

**SYNTHESIS AND STRUCTURAL STUDIES OF
HYBRID ORGANIC–INORGANIC NANOCOMPOSITES**

Kittipong Chainok

**A Thesis Submitted in Partial Fulfillment of the Requirements for
the Degree of Doctor of Philosophy in Chemistry**

Suranaree University of Technology

Academic Year 2008

การสังเคราะห์และศึกษาโครงสร้าง
ของสารประกอบนาโนรูปผลมอินทรีย์-อนินทรีย์

นายกิตติพงศ์ ไชยนอก

วิทยานิพนธ์นี้เป็นส่วนหนึ่งของการศึกษาตามหลักสูตรปริญญาวิทยาศาสตรดุษฎีบัณฑิต
สาขาวิชาเคมี
มหาวิทยาลัยเทคโนโลยีสุรนารี
ปีการศึกษา 2551

**SYNTHESIS AND STRUCTURAL STUDIES OF
HYBRID ORGANIC–INORGANIC NANOCOMPOSITES**

Suranaree University of Technology has approved this thesis submitted in partial fulfillment of the requirements for the Degree of Doctor of Philosophy.

Thesis Examining Committee



(Assoc. Prof. Dr. Malee Tangsathitkulchai)

Chairperson



(Assoc. Prof. Dr. Kenneth J. Haller)

Member (Thesis Advisor)



(Assoc. Prof. Dr. Adrian E. Flood)

Member



(Assoc. Prof. Dr. Albert Schulte)

Member

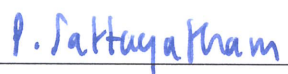


(Asst. Prof. Dr. Korakot Navakhun)

Member



(Assoc. Prof. Dr. Prapan Manyum)



(Prof. Dr. Pairote Sattayatham)

Vice Rector for Academic Affairs

Dean of Institute of Science

กิตติพงษ์ ไชยนอก : การสังเคราะห์และศึกษาโครงสร้างของสารประกอบนาโนรูปผสมอินทรีย์-อนินทรีย์ (SYNTHESIS AND STRUCTURAL STUDIES OF HYBRID ORGANIC-INORGANIC NANOCOMPOSITES) อาจารย์ที่ปรึกษา : รองศาสตราจารย์ ดร. เค็นเนท เจ. แสลดเลอร์, 407 หน้า.

วิทยานิพนธ์นี้ นำเสนอเกี่ยวกับการสังเคราะห์และศึกษาโครงสร้างผลึกเชิงเดี่ยวของสารประกอบนาโนรูปผสมอินทรีย์-อนินทรีย์ โดยส่วนที่หนึ่งของวิทยานิพนธ์กล่าวถึง การใช้หลักการวิศวกรรมผลึกและเคมีซูปราโมเลกูลาร์ เพื่อสังเคราะห์โครงสร้างใหม่ของวัสดุรูปผสมจำพวกสารประกอบโคออร์ดิเนชันโพลิเมอร์ที่มีหมู่ไซยาโน สารประกอบเชิงซ้อนไซยาโน และลิแกนด์ของออร์กาโนไซยาโนอยู่ในโครงสร้างผลึก พร้อมทั้งอธิบายความสัมพันธ์ระหว่างโครงสร้างและสมบัติแม่เหล็กของสารประกอบดังกล่าว

พบว่าเมื่อใช้สารประกอบเชิงซ้อนเตตระไซยาโนเฟอร์เรตของ $[Fe(L)(CN)_4]$ เป็นสารตั้งต้น โดยที่ L คือ ลิแกนด์ไบเดนเทต ได้สังเคราะห์สารประกอบจำพวกเฟอร์โรแมกเนติกที่มีโครงสร้างแบบสองมิติลักษณะคล้ายลูกฟูกของ $[Fe(2,2'-bipy)(CN)_4Mn] \cdot MeOH$ และโครงสร้างแบบท่อนาโนหนึ่งมิติของ $[Fe(2,2'-bipy)(CN)_4Mn(H_2O)_2]$ รวมทั้งสารประกอบจำพวกแอนไทเฟอร์โรแมกเนติกประกอบด้วยสารประกอบที่มีโครงสร้างคล้ายสี่เหลี่ยมจัตุรัสของ $[Fe(1,10-phen)(CN)_4Cu(tn)(H_2O)_2] \cdot 5H_2O$ และ $[Fe(2,2'-bipy)(CN)_4Cu(tn)] \cdot H_2O$ และสารประกอบที่มีโครงสร้างแบบหนึ่งมิติลักษณะคล้ายโซ่ฟันปลาของ $[Fe(2,2'-bipy)(CN)_4Ni(en)_2] \cdot solvent$ ขณะที่โมเลกุลเป็นเส้นตรงของสารประกอบเชิงซ้อนไดไซยาโนอาร์เจนเตท $[Ag(CN)_2]^-$ ถูกใช้เป็นบริดจิงลิแกนด์ที่ยาวกว่าเพื่อแทนที่หมู่ไซยาไนด์ของสารประกอบเชิงซ้อน $[Fe(L)(CN)_4]$ ข้างต้น ได้สังเคราะห์สารประกอบซูปราโมเลกูลาร์ใหม่ของ $[Ag(CN)_2]_2Mn(2,2'-bipy)_2 \cdot 2H_2O$ และ $[Ag(CN)_2Mn(2,2'-bipy)_2(H_2O)][Ag(CN)_2]$ ซึ่งแสดงสมบัติแม่เหล็กชนิดแอนไทเฟอร์โรแมกเนติก และสารประกอบโคออร์ดิเนชันโพลิเมอร์ใหม่ที่มีโครงสร้างแบบหนึ่งมิติคล้ายบันไดของ $[Ag_4(CN)_7\{Cd(2,2'-bipy)\}_2][ClO_4]$ และโครงสร้างแบบสามมิติของ $[Ag(CN)_2]_2Cd(2,2'-bipy)$ นอกจากนี้ยังพบว่าเมื่อใช้สารประกอบเชิงซ้อนทรงสี่เหลี่ยมจัตุรัสแบนราบของเตตระไซยาโนนิกเกิลเลต $[Ni(CN)_4]^{2-}$ เป็นลิแกนด์ ได้สังเคราะห์สารประกอบใหม่ที่มีโครงสร้างตาข่ายแบบสามมิติของ $[Ni(CN)_4Ni(en)] \cdot 2H_2O$ และ $[Ni(CN)_4Ni(tn)] \cdot H_2O \cdot MeOH$ ซึ่งทั้งสองสารประกอบนี้แสดงสมบัติแม่เหล็กชนิดเดียวกันคือ แอนไทเฟอร์โรแมกเนติก ขณะที่ลิแกนด์ออร์กาโนไดไนไตร์ของ ACCN และ AIBN ถูกใช้เพื่อเป็นบริดจิงลิแกนด์ในการศึกษาการเกิดโครงผลึกตาข่ายแบบสามมิติของสารประกอบเหล็ก (II) โคออร์ดิเนชันโพลิเมอร์ของ $[Fe(AIBN)_3][InCl_4]_2$ $[Fe(AIBN)_3][FeCl_4]_2$ $[Fe(ACCN)_3][InCl_4]_2$ และ $[Fe(ACCN)_3][FeCl_4]_2$ พบว่าโครงสร้างผลึกของสารประกอบดังกล่าว มีลักษณะคล้ายกับโครงผลึกตาข่ายแบบสามมิติ

ของแอลฟา-พอลิเอนิม โดยที่ผลึกของสารประกอบ AIBN อยู่ในระบบที่มีสมมาตรสูงของหมู่ปริภูมิ $R\bar{3}$ และแสดงการเปลี่ยนแปลงสมบัติทางแม่เหล็กเนื่องจากผลของอุณหภูมิ โดยเกิดการแทรนซิชันชนิดไม่สมบูรณ์แบบ “ครึ่ง” สปิน-ครอสส์โอเวอร์ ส่วนสารประกอบ ACCN พบว่าผลึกอยู่ในระบบสมมาตรที่ต่ำกว่าสารประกอบ AIBN ซึ่งอยู่ในหมู่ปริภูมิ $P\bar{1}$ และไม่แสดงการเกิดแทรนซิชันแบบสปิน-ครอสส์โอเวอร์ นอกจากนี้ยังได้ศึกษาและอธิบายการเกิดโครงสร้างซูปราโมเลกูลาร์ใหม่ของสารประกอบโคออร์ดิเนชันโพลิเมอร์ซิลเวอร์ (I) ไอออนและลิแกนด์ bmtz H_2bmtz และ bptz อีกด้วย

ส่วนที่สองของวิทยานิพนธ์นี้ กล่าวถึงการสังเคราะห์โครงสร้างผลึกใหม่ของวัสดุรูปผสมโลหะออกไซด์เพื่อเปรียบเทียบกับวัสดุจำพวกซีโอไลต์ สารประกอบใหม่ทั้งห้าของโลหะแทรนซิชันเวนาเดียมซึ่งถูกตัดแปลงด้วยสารอินทรีย์ สามารถสังเคราะห์ได้ด้วยวิธีไฮโดร/โซลโวเทอร์มัลโดยสารประกอบที่มีสารอินทรีย์ทำหน้าที่เหมือนเป็นเทมเพลตในโครงสร้างผลึก พบในโครงสร้างแบบสามมิติของ $[ImH][Mn_3(OH)_2(V_4O_{13})]$ ขณะที่สารประกอบของ $[M(Im)_4V_2O_6]$ เมื่อ M คือ แมงกานีส โคบอลต์ หรือ นิกเกิล และสารประกอบของ $[Mn(Im)_3(DMSO)V_2O_6]$ มีโครงสร้างแบบชั้นสองมิติ และพบว่าสารประกอบ $[M(Im)_4V_2O_6]$ เกิดการเปลี่ยนวิถึภาคแบบออร์เดอร์-ดีสออร์เดอร์ของหมู่ปริภูมิเนื่องด้วยผลของอุณหภูมิ โดยเกิดขึ้นระหว่างหมู่ปริภูมิที่ดีสออร์เดอร์ของ $P4_2/n$ ณ อุณหภูมิ 295 เคลวิน และหมู่ปริภูมิที่ออร์เดอร์ของ $I4_1/a$ (แมงกานีส และ โคบอลต์) หรือ $P2/n$ (นิกเกิล) ณ อุณหภูมิ 100 เคลวิน สำหรับสารประกอบ $[Mn(Im)_3(DMSO)V_2O_6]$ การถูกแทนที่ ณ ตำแหน่งอ็อกทอเวอรัลหนึ่งตำแหน่งของหมู่อิมิดาโซลบนรูปทรงออกตะฮีดรัลที่บิดเบี้ยวของแมงกานีส(II) ด้วยโมเลกุลของไดเมทิลซัลโฟไซด์ ทำให้โครงสร้างผลึกเสียสมมาตร ส่งผลให้เกิดการเปลี่ยนหมู่ปริภูมิจาก $P4_2/n$ ในสารประกอบ $[M(Im)_4V_2O_6]$ ไปสู่หมู่ปริภูมิที่มีสมมาตรต่ำกว่าของ $P2_1/n$ ณ อุณหภูมิ 295 เคลวิน อย่างไรก็ตามโครงสร้างร่างตาข่ายออกไซด์ของโลหะในสารประกอบ $[Mn(Im)_3(DMSO)V_2O_6]$ ยังคงมีลักษณะคล้ายๆ กับที่พบในสารประกอบของ $[M(Im)_4V_2O_6]$

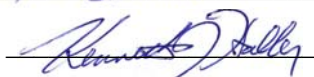
สาขาวิชาเคมี

ปีการศึกษา 2551

ลายมือชื่อนักศึกษา



ลายมือชื่ออาจารย์ที่ปรึกษา



KITTIPONG CHAINOK : SYNTHESIS AND STRUCTURAL STUDIES
OF HYBRID ORGANIC–INORGANIC NANOCOMPOSITES. THESIS
ADVISOR : ASSOC. PROF. KENNETH J. HALLER, Ph.D. 407 PP.

COORDINATION POLYMERS/CRYSTAL ENGINEERING/HYBRID ORGANIC–
INORGANIC/MAGNETIC PROPERTIES/SUPRAMOLECULAR/VANADATES

This thesis focuses on the single crystal growth and solid state structural studies of new hybrid organic-inorganic nanocomposites. The first part of this thesis deals with a rational synthetic strategy using the principles of crystal engineering and supramolecular chemistry for the construction of new hybrid coordination polymers containing cyano, metallocyano and organocyano bridging groups, and correlations between their structural and magnetic properties are described.

The use of tetracyanoferrate complexes of the type $[\text{Fe}(\text{L})(\text{CN})_4]$ as building blocks, where L is a bidentate ligand, two new ferromagnetic compounds with either a 2-D corrugated sheet structure, $[\text{Fe}(2,2'\text{-bipy})(\text{CN})_4\text{Mn}]\cdot\text{MeOH}$ or a 1-D nanotube-like structure, $[\text{Fe}(2,2'\text{-bipy})(\text{CN})_4\text{Mn}(\text{H}_2\text{O})_2]$, three antiferromagnetic compounds containing molecular square structures, $[\text{Fe}(1,10\text{-phen})(\text{CN})_4\text{Cu}(\text{tn})(\text{H}_2\text{O})_2]\cdot 5\text{H}_2\text{O}$ and $[\text{Fe}(2,2'\text{-bipy})(\text{CN})_4\text{Cu}(\text{tn})]\cdot\text{H}_2\text{O}$, and 1-D zigzag chains $[\text{Fe}(2,2'\text{-bipy})(\text{CN})_4\text{Ni}(\text{en})_2]\cdot\text{solvent}$ were synthesized. The linear $[\text{Ag}(\text{CN})_2]^-$ was used as a longer bridging ligand to replace the CN groups of the $[\text{M}(\text{L})(\text{CN})_4]$ building block. Two new supramolecular structures, $[\{\text{Ag}(\text{CN})_2\}_2\text{Mn}(2,2'\text{-bipy})_2]\cdot 2\text{H}_2\text{O}$ and $[\text{Ag}(\text{CN})_2\text{Mn}(2,2'\text{-bipy})_2(\text{H}_2\text{O})][\text{Ag}(\text{CN})_2]$ with display a weak antiferromagnetic behavior, and two new coordination polymers 1-D ladder-chains $[\text{Ag}_4(\text{CN})_7\{\text{Cd}(2,2'\text{-bipy})\}_2][\text{ClO}_4]$ and triple interpenetrated 3-D $[\{\text{Ag}(\text{CN})_2\}_2\text{Cd}(2,2'\text{-bipy})]$ were synthesized. Two new antiferromagnetic compounds composed of 3-D cyanide-bridged homometallic networks of $[\text{Ni}(\text{CN})_4\text{Ni}(\text{en})]\cdot 2\text{H}_2\text{O}$ and $[\text{Ni}(\text{CN})_4\text{Ni}(\text{tn})]\cdot\text{H}_2\text{O}\cdot\text{MeOH}$ were synthe-

sized by using the square planar ligand complex $[\text{Ni}(\text{CN})_4]^{2-}$.

The 2-connecting organodinitrile ligands ACCN and AIBN were used as bridging ligands for investigations of self-assembly processes in the construction of novel Fe(II) coordination polymer compounds: $[\text{Fe}(\text{AIBN})_3][\text{InCl}_4]_2$, $[\text{Fe}(\text{AIBN})_3][\text{FeCl}_4]_2$, $[\text{Fe}(\text{ACCN})_3][\text{InCl}_4]_2$, and $[\text{Fe}(\text{ACCN})_3][\text{FeCl}_4]_2$. The crystal structures consisted of 3-D α -Po like nets. The AIBN compounds crystallize in a highly symmetrical $R\bar{3}$ phase, and are display an interesting incomplete “half” spin-crossover (SCO). The ACCN compounds crystallize in a lower symmetrical $P\bar{1}$ phase, and no SCO transitions are observed. In addition, novel supramolecular architectures of Ag(I) coordination polymers formed with the multimodal ligands of bmtz, H_2bmtz , and bptz are also described.

The second aim of this thesis is to explore new metal oxide solid materials as analogues of zeolites. Five new organically modified transition metal vanadate compounds were hydro/solvothermally synthesized. The organic “templating” effect is well illustrated by the 3-D solid $[\text{ImH}][\text{Mn}_3(\text{OH})_2(\text{V}_4\text{O}_{13})]$. Isostructural compounds of formula $[\text{M}(\text{Im})_4\text{V}_2\text{O}_6]$, where M is Mn, Co, Ni, and $[\text{Mn}(\text{Im})_3(\text{DMSO})\text{V}_2\text{O}_6]$ have 2-D layer structure. Isostructural species $[\text{M}(\text{Im})_4\text{V}_2\text{O}_6]$ are display an interesting order-disorder crystallographic phase transition between the $P4_2/n$ at 295 K and $I4_1/a$ (Mn and Co) or $P2/n$ (Ni) space groups at 100 K. For compound $[\text{Mn}(\text{Im})_3(\text{DMSO})\text{V}_2\text{O}_6]$, the replacement of one equatorial imidazole on Mn(II) with a covalently coordinated DMSO results in a loss of symmetry from the parent $P4_2/n$ structure in isostructural compounds, lowering the space group to $P2_1/n$ at 295 K, but the topology of bimetallic oxide framework is otherwise similar.

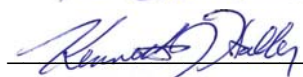
School of Chemistry

Academic Year 2008

Student's Signature



Advisor's Signature



ACKNOWLEDGEMENTS

Although I am indeed the sole author of this thesis, I am by no means the sole contributor. So many people have contributed to my thesis, to my education and to my life, and it is now my great pleasure to take this opportunity to thank them.

Firstly, I would like to gratefully thank my principal advisor, Assoc. Prof. Dr. Kenneth J. Haller for the unique opportunity to accomplish both M.Sc. and Ph.D degrees with him, his patience and knowledge whilst allowing me the room to work in my own way, and for offering several precious opportunities to attend and to make presentations in national and international academic conferences. I appreciate his manner of scientific thinking and his assistance in writing reports (*i.e.* grant proposals and scholarship applications).

Secondly, very special thanks are due to my co-supervisors at Monash University, Prof. Dr. Keith S. Murray and Assoc. Prof. Dr. Stuart R. Batten. I don't believe there are enough appropriate words to adequately thank them for the great support they have given to me. I am impressed by their scholarly performance, modesty and prudence, kindness and generosity, generous financial support, encouragement, discussion, sound advice, good teaching, good company, lots of good ideas, intensive proof reading of this thesis and friendship. These have been invaluable on both an academic and a personal level. I have learnt a lot from them. I will forever be proud for having worked under their guidance.

I am also very grateful to my co-supervisor at Research School of Chemistry, The Australian National University, Prof. Dr. A. David Rae, for his encouragement,

sound advice and good teaching me some nonroutine crystallography and proof reading many drafts of manuscript. Thanks to his least squares refinement program, RAELS. To Annas Rae (his wife), thanks for her help in taking care of me, when I was in Canberra and Sydney. I would like to thank Prof. Dr. Ray L. Withers, Dr. Lasse Norén and Dr. Yun Liu for organizing the solid state group at the Research School of Chemistry. I also thank Dr. Binh Nguyen for friendship and support.

I extend my warm and sincere thanks to Prof. Dr. Ian D. Williams for his continuous support of my work on vanadate project, encouragement and constant guidance during the course of my research at Hong Kong University of Science and Technology.

I would like to thank Dr. Suzanne Neville and Dr. Craig Forsyth (Monash University), Dr. Anthony Willis (ANU), and Dr. Herman Sung (HKUST), for help in collecting the data of single crystal X-ray, good sound advice and good teaching. I have learnt a lot from them.

To Dr. Boujemaa Moubaraki, thank you for your help with the SQUID magnetic measurements, useful discussion, good sound advice and good teaching, and friendship throughout the duration of the project in Monash University. I would also like to thank Assoc. Prof. Dr. John D. Cashion (Physics, Monash University) for help with Mössbauer spectra measurement, sound advice and good teaching.

I am very grateful to the Australian Government Department of Education, Science and Training (DEST) for providing financial support for undertaking research at Monash University and The Australian National University under the 2006 Endeavour Asia Award and the 2007 Endeavour Research Fellowship.

I would like to thank the International Union of Crystallography for a

Bursary Award to support my attendance at XX Congress (IUCr2005) in Florence, Italy. I would also like to thank the Society of Crystallographers in Australia and New Zealand for financial support of my attendance at SCANZ 2007 Conference-Crystal XXV, Hunter Valley, New South Wales, Australia.

I would like to thank the Liverpool Materials and Chemistry Group Portfolio Partnership for financial support to attend the summer school and workshops on Porous Materials, University California, Santa Barbara, USA. Also, thanks to Suranaree University of Technology for financial support of my attendance at the 31st and 34th STT conferences and the 6th NSGR, Thailand.

My best regards I sincerely give to who were my Australian Government of DEST advisors during the period of undertaking research in Australia, Ms. Cynthia Grant (Endeavour Project Manager), Ms. Mary Dykes (Endeavour Case Manager), Mr. Denise Miles (Endeavour Project Co-ordinator), for their suggestions, encouragement and friendship.

I am profoundly grateful to the official referees of this thesis, Assoc. Prof. Dr. Malee Tangsathitkulchai (chairperson), Assoc. Prof. Dr. Adrian E. Flood, Assoc. Prof. Dr. Albert Schulte and Asst. Prof. Dr. Korakot Nawakhun, for their constructive criticism, valuable suggestions and sparing their precious time for examining my thesis.

To former and current Haller group members: Dr. Auphatham Phothikanith, Dr. Preeyaporn Pookrod, Dr. Weenawan Somphon, Angkana Kiatpichitpong, Angkana Chatkon, Winya Dungkaew, Nongnaphat Khosavithikul, Samroeng Krachodnok, Saiphon Chanpaka, Ratchadaporn Puntharod, Kasada Sala, Pushpakumara Herath, Orrasa In-noi, Oratai Saisa-ard, Jittima Thisuwan, and Saifon

Kohnhorst, I would like to thank for their constant encouragement and helping me get through the difficult times.

Many thanks to former and current Murray and Batten group members: Dr. Boujemaa Moubaraki, Dr. Suzanne Neville, Dr. Jinzhen Lu, Dr. David Turner, Dr. Stuart Langley, Dr. Martin Duriska, Caspar Schneider, Tamsyn Ross, Ponco Prananto, and Anthony Chesman, for the very nice co-operation. It has always been a pleasure time to do experiments and discuss work together with them.

To former and current Williams members, especially to Dr. Fanny Shek, Dr. Alex Au-Yeung, and Pokka Pang, for their help and suggestions with the laboratory work in hydrothermal synthesis and friendship.

To Anchalee Suttikomala, thank you very much for support and time in sharing our faith. Also, to my dear brother, Winya Dungkaew and his girlfriend, Kamolwan Wichai, thanks for their constant encouragement and support during my Ph.D. candidature, especially at difficult moments.

I am indebted to my many student colleagues for providing a stimulating and fun environment in which to learn and grow. I wish to thank my best friend as an undergraduate (especially to Supakit Satkeaw) and my best friend as a graduate student (especially to Suparat Waranon, Sirinuch Loiha, Pongthanawat Khemtong, Surachai Artkla, Sittichai Kulawong, and Pairin Suwannasri) for all the emotional support, camaraderie, entertainment and caring they provided.

Last, but by no means least, I am deeply indebted to my parents, my brothers, and sisters for their support, patience and love, and I thank everyone for good chemistry and bad chemistry; you cannot create and develop without both.

Kittipong Chainok

CONTENTS

	Page
ABSTRACT IN THAI	I
ABSTRACT IN ENGLISH	III
ACKNOWLEDGEMENTS	V
CONTENTS	IX
LIST OF TABLES	XVII
LIST OF FIGURES	XXI
LIST OF ABBREVIATIONS	XXXI
 CHAPTER	
I A GENERAL INTRODUCTION	1
1.1 Supramolecular Chemistry	3
1.1.1 Supramolecular Host-Guest Chemistry	4
1.1.2 Self-Assembly	5
1.1.1 Supramolecular Interactions	10
1.2 Crystal Engineering of Coordination Polymers	26
1.2.1 Topology	26
1.2.2 Synthetic Strategies	27
1.3 Molecular-Based Magnetic Materials	32
1.3.1 Classification of Magnetic Materials	37
1.3.2 Spin-Crossover (SCO) Compounds	43
1.3.3 Cyanometallate Building Blocks	
In Molecular Magnetic Materials	51

CONTENTS (Continued)

	Page
1.3.4 [M(L)(CN) ₄] Building Blocks	53
1.3.5 [M ^{II} (CN) ₄] ²⁻ Building Blocks	59
1.3.6 [M ^I (CN) ₂] ⁻ Building Blocks in Framework Systems	60
1.4 Metal Oxide Framework Materials: Vanadates	63
1.4.1 Hydrothermal Synthesis of Hybrid Organic–Inorganic Framework Materials	64
1.4.2 Organovanadium Framework Materials of Relevance to the Present Thesis	65
1.5 Functional Applications of Hybrid Materials	68
1.6 The Present Study	70
1.7 References	73
 II SUPRAMOLECULAR	
ARCHITECTURE OF SILVER(I) COORDINATION	
POLYMERS CONTAINING MULTIMODAL LIGANDS	92
2.1 Introduction	92
2.2 Experimental Section	94
2.1.1 Materials and Physical Measurements	94
2.1.2 Syntheses	94
2.1.3 X-Ray Crystallographic Study	97
2.3 Results and Discussion	104
2.3.1 1-D Ribbons Structure of [Ag ₂ (bmtz)(ClO ₄)]ClO ₄ (2a)	104
2.3.2 1-D Ribbons Structure of [Ag(bmtz)]ClO ₄ ·MeCN (2b)	111

CONTENTS (Continued)

	Page
2.3.3 1-D Chain Structure of $[\{\text{Ag}(\text{tcm})\}_2(\text{H}_2\text{bmtz})(\text{MeCN})]$ (2c)	116
2.3.4 2-D Sheets Structure of $[\{\text{Ag}(\text{tcm})\}_2\text{bmtz}]$ (2d)	119
2.3.5 1-D Chain Structure of $[\text{Ag}(\text{bptz})(\text{NO}_3)]$ (2e)	123
2.3.6 Structural Description of $[\text{H}_2\text{bptz}](\text{NO}_3)_2$ (2f)	129
2.4 Conclusions	132
2.5 References	133
 III SYNTHESIS, STRUCTURES,	
AND MAGNETIC PROPERTIES OF	
NEW CYANIDE-BRIDGED BIMETALLIC COMPOUNDS	136
3.1 Introduction	136
3.2 Experimental Section	139
3.2.1 Materials and Physical Measurements	139
3.2.2 Syntheses	140
3.2.3 X-Ray Crystallographic Study	144
3.3 Results and Discussion	153
3.3.1 Synthesis and ATR-FTIR Spectra	153
3.3.2 Structural Description of $[\{\text{Fe}(2,2'\text{-bipy})(\text{CN})_4\}\text{Mn}]\cdot\text{MeOH}$ (3a)	157
3.3.3 Structural Description of $[\text{Fe}(2,2'\text{-bipy})(\text{CN})_4\text{Mn}(\text{H}_2\text{O})_2]$ (3b)	164
3.3.4 Structural Description of $[\text{Fe}(1,10\text{-phen})(\text{CN})_4\text{Cu}(\text{tn})(\text{H}_2\text{O})_2]\cdot 5\text{H}_2\text{O}$ (3c)	169

CONTENTS (Continued)

	Page
3.3.5 Structural Description of	
[Fe(2,2'-bipy)(CN) ₄ Cu(tn)]·H ₂ O (3d)	177
3.3.6 Structural Description of	
[Fe(2,2'-bipy)(CN) ₄ Ni(en) ₂]·Solvent (3e)	178
3.3.7 Magnetic Properties of	
[Fe(2,2'-bipy)(CN) ₄ Mn]·MeOH (3a)	183
3.3.8 Magnetic Properties of	
[Fe(2,2'-bipy)(CN) ₄ Mn(H ₂ O) ₂] (3b)	186
3.3.9 Magnetic Properties of the Molecular Squares	
[Fe(1,10-phen)(CN) ₄ Cu(tn)(H ₂ O) ₂]·5H ₂ O (3c)	
[Fe(2,2'-bipy)(CN) ₄ Cu(tn)]·H ₂ O (3d)	189
3.3.10 Magnetic Properties of	
[Fe(2,2'-bipy)(CN) ₄ Ni(en) ₂]·Solvent (3e)	191
3.4 Conclusions and Future Prospects	192
3.5 References	195
IV SUPRAMOLECULAR	
ARCHITECTURE AND COORDINATION	
POLYMERS WITH [Ag(CN)₂]⁻ AS BUILDING BLOCK	202
4.1 Introduction	202
4.2 Experimental Section	205
4.2.1 Materials and Physical Measurements	205
4.2.2 Syntheses	205

CONTENTS (Continued)

	Page
4.2.3 X-Ray Crystallographic Study	207
4.3 Results and Discussion	215
4.3.1 Synthesis and ATR-FTIR Spectra	215
4.3.2 Structural Description of <div style="padding-left: 80px;">$[\{\text{Ag}(\text{CN})_2\}_2\text{Mn}(2,2'\text{-bipy})_2]\cdot\text{H}_2\text{O}$ (4a)</div>	216
4.3.3 Structural Description of <div style="padding-left: 80px;">$[\text{Ag}(\text{CN})_2\text{Mn}(2,2'\text{-bipy})_2(\text{H}_2\text{O})]\text{Ag}(\text{CN})_2$ (4b)</div>	222
4.3.4 Structural Description of <div style="padding-left: 80px;">$[\text{Ag}_4(\text{CN})_7\{\text{Cd}(2,2'\text{-bipy})\}_2]\text{ClO}_4$ (4c)</div>	226
4.3.5 Structural Description of <div style="padding-left: 80px;">$[\{\text{Ag}(\text{CN})_2\}_2\text{Cd}(2,2'\text{-bipy})]$ (4d)</div>	231
4.3.6 Magnetic Properties of <div style="padding-left: 80px;">$[\text{Ag}(\text{CN})_2\text{Mn}(2,2'\text{-bipy})_2(\text{H}_2\text{O})]\text{Ag}(\text{CN})_2$ (4b)</div>	237
4.4 Conclusions	237
4.5 References	239
V SYNTHESIS, STRUCTURE, AND MAGNETIC PROPERTIES OF 3-D CYANIDE-BRIDGED HOMOMETALLIC COORDINATION POLYMERS	243
5.1 Introduction	243
5.2 Experimental Section	246
5.2.1 Materials and Physical Measurements	246
5.2.2 Syntheses	247

CONTENTS (Continued)

	Page
5.2.3 X-Ray Crystallographic Study	248
5.3 Results and Discussion	252
5.3.1 Syntheses	252
5.3.2 Structural Description of [Ni(CN) ₄ Ni(en)]·2H ₂ O (5a)	253
5.3.3 Structural Description of [Ni(CN) ₄ Ni(tn)]·H ₂ O·MeOH (5b)	259
5.3.4 Magnetic Properties	265
5.3.5 ATR-FTIR Spectra	267
5.3.6 Differential Thermal Analysis and Thermal Gravimetric Analysis	268
5.4 Conclusions	272
5.5 References	273
VI SYNTHESIS, STRUCTURES, AND SPIN-CROSSOVER PROPERTIES OF INFINITE 3-D FRAMEWORK IRON(II) CONTAINING ORGANODINITRILE BRIDGING LIGANDS	277
6.1 Introduction	277
6.2 Experimental Section	281
6.2.1 Materials and Physical Measurements	281
6.2.2 Syntheses	282
6.2.3 X-Ray Crystallographic Study	285

CONTENTS (Continued)

	Page
6.3 Results and Discussion	292
6.3.1 Syntheses and Characterizations	292
6.3.2 Structural Description of [Fe(AIBN) ₃][MCl ₄] ₂ , M = In (6a), Fe (6b)	294
6.3.3 Structural Description of [Fe(AIBN)H ₂ O][FeCl ₄] ₂ (6c)	304
6.3.4 Structural Description of [Fe(ACCN) ₃][MCl ₄] ₂ , M = In (6c), Fe (6d)	308
6.3.5 Magnetism	311
6.3.6 Mössbauer Spectroscopy	315
6.4 Conclusions	320
6.5 References	323
 VII HYDRO/SOLVOTHERMAL	
SYNTHESIS OF HYBRID ORGANIC-	
INORGANIC VANADIUM OXIDES COMPOUNDS	
327	
7.1 Introduction	327
7.2 Experimental Section	329
7.2.1 Materials and Physical Measurements	329
7.2.2 Syntheses	330
7.2.3 X-Ray Crystallographic Study	333
7.3 Results and Discussion	342
7.3.1 Syntheses and Characterizations	342

CONTENTS (Continued)

	Page
7.3.2 Structural Description of	
$[\text{Mn}_3(\text{OH})_2(\text{V}_4\text{O}_{13})][\text{ImH}]$ (7a)	344
7.3.3 Investigation of the Structure and Phase	
Transition of $[\text{M}(\text{Im})_4\text{V}_2\text{O}_6]_\infty$, $M = \text{Mn}$ (7b), Co (7c), Ni (7d)	349
7.3.4 Structural Description of	
$[\text{Mn}(\text{DMSO})(\text{Im})_3\text{V}_2\text{O}_6]$ (7e)	370
7.4 Conclusions	374
7.5 References	375
VIII CONCLUSIONS	278
APPENDICES	382
APPENDIX A CRYSTALLOGRAPHIC	
INFORMATION FILES (CD-ROM)	383
APPENDIX B SUPPLEMENTARY MATERIALS	385
APPENDIX C SUBMITTED ABSTRACTS	
AND PRESENTATIONS	402
CURRICULUM VITAE	407

LIST OF TABLES

Tables	Page
1.1 The van der Waals Radii used for observing hydrogen bonds	14
1.2 Classification and properties of hydrogen bonds	19
1.3 Some selected examples of possible prototypes	29
1.4 Comparison of calculated spin-only magnetic moments with experimental data for some octahedral complexes	37
1.5 Summary of different types of magnetic behavior	42
1.6 Experimental methods for monitoring the SCO in Fe(II) compounds	46
1.7 Selected examples and applications of inorganic oxides	64
2.1 Summary of crystallographic data for the compounds 2a–2f	99
2.2 Selected bond lengths and angles for 2a	100
2.3 Selected bond lengths and angles for 2b	101
2.4 Selected bond lengths and angles for 2c and 2d	102
2.5 Selected bond lengths and angles for 2e	103
2.6 Hydrogen bond geometries for 2a and 2b	109
2.7 Geometrical parameters of π – π interactions for 2a and 2b	110
2.8 Anion– π interactions for 2a and 2b	110
2.9 Intra- and intermolecular interactions for 2c and 2d	119
2.10 Geometrical parameters of π – π interactions for 2c	119
2.11 Hydrogen bond geometries for 2e and 2f	127
2.12 Geometrical parameters of π – π interactions for 2e and 2f	128
2.13 Anion– π interactions for 2e and 2f	129

LIST OF TABLES (Continued)

Tables	Page
3.1 Summary of crystallographic data for 3a–3c and 3e	147
3.2 Selected bond lengths and angles for 3a	148
3.3 Selected bond lengths and angles for 3b	150
3.4 Selected bond lengths and angles for 3c	151
3.5 Selected bond lengths and angles for 3e	152
3.6 Vibrational frequencies of the cyanide ligand in the present study	156
3.7 Hydrogen bond geometries for 3a	163
3.8 Geometrical parameters of π – π interactions in 3a	163
3.9 Hydrogen bond geometries for 3c	176
3.10 Geometrical parameters of π – π interactions in 3c	177
4.1 Summary of crystallographic data for the compounds 4a–4d	209
4.2 Selected bond lengths and angles for 4a and 4b	210
4.3 Selected bond lengths and angles for 4c	211
4.4 Selected bond lengths and angles for 4d	212
4.5 Hydrogen bond geometries for 4a and 4b	213
4.6 Geometrical parameters of π – π interactions in 4a–4d	214
5.1 Summary of crystallographic data for the compounds 5a and 5b	250
5.2 Selected bond lengths and angles for 5a and 5b	251
5.3 Hydrogen bond geometries for 5a and 5b	252
5.4 Vibrational frequencies for compounds 5a and 5b	269
6.1 Summary of crystallographic data for the compounds 6a–6b	287

LIST OF TABLES (Continued)

Tables	Page
6.2 Summary of crystallographic data for the compounds 6c–6e	288
6.3 Selected bond lengths and angles for [Fe(AIBN) ₃] ²⁺ cations in 6a and 6b at selected temperatures	289
6.4 Selected bond lengths and angles for [Fe(AIBN)(H ₂ O)] ²⁺ cations of [Fe(AIBN)(H ₂ O)][FeCl ₄] ₂ , 6c at 123 K	290
6.5 Hydrogen bond geometries for [Fe(AIBN)(H ₂ O)][FeCl ₄], 6c	290
6.6 Selected bond lengths and angles for [Fe(ACCN) ₃] ²⁺ cations in 6d and 6e at selected temperatures	291
6.7 Mössbauer data for [Fe(AIBN) ₃][MCl ₄] ₂ , M = In (6a), Fe (6b)	319
7.1 Summary of crystallographic data for the compounds 7a and 7e	337
7.2 Summary of crystallographic data for the compound 7b at selected temperatures	338
7.3 Summary of crystallographic data for the compound 7c at selected temperatures	339
7.4 Summary of crystallographic data for the compound 7d at 100 and 295 K	340
7.5 Refinement statistics for the compounds 7b–7d at selected temperatures	341
7.6 Selected bond lengths for 7a	346
7.7 Largest principal libration values for the imidazoles of the low temperature phase	363

LIST OF TABLES (Continued)

Tables	Page
7.8 Largest principal libration values for the imidazoles of the high temperature phase	364
7.9 Departure from equivalence of pseudo symmetry related imidazoles for the low temperature phase	364
7.10 Departure from equivalence of pseudo symmetry related imidazoles for the high temperature phase	364
7.11 Selected bond lengths of 7b and 7c at 100 K	367
7.12 Selected bond lengths of 7d at 100 K	368
7.13 Hydrogen bond geometries for 7b and 7c at 100 and 295 K	369
7.14 Hydrogen bond geometries for 7d at 100 and 295 K	370
7.14 Hydrogen bond geometries for 7e	373

LIST OF FIGURES

Figures	Page
1.1 Occurrence of the term hybrids organic-inorganic in titles of papers published between 1995 and 2007	2
1.2 Self-assembly of the circular helicate $[(Fe_5L_5)Cl]^{9+}$ from five tris-bpy ligand	4
1.3 Guest inclusion/removal in $[Fe_2(azpy)_4(NCS)_4] \cdot (guest)$	6
1.4 Self-assembly of nanosize coordination cages	8
1.5 (a) Ball-wires-sticks and (b) space-filling representations of the hexameric coordination capsule	9
1.6 View of the hexagonal packing of tubules composed of <i>p</i> -sulfonatocalix-[4]arene with intercalated pyridine <i>N</i> -oxide	10
1.7 (a) Ball-stick and (b) space filling model showing ion-dipole interactions in the cesium complex of [18]crown-6	12
1.8 Hydrogen bond geometry and partial charges	14
1.9 Structures of common hydrogen bond types	15
1.10 View of honeycomb hydrogen bonds sheets in $[Ni(Hbim)_3]^-$ building block	16
1.11 Schematic representation of (a) attractive and (b) repulsion of secondary hydrogen bonds interactions	17
1.12 (a) Ball-stick and (b) space filling representations of the enforced self-assembly of molecules of pyrido[4,3-dpyrimidine] into a hexamer	18

LIST OF FIGURES (Continued)

Figures	Page
1.13 Cation– π interactions between benzene and a potassium cation	20
1.14 (a) Ball-stick and (b) space-filling representations, showing anion– π interactions in $[\{\text{Ni}_5(\text{bptz})_5\text{C}(\text{CH}_3\text{CN})_{10}\}\text{SbF}_6](\text{SbF}_6)_9$	21
1.15 Schematic representations of aromatic–aromatic interactions	22
1.16 π – π interactions between <i>sym</i> -triphenethynyl- benzene and <i>sym</i> -tris(perfluorophenethynyl)benzene	24
1.17 Some of the simplest infinite 3-D nets	28
1.18 Coordination polymers compounds formed by the 4,4'-bipy bridging ligand with difference metal centers	31
1.19 2-D representation of spin	40
1.20 Schematic illustration of the magnetization, M , as a function of applied magnetic field, H	41
1.21 Schematic illustration of an Fe(II) SCO complex	44
1.22 Various types of SCO transition	45
1.23 Typical temperature evolution of (a) Mössbauer, (b) infrared, and (c) electronic d–d visible spectra for a SCO system of Fe(II)	47
1.24 (a) Coordination environment of Fe(II) ions and (b) a schematic presentation of the 3-D α -Po like network in $[\{\text{Fe}(\text{pbtz})_3\}(\text{ClO}_4)_2]\cdot 2\text{EtOH}$	49
1.25 A schematic presentation of the 3-D cubic network in Prussian blue	51

LIST OF FIGURES (Continued)

Figures	Page
1.26 Perspective view of a fragment of the 4,2-ribbon like chain in [$\{\text{Fe}(2,2'\text{-bipy})(\text{CN})_4\}_2\{\text{M}(\text{H}_2\text{O})_2\}] \cdot 4\text{H}_2\text{O}$, M = Co and Cu	54
1.27 (a) Side and (b) top views of a CNT-like coordination hexagonal tube structure in [$\text{Ru}(2,2'\text{-bipy})(\text{CN})_4\text{Mn}(\text{H}_2\text{O})_2$]	57
1.28 Perspective view of the structure of cyanide-bridged bimetallic, 3-D Hofmann-like networks in [$\text{Pt}(\text{CN})_4\text{Fe}(\text{pyz})$]·2H ₂ O	59
1.29 (a) A fragment in [$\text{Fe}(3\text{-I-py})_2\{\text{Au}(\text{CN})_2\}_2$]·0.5(3-I-py) (b) packing with emphasizing the aurophilic interactions	61
1.30 Metamorphosis of the vanadium coordination polyhedra	65
1.31 Polyhedral and ball-stick representations in [$\text{H}_2\text{en}][\text{Mn}_3(\text{V}_2\text{O}_7)_2(\text{H}_2\text{O})_2$]	67
2.1 (a) Thermal ellipsoid plot of a fragment and (b) coordination environments of the metal centres of 2a	105
2.2 (a) Packing diagram for 2a viewed down showing anion··· π and Ag··· π interactions and (b) the shortest contacts between perchlorate anions and the pyrimidine or tetrazine rings and Ag ions	106
2.3 Space-filling representations for 2a project Slightly onto <i>ab</i> plane showing <i>ef</i> C–H··· π interactions	108
2.4 Packing diagram for 2a showing weak π ··· π interactions	109

LIST OF FIGURES (Continued)

Figures	Page
2.5 Thermal ellipsoid plot of a fragment of 2b	111
2.6 1-D chain propagating along the <i>a</i> axis in 2b	112
2.7 The shortest contacts in 2b	113
2.8 Packing in 2b along the <i>a</i> axis showing the π - π stacking between pyrimidine rings	114
2.9 Perspective view of 2b along the <i>a</i> axis	115
2.10 Thermal ellipsoid plot of a fragment of 2c	116
2.11 1-D chain propagating along the <i>c</i> axis in 2c	118
2.12 Packing diagram in 2c view along the <i>b</i> axis showing the π - π interactions	118
2.13 Thermal ellipsoid plot of a fragment of 2d	120
2.14 View crystal structures of 2d along the (a) <i>c</i> and (b) <i>b</i> axis	122
2.15 Thermal ellipsoid plot of a fragment of 2e	123
2.16 Unit cell packing diagram showing different orientation of 1-D chains in 2e	125
2.17 View of π ·· π interactions in 2e	126
2.18 View of anion·· π interactions in 2e	126
2.19 The structure of 2f	130
2.20 (a) Wires-sticks and (b) space-filling representations showing 2-D sheet in 2f linked by N-H··O hydrogen bonds	131
3.1 Thermal ellipsoid plot of a fragment in 3a	158

LIST OF FIGURES (Continued)

Figures	Page
3.2 A projection along the <i>a</i> axis showing the 2-D corrugated sheets in 3a	160
3.3 Schematic view of the 2-D corrugated sheets of the bimetallic skeleton in 3a	161
3.4 Packing diagram of 3a viewed along along the <i>c</i> axis the <i>c</i> axis showing $\pi \cdots \pi$ stacking between the 2-D corrugated sheets	162
3.5 Ball and stick representation of the asymmetric unit in 3b	164
3.6 Views of (a) side, (b) top views of 1-D tubular structure, (c) Fe ₃ Mn ₃ hexanuclear arrangement, and (d) schematic view of the tube topology in 3b	166
3.7 Views of (a) packing of the three and (b) single 1-D tubes in 3b	167
3.8 (a) Stick and (b) space filling representations representation of seven 1-D tubes in top view of 3b	168
3.9 Ball and stick representation of the asymmetric unit in 3c	170
3.10 Views of 1-D tube like structure in 3c	173
3.11 View of 1-D chain linked <i>via</i> O–H \cdots N and O–H \cdots O hydrogen bonds in 3c along the <i>a</i> axis	174
3.12 2-D sheet generated through a combination of self- complementary O–H \cdots O hydrogen bonds and π – π stacking	175
3.13 Ball and stick representation showing the atom connectivity and coordination environment in 3d	178

LIST OF FIGURES (Continued)

Figures	Page
3.14 Thermal ellipsoid plot at the 50% probability level of 3e containing coordination environments of metals centre shown	179
3.15 View of the 1-D zigzag chains in 3e running parallel to the <i>b</i> axis	181
3.16 Stacking of four consecutive Fe–Ni bimetallic chains of 3e along the <i>c</i> axis	182
3.17 Plot of magnetic moment in fields of 0.01, 0.1, and 1 T for 3a	184
3.18 The DC magnetization isotherms (0–5 T) for 3a	186
3.19 Plot of magnetic moment in fields of 0.01, 0.1, and 1 T for 3b	187
3.20 The DC magnetization isotherms (0–5 T) for 3b	188
3.21 Temperature dependence (4–35 K) of FCM and ZFCM for 3b	189
3.22 Plot of magnetic moment, per [CuFe] for 3c–3d , and per [NiFe] for 3e	191
4.1 Perspective view of 4a with the atom-numbering scheme	217
4.2 Packing diagram of 4a view along the <i>c</i> axis	218
4.3 Views of supramolecular interactions in 4a	219
4.4 Crystal packing in 4a along the <i>c</i> axis	220
4.5 Histogram plot of distribution of Ag···Ag contacts between two [Ag(CN) ₂] fragments obtained from the CSD	221
4.6 Part of the crystal structure of 4a	222
4.7 Perspective view of 4b with the atom-numbering scheme	223
4.8 The 2-D sheet in 4b	225

LIST OF FIGURES (Continued)

Figures	Page
4.9 Perspective view of 4c with the atom-numbering scheme	226
4.10 View of 1-D ladder like chain in 4c	227
4.11 (a) Ball and stick and (b) space-filling representation showing two ladder chains in 4c viewed along the <i>b</i> axis	228
4.12 The 2-D sheet in 4c	230
4.13 Crystal packing in 4c along the <i>a</i> axis	230
4.14 Perspective view of 4d with the atom numbering scheme	231
4.15 The 2-D sheet with the (6,3) topology in 4c	232
4.16 Schematic view of the 3-D 4-connected network with $4^2.6^3.8$ topology for 4d	233
4.17 (a) Wires/sticks and (b) space filling representations of single 3-D framework with 1-D channels in 4d	234
4.18 (a) Ball and stick and (b) space-filling representations of the interpenetrating nets of 4d	235
4.19 Views of a fragment of the alternating nets in 4d showing (a) the Ag···Ag argentophilic and (b) C–H··· π and π ··· π interactions	236
4.20 Plot of magnetic moment in field of 1 T for 4b	237
5.1 View of 5a with the atom numbering scheme	254
5.2 The 2-D sheet motif in 5a	256
5.3 Projection of the 3-D network structure of 5a	257
5.4 The detailed view of the hydrogen bonds in the 5a	258
5.5 Perspective view of part of the structure in 5b	260

LIST OF FIGURES (Continued)

Figures	Page
5.6 View of 1-D of a square shaped [Ni–Ni] core in 5b	261
5.7 Perspective view of column structure in 5b	262
5.8 Perspective view of the cell packing in 5b	262
5.9 The detailed view of the hydrogen bonds in 5b	263
5.10 Schematic views of the 3-D 4-connected network for (a) 5a and (b) 5b	264
5.11 Temperature dependent magnetic behaviours of (a) 5a and (b) 5b	266
5.12 ATR-FTIR spectra of $K_2[Ni(CN)_4] \cdot H_2O$, 5a , and 5b	268
5.13 TGA (red) and DTA (blue) profiles for 5a	270
5.14 TGA (red) and DTA (blue) profiles for 5b	271
6.1 View showing asymmetric unit with the atom numbering in 6a	295
6.2 Comparison of Fe–N bond lengths in 6a and 6b at 103 and 233 K	297
6.3 Schematic representation for comparison of distorted octahedral geometry around Fe(II) centres in (a) 6a and (b) 6b	299
6.4 Views of AIBN ligands in (a) 6a and (b) 6b	301
6.5 (a) Views of the 3-D net in the structure of 6a at 103 K. (b) Schematic presentation of the α -Po related net in 6a	303
6.6 View showing the asymmetric unit with the atom numbering in 6c	305
6.7 View of 2-D (4,4) sheets in 6c along the <i>b</i> axis	306
6.8 View slightly offset from the <i>b</i> axis showing the the 2-D layered structure in 6c	307

LIST OF FIGURES (Continued)

Figures	Page
6.9 A view showing asymmetric unit with the atom numbering in 6c	308
6.10 (a) A view of the 3-D net in the structure of 6d . (b) Schematic presentation of the α -Po-related net in 6d	310
6.11 Schematic presentation in comparison of the α -Po related net for (a) 6a–6b and (b) 6d–6e	311
6.12 Magnetic behavior for compounds (a) 6a–6d and (b) 6b–6e in the form of $\chi_M T$ vs T plots	313
6.13 Magnetic behavior for compounds 6a–6d and 6b–6e in the form of μ_{eff} vs T plots	314
6.14 ^{57}Fe Mössbauer spectra of $[\text{Fe}(\text{AIBN})_3][\text{InCl}_4]_2$ (6a) recorded at (a) 77 and (b) 295 K	316
6.15 ^{57}Fe Mössbauer spectra of $[\text{Fe}(\text{AIBN})_3][\text{FeCl}_4]_2$ (6b) recorded at (a) 4.2, (b) 77, and (c) 295 K	318
7.1 SEM pictures of (a) 7a , (b) 7b , (c) 7c , (d) 7d , and (e) 7e	343
7.2 Simulation and experiment PXRD patterns of 7a , 7b , and 7e	344
7.3 Ball and stick representation of the asymmetric unit with numbering scheme in 7a	345
7.4 (a) Polyhedral and ball-and-stick representation of 7a viewed approximately along the a axis, and (b) wires/ stick and space-filling representation viewed along the b axis of 7a	347

LIST OF FIGURES (Continued)

Figures	Page
7.5 Perspective views of (a) polyhedral and (b) space-filling representations of anionic framework in 7a	348
7.6 Shows the asymmetric unit of (a) the $I4_1/a$ at 100 K, and (b) the $P4_2/n$ at 295 K structures of 7a	351
7.7 Polyhedral representations of single layer of compounds at (a) $I4_1/a$ and (b) $P4_2/n$, viewed along the c axis	353
7.8 Polyhedral representations of inorganic layers of compounds at (a) $I4_1/a$ for 7b and 7c , (b) $P2/n$ for 7d , and (c) $P4_2/n$ for 7b–7c	354
7.9 Hydrogen bonds about the pseudo inversion centers $3/4$, $1/4$, $1/2$ for the $I4_1/a$ structure at 100 K of (a) 7b , (b) 7c , and 0 , $1/2$, 1 for the $P4_2/n$ structure at 295 K of (c) 7b , (d) 7c	357
7.10 Hydrogen bonds about the inversion centres (a) 0 , 1 , $1/2$, and (b) $1/2$, $1/2$, $1/2$ for the ordered $P2/n$ structure of 7d at 100 K	360
7.11 Thermal ellipsoid plot of a fragment of 7e	371
7.12 Polyhedral representations of single layer of compound 7e	372
7.13 Polyhedral representations of a portion of bimetallic inorganic layers of compound 7e	373
B Supplementary figures	385

LIST OF ABBREVIATIONS

\AA	Angstrom
ΔJ	anisotropic in J
H	applied field
N	Avogadro's number
θ	Bragg angle or scattering angle
μ_B or B.M.	Bohr Magnetron
k	Boltzmann constant
Oe	centimeter-gram-second electromagnetic unit of magnetic intensity
C_g	centroids of ring
$\Delta\delta$	change of difference in δ
z	charge on an ionic species
H_C	critical fields
Δ	(i) crystal field splitting parameter (ii) spectra width
C	Curie constant
T_C	Curie temperature
$^{\circ}\text{C}$	degrees celsius
χ_{dia}	diamagnetic susceptibility
μ_{eff}	effective magnetic moment
ρ	electron density

LIST OF ABBREVIATIONS

χ_g	gram molar susceptibility
$-H\cdots$	hydrogen bond interaction
Γ	half-width at half-height
$d[-]$	interatomic bond distance for normal bonded atoms
$d[\cdots]$	interatomic bond distance involving a noncovalent atom
$\angle[-]$	interplanar dihedral angle
$\angle[- -]$	interatomic angle for normal bonded atoms
$\angle[- \cdots]$	interatomic angle involving a noncovalent interaction
$\angle[- - -]$	interatomic torsional angle
δ	isomer shift (IS)
$U[]$	isotropic atomic displacement parameter for the indicated atom
\cdots	noncovalent interaction or nonbonded interatomic separation
$-$	primarily covalent interaction or coordination interaction
μ	linear absorption coefficient
μ_0	magnetic constant, permeability of a vacuum
B	magnetic flux density
χ	magnetic susceptibility
Mg	Milligram
mm	millimeter
M	molar magnetization
χ_M	molar susceptibility
nm	nanometer

LIST OF ABBREVIATIONS

T_N	Néel temperature
Z	number of formula units in the unit cell or atomic number of an atom
n	number of unpaired spins
ΔE_Q	quadrupole splitting (QS)
J	rotation quantum number
M_s	saturation magnetization
H^2	second order field effects (Zeeman)
λ	spin orbit coupling constant
T	Teslar
T	temperature
S	total spin
$\bar{\lambda}$	wavelength of x-radiation
ν	wavenumbers
wt %	weight percent
Θ	Weiss constant
α, β, γ	unit cell angles
a, b, c	unit cell dimensions
1-D	one-dimensional
1,10-phen	1,10-phenanthroline
2-D	two-dimensional
2,2'-bipy	2,2'-bipyridine

LIST OF ABBREVIATIONS

3-D	three-dimensional
4AE	fourfold aryl embrace
4,4'-bipy	4,4'-bipyridine
AC	alternating current
ACCN	1,1'-azobiscyclohexanecarbonitrile
AIBN	2,2'-azobisisobutyronitrile
ampy	aminomethylpyridine
Anal	Analysis
ANU	The Australian National University
ATR-FTIR	Attenuated Total Reflection Fourier Transform Infrared
azpy	<i>trans</i> -4,4'-azopyridine
B.C.	Before Christ
bmtz	3,6-bis(2'-pyrimidyl)-1,2,4,5-tetrazine
bppn	bis(2'-pyridyl)-1,2-pyridazine
bpm	bis(1-pyrazolyl)methane
bptz	3,6-bis(2-pyridyl)-1,2,4,5-tetrazine
bpym	2,2'-bipyrimidine
btr	tris(4,4'-bis-1,2,4-triazole)
btzb	1,4-bis(tetrazol-1-yl)butane-N ₄ ,N ₄ '
btzpol	1,3-bis(tetrazol-1-yl)-2-propanol
calcd	calculated
cddt	2-chloro-4,6-bis(dipyrid-2-ylamino)-1,3,5-triazine
CD-ROM	Compact Disk Read Only Memory

LIST OF ABBREVIATIONS

CN ⁻	cyanide
CNT	carbon nanotube
CIF	IUCr Crystallographic Information File
dabn	1,4-diaminobutane
dapn	1,5-diaminopentane
DC	direct current
dca ⁻	dicyanamide
dien	diethylenetriamine
ditz	bis(tetrazol-1-yl)alkane-N4,N4'
dmbpy	4,4'-dimethyl-2,2'-bipyridine
dmptacn	1,4-bis(2-pyridylmethyl)-1,4,7-triazacyclononane
dpap	2,6-(<i>N,N'</i> -di(4-pyridyl)amino)pyridine
dmit	2-thioxo-1,3-dithiole-4,5-dithiolate
DMF	Dimethylformamide
DNA	deoxyribonucleic acid
dpap	2,6-(<i>N,N'</i> -di(4-pyridyl)amino)pyridine)
dpa	dipyridyl amine
DTA	Differential Thermal Analysis
EDX	Energy Dispersive X-ray analysis
<i>eg.</i>	Exempli gratia, in Latin meaning “for example”
<i>ef</i>	Edge-to-Face interaction
emu	Electro-magnetic unit
en	1,2-ethylenediamine

LIST OF ABBREVIATIONS

EPR	electron paramagnetic resonance
Eq	Equation
<i>et al.</i>	Et al ii, in Latin meaning “and others”
<i>etc.</i>	etcetera (redirects here); et means “and”, cetera means “the rest”
EtOH	ethanol
EvalCCD	data reduction software from Bruker Nonius
FCM	field- cooled magnetization
gof	estimated standard deviation of an observation of unit weight, or goodness of fit
Hbim	biimidazolium
H ₂ bmtz	1,4-dihydro-3,6-bis(2'-pyrimidyl)-1,2,4,5-tetrazine
Hdpa	protonated di-2-pyridylamine
HKUST	Hong Kong University of Science and Technology
HS	high-spin
<i>i.e.</i>	Id est, in Latin meaning “that is”
Im	imidazole
ImH ⁺	imidazolium
IUCr	International Union of Crystallography
K	Kelvin
kJ	kilojoules
kV	kilovolts
LIESST	Light-Induced Excited Spin State Trapping

LIST OF ABBREVIATIONS

LS	low-spin
MeCN	acetonitrile
MeOH	methanol
MOFs	metal-organic frameworks
M_r	Molecular Mass
MW	molecular weight
oct	octahedron
<i>off</i>	Offset Face-to-Face interaction
ORTEP	Oak Ridge Thermal Ellipsoid Plot program
PB	Prussian blue
PBs	Prussian blue analogs
POMs	polyoxometallates
pbtz	1,3-di(tetrazol-2-yl)propane
pmd	pyrimidine
pn	1,2-diaminopropane
PXRD	powder X-ray diffraction
py	pyridine
pyz	pyrazine
PTMTC	tris(4-carboxylato-2,3,5,6-tetrachlorophenyl)methane
P4AE	Parallel Fourfold Aryl Embrace
R_1	conventional crystallographic discrepancy index
r.m.s	root mean square
RNA	ribonucleic acid

LIST OF ABBREVIATIONS

SCMs	single chain magnets
SCO	spin-crossover
SEM	scanning electron microscope
SHELXL-97	least squares structure refinement program
SHELXS-97	least squares structure solution program
S.I.	International System of Units
SIR97	direct methods structure solution software
SMMs	single-molecule magnets
SQUID	Superconducting Quantum Interference Devices
SUT	Suranaree University of Technology
tacn	1,4,7-triazacyclononane
tcn ⁻	tricyanomethanide
tet	tetrahedron
TGA	Thermogravimetric Analysis
TIP	temperature independent susceptibility
tn	1,3-diaminopropane
tpa	tris(2-pyridylmethyl)amine
tptz	2,4,6-tri(2-pyridyl)-s-triazine
tren	tris(2-aminoethyl)amine
trine	triethylenetetraamine
wR_2	weighted crystallographic discrepancy index
ZFCM	zero-field- cooled magnetization
ZFS	zero-field splitting

CHAPTER I

A GENERAL INTRODUCTION

In the last decade, there has been much interest in nanotechnology because of its broad applications across many fields of science and engineering. Creation of localized scientific community networks dedicated to identification, development, and commercialization of inventions from nanotechnology remains important to the overall success of any region attempting to benefit from the tremendous economic potential of nanotechnology. Porous materials have attracted the attention of chemists, physicists, and materials scientists due to their interest in the creation of nanometer sized spaces and the novel phenomena that occur in them.

Hybrid organic-inorganic materials are an important subclass of porous materials that usually possess open-framework structures, and are of great contemporary interest in materials science and chemical research, Figure 1.1. They are currently one of the hot topics in the development of nanoscience and nanotechnology (Rao *et al.*, 2007). These hybrid materials are very attractive because properties of organic materials (*eg.* optical, electrical, and magnetic functionality, porosity, and hydrophobicity) are combined with those of inorganic materials (*eg.* rigidity, high surface area, thermal stability, and mechanical stability). The hybrid concept has made accessible an immense new area of materials science with extraordinary implications for the development of multifunctional advance materials such as optical materials, magnetic materials, electrical materials, solid electrolytes,

chemical sensors, catalysts, separation membranes, and gas storage materials (Rao *et al.*, 2004; 2007).

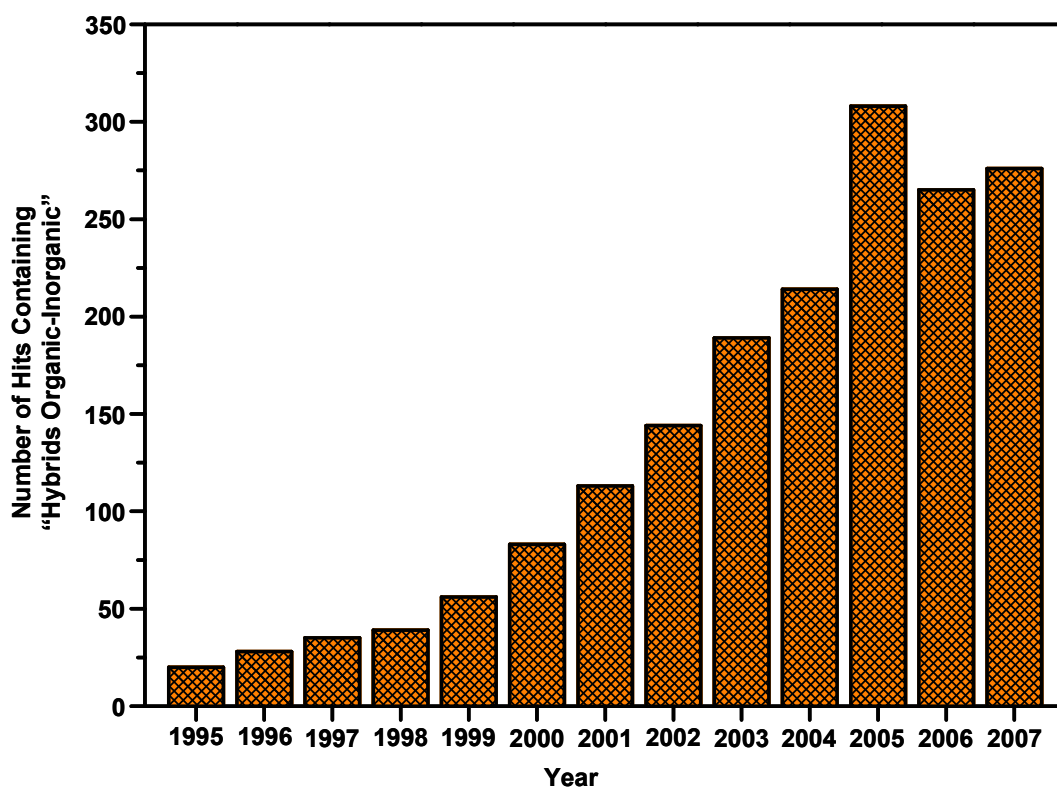


Figure 1.1 Occurrence of the term “hybrids organic-inorganic” in titles of papers published between 1995 and 2007 (SciFinder Scholar search: July, 2008).

A precise definition of hybrid organic-inorganic framework materials has been given by Cheetham *et al.* (2004) as “*compounds that contain both inorganic and organic moieties as integral parts of a network with infinite bonding connectivity in at least 1-D*”. Such materials can be conveniently divided into two categories, firstly, called “*coordination polymers*”, which are defined as extended arrays composed of

metal atoms or clusters bridged by polyfunctional organic molecules (Batten, 2001; 2004), and secondly, “*hybrid metal oxides*”, which contain infinite metal–oxygen–metal (M–O–M) arrays as a part of their structures (Cheetham *et al.*, 1998). For other materials, where the organic part is located within the pores and does not bond to the framework except through van der Waals, coulombic, or hydrogen bond interactions, the term “*organically templated porous solids*” is used.

1.1 Supramolecular Chemistry

Supramolecular chemistry has its roots in nature, and is one of the most popular and fastest growing areas of experimental science. It combines knowledge from chemistry, biology, and physics while utilizing the most modern research technology (Lehn, 1990; Steed and Atwood, 2000). One precise definition of supramolecular chemistry has been given by Jean-Marie Lehn, who received a Nobel Prize for his pioneering work on supramolecular chemistry in 1987, as “*chemistry of the intermolecular bond, covering the structures and functions of the entities formed by association of two or more chemical species*” (Lehn, 1988). An example of a supramolecular assembly reported by Lehn and co-workers is shown in Figure 1.2. More extended definitions, including the nature of the interactions have been recently offered; “*the study of systems involving aggregates of molecules or ions held together by non-covalent interactions, such as electrostatic interactions, hydrogen bonding, dispersion interactions and solvophobic effects*” (Steed *et al.*, 2007).

More recently, using concepts in the area of supramolecular chemistry based on size and shape of materials, supramolecular chemistry can be split into two broad categories: (i) host-guest chemistry and (ii) self-assembly (Steed *et al.*, 2007).

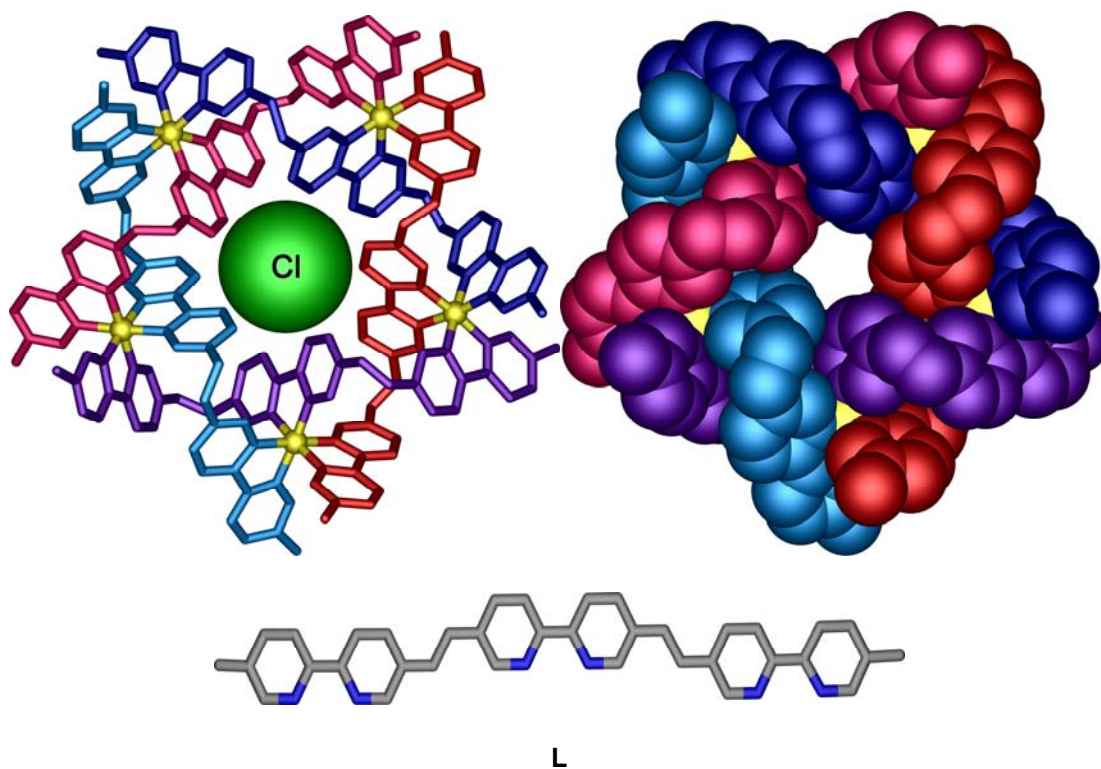


Figure 1.2 Self-assembly of the circular helicate $[(\text{Fe}_5\text{L}_5)\text{Cl}]^{9+}$ from five tris-bpy ligand strands L and five equivalents of FeCl_2 . Drawn from coordinates from CSD, after Hasenknopf *et al.*, 1996.

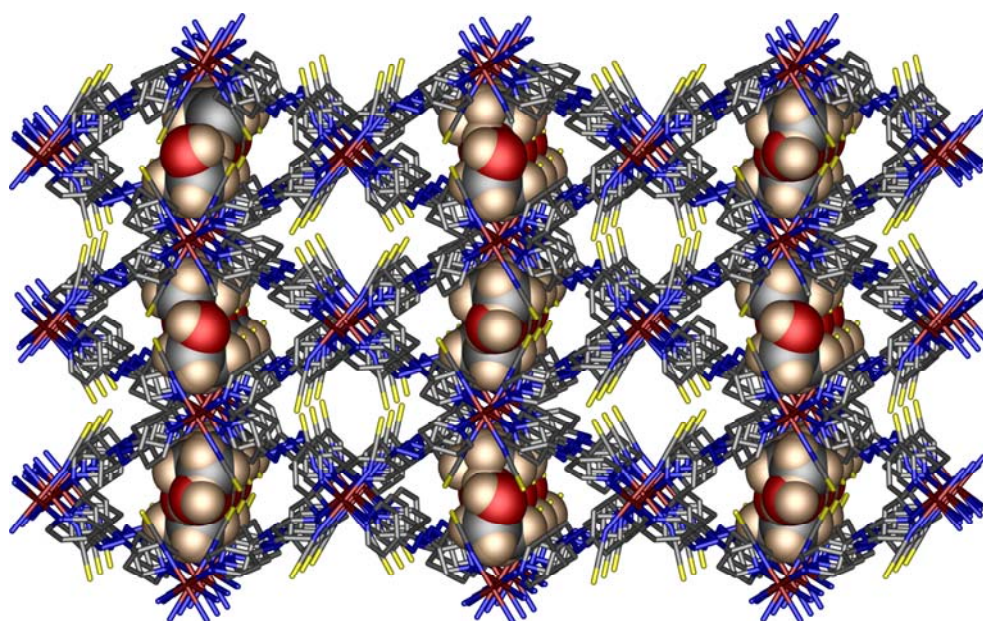
1.1.1 Supramolecular Host-Guest Chemistry

The definition of host-guest is very broad. In supramolecular chemistry, according to the statement by Steed *et al.* (2007), the term of “*host*” is used when one molecule is significantly larger than another molecule, whereas the smaller molecule is the “*guest*” and the large host molecules are capable of enclosing the smaller guest molecules *via* noncovalent interactions. A representative example of supramolecular solid state host-guest chemistry is the guest-dependent spin crossover (SCO) in the nanoporous molecular framework material of $[\text{Fe}_2(\text{azpy})_4(\text{NCS})_4] \cdot (\text{guest})$, azpy =

trans-4,4'-azopyridine, Figure 1.3. In this structure, pore size and thermal behavior of the material depend on the presence of small molecules (low molecular weight alcohols) in the lattice. Such complexes are referred to as host-guest complexes, where the lattice provides the “*host*” and the small, sorbed molecules are the “*guests*”. The most striking feature of the material is the change in the magnetic and optical properties. SCO behavior was successfully controlled by both guest removal and sorption. In the presence of guest molecules, 50% of the high-spin (HS) Fe(II) atoms became low-spin (LS) below 50 K. However, in the absence of guest, no SCO occurred (Halder *et al.*, 2002). More recent reviews of supramolecular solid state host-guest chemistry are available (Beatty, 2003; Wan *et al.*, 2006; Dalgarno *et al.*, 2008).

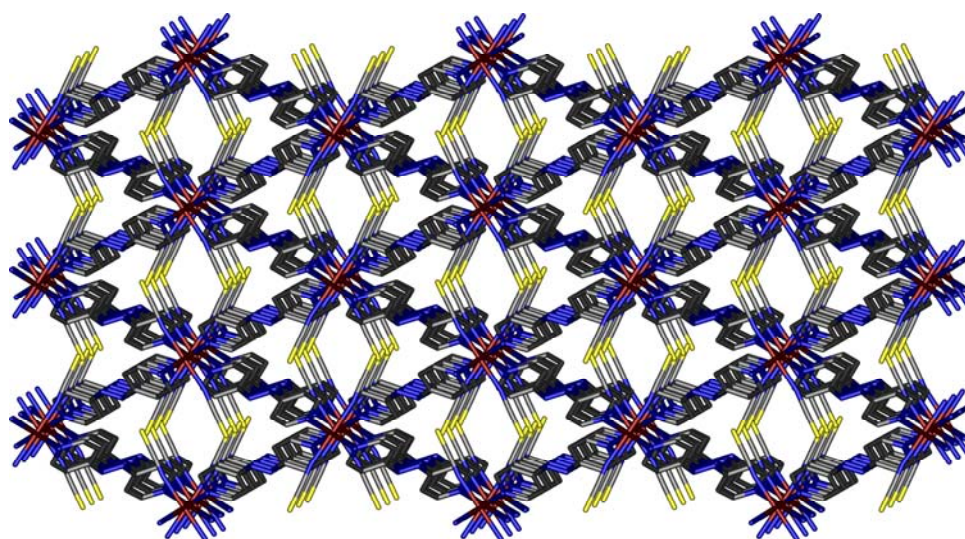
1.1.2 Self-Assembly

When there is no significant difference in size, and no species is acting as a host for another, the joining of two or more species is termed “*self-assembly*”. Steed *et al.* (2007) has given the generic definition broadened over time to incorporate many aspects of biochemistry and nanotechnology as “*the spontaneous and reversible association of molecular species to form larger, more complex supramolecular entities according to the intrinsic information contained in the components*”. This process is usually spontaneous but may be influenced by solvation or templation effects or in the case of solids by the nucleation and crystallisation processes. Many examples of self-assembly process are metal-ligand complexes. Fujita and co-workers has reacted pyridyl or pyrimidyl functionalised planar or near planar ligands with *cis*-protected Pd in order to synthesize a substantial series of metal-organic cages (Umemoto *et al.*, 2001; Chand *et al.*, 2002; Tominaga *et al.*, 2004; Sato *et al.*, 2006;



Monoclinic ($C2/c$, $T = 150(2)$ and $25(2)$ K), spin-crossover

↓ Heating to 375 K
under dry N_2



Orthorhombic ($Ibam$, $T = 375(2)$ K), no spin-crossover

Figure 1.3 Guest inclusion/removal in $[Fe_2(azpy)_4(NCS)_4] \cdot (guest)$. Drawn from coordinates from CSD, after Halder *et al.*, 2002.

Suzuki *et al.*, 2007; Yoshizawa *et al.*, 2007). An impressive example from their works uses V-shaped ligands of 1,3-bis(4-pyridyl)-5-benzyl ester ethyl ester which bind with naked palladium centers to afford finite spherical coordination cages that have a diameter of *ca.* 3 nm, Figure 1.4a (Tominaga *et al.*, 2004). In related work, Stang and co-workers have used $\text{Pt}(\text{PMe}_3)_2(\text{OTf})_2$ as a V-shaped metallic building unit reacted with triangular shaped 1,3,5-tris(4-pyridyl-trans-ethenyl)benzene in a 3:2 ratio to build discrete supramolecular architectures of *ca.* 1–1.5 nm of size, Figure 1.4b (Schweiger *et al.*, 2005). Similarly, Dalcanale and co-workers synthesized nano cages formed by picolyl-bridged cavitands, preorga-nized for cage self-assembly *via* coordination to Pt metal precursors, and its structure was determined using synchrotron radiation at low temperature, Figure 1.4c (Pinalli *et al.*, 2004).

Self-assembled metallo-supramolecular capsules are of contemporary great interest research due to their potential application in the fields of sensors and catalysis (Dalgarno *et al.*, 2008). Strategies developed in their construction have mainly relied on self-assembly or arranging molecules through metal-ligand interactions or the use of hydrogen bonds (Prins *et al.*, 2001; Steed 2001; Cho *et al.*, 2002; McKinlay *et al.*, 2005). Atwood and co-workers reported interesting nano capsules composed of a large neutral discrete pseudo-spherical coordination complexes assembled from 6 pyrogallol[4]arene ligands and 24 Cu(II) metal ions, Figure 1.5. Amazingly, this coordination capsule is structurally analogous to its hydrogen bonded counterpart. The result shows the robust ability of pyrogallol[4]arene molecules to self-assemble into large hexameric cage structures from either hydrogen-bonding or metal-ligand coordination processes (McKinlay *et al.*, 2005).

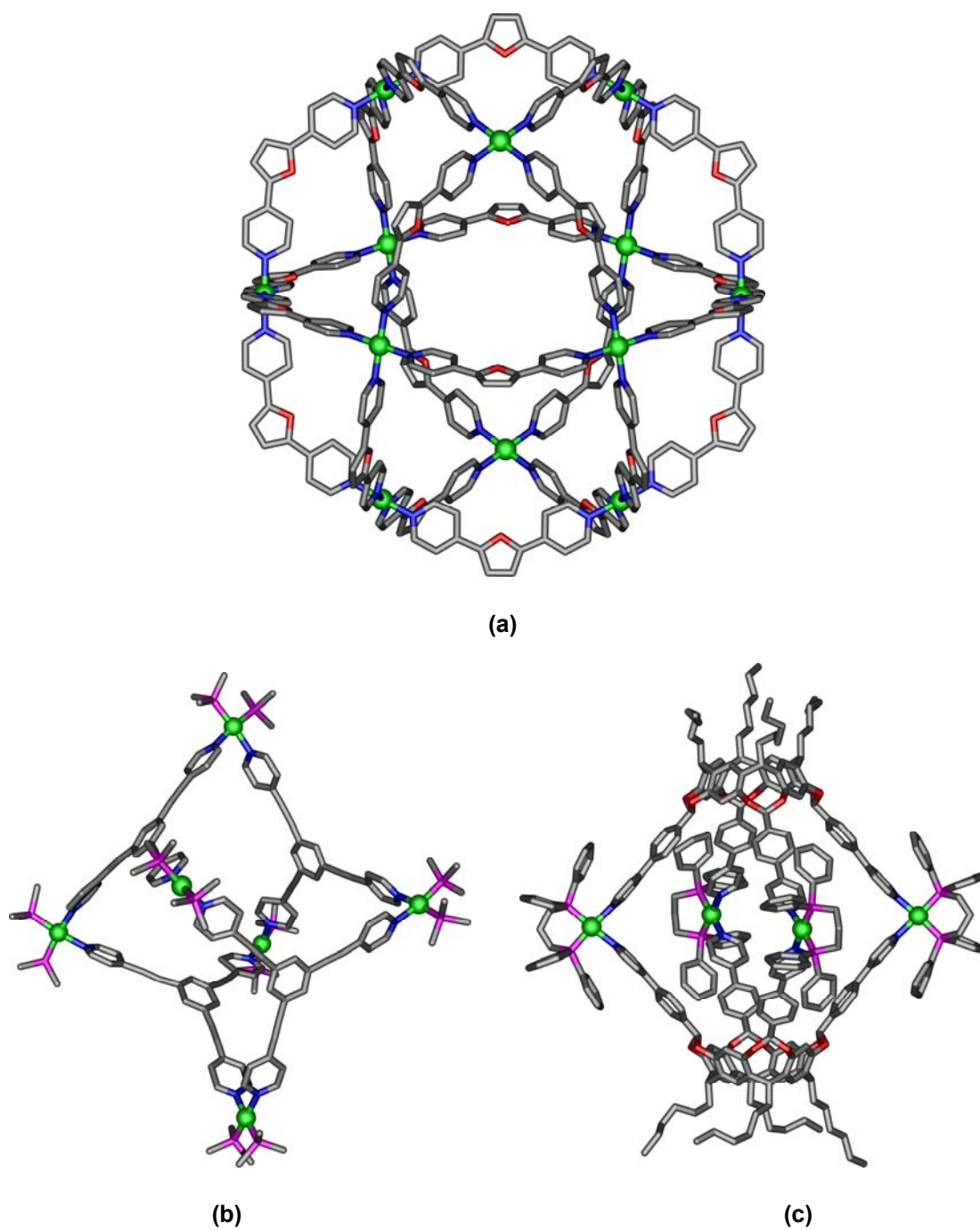


Figure 1.4 Self-assembly of nanosize coordination cages. Drawn from coordinates from CSD, after (a) Tominaga *et al.*, 2004, (b) Schweiger *et al.*, 2005, and (c) Pinalli *et al.*, 2004.

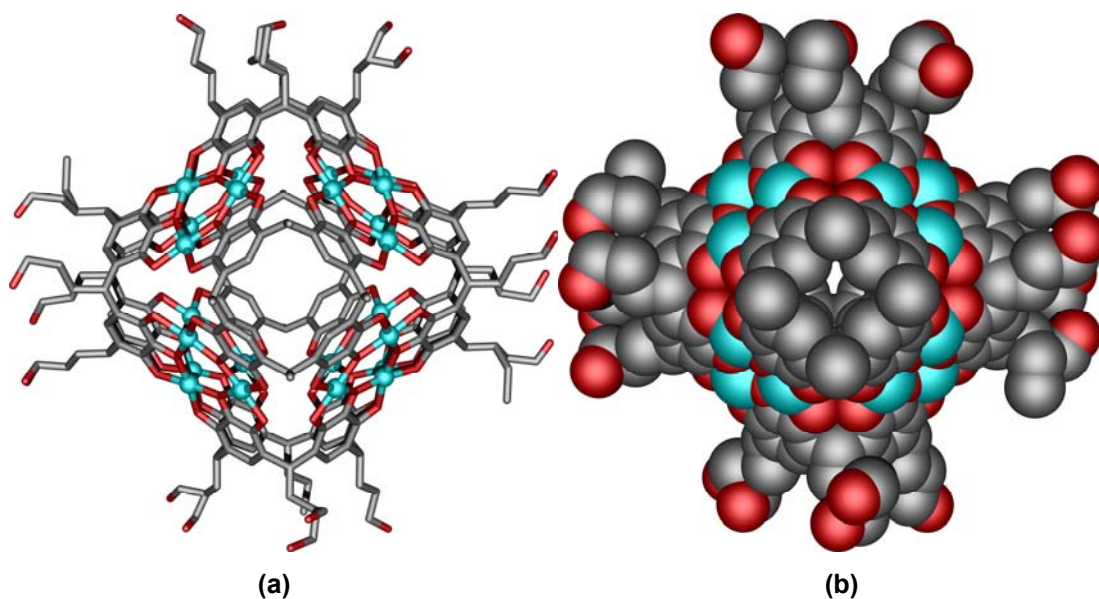


Figure 1.5 (a) Ball-wires-sticks and (b) space-filling representations of the hexameric coordination capsule showing the metal-directed self-assembly of part of 6 pyrogallol[4]arenes and 24 Cu(II) ions. Drawn from coordinates from CSD, after McKinlay *et al.*, 2005.

Another example is a molecular tubular assembly which was also discovered by Atwood and co-workers (Orr *et al.*, 1999). In this structure, the authors successfully react amphiphilic polyhedron-shaped *p*-sulfonatocalix[4]arene pyridine *N*-oxide ligands with lanthanide ions to afford spherical and helical tubular structures. The tube is *ca.* 1.5 nm in diameter. These tubular assemblies are arranged in a hexagonal array as shown in Figure 1.6. A related system has been obtained in the present work and described in Chapter III.

Weak, noncovalent interactions between molecules control many biological functions (Jeffrey and Saenger, 1991; Desiraju and Steiner, 1999). In chemistry,

noncovalent interactions are now exploited for the synthesis in solution of large supramolecular aggregates. The aim of these syntheses is not only the creation of a particular structure, but also the introduction of specific chemical functions in these supramolecules.

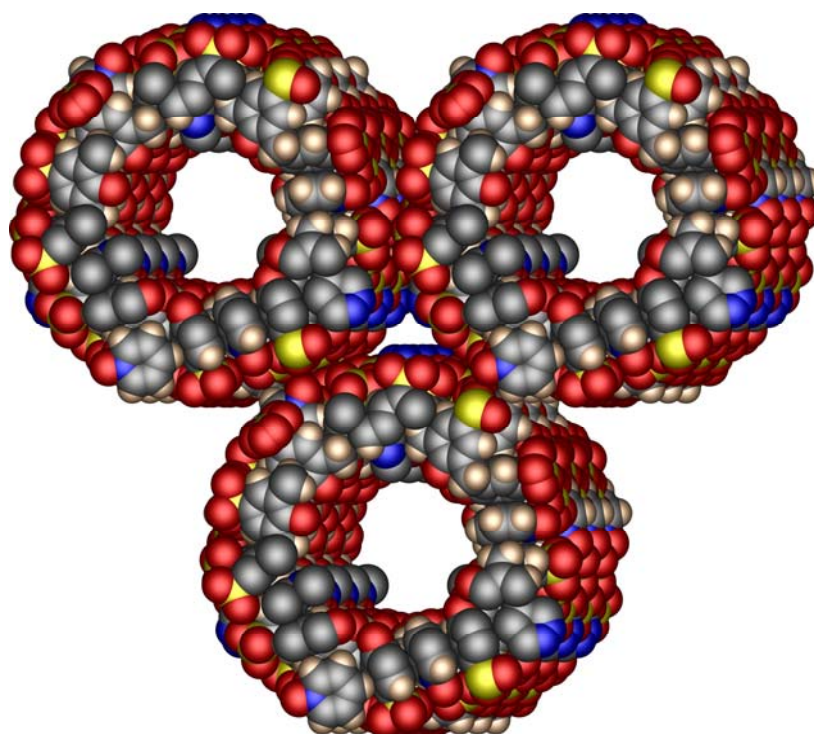


Figure 1.6 View of the hexagonal packing of tubules composed of *p*-sulfonatocalix[4]arene with intercalated pyridine *N*-oxide. Drawn from coordinates from CSD, after Orr *et al.*, 1999.

1.1.3 Supramolecular Interactions

The phrase “*supramolecular interactions*” throughout this thesis is intended to should be assumed to mean noncovalent interactions, unless specified otherwise. Covalent bonds are a common type of bonding formed as a result of the sharing of one or more pairs of bonding electrons, *i.e.* formed by overlapping of partially

occupied orbital of interacting atoms. In contrast, the formation of noncovalent interactions does not involve the sharing of pairs of electrons, because the attraction comes from the electrical properties of the building blocks (Muller-Dethlefs and Hobza, 2000). Covalent bonds are generally shorter than 2 Å, while noncovalent interactions function within a range of several angstroms. Covalent interactions range between *ca.* 150 kJ mol⁻¹ to 450 kJ mol⁻¹ for single bonds, and are considerably stronger than noncovalent interactions, which can range from 2 kJ mol⁻¹ for dispersion interactions to 300 kJ mol⁻¹ for ion–ion interactions (Steed *et al.*, 2007). Noncovalent interactions lead to the formation of a molecular cluster while covalent interactions lead to the formation of a classical molecule. The noncovalent interactions involved in supramolecular entities may be a combination of several types of interaction as follows.

Ion–ion interactions (200–300 kJ mol⁻¹) are attractive interactions between a positive ion and a negative ion or repulsion between two ions of the same charge. This supramolecular ion–ion interaction is non-directional in nature which means that the interaction can occur in any orientation, and is comparable with covalent interactions. An example of a supramolecular ion–ion interaction can be seen in the crystal structure of sodium chloride (Klewe and Pedersen, 1974).

Ion–dipole interactions (40–210 kJ mol⁻¹) are the electrostatic attractions between ions and dipoles (the separation of charge in a bond or a molecule with a positively charged end and a negatively charged end) of molecules. An example of a ion–dipole interaction is the alkali metal Cs cation interacting with polar [18]crown-6, Figure 1.7, in the structure of Cs₂([18]crown-6)₃[Ni(dmit)₂]₂, dmit = 2-thioxo-1,3-dithiole-4,5-dithiolate (Akutagawa *et al.*, 2005). Other examples of this interaction are

a series of the alkali metals (*i.e.* Li, Na, K, Rb, and Cs) with macrocyclic crown ether molecules reviewed by Steed (2001).

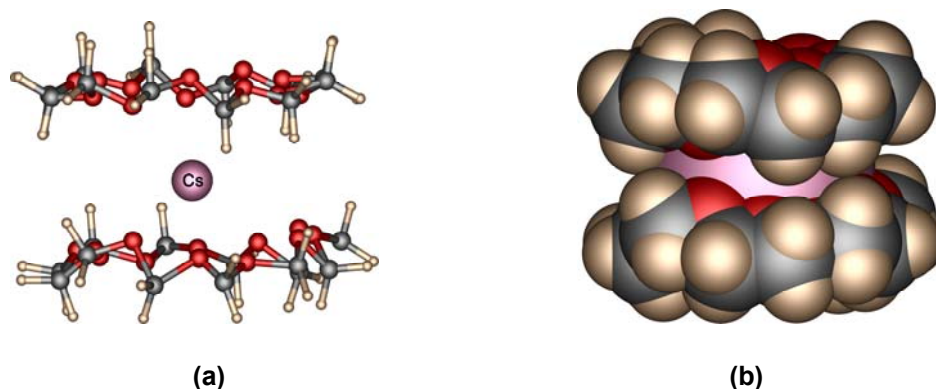


Figure 1.7 (a) Ball-stick and (b) space filling model showing ion-dipole interactions in the cesium complex of [18]crown-6. Drawn from coordinates from CSD, after Akutagawa *et al.*, 2005.

Dipole–dipole interactions ($5\text{--}50\text{ kJ mol}^{-1}$) are intermolecular or intramolecular interactions between molecules or groups of atoms having permanent electric dipole moments. The strength of the interaction depends on the distance, strength of the dipoles, and relative orientation of the dipoles. The term also applies to intramolecular interactions between bonds having permanent dipole moments. Allen and co-workers reported the investigation of geometries and attractive energies of dipole–dipole carbonyl–carbonyl interactions by using crystallographic data and *ab initio* molecular-orbital calculations (Allen *et al.*, 1998). Three common interaction motifs are observed in crystal structures: (i) a slightly sheared antiparallel motif interactions, 22.3 kJ mol^{-1} , (ii) a perpendicular motif, 20 kJ mol^{-1} , and (iii) a highly sheared parallel motif, 7.6 kJ mol^{-1} . These energies are comparable to those of

medium-strength hydrogen bonds. An example of these interactions is antiparallel carbonyl–carbonyl interaction between the positive polarity carbon atom and the negative polarity oxygen atom of adjacent carbonyl groups in pyridine-3,5-dicarboxylic acid (Cowan *et al.*, 2005).

Hydrogen bond interactions (4–120 kJ mol⁻¹) are bonding interactions between acidic hydrogen atoms and negatively charged or negatively polarized atoms with (or without) lone-pairs as depicted in Figure 1.8a. They are described by the formula D–H···A (where D represents the donor atom that is bonded to the acidic hydrogen atom, and A represents the acceptor atom to which the acidic hydrogen atom is bonded). Hydrogen bonds are widely exploited in molecular crystal engineering (Desiraju, 1996; 2002; 2003), have been used extensively in molecular recognition applications (Hosseini, 2003), and are especially important because they best combine both strength and directionality (Jeffrey, 1997; Scheiner, 1997; Braga and Grepioni, 2001).

The most commonly used criteria for identification of a strong hydrogen bond, are the interatomic distances H···A and D···A, and the angle (θ), illustrated in Figure 1.8b. If the distance between the hydrogen and acceptor atoms is significantly shorter than the sum of van der Waals radii, and if θ is close to 180°, a hydrogen bond is usually present. Several studies have shown the angular dependence of θ to be related to the strength of the hydrogen bond (Bernstein *et al.*, 1994). Stronger hydrogen bonds tend to show a shorter H···A distance, correlated with an elongated D–H bond and a θ between 170–180°. In cases where the acceptor is a carbonyl (C=O), the ϕ angle is most frequently between 110° and 130°, corresponding to the regions of the lone electron pairs (Braga *et al.*, 1994). Irrespective of the criteria listed

above, it has become widely accepted that there is a hydrogen bond interaction whenever the H \cdots A and/or the D \cdots A distances are less than the sum of the van der Waals radii. Accordingly, a list of van der Waals radii, such as that in Table 1.1 for some common atoms, with comparison between Pauling (1945), Bondi (1964), and Rowland and Taylor (1996) radii is an essential tool for observing hydrogen bonds.



Figure 1.8 Hydrogen bond geometry and partial charges. (a) Donor and acceptor atoms and (b) angular dependence in a primary hydrogen bonds interactions.

Table 1.1 The van der Waals radii (in Å) used for observing hydrogen bonds.

Element	Pauling (1945)	Bondi (1961)	Rowland and Taylor (1996)
H	1.20	1.20	1.09
C		1.70	1.75
N	1.50	1.55	1.61
O	1.40	1.52	1.56
F	1.35	1.47	1.44
S	1.85	1.80	1.79
Cl	1.80	1.75	1.74
Br	1.95	1.85	1.85
I	2.15	1.98	2.00

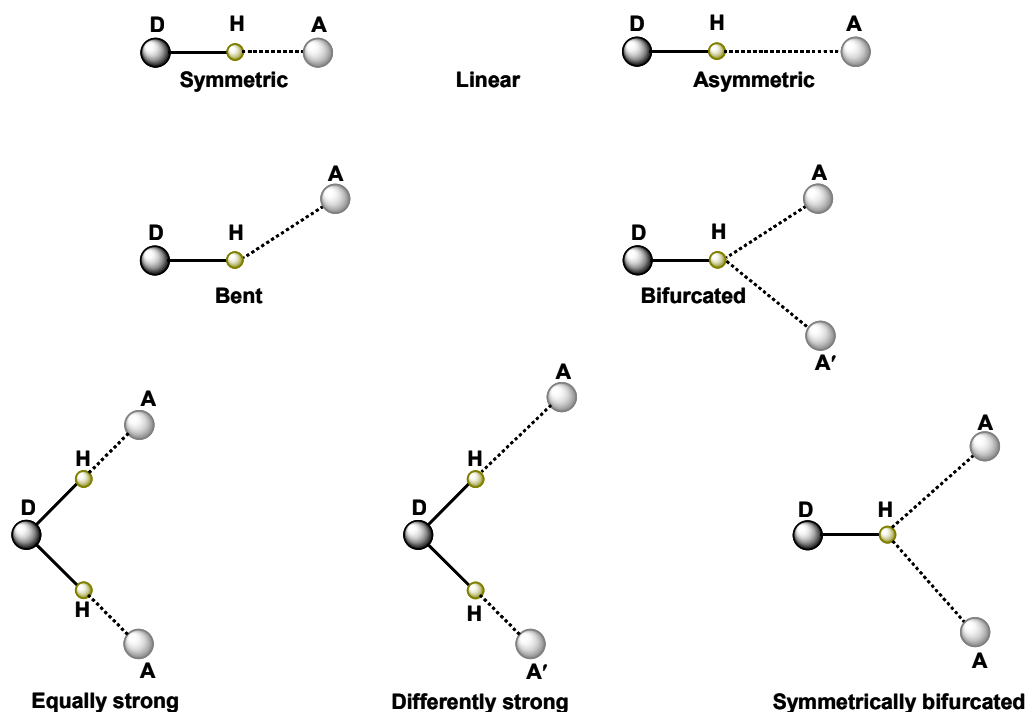


Figure 1.9 Structures of common hydrogen bond types. Redrawn after Lutz, 2003.

The structure and strength of hydrogen bonds in inorganic solids has recently been examined by Lutz (2003). He remarked that they depend on several factors, including the various $D-H\cdots A$ motifs possible, the inherent hydrogen bond donor strength of the acid hydrogen atom, the inherent acceptor capability of the respective acceptor groups, collective phenomena (cooperative, competitive, and synergetic effects), and structural features, such as the number of acceptors *eg.* two-center, three-center (bifurcated), etc. hydrogen bonds, and the hydrogen bond angles $D-H\cdots A$ (linear or bent) and $H\cdots A-R$. As already mentioned, the nature and strength of hydrogen bonds strongly depends on both the hydrogen-bond donors and acceptors involved and the structural arrangement of the hydrogen bonds. Therefore, the

structural arrangement including geometry, coordination, and configuration is essential for understanding hydrogen bonding. Figure 1.9 illustrates the structures of several common hydrogen bond types. A simple example of hydrogen bonds exhibiting directional properties are the 2-D honeycomb networks based upon $[\text{Ni}(\text{Hbim})_3]^-$ building blocks (Hbim = biimidazolium) linked by $\text{N}-\text{H}\cdots\text{N}$ hydrogen bonds in an $R_2^2(10)$ synthon (Tadokoro *et al.*, 1999), as shown in Figure 1.10.

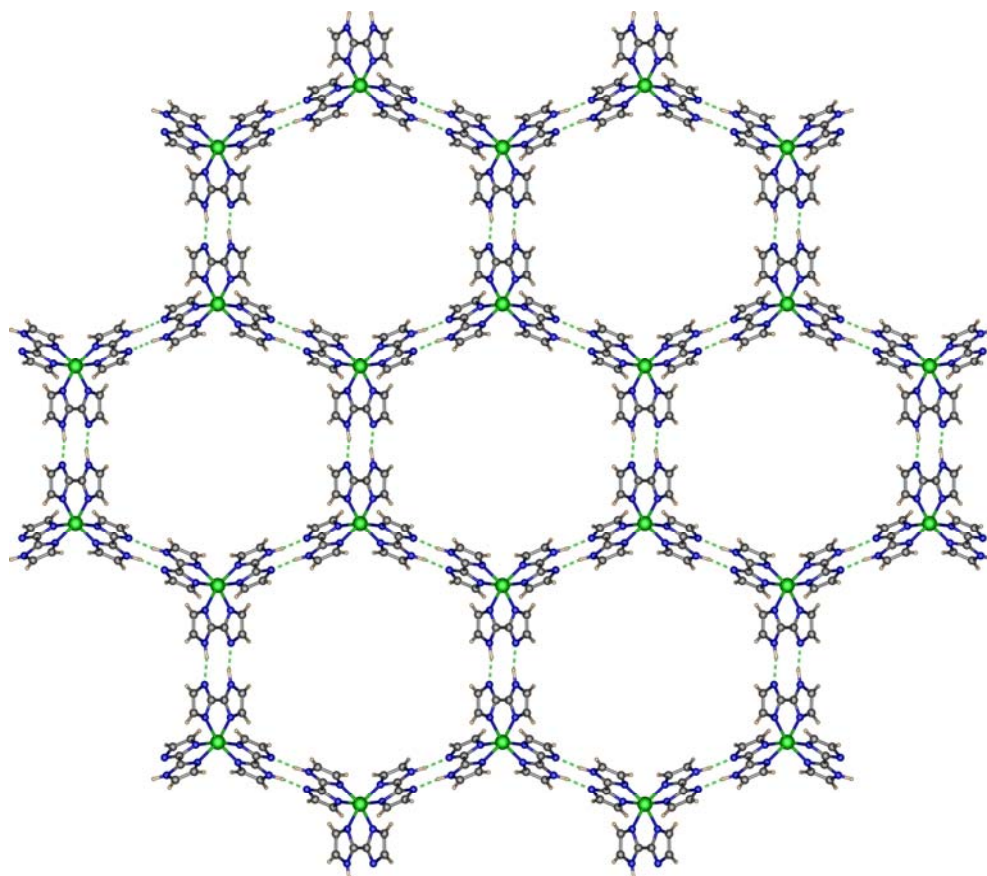


Figure 1.10 View of honeycomb hydrogen bonds sheets in $[\text{Ni}(\text{Hbim})_3]^-$ building block. Drawn from coordinates from CSD, after Tadokoro *et al.*, 1999.

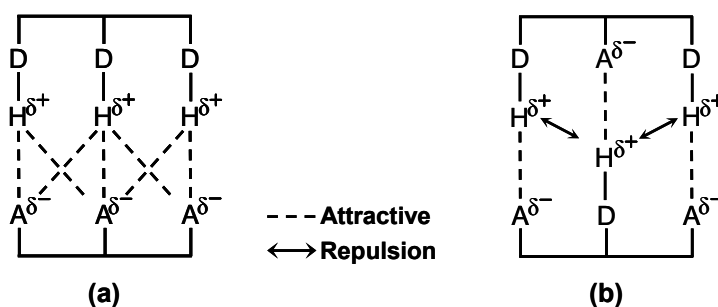


Figure 1.11 Schematic representation of (a) attractive and (b) repulsion of secondary hydrogen bonds interactions. Redrawn after Steed *et al.*, 2007.

The above example contains “*primary hydrogen bond interactions*” in which the hydrogen bonds are formed by a directional interaction between the donor and the acceptor groups. However, there are also “*secondary hydrogen bond interactions*” possible between neighboring groups, as illustrated in Figure 1.11. In these interactions stabilization arises from electrostatic attractions between positively and negatively polarized atoms in adjacent hydrogen bonds. Destabilization is likewise possible as a result of electrostatic repulsion between two positively or negatively polarized atoms. These hydrogen bonds have structural role in proteins and other biomolecules such as in the double helix of DNA (Bikadi *et al.*, 2007). Mascali and co-workers (1996) have synthesized a DNA-base hybrid designed to function exclusively as the corner piece of a hexagon. The combination of the A–A–D sequence of cytosine and the complementary D–D–A sequence of guanine at an angle of 120° to each other in pyrido[4,3-dpyrimidine], leads to the assembly of independent hexagonal aggregates in the solid state, Figure 1.12. This is a beautiful example of the communication of programmed, hydrogen bonding information.

The importance of weak hydrogen bonds has been established, and is recognized to be of importance in crystal engineering (Desiraju, 2007), as well as found to play important roles in the physical, chemical, and biological properties of a variety of substances (Desiraju and Steiner, 1999; Panigrahi and Desiraju, 2007). The C–H \cdots π interaction is a weak hydrogen-bond occurring between soft acids and soft bases (Nishio *et al.*, 1998). Examples of this interaction can be found in when C–H bonds point directly towards the π -cloud of the benzene rings or C \equiv C groups. Many examples of these interactions are available in reviews articles (Andrews *et al.*, 1999; Lewiński *et al.*, 2005).

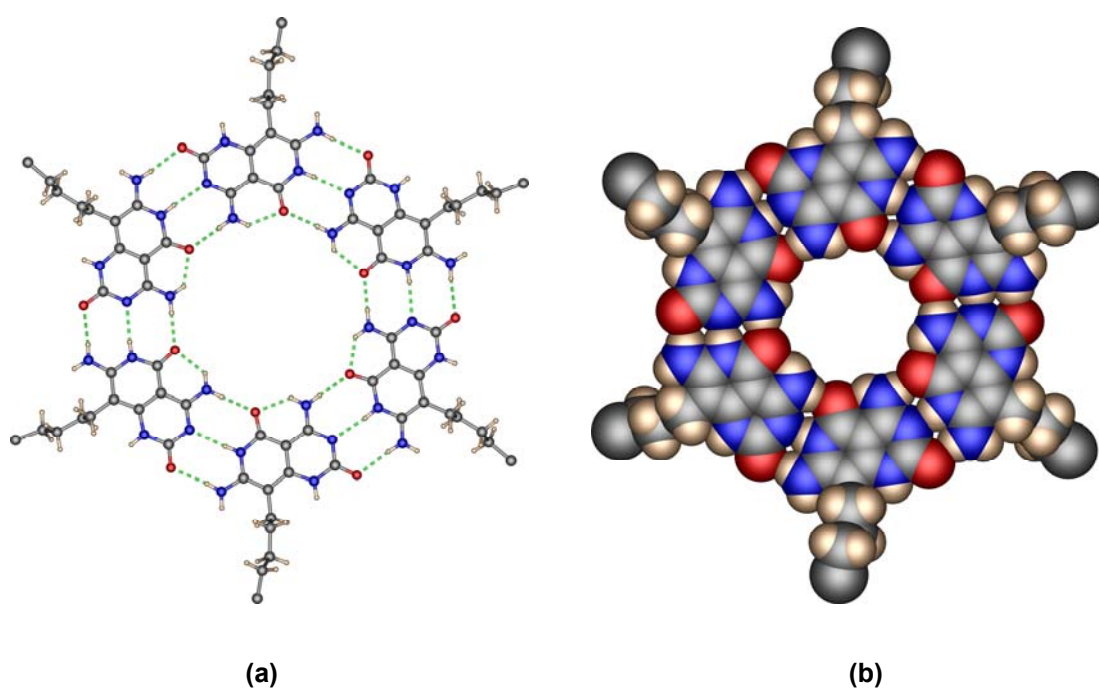


Figure 1.12 (a) Ball-stick and (b) space filling representations of the enforced self-assembly of molecules of pyrido[4,3-d]pyrimidine into a hexamer. Drawn from coordinates from CSD, after Mascall *et al.*, 1996.

The geometry of a hydrogen bond and the type of donor and acceptor groups determine the strength, length, and nature of the interactions. From these criteria, hydrogen bonds have been classified into three different types: (i) weak or double-well hydrogen bonds, (ii) moderate or low barrier hydrogen bonds, and (iii) very strong or single-well hydrogen bonds (Prins *et al.*, 2001). Classification and properties of hydrogen bonds adapted from Table 1 in *The Weak Hydrogen Bond in Structural Chemistry and Biology* by Desiraju and Steiner (1999) and Table 1.2 in *Core Concepts in Supramolecular Chemistry and Nanochemistry* by Steed, Turner, and Wallace (2007), are listed in Table 1.2.

Table 1.2 Classification and properties of hydrogen bonds.

Interaction/property	Strong	Moderate	Weak
D–H···A	Mainly covalent	Mainly electrostatic	Electrostatic
Bond energy (kJ mol ⁻¹)	60–120	16–60	< 12
Bond length (Å)	D–H ≈ H···A	D–H < H···A	D–H ≪ H···A
Lightening of D–H (Å)	0.05–0.2	0.01–0.05	≤ 0.01
H···A (Å)	1.2–1.5	1.5–2.2	2.2–3.2
D···A (Å)	2.2–2.5	2.5–3.2	3.2–4.0
Bonds shorter than H···A vdW separation (%)	100	Almost 100	30–80
D–H···A angle (°)	175–180	130–180	90–150
Effect on crystal packing	Strong	Distinctive	Variable
Utilized in crystal engineering	Unknown	Useful	Partly useful
Covalency	Pronounced	Weak	Vanishing
Electrostatic contribution	Significant	Dominant	Moderate
Examples	[F···H···F] ⁻ [F···H···N] ⁺ [F–OH···O=P]	Acids Alcohols DNA/RNA	C–H···A D–H···π

Cation- π interactions (4–120 kJ mol⁻¹) are a noncovalent molecular interaction between the face of an electron-rich π system, a quadrupole *eg.* benzene, ethylene, with an adjacent cation, a monopole *eg.* Li⁺, Na⁺, K⁺ (Mecozzi *et al.*, 1996; Ma and Dougherty, 1997; Gokel *et al.*, 2002), Figure 1.13. Cation- π interaction energies are of the same order of magnitude of hydrogen bonds, and play an important role in molecular recognition (Dougherty, 1996). Numerous examples of cation- π interactions in many organic and biochemical systems have been recently reported (Meyer *et al.*, 2003).

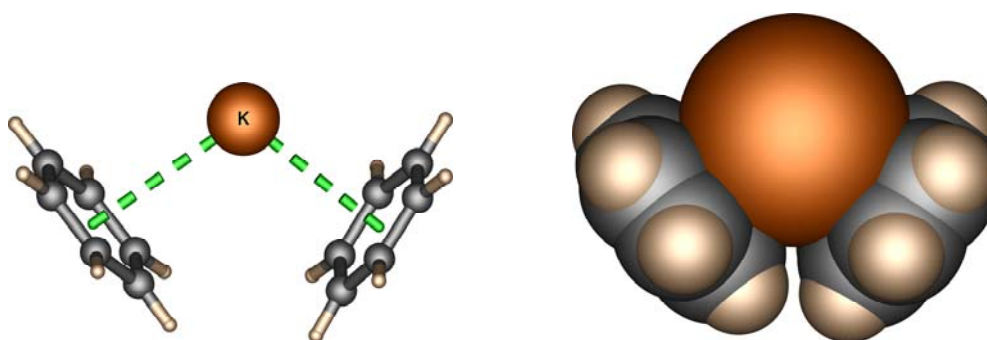


Figure 1.13 Cation- π interactions between benzene and a potassium cation.

Anion- π interactions are binding interactions between an electron-rich molecule and a π -acidic heteroaromatic ring (Quiñonero *et al.*, 2002; Mooibroek *et al.*, 2008). Such interactions are opposite to cation- π interaction and significantly fewer examples of anion- π interactions are known to date. However examples are increasingly reported in the recent literature of both experimental and theoretical investigations (Hoog *et al.*, 2004; Mascari *et al.*, 2007; Quiñonero *et al.*, 2007; Zhou *et al.*, 2007). The anion- π effect is advantageously exploited in chemical sensors for specific anions (Francis *et al.*, 2004). An illustrative example of this category has

been recently reported by Dunbar and co-workers. As shown in Figure 1.14, this structure displays $[\text{SbF}_6]^-$ anions encapsulated inside cavities formed by five 1,2,4,5-tetrazine rings of 3,6-bis(2-pyridyl)-1,2,4,5-tetrazine (bptz) ligands. The $[\text{SbF}_6]^-$ centroid distances are between 3.275 and 3.517 Å, which are indicative of strong anion- π interactions (Campos-Fernandez *et al.*, 2005). In a subsequent recent paper, Dunbar and co-workers have also used same ligand (bptz) and a related one, 3,6-bis(2'-pyridyl)-1,2-pyridazine (bppn) with the AgX salts ($\text{X}^- = [\text{BF}_4]^-$, $[\text{AsF}_6]^-$, $[\text{PF}_6]^-$, and $[\text{SbF}_6]^-$) to further explore of anion- π interactions (Schottel *et al.*, 2006). From the systems studied, the authors concluded that anion- π interactions play an important role in the outcome of self-assembly reactions.

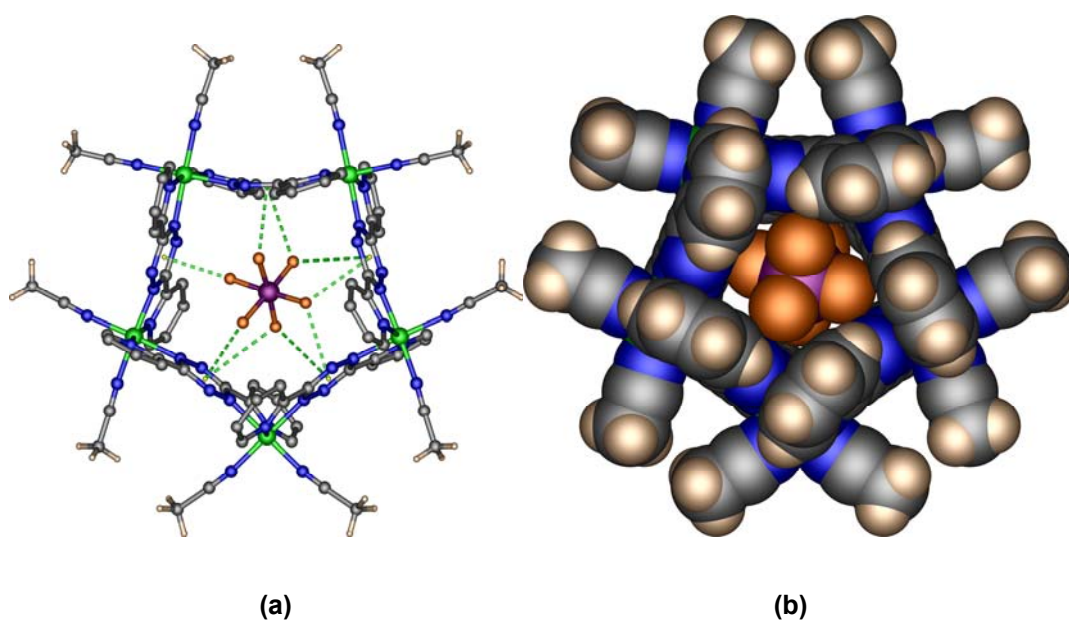


Figure 1.14 (a) Ball-stick and (b) space-filling representations, showing anion- π interactions in $[\{\text{Ni}_5(\text{bptz})_5\text{C}(\text{CH}_3\text{CN})_{10}\}\text{SbF}_6](\text{SbF}_6)_9$. Drawn from coordinates from CSD, after Campos-Fernandez *et al.*, 2005.

π - π interactions (0 – 50 kJ mol^{-1}) are weak electrostatic interactions that occur between aromatic moieties which can interact in different physical arrangements: face-to-face stacked arrangement (offset, slipped, or parallel displaced), and edge-to-face or point-to-face, T-shaped conformations. These orientations come from $\text{C-H}\cdots\pi$ interactions between positively charged hydrogen atoms (the C-H bond generally having a small dipole moment) and a negatively charged π -cloud of the aromatic system. The perfect facial alignment of an eclipsed face-to-face orientation is unlikely because all the electrostatic interactions would be repulsive between the two negatively charged π -systems of the aromatic rings and between the positive ends of the C-H dipoles (Hunter and Sanders, 1990). The distance between the aromatic faces in a π - π interaction is *ca.* 3.3 – 3.8 \AA (Janiak, 2000). Types of aromatic–aromatic interactions are illustrated in Figure 1.15.

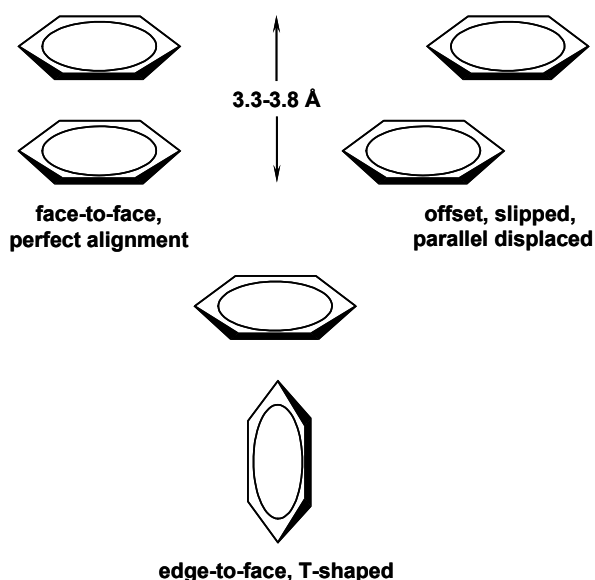


Figure 1.15 Schematic representations of aromatic–aromatic interactions.

A representative example is provided in the stacking of 1,3,5-tris(phenethynyl)benzene and 1,3,5-tris(perfluorophenethynyl)benzene in the solid state as shown in Figure 1.16. While the former slipped stacks with their terminal aryl rings twisted with respect to the plane of the central ring when crystallized separately, the 1:1 heterocomplex is essentially planar with markedly less slippage. These results provide excellent evidence for the structural control attainable when using the phenyl-perfluorophenyl synthon (Ponzini *et al.*, 2000).

Metallophilic interactions, in this thesis, refer to (i) *argentophilic* ($\text{Ag}^{\text{I}}\cdots\text{Ag}^{\text{I}}$), (ii) *aurophilic* ($\text{Au}^{\text{I}}\cdots\text{Au}^{\text{I}}$), and (iii) *cuprophilic* ($\text{Cu}^{\text{I}}\cdots\text{Cu}^{\text{I}}$) interactions. These interactions are useful tools for constructing supramolecular structures in the solid state (Fu *et al.*, 2004; Mohr *et al.*, 2004; Chu *et al.*, 2005). The strengths of the argentophilic interactions are within the range of typical hydrogen bonds. Compared with aurophilic interactions (25–50 kJ mol^{-1}), argentophilic interactions are weaker but stronger than the related cuprophilic interactions (up to 16 kJ mol^{-1}). Theoretical studies on dimeric models of linear two-coordinate complexes indicate that metalophilicity decreases as $\text{Au}^{\text{I}} > \text{Ag}^{\text{I}} > \text{Cu}^{\text{I}}$ (Magnko *et al.*, 2002). Representative examples of argentophilic interactions can be found in a recent review by Young and Hanton (2008).

van der Waals interactions ($< 5 \text{ kJ mol}^{-1}$) are dispersion forces of relatively weak intermolecular interactions of two components, *i.e.* the *London* interactions and the *exchange* and *repulsion* interactions (Scheider, 2004). These interactions are non-directional, and do not feature highly in supramolecular design but they are important in the formation of inclusion compounds (Steed *et al.*, 2007).

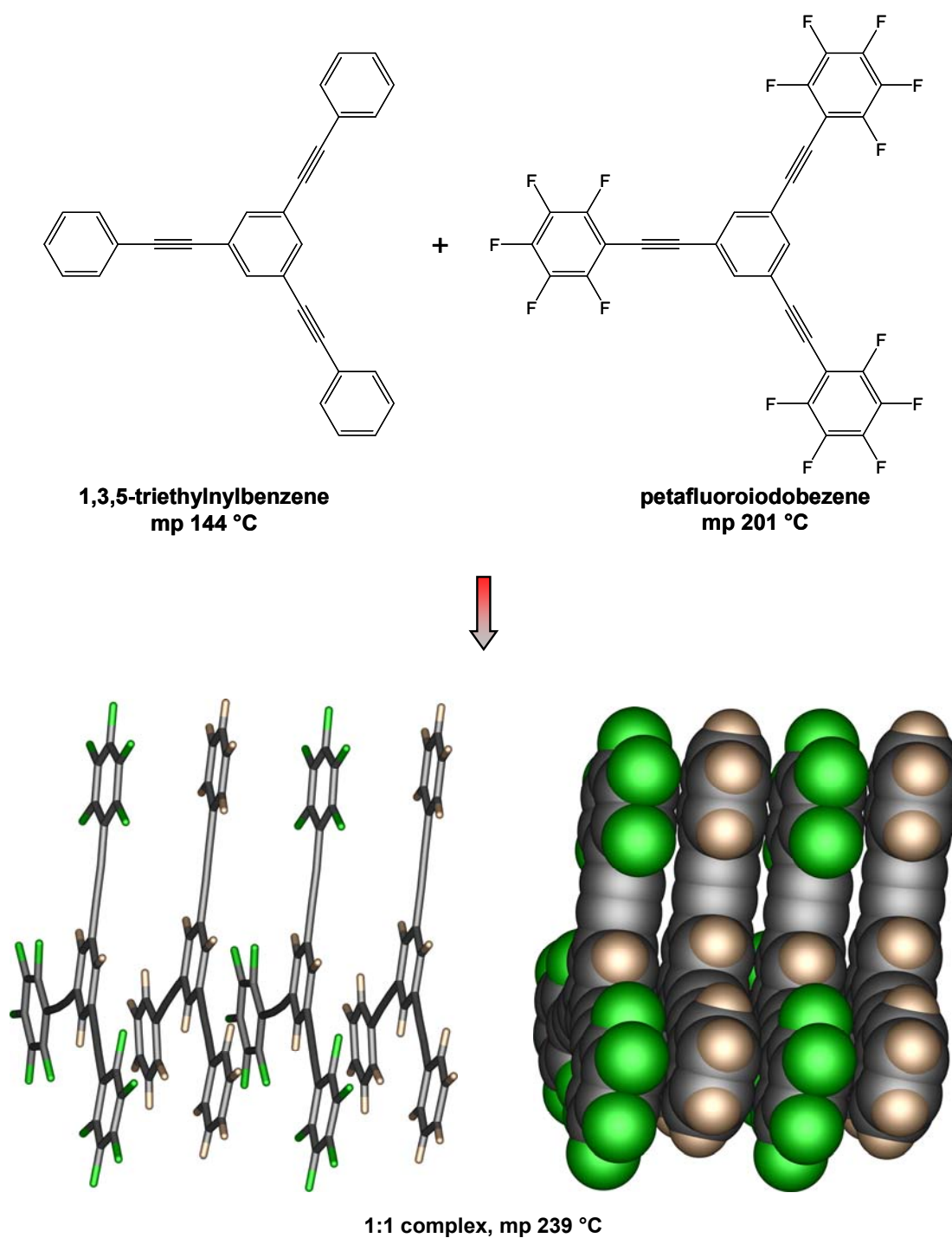


Figure 1.16 π - π interactions between *sym*-triphenylbenzene and *sym*-tris(perfluorophenyl)benzene. Drawn from coordinates from CSD, after Ponzini *et al.*, 2000.

Hydrophobic effects are the properties of those non-polar molecules that tend to form intermolecular aggregates in aqueous medium and analogous intramolecular interactions (Blokzijl and Engberts, 1993; Chandler, 2005). These interactions are of importance in many chemical and/or biological disciplines, including the chemistry of *in vivo* processes, enzyme-substrate interactions, the assembly of lipids in biomembranes, surfactant aggregation, and kinetic solvent effects in water-rich solutions (Pratt and Pohorille, 2002). Atwood and co-workers have described a simple model system that exemplifies proton transfer in a largely hydrophobic environment of calix[4]arene anion, NH_4 cation and molecule of NH_3 . They show that the overriding preference for the ammonium cation is to associate directly with the deprotonated phenolic oxygen atom. This suggests that electrostatic interactions may play a key role in the stabilization of intermediate species in the initial stages of complex multistep proton-transfer processes such as those found in biological systems. This represents one example of such effects that occurred in supramolecular systems (Atwood *et al.*, 2002).

Noncovalent interactions play an important role in chemistry and especially in biology. Due to the presence of a great number of cation- π and π - π interactions in biological systems, this effect is important and helps us understand some biological processes where the interplay between both interactions exist. Today, it also should be taken into account in the supramolecular chemistry of the crystal engineering field, the design of new solids with desired physical and chemical properties.

1.2. Crystal Engineering of Coordination Polymers

Single crystals are the most orderly manifestations of any state of matters, and are also the perfect example of a supramolecular assembly (Desiraju, 2003). The term “*crystal engineering*” was defined by G. R. Desiraju in 1989 as “*the understanding of intermolecular interactions in the context of crystal packing and the utilization of such understanding in the design of new solids with desired physical and chemical properties*” (Desiraju, 1989). Crystal engineering and design of solid-state architectures has become an area of recent increasing interest. (Batten and Robson, 1998; Moulton and Zaworotko, 2001; Hollingsworth, 2002; Yaghi *et al.*, 2003; Kitagawa *et al.*, 2004; Sieklucka *et al.*, 2005; Khuong *et al.*, 2006; Glaser, 2007).

Metal ligand compounds formed *via* coordination bonds that extend infinitely into 1-D to 3-D, are called “*coordination polymers*” (Batten, 2001; 2004). The crystal engineering of coordination polymers has received considerable attention in recent years since the first steps were taken with the seminal reports of Prof. Richard Robson, University of Melbourne, in eighteen years ago (Robson and Hoskins, 1990). Presently, this field is an attractive area of research owing to the inherent stability of coordination bonds and also to the versatility of coordination modes of transition metal atoms. The predictable formation of coordination networks in order to design the entire crystal lattice have often been proposed or supported for the targeted synthesis of new materials (Ockwig *et al.*, 2005; Champness, 2006).

1.2.1 Topology

One conceptual approach to building framework structures or topologies is based on the idea of a net (*consisting of a collection of points or nodes*). According to Wells (Wells, 1977), one notation for describing the topologies of coordination

networks in terms of the connectivity of the nodes has the general symbol (n, p) , where n is the number of nodes in the smallest closed circuits in the net, and p is the number of connections to neighboring nodes that radiate from any center or node. A more complete notation of Schläfli symbols is also described (Batten and Robson, 1998).

The topology of 3-D networks can be described in similar manners. Some 3-D structures have recently been reported to have the following topologies: boracite, CdSO_4 , CaB_6 , NbO , perovskite, Pt_3O_4 , PtS , rutile, SrSi_2 , and tungsten bronze (Batten and Robson, 1998; Robson, 2000; Delgado-Friedrichs *et al.*, 2005). The simplest infinite 3-D nets are depicted in Figure 1.17, and listed in Table 1.3.

1.2.2 Synthetic Strategies

The most significant goals in the field of crystal engineering are to tailor the chemical and/or physical properties of crystalline solids through crystal design at the molecular level (Seddon and Zaworotko, 1999; Braga and Crepioni, 2007). Two different design philosophies have been employed: (i) to use coordination bonds and (ii) to use highly directional hydrogen bonds and/or other weak electrostatic interactions as a very powerful and versatile strategy in material synthesis and/or controlling self assembly in supramolecular systems.

In theory, through the careful choice of metal ions, ligands and framework motifs can be rational synthesized to realize a certain desired framework. For example, if a tetrahedral node is employed, most commonly a tetrahedrally coordinating transition metal cation *eg.* Cu(I) , then by far the most commonly observed structure is the diamond net (Hoskins and Robson, 1990). However, in fact, there are several factors such as metal to ligand ratios, metal coordination modes and

the presence of anions and guest molecules, which affects the formation of the expected polymeric or discrete supramolecular aggregates.

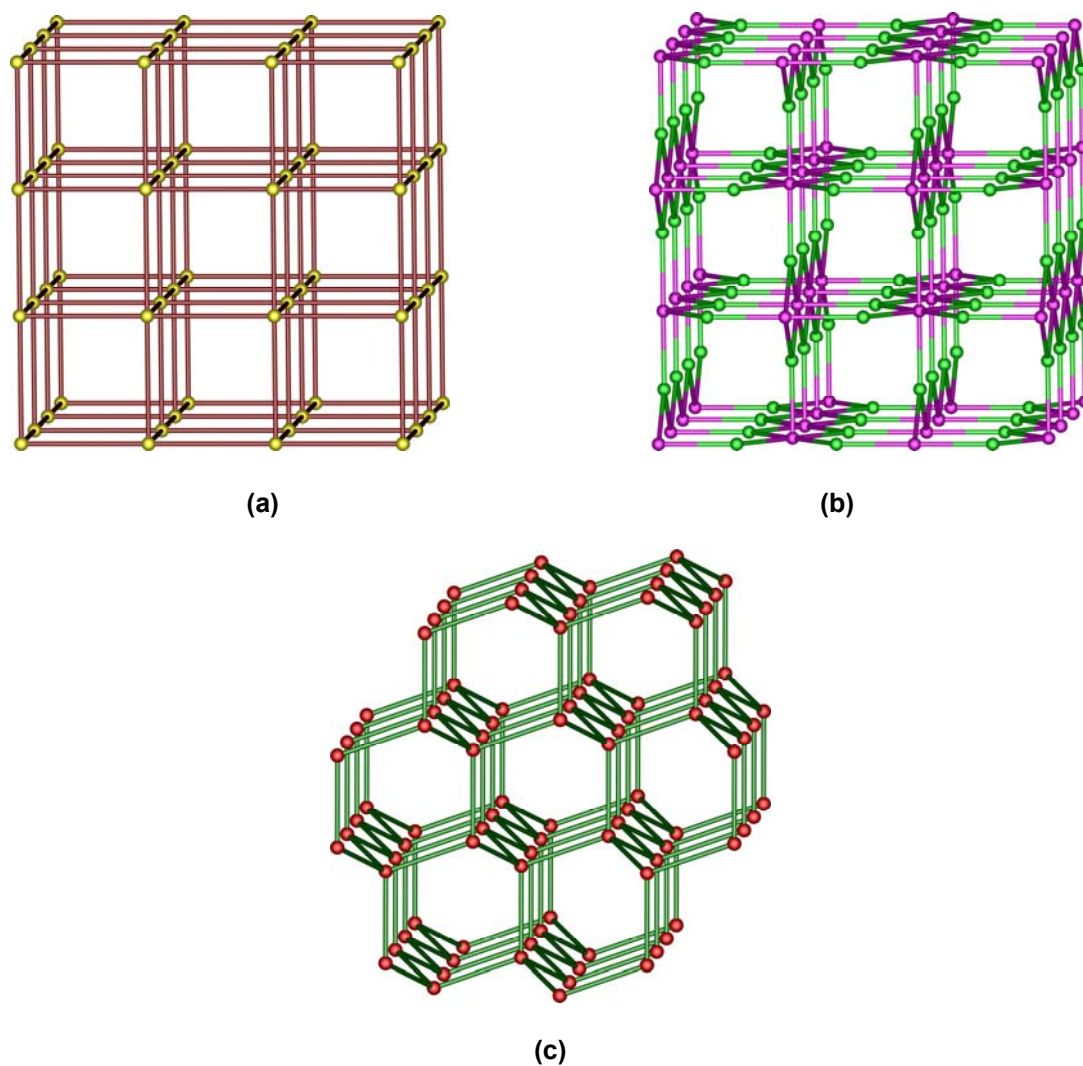


Figure 1.17 Some of the simplest infinite 3-D nets. (a) the 6-connected in α -Po net (or NaCl), (b) the (3,6)-connected in rutile net and (c) the 4-connected in diamond net.

Table 1.3 Some selected examples of possible prototypes.

Center A	Center B	Ratio	Prototype
Octahedral	–	–	α -Po
Octahedral	Trigonal	1:2	Rutile (TiO ₂), α -PbO ₂
Tetrahedral	–	–	Diamond
	–	–	Lonsdalite
Tetrahedral	Square Planar	1:1	PtS
Tetrahedral	Trigonal	3:4	Ge ₃ N ₄
Square Planar	–	–	NbO
Square Planar	Trigonal	3:4	Na _x Pt ₃ O ₄
Trigonal	–	–	ThSi ₂

(Batten, 1995)

The preferred coordination number and geometry of the metal ion is one of important factors influencing the formation of a coordination network. Divalent and trivalent first-row transition metals have well known coordination preferences that often depend upon the identity of the ligand environment. For example, Cr^{III} is always octahedral, while Mn^{II} is typically octahedrally coordinated by oxygen. Co^{II} is more versatile and ranges from tetrahedral through pentacoordinated to octahedral, while Ni^{II} is usually octahedral when surrounded by oxygen, but may be square planar in nitrogen environments. Isolated Cu^{II} is relatively inflexible, and is constrained by its need to accommodate the *Jahn-Teller* distortion that is characteristic of d⁹ ions. Zn^{II}, which has been widely used in studies on hybrid frameworks, is very versatile and behaves somewhat like Co^{II}.

For example, the rigid rod-like bidentate ligand of 4,4'-bipyridine (4,4'-bipy) reacts with different transition metal cations to yield very different final products depending on the metal centers. Yaghi and Li (1996) have shown how the 4,4'-bipy

ligand reacts with AgNO_3 under mild hydrothermal condition to form extended 1-D chains, Figure 1.18a. Interestingly, adjacent chains are cross-linked in an almost perpendicular fashion by *argentophilic* ($\text{Ag}\cdots\text{Ag}$) interactions leading to a 3-D open network. Recently, Pedireddi and co-workers have used the 4,4'-bipy ligand with Cu(I) centers in the presence of an ionic liquid of 1-ethyl-3-methylimidazolium tetrafluoroborate to synthesize a diamondoid network, Figure 1.18b, in which each copper has tetrahedral geometry (Pedireddi *et al.*, 2006). In contrast, the product obtained from a hydrothermal reaction was found to be a polymer containing trigonal metal ions (MacGillivray *et al.*, 1994). Subramanian and Zaworotko (1995) have found that the 2-D square grid networks formed by the 4,4'-bipy ligand with Zn(II) can be linked with $[\text{SiF}_6]^-$ counter ions in order to form a 3-D network with large channels, Figure 1.8c.

The role of the anions in the systems is clearly very important. Bu and co-workers have reported that the reactions of various Cu(II) salts with 2,5-bis(3-pyridyl)-1,3,4-oxadiazole in $\text{CH}_3\text{CN}/\text{H}_2\text{O}$ medium affords different complexes depending on the nature of the copper salt's counter ion (Du *et al.*, 2003). Similarly, recently studies by Dong and co-workers (Dong *et al.*, 2007) focused on temperature and anion-dependent synthesis of metal-organic frameworks. The authors have used a flexible ethylene glycol ether-bridging tetradentate ligand with bidirectional coordination donors of AgX ($\text{X} = \text{BF}_4^-$ or SbF_6^-) to synthesize four Ag coordination polymers. Recently, it has been demonstrated that a pentamer can also be templated by counter anion such as bromide or iodide (García *et al.*, 2004).

The influence of different ancillary solvent ligands such as CH_3CN , CH_3OH , and H_2O on the crystallization process is also one of factors affecting the formation of

the final network structure (Lee *et al.*, 2004; Dong *et al.*, 2006). For example, Wang and co-workers examined the solvent effects on the network structure formed. The authors used a flexible ligand $\text{dpap} \cdot 2\text{H}_2\text{O}$ ($\text{dpap} = 2,6\text{-}(N,N'\text{-di}(4\text{-pyridyl})\text{amino})\text{pyridine}$) with 2 equivalents of $\text{Cu}(\text{CH}_3\text{COO})_2 \cdot 2\text{H}_2\text{O}$ in various solvents (CH_3CN , CH_2Cl_2 , CHCl_3 and CH_3OH), and obtained five coordination polymers in which the structures are influenced by the nature of the solvent (Wang *et al.*, 2007).

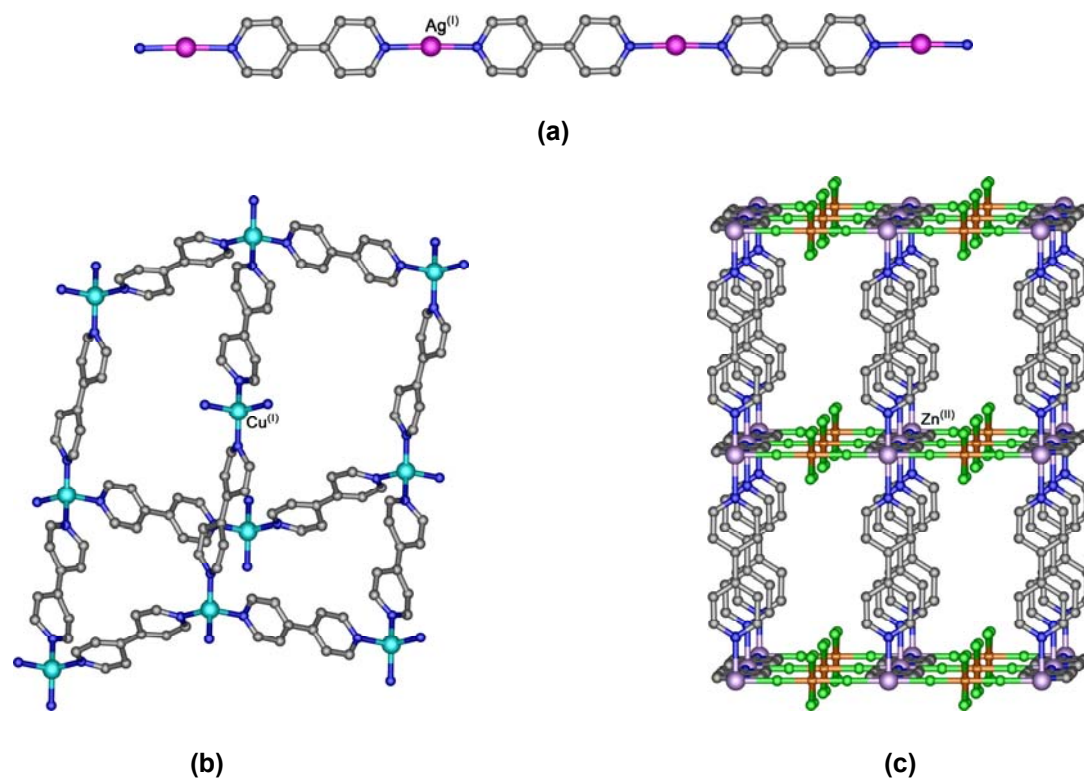


Figure 1.18 Coordination polymers compounds formed by the 4,4'-bipy bridging ligand with difference metal centers: (a) 1-D chain in $[\text{Ag}(4,4'\text{-bipy})](\text{NO}_3)$, (b) diamondoid network in $[\text{Cu}(4,4'\text{-bipy})](\text{NO}_3)$, and (c) 3-D network in $[\text{Zn}(4,4'\text{-bipy})_2(\text{SiF}_6)]_n \cdot x\text{DMF}$. Drawn from coordinates from CSD.

Many challenges in crystal engineering are still on the angstrom scale, but it may be extended to a controlled formation of nano-structured systems and even into the mesoscopic range, where optoelectronics and photonics open up new horizons for organic solids. Metal-organic frameworks (MOFs), a class of nanoporous coordination polymers, are of significant contemporary interest due to scientific interest in the creation of nanometer-sized spaces and their potential applications in molecular sieves, gas storage and heterogeneous catalysis (Yaghi *et al.*, 2003; Kitagawa *et al.*, 2004; Ferey *et al.*, 2005). Early examples in the MOFs area can be found in the work of the groups of Yaghi (Li *et al.*, 1999), Rossensinsky (Kepert *et al.*, 1999) and Williams (Chui *et al.*, 1999) in the late 1990s. Recently, several excellent comprehensive reviews on coordination networks have been reported (Kitagawa *et al.*, 2004; 2007; Kawano and Fujita, 2007; Fromm *et al.*, 2008; Suh *et al.*, 2008).

1.3 Molecule-Based Magnetic Materials

The history of magnetism dates back to earlier than 600 B.C., but it is only in the twentieth century that scientists have begun to understand it, and develop technologies based on this understanding. Magnetic materials are essential for the operation of many of the devices used in modern industry such as recording devices. Depending on their ability to retain magnetization over long times, magnets are divided into two groups. “Soft” magnetic materials that lose their magnetic moment completely if the applied magnetic field is removed. “Hard” magnetic materials that keep their magnetic moment over many years without applying a magnetic field. Presently, the hard ferrites are the most used commercially available magnets, but

rare-earth-based magnets are developing rather quickly, both qualitatively and quantitatively.

All materials have an inherent magnetic character arising from the movements of their electrons. Magnetic properties arise from the interactions of unpaired electrons spins. These properties are traditionally found in transition metals, lanthanides, and their compounds due to the unpaired d- and f-electrons on the metal. In paramagnets, the net magnetic moment of the bulk material is zero due to the spin sites behaving independently and undergoing thermal motion. However, when a strong magnetic field is applied, the spins tend to align parallel to the field direction and it responds by producing a magnetic field, called the magnetization, M (Kahn, 1993; Miller and Drillon, 2002). This magnetization is defined as the amount of magnetic moment per unit volume of the materials. The field that is applied to the material is called the applied field, H , and is the total field that would be present if the field were applied to a vacuum. Another important parameter is the magnetic flux density, B (Kahn, 1993). When magnetic materials are placed in the field, the density of the lines of forces is decreased or increased for diamagnetic or paramagnetic materials, respectively. B , H and M are related by Eq. 1.1 in S.I. units.

$$B = \mu_0(H + M) \quad \text{Eq. 1.1}$$

where μ_0 is the magnetic constant.

However, the magnetization is usually discussed in terms of the degree of magnetization of a material in response to an applied magnetic field, and it is called the magnetic susceptibility, χ (Kahn, 1993; Miller and Drillon, 2002). Experimentally, in this work the M value is obtained from the SQUID instrument output and it is then

converted into χ_g (per gram), Eq. 1.2.

$$\chi = \frac{M}{H}$$

$$\chi_g = \frac{M}{H \times \text{mass(g)}} \quad \text{Eq. 1.2}$$

In magnetochemistry, χ_g is converted to the molar susceptibility, (χ_M) and the ligand diamagnetic contributions are made, Eq. 1.3. χ_{dia} is a negative term, and is obtained from Pascal's tables or measured directly.

$$\chi_M = \chi_g \times (\text{MW}) - \chi_{\text{dia}} \quad \text{Eq. 1.3}$$

Accordingly, the Curie-Weiss law indicates that the molecular susceptibility (χ_M) of paramagnetic materials is inversely proportional to their Kelvin temperature (T), Eq. 1.4. This law is only valid under conditions of when χ is independent of the applied magnetic field (H). This is the linear region of the M versus H plot given in 20 for paramagnets and ferromagnetic coupling at low H values.

$$\chi_M = \frac{C}{T - \Theta} \quad \text{Eq. 1.4}$$

where C is the Curie constant, Θ is the Weiss constant.

The χ_M values are often transformed into the effective magnetic moment, μ_{eff} (Kahn, 1993; Miller and Drillon, 2002). When Θ is zero in Eq. 1.4 (Curie law, $\chi_M = C/T$), this is independent of temperature as well as external field strength for paramagnetic materials which is a convenient measure of a material's magnetic

properties. The μ_{eff} is defined in Eq. 1.5, has the non S.I. unit of Bohr Magnetron (B.M., μ_B or β), and χ_M is in $\text{cm}^3 \text{mol}^{-1}$.

$$\mu_{\text{eff}} = \left(\frac{3k}{N(\mu_B)^2} \right)^{1/2} \sqrt{\chi_M T}$$

$$\mu_{\text{eff}} = 2.828 \sqrt{\chi_M T} \mu_B \quad \text{Eq. 1.5}$$

where k is Boltzmann constant, N is Avogadro's number

It is common now to use $\chi_M T$ (in $\text{cm}^3 \text{mol}^{-1} \text{K}$) at a particular T instead of converting to μ_{eff} .

For first row transition metal ions in the free ion state, *i.e.* isolated ions in a vacuum, all five 3d orbitals are degenerate. In octahedral complexes, a simple crystal field theory approach suggests that for these ions the d orbitals are no longer degenerate but are split such that two orbitals, the $d_{x^2-y^2}$ and the d_{z^2} are at higher energy than the d_{xy} , d_{xz} , d_{yz} . For ions with between four and seven d electrons, this gives rise to two possible arrangements called high-spin or low-spin (or weak-field or strong-field), respectively. The energy gap, Δ_{oct} , is dependent on the position of the coordinated ligands in the spectrochemical series (Cotton *et al.*, 2006). In tetrahedral complexes the orbitals are again split, such that two orbitals (the $d_{x^2-y^2}$ and the d_{z^2}) are now at lower energy than the remaining three. Tetrahedral complexes are all high spin since the difference between the two subsets of orbitals is much smaller than is found in octahedral complexes ($\Delta_{\text{tet}} = 4/9 \Delta_{\text{oct}}$). The “spin-only” formulae most frequently used to calculate magnetic moment of first row transition metal ion

complexes is given in Eq. 1.6. When the ground term for the metal ion is either A_{2g} or E_g , spin-orbit coupling can “mix-in” some orbital degeneracy from higher T terms and in orbitally non-degenerate systems ($d_{tet}^1, d_{oct}^9; d_{tet}^2, d_{oct}^8; d_{tet}^3, d_{oct}^7; d_{tet}^4, d_{oct}^6; d_{tet}^5, d_{oct}^5$) Eq. 1.7 is used.

$$\begin{aligned}\mu_{\text{eff}} &\approx \mu_{\text{spin-only}} = 2\sqrt{S(S+1)} \mu_B \\ &= \sqrt{n(n+2)} \mu_B\end{aligned}\quad \text{Eq. 1.6}$$

$$\mu_{\text{eff}} = \mu_{\text{spin-only}} \left(1 - \frac{\alpha\lambda}{\Delta}\right) \quad \text{Eq. 1.7}$$

where S is total spin (*eg.* $S = 3/2$ for d^3), n is number of unpaired spins (*eg.* 3 for d^3), α is a constant = 2 for E and 4 for A ground terms, λ is the spin orbit coupling constant, and Δ is the crystal field splitting parameter that can often be obtained from the visible spectrum of the complex. The calculated spin-only and experimental of magnetic moment data for some octahedral complexes are listed in Table 1.4. Note that Eq. 1.7 yields Curie-Weiss behavior (Eq. 1.4), except for d_{oct}^5 (${}^6A_{1g}$) which is Curie, and a small temperature dependent μ_{eff} results from Eq. 1.5 (Kahn, 1993).

Note also that the deviations from Eq. 1.7 that μ_{obs} show (*eg.* Ni(II) oct, μ_{obs} *ca.* $3.1 \mu_B$; $\mu_{\text{spin-only}} = 2.83 \mu_B$) depend on the size and sign of λ (negative for d^8 , Ni(II)) and on the size of α and Δ . The μ_{obs} values often, but not always, differ significantly for T ground term systems because the orbital degeneracy is affected directly by spin orbital coupling. Curie-Weiss law applies to χ_M and Θ can be large and negative so that μ_{eff} varies with temperature.

Table 1.4 Comparison of calculated spin-only magnetic moments with experimental data for some octahedral complexes.

Ion	Configuration	Ground term	$\mu_{\text{spin-only}} (\mu_{\text{B}})$	$\mu_{\text{obs}} (\mu_{\text{B}})$
Ti ^(III)	d ¹ (t _{2g} ¹)	² T _{2g}	(3) ^{1/2} = 1.73	1.6–1.7
V ^(III)	d ² (t _{2g} ²)	³ T _{1g}	(8) ^{1/2} = 2.83	2.7–2.9
Cr ^(III)	d ³ (t _{2g} ³)	⁴ A _{2g}	(15) ^{1/2} = 3.88	3.7–3.9
Cr ^(II)	d ⁴ high spin (t _{2g} ³ e _g ¹)	⁵ E _g	(24) ^{1/2} = 4.90	4.7–4.9
Cr ^(II)	d ⁴ low spin (t _{2g} ⁴)	³ T _{1g}	(8) ^{1/2} = 2.83	3.2–3.3
Mn ^(II) /Fe ^(III)	d ⁵ high spin (t _{2g} ³ e _g ²)	⁶ A _{1g}	(35) ^{1/2} = 5.92	5.6–6.1
Mn ^(II) /Fe ^(III)	d ⁵ low spin (t _{2g} ⁵)	² T _{2g}	(3) ^{1/2} = 1.73	1.8–2.1
Fe ^(II)	d ⁶ high spin (t _{2g} ⁴ e _g ²)	⁵ T _{2g}	(24) ^{1/2} = 4.90	5.1–5.7
Co ^(III) , Fe ^(II)	d ⁶ low spin (t _{2g} ⁶)	¹ A _{1g}	0	0–0.6 ^[*]
Co ^(II)	d ⁷ high spin (t _{2g} ⁵ e _g ²)	⁴ T _{1g}	(15) ^{1/2} = 3.88	4.3–5.2
Co ^(II)	d ⁷ low spin (t _{2g} ⁶ e _g ¹)	² E _g	(3) ^{1/2} = 1.73	1.8
Ni ^(II)	d ⁸ (t _{2g} ⁶ e _g ²)	² A _{2g}	(8) ^{1/2} = 2.83	2.9–3.3
Cu ^(II)	d ⁹ (t _{2g} ⁶ e _g ³)	² E _g	(3) ^{1/2} = 1.73	1.7–2.2

[*]Second order field effects (Zeeman), H^2 , can give small positive μ_{eff} values, the corresponding χ_{M} called “temperature independent susceptibility”, TIP.

1.3.1 Classification of Magnetic Materials

The origin of magnetism lies in the orbital and spin motions of electrons, and how the electrons interact with one another and with the field, H . The magnetic moments associated with atoms have three origins. These are the electron orbital motion, the change in orbital motion caused by an external magnetic field, and the spin of the electrons. The magnetic behavior of materials can be classified into the following five major groups depending on their bulk magnetic susceptibility as shown in Figures 1.19 and 1.20. A summary of different types of magnetic behavior

for each type of material is listed in Table 1.5.

Diamagnetism: the substances are composed of atoms which have no net magnetic moments when there is no applied field, namely, all the orbital shells are filled, and there are no unpaired electrons (Figure 1.19a). However, when exposed to a field, they have a very weak and negative susceptibility to magnetic fields. Most elements in the periodic table, including d- and f-block metal ions are diamagnetic. Of importance here are the diamagnetic ligands.

Paramagnetism: the unpaired electrons are randomly arranged, Figure 1.19b. Their properties are due to the presence of some unpaired electrons, and from the of the electron orbits caused by the external magnetic field. However, when the field is removed, the individual magnetic moments do not interact magnetically (like diamagnetism), the magnetization is zero. Paramagnetic materials include most mononuclear d- and f-blocks complexes.

Ferromagnetism: the unpaired electrons are all aligned parallel (Figures 1.19c, and 1.19d). The materials have a large and positive susceptibility to an external magnetic field. They exhibit a strong attraction to magnetic fields, and are able to retain their magnetic properties after the external field has been removed. Ferromagnetic materials have some unpaired electrons, and their atoms have a net magnetic moment. They get their strong magnetic properties due to the presence of magnetic domains. In these domains, the unpaired electron spins to line up parallel with each other in a region so that the magnetic force within the domain is strong. When a ferromagnetic material is in the unmagnetized state, the domains are nearly randomly organized, and the net magnetic field for the part as a whole is zero. When

a magnetizing force is applied, the domains become aligned to produce a strong magnetic field within the part.

All ferromagnets have a maximum temperature where the ferromagnetic property disappears as a result of thermal agitation. Below this temperature all spins are “ordered”. This temperature is called the Curie temperature, T_C (Kahn, 1993; Miller and Drillon, 2002). Metals such as, Fe ($T_C = 770\text{ °C}$), Co ($T_C = 1131\text{ °C}$) and Ni ($T_C = 358\text{ °C}$) are ferromagnetic at and above room temperature. The Curie temperature is an essential temperature for a ferromagnetic material. At temperature below the Curie temperature, the material has a net spontaneous magnetization, which means that the material becomes ferromagnetic, or “magnetic”. If a ferromagnetic material is at a temperature above its Curie temperature, then the material becomes paramagnetic the spins are randomized, and it is no longer a “magnet”.

Antiferromagnetism: the unpaired electron spins are lined up parallel opposite of one another (Figure 1.19e). The clue to antiferromagnetism is the behavior of susceptibility above a critical temperature, called the Néel temperature, T_N , (Kahn, 1993; Miller and Drillon, 2002). Above T_N , the susceptibility obeys the Curie-Weiss law for paramagnets but with a negative intercept (θ) indicating negative exchange coupling interactions. Note that this is a different reason for negative θ than described on page 38 for monomeric compounds. The only metallic element exhibiting antiferromagnetism at room temperature is chromium. Oxides such as MnO are classical antiferromagnets.

Ferrimagnetism: the electron spins are orientated antiparallel to one another but, due to an inequality in the number of spins in each orientation, there exists an

overall (net) magnetic moment, (Figure 1.19f). Ferrimagnetism is only observed in compounds which have more complex crystal structures than have pure the metallic elements. Metal oxides such as iron oxides are ferrimagnetic materials.

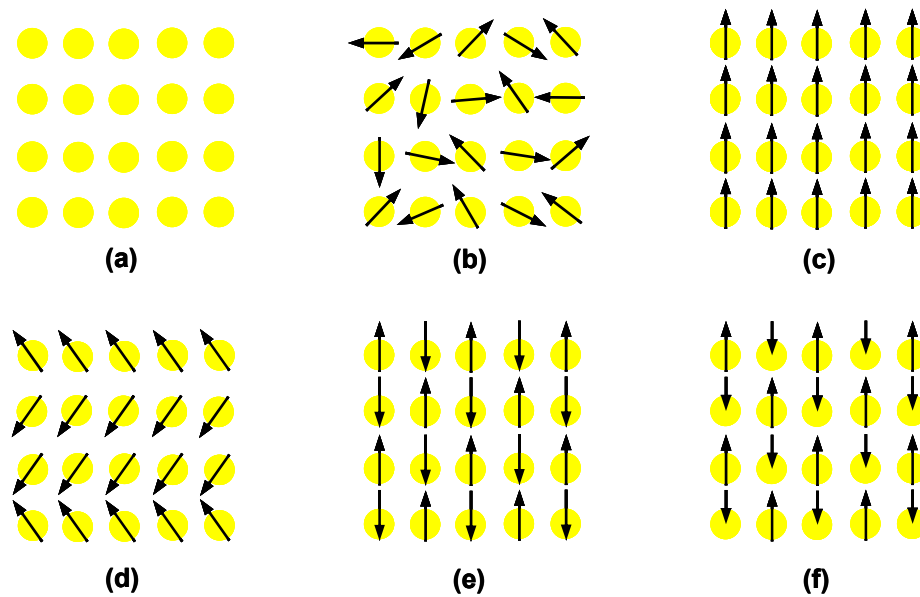


Figure 1.19 2-D representation of spin alignment for (a) diamagnet, (b) paramagnet, (c) ferromagnet, (d) canted ferromagnet, (e) antiferromagnet, and (f) ferrimagnet behavior. Redrawn after Miller and Epstein, 1994.

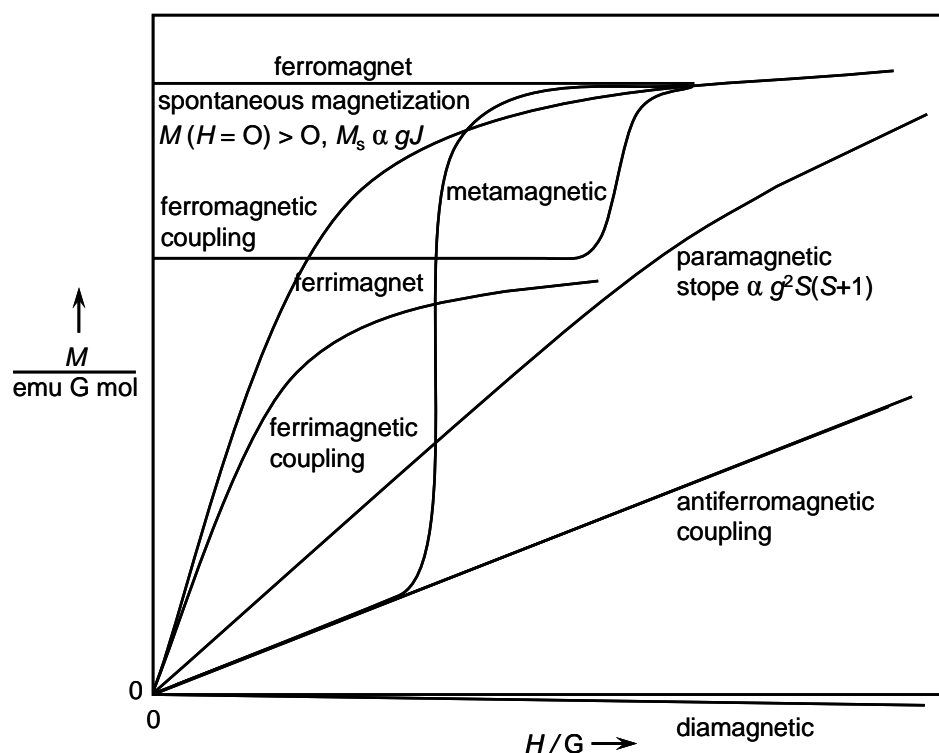


Figure 1.20 Schematic illustration of the magnetization, M , as a function of applied magnetic field, H , for several types of commonly observed in magnetic behavior. Redrawn after Miller *et al.*, 1988.

Of particular relevance to the present study is the subject of molecular materials (molecular-based magnets) that has developed vigorously during the last twenty years. These d- or f-block metal-organic compounds contain, usually, bridging ligands (such as CN^-) that “couple” spins on neighboring metal ions such that long-range order of the types shown in Figure 1.19 can occur below T_C (or T_N) temperatures that are usually well below room temperature.

Table 1.5 Summary of different types of magnetic behavior.

Type	Susceptibility, χ_M	Atomic (metals) ^[a]
Diamagnetic	Small & negative	Atoms have no magnetic moment
Paramagnetic	Small & positive	Atoms have randomly oriented magnetic moments
Ferromagnetic	Large & positive, function of applied field ^[b] , microstructure dependent	Atoms have parallel aligned magnetic moments
Antiferromagnetic	Small & positive close to zero	Atoms have mixed equal antiparallel aligned magnetic moments
Ferrimagnetic	Large & positive, function of applied field, microstructure dependent	Atoms have anti-parallel aligned unequal magnetic moments

^[a] In “molecular” species such as d- or f-block metal complexes, organic radicals or metal-organic radicals, these kinds of magnetic behaviors are now known (Kahn, 1993).

^[b] Note that in small cluster (ligand-bridged) complexes, ferromagnetic (or antiferromagnetic) coupling of spins, within the clusters does not involve long-range magnetic order and χ_M does not depend on the field, H , thus ferromagnetic coupling does not mean the materials is an ordered ferromagnet (unless T_C can be observed at very low temperature).

1.3.2 Spin-Crossover (SCO) Compounds

Recently, research into the preparation and properties of complexes that exhibit the SCO phenomenon has been extensive due to their potential applications for molecular switches and information storage and display devices (Kahn and Martinez, 1998; Miller, 2003; Sato, 2003). SCO is quite frequently observed in octahedral complexes of some transition metal ions with electronic configurations of $3d^4$ to $3d^7$ (Gütlich and Goodwin, 2004; Bousseksou *et al.*, 2007). These can adopt either a HS or a LS ground state depending on the ligand field strength relative to the mean spin-pairing energy (Gütlich *et al.*, 1994). A crossover between these states is observed when the difference between the ligand field strength and the mean spin-pairing energy is in the range of the thermal energy. As illustrated in Figure 1.21, this phenomenon can be induced by a change external constraints, *i.e.* temperature, pressure or electromagnetic radiation, Light-Induced Excited Spin State Trapping (LIESST) effect (Gütlich *et al.*, 2005; Klokishner, and Linares, 2007; Grunert *et al.*, 2008; Neville *et al.*, 2008). Changes in colour, magnetic moment and structural properties (*eg.* metal–ligand distances) are observed when SCO occurs.

In addition to the inner coordination sphere (ligand) effects, the influence of anions, solvate molecules, noncovalent interactions will also affect the nature of SCO and the cooperativity (see below), as has been discussed above. The use of supramolecular chemistry to design such SCO materials have been extensively investigated (Yamada *et al.*, 2006). These interactions can cause mechanical and/or electronic coupling of the centers, and thereby modify the properties of the materials cooperativity in solid materials is when the spin centers interact together. Strong cooperativity leads to an abrupt spin transition and/or thermal hysteresis, or it can

yield multiple stable states weak cooperativity leads to gradual spin transitions. Types of SCO are provided in Figure 1.22.

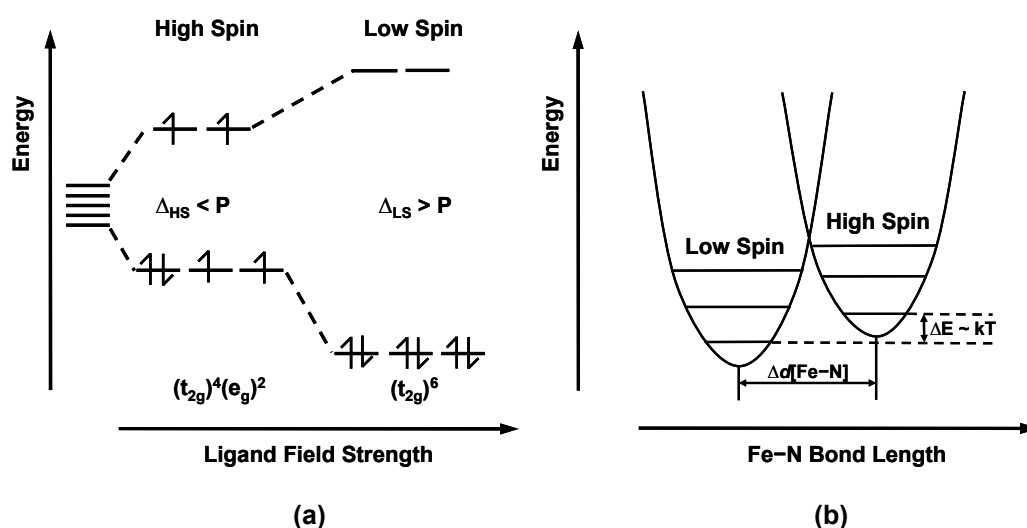


Figure 1.21 Schematic illustration of an Fe(II) SCO complex, (a) d-orbital splitting and the electronic distribution in the low-spin and high-spin states in an octahedral ligand field, and (b) the corresponding oscillator potentials of the totally symmetric mode of the complex as well as showing bond length change between spin states. In SCO compounds the energy difference $\Delta E \approx k_B T$ between the lowest vibronic levels and the much higher density of high-spin states leads to a reversible spin transition well below the decomposition temperature. Also light of different wavelengths switches between the low-spin and the metastable high-spin state at low temperatures.

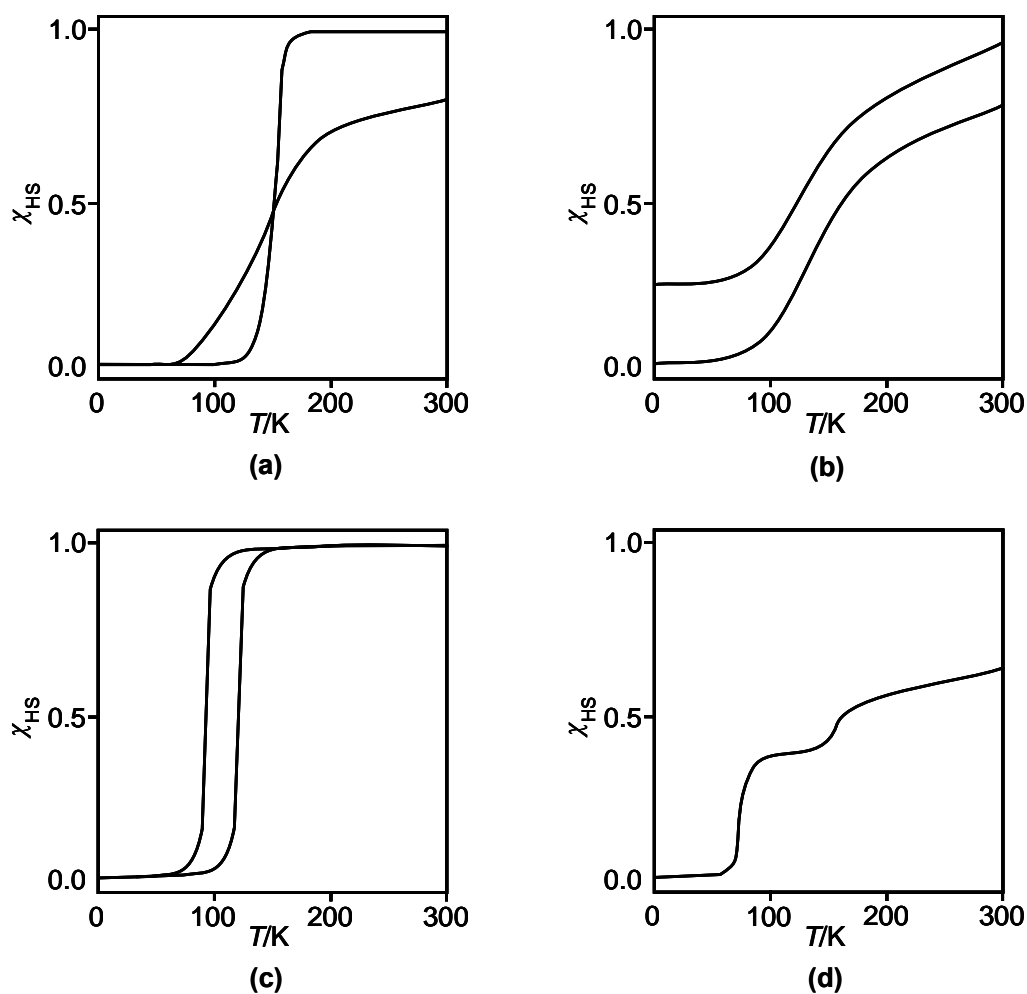


Figure 1.22 Various types of SCO transition. (a) smooth transition occurring within a few K, or a gradual transition occurring within a large temperature interval, (b) complete transition at both a low ($\chi_{HS} = 0$) and a high temperature ($\chi_{HS} = 1$), or incomplete at a low temperature ($\chi_{HS} > 0$) or at a high temperature ($\chi_{HS} < 1$), (c) transition with the thermal hysteresis effect, the critical temperature upon heating T_C is higher than that upon cooling T_C , and (d) two-step (incomplete) SCO. γ_{HS} is the fraction of HS. Note that $T_C = T_{1/2}$ is when $\gamma_{HS} = \gamma_{LS} = 0.5$. Redrawn after Gülich *et al.*, 1994.

Table 1.6 Experimental methods used to monitor the SCO transition in *eg.* Fe^{II} compounds.

Experimental Methods	Monitored Property	LS	HS
Magnetic measurements	Magnetic susceptibility, effective magnetic moment	Low	High
Calorimetric measurements	Heat capacity	Low	High
Mössbauer spectra	Quadrupole splitting, ΔE_Q	Low	High
X-ray diffraction	Cell parameters, metal–ligand distances	Low	High
Nuclear magnetic resonance	Paramagnetic shift, effective magnetic moment	Low	High
Volumetric measurements	Partial molar volume	Low	High
Vibrational spectra	M–L stretching wavenumber	High	Low
Electron spin resonance	Absorption, <i>g</i> -factor	No	Yes
Optical spectroscopy	Excitation energy	Low	High
LIESST (photomagnetism)	Photoexcited HS state	High	Low

(Gütlich and Goodwin, 2004)

Several techniques used to directly monitor substances in the LS and the HS states spin state, and the monitored property, are summarised in Table 1.6. Typical results for a Fe(II) SCO from Mössbauer, IR [$\nu(\text{Fe}^{\text{II}}-\text{N})$], and d–d visible spectra techniques are also shown in Figure 1.23.

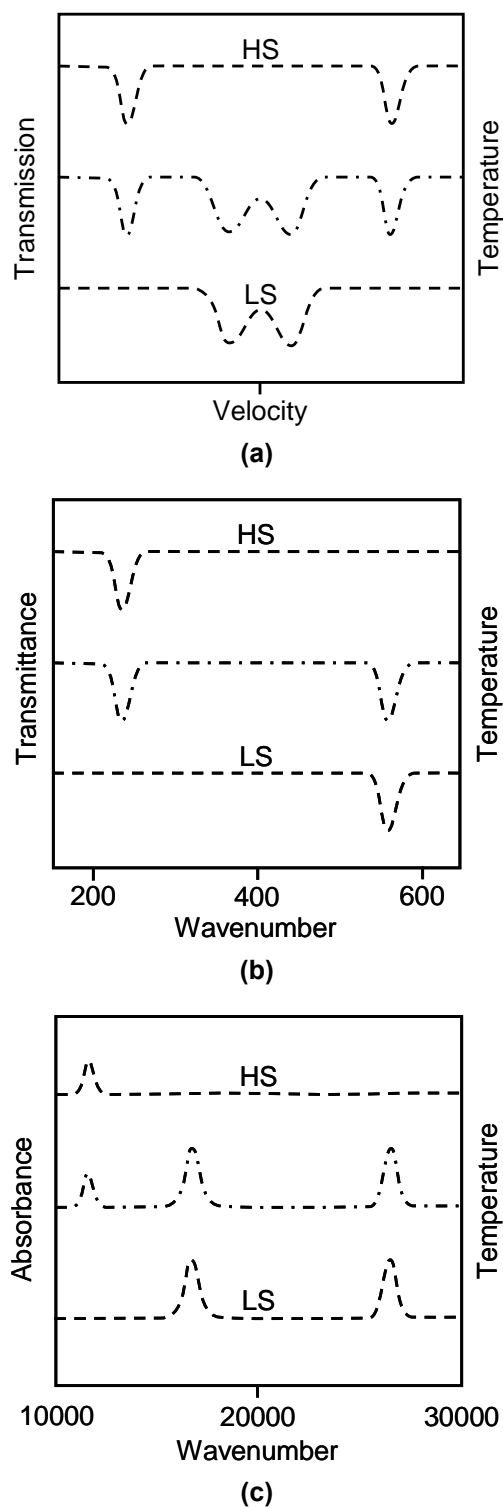


Figure 1.23 Typical temperature evolutions of (a) Mössbauer, (b) Infrared, and (c) Electronic d-d visible spectra for a SCO system of Fe(II). Redrawn after Gütllich and Goodwin, 2004.

Mononuclear Fe(II) complexes with six N (pyridyl type) donor have been extensively studied, and many modern aspects have been recovered (Gütlich and Goodwin, 2004). Recently, interest has been turned to polynuclear species, particularly of Fe(II). Representative examples of SCO are dinuclear Fe(II) compounds which recent reports by the group of Murray (2008), Leita *et al.* (2004; 2007), Klingele *et al.* (2005), Amore *et al.* (2006), and Schneider *et al.* (2007), the group of Kaizaki, Nakano *et al.* (2004), Nakano *et al.* (2005), Yoneda *et al.* (2006), and the group of Real, Ortega-Villar *et al.* (2005), Gaspar *et al.* (2006), Bousseksou *et al.* (2007). The spin transitions in these dinuclear Fe(II) systems proceed through $[\text{HS-HS}] \leftrightarrow [\text{HS-LS}] \leftrightarrow [\text{LS-LS}]$ or by the direct $[\text{HS-HS}] \leftrightarrow [\text{LS-LS}]$ transformations.

Recently, great progress has been made in the area of SCO complexes that display infinite 1-D to 3-D coordination polymeric arrays (Murray and Kepert, 2004; Gaspar *et al.*, 2005; Mroziński, 2005; Molnár *et al.*, 2007). The purpose of this polymers approach was to try and enhance, and fine tune of cooperative properties by the strong covalent links between the metallic centers in the polymers. Murray and co-workers have reported the synthesis series of four isostructural 1-D polymeric Fe(II) SCO materials containing the ligand 2-chloro-4,6-bis(dipyrid-2-ylamino)-1,3,5-triazine (cddt) (Neville *et al.*, 2007; Murray, 2008). Reedijk and co-workers have used the 1,3-bis(tetrazol-1-yl)-2-propanol (btzpol) ligand with $\text{Fe}(\text{BF}_4)_2 \cdot 6\text{H}_2\text{O}$, in CH_3CN , to yield the remarkable 2-D coordination polymer $[\text{Fe}(\text{btzpol})_{1.8}(\text{btzpol-OBF}_3)_{1.2}](\text{BF}_4)_{0.8} \cdot (\text{H}_2\text{O})_{0.8} \cdot (\text{CH}_3\text{CN})$. It shows spin-transition properties induced by both temperature and light (Quesada *et al.*, 2007).

A beautiful example of a 3-D coordination polymer incorporating SCO Fe(II) centers is found in the α -Po like structure of $[\{\text{Fe}(\text{pbtz})_3\}(\text{ClO}_4)_2 \cdot 2\text{EtOH}]$, where pbtz is the 2-connecting di-tetrazole 1,3-di(tetrazol-2-yl)propane, Figure 1.24, was reported by Bronisz (2007), and provided the opportunity to characterize the mixed LS–HS spin state by X-ray crystallography. The single crystal X-ray diffraction studies at 90 K have confirmed that the structure undergoes the thermally induced spin transition $\text{HS} \leftrightarrow \text{LS}$. The $\chi_{\text{M}}T$ dependence in the range 200–75 K shows a gradual SCO. Below 75 K, the transition is complete, and *ca.* 20% of the HS fraction is presented in the LS sample. The $\text{HS} \rightarrow \text{LS}$ transition is accompanied by a shortening of the Fe–N bonds of 0.15 Å. The 2-connecting di-tetrazoles such as pbtz are relevant to the present work the same 2-connecting di-organonitriles have been used to make Fe(II) SCO network, as described in Chapter VI of this thesis.

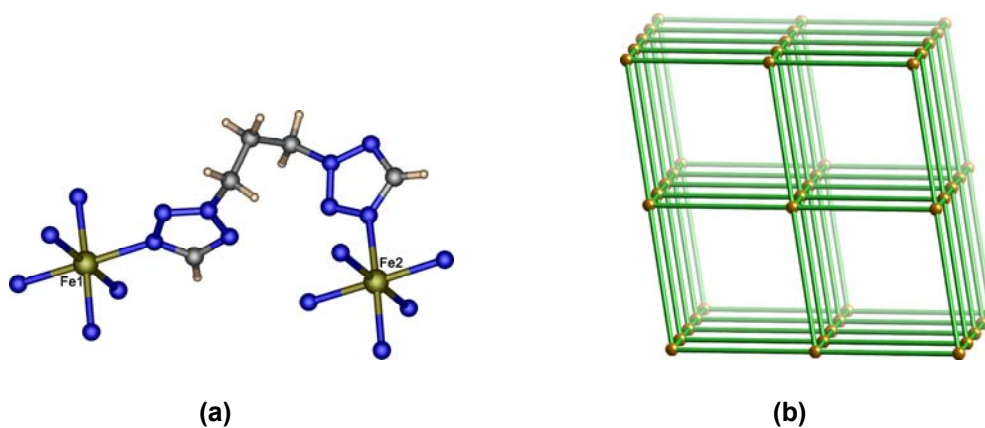


Figure 1.24 (a) Coordination environment of Fe(II) ions and (b) a schematic presentation of the 3-D α -Po like network in $[\{\text{Fe}(\text{pbtz})_3\}(\text{ClO}_4)_2] \cdot 2\text{EtOH}$, pbtz molecules represented as green solid lines. Perchlorate anions and ethanol molecules are omitted for clarity. Drawn from coordinates from CSD, after Bronisz, 2007.

Other coordination compounds of 3d transition elements such as Cr^{II} , d^4 (Halepoto *et al.*, 1989; Meredith *et al.*, 2006), Fe^{III} , d^5 (Imatomi *et al.*, 2007), Mn^{II} , d^5 (Hebendanz *et al.*, 1986), Mn^{III} , d^4 (Morgan *et al.*, 2006), Co^{II} , d^7 (Brooker *et al.*, 1999; Krivokapic *et al.*, 2007), and Co^{III} , d^6 (Klaeui *et al.*, 1987; Wasbotten and Ghosh, 2007) were also found the similar SCO phenomena.

1.3.3 Cyanometallate Building Blocks in Molecular Magnetic Materials

The engineering of molecular magnetic systems may be considered as a facet of supramolecular chemistry, since it results from the collective features of components bearing free spins and on their arrangement in organized assemblies. The approach requires the judicious choice of the building blocks and their arrangement in suitable supramolecular architectures.

During recent years, bridging cyanometallate units have been used in concert with coordinately unsaturated complexes of simple transition metal ions to create multidimensional supramolecular polymers which exhibit very interesting spectroscopic, magnetic, and magneto-optical properties. Some recent literatures are found in papers by Beltran and Long (2005), Sieklucka *et al.* (2005), and Przychodzeń *et al.* (2006).

Prussian blue (PB), $[\text{Fe}^{\text{III}}_4\{\text{Fe}^{\text{II}}(\text{CN})_6\}_3] \cdot x\text{H}_2\text{O}$, is the iconic and original CN^- linked coordination compound. This complex was synthesized many years ago by mixing together the aqueous solutions of $\text{K}_4[\text{Fe}^{\text{II}}(\text{CN})_6]$ and $\text{Fe}(\text{III})$ chloride affording a beautiful deep-blue color. The structure, Figure 1.25, is a mixed-valence cyanide-bridged cubic network containing LS Fe^{II} ($S = 0$) surrounded by carbon and HS Fe^{III} ($S = 5/2$) linked to the nitrogen atoms of the cyanide bridge (Buser *et al.*, 1977). It orders ferromagnetically below $T_C = 5.6$ K (Herren *et al.*, 1980). Using the same

approach, closely framework compounds related to PB with interesting magnetic properties have also been synthesized by the reaction of hexacyanometalates $[\text{M}^{\text{III}}(\text{CN})_6]^{3-}$, $\text{M}^{\text{III}} = \text{Cr}, \text{Mn}, \text{Fe}, \text{and Co}$, with transition metal Lewis acid aqua salts, $\text{M}^{\text{II}} = \text{Mn}, \text{Co}, \text{Ni}, \text{and Cu}$ (Miller and Drillon, 2005).

The most common problem dealing with the characterization of PB related compounds is their poor crystallinity and consequently, the difficulty in growing single crystals. Moreover, although the PB phases exhibit remarkable magnetic properties, their face-centered cubic structures mean that no magnetic anisotropy can be expected. In an attempt to address this problem, a number of research groups have turned their attention to investigate Prussian blue analogs (PBs) and developed an alternative synthetic route that commonly involves the reaction of a cyanometallate such as $[\text{Fe}^{\text{III}}(\text{CN})_6]^{3-}$ with a metal chelate such as $[\text{Ni}(\text{en})_3]^{2+}$. Many such heterometallic frameworks have been reported with reviews by Kahn *et al.* (1993).

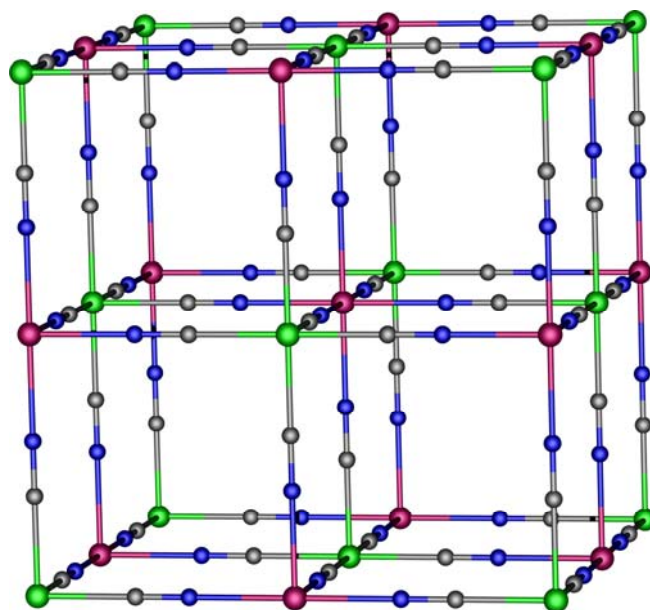


Figure 1.25 A schematic presentation of the 3-D cubic network in Prussian blue.

Chelated metal-cyano species have been used to direct the topology and nuclearity of clusters and extended networks. In clusters such as squares, a tetradentate chelate can block four positions around the M ions, *eg.* in $[M(\text{tpa})(\text{CN})_2]$ to react with $[M'(\text{tpa})(\text{H}_2\text{O})_2]^{2+}$ or $[M'(2,2'\text{-bipy})_2(\text{H}_2\text{O})_2]^{2+}$, where tpa = tris(2-pyridylmethyl)amine, to yield the square (Nihei *et al.*, 2005). In cubes, use of a facial tridentate ligand will leave three facial sites pointing in toward the cube *eg.* $[M^{\text{II}}(\text{tacn})(\text{CN})_3]^-$ for reaction with $[\text{Mn}(\text{tacn})\text{M}(\text{H}_2\text{O})_3]^{2+}$, where tacn = 1,4,7-triazacyclononane, to yield CN-bridged cubes (Beltran and Long, 2005). Thus, one of the initial aim of the present study was to use bidentate chelates in precursors such as $[M(\text{en})(\text{CN})_4]^{2-}$ to produce CN-bridged square tube species upon reaction with $[M(\text{bidentate})(\text{H}_2\text{O})_4]^{2+}$. The background to such precursor is given.

The detailed investigation of compounds requires a combination of a number of different experimental techniques (*eg.* chemical analysis, infrared spectroscopy, single and powder X-ray diffraction, *etc.*) and the theoretical description of the electronic structure obtained from magnetic, spectral, Mössbauer (Fe), and EPR methods.

1.3.4 $[M(\text{L})(\text{CN})_4]$ Building Blocks

To investigate the structure and magnetic properties of low dimensional PBs compounds, a few research groups have recently explored the possibilities of using the mononuclear precursor of formula $[M(\text{L})(\text{CN})_4]^{z-}$, where $z = 1, 2$; $M = \text{Cr}^{\text{III}}, \text{Fe}^{\text{II}}, \text{Fe}^{\text{III}}$, and Ru^{II} , $L =$ bidentate nitrogen donor, *i.e.* 1,10-phenanthroline (1,10-phen), 2-aminomethylpyridine (ampy), 2,2'-bipyridine (2,2'-bipy), 4,4'-dimethyl-2,2'-bipysridine (dmbpy), as building blocks toward transition metal ions. Julve and co-workers have reacted a 1:1 molar ratio of the $[\text{Fe}^{\text{III}}(2,2'\text{-bipy})(\text{CN})_4]^-$ and

$[M^{II}(H_2O)_6]^{2+}$, where $M^{II} = Mn$ and Zn , in aqueous solution to afford trinuclear neutral complexes with formula $[\{Fe^{III}(2,2'\text{-bipy})(CN)_4\}_2M^{II}(H_2O)_4]\cdot 4H_2O$, where $M = Mn$ and Zn (Lescouëzec *et al.*, 2002). In the structure of the centrosymmetric trinuclear species, the $[Fe^{III}(2,2'\text{-bipy})(CN)_4]^-$ unit acts as a monodentate ligand toward $[M(H_2O)_4]^{2+}$ ($M = Mn$ and Zn) through one cyanide group, the other three ones remaining terminal. The intramolecular Fe–M distances are 5.126(1) (Mn) and 5.018(1) Å (Zn). The analysis of the magnetic properties of both compounds show the occurrence of very weak antiferromagnetic behaviors. More interestingly, the manganese derivative show the occurrence of very weak antiferromagnetic interactions between the adjacent LS Fe(III) and HS Mn(II) ions through the bridging cyanide ($J = -0.9\text{ cm}^{-1}$) and between the peripheral LS Fe(III) ions through the –CN–Mn–NC– bridging framework ($J = -1.3\text{ cm}^{-1}$).

In a similar study by the same group, the use of $[Fe^{III}(2,2'\text{-bipy})(CN)_4]^-$ with the fully hydrated $[Co(H_2O)_4]^{2+}$ or $[Cu(H_2O)_4]^{2+}$ in aqueous solution in 1:1 stoichiometry yielded the isostructural 4,2-ribbon like bimetallic chain of formula $[\{Fe^{III}(2,2'\text{-bipy})(CN)_4\}_2M^{II}(H_2O)_2]\cdot 4H_2O$, where $M = Co$ (Lescouëzec *et al.*, 2003) and Cu (Toma *et al.*, 2004). The crystal structures of these two complexes are made up of neutral cyanide-bridged M^{II} – Fe^{III} double zigzag chains and uncoordinated water molecules which are linked through van der Waals forces and hydrogen bonds. Within each chain, the $[Fe^{III}(2,2'\text{-bipy})(CN)_4]^-$ entity acts as a bimonodentate ligand towards two *trans*-diaquametal(II) units through two of its four cyanide groups in *cis*-positions affording bimetallic double chains which run parallel to the *a* axis as illustrated in Figure 1.26. The magnetic behavior corresponds to that of a ferromagnetically coupled chain of LS Fe(III) and M(II) ions with frequency

dependence of the out-of-phase AC susceptibility at $T < 8.0$ and 4.0 K for $M^{II} = \text{Co}$ and Cu , respectively, which indicating that they are examples of single chain magnets (SCMs).

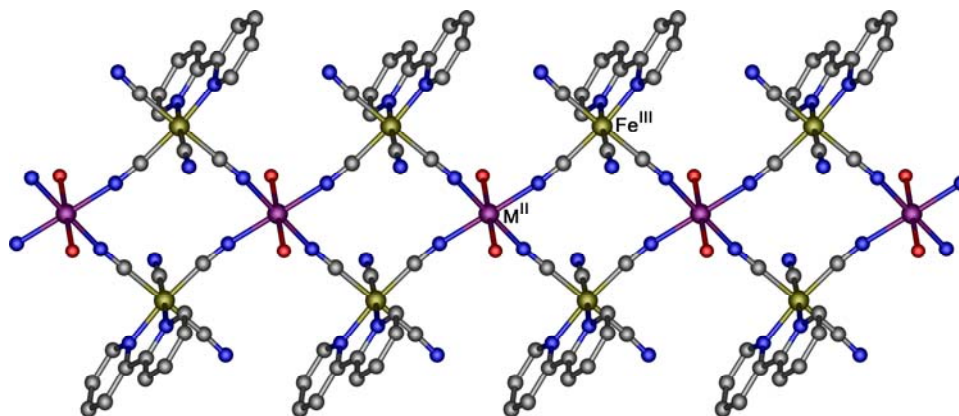


Figure 1.26 Perspective view of a fragment of the 4,2-ribbon like chain in $[\{\text{Fe}^{\text{III}}(2,2'\text{-bipy})(\text{CN})_4\}_2\text{M}^{\text{II}}(\text{H}_2\text{O})_2] \cdot 4\text{H}_2\text{O}$, $M^{\text{II}} = \text{Co}$ and Cu . Hydrogen atom and isolated water molecules are omitted for clarity. Drawn from coordinates from CSD, after Lescouëzec *et al.*, 2003.

Using the LS Fe(III) precursor, Julve and co-workers have also used the related chelate species of $[\text{Fe}^{\text{III}}(1,10\text{-phen})(\text{CN})_4]^-$ as building block with the fully hydrated species $[\text{M}(\text{H}_2\text{O})_6]^{2+}$ to synthesized an impressive series of cyanide-bridged bimetallic coordination polymers with interesting magnetic properties: the 4,2-ribbon like of formula $[\{\text{Fe}^{\text{III}}(1,10\text{-phen})(\text{CN})_4\}_2\text{M}^{\text{II}}(\text{H}_2\text{O})_2] \cdot 4\text{H}_2\text{O}$, where $M = \text{Mn}$, Zn (Lescouëzec *et al.*, 2001), Co (Lescouëzec *et al.*, 2003), and Ni (Toma *et al.*, 2007). The Mn structure exhibits 1-D ferrimagnetic behaviour due to the non-compensation of the local interacting spins ($S_{\text{Mn}} = 5/2$ and $S_{\text{Fe}} = 1/2$) which interact antiferromagnetically through the bridging cyano groups. The magnetic properties of Zn

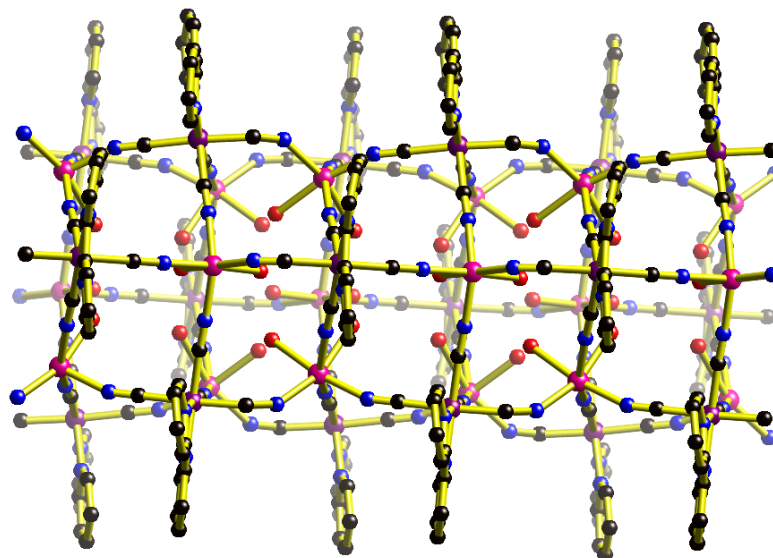
structure correspond to the sum of two magnetically isolated spin triplets, the magnetic coupling between the LS Fe(III) centers through the $-\text{CN}-\text{Zn}-\text{NC}-$ bridging skeleton (Fe \cdots Fe separation larger than 10.2 Å) being negligible. The Co and Ni analogue exhibit ferromagnetically coupled chain of low spin Fe(III) and M(II) ions with frequency dependence of the out-of-phase AC susceptibility at $T < 8.0$ and 3.5 K, respectively, again indicating of SCMs behavior.

In an attempt to extend cyanide bridging chemistry to the molecular regime, the Julve group has also used quite stable paramagnetic of cyanide-bearing Cr(III) building blocks ($S_{\text{Cr}} = 3/2$) of the formula $[\text{Cr}^{\text{III}}(\text{L})(\text{CN})_4]^-$, where L = 1,10-phen, 2,2'-bipy, and ampy, towards fully hydrated Mn(II) ions afforded a wide variety of topologies of polynuclear species with interesting magnetic properties: the neutral trinuclear species $[\{\text{Cr}(2,2'\text{-bipy})(\text{CN})_4\}_2\text{Mn}(\text{H}_2\text{O})_4]\cdot 4\text{H}_2\text{O}$ and two 1-D compounds of formula $[\{\text{Cr}(2,2'\text{-bipy})(\text{CN})_4\}_2\text{Mn}(\text{H}_2\text{O})_2]$ and $[\{\text{Cr}(2,2'\text{-bipy})(\text{CN})_4\}_2\text{Mn}(\text{H}_2\text{O})]\cdot \text{H}_2\text{O}\cdot \text{CH}_3\text{CN}$ (Toma *et al.*, 2004), and the 4,2-ribbon-like bimetallic chains $[\{\text{Cr}(1,10\text{-phen})(\text{CN})_4\}_2\text{Mn}(\text{H}_2\text{O})_2]\cdot 4\text{H}_2\text{O}$ and $[\{\text{Cr}(\text{ampy})(\text{CN})_4\}_2\text{Mn}(\text{H}_2\text{O})]\cdot 6\text{H}_2\text{O}$ (Toma *et al.*, 2005).

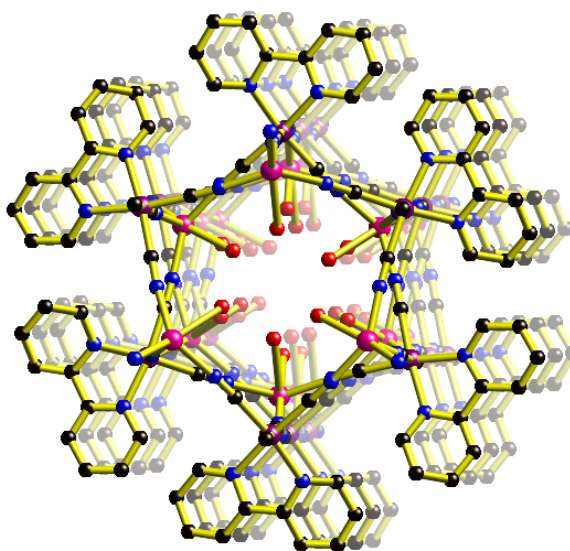
Related to the research mentioned above, recent work by Gao and co-workers have used the same building blocks of $[\text{Cr}^{\text{III}}(2,2'\text{-bipy})(\text{CN})_4]^-$ with secondary and/or tertiary coligands as modulators to synthesized a large family of multinuclear polymeric complexes as well as many topologies, but not 1-D tube species. These compounds in general exhibit antiferromagnetic interactions and either long-rang magnetic ordering including metamagnetism over the lattice, depending on the magnetic interactions (Zhang *et al.*, 2004; 2005; 2006).

Very recently, Cheng and co-workers reported an impressive example of what they described as carbon nanotube (CNT)-like structure bridged by cyanide groups which has been first observed in coordination polymers (Xia *et al.*, 2007). When the $\text{K}_2[\text{Ru}^{\text{II}}(2,2'\text{-bipy})(\text{CN})_4]$ building block with MnCl_2 in a 1:1 stoichiometry were self-assembled in aqueous solution, orange cube-like crystals of $[\text{Ru}^{\text{II}}(2,2'\text{-bipy})(\text{CN})_4\text{Mn}^{\text{II}}(\text{H}_2\text{O})_2]$ were formed. In the solid state structure, three Mn(II) ions and three Ru(II) ions form a basic hexanuclear unit, Ru_3Mn_3 , bridged by cyanide groups with the distance between Mn(II) and Ru(II) ions being 4.969 Å. All the hexanuclear units are assembled alternately to form an infinite 1-D single (hexagonal tube) pipe structure as shown in Figure 1.27. The magnetic susceptibilities of this compound obey the Curie–Weiss law, which indicated paramagnetic Mn(II) ion ($S = 5/2$) behaviour. It can be ascribed to the diamagnetic nature of $[\text{Ru}^{\text{II}}(2,2'\text{-bipy})(\text{CN})_4]^{2-}$, and the Mn–Mn interaction through the long diamagnetic NC–Ru–CN bridge (more than 10 Å) is very weak. Interestingly, this compound exhibits high thermal stability and does not decompose until 500 °C.

It is interesting to note, but different to provide the reason for the different structures and topologies that $\{[\text{M}(\text{L})(\text{CN})_4]^{2-} + [\text{M}'(\text{H}_2\text{O})_6]^{2+}\}$ reaction yield in contrast to our proposed use of $[\text{M}'(\text{L})(\text{H}_2\text{O})_4]^{2+}$ acceptors, there is no chelate directing or blocking preference using $[\text{M}'(\text{L})(\text{H}_2\text{O})_6]^{2+}$.



(a)



(b)

Figure 1.27 (a) Side and (b) top views of a CNT-like coordination hexagonal tube structure in $[\text{Ru}^{\text{II}}(2,2'\text{-bipy})(\text{CN})_4\text{Mn}^{\text{II}}(\text{H}_2\text{O})_2]$. Drawn from coordinates from CSD, after Xia *et al.*, 2007.

1.3.5 $[\text{M}^{\text{II}}(\text{CN})_4]^{2-}$ Building Blocks

Real and co-workers reported the syntheses and characterization of cyanide-bridged bimetallic 3-D Hofmann-like networks with cooperative SCO behaviour of formula $[\text{Fe}^{\text{II}}(\text{pyz})\text{M}^{\text{II}}(\text{CN})_4] \cdot n\text{H}_2\text{O}$, where pyz = pyrazine, $\text{M} = \text{Ni}$, $n = 2$; Pd , $n = 2.5$, and Pt , $n = 2.5$ (Niel *et al.*, 2001). The samples were obtained as microcrystalline materials when a solution of $\text{K}_2[\text{M}(\text{CN})_4]$ in distilled H_2O is added with constant stirring to a solution which contains stoichiometric amounts of pyz and $\text{Fe}(\text{BF}_4)_2 \cdot 6\text{H}_2\text{O}$ in $\text{MeOH}/\text{H}_2\text{O}$ (1:1). They have exactly the same X-ray powder diffraction patterns. Ab initio crystal structure studies were carried out in order to confirm their 3-D nature in the absence of single crystals. The structure consists of the pyz ligands bridging the $\text{Fe}(\text{II})$ atoms of consecutive sheets thus achieving a pillaring of the 2-D sheets by vertical columns of the pz bridge to give a 3-D overall structure, Figure 1.28. Subsequently, the authors have also reported spectroscopic evidence for light-induced spin transition at room temperature in $[\text{Pt}(\text{CN})_4\text{Fe}(\text{pyz})] \cdot 2\text{H}_2\text{O}$ by applying a one-shot laser pulse of irradiation (Bonhommeau *et al.*, 2005).

The absorption and/or desorption of guest molecules may reveal potential applications in the areas of separation and catalysis. Iwamoto and co-workers have used tetracyanonickelate(II) as building block to synthesize the Hofmann type clathrate (porous) framework, which are potentially useful as analogues of zeolites. The authors showed that the rigidity of the Hofmann type frameworks allows for shape and size selective inclusion of organic solvents or water molecules to fill up the void space stabilizing the crystal structure (Nishikiori and Iwamoto, 1986; Yuge and Iwamoto, 1993; 1994; Yuge *et al.*, 1995; 1996). Particularly typical in porous CN-

bridged (PB) framework is the study of their hydrogen absorbing capacity. Kepert *et al.* (2005) and Long *et al.* (2006) have recently reported encouraging results on such species.

From the magnetic point of views, the tetracyanometallate moieties, generally formed by d^8 metal ions, are LS and diamagnetic. Currently, the use of square planar $[M(CN)_4]^{2-}$ building blocks has received little attention for designing magnetically ordered coordination polymers in contrast to their importance in SCO studies (Boldog *et al.*, 2008).

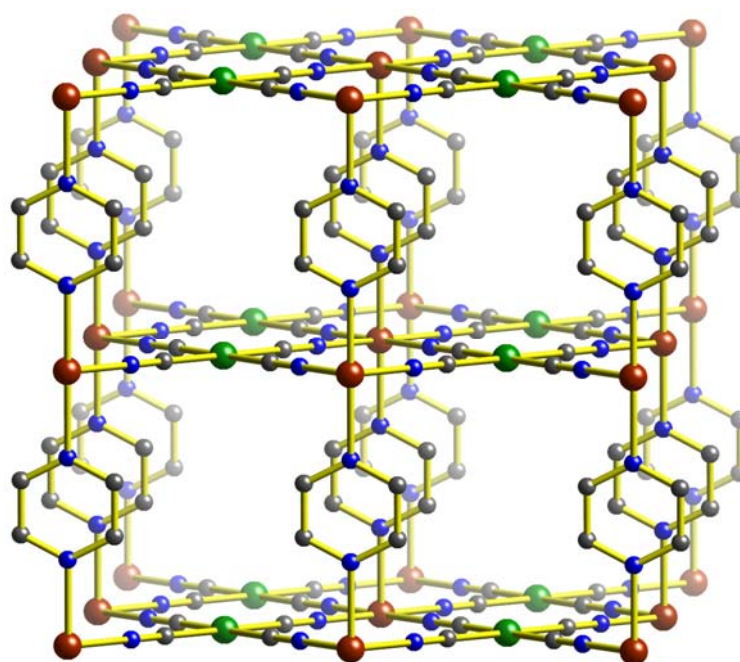


Figure 1.28 Perspective view of the structure of cyanide-bridged bimetallic 3-D Hofmann-like networks in $[Pt(CN)_4Fe(pyz)] \cdot 2H_2O$. Drawn from coordinates from CSD, after Niel *et al.*, 2001.

1.3.6 $[M^I(CN)_2]^-$ Building Blocks in Framework Systems

The polycyanide anions like $[M^I(CN)_2]^-$, where $M^I = Ag, Au, \text{ or } Cu$, are of particular interest when used as bridging ligands for the construction of multidimensional cyanometalate coordination polymers having interesting magnetic properties. They have shown versatile abilities to coordinate to metal ions in different modes and numbers such as (i) rod-shaped or a linear bridging motif (Dong *et al.*, 2003), (ii) a discrete anion playing the role of space filler (Omary *et al.*, 1996), and (iii) as a unidentate ligand that blocking some coordination sites of the central atom (Soma and Iwamoto, 1998).

Unlike other related two-connecting bridging ligands such as the non-metallic dicyanamide $[N(CN)_2]^-$ (Batten and Murray, 2003), interestingly, the $[M^I(CN)_2]^-$ can also possess the ability to further stabilize the polymeric structures through interactions between closed-shell $d^{10}\cdots d^{10}$ *argentophilic* ($Ag^I\cdots Ag^I$) which has effectively increased its dimensionality from a 1-D chain to a 3-D network structure (Pyykko, 1997; Liu *et al.*, 2006).

During recent years, Real and co-workers have systematically been investigating new Hofmann type Fe(II) SCO compounds with polymeric structures based on $[M^I(CN)_2]^-$ (where $M^I = Ag \text{ or } Au$) as bridging ligands. By doing so, the authors have shown a number of beautiful examples in which those materials offer the opportunity to investigate the interplay between different switchable molecular and/or supramolecular components, and the collective properties that may arise from the synergy between the individual component properties. Compounds combine their cooperative SCO properties (magnetic, spectral chromatic, and structural) with different chemical properties such as crystalline-state reactions with allosteric effects

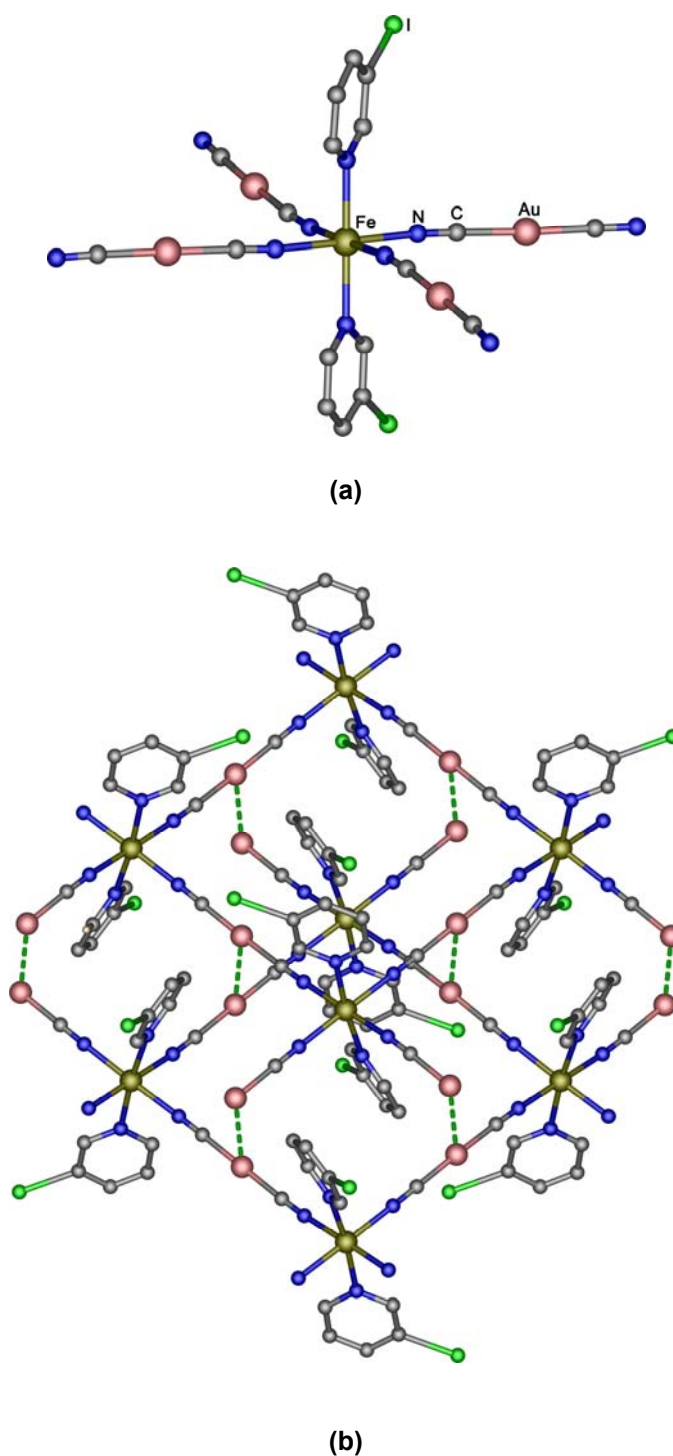


Figure 1.29 (a) A fragment in $[\text{Fe}(\text{3-I-py})_2\{\text{Au}(\text{CN})_2\}_2] \cdot 0.5(\text{3-I-py})$, (b) packing with emphasizing the aurophilic interactions (dotted green lines). Drawn from coordinates from CSD, after Agustí *et al.*, 2008.

found in $[\text{Fe}(\text{pmd})(\text{H}_2\text{O})\{\text{M}^{\text{I}}(\text{CN})_2\}_2]\cdot\text{H}_2\text{O}$, $\text{M}^{\text{I}} = \text{Ag}$ and Au , $\text{pmd} = \text{pyrimidine}$, (Niel *et al.*, 2003), SCO tuned metallophilicity as in $[\text{Fe}(\text{3-cyanopyridine})\{\text{Ag}(\text{CN})_2\}_2]\cdot 1/3\text{H}_2\text{O}$ (Galet *et al.*, 2003), triple-interpenetrated 3-D network of $[\text{Fe}(\text{pmd})\text{Ag}_2(\text{CN})_3\text{Ag}(\text{CN})_2]$, which display a thermal and light induced spin transition and spin dependent ligand unsupported argentophilic interactions (Niel *et al.*, 2005). A great series of compounds cooperative with SCO behaviours of formulated $[\text{Fe}(\text{3-X-py})_2\{\text{Ag}(\text{CN})_2\}_2]$, where $\text{X} = \text{F}$, Cl , Br , and I ; $\text{py} = \text{pyridine}$, and $[\{\text{Fe}(\text{3-X-py})_2\text{Ag}(\text{CN})_2\}_2\text{Ag}(\text{3-X-py})(\text{CN})_2]\cdot 3\text{-X-py}$, where $\text{X} = \text{Br}$ and I , have also been synthesized (Munoz *et al.*, 2007). Very recently, the clathrate derivative $[\text{Fe}(\text{3-I-py})_2\text{Au}(\text{CN})_2]\cdot 0.5(\text{3-I-py})$ was reported by the same group. The structure is made up of parallel stacks of corrugated $[\text{Fe}\{\text{Au}(\text{CN})_2\}_2]_n$ grids and cross-link *via* aurophilic interactions to give 3-D networks structure, Figure 1.29.

1.4 Metal Oxides Framework Materials: Vanadates

Inorganic oxide materials have attracted considerable interest over many years owing to their intriguing structures and wide potential applications in a variety of areas such as those listed in Table 1.7. Recently, inorganic oxides have been used to produce functional nanosystems, an area representing one of the greatest challenges in physics, chemistry and materials science (Wight and Davis, 2002; Rao *et al.*, 2004). Control over the cluster arrangements in the molecular-assemblies is important in allowing the construction of solid state inorganic oxides of nanoscale dimensions, and these aspects have been discussed recently (Akutagawa *et al.*, 2007; Alam *et al.*, 2008).

1.4.1 Hydrothermal Synthesis of Hybrid Organic-Inorganic Framework Materials

One approach to the rational design and syntheses of solid frameworks is to mimic nature's use of organic molecules to modify inorganic structures (Cheetham *et al.*, 1999). Organic templates may be used to introduce secondary inorganic metal sites. Of particular use are aliphatic amines which can have multiple roles, such as (i) space-filling, (ii) charge-compensating, or (iii) structure directing, dependent on their coordination preferences and range of binding interactions (Hagman *et al.*, 1999). The use of organic templates in the fabrication of self-assembled frameworks has long been used in zeolite synthesis, and has recently been demonstrated for a number of metal oxide frameworks made using hydrothermal synthetic methods (Hagman *et al.*, 2001). Reactions are typically performed in the temperature range 110–240 °C under autogenous pressure in a sealed reaction vessel (Byrappa and Ohachi, 2007). This allows the self-assembly of the products from precursors which would be insoluble or unreactive under ambient conditions. Different phase pure products are obtained by changing physical conditions such as pH, stoichiometry, temperature, time, and concentration (Law and Williams, 2000; Forster *et al.*, 2005). This approach has produced a variety of hybrid metal oxide structures (*eg.* 0-D discrete clusters, 1-D infinite chains, 2-D sheets, and 3-D frameworks) with potential functionality (Zavalij and Whittingham, 1999).

Table 1.7 Selected examples and applications of inorganic oxides.

Metal class	Examples	Applications
Magnetic Oxides	CrO ₂ , ferrites, spinels	Magnetic tapes, transformer cores, computer memories
Oxide sensors	BaTiO ₃ , PbZrO ₃	Temperature sensors, piezo speakers
Phosphors	Doped Zn ₂ SiO ₄ , Y ₂ O ₃	Oscilloscope tubes
Electronic materials	BaTiO ₃ , ZnO	Surge protectors, high T semiconductors
Ceramics	Al ₂ O ₃ , PbZr _{1-x} Ti _x O ₃	Ferroelectrics
Catalysts	(VO) ₂ P ₂ O ₇ , Bi ₂ Mo ₂ O ₉ , V ₂ O ₅ /TiO ₂	Selective oxidations, oxidative dehydrogenation, polymerization
Ion exchange	NASICON, zeolites	Fast ion conductors, detergents
Molecular sieves	Zeolites	Separating agents
Biomaterials	Organoapatites	Artificial bone
Optical materials	LiNbO ₃ , KTiOPO ₄ , Nd: YAG	Harmonic generators, frequency mixers, lasers
Construction oxides	CaO	Concrete, trap for desulfurization
High temperature materials	Vitreous silica	1000–1300 °C containers

Hagman *et al.*, 2001

1.4.2 Organovanadium Framework Materials of Relevance to the Present Thesis

Vanadium is often found in oxides in all the oxidation states (+5), (+4), (+3), and even (+2). In mineral chemistry, vanadium exhibits three oxidation states V⁽⁺⁵⁾, V⁽⁺⁴⁾, and V⁽⁺³⁾ which gives many isopolyvanadates that exhibits a large variety of structures. The structure of the frameworks shown schematically in Figure 1.30 is defined in substantial part by the vanadium–oxygen coordination polyhedra, which

vary from tetrahedron to trigonal pyramid, square pyramid, distorted octahedron and regular octahedron, while the oxidation state change from (+5) to (+3), with vanadium–oxygen doubling bonding playing a part in the (+5) and (+4) states.

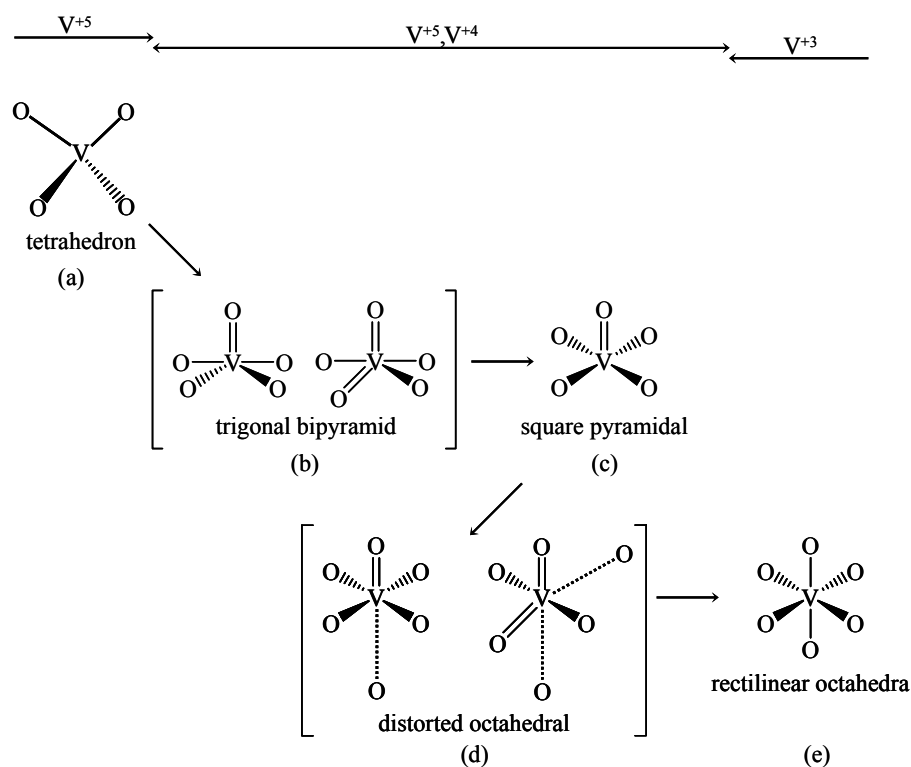


Figure 1.30 Metamorphosis of the vanadium coordination polyhedra: (a) tetrahedral, (b) “3 + 2” and “4 + 1” trigonal pyramidal, (c) “4 + 1” square pyramidal, (d) “4 + 1 + 1” and “2 + 2 + 2” distorted octahedral, and (e) regular octahedral. Redrawn after Zavalij and Whittingham, 1999.

The synthesis of extended structure solids based on vanadium oxides is of much currently interest. This is mainly due to their fascinating structures and attractive possibilities for their catalytic or magnetic properties (V^{+4} , V^{+3}), and the development of new cathode materials for Li batteries (Liu *et al.*, 2002; Weckhuysen and Keller, 2003). Many interesting new systems containing tetrahedral $\{VO_4\}$,

square pyramidal $\{\text{VO}_5\}$, and octahedral $\{\text{VO}_6\}$ units with vanadium centers have been synthesized and characterized. The tetrahedral $\{\text{VO}_4\}$ linking unit is often observed among the solid state polyhedra of vanadium oxide structures. This is analogous to the use of AlO_4 and SiO_4 in aluminasilicate based zeolites, tetrahedral oxyanions such as PO_4^{3-} , SO_4^{2-} , and AsO_4^{3-} , and tetrahedral $\{\text{ZnO}_4\}$, which can produce similar topologies. The tetrahedral $\{\text{VO}_4\}$ unit may be regarded as a potentially versatile motif for constructing oxovanadate based open framework solid structures. These could be remarkable redox catalysts unlike zeolites that do not show such characteristic reactivity and redox chemistry (Whittingham, 2004).

Several open-frameworks of vanadate solids can be prepared by self-assembly of three main building blocks, *i.e.* an organoamine ligand, a transition metal cation, and an oxovanadate, under mild hydro/solvothermal conditions. In 1996, Zubieta and co-workers reported a new class of hydrothermally synthesized mixed-valence vanadium oxides that possesses a layered structure and displayed interesting ion-exchange and magnetic properties (Zhang *et al.*, 1996). Williams and co-workers prepared the first example of 3-D organically templated manganese divanadates of $[\text{H}_2\text{en}][\text{Mn}_3^{\text{II}}(\text{V}_2^{\text{V}}\text{O}_7)_2(\text{H}_2\text{O})_2]$ by hydrothermal reaction of $[\text{Mn}_3\text{O}(\text{OAc})_6(\text{py})_3][\text{BF}_4]$, V_2O_5 , en, and H_3BO_3 in a 0.67: 1: 6: 10 ratio with pH = 8 at 140 °C. This compound was of magnetic interest, since the Mn^{II} centers associated as trimers or ladder-like chains, Figure 1.31. Subsequently, a vast of polymeric metal oxide framework materials with interesting properties has been recently discovered (Chesnut *et al.*, 1999; Wight and Davis, 2002; Coronado *et al.*, 2005; Akutagawa *et al.*, 2007).

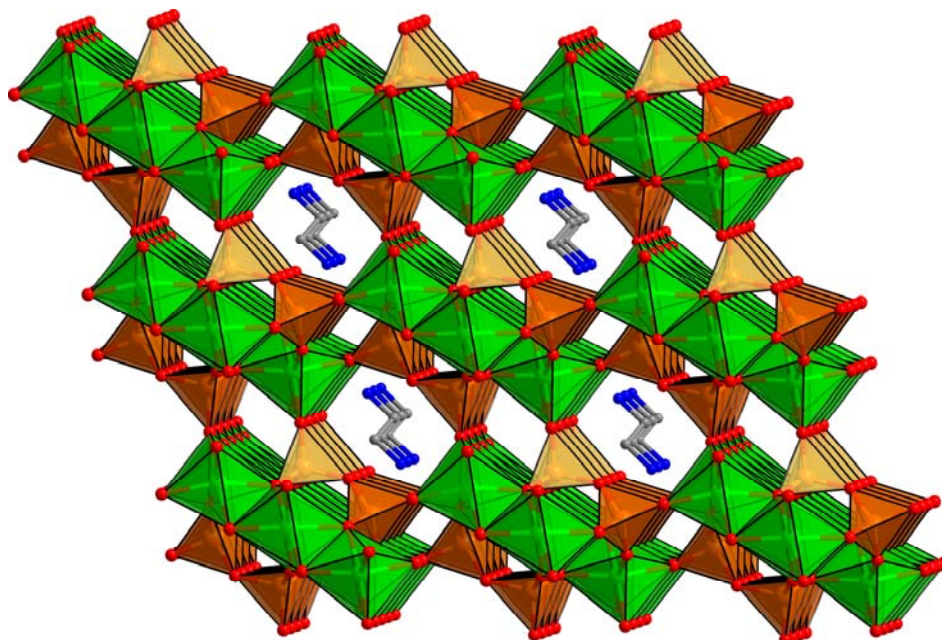


Figure 1.31 Polyhedral and ball-stick representations in $[\text{H}_2\text{en}][\text{Mn}_3(\text{V}_2\text{O}_7)_2(\text{H}_2\text{O})_2]$.

The $[\text{enH}_2]^{2+}$ group are in the cavities. Hydrogen atoms are omitted for clarity. Drawn from coordinates from CSD, after Williams *et al.*, 2000.

1.5 Functional Applications of Metal–Organic Hybrid Framework

Materials

In comparison to the enormous number of commercial applications of the aluminosilicate zeolites, hybrids offer certain advantages because of (i) the relative ease with which they can be functionalized, post-synthesis, (ii) the simplicity with which the pore size can be tuned over a wide range of sizes, and (iii) the manner in which enantiomerically-pure chiral frameworks can be created (Cheetham *et al.*, 2004). Many interesting new hybrid materials have already been recently prepared with remarkable properties. These functional hybrids are considered as innovative

advance materials and promising applications, are expected in many fields (Gómez-Romero and Sánchez, 2004).

The practical usage standard for H₂ storage of 6.5 wt % set by the U. S. Department of Energy at ambient temperature and low pressure is a big challenge and none of storage materials, such as metal hydrides, zeolites, and activated carbon adsorbents can meet such criterion. MOFs have some advantages on pore designable and large surface area over zeolites. They have been recently considered as the most hopeful hydrogen storage adsorbents. But the effectiveness of MOFs materials in hydrogen adsorption has mainly focused on the low temperature and the high pressure. Yaghi and co-workers have been recently synthesized and studies gas absorptions of a number of MOFs (Yaghi *et al.*, 2003). A most impressive example in this series is MOF-5, which is a very low-density material, and there is a good deal of data on the gas storage capacities, including hydrogen and methane (Li *et al.*, 1999). The design and preparation of MOF materials used as the gas storage materials, at an ambient temperature, is currently investigated by several research groups (Peterson *et al.*, 2006; Kubas, 2007; Lin *et al.*, 2007; Collins *et al.*, 2008; Suh *et al.*, 2008).

Porous, homochiral MOFs and their application in the heterogeneous asymmetric catalysis with the activity and the stereoselectivity rivalling their homogeneous counterparts have been reported in the recent literature (Soo *et al.*, 2000; Wu *et al.*, 2005; Dybtsev *et al.*, 2006; Wu and Lin, 2007). Catalysis using organically pillared zirconium phosphate/phosphonate catalysts has also recently been reviewed by Clearfield and Wang (2002).

The exploitation of chemical functionalization within coordination framework structures has been reviewed (Decurtins *et al.*, 1999; Maspoch *et al.*, 2003; Kitagawa

et al., 2004; Murray and Kepert, 2004). One of the impressive examples of multifunctional material exhibiting both porosity and guest-responsive magnetic properties is $[\text{Cu}_3(\text{PTMTC})_2(\text{pyridine})_6(\text{EtOH})_2(\text{H}_2\text{O})]$, where PTMTC = tris(4-carboxylato-2,3,5,6-tetrachlorophenyl)methane (MasPOCH *et al.*, 2003). The inclusion of the ethanol guest species is accompanied by a breathing of the structure that significantly influences the magnetic properties of the framework which behaved similar to that found in $[\text{Fe}_2(\text{azpy})_4(\text{NCS})_4]\cdot\text{guest}$ (Halder *et al.*, 2003). In addition, the optical properties of hybrid frameworks are also of considerable interest (Lacroix *et al.*, 2001; Thushari *et al.*, 2005; Bidault *et al.*, 2006; Li *et al.*, 2006).

As already mentioned, hybrid organic-inorganic materials are ubiquitous materials possessing the extensive compositional range, structural diversity, and many potential applications. Therefore, these materials are an interesting target for the present research project.

1.6 The Present Study

This study was carried out at the School of Chemistry, Suranaree University of Technology, Thailand (Chapter VII), School of Chemistry, Monash University, Australia (Chapters II–VI), Department of Chemistry, Hong Kong University of Science and Technology, Hong Kong (Chapter VII), and the Research School of Chemistry, The Australian National University, Canberra, Australia (Chapter VII).

The study at the School of Chemistry, Monash University, was the primary focus of the projects with the aim of using the principles of crystal engineering to synthesize, for the first time, 1-D tube-like motifs of cyanide-bridged bimetallic coordination polymers. Making comparisons to 2- and 3-D Prussian blue analogues

were important. A more general aim was to study the structural diversity and magnetic properties of cyanide-bridged bimetallic compounds that formed from the attempts to make the 1-D tubes. In attempts to synthesize the 1-D tube motifs, the complexes of formulae $[M(L)(CN)_4]$ and $[M'(L')(solvent)_4]$ (where $M = Fe^{II}$ and Fe^{III} ; $M' =$ first row transition metals; $L = 1,10\text{-phen}, 2,2'\text{-bipy}, en, tn$; $L' = en, tn$) were chosen as building blocks to form the tube motifs (Chapter III).

Other metallocyano and organocyano bridging groups were explored. For examples, a linear dicyanoargentate $[Ag(CN)_2]^-$ was used as longer bridging ligand to replace the CN groups of the $[M(L)(CN)_4]^{2-}$ building block (Chapter III). The ideal candidate for this study was also expected to produce 1-D tube-like motifs of $[Ag(CN)_2]$ bridged bimetallic coordination polymers. Other new supramolecular complexes involving the $[Ag(CN)_2]^-$ groups could also form their structures by involving $d^{10}\cdots d^{10}$ argentophilic ($Ag\cdots Ag$) interactions (Chapter IV). The “ligand complex” of square planar tetracyanonickelate, $[Ni(CN)_4]^{2-}$, was also employed as a building block for the construction of supramolecular coordination polymers (Chapter V).

The 2-connecting organodinitrile ligand, ACCN and AIBN, were used as bridging ligands for investigations of self-assembly processes in the construction of 3-D Fe(II) coordination polymer compounds, for which early reports in the AIBN compound (Zuur *et al.*, 1981) had suggested they would exhibit thermally induced SCO behaviour. The structure and SCO magnetic properties of the $[Fe^{II}(L)_3](M^{III}Cl_4)_2$ materials, where $L = ACCN$ or $AIBN$, $M^{III} = Fe, In$, are described here (Chapter VI).

In order to obtain information at the basic structural level as well as try to understand the details of the self-assembly process, which should be of general

interest for the crystal engineering of novel supramolecular metal coordination polymers, the covalent and noncovalent interactions of 3,6-bis(2'-pyrimidyl)-1,2,4,5-tetrazine (bmtz) and 3,6-bis(2-pyridyl)-1,2,4,5-tetrazine (bptz) were investigated upon reaction with Ag(I) ion (Chapter II).

The study on open framework, hybrid organic-inorganic vanadium oxides (analogs of zeolite) was carried out at SUT, HKUST, and ANU. The aim was to use the aromatic diamine planar geometry of imidazole and hydro/solvothermal syntheses to introduce inorganic metal sites. This molecule is different from the aliphatic diamines previously used (Law *et al.*, 2000; Law and Williams, 2000; Williams *et al.*, 2000) in terms of basicity, size, shape, ligation ability, hydrogen bond capacity and charge, and this could allow different and more diverse framework structures. The framework structures were studied by single crystal X-ray analysis with physical techniques such as elemental analyses, XRD, EDX and TGA, used to support the structure analysis (Chapter VII).

The overarching themes of the project were to investigate metal coordination polymers of varying dimensionalities, with emphasis on synthesis, crystal growing, structural and magnetic properties. Cyanide-, metallocyanide- and organocyanobridging modes were of particular interest. Each chapter is designed to be self-contained with its own relevant introduction, so the chapters need not be read sequentially. The introduction provides a general underpinning to the chemical, structural and magnetic aspects of the project.

1.7 References

- Agustí, G., Muñoz, M. C., Gaspar, A. B., and Real, J. A. (2008). **Inorg. Chem.** 47(7): 2552-2561.
- Akutagawa, T., Endo, D., Noro, S.-I., Cronin, L., and Nakamura, T. (2007). **Coord. Chem. Rev.** 251(21-24): 2547-2561.
- Akutagawa, T., Shitagami, K., Nishihara, S., Takeda, S., Hasegawa, T., Nakamura, T., Hosokoshi, Y., Inoue, K., Ikeuchi, S., Miyazaki, Y., and Saito, K. (2005). **J. Am. Chem. Soc.** 127(12): 4397-4402.
- Alam, Md. A., Kim, Y.-S. Ogawa, S., Tsuda, A., Ishii, N., and Aida, T. (2008). **Angew. Chem., Int. Ed.** 47(11): 2070-2073.
- Allen, F. H., Baalham, C. A., Lommerse, J. P. M., and Raithby, P. R. (1998). **Acta Crystallogr., Sect. B: Struct. Sci.** 54: 320-329.
- Amoore, J. J., Kepert, C. J., Cashion, J. D., Moubaraki, B., Neville, S. M., and Murray, K. S. (2006). **Chem. Eur. J.** 12(32): 8220-8227.
- Andrews, P. C., Hardie, M. J., and Raston, C. L. (1999). **Coord. Chem. Rev.** 189(1): 169-198.
- Assefa, Z., Shankle, G., Patterson, H. H., and Reynolds, R. (1994). **Inorg. Chem.** 33(10): 2187-2195.
- Atwood, J. L., Barbour, L. J., and Jerga, A. (2002). **J. Am. Chem. Soc.** 124(10): 2122-2123.
- Batten, S. R. (1995). **Doctoral Dissertation.** University of Melbourne.
- Batten, S. R. (2001). **Curr. Opin. Solid State Mater. Sci.** 5(2-3): 107-114.
- Batten, S. R. (2004). Coordination polymers. **Encyclopedia of Supramolecular.** New York: Marcel Dekker, pp 1-13.

- Batten, S. R., and Robson, R. (1998). *Angew. Chem., Int. Ed.* 37(11): 1460-1494.
- Beatty, A. M. (2003). *Coord. Chem. Rev.* 246(1-2): 131-143.
- Beltran, L. M. C., and Long, J. R. (2005). *Acc. Chem. Res.* 38(4): 325-334.
- Bernstein, J., Etter, M. C., and Leiserowitz, L. (1994). **The Role of Hydrogen Bonding in Molecular Assemblies: Structure Correlation**. Vol. 2. Bürgi, H.-B., Dunitz, J. D., Eds., Weinheim, New York, pp 431-500.
- Bidault, S., Viau, L., Maury, O., Brasselet, S., Zyss, J., Ishow, E., Nakatani, K., and Le Bozec, H. (2006). *Adv. Funct. Mater.* 16(17): 2252-2262.
- Bikadi Z., Demko L., and Hazai E. (2007). *Arch. Biochem. Biophys.* 461(2): 225-234.
- Blokzijl, W., and Engberts, J. B. F. N. (1993). *Angew. Chem., Int. Ed.* 32(11): 1545-1579.
- Boldog, I., Gaspar, A. B., Martínez, C., Pardo-Ibañez, P., Ksenofontov, V., Bhattacharjee, A., Gütllich, P., and Real, J. A. (2008). *Angew. Chem., Int. Ed.* 47(34): 6433-6437.
- Bondi, A. (1964). *J. Phys. Chem.* 68(3): 441-451.
- Bonhommeau, S., Molnár, G., Galet, A., Zwick, A., Real, J.-A., McGarvey, J. J., and Bousseksou, A. (2005). *Angew. Chem., Int. Ed.* 44(26): 4069-4073.
- Bousseksou, A., Molnár, G., Real, J. A., and Tanaka, K. (2007). *Coord. Chem. Rev.* 251(13-14): 1822-1833.
- Braga, D., and Grepioni, F. (2001). *Acc. Chem. Res.* 33(9): 601-608.
- Braga, D., and Grepioni, F. (2007). **Making Crystals by Design: Methods, Techniques and Applications**. Wiley-VCH Verlag GmbH & Co. KGaA, Weinheim.

- Braga, D., Grepioni, F., Sabatino, P., and Desiraju, G. (1994). **Organometallics** 13 (9): 3532-3543.
- Brooker, S., Plieger, P. G., Moubaraki, B., and Murray, K. S. (1999). **Angew. Chem., Int. Ed.** 38(3): 408-410.
- Bronisz, R. (2007). **Inorg. Chem.** 46(16): 6733-6739.
- Buser, H. J., Schwarzenbach, D., Petter, W., and Ludi, A. (1977). **Inorg. Chem.** 16 (11): 2704-2710.
- Byrappa, K., and Ohachi, T. (2007). **Crystal Growth Technology**. Springer-Verlag Berlin Heidelberg, New York.
- Campos-Fernandez, C. S., Schottel, B. L., Chifotides, H. T., Bera, J. K., Bacsa, J., Koomen, J. M., Russell, D. H., and Dunbar, K. R. (2005). **J. Am. Chem. Soc.** 127(37): 12909-12923.
- Černák, J., Orendáč, M., Potočňák, I., Chomič, J., Orendáčová, A., Skoršepa, J., and Feher, A. (2002). **Coord. Chem. Rev.** 224(1-2): 51-66.
- Champness, N. R. (2006). **J. Chem. Soc., Dalton Trans.** (7): 877-880.
- Chandler, D. (2005). **Nature** 437: 640-647.
- Chapman, K. W., Southon, P. D., Weeks, C. L., and Kepert, C. J. (2005). **Chem. Commun.** (26): 3322-3324.
- Cheetham, A. K., Férey, G., and Loiseau, T. (1999). **Angew. Chem., Int. Ed.** 38(22): 3268-3292.
- Cheetham, A. K., and Forster, P. M. (2004). **Chemistry of Nanomaterials**. Rao, C. N. R.; Müller, A.; Cheetham, A. K. Eds. Vol. 2. Weinheim: Wiley-VCH; Chichester: John Wiley.
- Chesnut, D. J., Hagrman, D., Zapf, P. J., Hammond, R. P., LaDuca Jr., R., Haushalter, R. C., and Zubieta, J. (1999). **Coord. Chem. Rev.** 190-192: 737-

769.

Cho, Y. L., Rudkevich, D. M., Shivanyuk, A., Rissanen, K., and Rebek, J. Jr. (2000).

Chem. Eur. J. 6(20): 3788-3796.

Chu, Q., Swenson, D. C., and MacGillivray, L. R. (2005). **Angew. Chem., Int. Ed.**

44(23): 3569-3572.

Chui, S. S.-Y., Lo, S. M.-F., Charmant, J. P. H., Orpen, A. G., and Williams, I. D.

(1999). **Science** 283: 1148-1150.

Clearfield, A., and Wang, Z. (2002). **J. Chem. Soc., Dalton Trans.** (15): 2937-2947.

Colacio, E., Lloret, F., Kivekals, R., Suárez-Varela, J., Sunberg, M. R., and Uggla, R.

(2003). **Inorg. Chem.** 42(2): 560-565.

Collins, D. J., and Zhou, H.-C. (2007). **J. Mater. Chem.** (30): 3154-3160.

Coronado, E., Giménez-Saiz, C., and Gómez-García, C. J. (2005). **Coord. Chem.**

Rev. 249(17-18): 1776-1796.

Cotton, A. F., Murillo, C. A., and Bochmann, M. (2006). **Advanced Inorganic**

Chemistry. 6th Edition, John Wiley and Sons: New York.

Cowan, J. A., Howard, J. A. K., McIntyre, G. J., Lo, S. M.-F., and Williams, I. D.

(2005). **Acta Crystallogr., Sect. B: Struct. Sci.** 61: 724-730.

Delgado-Friedrichs, O., Foster, M. D., O'Keeffe, M., Proserpio, D. M., Treacy, M.

M. J., Yaghi, M. O. (2005). **J. Solid State Chem.** 178(8): 2533-2554.

Delgado-Friedrichs, O'Keeffe, O., and Yaghi, O. M. (2003). **Solid State Sci.** 5(1):

73-78.

Dalgarno, S. J., Power, N. P., and Atwood, J. L. (2008). **Coord. Chem. Rev.** 252(8-

9): 825-841.

Decurtins, S., Pellaux, R., Antorrena, G., and Palacio, F. (1999). **Coord. Chem. Rev.**

190-192: 841-854.

Desiraju, G. R. (1989). **Crystal Engineering: The Design of Organic Solids.**

Elsevier, Amsterdam.

Desiraju, G. R. (1996). **The Crystal as a Supramolecular Entity.** Chichester: New

York: Wiley.

Desiraju, G. R. (2002). **Acc. Chem. Res.** 35(7): 565-573.

Desiraju, G. R. (2003). **Crystal Design: Structure and Function.** Chichester: John

Wiley Sons Ltd.

Desiraju, G. R. (2003). **Angew. Chem., Int. Ed.** 46(44): 8342-8356.

Desiraju G. R., and Steiner, T. (1999). **The Weak Hydrogen Bond in Structural**

Chemistry and Biology. New York: Oxford University Press.

Dong, W., Wang, Q.-L., Si, S.-F., Liao, D.-Z., Jiang, Z.-H., Yan, S.-P., and Cheng, P.

(2003). **Inorg. Chem. Commun.** 6(7): 873-876.

Dong, Y.-B., Jiang, Y.-Y., Li, J., Ma, J.-P., Liu, F.-L., Tang, B., Huang, R.-Q., and

Batten, R. B. (2007). **J. Am. Chem. Soc.** 129(15): 4520-4521.

Dong, Y.-B., Xu, H.-X., Ma, J.-P., and Huang, R.-Q. **Inorg. Chem.** 45(8): 3325-

3343.

Dougherty, D. A. (1996). **Science** 271: 163-168.

Du, M., Bu, X.-H., Huang, Z., Chen, S.-T., and Guo, Y.-M. (2003). **Inorg. Chem.**

42(2): 552-559.

Dybtsev, D. N., Nuzhdin, A. L., Chun, H., Bryliakov, K. P., Talsi, E. P., Fedin, V. P.,

and Kim, K. (2006). **Angew. Chem., Int. Ed.** 45(6): 916-920.

Ferey, G., Mellot-Draznieks, C., Serre, C., and Millange, F. (2005). **Acc. Chem. Res.**

38(4): 217-225.

- Fernandez, E. J., Lopez-de-Luzuriaga, J. M., Monge, M., Rodriguez, M. A., Crespo, O., Gimeno, M. C., Laguna, A., and Jones, P. G. (1998). **Inorg. Chem.** 37(23): 6002-6006.
- Forster, P. M., Stock, N., and Cheetham, A. K. (2005). **Angew. Chem., Int. Ed.** 44(46): 7608-7611.
- Francis, P. S., Barnett, N. W., Lewis, S. W., and Lim, K. F. (2004). **Luminescence** 19(2): 94-115.
- Fromm, K. M. (2008). **Coord. Chem. Rev.** 252(8-9): 856-885.
- Fu, W.-F., Gan, X., Che, C.-M., Cao, Q.-Y., Zhou, Z.-Y., and Zhu, N. N.-Y. (2004). **Chem. Eur. J.** 10(9): 2228-2236.
- Galet, A., Munoz, M. C., Gaspar, A. B., and Real, J. A. (2005). **Inorg. Chem.** 44(24): 8749-8755.
- Galet, A., Niel, V., Munoz, M. C., and Real, J. A. (2003). **J. Am. Chem. Soc.** 125(47): 14224-14225.
- Gallivan, J. P., and Dougherty, D. A. (1999). **Proc. Nat. Acad. Sci. U.S.A.** 96(17): 9459-9463.
- García, F., Goodman, J. M., Kowenicki, R. A., Kuzu, I., McPartlin, M., Silva, M. A., Riera, L., Woods, A. D., and Wright, D. S. (2004). **Chem. Eur. J.** 10(23): 6066-6072.
- Gaspar, A. B., Ksenofontov, V., Reiman, S., Gülich, P., Thompson, H. L., Goeta, A. E., Muñoz, M. C., and Real, J. A. (2006). **Chem. Eur. J.** 12(36): 9289-9298.
- Gaspar, A. B., Ksenofontov, V., Seredyuk, M., and Gülich, P. (2005). **Coord. Chem. Rev.** 249(23): 2661-2676.
- Glaser, R. (2007). **Acc. Chem. Res.** 40(1): 9-17.

- Gómez-Romero, P., and Sánchez, C. (Eds). (2004). **Functional Hybrid Materials**. Wiley–VCH, Weinheim.
- Gokel, G. W., Barbour, L. J., Ferdani, R., and Hu, J. (2002). **Acc. Chem. Res.** 35 (10): 878-886.
- Greer, M. L., and Blackstock, S. C. (1997). **J. Am. Chem. Soc.** 119(46): 11343-11344.
- Grunert, C. M., Reiman, S., Spiering, H., Kitchen, J. A., Brooker, S., and Gütllich, P. (2008). **Angew. Chem., Int. Ed.** 47(16): 2997-2999.
- Gütllich, P., and Goodwin, H. A. (2004). **Spin Crossover in Transition Metal Complexes**. Vols. I–III, Springer, Heidelberg.
- Gütllich, P., Hauser, A., and Spiering, H. (1994). **Angew. Chem., Int. Ed.** 33(20): 2024-2054.
- Gütllich, P., Ksenofontov, V., and Gaspar, A. B. (2005). **Coord. Chem. Rev.** 249(17-18): 1811-1829.
- Halder, G. J., Kepert, C. J., Moubaraki, B., Murray, K. S., and Cashin, J. D. (2002). **Science** 298: 1762-1765.
- Hagrman, P. J., Finn, R. C., and Zubieta, J. (2001). **Solid State Sci.** 3(7): 745-774.
- Hagrman, P. J., Hagrman, D., and Zubieta, J. (1999). **Angew. Chem., Int. Ed.** 38(18): 2638-2684.
- Halepoto, D. M., Holt, D. G. L., Larkworthy, L. F., Leigh, G. J., Povey, D. C., and Smith, G. W. (1989). **Chem. Commun.** (18): 1322-1323.
- Hasenknopf, B., Lehn, J.-M., Kneisel, B. O., Baum, G., and Fenske, D. (1996). **Angew. Chem., Int. Ed.** 35(16): 1838-1840.
- Hebendanz, N., Koehler, F. H., Mueller, G., and Riede, J. (1986). **J. Am. Chem. Soc.**

108(12): 3281-3289.

Herren, F., Fischer, P., Ludi, A., and Haelg, W. (1980). **Inorg. Chem.** 19(4): 956-959.

Hollingsworth, M. D. (2002). **Science** 295: 2410-2413.

Holman, K. T., Pivovar, A. M., and Ward, M. D. (2001). **Science** 294: 1907-1911.

Hoog, P. D., Gamez, P., Mutikainen, I., Turpeinen, U., and Reedijk, J. (2004). **Angew. Chem., Int. Ed.** 43(43): 5815-5817.

Hasegawa, S., Horike, S., Matsuda, R., Furukawa, S., Mochizuki, K., Kinoshita, Y., and Kitagawa, S. (2007). **J. Am. Chem. Soc.** 129(9): 2607-2614.

Hoskins, B. F., and Robson, R. (1990). **J. Am. Chem. Soc.** 112(4): 1546-1554.

Hosseini, M. W. (2003). **Coord. Chem. Rev.** 240(1-2): 157-166.

Jeffrey, G. A. (1997). **An Introduction to Hydrogen Bonding**. Oxford, University Press, New York.

Jeffrey G. A., and Saenger W. (1991). **Hydrogen Bonding in Biological Structures**. Berlin: Springer-Verlag.

Kahn, O. (1993). **Molecular Magnetism**. VCH, New York.

Kahn, O., and Martinez, C. J. (1998). **Science** 279: 44-48.

Kawano, M., and Fujita, M. (2007). **Coord. Chem. Rev.** 251(21-24): 2592-2605.

Kaye, S. S., and Long, J. R. (2005). **J. Am. Chem. Soc.** 127(18): 6506-6507.

Kepert, C. J., and Rosseinsky, M. J. (1999). **Chem. Commun.** (4): 375-376.

Kitagawa, S., and Matsuda, R. (2007). **Coord. Chem. Rev.** 251(21-24): 2490-2509.

Kitagawa, S., Kitaura, R., and Noro, S. (2004). **Angew. Chem., Int. Ed.** 43(18): 2334-2375.

Kitaura, R., Kitagawa, S., Kubota, Y., Kobayashi, T. C., Kindo, K., Mita, Y., Matsuo,

- A., Kobayashi, M., Chang, H.-C., Ozawa, T. C., Suzuki, M., Sakata, M., and Takata, M. (2002). **Science** 298: 2358-2361.
- Khuong, T.-A. V., Nunez, J. E., Godinez, C. E., and Garcia-Garibay, M. A. (2006). **Acc. Chem. Res.** 39(6): 413-422.
- Klaeui, W., Eberspach, W., and Gütlich, P. (1987). **Inorg. Chem.** 26(24): 3977-3982.
- Klewe, B., and Pedersen, B. (1974). **Acta Crystallogr., Sect. B: Struct. Sci.** 30: 2363-2371.
- Klinge, M. H., Moubaraki, B., Cashion, J. D., Murray, K. S., and Brooker, S. (2005). **Chem. Commun.** (8): 987-989.
- Klokishner, S., and Linares, J. (2007). **J. Phys. Chem. C** 111(28): 10644-10651.
- Krivokapic, I., Zerara, M., Daku, M. L., Vargas, A., Enachescu, C., Ambrus, C., Tregenna-Piggott, P., Amstutz, N., Krausz, E., and Hauser, A., (2007). **Coord. Chem. Rev.** 251(3-4): 364-378.
- Kubas, G. J. (2007). **Chem. Rev.** 107(10): 4152-4205.
- Lacroix, P. G. (2001). **Eur. J. Inorg. Chem.** 339-348.
- Law, T. S.-C., and Williams, I. D. (2000). **Chem. Mater.** 12(8): 2070-2072.
- Lee, I. S., Shin, D. M., and Chung, Y. K. (2004). **Chem. Eur. J.** 10(13): 3158-3165.
- Lehn, J.-M. (1990). **Angew. Chem., Int. Ed.** 29(11): 1304-1319.
- Lehn, J.-M. (1995). **Supramolecular Chemistry**. VCH, Weinheim, Germany.
- Lehn, J.-M., Atwood, J. L., Davies, J. E. D., MacNicol, D. D., Vögtle, F. (1996). **Comprehensive Supramolecular Chemistry**. Pergamon, Oxford, UK.
- Leita, B. A., Moubaraki, B., Murray, K., Smith, J. P., and Cashion, J. D. (2004). **Chem. Commun.** (2): 156-157.

- Lescouëzec, R., Toma, L. M., Vaissermann, J., Verdaguer, M., Delgado, F. S., Ruiz-Pérez, C., Lloret, F., and Julve, M. (2005). **Coord. Chem. Rev.** 249(23): 2691-2729.
- Lescouëzec, R., Lloret, F., Julve, M., Vaissermann, J., Verdaguer, M., Llusar, R., and Uriel, S. (2001). $[\text{Fe}(\text{phen})(\text{CN})_4]^-$: **Inorg. Chem.** 40(9): 2065-2072.
- Lescouëzec, R., Lloret, F., Julve, M., Vaissermann, J., and Verdaguer, M. (2002). **Inorg. Chem.** 41(4): 818-826.
- Lescouëzec, R., Vaissermann, J., Ruiz-Pérez, C., Lloret, F., Carrasco, R., Julve, M., Verdaguer, M., Dromzee, Y., Gatteschi, D., and Wernsdorfer, W. (2003). **Angew. Chem., Int. Ed.** 42(13): 1483-1486.
- Lewiński, J., Zachara, J., Justyniak, I., and Dranka, M. (2005). **Coord. Chem. Rev.** 249(11-12): 1185-1199.
- Leznoff, D. B., Xue, B.-Y., Batchelor, R. J., Einstein, F. W. B., and Patrick, B. O. (2001). **Inorg. Chem.** 40(23): 6026-6034.
- Li, H., Eddaoudi, M., O'Keeffe, M., and Yaghi, O. M. (1999). **Nature** 402: 276-279.
- Li, S.-L., Wu, J.-Y., Tian, Y.-P., Ming, H., Wang, P., Jiang, M.-H., and Fun, H.-K. (2006). **Eur. J. Inorg. Chem.** (14): 2900-2907.
- Lin, X., Jia, J., Hubberstey, P., Schröder, M., and Champness, N. R. (2007). **CrystEngComm.** (6): 438-448.
- Liu, X., Guo, G.-C., Fu, M.-L., Liu, X.-H., Wang, M.-S., and Huang, J.-S. (2006). **Inorg. Chem.** 45(9): 3679-3685.
- Lin, Z.-z., Jiang, F.-l., Yuan, D.-q., Chen, L., Zhou, Y.-f., and Hong, M.-c. (2005). **Eur. J. Inorg. Chem.** (10): 1927-1931.
- Lu, J.-M., Rosokha, S. V., and Kochi, J. K. (2003). **J. Am. Chem. Soc.** 125(40):

12161-12171.

Liu, P., Lee, S.-H., Tracy, C. E., Yan, Y., and Turner, J. A. (2002). **Adv. Mater.**

14(1): 27-30.

Lutz, H. D. (2003). **J. Mol. Struct.** 646(1-3): 227-234.

Ma, C., and Dougherty, D. A. (1997). **Chem. Rev.** 97(5): 1303-1324.

MacGillivray, L. R., Subramanian, S., and Zaworotko, M. J. (1994). **Chem.**

Commun. (11): 1325-1326.

Magnko, L., Schweizer, M., Rauhut, G., Schütz, M., Stoll, H., and Werner, H.-S.

(2002). **Phys. Chem. Chem. Phys.** (6): 1006-1013.

Mascal, M., Hext, N. M., Warmuth, R., Moore, M. H., and Turkenburg, J. P. (1996).

Angew. Chem., Int. Ed. 108(19): 2203-2206.

Mascal, M., Yakovlev, I., Nikitin, E. B., and Fettingner, J. C. (2007). **Angew. Chem.,**

Int. Ed. 119(46): 8938-8940.

Maspoch, D., Ruiz-Molina, D., and Veciana, J. (2004). **J. Mater. Chem.** (18): 2713-

2723.

Maspoch, D., Ruiz-Molina, D., Wurst, K., Domingo, N., Cavallini, M., Biscarini, F.,

Tejada, J., Rovira, C., and Veciana, J. (2003). **Nat. Mat.** 2: 190-195.

McKinlay, R. M., Cave, G. W. V., and Atwood, J. L. (2005). **Proc. Nat. Acad. Sci.**

U.S.A. 102: 5944-5948.

McKinlay, R. M., Thallapally, P. K., Cave, G. W. V., and Atwood, J. L. (2005).

Angew. Chem., Int. Ed. 44(35): 5733-5736.

Mecozzi, S., West, A. P., and Dougherty, D. A. (1996). **J. Am. Chem. Soc.** 118(9):

2307-2308.

Meredith, M. B., Crisp, J. A., Brady, E. D., Hanusa, T. P., Yee, G. T., Brooks, N. R.,

- Kucera, B. E., and Young, V. G., Jr. (2006). **Organometallics** 25(21): 4945-4952.
- Meyer, E. A., Castellano, R. K., and Diederich, F. (2003). **Angew. Chem., Int. Ed.** 42(11): 1210-1250.
- Miller, J. S. (2003). **Angew. Chem., Int. Ed.** 42(1): 27-29.
- Miller, J. S., and Drillon, M. (2002). **Magnetism: Molecules to Materials I**. Weinheim, Wiley-VCH.
- Miller, J. S., and Drillon, M. (2005). **Magnetism: Molecules to Materials V**. Weinheim, Wiley-VCH.
- Miller, J. S., and Epstein, A. J. (1994). **Angew. Chem., Int. Ed.** 33(4): 385-415.
- Miller, J. S., Epstein, A. J., and Reiff, W. M. (1988). **Chem. Rev.** 88(1): 201-220.
- Mohr, F., Jennings, M. C., and Puddephatt, R. J. (2004). **Angew. Chem., Int. Ed.** 43(8): 969-971.
- Molnár, G., Cobo, S., Real, J. A., Carcenac, F., Daran, E., Vieu, C., and Bousseksou, A. (2007). **Adv. Mater.** 19(16): 2163-2167.
- Mooibroek, T. J., Black, C. A., Gamez, P., and Reedijk, J. (2008). **Cryst. Growth Des.** 8(9): 3187-3192.
- Morgan, G. G., Murnaghan, K. D., Müller-Bunz, H., McKee, V., and Harding, C. J. (2006). **Angew. Chem., Int. Ed.** 45(43): 7192-7195.
- Moulton, B., and Zaworotko, M. J. (2001). **Chem. Rev.** 101(6): 1629-1658.
- Mroziński, J. (2005). **Coord. Chem. Rev.** 249(21-22): 2534-2548.
- Muga, I., Gutiérrez-Zorrilla, J. M., Vitoria, P., Román, P., Lezama, L., and Beitia, J. I. (2004). **Eur. J. Inorg. Chem.** (9): 1886-1893.
- Muller-Dethlefs, K., and Hobza, P. (2000). **Chem. Rev.** 100(1): 143-168.

- Munoz, M. C., Gaspar, A. B., Galet, A., and Real, J. A. (2007). **Inorg. Chem.** 46(20): 8182-8192.
- Murray, K. S., and Kepert, C. J. (2004). **Top. Inorg. Chem.** 233: 195-228.
- Nakano, K., Kawata, S., Yoneda, K., Fuyuhiko, A., Yagi, T., Nasu, S., Morimoto, S., and Kaizaki, S. (2004). **Chem. Commun.** (24): 2892-2893.
- Nakano, K., Suemura, N., Yoneda, K., Kawata, S., and Kaizaki, S. (2005). **J. Chem. Soc., Dalton Trans.** (4): 740-743.
- Neville, S. M., Leita, B. A., Offermann, D. A., Duriska, M. B., Moubaraki, B., Chapman, K. W., Halder, G. J., and Murray, K. S. (2007). **Eur. J. Inorg. Chem.** (8): 1073-1085.
- Neville, S. M., Halder, G. J., Chapman, K. W., Duriska, M. B., Southon, P. D., Cashion, J. D., Letard, J.-F., Moubaraki, B., Murray, K. S., and Kepert, C. J. (2008). **J. Am. Chem. Soc.** 130(9): 2869-2876.
- Niel, V., Martinez-Agudo, J. M., Munoz, M. C., Gaspar, A. B., and Real, J. A. (2001). **Inorg. Chem.** 40(16): 3838-3839.
- Niel, V., Munoz, M. C., Gaspar, A. B., Galet, A., Levchenko, G., and Real, J. A. (2002). **Chem. Eur. J.** 8(11): 2446-2453.
- Niel, V., Thompson, A. L., Goeta, A. E., Enachescu, C., Hauser, A., Galet, A., Munoz, M. C., and Real, J. A. (2005). **Chem. Eur. J.** 11(7): 2047-2060.
- Niel, V., Thompson, A. L., Muñoz, M. C., Galet, A., Goeta, A. E., and Real, J. A. (2003). **Angew. Chem., Int. Ed.** 42(32): 3760-3763.
- Nihei, M., Ui, M., Yokota, M., Han, L., Maeda, A., Kishida, H., Okamoto, H., and Oshio, H. (2005). **Angew. Chem., Int. Ed.** 44(40): 6484-6487.
- Nishikiori, S., and Iwamoto, T. (1986). **Inorg. Chem.** 25(6): 788-794.

- Nishio, M., Hirota, M., and Umezawa, Y. (1998). **The C–H \cdots π Interaction: Evidence, Nature, and Consequences.** Wiley-VCH, New York.
- Ockwig, N. W., Delgado-Friedrichs, O., O'Keeffe, M., and Yaghi, O. M. (2005). **Acc. Chem. Res.** 38(3): 176-182.
- Oh, M., and Mirkin, C. A. (2005). **Nature** 438: 651-654.
- O'Keeffe, M., Eddaoudi, M., Li, H., Reineke, T., and Yaghi, O. M. (2000). **J. Solid State Chem.** 152(1): 3-20.
- Omary, M. A., Webb, T. R., Assefa, Z., Shankle, G. E., and Patterson, H. H. (1998). **Inorg. Chem.** 37(6): 1380-1386.
- Orr, G. W., Barbour, L. J., and Atwood, J. L. (1999). **Science** 285: 1049-1052.
- Ortega-Villar, N., Thompson, A. L., Muñoz, M. C., Ugalde-Saldívar, V. M., Goeta, A. E., Moreno-Esparza, R., and Real, J. A. (2005). **Chem. Eur. J.** 11(19): 5721-5734.
- Panigrahi, S. K., and Desiraju, G. R. (2007). **Proteins: Structure, Function, and Bioinformatics** 67(1): 128-141.
- Pauling, L. (1945). **The Nature of the Chemical Bond.** Cornell University Press, USA.
- Pedireddi, V. R., Shimpi, M. R., and Yakhmi, J. V. (2006). **Macromol. Symp.** 241: 83-87.
- Peterson, V. K., Liu, Y., Brown, C. M., and Kepert, C. J. (2006). **J. Am. Chem. Soc.** 128(49): 15578-15579.
- Pinalli, R., Cristini, V., Sottili, V., Geremia, S., Campagnolo, M., Caneschi, A., and Dalcanale, E. (2004). **J. Am. Chem. Soc.** 126(21): 6516-6517.
- Ponzini, F., Zaghera, R., Hardcastle, K., and Siegel, J. S. (2000). **Angew. Chem., Int.**

- Ed. 39(13): 2323-2325.
- Pratt, L. R., and Pohorille, A. (2002). **Chem. Rev.** 102(8): 2671-2692.
- Prins, L. J., Reinhoudt, D. N., and Timmerman, P. (2001). **Angew. Chem., Int. Ed.** 40(13): 2382-2426.
- Przychodzeń, P., Korzeniak, T., Podgajny, R., and Sieklucka, B. (2006). **Coord. Chem. Rev.** 250(17-18): 2234-2260.
- Pyykko, P. (1997). **Chem. Rev.** 97(3): 597-636.
- Quesada, M., Prins, F., Roubeau, O., Gamez, P., Teat, S. J., van Koningsbruggen, P. J., Haasnoot, J. G., and Reedijk, J. (2007). **Inorg. Chim. Acta** 360(13): 3787-3796.
- Quiñonero, D., Garau, C., Rotger, C., Frontera, A., Ballester, P., Costa, A., and Deyà, P. M. (2002). **Angew. Chem., Int. Ed.** 41(18): 3389-3392.
- Quiñonero, D., Frontera, A., Escudero, D., Ballester, P., Costa, A., and Deyà, P. M. (2007). **ChemPhyChem.** 8(8): 1182-1187.
- Rao, C. N. R., Müller, A., and Cheetham, A. K. (Eds). (2004). **The Chemistry of Nanomaterials: Synthesis, Properties and Applications.** Wiley-VCH Verlag GmbH & Co. KGaA.
- Rao, C. N. R., Müller, A., and Cheetham, A. K. (2007). **Nanomaterials Chemistry.** Wiley-VCH Verlag GmbH & Co. KGaA.
- Ren, X. M., Akutagawa, T., Nishihara, S., Nakamura, T., Fujita, W., and Awaga, K. (2005). **J. Phys. Chem. B.** 109(35): 16610-16615.
- Robson, R. (2000). **J. Chem. Soc., Dalton Trans.** (21): 3735-3744.
- Rotger, C., Soberats, B., Quiñonero, D., Frontera, A., Ballester, P., Benet-Buchholz, J., Deyà, P. M., and Costa, A. (2008). **Eur. J. Org. Chem.** (11): 1864-1868.

- Rowland, R. S., and Taylor, R. (1996). **J. Phys. Chem.** 100(18): 7384-7391.
- Sato, O. (2003). **Acc. Chem. Res.** 36(9): 692-700.
- Sato, S., Iida, J., Suzuki, K., Kawano, M., Ozeki, T., and Fujita, M. (2006). **Science** 313: 1273-1276.
- Seddon, K. R., and Zaworotko, M. (1999). **Crystal Engineering the Design and Application of Functional Solids**. Kluwer Academic Publishers.
- Sieklucka, B., Podgajny, R., Przychodzeń, P., and Korzeniak, T. (2005). **Coord. Chem. Rev.** 249(21-22): 2203-2221.
- Sparkes, H. A., Raithby, P. R., Clot, E., Shields, G. P., Chisholm, J. A., and Allen, F. H. (2006). **CrystEngComm**. 8: 563-570.
- Schneider, C. J., Cashion, J. D., Moubaraki, B., Neville, S. M., Batten, S. R., Turner, D. R., and Murray, K. S. (2007). **Polyhedron** 26(9-11): 1764-1772.
- Schneider, H.-J. (2004). **van der Waals forces in Encyclopedia of Supramolecular Chemistry**. Vol. 2. Steed, J. W. and Atwood, J. L. (Eds), Marcel Dekker, New York, NY, USA, pp. 1550-1556.
- Scheiner, S. (1997). **Hydrogen Bonding**. Oxford University Press, New York.
- Schweiger, M., Yamamoto, T., Stang, P. J., Bläser, D., and Boese, R. (2005). **J. Org. Chem.** 70(12): 4861-4864.
- Schottel, B. L., Chifotides, H. T., Shatruk, M., Chouai, A., Perez, L. M., Bacsá, J., and Dunbar, K. R. (2006). **J. Am. Chem. Soc.** 128(17): 5895-5912.
- Seo, J. S., Whang, D., Lee, H., Jun, S. I., Oh, J., Jeon, Y. J., and Kim, K. (2000). **Nature** 404: 982-986.
- Sieklucka, B., Podgajny, R., Przychodzeń, P., and Korzeniak, T. (2005). **Coord. Chem. Rev.** 249(21-22): 2203-2221.

- Soo, S. J., Dongmok, W., Hyoyoung, L., Im, J. S., Jinho, O., Jin, J. Y., and Kimoon, K. (2000). **Nature** 404(6781): 982-986.
- Steed, J. W. (2001). **Science** 298: 976-977.
- Steed, J. W. (2001). **Coord. Chem. Rev.** 215(1): 171-221.
- Steed, J. W., and Atwood, J. L. (2000). **Supramolecular Chemistry**. Chichester: England.
- Steed, J. W., Turner, D. R., and Wallace, K. J. (2007). **Core Concepts in Supramolecular Chemistry and Nanochemistry**. John Wiley & Sons, Ltd.
- Subramanian, S., and Zaworotko, M. J. (1995). **Angew. Chem., Int. Ed.** 34(19): 2127-2129.
- Sudik, A. C., Millward, A. R., Ockwig, N. W., Cote, A. P., Kim, J., and Yaghi, O. M. (2005). **J. Am. Chem. Soc.** 127(19): 7110-7118.
- Suh, M. P., Cheon, Y. E., and Lee, E. Y. (2008). **Coord. Chem. Rev.** 252(8-9): 1007-1026.
- Suzuki, K., Kawano, M., and Fujita, M. (2007). **Angew. Chem., Int. Ed.** 46(16): 2819-2822.
- Tadokoro, M., Isobe, K., Uekusa, H., Ohashi, Y., Toyoda, J., Tashiro, K., and Nakasuji, K. (1999). **Angew. Chem., Int. Ed.** 38(1-2): 95-98.
- Thushari, S., Cha, J. A. K., Sung, H. H.-Y., Chui, S. S.-Y., Leung, A. L.-F., Yen, Y.-F., and Williams, I. D. (2005). **Chem. Commun.** (44): 5515-5517.
- Toma, L. M., Delgado, F. S., Ruiz-Pérez, C., Carrasco, R., Cano, J., Lloret, F., and Julve, M. (2004). **J. Chem. Soc., Dalton Trans.** (18): 2836-2846.
- Toma, L. M., Lescouëzec, R., Vaissermann, J., Delgado, F. S., Ruiz-Pérez, C., Carrasco, R., Cano, J., Lloret, F., and Julve, M. (2004). **Chem. Eur. J.** 10(23):

6130-6145.

Toma, L. M., Lescouëzec, R., Vaissermann, J., Herson, P., Marvaud, V., Lloreta, F., and Julve, M. (2005). **New J. Chem.** (1): 210-219.

Toma, L. M., Lescouëzec, R., Uriel, S., Llusar, R., Vaissermann, C. R.-P. J., Lloret, F., and Julve, M. (2007). **J. Chem. Soc., Dalton Trans.** (33): 3690-3698.

Tominaga, M., Suzuki, K., Kawano, M., Kusukawa, T., Ozeki, T., Sakamoto, S., Yamaguchi, K., and Fujita, M. (2004). **Angew. Chem., Int. Ed.** 43(42): 5621-5625.

Umemoto, K., Tsukui, H., Kusukawa, T., Biradha, K., and Fujita, M. (2001). **Angew. Chem., Int. Ed.** 40(14): 2620-2622.

Wan, Y., Yang, H., and Zhao, D. (2006). **Acc. Chem. Res.** 39(7): 423-432.

Wang, C.-J., Ma, H.-R., Wang, Y.-Y., Liu, P., Zhou, L.-J., Shi, Q.-Z., and Peng, S.-M. (2007). **Cryst. Growth Des.** 7(9): 1811-1817.

Wasbotten, I. H., and Ghosh, A. (2007). **Inorg. Chem.** 46(19): 7890-7898.

Weckhuysen, B. M., and Keller, D. E. (2003). **Catal. Today** 78(1-4): 25-46.

Wells, A. F. (1977). **Three-Dimensional Nets and Polyhedra.** John Wiley & Sons, Inc., New York, NY, USA.

Whittingham, M. S. (2004). **Chem. Rev.** 104(10): 4271-4302.

Wight, A. P., and Davis, M. E. (2002). **Chem. Rev.** 102(10): 3589-3614.

Williams, I. D., Law, T. S.-C., Sung, H. H.-Y., Wen, G.-H., and Zhang, X.-X. (2000). **Solid State Sci.** 2(1): 47-55.

Wu, C.-D., Hu, A., Zhang, L., and Lin, W. (2005). **J. Am. Chem. Soc.** 127(25): 8940-8941.

Wu, C.-D., and Lin, W. (2007). **Angew. Chem., Int. Ed.** 46(7): 1075-1078.

- Xia, J. Shi, W., Chen, X.-Y., Wang, H.-S., Cheng, P., Liao, D.-Z., and Yan, S. P. (2007). **J. Chem. Soc., Dalton Trans.** (23): 2373-2375.
- Yaghi, O. M., and Li, H. (1996). **J. Am. Chem. Soc.** 118(1): 295-296.
- Yaghi, O. M., O'Keeffe, M., Ockwig, N. W., Chae, H. K., Eddaoudi, M., and Kim, J. (2003). **Nature** 423: 705-714.
- Yamada, M., Hagiwara, H., Torigoe, H., Matsumoto, N., Kojima, M., Dahan, F., Tuchagues, J.-P., Re, N., and Iijima, S. (2006). **Chem. Eur. J.** 12(17): 4536-4549.
- Yoneda, K., Adachi, K., Hayami, S., Maeda, Y., Katada, M., Fuyuhiko, A., Kawata, S., and Kaizaki, S. (2006). **Chem. Commun.** (1): 45-47.
- Yoshizawa, M., Tamura, M., and Fujita, M. (2007). **Angew. Chem., Int. Ed.** 46(21): 3874-3876.
- Young, A. G., and Hanton, L. A. (2008). **Coord. Chem. Rev.** 252(12-14): 1346-1386.
- Yuge, M., Mamada, A., Asai, M., Nishikiori, S.-i., and Iwamoto, T. (1995). **J. Chem. Soc., Dalton Trans.** (19): 3195-3205.
- Yuge, H., Noda, Y., and Iwamoto, T. (1996). **Inorg. Chem.** 35(7): 1842-1848.
- Zavalij, P. Y., and Whittingham, M. S. (1999). **Acta Crystallogr., Sect. B: Struct. Sci.** 55: 627-663.
- Zhang, Y., DeBord, J. R. D., O'Connor, C. J., Haushalter, R. C., Clearfield, A., and Zubieta, J. (1996). **Angew. Chem., Int. Ed.** 35(9): 989-991.
- Zhang, Y.-Z., Gao, S., Sun, H.-L., Su, G., Wang, Z.-M., and Zhang, S.-W. (2004). **Chem. Commun.** (17): 1906-1907.
- Zhang, Y.-Z., Gao, S., Wang, Z.-M., Su, G., Sun, H.-L., and Pan, F. (2005). **Inorg.**

Chem. 44(13): 4534-4545.

Zhang, Y.-Z., Wang, Z.-M., and Gao, S. (2006). **Inorg. Chem.** 45(26): 10404-10406.

Zhou, X.-P., Zhang, X., Lin, S.-H., and Li, D. (2007). **Cryst. Growth Des.** 7(3): 485-487.

Zuur, A. P., Driessen, W. L., and Everstijn, P. L. A. (1981). **Inorg. Nucl. Chem. Lett.** 17: 15-18.

CHAPTER II

SUPRAMOLECULAR

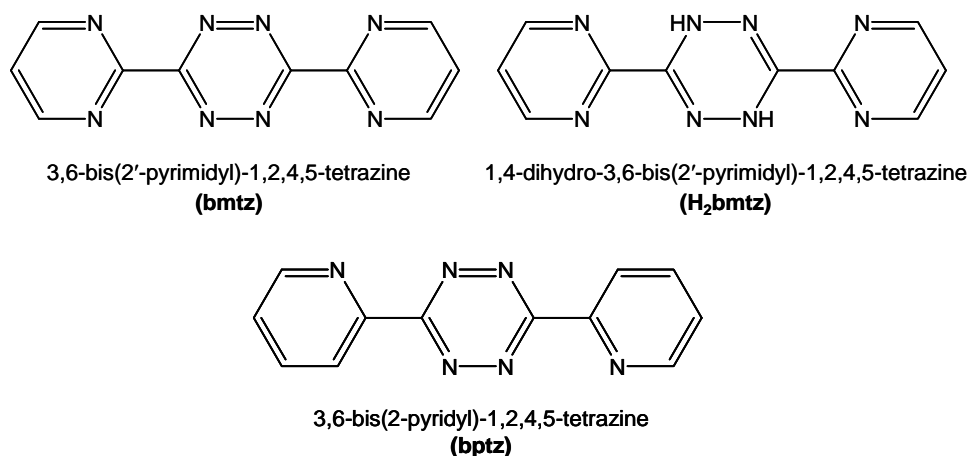
ARCHITECTURE OF SILVER(I) COORDINATION

POLYMERS CONTAINING MULTIMODAL LIGANDS

2.1 Introduction

One of the principal challenges of modern chemistry is that of the crystal engineering of new crystal structures with specific target properties (Sommerdijk, 2003; Tiekink and Vittal, 2006; Desiraju, 2007). In the context of coordination polymers, the combinations of coordinate covalent bonds and noncovalent interactions (eg. hydrogen bonds, π - π stacking) have been employed in the construction of various dimensional supramolecular architectures (Batten, 2001; Batten and Murray, 2005; Holliday and Mirkin, 2001; Moulton and Zaworotko, 2001). Ideally, the overall topology of coordination polymers can be controlled by means of the coordination preferences of the metal center and the structure of the bridging ligand (Batten and Robson, 1998; Batten, 2005; Ockwig *et al.*, 2005). However, in practice from many previous examples, solvent molecules or anion templates as well as the strength of noncovalent interactions were found to produce a dramatic effect on the extended structure of the network (Du *et al.*, 2003; Dong *et al.*, 2006; 2007). Therefore, it still requires the investigating and understanding the details of the assembly process of the coordination network.

Multidimensional coordination polymers based on Ag(I) and N-donor ligands are known in the literature (Khlobystov *et al.*, 1991; Young and Hanton, 2008; Steel and Fitchett, 2008). To study types of intermolecular forces which may lead to new supramolecular architectures. The reaction of the multimodal ligands 3,6-bis(2'-pyrimidyl)-1,2,4,5-tetrazine (bmtz), 1,4-dihydro-3,6-bis(2'-pyrimidyl)-1,2,4,5-tetrazine (H_2 bmtz) and 3,6-bis(2-pyridyl)-1,2,4,5-tetrazine (bptz), Scheme 1, are investigated with Ag(I) ions. The coordination sphere of Ag(I), d^{10} configuration, is very flexible and can adopt coordination numbers between two and six and various geometries from linear through trigonal to tetrahedral, trigonal pyramidal and octahedral (Venkataraman *et al.*, 1997). The ligands are studied here not only have rich coordination modes with the capability of chelating metal ions, but are also able to form noncovalent interactions. It is anticipated that weak association of interactions such as $Ag \cdots Ag$, $Ag \cdots \pi$, $C-H \cdots \pi$, $\pi \cdots \pi$, and anion $\cdots \pi$ interactions will help to provide diversity to the architectures of the various dimensional coordination polymers formed. This study will advance our understanding of the development of supramolecular chemistry and the tuning and prediction of the crystal structures.



Scheme 1 The ligands bmtz, H_2 bmtz and bptz used for this study.

2.2 Experimental Section

2.2.1 Materials and Physical Measurements

The bmtz and H₂bmtz (Kaim and Fees, 1995), and bptz (Geldard and Lions, 1965) ligands were prepared following procedures reported previously. All chemicals were purchased from commercially available sources and were used without further purification.

Caution!: Perchlorate salts of metal complexes with organic ligands are potentially explosive. Only small amounts of material should be prepared, and these should be handled with care. Reactions were performed under a fume hood.

Microanalytical measurements (C, H, N) were performed by Campbell Microanalytical Laboratory, Chemistry Department, University of Otago, Dunedin, New Zealand. Infrared spectra of Nujol mulls were recorded in the range on a Bruker Opus/IR IFS 55 spectrometer in the range of 600–4000 cm⁻¹ (50 scans, resolution ±4 cm⁻¹].

2.2.2 Syntheses

Preparation of Ag(tcm)

Ag(tcm) was prepared by a literature procedure (Konnert and Britton, 1966). Typically, AgNO₃ (3.40 g, 0.020 mol) in H₂O (20 mL) was added to a solution of K(tcm) (2.55 g, 0.020 mol) in H₂O (20 mL). After the mixture had been stirred for 30 minutes, an amorphous white powder was filtered off and dried at room temperature (3.70 g, 86% yield).

Preparation of [Ag₂(bmtz)(ClO₄)]ClO₄ (2a)

AgClO₄ (82.7 mg, 0.4 mmol) was dissolved in 1 mL MeNO₂ and pipetted into one side of a H-shaped tube. bmtz (23.7 mg, 0.1 mmol) was dissolved in 2 mL of

MeNO₂ and pipetted into the other side. The H-shaped tube was then carefully filled with MeNO₂. The solutions were allowed to slowly diffuse into each other, and dark-green block X-ray quality single crystals of **2a** were obtained after 2 weeks. Yield: 11.0 mg, 45% based on bmtz. Anal. Found (calcd) for C₁₀H₆Ag₂Cl₂N₈O₈ (*M_r* = 652.87 g/mol): C, 18.32(18.40), H, 1.01(0.93), N, 17.11(17.17). ATR-FTIR (*v_{max}*/cm⁻¹): 617m, 647w, 754m, 793w, 822w, 923w, 954w, 1030w, 1082w, 1179m, 1381s, 1441w, 1565w, 1581s, 1983w, 2166m, 2235w, 2324w, 3101w.

Preparation of [Ag(bmtz)]ClO₄·MeCN (**2b**)

AgClO₄ (83.1 mg, 0.4 mmol) was dissolved in 1 mL MeCN and pipetted into one side of a H-shaped tube. bmtz (24.1 mg, 0.1 mmol) was dissolved in 2 mL of MeCN and pipetted into the other side. The H-shaped tube was then carefully filled with MeCN. The solutions were allowed to slowly diffuse into each other, and emerald-green column X-ray quality single crystals of **2b** were obtained after 2 weeks. Yield: 17.0 mg, 70% based on bmtz. Anal. Found (calcd) for C₁₂H₉AgClN₉O₄ (*M_r* = 486.60 g/mol): C, 29.58(29.62), H, 1.80(1.86), N, 25.89(25.91). ATR-FTIR (*v_{max}*/cm⁻¹): 619m, 652w, 744m, 802w, 815w, 978w, 999w, 1041w, 1095w, 1199w, 1401s, 1441w, 1582w, 1593s, 1967w, 2171m, 2435w, 2504w.

Preparation of [{Ag(tcm)}₂(H₂bmtz)(MeCN)] (**2c**)

A hot solution of Ag(tcm) (371.7 mg, 2 mmol) in 10 mL MeCN was added dropwise to a hot solution of the H₂bmtz ligand (276.3 mg, 1 mmol) in 10 mL MeCN with stirring to give an orange solution and left to stand at room temperature. After two days, orange-yellow block single crystals of **2c** suitable for structure determination were obtained. Yield: 248.0 mg, 90% based on H₂bmtz. Anal. Found (calcd) for C₂₀H₁₁Ag₂N₁₅ (*M_r* = 677.18 g/mol): C, 35.59(35.47), H, 1.66(1.64), N,

31.14(31.03). ATR-FTIR (ν_{max}/cm^{-1}): 638w, 660w, 805w, 1004w, 1118w, 1242w, 1279w, 1385m, 1438m, 1561m, 1635w, 2162s, 2234w, 3236w.

Preparation of $[\{\text{Ag}(\text{tcm})\}_2\text{bmtz}]$ (2d**)**

A hot solution of Ag(tcm) (372.1 mg, 2 mmol) in 10 mL MeCN was added dropwise to a solution of the bmtz ligand (238.1 mg, 1 mmol) in 10 mL MeCN with stirring to give a red solution and left to stand at room temperature. After two days, orange-red block single crystals of **2d** suitable for structure determination were obtained. Yield: 219.0 mg, 92% based on bmtz. Anal. Found (calcd) for $\text{C}_{18}\text{H}_6\text{Ag}_2\text{N}_{14}$ ($M_r = 634.11$ g/mol): C, 34.37(34.09), H, 1.00(0.95), N, 31.11(30.93). ATR-FTIR (ν_{max}/cm^{-1}): 669w, 959w, 1019m, 1070w, 1095w, 1317w, 1395w, 1452w, 1597s, 1982w, 2163s, 2324w, 2867w, 2908w, 2960w, 3189w, 3285m, 3340m, 3580m, 3857s.

Preparation of $[\text{Ag}(\text{bptz})(\text{NO}_3)]$ (2e**)**

AgNO_3 (34.0 mg, 0.2 mmol) was dissolved in 1 mL MeCN and pipetted into one side of a H-shaped tube. bptz (47.5 mg, 0.2 mmol) was dissolved in 2 mL of MeCN and pipetted into the other side. The H-shaped tube was then carefully filled with MeCN. The solutions were allowed to slowly diffuse into each other at 4 °C, and the red plate X-ray quality single crystals of **2e** were obtained after 2 days. Yield: 34.2 mg, 72% based on bptz. Anal. Found (calcd) for $\text{C}_{12}\text{H}_8\text{AgN}_7\text{O}_3$ ($M_r = 406.11$ g/mol): C, 35.48(35.50), H, 1.87(1.99), N, 24.10(24.14). ATR-FTIR (ν_{max}/cm^{-1}): 623m, 644w, 703m, 726w, 733w, 912w, 944w, 1189w, 1352w, 1501m, 1589s, 1677w, 1965w, 1991w, 2104m, 2335w, 2584w, 3231w.

Preparation of [H₂bptz](NO₃)₂ (**2f**)

Fe(NO₃)₃·9H₂O (81.2 mg, 0.2 mmol) was dissolved in 1 mL of MeCN and pipetted into one side of a H-shaped tube. bptz (47.1 mg, 0.2 mmol) was dissolved in 2 mL of MeCN and pipetted into the other side. The H-shaped tube was then carefully filled with MeCN. The solutions were allowed to slowly diffuse into each other at 4 °C, and the red plate X-ray quality single crystals of **2f** were obtained after 3 days. Yield: 14.2 g, 30% based on bptz. Anal. Found (calcd) for C₂₄H₂₀N₁₆O₁₂ (*Mr* = 724.56 g/mol): C, 39.81(39.79), H, 2.73(2.78), N, 25.89(25.02). ATR-FTIR (ν_{max}/cm^{-1}): 623m, 639w, 678m, 705w, 814w, 889w, 934w, 1010w, 1139w, 1365m, 1465s, 1784w, 2324w, 3241w.

2.2.3 X-Ray Crystallographic Study

Single crystals of **2a–2f** were mounted on a MiTeGen MicroMounts fiber in a small amount of oil prior to measurements made by Dr. Suzanne M. Neville and Dr. Craig Forsyth, Monash University. Reflection intensities were collected on a Bruker X8 APEX CCD diffractometer (Mo K_{α} radiation, $\bar{\lambda} = 0.71073 \text{ \AA}$) and equipped with an Oxford Instruments nitrogen gas Cryostream. Empirical absorption corrections were applied to all data using SADABS (Blessing, 1995). The structures were solved using SHELXS-97 (Sheldrick, 1997) and refined on F^2 using SHELXL-97 (Sheldrick, 1997) with X-SEED (Barbour, 2001) as a graphical interface.

In the final cycles of refinement, all atoms except hydrogen atoms were refined anisotropically. All hydrogen atoms were placed in idealized positions and constrained to ride on their parent atoms, with C/N–H distances in the range 0.95 to 0.99 Å, with $U_{iso}(\text{H}) = 1.2U_{eq}(\text{C, N})$ [$1.5U_{eq}(\text{C})$ for methyl hydrogen atoms]. For compounds **2a** and **2b** the [ClO₄][−] anions were found to be disordered, and were

modeled in two different orientations. The total occupancy of both orientations was fixed to one. Crystal data and details of the data collection and structure refinement for compounds **2a–2f** are summarized in Table 2.1. Selected interatomic bond lengths and angles for compounds **2a–2b**, **2c–2d** and **2e** are given in Tables 2.2, 2.3, and 2.4, respectively. The bond lengths and angles and other crystallographic data are given as supplementary material in the CIF which can be found on the attached CD-ROM.

Table 2.1 Summary of crystallographic data for the compounds **2a–2f**.

Identification code	2a	2b	2c	2d	2e	2f
Formula	C ₁₀ H ₆ Ag ₂ Cl ₂ N ₈ O ₈	C ₁₂ H ₉ AgClN ₉ O ₄	C ₂₀ H ₁₁ Ag ₂ N ₁₅	C ₁₈ H ₆ Ag ₂ N ₁₄	C ₃₆ H ₂₄ Ag ₃ N ₂₁ O ₉	C ₂₄ H ₂₀ N ₁₆ O ₁₂
<i>Mr</i>	652.87	486.60	677.18	634.11	1218.37	724.56
Crystal system	orthorhombic	orthorhombic	triclinic	monoclinic	triclinic	monoclinic
Crystal color/habit	green/block	red-green/column	orange/block	orange/block	red/plate	red/block
Crystal size (mm)	0.04 × 0.04 × 0.12	0.07 × 0.10 × 0.21	0.10 × 0.14 × 0.25	0.12 × 0.14 × 0.24	0.25 × 0.13 × 0.05	0.25 × 0.25 × 0.25
Space group	<i>Pnma</i>	<i>Pnma</i>	<i>P</i> -1	<i>P</i> 2 ₁ / <i>c</i>	<i>P</i> -1	<i>C</i> 2/ <i>c</i>
<i>a</i> (Å)	15.6189(9)	10.484(2)	7.5846(4)	6.9167(5)	8.3748(3)	18.1292(6)
<i>b</i> (Å)	11.2218(7)	16.466(3)	11.6431(7)	8.5461(5)	13.6582(5)	7.8219(2)
<i>c</i> (Å)	9.7123(6)	18.343(4)	13.6203(9)	16.9167(12)	19.0224(7)	11.7806(4)
α (°)	90	90	99.748(2)	90	74.578(2)	90
β (°)	90	90	99.023(2)	95.348(2)	78.091(2)	121.711(1)
γ (°)	90	90	94.555(2)	90	77.000(2)	90
<i>V</i> (Å ³)	1702.30(18)	3166.4(11)	1163.8(1)	995.61(12)	2018.74(13)	1421.15(8)
<i>Z</i>	4	8	2	2	2	2
<i>D</i> _{calc} (Mg m ⁻³)	2.547	2.041	1.933	2.115	2.004	1.693
Temperature (K)	123(2)	123(2)	123(2)	123(2)	123(2)	123(2)
μ (MoK α) (mm ⁻¹)	2.68	1.488	1.73	2.01	1.527	0.140
<i>F</i> (000)	1256	1290.0	660	612	1200	744
θ range (°)	3.0 – 29.2	1.7 – 30.7	1.5 – 33.8	2.4 – 30.6	1.7 – 27.5	1.6 – 27.5
Limiting indices <i>h</i>	–18 → 18	–8 → 12	–9 → 5	–8 → 8	–10 → 10	–21 → 22
<i>k</i>	–8 → 13	–21 → 5	–13 → 10	0 → 10	–17 → 17	–9 → 10
<i>l</i>	–11 → 6	–23 → 6	–13 → 10	0 → 20	–24 → 24	–15 → 14
<i>T</i> _{min} / <i>T</i> _{max}	0.879/0.898	0.836/0.901	0.748/0.841	0.721/0.786	0.788/0.926	0.966/0.966
Reflections collected/unique	5595/1583	6642/3316	2986/2837	1750/1750	28207/8495	4753/1551
<i>R</i> _{int}	0.029	0.079	0.108	0.054	0.036	0.0213
Data/restraints/parameters	1482/42/169	1973/42/284	2403/0/335	1564/0/154	7711/0/622	1443/0/122
<i>R</i> ₁ , <i>wR</i> ₂ [all data]	0.042, 0.109	0.060, 0.146	0.032, 0.082	0.033, 0.068	0.061, 0.104	0.038, 0.091
<i>R</i> ₁ , <i>wR</i> ₂ [<i>I</i> > 2 σ (<i>I</i>)]	0.040, 0.106	0.106, 0.176	0.041, 0.099	0.028, 0.064	0.053, 0.101	0.035, 0.088
Goodness of fit, <i>S</i>	1.12	1.01	0.84	0.94	1.25	1.09
$\Delta\rho_{\min}$, $\Delta\rho_{\max}$ (e Å ⁻³)	2.37, –1.18	1.15, –1.13	0.60, –0.87	0.84, –0.65	0.85, –1.15	0.22, –0.27

Computer programs: Diamond v. 3e (Brandenburg and Putz, 2006), SADABS (Blessing, 1995), SHELXL-97 (Sheldrick, 1997), SHELXS-97 (Sheldrick, 1997) and X-SEED (Barbour, 2001).

Table 2.2 Selected bond lengths and angles for **2a** (Å, °). ^a

Ag1–N1	2.353(5)	Ag2–N4	2.529(5)
Ag1–N2	2.464(5)	Ag2–O2 ⁱ	2.499(9)
Ag1–O1	2.328(8)	Ag2⋯O5 ⁱⁱ	2.667(6)
Ag2–N3	2.392(5)	Ag2⋯O7	3.174(6)
Ag1⋯Ag1 ⁱⁱⁱ	7.614(1)	Ag1⋯Ag2	6.378(1)
Ag2⋯Ag2 ^v	7.757(1)	Ag1⋯Ag2 ^{iv}	4.289(1)
<hr/>			
N1–Ag1–N1 ^v	105.7(2)	N3–Ag2–N3 ^{vi}	103.3(3)
N1–Ag1–N2	67.8(1)	N3–Ag2–N4	66.9(1)
N1–Ag1–N2 ^v	142.5(1)	N3–Ag2–N4 ^{vi}	137.1(1)
N1–Ag1–O1	112.1(1)	N3–Ag2–O2 ⁱ	116.0(3)
N2–Ag1–N2 ^v	94.5(2)	N4–Ag2–N4 ^{vi}	91.6(2)
N2–Ag1–O1	104.0(1)	N4–Ag2–O2 ^{vii}	75.3(3)

^a Estimated standard deviations of the least significant digits are given in parentheses. Symmetry codes: (i) $x, -y+1/2, z$; (ii) $1/2+x, 1/2-y, 1/2-z$; (iii) $-x, 1/2+y, -z$; (iv) $-x, y-1/2, -z$; (v) $-x, y-1/2, -z$; (vi) $x, -y-1/2, z$; (vii) $-x, -y, -z$.

Table 2.3 Selected bond lengths and angles for **2b** (Å, °). ^a

Ag1–N1	2.478(7)	Ag1–N6	2.522(7)
Ag1–N2	2.481(6)	Ag1–N7 ⁱ	2.583(7)
Ag1–N5	2.440(7)	Ag1–N8 ⁱ	2.456(7)
Ag1–Ag1 ⁱⁱ	4.283(1)	Ag1–Ag1 ⁱⁱⁱ	6.488(1)
Ag1–Ag1 ^{iv}	7.774(1)		
<hr/>			
N1–Ag1–N2	67.3(2)	N2–Ag1–N8 ⁱ	122.0(2)
N1–Ag1–N5	153.0(2)	N5–Ag1–N6	66.5(2)
N1–Ag1–N6	106.7(2)	N5–Ag1–N7 ⁱ	82.9(2)
N1–Ag1–N7 ⁱ	117.0(2)	N5–Ag1–N8 ⁱ	113.7(2)
N1–Ag1–N8 ⁱ	92.1(2)	N6–Ag1–N7 ⁱ	130.1(2)
N2–Ag1–N5	102.7(2)	N6–Ag1–N8 ⁱ	91.4(2)
N2–Ag1–N6	145.5(2)	N7 ⁱⁱⁱ –Ag1–N8 ⁱ	65.3(2)
N2–Ag1–N7 ⁱ	77.0(1)		

^a Estimated standard deviations of the least significant digits are given in parentheses. Symmetry codes: (i) $x+1/2, y, -z+1/2$; (ii) $x, 1/2-y, z$; (iii) $x-1/2, y, 1/2-z$; (iv) $x-1/2, 1/2-y, 1/2-z$.

Table 2.4 Selected bond lengths and angles for **2c** and **2d** (Å, °). ^a

2c			
Ag1–N1	2.491(4)	Ag2–N5	2.395(3)
Ag1–N2	2.364(4)	Ag2–N7	2.373(4)
Ag1–N9	2.230(3)	Ag2–N12	2.174(4)
Ag1–N10	2.294(4)	Ag2–N15	2.629(5)
N1–Ag1–N2	68.5(1)	N5–Ag2–N7	69.5(1)
N1–Ag1–N9	118.9(1)	N5–Ag2–N12	152.6(1)
N1–Ag1–N10	103.6(1)	N5–Ag2–N15	86.8(1)
N2–Ag1–N9	139.2(1)	N7–Ag2–N12	137.5(1)
N2–Ag1–N10	108.2(1)	N7–Ag2–N15	100.3(1)
N9–Ag1–N10	108.1(1)	N12–Ag2–N15	90.2(1)
2d			
Ag1–N1	2.332(4)	Ag2–N6 ⁱ	2.461(4)
Ag1–N2	2.627(4)	Ag2–N7 ⁱⁱ	2.423(3)
Ag2–N5	2.237(4)		
N1–Ag1–N2	66.3(1)	N2–Ag1–N6 ⁱ	82.8(1)
N1–Ag1–N5	163.1(1)	N2–Ag1–N7 ⁱⁱ	146.9(1)
N1–Ag1–N6 ⁱ	106.1(1)	N5–Ag1–N6 ⁱ	87.9(1)
N1–Ag1–N7 ⁱⁱ	89.4(1)	N5–Ag1–N7 ⁱⁱ	89.6(1)
N2–Ag1–N5	107.1(1)	N6 ⁱ –Ag1–N7 ⁱⁱ	127.3(1)

^a Estimated standard deviations of the least significant digits are given in parentheses.

Symmetry codes: (i) $-x, y-1/2, -z+1/2$; (ii) $-x, y+1/2, -z+1/2$.

Table 2.5 Selected bond lengths and angles for **2e** (Å, °). ^a

Ag1–N1	2.293(4)	Ag2–O4	2.598(5)
Ag1–N2	2.540(4)	Ag3–N11	2.467(4)
Ag1–N17 ⁱ	2.561(4)	Ag3–N12	2.278(4)
Ag1–N18 ⁱ	2.237(4)	Ag3–N13	2.244(4)
Ag1–O1	2.514(4)	Ag3–N14	2.734(3)
Ag2–N5	2.543(4)	Ag3–O7	2.577(4)
Ag2–N6	2.303(4)	Ag1⋯Ag2	7.667(1)
Ag2–N7	2.287(4)	Ag1⋯Ag3 ⁱ	7.517(1)
Ag2–N8	2.578(4)	Ag2⋯Ag3	7.473(1)
N1–Ag1–N2	68.1(1)	N5–Ag2–O4	105.6(1)
N1–Ag1–N17 ⁱ	101.8(1)	N6–Ag2–N7	157.2(1)
N1–Ag1–N18 ⁱ	152.3(1)	N6–Ag2–N7	103.8(1)
N1–Ag1–O1	80.3(1)	N6–Ag2–O4	93.3(1)
N2–Ag1–N17 ⁱ	164.1(1)	N7–Ag2–N8	69.1(1)
N2–Ag1–N18 ⁱ	113.4(1)	N7–Ag2–O4	109.5(1)
N2–Ag1–O1	78.6(1)	N8–Ag2–O4	105.1(1)
N17 ⁱ –Ag1–N18 ⁱ	69.2(1)	N11–Ag3–N12	69.8(1)
N17 ⁱ –Ag1–O1	112.7(1)	N11–Ag3–N13	114.6(1)
N18 ⁱ –Ag1–O1	127.3(1)	N11–Ag3–O7	103.4(1)
N5–Ag2–N6	68.4(1)	N12–Ag3–N13	156.3(1)
N5–Ag2–N7	105.7(1)	N12–Ag3–O7	99.3(1)
N5–Ag2–N8	148.6(1)	N13–Ag3–O7	101.8(1)

^a Estimated standard deviations of the least significant digits are given in parentheses.

Symmetry code: (i) $x-2, y, z+1$.

2.3 Results and Discussion

2.3.1 1-D Ribbons Structure of $[\text{Ag}_2(\text{bmtz})(\text{ClO}_4)]\text{ClO}_4$ (**2a**)

The complex **2a** was prepared as deep green blocks from the 4:1 reaction of AgClO_4 and the bmtz ligand in MeNO_2 solution at room temperature. Attempts to grow single crystals by change of counter anions from AgClO_4 to AgBF_4 and AgSbF_6 using the same procedure as in **2a** were unsuccessful. Figure 2.1 shows the asymmetric unit with atomic numbering and the detailed coordination environment for the Ag(I) ions. There are two types of crystallographically and chemically different Ag(I) ions. The Ag1 center adopts a square pyramidal five coordinate geometry with four nitrogen atoms from two different bmtz ligands and one oxygen atom from a coordinated perchlorate counter ion in axial position. The geometry is evaluated by the parameter, $\tau = (\alpha - \beta)/60$, where α and β are the angles between the nitrogen donor atoms forming the basal plane in square pyramidal geometry. For ideal square pyramidal and trigonal bipyramidal geometry τ is equal to 0 and 1, respectively (Addison *et al.*, 1984). The calculated values of the τ parameter for the Ag1 ion is equal to 0, indicating that Ag1 geometry in **2a** is perfectly square pyramidal. The Ag2 center has a five coordinate geometry formed by four nitrogen donor of two different bmtz ligands and an oxygen of a perchlorate counter ion in the axial position. However, Ag2 also weakly bonded by another oxygen atom from a different perchlorate counter ion to give a pseudo trigonal prismatic arrangement.

The Ag–N bond lengths range from 2.328(8) to 2.529(5) Å. This range is comparable to that found in the square-pyramidal geometry of $[\text{Ag}_2(\text{bptz})_2(\text{CH}_3\text{CN})_2][\text{PF}_6]_2$ (Schottel *et al.*, 2006). The Ag–O bond lengths are 2.328(1) and 2.521(10) Å for Ag1–O1 and Ag2–O2, respectively. These values are shorter than the mean value

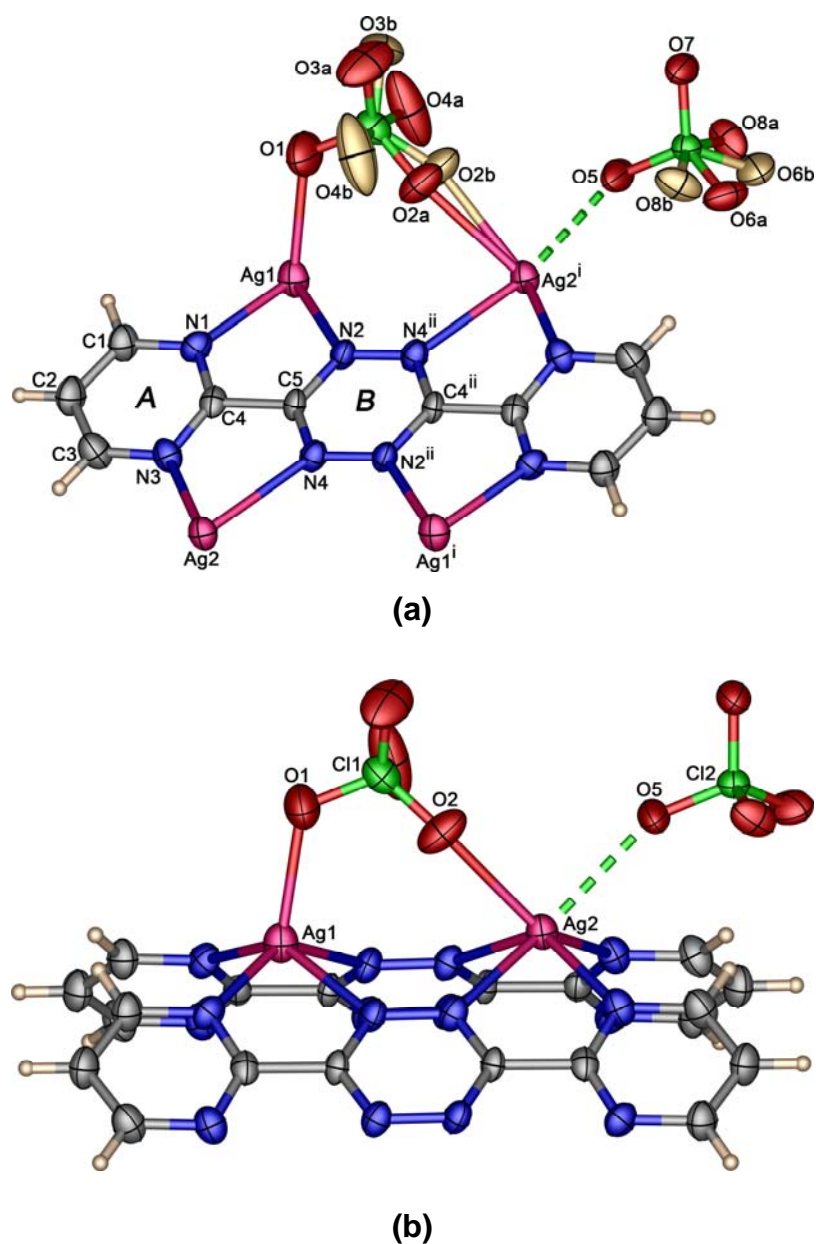


Figure 2.1 (a) Thermal ellipsoid plot of a fragment at the 50% probability level containing the asymmetric unit with atom numbering and (b) coordination environments of the metal centers of **2a**. The labeling scheme, *A* and *B*, applied for the phenyl rings are used to identify the rings in subsequent discussion. Symmetry codes: (i) $-x, -0.5+y, -z$; (ii) $-x, 0.5+y, -z$.

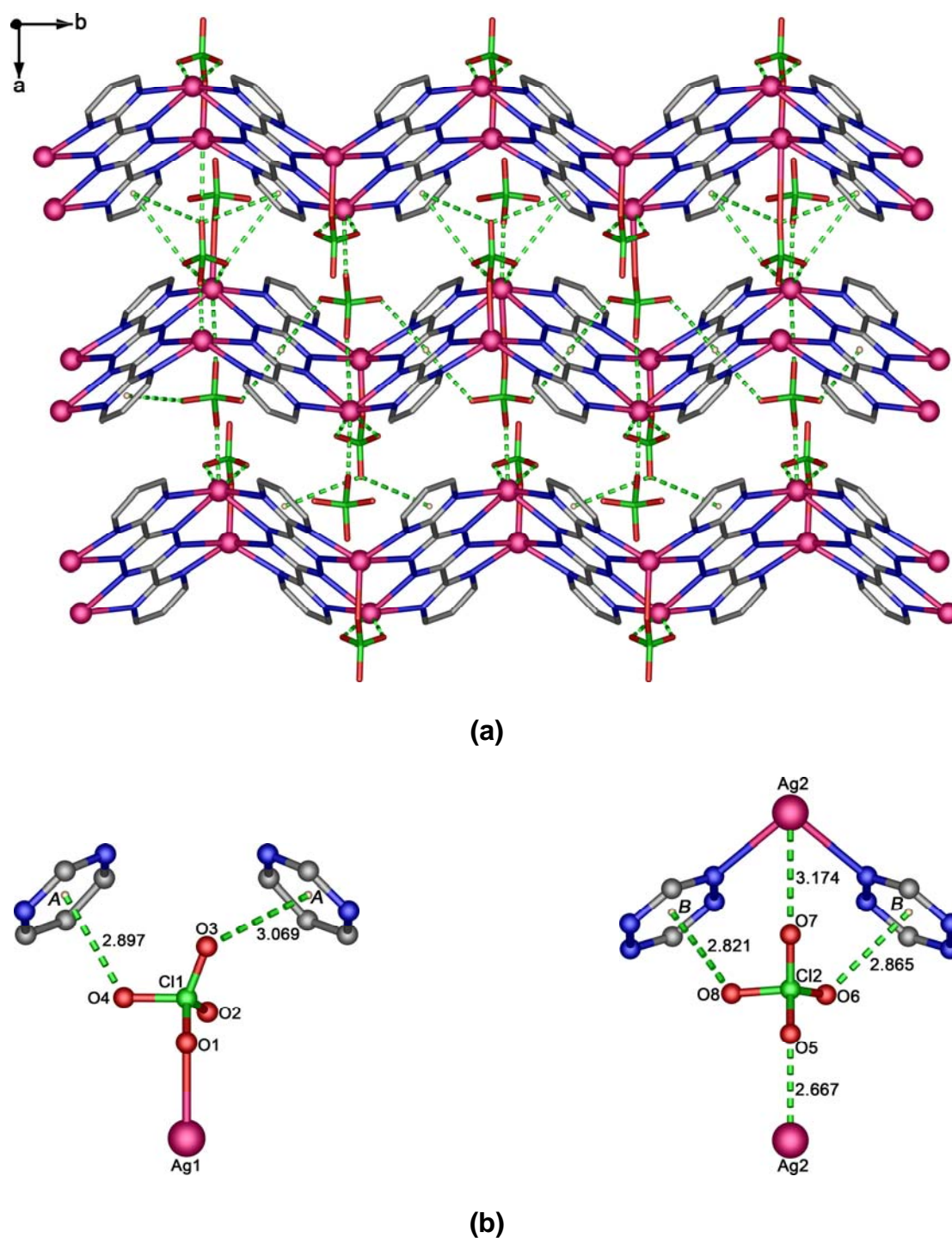


Figure 2.2 (a) Packing diagram for **2a** viewed down the c axis and showing anion $\cdots\pi$ and Ag $\cdots\pi$ interactions and (b) the shortest contacts between perchlorate anions and the pyrimidine or tetrazine rings and Ag ions.

of 2.53 Å for Ag–O(ClO₃[−]) from 370 datasets with 752 occurrences obtained from the CSD (Allen *et al.*, 1991). The Ag²⋯O5 bond length is 2.667(6) Å. This value is considered to be a weak interaction and not a formal Ag–O bond (Young and Hanton, 2008). The values of the intra ligand N–C and C–C bond distances have typical values, and are in agreement with those reported for the free bmtz molecule (Glöckle *et al.*, 2001). The pyrimidine and the tetrazine rings of the bmtz ligand are planar, but the ligand as a whole is not. The mean deviation (r. m. s. deviation of fitted atoms) from the best plane calculated using eighteen atoms is 0.046 Å with the largest deviation being 0.091(4) Å at N2. Each bmtz molecule is *bis*-chelating to two Ag(I) ions in the *syn* orientation. The Ag⋯Ag separation along the length of the bmtz ligands is 4.289(1) Å. The Ag⋯Ag separations across the bridging bmtz ligands range from 6.378(1) to 7.757(1) Å (Table 2.2).

The structure of **2a** consists of 1-D [Ag(bmtz)]⁺ cation ribbons running parallel to the crystallographic *b* axis, and the perchlorate counter anions lie between the cationic chains. The self-assembly of the supramolecular coordination polymers in **2a** is the result of combinations of forces including strong silver–bmtz coordination bonds (Table 2.2) and weak interactions of intermolecular anion⋯π, C–H⋯O, C–H⋯π hydrogen bonds and π–π stacking (Tables 2.6–2.8). These interactions help to stabilize the assembly as well as increase the dimensionality of the structure.

Along the crystallographic *c* axis, each ribbon is connected to two adjacent ribbons *via* anion⋯π, Ag⋯N, *ef* C–H⋯π and C–H⋯O interactions. Each anion interacts with the centroid (*C_g*) of a pyrimidine or tetrazine ring with the O⋯*C_g*(pyrimidine)/*C_g*(tetrazine) ranging from 2.882(8) to 3.151(20) Å. The Ag⋯O distances of 2.667(6) [Ag²⋯O5 (1/2+*x*, 1/2−*y*, 1/2−*z*)] and 3.174(6) Å [Ag²⋯O7] are

significantly shorter the sum of the van der Waals radii of Ag and O, 3.22 Å (Bondi, 1964), indicating the existence of Ag \cdots O interactions, Figure 2.2. One feature of **2a** is the formation of *ef* C–H \cdots π interactions. Hydrogen atoms, H2, of the stacked pyrimidine rings point towards the C_g faces of pyrimidine rings of N1/N2/C1/C2/C3/C4 (ring *A*) at distance 3.192(9) Å with dihedral angle of 39.4(9)°, Figure 2.3.

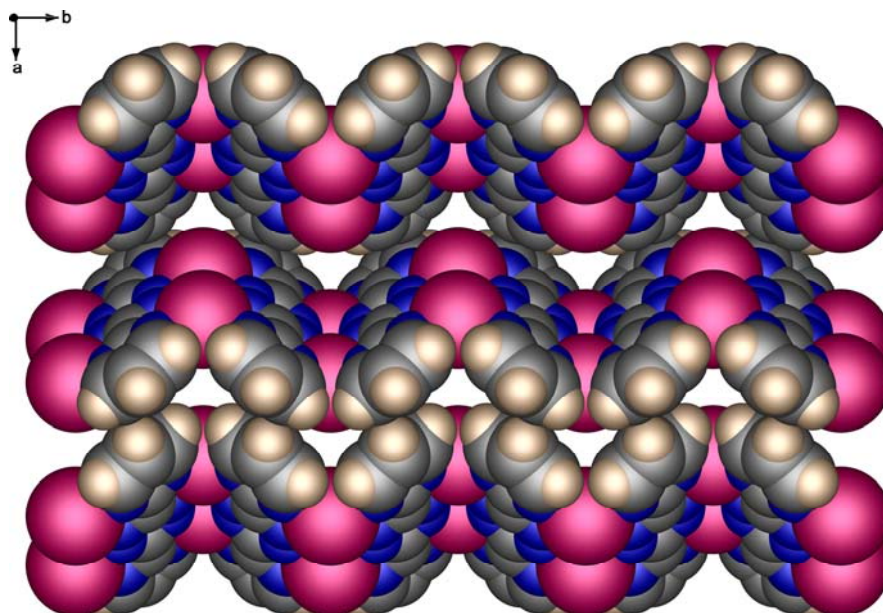


Figure 2.3 Space-filling representations for **2a** project slightly onto *ab* plane showing *ef* C–H \cdots π interactions.

The shortest C \cdots C distance between the pyrimidine rings (ring *A*) of the [Ag(bmtz)]⁺ moiety is 3.325(9) Å at C1, indicating the presence of weak offset $\pi\cdots\pi$ interactions (Desiraju and Steiner, 1999), Figure 2.4. Further investigation of the packing structure showed that the assembly of the 1-D ribbons of **2a** into a 3-D supramolecular architecture is accomplished *via* additional C–H \cdots O hydrogen bonds involving the anions and the bmtz ligands.

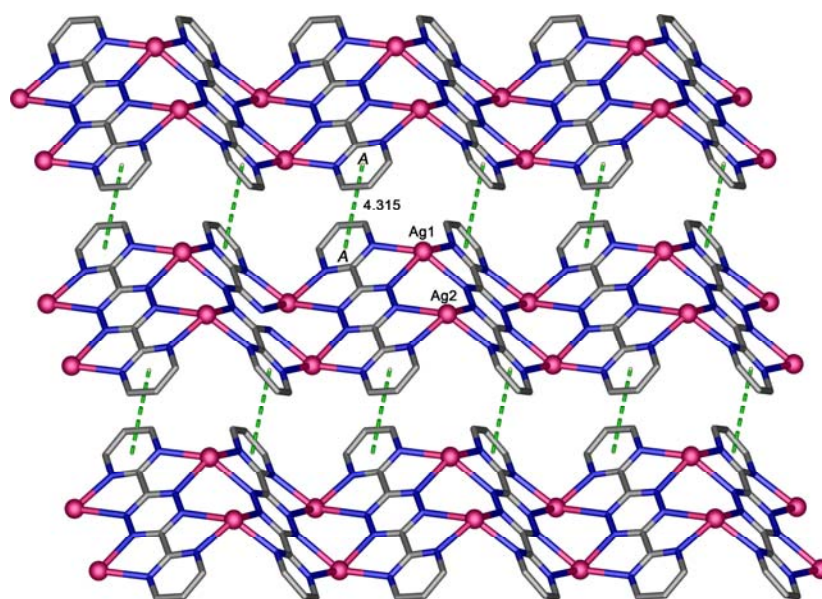


Figure 2.4 Packing diagram for **2a** showing weak $\pi\cdots\pi$ interactions.

Table 2.6 Hydrogen bond geometries for **2a** and **2b** (Å, °).^a

D–H \cdots A	d[D–H]	d[H \cdots A]	d[D \cdots A]	\angle [D–H–A]
2a				
C2–H2 \cdots O4 ⁱ	0.95	2.50	3.220(10)	144.4
C2–H2 $\cdots\pi$ (ring A ⁱⁱ)	0.95	3.192(9)	3.790(10)	39.4(2)
2b				
C3–H3 \cdots O2 ⁱⁱⁱ	0.95	2.53	3.179(15)	125.2
C6–H6 \cdots O4a ⁱⁱⁱ	0.95	2.16	2.918(17)	135.4
C6–H6 \cdots O4b ^{iv}	0.95	2.76	3.140(17)	104.8
C7–H7 \cdots O4a ⁱⁱⁱ	0.95	2.90	3.253(18)	103.4
C7–H7 \cdots O4b ^{iv}	0.95	2.76	3.140(30)	104.8
C8–H8 \cdots O4b ^{iv}	0.95	2.28	2.920(30)	124.5

^a Estimated standard deviations of the least significant digits are given in parentheses. Symmetry codes: (i) $-x, 1/2+y, 1-z$; (ii) $1/2-x, -y, 1/2+z$; (iii) $1-x, -y, 1-z$; (iv) $1/2-x, -y, z-1/2$; (v) $1/2-x, -y, -1/2-z$.

Table 2.7 Geometrical parameters of π - π interactions for **2a** and **2b** (Å, °). ^a

π - π	Ceter to ceter distance ($C_g \cdots C_g$)	Closest distance of approach	Interplanar angle
2a			
ring <i>A</i> \cdots ring <i>A</i> ⁱ	4.315	3.325(9), C1	0.0(3)
2b			
ring <i>C</i> \cdots ring <i>D</i> ⁱ	4.084	3.168(13), C7	11.0(4)

^a Estimated standard deviations of the least significant digits are given in parentheses.

2a: ring *A* = N1/N3/C1/C2/C3/C4. **2b:** ring *C* = N1/N3/C1/C2/C3/C4; ring *D* = N6/N8/C6/C7/C8/C9. C_g is centroid of a ring. Symmetry code: (i) $-x, -y, 1-z$.

Table 2.8 Anion- π interactions for **2a** and **2b** (Å, °). ^a

[D-X \cdots ring]	d[X \cdots C_g]	d[X \cdots Plane]	\angle [D-X- C_g]
2a			
Cl1-O3 \cdots ring <i>A</i>	3.069	2.843(11)	114.7
Cl1-O4 \cdots ring <i>A</i>	2.897	2.840(14)	120.6
Cl2-O6 \cdots ring <i>B</i>	2.865	2.809(12)	123.7
Cl2-O8 \cdots ring <i>A</i>	2.821	2.781(10)	124.9
2b			
Cl1-O2 \cdots ring <i>F</i>	2.967	2.758(9)	109.7
Cl1-O3 \cdots ring <i>D</i>	2.895	2.849(13)	124.6
Cl1-O3 \cdots ring <i>F</i>	2.951	2.878(13)	123.3
Cl2-O5b \cdots ring <i>D</i>	3.103	3.051(47)	113.7

^a Estimated standard deviations of the least significant digits are given in parentheses.

2a: ring *A* = N1/N2/C1/C2/C3/C4; ring *B* = N1ⁱ/N2/N3ⁱ/N4/C5/C5ⁱ. **2b:** ring *D* = N2/N2ⁱⁱ/N4/N4ⁱⁱ/C5/C5ⁱⁱ; ring *F* = N5/N5ⁱⁱ/N7/N7ⁱⁱ/C10/C10ⁱⁱ. C_g is centroid of a ring. Symmetry codes: (i) $-x, -y, -z$; (ii) $x, 1/2-y, z$.

2.3.2 1-D Chain Structure of [Ag(bmtz)]ClO₄·MeCN (**2b**)

Using the same stoichiometric ratio of the metal and ligand as in **2a**, but with the diffusion solvent changed from MeNO₂ to MeCN, emerald-green column-shaped crystals of **2b** were obtained in high yield. Attempts to grow single crystals by change of counter ions from AgClO₄ to AgBF₄, AgCF₃SO₃, AgNO₃ and AgSbF₆ were unsuccessful.

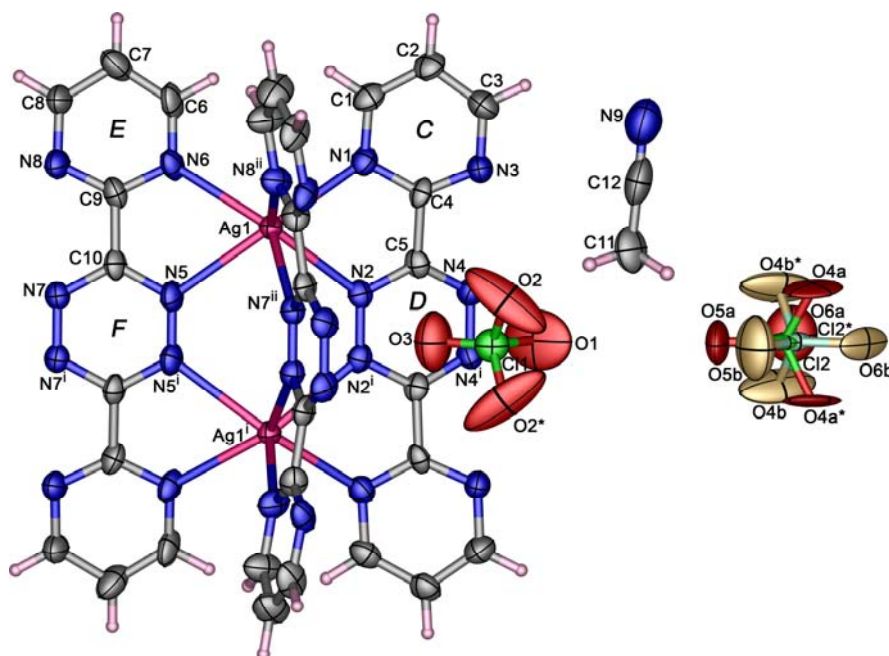


Figure 2.5 Thermal ellipsoid plot of a fragment of **2b** at the 50% probability level containing its asymmetric unit with atom numbering and showing coordination environments of metals ceter. The two orientations of the disordered of perchlorate are shown in different colors. Hydrogen atoms are shown as small spheres of arbitrary radii. The labeling scheme, *C–F*, applied for the phenyl rings are used to identity the rings in the subsequent discussion. Symmetry codes: (i) $x, 0.5-y, z$; (ii) $0.5+x, y, 0.5-z$.

The single crystal X-ray determination of **2b** revealed that MeCN solvent is present in the structure. The asymmetric unit consists of one Ag(I) cation, two half of a bmtz ligand, one perchlorate counter anion, and one solvent MeCN molecule. Each Ag(I) ion adopts a six-coordinate geometry with six nitrogen atoms from three bmtz moieties in a trigonal prismatic arrangement as shown in Figure 2.5. The Ag \cdots Ag (x , $0.5-y$, z) separation along the bmtz ligand is 4.284(1) Å. The Ag–N distances are in the range 2.440(7) to 2.583(7) Å, comparable to that observed in [Ag₂(bptz)₃][SbF₆]₂ (Schottel *et al.*, 2006). The bond lengths and angles of the bmtz molecule in **2b** are also comparable to those in **2a**.

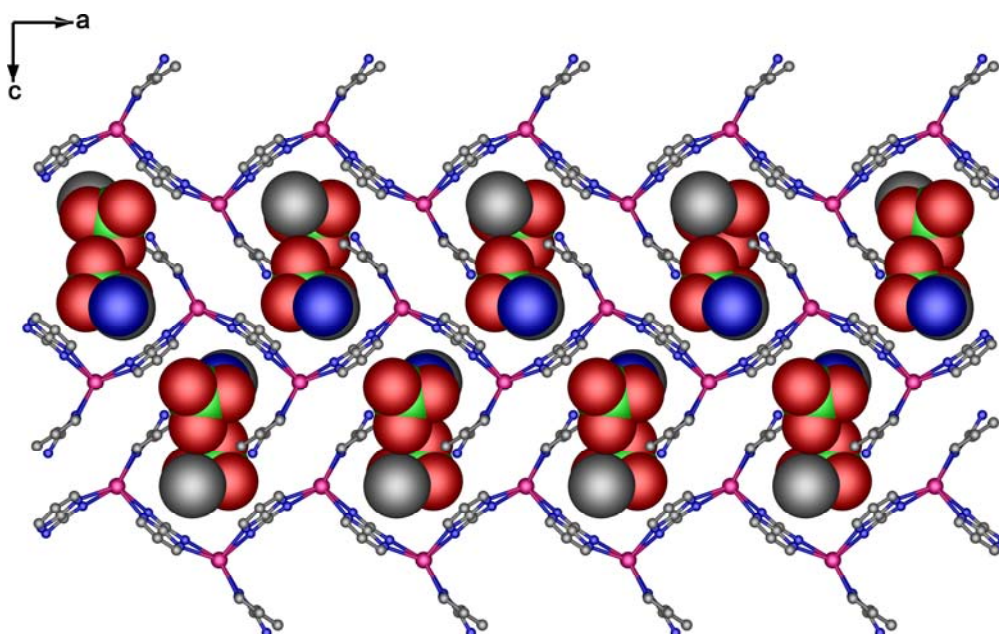


Figure 2.6 1-D chain propagating along the a axis in **2b**. The MeCN solvent and disordered counter ions are represented in space filling mode, and are located between the chains. Hydrogen atoms are omitted for clarity.

A view depicting the solid state packing in **2b** is shown in Figure 2.6. The structure has 1-D ladder ribbons running parallel to the crystallographic *a* axis. The [ClO₄] counter ions and solvent MeCN molecules lie between the ribbons and establish intermolecular interactions which cross-link the neighboring ribbons *via* anion $\cdots\pi$, C–H \cdots O and C–H $\cdots\pi$ hydrogen bonds. As illustrated in Figure 2.7, the perchlorate (Cl1) anion interacts with three tetrazine rings (rings *D* and *F*). Each oxygen atom of the [ClO₄] counter anions is oriented toward the *C_g* of tetrazine ring with the O \cdots C_{*g*} distances in the range 2.895 to 2.967 Å. Further investigation of the packing structure found that the distance of O5b \cdots C_{*g*} (ring *D*) is 3.103 Å, which indicating the existence of anion $\cdots\pi$ interactions (Hoog *et al.*, 2004) between the ribbons, Figure 2.7b.

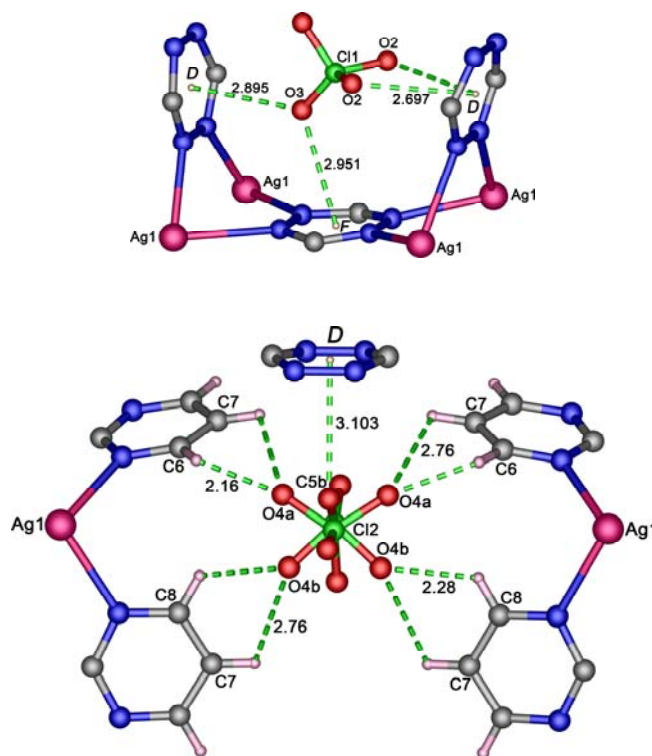


Figure 2.7 The shortest contacts in **2b**.

Furthermore, the pyrimidine moiety of the bmtz ligand is in close proximity to a neighbouring $[\text{ClO}_4]$ anions (which lie on mirror planes) with the $\text{C}\cdots\text{O}$ distances ranging from 2.918(17) to 3.179(15) Å, indicating the existence of weak hydrogen bonds (Desiraju and Steiner, 1999). Additionally, the hydrogen atoms of the MeCN solvent molecules act as hydrogen bonds donor towards C_g of pyrimidine rings of bmtz moieties (rings *C* and *D*) to form $\text{C}-\text{H}\cdots\pi$ interactions.

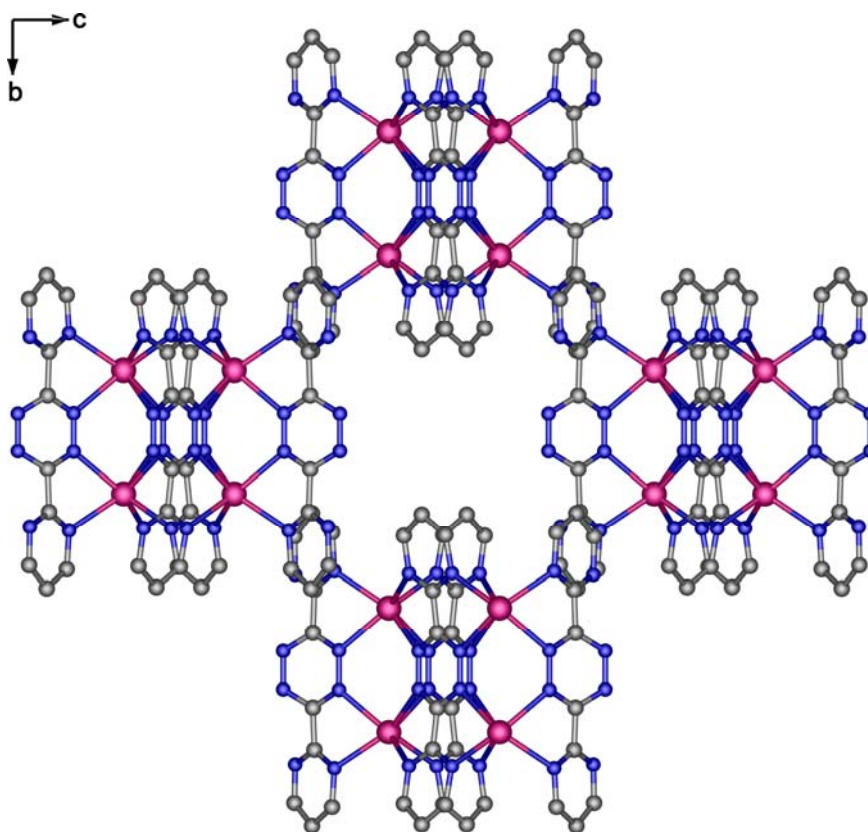


Figure 2.8 Packing in **2b** along the *a* axis showing the π - π stacking interactions between pyrimidine rings. $[\text{ClO}_4]$ counter ions, MeCN molecules, and hydrogen atoms are omitted for clarity.

Unlike the complex **2a**, in which each Ag(I) is coordinated by two bmtz moieties, **2b** adopts a *tris*-chelate Ag(I) environment. There are significant weak π - π intermolecular interactions between the pyrimidine rings of bmtz ligands from neighboring chains which are almost parallel to each other, with a $C_g \cdots C_g$ distance of 4.084 Å. Interestingly, the coexistence of a [Ag(bmtz)] coordination network with the intermolecular π - π stacking results in a highly symmetric arrangement of the 3-D supramolecular architecture as shown in Figures 2.8 and 2.9.

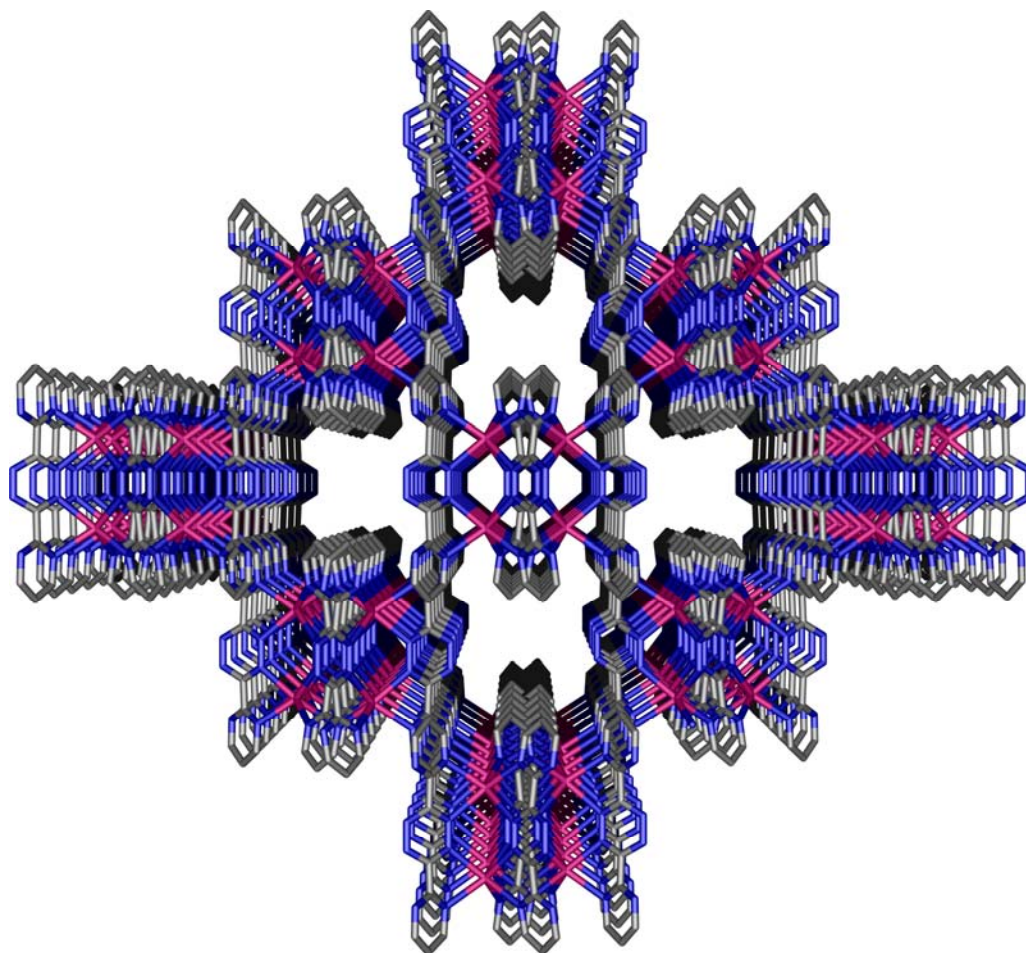


Figure 2.9 Perspective views of **2b** along the crystallographic *a* axis. [ClO₄] counter ions, MeCN molecules, and hydrogen atoms are omitted for clarity.

2.3.3 1-D Chain Structure of $[\{Ag(tcm)\}_2(H_2bmtz)(MeCN)]$ (**2c**)

A 1-D coordination polymer is formed by the 2:1 reaction of Ag(tcm) and H₂bmtz in MeCN solution, and subsequent solvent evaporation at ambient temperature. The asymmetric unit contains two Ag(I), two tcm, one H₂bmtz, and one MeCN molecule as shown in Figure 2.10. The 1-D polymeric chains contain two unique Ag(I) ions. One Ag(I) atom has a distorted tetrahedral coordination, with two bonds to two nitrogen atoms from the H₂bmtz ligand and to two nitrogen atoms from the tcm ligand. The silver atoms have relatively long bonds to H₂bmtz and short bonds to tcm ligands. The Ag–N distances are 2.491(4), 2.364(4), 2.230(3), and 2.294(4) Å for Ag1–N1, Ag1–N2, Ag1–N9, and Ag1–N10, respectively.

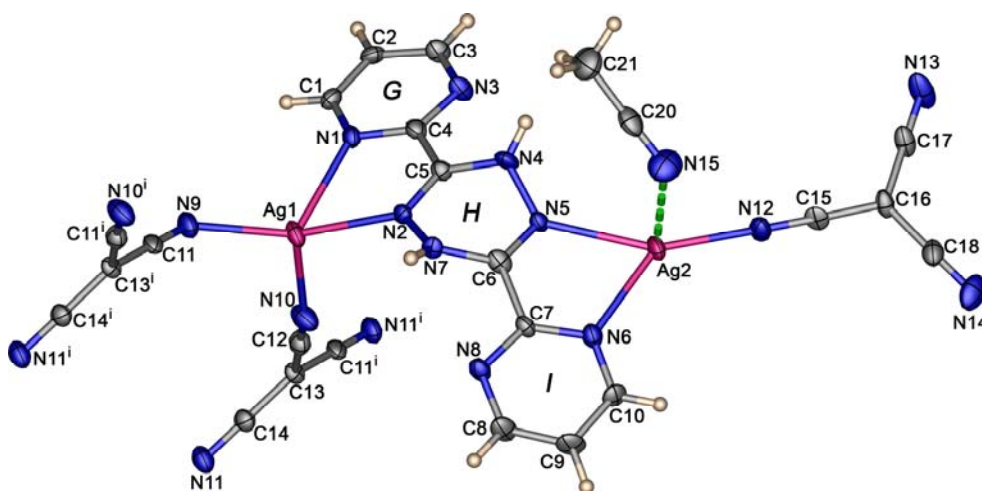


Figure 2.10 Thermal ellipsoid plot of a fragment of **2c** at the 50% probability level containing its asymmetric unit with atom numbering. Hydrogen atoms are shown as small spheres of arbitrary radii. The labeling scheme, *G–I*, applied for the phenyl rings are used to identify the rings in subsequent discussion. Symmetry codes: (i) $-x, -0.5+y, -z$; (ii) $-x, 0.5+y, -z$.

These Ag–N bond distances are comparable to those found in the Ag(I) containing aromatic N–donor and tcm ligands complexes such as [Ag(tcm)(phz)_{1/2}] and [Ag(tcm)(pyz)] (Batten *et al.*, 1998). The N–Ag–N bond angles range from 103.7(1) to 108.3(1)°. The H₂bmtz ligand exhibits an acute N··N bite distance of 2.735(6) Å [N1··N2]. The bite angle of H₂bmtz is 68.5(1)° for N1–Ag1–N2. As a result, the Ag1 coordination sphere is distorted from ideal tetrahedral geometry. The ligand as a whole is not planar (r. m. s. = 0.488 Å and the largest deviation = 0.916(4) Å at N4). Ag2 has distorted trigonal planar geometry, coordinating to two nitrogen atoms of H₂bmtz ligands and one nitrogen atom of a tcm ligand. Again, the Ag–N distances have relatively long bonds to the H₂bmtz ligand with 2.395(3) and 2.373(4) Å for Ag2–N5 and Ag2–N7, respectively, and a short bond to the tcm ligand at 2.174(4) Å (Ag2–N12). There is a MeCN molecule which bonds weakly [Ag2··N15 = 2.629(5) Å] in an axial position. The bond angles in the equatorial plane of Ag(I) differ considerably from the ideal trigonal angle of 120°, with two large angles of 152.6(1)° (N5–Ag2–N12) and 137.5(1)° (N7–Ag2–N12), and one small angle of 69.6(1)° (N5–Ag2–N7). The Σ_{Ag} is 359.7° (360° for ideal).

All tcm ions are very nearly trigonal planar, as was observed for the K(tcm) structures (Witt and Britton, 1971). As shown in Figure 2.11, the Ag1 ions are bridged by $\mu_{1,5}$ tcm anions (Batten and Murray, 2003) into 1-D chains. The Ag1 centers of the chains are also coordinated to H₂bmtz ligands, which in turn coordinate to Ag2 ions. These Ag2 ions are also coordinated to the MeCN molecules and to terminal μ_1 tcm anions. As a result, pendant Ag1–H₂bmtz–Ag2(tcm)(MeCN) ‘arms’ are created, which are attached to the Ag1(tcm) chains. These chains are further connected into a 3-D network by weak Ag··N interactions between the uncoordinated nitrogen atoms

of the μ_1 tcm anions and the Ag atoms of adjacent chains ($\text{Ag1}\cdots\text{N15} = 2.782(2) \text{ \AA}$, $\text{Ag2}\cdots\text{N16} = 2.816(2) \text{ \AA}$). Furthermore, supramolecular layers are formed by Ag– π (C_g ring *G*), π – π stacking (C_g ring *I* \cdots C_g ring *I*) and C–H \cdots π interactions as shown in Figures 2.11 and 2.12. All relevant interactions are listed in Tables 2.9–2.10.

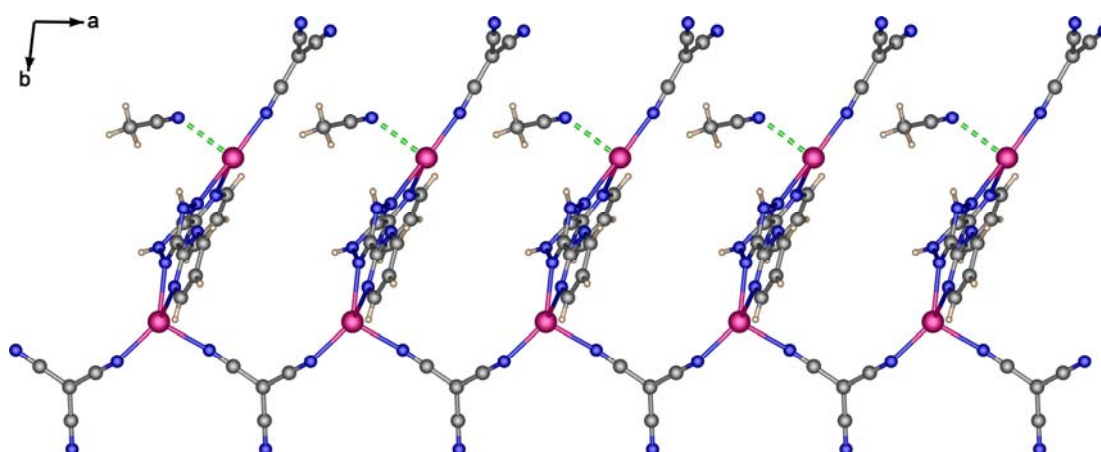


Figure 2.11 1-D chain propagating along the crystallographic *c* axis in **2c**.

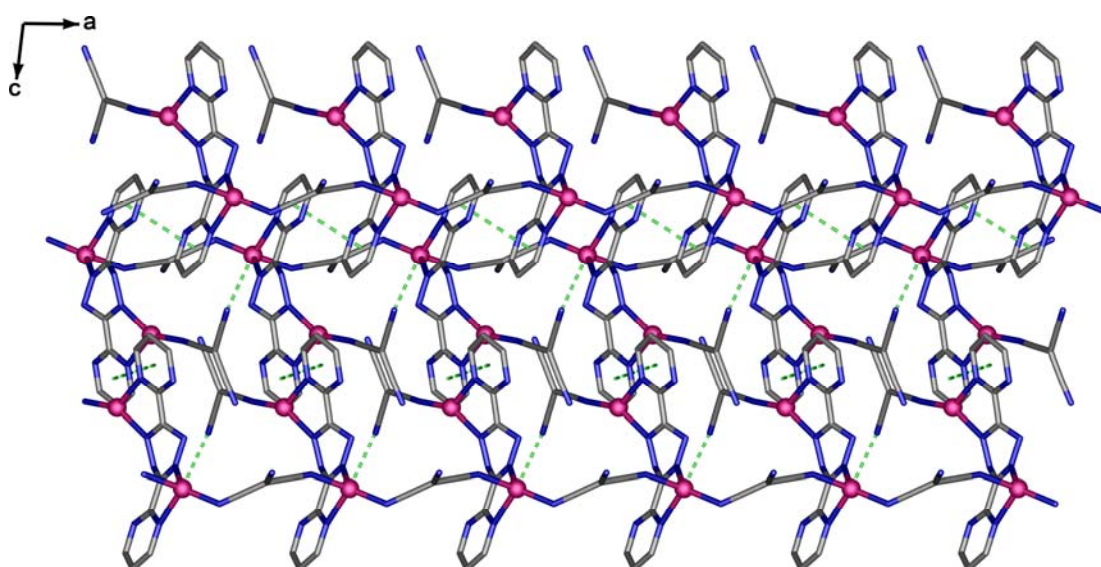


Figure 2.12 Packing diagram in **2c** view along the *b* axis showing the π – π interactions (dashed lines).

Table 2.9 Intra- and intermolecular interactions for **2c** and **2d** (Å, °).^a

D–H⋯A	d[D–H]	d[H⋯A]	d[D⋯A]	∠[D–H–A]
2c				
C1–H1⋯N11 ⁱ	0.95	2.82	3.312(8)	113.4
C2–H2⋯N14 ⁱⁱ	0.95	2.58	3.313(8)	134.0
N4–H4⋯N11 ⁱⁱⁱ	0.88	2.53	2.975(7)	111.8
N5–H5⋯N13 ^{vi}	0.88	2.55	2.961(8)	109.1
Ag1⋯N13 ^{iv}			2.781(6)	
Ag2⋯N11 ⁱⁱⁱ			3.091(5)	
Ag2⋯N14 ^v			2.817(5)	
2d				
C2–H2⋯N3 ^{vi}	0.95	2.57	3.356(5)	140.3
C3–H3⋯N4 ^x	0.95	2.74	3.615(5)	153.2
Ag⋯π (ring <i>J</i>) ^{vii}			3.551(2)	

^a Estimated standard deviations of the least significant digits are given in parentheses. Symmetry codes: (i) $-x, -y, -z$; (ii) $x-1, y-1, z-1$; (iii) $1+x, 1+y, z$; (iv) $x-1, y-1, z$; (v) $2-x, 2-y, 1-z$; (vi) $1-x, 1/2-y, 3/2-z$; (vii) $1-x, 2-y, 1-z$.

Table 2.10 Geometrical parameters of π – π interactions for **2c** (Å, °).^a

π – π	Ceter to ceter distance (C_g ⋯ C_g)	Closest distance of approach	Interplanar angle
ring <i>G</i> ⋯ring <i>G</i> ⁱ	3.607	3.291(5), N3	0.0(2)
ring <i>I</i> ⋯ring <i>I</i> ⁱ	3.781	3.465(6), C9	0.0(5)

^a Estimated standard deviations of the least significant digits are given in parentheses. Symmetry code: (i) $1-x, 1-y, -z$.

2.3.4 2-D Sheets Structure of [$\{\text{Ag}(\text{tcm})\}_2\text{bmtz}$] (**2d**)

Analogous to **2c**, reaction of a 2:1 molar ratio of Ag(tcm) with bmtz in MeCN gave an orange-red polymer [$\{\text{Ag}(\text{tcm})\}_2\text{bmtz}$], **2d**. The asymmetric unit consists of

one Ag(I), one tcm, and half a bmtz ligand as shown in Figure 2.13. The Ag and tcm moieties lie on general positions, however, the bmtz lies across an inversion center. No solvent molecules are present in the structure. The Ag atom exhibits a distorted square pyramidal AgN₅ environment, the value of the trigonality parameter τ being 0.27 (Addison *et al.*, 1984). The equatorial positions around the Ag atom are defined by four nitrogen atoms, two from the bmtz ligand (N1 and N2), and another two from a bridging tcm (N5 and N7). The apical position is filled by a nitrogen atom of another tcm bridge (N6).

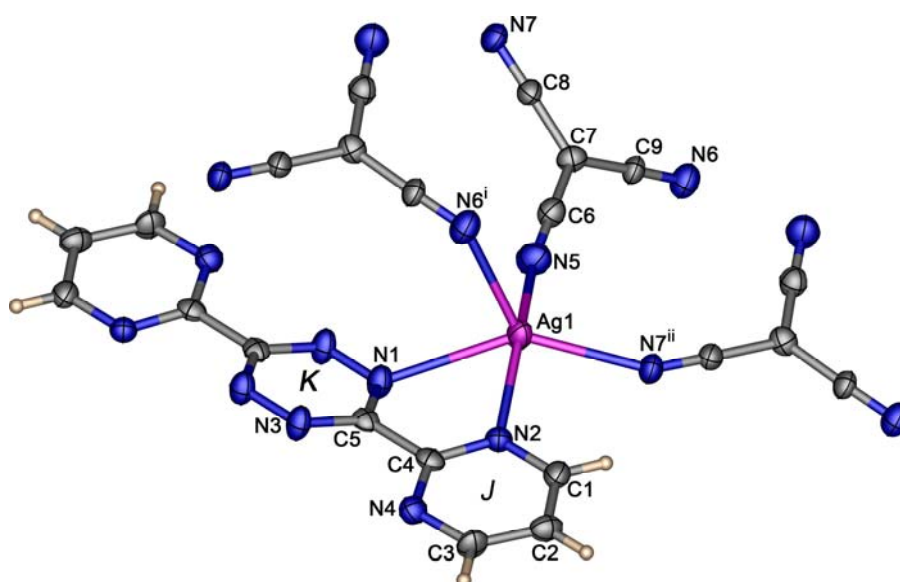


Figure 2.13 Thermal ellipsoid plot of a fragment of **2d** at the 50% probability level containing the asymmetric unit with atom numbering and showing coordination environments of the metal center. Hydrogen atoms are shown as small spheres of arbitrary radii. The labeling scheme, *K* and *L*, applied to the phenyl rings are used to identify the rings in the subsequent discussion. Symmetry codes: (i) $-x, -0.5+y, 0.5-z$; (ii) $-x, 0.5+y, 0.5-z$.

The two Ag–N_{bmtz} bond distances are 2.332(4) and 2.627(4) Å for Ag1–N1 and Ag1–N2, respectively. These values are comparable to those observed in the related *bis*-chelate of the dptz-containing Ag(I) complex [Ag(bptz)][PF₆] (Schottel *et al.*, 2006). The Ag–N_{tcm} bond distances vary in the range 2.337(4) to 2.461(4) Å. These observations are similar to those observed in [Ag(tcm)(phz)_{1/2}] and [Ag(tcm)(pyz)] (Batten *et al.*, 1998). The bmtz ligand exhibits an usual acute N··N bite distance of 2.725(5) Å [N1··N2] with a bite angle of 66.3(1)° [N1–Ag1–N2]. The reduced bite of the *bis*-chelated bmtz ligand is the main source of distortion of the ideal square pyramidal environment of the Ag(I) atoms. The N1/N2/Ag1/N5/N7 set of atoms defines the basal plane, and the largest deviation from their mean plane is 0.352(1) Å at Ag1, which is shifted from the mean basal plane toward the apical position. The Ag··Ag separations across bridging 1,2-bmtz and tcm ligands are 7.725(1) Å [Ag1··Ag1(1–*x*, 1–*y*, 1–*z*)] and 7.601(1) Å [Ag1··Ag1 (–*x*, 0.5+*y*, 0.5–*z*)], respectively.

As shown in Figure 2.12, the structure of **2d** contains distorted square pyramidal Ag atoms, which are coordinated to three tcm anions and one bmtz ligand. The tcm anions bridge in a tridentate μ -1,3,5 fashion (Batten and Murray, 2003), which is similar to those observed in M(tcm)₂, where M = Cr, Mn, Fe, Co, Ni, Cu, Zn, Cd, or Hg (Batten *et al.*, 1999), and connect the Ag(I) atoms into ladder-like motifs. These ladders are then cross-linked by the bridging bmtz ligands to generate a 2-D sheet as shown in Figure 2.14.

There are no π – π interactions between adjacent bmtz rings. The shortest distance between C_g to C_g of pyrimidine rings of bmtz ligands is 5.773(7) Å, which is out the range (3.3–3.8 Å) considered for significant π ·· π interactions (Janiak, 2000).

There are, however, weak $\text{Ag}\cdots\pi$ interaction at 3.551(2) Å between adjacent sheets. The sheets are further stacked along the crystallographic b axis by weak $\text{C-H}\cdots\text{N}$ hydrogen bonds (Table 2.2) assembled to a 3-D supramolecular architecture.

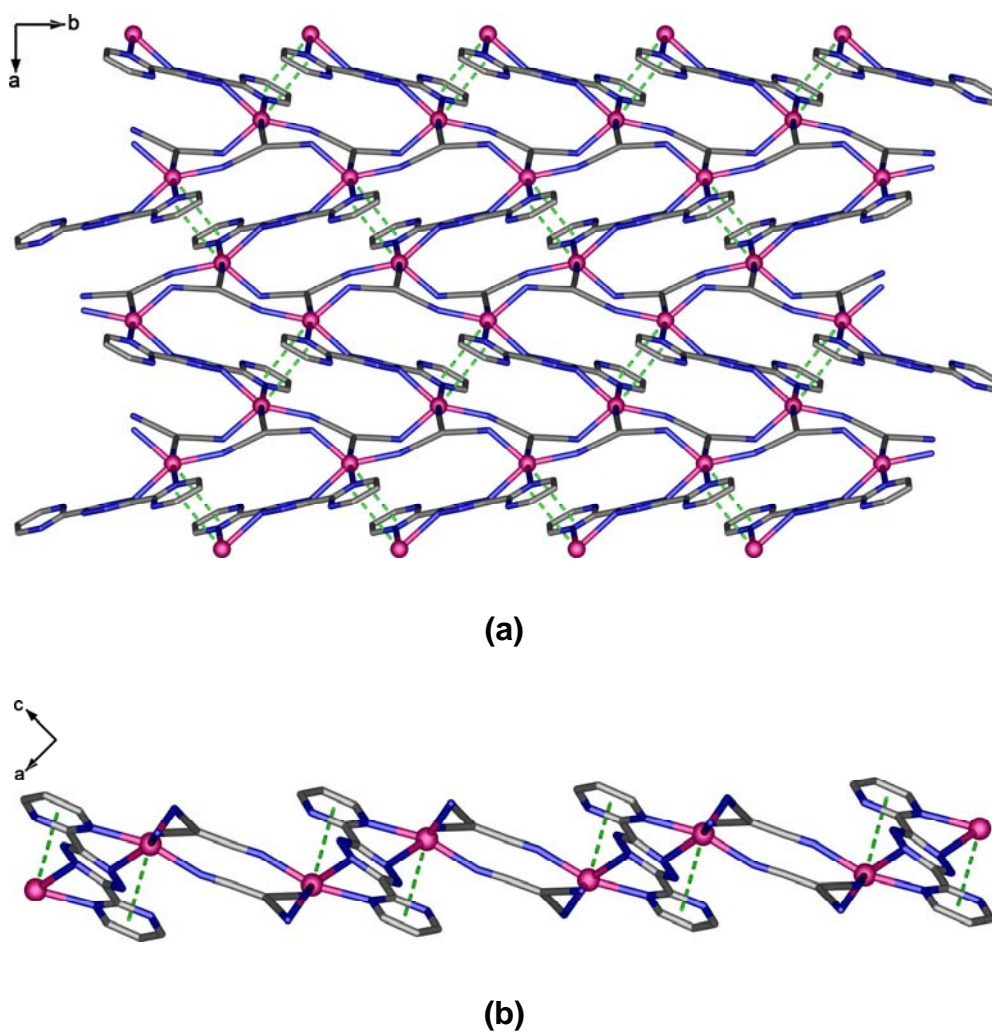


Figure 2.14 View crystal structures of **2d** along the crystallographic (a) c and (b) b axis, showing the ladder-like motifs and $\text{Ag}\cdots\pi$ interactions (indicated with dashed lines).

2.3.5 1-D Chain Structure of [Ag(bptz)(NO₃)] (**2e**)

The equivalent molar reaction of AgNO₃ and bptz in MeCN gave dark red crystals of complex [Ag(bptz)(NO₃)], **2e**. Change of mole ratio of Ag(I) metal and bptz to 1:2 and 1:4 do not have any significant effect on the nature of the products, provided the reactant ratios of 1:1 remain the same as evidenced by single crystal X-ray analysis. The unit cell parameters of a representative of those crystals were identical to the cell parameters in compound **2e**. Attempts to grow single crystals by change of counter anions from AgNO₃ to AgBF₄, AgCF₃SO₃, AgClO₄, and AgSbF₆ using the same procedure as in **2e** were unsuccessful.

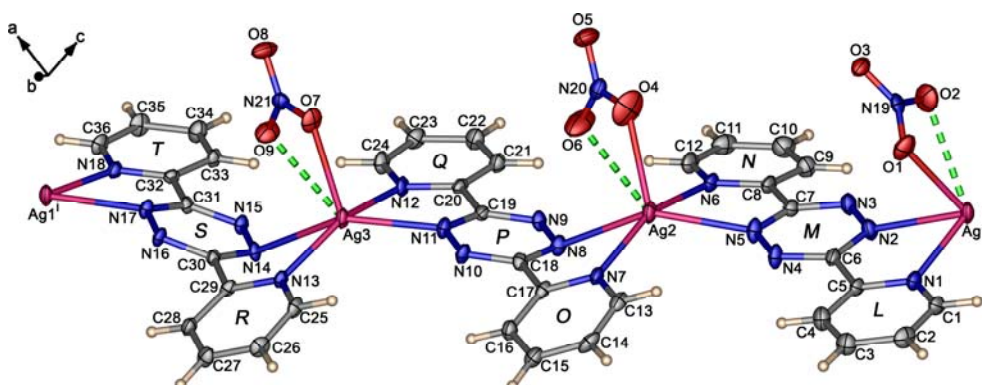


Figure 2.15 Thermal ellipsoid plot of a fragment of **2e** at the 50% probability level containing its asymmetric unit with atom numbering. Hydrogen atoms are shown as small spheres of arbitrary radii. The labeling scheme, *L-T*, applied to the phenyl rings are used to identify the rings in subsequent discussion. Symmetry code: (i) $2+x, y, -1+z$.

Compound **2e** is isostructural with the analogous PF₆ salt, [Ag(bptz)]·PF₆ (Schottel *et al.*, 2006). The asymmetric unit is shown in Figure 2.15, and consists of three Ag(I), each of which reside on an inversion center, three bptz ligands, and three

nitrate molecules. Each Ag(I) ion has the same environment. The Ag(I) ions exhibit a square pyramidal geometry with chelating bptz ligands forming the basal plane, and an oxygen atom belonging to a nitrate counter anions coordinated in the apical position.

The Ag–N bond lengths range from 2.237(4) to 2.734(3) Å and are comparable to those found in compounds **2a-2b**, and other related Ag(I) containing bptz complexes such as [Ag₂(bptz)₃](AsF₆)₂ (Schottel *et al.*, 2005) and [Ag(bptz)]·PF₆ (Schottel *et al.*, 2006). The Ag–O bond lengths range from 2.514(4) to 2.598(5) Å, and are within the expected range and comparable to the calculated average value of 2.51 Å from 370 datasets with 752 occurrences for Ag–O(NO₂)[−] obtained from the CSD (Allen *et al.*, 1991). The bptz ligand exhibits acute N···N bite distances ranging from 2.716(6) to 2.824(6) Å with bite angles of between 68.1(1) and 69.8(1)°. The axial N–Ag–N bond angles are 177.7(1) to 108.3(1)°. The calculated values of the τ parameter for Ag1, Ag2 and Ag3 ions are 0.195, 0.143 and 0.123, respectively, indicating that all geometries are close to square pyramidal. These indicate that the Ag coordination sphere is distorted from an ideal square pyramidal. The Ag···Ag separations across the bridging bptz ligands are 7.667(1) and 7.473(1) and 7.517(1) Å, for Ag1···Ag2 Ag2···Ag3 and Ag1···Ag3 ($x-2, y, z+1$), respectively. In addition, the bptz ligand as a whole is not planar. The mean deviation (r. m. s. deviation of fitted atoms) from the best plane calculated using eighteen atoms are 0.146, 0.214 and 0.282 Å for rings L/M/N, O/P/Q, and R/S/T, respectively. The largest deviations are −0.274(5) at C10, −0.400(4) at C15 and −0.515(4) Å at C27 for rings L/M/N, O/P/Q, and R/S/T, respectively. The values of the intra ligand N–C and C–C bond distances

have their typical values, and are in agreement with those reported for the free bmtz molecule (Glöckle *et al.*, 2001).

The 1-D polymer in **2e** comprises two very similar chains running along the crystallographic *b* axis, which each chain containing three unique Ag(I) ions as shown in Figure 2.16. Significant π - π stacking and anion- π interactions occur between the 1-D chains, generating a 2-D ladder supramolecular architecture as shown in Figures 2.17 and 2.18. The π - π contacts ($C_g \cdots C_g$ distances) are in between 3.571 to 4.440 Å. The anion- π ($O \cdots C_g$ distances) interactions range from 2.672 to 3.241 Å. The neighbouring layers are additionally interlinked by C-H \cdots O hydrogen bonds. The combination of the anion- π , π - π , and C-H \cdots O interactions generates a 3-D supramolecular architecture. All relevant interactions in **2e** are listed in Tables 2.11 to 2.13.

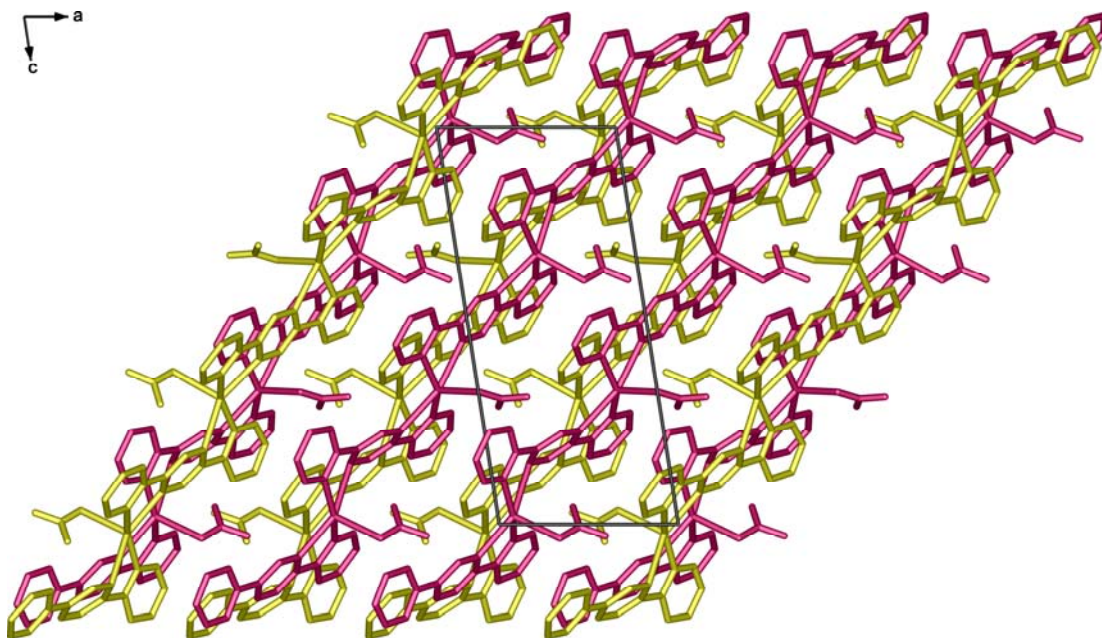


Figure 2.16 Unit cell packing diagram showing different orientation of 1-D chains in **2e**.

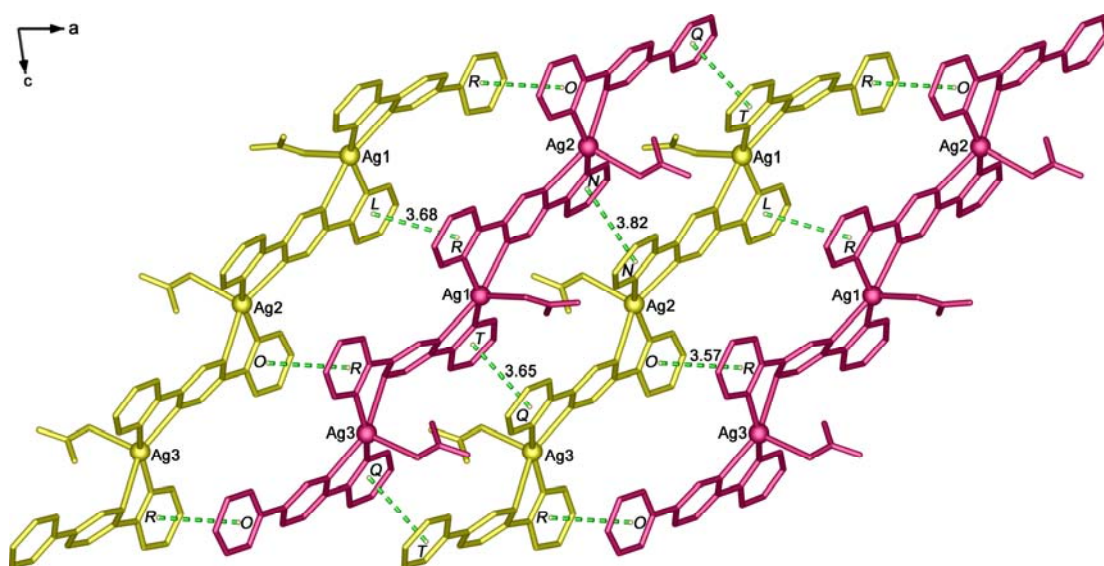


Figure 2.17 View of $\pi\cdots\pi$ interactions in **2e**.

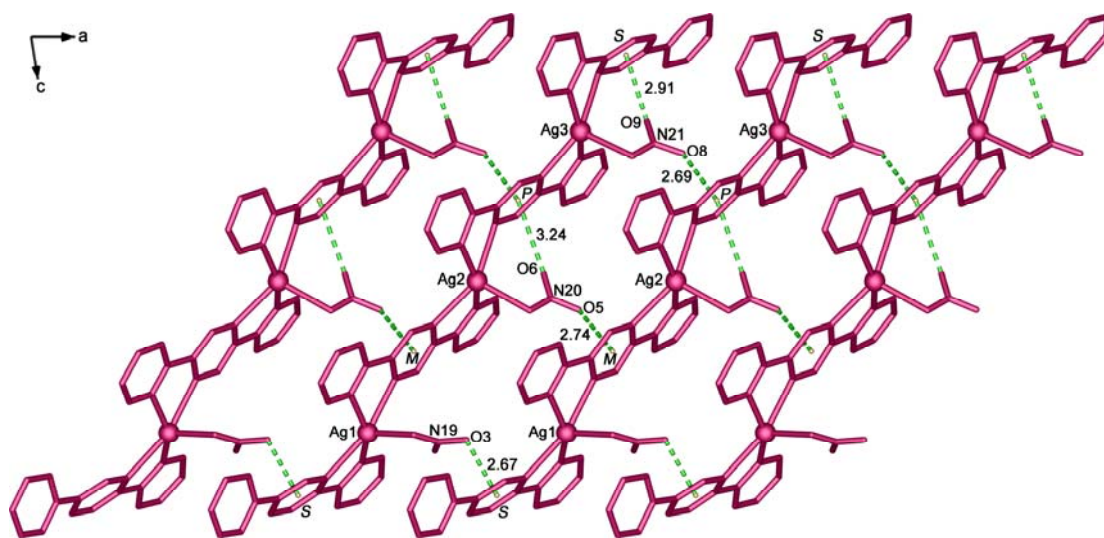


Figure 2.18 View of anion··· π interactions in **2e**.

Table 2.11 Hydrogen bond geometries for **2e** and **2f** (Å, °). ^a

D–H⋯A	d[D–H]	d[H⋯A]	d[D⋯A]	∠[D–H–A]
2e				
C2–H2⋯O4 ⁱ	0.95	2.19	3.136(6)	171.1
C3–H3⋯O3 ⁱ	0.95	2.39	3.157(6)	137.4
C4–H4⋯O1 ⁱ	0.95	2.53	3.268(6)	134.4
C14–H14⋯O1 ⁱ	0.95	2.49	3.263(7)	139.1
C15–H15⋯O8 ⁱⁱ	0.95	2.49	3.263(7)	139.1
C21–H21⋯O2 ⁱⁱⁱ	0.95	2.63	3.238(6)	122.3
C25–H25⋯O7 ⁱⁱ	0.95	2.60	3.238(6)	121.7
C26–H26⋯O7 ⁱⁱ	0.95	2.47	3.123(6)	125.6
2f				
N1–H1a⋯O3	0.93(3)	1.83(2)	2.772(1)	159.5(1)
C2–H2⋯O1 ^{iv}	0.95	2.50	3.203(1)	130.7
C4–H4⋯O1 ^v	0.95	2.37	3.072(1)	130.1

^a Estimated standard deviations of the least significant digits are given in parentheses. Symmetry codes: (i) $-x, 2-y, 1-z$; (ii) $2-x, 2-y, -z$; (iii) $1-x, 1-y, 1-z$; (iv) $x-1/2, 1/2-y, 1/2-z$; (v) $x-1/2, 1/2+y, z$; (vi) $1/2-x, 1/2-y, -z$.

Table 2.12 Geometrical parameters of π - π interactions for **2e** and **2f** (Å, °). ^a

π - π	Ceter to ceter distance ($C_g \cdots C_g$)	Closest distance of approach	Interplanar angle
2e			
ring $L \cdots$ ring L^i	3.682	3.268(6), C4	0.0(2)
ring $L \cdots$ ring M^{ii}	4.440	3.249(7), N5	6.4(2)
ring $N \cdots$ ring N^{iii}	3.823	3.696(5), C9	0.0(2)
ring $N \cdots$ ring T^{iv}	3.823	3.352(7), C32	5.6(2)
ring $O \cdots$ ring R^v	3.571	3.237(7), C29	1.2(2)
ring $O \cdots$ ring S^{vi}	4.294	3.166(4), N16	40.7(1)
ring $P \cdots$ ring R^{vi}	4.105	2.378(8), N13	29.7(1)
ring $Q \cdots$ ring Q^{iv}	3.776	3.516(6), C22	0.0(2)
ring $Q \cdots$ ring T^{vi}	3.651	3.466(6), C36	4.3(2)
2f			
ring $U \cdots$ ring U^{vii}	4.548	2.889(2), C1	39.0(1)
ring $V \cdots$ ring U^{viii}	4.638	1.737(1), C4	19.5(1)

^a Estimated standard deviations of the least significant digits are given in parentheses. **2e**: ring L = N1/C1/C2/C3/C4/C5; ring M = N2/N3/N4/N5/C6/C7; ring N = N6/C8/C9/C10/C11/C12; ring O = N7/C13/C14/C15/C16/C17; ring P = N8/N9/10/N11/C18/C19; ring Q = N12/C20/C21/C22/C23/C24; ring R = N13/C25/C26/C27/C28/C29; ring S = N14/N15/N16/N17/C30/C31; ring T = N18/C32/C33/C34/C35/C36. **2f**: ring U = N1/C1/C2/C3/C4/C5; ring V = N2/N2^{ix}/N3/N3^{ix}/C6/C6^{ix}. C_g is centroid of a ring. Symmetry codes: (i) $-1-x, 2-y, 1-z$; (ii) $-x, 2-y, 1-z$; (iii) $1-x, 1-y, 1-z$; (iv) $2-x, 1-y, -z$; (v) $1-x, 2-y, -z$; (vi) $2-x, 2-y, -z$; (vii) $1/2-x, 1/2+y, -z-1$; (viii) $1-x, 1-y, -z$; (ix) $1-x, y, 1/2-z$.

Table 2.13 Anion– π interactions for **2e** and **2f** (Å, °). ^a

[D–X⋯ring]	d[X⋯C _g]	d[X⋯Plane]	∠[D–X–C _g]
2e			
N19 ⁱ –O3 ⁱ ⋯ring <i>S</i>	2.672	2.665(3)	117.5
N20 ⁱⁱ –O5 ⁱⁱ ⋯ring <i>M</i>	2.745	2.676(4)	133.1
N20–O6⋯ring <i>P</i>	3.241	2.723(5)	144.0
N21 ⁱⁱ –O8 ⁱⁱ ⋯ring <i>P</i>	2.696	2.621(4)	139.3
N21–O9⋯ring <i>S</i>	2.913	2.802(4)	147.1
2f			
N4 ⁱⁱⁱ –O1 ⁱⁱⁱ ⋯ring <i>U</i>	3.396	2.970(1)	112.4
N4 ^{iv} –O2 ^{iv} ⋯ring <i>V</i>	3.271	2.899(1)	113.2
N4 ^v –O3 ^v ⋯ring <i>V</i>	3.485	2.988(1)	141.1

^a Estimated standard deviations of the least significant digits are given in parentheses.

2e: ring *M* = N2/N3/N4/N5/C6/C7; ring *P* = N8/N9/10/N11/C18/C19; ring *S* = N14/N15/N16/N17/C30/C31; **2f**: ring *U* = N1/C1/C2/C3/C4/C5; Ring *V* = N2/N2^{vi}/N3/N3^{vi}/C6/C6^{vi}. C_g is centroid of a ring. Symmetry codes: (i) 1+x, y, z–1; (ii) x–1, y, z; (iii) 1–x, –y, –z; (iv) x, –y, 1/2+z; (v) 1–x, 1–y, –z; (vi) 1–x, y, 1/2–z.

2.3.6 Structural Description of [H₂bptz](NO₃)₂ (**2f**)

Unexpected red crystals of composition [H₂bptz](NO₃)₂ were obtained by the 1:1 metal:ligand ratio reaction of Fe(NO₃)₃·9H₂O and bptz in MeCN at 4 °C. The crystal structure of **2f** contains a half molecule of H₂bptz (generated by inversion symmetry to the other half) and one nitrate anion in the asymmetric unit as shown in Figure 2.19. **2f** is a protonated amine salt compound in which the positive charge is localized at the H₂bptz atom N1. The protonation of the H₂bptz ligand is most likely the result of hydrolysis of the Fe^{III} (Batten *et al.*, 1998). The bond lengths of the H₂bptz ligand are within the normal range (Klein *et al.*, 1998). The ligand as a whole

is not planar due to the strengths of the noncovalent interactions which occur between the moieties.

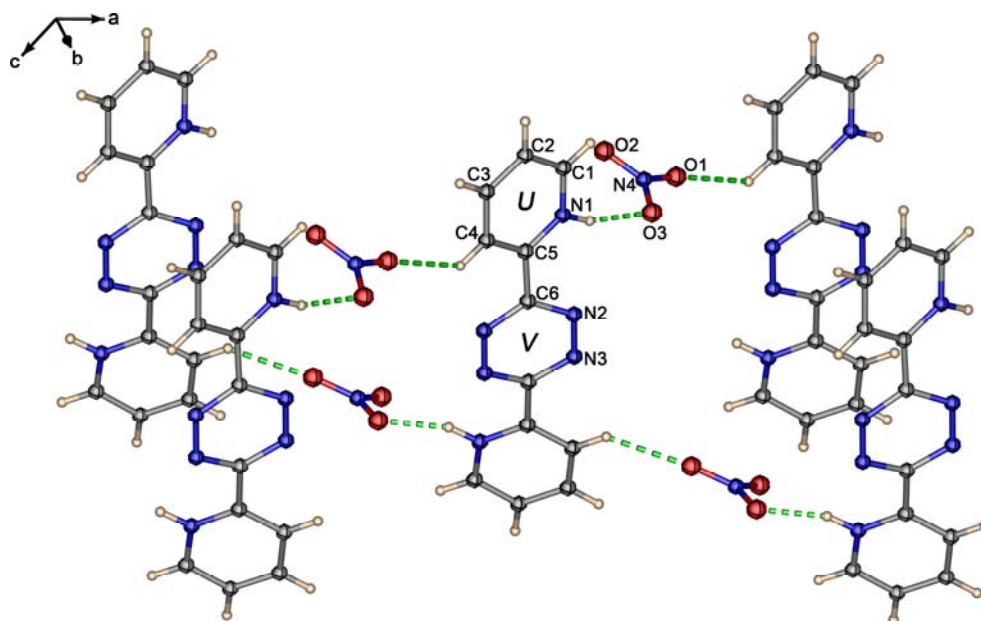


Figure 2.19 The structure of **2f**, showing 50% probability displacement ellipsoids with atom numbering scheme. Hydrogen atoms are shown as small spheres of arbitrary radii. Hydrogen bonds are shown as dash lines. The labeling scheme, *A* and *B*, applied for phenyl rings and are used to identify the rings in subsequent discussion.

Each cation molecule of H₂bptz is connected to two different H₂bmtz cations by the nitrate anion into a 2-D sheet *via* strong N–H···O and weak C–H···O hydrogen bonds (Table 2.11). Atoms N1 and C4 act as hydrogen bond donors atoms O3 and O1 (–0.5+*x*, 0.5+*y*, *z*), respectively, [N1–H1···O3 = 2.772(1) Å, C4–H4···O1 (1/2–*x*, 1/2–*y*, –*z*) = 3.072(1) Å], generating open square grid cavities with distorted (4,4) topology, as shown in Figure 2.20. The 2-D sheets are then interact to each other

through intermolecular anion- π , π - π stacking, and additional weak C-H \cdots O hydrogen bonding interactions to produce a 3-D supramolecular architecture (Tables 2.11 to 2.13).

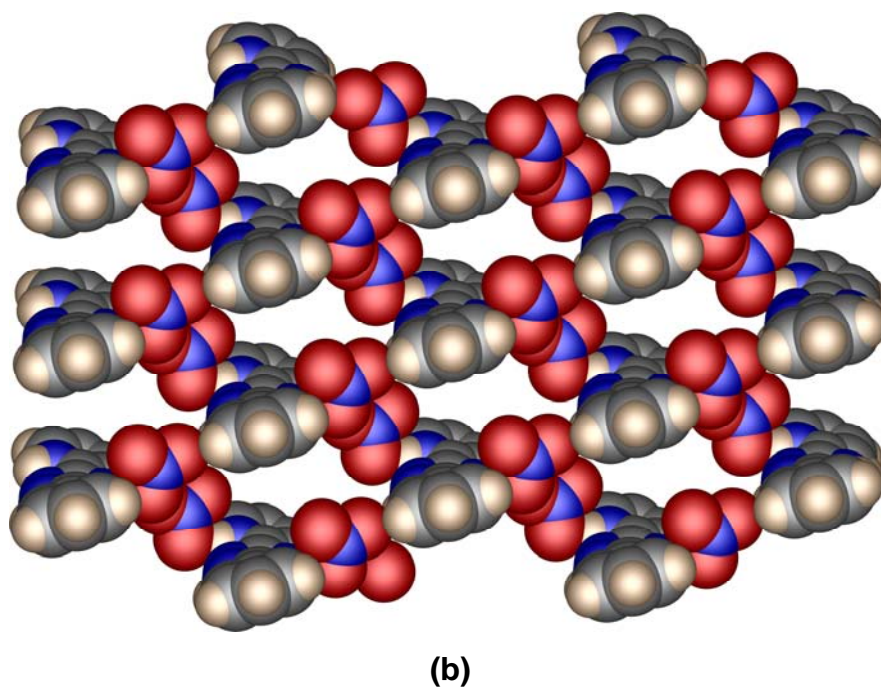
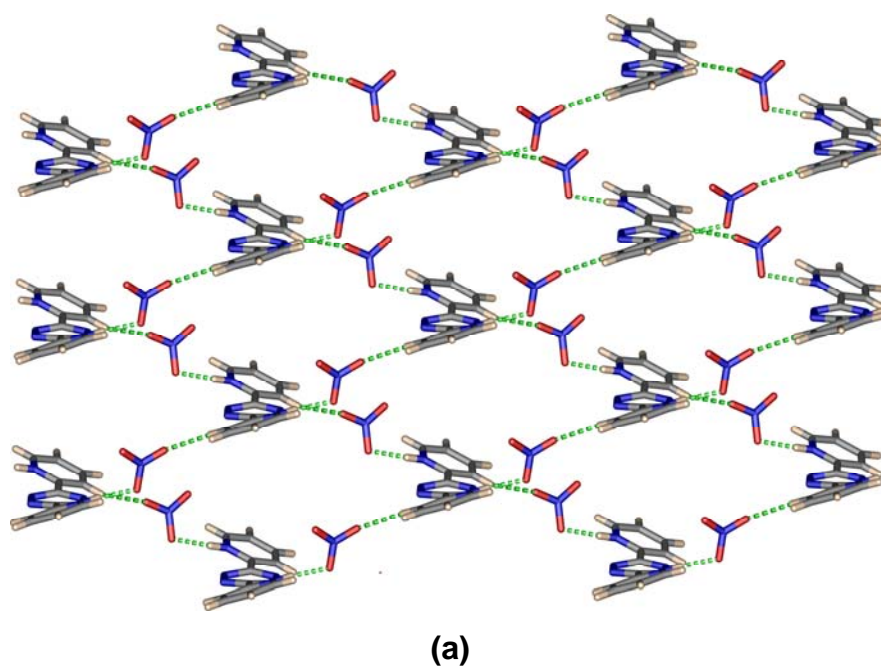


Figure 2.20 (a) Wires-sticks and (b) space-filling representations showing 2-D sheet in **2f** linked by N-H \cdots O hydrogen bonds.

2.4 Conclusions

This chapter describes new silver(I) coordination polymers, which are built up through the combination of silver-coordination, Ag- π , anion- π , hydrogen bonding, and π - π stacking interactions to generate novel supramolecular architectures. Structural studies on the resulting complexes demonstrate that the multidonal N-donor bmtz, H₂bmtz and bptz ligands can act as useful multiple bridging ligands for the Ag(I) ion. Reaction of the bmtz ligand with AgClO₄ gave 1-D chains of **2a** and **2b**. The [ClO₄] ions are coordinated to the Ag(I) ions in **2a**, but they are isolated in **2b**. The structures also differ by the incorporation of solvent molecules (**2b**). When the H₂bmtz and bmtz ligands are mixed with Ag(tcm) in MeCN, they afford different kinds of coordination polymers: 1-D chains (**2c**) and 2-D sheets (**2d**). The reaction of bptz ligand with 1 equivalent of AgNO₃ in MeCN gave a 1-D chain (**2e**). The nitrate ion in **2e** is coordinated to the silver ions, similar to the perchlorate ion found in **2a**. When the same ligand is employed with Fe(NO₃)₃·9H₂O in MeCN, the unexpected salt **2f** is obtained. Interestingly, the component ions in **2f** are connected into a 2-D sheet *via* strong and weak hydrogen bonds. The 2-D sheet is further constructed to a 3-D supramolecular structure through anion- π interactions.

2.5 References

- Addison, A. W., Rao, T. N., Reedijk, J., Rijn, J. v., and Verschoor, G. C. (1984). **J. Chem. Soc., Dalton Trans.** (7): 1349-1356.
- Allen, F. H., Davies, J. E., Galloy, J. J., Johnson, O., Kennard, O., Macrae, C. F., Mitchell, E. M., Mitchell, G. F., Smith, J. M., and Watson, D. G. (1991). **J. Chem. Inf. Comput. Sci.** 31: 187-204.
- Barbour, L. J. (2001). **J. Supra. Chem.** 1(4-6): 189-191.
- Batten, S. R. (2001). **Curr. Opin. Solid State Mater. Sci.** 5(2-3): 107-114.
- Batten, S. R. (2005). **J. Solid State Chem.** 178: 2475-2479.
- Batten, S. R., Hoskins, B. F., Moubaraki, B., Murray, K. S., and Robson, R. (1999). **J. Chem. Soc., Dalton Trans.** (17): 2977-2986.
- Batten, S. R., Jeffery, J. C., and Ward, M. D. (1999). **Inorg. Chim. Acta** 292(2): 231-237.
- Batten, S. R., and Murray, K. S. (2001). **Aus. J. Chem.** 54: 605-609.
- Batten, S. R., and Robson, R. (1998). **Angew. Chem., Int. Ed.** 37(11): 1461-1494.
- Batten, S. R., Hoskins, B. F., Moubaraki, B., Murray, K. S., and Robson, R. (2001). **CrystEngCommun.** (8): 33-35.
- Batten, R. S., Hoskins, B. F., and Robson, R. (1998). **New J. Chem.** (2): 173-175.
- Blessing, R. H. (1995). **Acta Crystallogr., Sect. A: Found. Crystallogr.** 51: 33-38.
- Brandenburg, K., and Putz, H. (2006). **DIAMOND**. Version 3.1e, Crystal Impact GbR, Bonn, Germany.
- Desiraju, G. R. (2007). **Angew. Chem., Int. Ed.** 46(44): 8342-8356.
- Desiraju, G. R., and Steiner, T. (1999). **The Weak Hydrogen Bond in Structural Chemistry and Biology**. New York, Oxford University Press.

- Dong, Y.-B., Jiang, Y.-Y., Li, J., Ma, J.-P., Liu, F.-L., Tang, B., Huang, R.-Q., and Batten, R. B. (2007). **J. Am. Chem. Soc.** 129(15): 4520-4521.
- Dong, Y.-B., Xu, H.-X., Ma, J.-P., and Huang, R.-Q. (2007). **Inorg. Chem.** 45(8): 3325-3343.
- Du, M., Bu, X.-H., Huang, Z., Chen, S.-T., and Guo, Y.-M. (2003). **Inorg. Chem.** 42(2): 552-559.
- Geldard, J. F., and Lions, F. J. (1965). **J. Org. Chem.** 30(1): 318-319.
- Glöckle, M., Hubler, K., Kummerer, H.-J., Denninger, G., and Kaim, W. (2001). **Inorg. Chem.** 40(10): 2263-2269.
- Hoog, P. D., Gamez, P., Mutikainen, I., Turpeinen, U., and Reedijk, J. (2004). **Angew. Chem., Int. Ed.** 43(43): 5815-5817.
- Holliday, B. J., and Mirkin, C. A. (2001). **Angew. Chem., Int. Ed.** 40(11): 2022-2043.
- Janiak, C. (2000). **J. Chem. Soc., Dalton Trans.** (21): 3885-3896.
- Kaim, W., and Fees, J. (1995). **Z. Naturforsch., B: Chem. Sci.** 50: 123-127.
- Klein, A., McInnes, E. J. L., Scheiring, T., and Zališ, S. (1998). **J. Chem. Soc., Faraday Trans.** 94(19): 2979-2984.
- Ockwig, N. W., Delgado-Friedrichs, O., O'Keeffe, M., and Yaghi, O. M. (2005). **Acc. Chem. Res.** 38(3): 176-182.
- Khlobystov, A. N., Blake, A. J., Champness, N. R., Lemenovskii, D. A., Majouga, A. G., Zyk, N. V., and Schröder, M. (2001). **Coord. Chem. Rev.** 222(1): 155-192.
- Konnert, J., and Britton, D. (1966). **Inorg. Chem.** 5(7): 1193-1196.
- Moulton, B., and Zaworotko, M. J. (2001). **Chem. Rev.** 101(6): 1629-1658.

- Schottel, B. L., Bacsá, J., and Dunbar, K. R. (2005). **Chem. Commun.** (1): 46-47.
- Schottel, B. L., Chifotides, H. T., Shatrúk, M., Chouai, A., Pérez, L. M., Bacsá, J., and Dunbar, K. R. (2006). **J. Am. Chem. Soc.** 128(17): 5895-5912.
- Sheldrick, G. M. (1997). **SHELXL-97**: A program for crystal structure refinement, University of Göttingen, Germany.
- Sheldrick, G. M. (1997). **SHELXS-97**: A program for automatic solution of crystal structure, University of Göttingen, Germany.
- Sommerdijk, N. A. J. M. (2003). **Angew. Chem., Int. Ed.** 42(31): 3572-3574.
- Steel, P. J., and Fitchett, C. M. (2008). **Coord. Chem. Rev.** 252(8-9): 990-1006.
- Tiekink, E. R. T., and Vittal, J. J. (2006). **Frontiers in Crystal Engineering**. John Wiley & Sons Ltd.
- van der Sluis, P., and Spek, A. L. (1990). **Acta Crystallogr., Sect. A: Found. Crystallogr.** 46: 194-201.
- Venkataraman, D., Du, Y., Wilson, S. R., Hirsch, K. A., Zhang, P., and Moore, J. S. (1997). **J. Chem. Educ.** 74(8): 915-918.
- Witt, J. R., and Britton, D. (1971). **Acta Crystallogr., Sect. B: Struct. Sci.** 27: 1835-1836.
- Young, A. G., and Hanton, L. R. (2008). **Coord. Chem. Rev.** 252(12-14): 1346-1386.

CHAPTER III

SYNTHESIS, STRUCTURES

AND MAGNETIC PROPERTIES OF NEW CYANIDE- BRIDGED BIMETALLIC COMPOUNDS

3.1 Introduction

An enormous amount of research work has been considerable interest in the design and elaboration of multidimensional coordination polymer materials (Robson *et al.*, 1992; Leininger *et al.*, 2001; Batten, 2001; 2004; 2005; Moulton and Zaworotko, 2002, Janiak, 2003; Yaghi *et al.*, 2003; Kitagawa *et al.*, 2004; Kepert, 2006) due to their intriguing structural richness and also potential applications in electrical conductivity (Sato, 2003), molecular based magnets (Kahn and Martinez, 1998; Jensen *et al.*, 1999; Ammala *et al.*, 2000; Moliner *et al.*, 2000; Niel *et al.*, 2001; Maspoch *et al.*, 2004; Chippindale *et al.*, 2005), molecular absorption (Chui *et al.*, 1999; Eddaoudi *et al.*, 2002; Forster and Cheetham, 2002; Bradshaw *et al.*, 2005; Kesanli *et al.*, 2005; Dincá *et al.*, 2006), and biological relevance (Henkel and Krebs, 2004). In the field of cyanide bridged metal chemistry, there has been carried out intensive research during the last three decades by chemists, physicists and materials scientists dealing with the highly insoluble 3-D Prussian blue (PB) and their more soluble Prussian blue analogues (PBs). This is because of their spectacular properties such as in the fields of spectroscopy (Franz *et al.*, 2004; Szaciowski *et al.*, 2006; Ward, 2006), nanoporosity *i.e.* the related properties of gas storage (Chapman *et al.*,

2005; Kaye and Long, 2005, 2007), molecular magnetism *eg.* single-molecule magnets, SMMs (Berlinguette *et al.*, 2003; Wang *et al.*, 2006), single-chain magnets, SCMs, (Salman *et al.*, 2006), molecular-based photomagnets (Ohkoshi *et al.*, 2006), highest T_C molecule-based materials (Gadet *et al.*, 1992; Arrio *et al.*, 1996; Buschmann *et al.*, 1998), and spin crossover materials (Kosaka *et al.*, 2005; Nihei *et al.*, 2005; Guennic *et al.*, 2007; Munoz *et al.*, 2007).

Cyanometallates of varying coordination geometry, such as heptacyanometallates(III) $[M(CN)_7]^{4-}$, hexacyanometallates $[M(CN)_6]^{3-}$, $[Fe(CN)_6]^{4-}$, pentacyanometallates $[ML(CN)_5]^{3-}$ or tetracyanometallates $[ML(CN)_4]^{2-}$ and $[ML(CN)_4]^-$ (where M = a paramagnetic transition metal center, L = bidentate chelating ligand) have been employed as building blocks to make polynuclear species. The L ligand not only allows solubilization of reactants but also allow lowering of dimensionality of the PBs into the molecular regime. (Verdaguer *et al.*, 1999; Ohba *et al.*, 2000; Bernhardt *et al.*, 2005; Culp *et al.*, 2005; Lescouëzec *et al.*, 2005).

Using some examples of hexacyanometallate-based coordination polymers, Okawa and co-workers have prepared a 3-D network containing the cubic $\{Fe_8Ni_{12}\}$ unit in compound of type $[Ni^{II}(L)_2]_3[Fe^{II}(CN)_6]X_2$, where L = 1,2-ethylenediamine, trimethylenediamine, X = PF_6^- , ClO_4^- using hexacyanoferrate(II) anion $[Fe^{II}(CN)_6]^{4-}$ as a building block. These compounds display a ferromagnetic interaction between the nearest Ni^{II} ions through the diamagnetic $[Fe^{II}(CN)_6]^{4-}$ ($S = 0$) ion (Fukita *et al.*, 1998). For the Fe^{III} ($S = 1/2$) analogue, reactions of the $[Fe^{III}(CN)_6]^{3-}$ building block with $[Cu^{II}(tn)(H_2O)_n]^{2+}$, afforded the compounds $[Cu^{II}(tnH)_2(H_2O)_2Fe^{II}(CN)_6] \cdot 2H_2O$ (1-D structure), $[\{Cu^{II}(tn)\}_2Fe^{II}(CN)_6] \cdot KCl \cdot 5H_2O$ (2-D structure), and $[\{Cu^{II}(tn)\}_2Fe^{II}(CN)_6] \cdot 4H_2O$ (3-D structure), where tn = 1,3-diaminopropane. The magnetic

properties of compounds show the presence of weakly coupled Cu^{II} ions with weak ferromagnetic (2-D) or antiferromagnetic (1- and 3-D) interactions (Triki *et al.*, 2006). For all these compounds, the synthetic processes involve the spontaneous reduction of the paramagnetic $[\text{Fe}^{\text{III}}(\text{CN})_6]^{3-}$ anion into the diamagnetic $[\text{Fe}^{\text{II}}(\text{CN})_6]^{4-}$. The reduction of Fe^{III} to Fe^{II} in water is similar to those observed in the works of Murray, Spiccia and co-workers when making heptanuclear cluster of type $[\{\text{Cu}^{\text{II}}(\text{tpa})\}_6\text{Fe}^{\text{II}}(\text{CN})_6]^{8+}$, where tpa = tris(2-pyridylmethyl)amine (Parker *et al.*, 1996; Spiccia and Murray, 2004).

Recently, Julve *et al.* (Lescouëzec *et al.*, 2005), and Gao *et al.* (Zhang *et al.*, 2005) have prepared a number of low-dimensional assemblies of cyanide-bridged heterobimetallic by using low-spin trivalent transition metal ion of formula $[\text{M}(\text{bidentate})(\text{CN})_4]$, where $\text{M} = \text{Fe}^{\text{III}}$ and Cr^{III} as building blocks. For example, single-chain magnets (SCMs) nanowires of ferrimagnetic bimetallic compounds $[\{\text{Fe}^{\text{III}}(\text{L})(\text{CN})_4\}_2\text{Co}^{\text{II}}(\text{H}_2\text{O})_2] \cdot 4\text{H}_2\text{O}$, where $\text{L} = 1,10\text{-phen}$, $2,2'\text{-bipy}$, were shown to exhibit slow magnetic relaxation and hysteresis effects (Lescouëzec *et al.*, 2003). 4,2-ribbon like bimetallic chains in $[\{\text{Cr}^{\text{III}}(1,10\text{-phen})(\text{CN})_4\}_2\text{Mn}(\text{H}_2\text{O})_2] \cdot 4\text{H}_2\text{O}$ show ferromagnetic hysteresis loops with coercive fields $H_c < 5000$ G (Toma *et al.*, 2005). Zigzag chains in $[\text{Cr}^{\text{III}}(2,2'\text{-bipy})(\text{CN})_4\text{Mn}^{\text{II}}(\text{dca})(2,2'\text{-bipy})(\text{H}_2\text{O})] \cdot \text{H}_2\text{O}$, and a ladder chains in $[\text{Cr}^{\text{III}}(2,2'\text{-bipy})(\text{CN})_4\text{Mn}^{\text{II}}(\text{N}_3)(\text{CH}_3\text{OH})] \cdot 2\text{H}_2\text{O}$ display magnetic ordering with different critical temperatures (T_C) and critical fields (H_C) (Zhang *et al.*, 2005). The Ru^{II} analogs $[\text{Fe}^{\text{II}}(\text{L})(\text{CN})_4]^{2-}$ have also been used extensively to make framework species and their emission spectral properties have been investigated (Ward, 2006; Xial *et al.*, 2007)

In the above work using $[\text{M}^{\text{III}}(\text{bidentate})(\text{CN})_4]^-$ plus $[\text{M}(\text{H}_2\text{O})_2]^{n+}$ or $[\text{M}(\text{X})_{\text{eq}}]$, where $\text{X} = \text{N}_3^-$, $\text{N}(\text{CN})_2^-$ (dca^-), there has been little effort given to directing the topology of the PB analog. The aim of the present work is to use the principles of crystal engineering to synthesize 1-D tube-like motifs of cyanide-bridged bimetallic coordination polymers, and if successful, to make in comparisons to 2- and 3-D Prussian blue analogues. The main strategy is to combine the chelated tetracyanoferrate building block of formula $[\text{M}(\text{L})(\text{CN})_4]^{x-}$ and $[\text{M}'(\text{L}')(\text{solvent})_4]$ (where $x = 1, 2$; $\text{M} = \text{Fe}^{\text{II}}$ and Fe^{III} ; $\text{M}' =$ first row transition metals; $\text{L} = 1,10\text{-phen}$, $2,2'\text{-bipy}$, en , tn ; $\text{L}' = \text{en}$, tn). Since other dimensionality products (2-D and 3-D) or discrete CN-bridged clusters (square, etc.) are possible, the structural diversity and magnetic properties of such bimetallic compounds that formed during the attempts to make the 1-D tubes are also of much interest to the project. The synthesis, structural and magnetic properties of a range of new cyanide-bridged complexes $[\text{Fe}^{\text{II}}(2,2'\text{-bipy})(\text{CN})_4\text{Mn}^{\text{II}}] \cdot \text{MeOH}$ (**3a**), $[\text{Fe}^{\text{II}}(2,2'\text{-bipy})(\text{CN})_4\text{Mn}^{\text{II}}(\text{H}_2\text{O})_2] \cdot \text{H}_2\text{O}$ (**3b**), $[\text{Fe}^{\text{II}}(1,10\text{-phen})(\text{CN})_4\text{Cu}^{\text{II}}(\text{tn})(\text{H}_2\text{O})_2] \cdot 5\text{H}_2\text{O}$ (**3c**), $[\text{Fe}^{\text{II}}(2,2'\text{-bipy})(\text{CN})_4\text{Cu}^{\text{II}}(\text{tn})] \cdot \text{H}_2\text{O}$ (**3d**), and $[\text{Fe}^{\text{II}}(2,2'\text{-bipy})(\text{CN})_4\text{Ni}^{\text{II}}(\text{en})_2] \cdot \text{solvent}$ (**3e**) are reported.

3.2 Experimental Section

3.2.1 Materials and Physical Measurements

$\text{Mn}(\text{CH}_3\text{COO})_2 \cdot 4\text{H}_2\text{O}$, $\text{Ni}(\text{NO}_3)_2 \cdot 6\text{H}_2\text{O}$, $\text{Ni}(\text{ClO}_4)_2 \cdot 6\text{H}_2\text{O}$, $\text{Cu}(\text{ClO}_4)_2 \cdot 6\text{H}_2\text{O}$, $\text{Cu}(\text{NO}_3)_2 \cdot 6\text{H}_2\text{O}$, 1,10-phen, 2,2'-bipy, en, and tn were purchased from commercial sources and used without further purification. $\text{K}_2[\text{Fe}^{\text{II}}(\text{en})(\text{CN})_4] \cdot 3\text{H}_2\text{O}$ and $\text{K}_2[\text{Fe}^{\text{II}}(\text{tn})(\text{CN})_4] \cdot 3\text{H}_2\text{O}$ (Goto, 1986), and $\text{K}_2[\text{Fe}^{\text{II}}(2,2'\text{-bipy})(\text{CN})_4] \cdot 3\text{H}_2\text{O}$, $\text{H}[\text{Fe}^{\text{III}}(2,2'\text{-bipy})(\text{CN})_4] \cdot 2\text{H}_2\text{O}$, $\text{K}_2[\text{Fe}^{\text{II}}(1,10\text{-phen})(\text{CN})_4] \cdot 4\text{H}_2\text{O}$, and $\text{H}[\text{Fe}^{\text{III}}(1,10\text{-phen})(\text{CN})_4] \cdot \text{H}_2\text{O}$

(Schilt, 1960) were prepared according to the literature.

Caution!: Cyanide is very poisonous. Great care was taken so that its salts did not come into contact with acid, which would liberate highly toxic hydrogen cyanide gas. Since CN^- salts should not be touched with the fingers; use a spatula or handle small pieces with pincers, and reactants were performed under a fume hood.

Microanalytical measurements (C, H, N) were performed by Campbell Microanalytical Laboratory, Chemistry Department, University of Otago, Dunedin, New Zealand. Infrared spectra of Nujol mulls were recorded using a diamond-ATR cell on a Bruker Opus/IR IFS 55 spectrometer in the range of $600\text{--}4000\text{ cm}^{-1}$ (50 scans, resolution $\pm 4\text{ cm}^{-1}$). Variable-temperature magnetic susceptibility data were obtained by Dr. Boujemaa Moubaraki, Monash University using a Quantum Design MPMS 5 SQUID magnetometer for DC magnetization measurements.

3.2.2 Syntheses

Preparation of Precursor Complex $[\text{Ni}(\text{en})(\text{H}_2\text{O})_4](\text{NO}_3)_2$

The 1:1 complex $[\text{Ni}(\text{en})(\text{H}_2\text{O})_4](\text{NO}_3)_2$ readily crystallizes as large blue plates from methanolic solutions of nickel nitrate hexahydrate and ethylenediamine mixed in 1:1 stoichiometric amounts. Typically, a methanol solution (15 mL) of ethylenediamine (0.60 g, 0.01 mol) was added dropwise to a methanol solution (15 mL) of $\text{Ni}(\text{NO}_3)_2 \cdot 6\text{H}_2\text{O}$ (2.91 g, 0.01 mol) with constant stirring for one hour and filtered to remove any undissolved solid. The filtrate was allowed to stand to slowly evaporate, at room temperature. After one month, large blue plates were obtained (Yield 2.55 g, 88%). The unit cell parameters of a representative crystal were identical to the cell parameters reported by McDougall and Hancock (1980). Anal. Found (calcd) for $\text{C}_2\text{H}_{16}\text{N}_4\text{NiO}_{10}$ ($M_r = 314.86\text{ g/mol}$): C, 7.60(7.63); H, 5.08(5.12),

N, 17.82(17.79). ATR-FTIR (ν_{max}/cm^{-1}): 684s, 843w, 863w, 924w, 1047w, 1098s, 1115m, 1163s, 1292w, 1341w, 1396w, 1438w, 1463m, 1575s, 1982w, 2115w, 2324w, 2657w, 2853s, 2926s, 3123m, 3222s, 3286s. $\mu_{\text{eff}}(\text{RT}) = 3.2 \mu_{\text{B}}$.

Preparation of $[\text{Fe}^{\text{II}}(2,2'\text{-bipy})(\text{CN})_4\text{Mn}^{\text{II}}]\cdot\text{MeOH}$ (**3a**)

A single crystal of **3a** suitable for X-ray crystallographic analysis was obtained by slow diffusion in which aqueous methanolic (1:1, v/v) solutions of 14 mL capacity were contained in an H-shaped tube and left in the dark. In a typical experiment, $\text{Mn}(\text{CH}_3\text{COO})_2\cdot 4\text{H}_2\text{O}$ (245 mg, 1 mmol) was dissolved in 3 mL of MeOH/H₂O to form a colorless solution and this was pipetted into one side of the H-tube. $\text{K}_2[\text{Fe}^{\text{II}}(2,2'\text{-bipy})(\text{CN})_4]\cdot 3\text{H}_2\text{O}$ (113 mg, 0.25 mmol) was dissolved in 3 mL of distilled water to give a deep red solution and this was pipetted into the other side arm of the H-tube. The H-tube was then carefully filled with MeOH/H₂O. Upon slow diffusion for two weeks, red plate-shaped single crystals of **3a** were formed in the iron-containing side of the H-tube. Yield: 42 mg, 37% based on $\text{K}_2[\text{Fe}(2,2'\text{-bipy})(\text{CN})_4]\cdot 3\text{H}_2\text{O}$. Anal. Found (calcd) for $\text{C}_{29}\text{H}_{20}\text{Fe}_2\text{Mn}_2\text{N}_{12}\text{O}$ ($M_r = 774.12$ g/mol): C, 44.26(44.69); H, 2.89(3.00), N, 20.51(20.85). ATR-FTIR (ν_{max}/cm^{-1}): 649br, 731s, 766s, 1008m, 1062w, 1155m, 1244w, 1314w, 1425w, 1441m, 1470s, 1603s 2056s. $\mu_{\text{eff}}(300\text{ K}) = 8.01 \mu_{\text{B}}$, per Fe_2Mn_2 .

Preparation of $[\text{Fe}^{\text{II}}(2,2'\text{-bipy})(\text{CN})_4\text{Mn}^{\text{II}}(\text{H}_2\text{O})_2]$ (**3b**)

A sample of **3b** was prepared in analogous way to **3a** in which $\text{H}[\text{Fe}^{\text{III}}(2,2'\text{-bipy})(\text{CN})_4]\cdot 2\text{H}_2\text{O}$ was used instead of $\text{K}_2[\text{Fe}^{\text{II}}(2,2'\text{-bipy})(\text{CN})_4]\cdot 3\text{H}_2\text{O}$. Red block-shaped crystals of **3b** were formed in the manganese-containing side of the H-tube within three weeks. The Fe^{III} precursor was reduced to Fe^{II} . Yield: 23 mg, 33% based

on $\text{H}[\text{Fe}^{\text{III}}(2,2'\text{-bipy})(\text{CN})_4]\cdot 2\text{H}_2\text{O}$. Anal. Found (calcd) for $\text{C}_{14}\text{H}_{12}\text{FeMnN}_6\text{O}_2$ ($M_r = 407.08$ g/mol): C, 41.04(41.31); H, 2.61(2.97), N, 20.27(20.65). ATR-FTIR ($\nu_{\text{max}}/\text{cm}^{-1}$): 717w, 856w, 958w, 1178s, 1217s, 1369m, 1388m, 1438w, 1461w, 1599m, 1982w, 2051w, 2166w, 2286m, 2314w, 2944w, 2996m, 3404w. μ_{eff} (300 K) = 5.93 μ_{B} , per FeMn.

Preparation of $[\text{Fe}^{\text{II}}(1,10\text{-phen})(\text{CN})_4\text{Cu}^{\text{II}}(\text{tn})(\text{H}_2\text{O})_2]\cdot 5\text{H}_2\text{O}$ (**3c**)

A sample of **3c** was prepared following the procedure described above for **3a** using aqueous solutions, except that $\text{K}_2[\text{Fe}^{\text{II}}(1,10\text{-phen})(\text{CN})_4]\cdot 4\text{H}_2\text{O}$ was used instead of $\text{K}_2[\text{Fe}^{\text{II}}(2,2'\text{-bipy})(\text{CN})_4]\cdot 3\text{H}_2\text{O}$. Typically, $\text{Cu}(\text{ClO}_4)_2\cdot 6\text{H}_2\text{O}$ (70 mg, 0.2 mmol), and tn (stock solution, 0.01 mL, 0.2 mmol) were dissolved in 3 mL of distilled H_2O to form a blue solution of $[\text{Cu}^{\text{II}}(\text{tn})(\text{H}_2\text{O})_n]^{2+}$, *in situ*, and this was pipetted into one side of the H-tube. $\text{K}_2[\text{Fe}^{\text{II}}(1,10\text{-phen})(\text{CN})_4]\cdot 4\text{H}_2\text{O}$ (90 mg, 0.2 mmol) was dissolved in 3 mL of distilled H_2O to give a deep red solution and this was pipetted into the other side arm of the H-tube. The H-tube was then carefully filled with distilled H_2O . Slow diffusion for three weeks yielded dark red needle-shaped crystals of **3c**, which were formed in the $[\text{Cu}^{\text{II}}(\text{tn})(\text{H}_2\text{O})_n]^{2+}$ containing side. Yield: 50 mg, 72% based on $\text{K}_2[\text{Fe}(1,10\text{-phen})(\text{CN})_4]\cdot 4\text{H}_2\text{O}$. Anal. Found (calcd) for $\text{C}_{19}\text{H}_{28}\text{CuFeN}_8\text{O}_5$ ($M_r = 603.90$ g/mol): C, 37.58(37.79); H, 5.32(5.34), N, 18.42(18.56). ATR-FTIR ($\nu_{\text{max}}/\text{cm}^{-1}$): 649br, 731s, 766s, 1008m, 1062w, 1155m, 1244w, 1314w, 1425w, 1441m, 1470s, 1603s, 2056s, 2123w, 2254m, 2309w, 2943w, 3012m, 3414w. μ_{eff} (300 K) = 2.02 μ_{B} , per FeCu.

Preparation of $[\text{Fe}^{\text{II}}(2,2'\text{-bipy})(\text{CN})_4\text{Cu}^{\text{II}}(\text{tn})]\cdot\text{H}_2\text{O}$ (**3d**)

A sample of **3d** was prepared analogously to **3c** in which $\text{K}_2[\text{Fe}^{\text{II}}(2,2'\text{-bipy})(\text{CN})_4]\cdot 3\text{H}_2\text{O}$ was used instead of $\text{K}_2[\text{Fe}^{\text{II}}(1,10\text{-phen})(\text{CN})_4]\cdot 4\text{H}_2\text{O}$. Brown-red needle-shaped crystals **3d** were formed in the $[\text{Cu}^{\text{II}}(\text{tn})(\text{H}_2\text{O})_n]^{2+}$ containing side within three weeks. Yield: 48 mg, 68% based on $\text{K}_2[\text{Fe}(2,2'\text{-bipy})(\text{CN})_4]\cdot 3\text{H}_2\text{O}$. Anal. Found (calcd) for $\text{C}_{17}\text{H}_{19}\text{CuFeN}_8\text{O}$ ($M_r = 470.78$ g/mol): C, 43.48(43.37); H, 4.38 (4.07), N, 23.89(23.80). ATR-FTIR ($\nu_{\text{max}}/\text{cm}^{-1}$): 647w, 732w, 761w, 963w, 1025w, 1159w, 1240w, 1278w, 1313w, 1425w, 1444w, 1582m, 1603m, 1995w, 2056s, 2103m, 2904w, 3161br, 3256br. $\mu_{\text{eff}}(300\text{ K}) = 1.78 \mu_{\text{B}}$, per FeCu.

Preparation of $[\text{Fe}^{\text{II}}(2,2'\text{-bipy})(\text{CN})_4\text{Ni}^{\text{II}}(\text{en})_2]\cdot\text{Solvent}$ (**3e**)

A sample of **3e** was prepared following the procedure described above for **3a** using aqueous methanolic (1:1, v/v) solutions. In a typical experiment procedure, $[\text{Ni}(\text{en})(\text{H}_2\text{O})_4](\text{NO}_3)_2$ (63 mg, 0.2 mmol) was dissolved in 3 mL of MeOH/H₂O solution to form a bright blue solution and this was pipetted into one side of the H-tube. $\text{K}_2[\text{Fe}(2,2'\text{-bipy})(\text{CN})_4]\cdot 3\text{H}_2\text{O}$ (90 mg, 0.2 mmol) was dissolved in 3 mL of MeOH/H₂O solution to give a bright yellow solution and this was pipetted into the other side arm of the H-tube. The H-tube was then carefully filled with MeOH/H₂O solution. Upon slow diffusion for two months, deep red plate shaped single crystals of **3e** were formed in both sides of the H-tube with red powder precipitate. Yield: 18 mg, 15% based on $\text{K}_2[\text{Fe}^{\text{II}}(2,2'\text{-bipy})(\text{CN})_4]\cdot 3\text{H}_2\text{O}$. ATR-FTIR ($\nu_{\text{max}}/\text{cm}^{-1}$): 990w, 1421w, 1444w, 1467w, 1570w, 1592w, 2051s, 2067w, 2091m, 2325w, 2879m, 2929m, 3167w, 3245w, 3295w, 3318w, 3342w, 3358w, 3443w, 3634s. $\mu_{\text{eff}}(300\text{ K}) = 3.08 \mu_{\text{B}}$, per FeNi.

3.2.3 X-Ray Crystallographic Study

Single crystals of **3a–3e** were mounted on a MiTeGen MicroMounts fiber in a small amount of oil and quench cooled to 123(2) K prior to measurements made by Dr. Suzanne M. Neville and Dr. Craig Forsyth, Monash University. Reflection intensities were collected on a Bruker X8 APEX CCD diffractometer (Mo K_α radiation, $\bar{\lambda} = 0.71073 \text{ \AA}$) and equipped with an Oxford Instruments nitrogen gas Cryostream. Empirical absorption corrections were applied to all data using SADABS (Blessing, 1995). The structures were solved using SHELXS-97 and refined on F^2 using SHELXL-97 (Sheldrick, 1997) with X-SEED (Barbour, 2001) as a graphics interface. In the final cycles of refinement, all atoms except hydrogen atoms and disordered molecules were refined anisotropically. However, special crystal structure refinement details for each compound are described below.

3a: The methanol molecules were found to be disordered about a 2_1 screw axis, and were modeled in two different orientations. The total occupancy of both orientations was fixed to one. Restraints were applied to the displacement parameters of this disordered molecule. In the final cycles of refinement, all atoms except hydrogen atoms were refined anisotropically. Hydrogen atoms attached to carbon atoms of 2,2'-bipy molecules were placed in idealized positions and constrained to ride on their parent atoms, with C–H distance at 0.95 \AA , with $U_{\text{iso}}(\text{H}) = 1.2U_{\text{eq}}(\text{C}, \text{N})$ [$1.5U_{\text{eq}}(\text{C})$ for methyl hydrogen atoms].

3b: The coordinated water molecules exhibited large displacement parameters, were modeled assuming a three-site disorder about a $\bar{3}$ axis; the occupancy factors for the three components were allowed to vary and their summation was set to one. The poor crystal quality also resulted in broad diffraction peaks. The hydrogen atoms of

the water molecules are very labile and difficult to locate. Thus no hydrogen atoms were located for any of the water molecules. Hydrogen atoms attached to carbon atoms of 2,2'-bipy molecules were placed in idealized positions and constrained to ride on their parent atoms, with C–H distance at 0.95 Å, with $U_{\text{iso}}(\text{H}) = 1.2U_{\text{eq}}(\text{C}, \text{N})$.

3c: Hydrogen atoms attached to oxygen atoms of the water molecules were located in a difference Fourier map and refined as riding in their as-found positions with a DFIX restraint of O–H distance at 0.90 Å, with $U_{\text{iso}}(\text{H}) = 1.2U_{\text{eq}}(\text{O})$. Hydrogen atoms bound to carbon or nitrogen atoms of tn molecules were positioned geometrically and refined as riding atoms with C–H and N–H distances of 0.97 and 0.86 Å, respectively, and $U_{\text{iso}}(\text{H})$ values of $1.2U_{\text{eq}}(\text{C}, \text{N})$. Hydrogen atoms attached to carbon atoms of 1,10-phen molecules were placed in idealized positions and constrained to ride on their parent atoms, with C–H distance at 0.95 Å, with $U_{\text{iso}}(\text{H}) = 1.2U_{\text{eq}}(\text{C}, \text{N})$.

3d: The cell parameters of **3d** indicated a triclinic cell ($a = 6.6150$ Å, $b = 12.0449$ Å, $c = 15.1964$ Å, $\alpha = 69.659^\circ$, $\beta = 77.970^\circ$, $\gamma = 80.201^\circ$, $V = 1104.04$ Å³) and the R_{int} value for the triclinic crystal system was 0.187. The structure was solved in the triclinic space group $P\bar{1}$ using direct methods. After encountering severe problems during structure solution, anisotropic refinement remained stalled at $R_1 = 0.131$ and $wR_2 = 0.357$, with several atoms going nonpositive definite. Despite many attempts to re-grow the crystals, the only brown-red needle microcrystals obtained were always small and often twinned and of poor quality. However, the elementary analysis of the obtained crystalline product is consistent with the C, H and N values expected for the formula of $[\text{Fe}^{\text{II}}(2,2'\text{-bipy})(\text{CN})_4\text{Cu}^{\text{II}}(\text{tn})]\cdot\text{H}_2\text{O}$.

3e: Solvents molecules were found to be disordered, and were modeled in two different orientations. The total occupancy of both orientations was fixed to one. Hydrogen atoms bound to carbon or nitrogen atoms of en molecules were positioned geometrically and refined as riding atoms with C–H and N–H distances of 0.97 and 0.86 Å, respectively, and $U_{\text{iso}}(\text{H})$ values of $1.2U_{\text{eq}}(\text{C,N})$. Hydrogen atoms attached to carbon atoms of 2,2'-bipy molecules were placed in idealized positions and constrained to ride on their parent atoms, with C–H distance at 0.95 Å, with $U_{\text{iso}}(\text{H}) = 1.2U_{\text{eq}}(\text{C, N})$.

Crystal data and details of the data collection and structure refinement for compounds **3a–3c** and **3e** are summarized in Table 3.1. The relatively high R values for some compounds were due to the low quality of the crystals and disorder of solvent molecules. Selected interatomic bond lengths and angles for compounds **3a–3c** and **3e** are given in Tables 3.2 to 3.5. The bond lengths and angles, hydrogen bonds geometry, and other crystallographic data are given as supplementary material in the CIF which can be found on the attached CD-ROM.

Table 3.1 Summary of crystallographic data for the compounds **3a–3c** and **3e**.

Identical code	3a	3b	3c	3e
Formula	C ₂₉ H ₂₀ Fe ₂ Mn ₂ N ₁₂ O	C ₁₄ H ₁₂ FeMnN ₆ O ₂	C ₁₉ H ₂₈ CuFeN ₈ O ₅	C ₂₀ H ₃₂ FeNiN ₁₀ O ₃
<i>Mr</i>	774.15	407.07	567.86	575.10
Crystal system	monoclinic	trigonal	triclinic	monoclinic
Crystal color/habit	red/plate	red/block	dark-red/needle	red/plate
Crystal size (mm)	0.22 × 0.14 × 0.12	0.10 × 0.10 × 0.05	0.14 × 0.09 × 0.05	0.20 × 0.02 × 0.02
Space group	<i>P</i> 2 ₁ / <i>c</i> (No. 14)	<i>R</i> -3 (No. 148)	<i>P</i> -1 (No. 2)	<i>P</i> 2 ₁ / <i>n</i> (No. 15)
<i>a</i> (Å)	9.7468(5)	29.3328(7)	6.6989(6)	11.8757(6)
<i>b</i> (Å)	25.0289(12)	29.3328(7)	12.3558(11)	9.6645(5)
<i>c</i> (Å)	13.0520(6)	9.5650(3)	15.1625(14)	19.6343(9)
α (°)	90	90	104.420(2)	90
β (°)	95.118(1)	90	98.997(2)	97.023(2)
γ (°)	90	120	105.521(2)	90
<i>V</i> (Å ³)	3171.4(3)	7127.3(3)	1137.2(1)	2236.57(19)
<i>Z</i>	4	18	2	4
<i>D</i> _{calc} (Mg m ⁻³)	1.621	1.690	1.632	1.551
Temperature (K)	123(2)	123(2)	123(2)	123(2)
μ (Mo <i>K</i> α) (mm ⁻¹)	1.72	1.73	1.619	1.524
<i>F</i> (000)	1552.0	3618.0	576	1084
θ range (°)	1.8 – 25.0	2.3 – 25.0	2.6 – 25.0	2.4 – 25.0
Data completeness	0.992	1.000	0.970	0.986
Limiting indices <i>h</i>	-11 → 11	-34 → 22	-4 → 7	-14 → 14
<i>k</i>	-29 → 23	-27 → 34	-14 → 14	-11 → 11
<i>l</i>	-15 → 8	-11 → 11	-18 → 18	-21 → 23
Reflections collected/unique	18474/5543	20183/?	7623/3876	19097/3882
<i>R</i> _{int}	0.052	0.083	0.030	0.066
Data/restraints/parameters	4661/2/428	2670/0/230	3594/16/337	2890/13/347
<i>R</i> ₁ , <i>wR</i> ₂ [all data]	0.086, 0.185	0.114, 0.205	0.071, 0.142	0.082, 0.151
<i>R</i> ₁ , <i>wR</i> ₂ [<i>I</i> > 2 σ (<i>I</i>)]	0.072, 0.175	0.109, 0.201	0.066, 0.140	0.056, 0.137
Goodness of fit, <i>S</i>	1.11	1.34	1.28	1.053
$\Delta\rho_{\min}$, $\Delta\rho_{\max}$ (e Å ⁻³)	1.86, -1.12	0.99, -0.98	0.90, -1.21	1.97, -1.32

Computer programs: Crystal Maker (2006), Diamond v. 3e (Brandenburg and Putz, 2006), SADABS (Blessing, 1995), SHELXL-97 (Sheldrick, 1997), SHELXS-97 (Sheldrick, 1997), and X-SEED (Barbour, 2001).

Table 3.2 Selected bond lengths and angles for **3a** (Å, °). ^a

Fe1–C1	1.918(7)	Fe2–N11	1.982(6)
Fe1–C2	1.896(8)	Fe2–N12	2.001(5)
Fe1–C3	1.889(9)	Mn1–N1	2.071(5)
Fe1–C4	1.915(6)	Mn1–N5	2.058(6)
Fe1–N9	1.973(6)	Mn1–N4 ⁱⁱ	2.094(5)
Fe1–N10	1.987(6)	Mn1–N8 ⁱ	2.057(6)
Fe2–C5	1.868(7)	Mn2–N2	2.057(7)
Fe2–C6	1.908(7)	Mn2–N3 ⁱⁱⁱ	2.110(8)
Fe2–C7	1.920(7)	Mn2–N6	2.080(6)
Fe2–C8	1.869(7)	Mn2–N7 ^{iv}	2.114(6)
Fe1⋯Mn1	4.997(1)	Fe2⋯Mn1	5.027(1)
Fe1⋯Mn2	5.096(1)	Fe2⋯Mn2	5.073(1)
Fe1⋯Mn1 ^v	5.036(1)	Fe2⋯Mn1 ^{vii}	5.050(1)
Fe1⋯Mn2 ^{vi}	5.163(1)	Fe2⋯Mn1 ^{viii}	5.003(1)
C1–Fe1–C2	87.2(3)	C5–Fe2–C8	91.1(3)
C1–Fe1–C3	91.5(3)	C5–Fe2–N11	174.0(2)
C1–Fe1–C4	175.7(3)	C5–Fe2–N12	94.6(2)
C1–Fe1–N9	89.1(3)	C6–Fe2–C7	174.5(3)
C1–Fe1–N10	94.9(3)	C6–Fe2–C8	89.6(3)
C2–Fe1–C3	91.5(4)	C6–Fe2–N11	89.8(3)
C2–Fe1–C4	90.0(3)	C6–Fe2–N12	94.2(3)
C2–Fe1–N9	173.0(3)	C7–Fe2–C8	86.8(3)
C2–Fe1–N10	94.0(3)	C7–Fe2–N11	94.6(2)
C3–Fe1–C4	85.3(3)	C7–Fe2–N12	89.8(2)
C3–Fe1–N9	94.5(4)	C8–Fe2–N11	93.9(3)
C3–Fe1–N10	171.7(3)	C8–Fe2–N12	173.4(3)
C4–Fe1–N9	94.1(2)	N11–Fe2–N12	80.6(2)
C4–Fe1–N10	88.5(2)	N1–Mn1–N4 ⁱⁱ	120.3(2)
N9–Fe1–N10	80.5(3)	N1–Mn1–N5	111.8(2)
C5–Fe2–C6	86.9(3)	N1–Mn1–N8 ⁱ	104.4(3)
C5–Fe2–C7	89.0(3)	N4 ⁱⁱ –Mn1–N5	101.9(2)

Table 3.2 (Continued).

N4 ⁱⁱ –Mn1–N8 ⁱ	106.1(2)	Fe2–C5–N5	176.5(6)
N5–Mn1–N8 ⁱ	112.4(2)	Fe2–C6–N6	176.5(6)
N2–Mn2–N3 ⁱⁱⁱ	128.2(4)	Fe2–C7–N7	174.2(6)
N2–Mn2–N6	107.9(3)	Fe2–C8–N8	176.6(7)
N2–Mn2–N7 ^{iv}	107.3(3)	Mn1–N1–C1	152.2(6)
N3 ⁱⁱⁱ –Mn2–N6	92.7(3)	Mn1–N4 ^{iv} –C4 ^{iv}	155.2(5)
N3 ⁱⁱⁱ –Mn2–N7 ^{iv}	101.1(3)	Mn1–N5–C5	165.4(5)
N6–Mn2–N7 ^{iv}	120.6(3)	Mn1–N8 ⁱⁱⁱ –C8 ⁱⁱⁱ	168.9(6)
Fe1–C1–N1	178.3(7)	Mn2–N2–C2	173.9(9)
Fe1–C2–N2	177.1(7)	Mn2–N3 ⁱ –C3 ⁱ	176.8(10)
Fe1–C3–N3	175.3(6)	Mn2–N6–C6	162.0(6)
Fe1–C4–N4	177.5(6)	Mn2–N7 ⁱⁱ –C7 ⁱⁱ	152.7(6)

^a Estimated standard deviations are given in parentheses.

Symmetry codes: (i) $x, -y+1/2, z-1/2$; (ii) $x-1, y, z$; (iii) $x, -y+1/2, z+1/2$; (iv) $x+1, y, z$; (v) $1+x, y, z$; (vi) $x, 0.5-y, -0.5+z$; (vii) $x, 0.5-y, 0.5+z$; (viii) $-1+x, y, z$.

Table 3.3 Selected bond lengths and angles for **3b** (Å, °).^a

Fe1–C1	1.940(10)	Mn1–N1	2.165(9)
Fe1–C2	1.870(10)	Mn1–N2 ⁱ	2.114(10)
Fe1–C3	1.879(10)	Mn1–N3 ⁱⁱ	2.133(9)
Fe1–C4	1.912(11)	Mn1–N3 ⁱⁱⁱ	2.141(9)
Fe1–N5	1.997(9)	Mn1–O1	2.340(9)
Fe1–N6	1.980(8)	Mn1–O1	2.480(20)
Fe1⋯Mn1	4.861(2)		
C1–Fe1–C2	86.4(4)	N1–Mn1–N2 ⁱ	103.0(4)
C1–Fe1–C3	86.0(4)	N1–Mn1–N3 ⁱⁱ	108.0(4)
C1–Fe1–C4	175.1(4)	N1–Mn1–N4 ⁱⁱⁱ	108.2(3)
C1–Fe1–C5	92.4(4)	N1–Mn1–O1	84.7(3)
C1–Fe1–C6	93.9(4)	N1–Mn1–O2	162.0(8)
C2–Fe1–C3	91.0(4)	N2 ⁱ –Mn1–N3 ⁱⁱ	146.1(4)
C2–Fe1–C4	89.8(4)	N2 ⁱ –Mn1–N4 ⁱⁱⁱ	92.3(4)
C2–Fe1–C5	95.5(4)	N2 ⁱ –Mn1–O1	85.5(3)
C2–Fe1–C6	175.6(4)	N2 ⁱ –Mn1–O2	73.0(7)
C3–Fe1–C4	91.1(4)	N3 ⁱⁱ –Mn1–N4 ⁱⁱⁱ	90.8(3)
C3–Fe1–C5	173.3(4)	N3 ⁱⁱ –Mn1–O1	84.2(3)
C3–Fe1–C6	93.5(4)	N3 ⁱⁱ –Mn1–O2	73.3(7)
C4–Fe1–C5	90.9(4)	N4 ⁱⁱⁱ –Mn1–O1	167.0(3)
C4–Fe1–C6	90.2(4)	N4 ⁱⁱⁱ –Mn1–O2	89.6(8)
C5–Fe1–C6	80.1(4)	O1–Mn1–O2	77.5(8)

^a Estimated standard deviations are given in parentheses.

Symmetry codes: (i) $x-y+1/3, x-1/3, -z+2/3$; (ii) $y+1/3, -x+y+2/3, -z+2/3$; (iii) $x, y, z-1$; (iv) $x, y, z+1$.

Table 3.4 Selected bond lengths and angles for **3c** (Å, °). ^a

Fe1–C1	1.874(6)	Cu1–N1	1.982(5)
Fe1–C2	1.879(7)	Cu1–N2 ⁱ	1.980(6)
Fe1–C3	1.932(7)	Cu1–N7	2.011(5)
Fe1–C4	1.929(7)	Cu1–N8	2.023(5)
Fe1–N5	2.001(5)	Cu1–O1	2.630(5)
Fe1–N6	2.008(5)	Cu1–O2	2.470(5)
Fe1⋯Cu1	4.953(1)		
C1–Fe1–C2	90.6(3)	Fe1–C4–N3	179.8(6)
C1–Fe1–C3	90.9(3)	C1–N1–Cu1	160.6(5)
C1–Fe1–C4	88.7(3)	C2–N2–Cu1 ⁱ	160.2(5)
C1–Fe1–N5	93.8(2)	N1–Cu1–N2 ⁱ	91.4(2)
C1–Fe1–N6	174.4(2)	N1–Cu1–N7	87.4(2)
C2–Fe1–C3	88.2(3)	N1–Cu1–N8	177.2(2)
C2–Fe1–C4	89.7(3)	N1–Cu1–O1	93.2(2)
C2–Fe1–N5	175.1(2)	N1–Cu1–O2	90.8(2)
C2–Fe1–N6	94.3(2)	N2 ⁱ –Cu1–N7	178.8(2)
C3–Fe1–C4	177.8(3)	N2 ⁱ –Cu1–N8	86.1(2)
C3–Fe1–N5	89.5(2)	N2 ⁱ –Cu1–O1	93.3(2)
C3–Fe1–N6	92.1(2)	N2 ⁱ –Cu1–O2	91.9(2)
C4–Fe1–N5	92.7(2)	N7–Cu1–N8	95.0(2)
C4–Fe1–N6	88.5(2)	N7–Cu1–O1	86.5(2)
N5–Fe1–N6	81.4(2)	N7–Cu1–O2	88.4(2)
Fe1–C1–N1	178.1(6)	N8–Cu1–O1	88.3(2)
Fe1–C2–N2	177.3(6)	N8–Cu1–O2	88.0(2)
Fe1–C3–N3	178.0(6)	O1–Cu1–O2	173.4(2)

^a Estimated standard deviations are given in parentheses.

Symmetry code: (i) $-x, -y, -z$.

Table 3.5 Selected bond lengths and angles for **3e** (Å, °). ^a

Fe1–C1	1.880(6)	Ni1–N1	2.086(5)
Fe1–C2	1.900(6)	Ni1–N2 ⁱ	2.064(5)
Fe1–C3	1.929(7)	Ni1–N7	2.109(6)
Fe1–C4	1.935(7)	Ni1–N8	2.111(5)
Fe1–N5	1.984(4)	Ni1–N9	2.081(6)
Fe1–N6	1.995(5)	Ni1–N10	2.151(5)
Fe1⋯Ni1	4.813(1)	Fe1⋯Ni1 ⁱⁱ	4.959(1)
Fe1⋯Fe1 ⁱ	8.494(1)	Ni1⋯Ni1 ⁱⁱ	6.064(1)
C1–Fe1–C2	89.1(2)	N1–Ni1–N2 ⁱ	95.2(2)
C1–Fe1–C3	87.2(2)	N1–Ni1–N7	90.3(2)
C1–Fe1–C4	89.6(2)	N1–Ni1–N8	170.6(2)
C2–Fe1–C3	91.7(2)	N1–Ni1–N9	93.9(2)
C1–Fe1–N5	96.1(2)	N1–Ni1–N10	84.8(2)
C1–Fe1–N6	175.5(2)	N2 ⁱ –Ni1–N7	90.5(2)
C2–Fe1–C4	85.0(2)	N2 ⁱ –Ni1–N8	90.7(2)
C2–Fe1–N5	172.2(2)	N2 ⁱ –Ni1–N9	93.0(2)
C2–Fe1–N6	94.7(2)	N2 ⁱ –Ni1–N10	175.0(2)
C3–Fe1–C4	175.4(2)	N7–Ni1–N8	82.3(2)
C3–Fe1–N5	94.4(2)	N7–Ni1–N9	174.2(2)
C3–Fe1–N6	90.3(2)	N7–Ni1–N10	94.5(3)
C4–Fe1–N5	89.2(2)	N8–Ni1–N9	93.1(2)
C4–Fe1–N6	93.2(2)	N8–Ni1–N10	89.9(2)
N5–Fe1–N6	80.4(2)	N9–Ni1–N10	82.0(2)
Fe1–C1–N1	175.5(5)	Fe1–C4–N4	177.5(5)
Fe1–C2–N2	173.1(5)	Ni1–C1–N1	142.0(4)
Fe1–C3–N3	177.8(5)	Ni1–C2 ⁱⁱ –N2 ⁱⁱ	154.9(5)

^a Estimated standard deviations are given in parentheses.

Symmetry codes: (i) $-x, y-1/2, -z+1/2$; (ii) $-x, y+1/2, -z+1/2$.

3.3 Results and Discussion

3.3.1 Synthesis and ATR-FTIR Spectra

Many attempts were made to grow single crystals of the proposed 1-D tube motifs in cyanide-bridged bimetallic products by using the complexes of formula $[M(L)(CN)_4]$ and $[M'(L')(\text{solvent})_4]$ (where $M = Fe^{II}$ and Fe^{III} ; $M' = Mn^{II}$, Co^{II} , Ni^{II} , Cu^{II} , Zn^{II} , and Cd^{II} ; $L = 1,10\text{-phen}$, $2,2'\text{-bipy}$, en , tn ; $L' = en$, tn) as building blocks. Initially, the precursor $Na_2[Fe^{II}L(CN)_4] \cdot 3H_2O$, where L is an aliphatic diamine en and tn , were chosen as building blocks in order to minimize any chelate ligand steric effects on trying to form the $[(L)-Fe-(CN)_2-M'-(L')]_2$ square moieties. These iron-cyano building blocks were successfully prepared, in large scale and high yield, by a literature procedure (Goto *et al.*, 1986), and were phase pure as evidenced by microscopic examination and microelemental analysis. The first compound in this “square tube” study was successfully synthesized *via* in situ reaction, at room temperature, using $Na_2[Fe(tn)(CN)_4] \cdot 3H_2O$ and $[Ni(tn)(H_2O)_4](NO_3)_2$ as building blocks. Two different types of crystals, with distinctly different crystal morphologies and colors, were grown. The crystals were small red blocks and large purple blocks. Magnetic measurement on polycrystalline bulk samples display interesting long-range magnetic order with an ordering temperature, $T_C = 16.0$ K.

Surprisingly, single crystal X-ray crystallographic studies, and subsequent confirm of the metal content by EDX, revealed that no iron was detectable in both types of crystal. The crystal structure showed that a cyanide-bridged homometallic compound $[Ni(CN)_4Ni(tn)]$ had formed that contains two kinds of coordination geometry around Ni centres, *i.e.* octahedron and square planar, in a 3-D network array. This prompted further investigations of the “ligand complex” tetracyanonic-

kelate, $[\text{Ni}^{\text{II}}(\text{CN})_4]^{2-}$. This square-planar moiety was employed as a building block to react with $[\text{Ni}(\text{tn})(\text{H}_2\text{O})_4](\text{NO}_3)_2$ in aqueous methanolic (1:1) solutions, to afford a 3-D cyanide-bridged network complex $[\text{Ni}^{\text{II}}(\text{CN})_4\text{Ni}^{\text{II}}(\text{tn})]\cdot\text{H}_2\text{O}\cdot\text{MeOH}$ (**5b**), in which elucidation of the magnetic measurements provided results consistent with the single crystal X-ray crystallographic and elemental (C, H, N) analyses (see Chapter V). Therefore, the long-range magnetic order first observed was presumably due to the presence of impurity phases in the initial bulk sample. The identify of the impurity phase is not known but we note that $\text{Fe}^{\text{III}}\text{-CN-Ni}^{\text{II}}$ coordination polymer often yield T_C values of similar size (Ohba *et al.*, 1994).

This result showed that the mono-chelated Fe(II) complexes $[\text{Fe}^{\text{II}}(\text{L})(\text{CN})_4]^{2-}$, L = en and tn, are labile in aqueous media, and prone to Fe^{II} substitution, *eg.* by Ni^{II} , as well as loss of the diamine. So far, although four structures have been solved and refined by single crystal X-ray analysis, the mono-chelated en- or tn-Fe(II) complexes were not found in the products. Therefore, this prompted use of the 2,2'-bipy and 1,10-phen chelate ligands instead which, though having bulkier size, form LS Fe(II) complexes that are usually more stable and less prone to loss of the bidentate ligand than are the mono-chelated Fe(II) complex of en and tn.

The $[\text{Fe}(1,10\text{-phen or } 2,2'\text{-bipy})(\text{CN})_4]^{2-}$ building block has excellent solubility in water but very small solubility in common organic solvents, *i.e.* MeOH, EtOH, and MeCN. Mixed aqueous solvents such as $\text{H}_2\text{O}/\text{MeOH}$, $\text{H}_2\text{O}/\text{EtOH}$, $\text{H}_2\text{O}/\text{MeCN}$, $\text{H}_2\text{O}/\text{DMF}$ were also used as crystallization solvents in order to avoid solvents in which the precursor is too soluble and tend to give too small a size in the product crystals. After many attempts, it was found that the best solvent combination needed to obtain single crystals suitable for X-ray structure determination was the

mixtures of water and methanol (**3a**, **3b**, and **3e**) or water alone (**3c** and **3d**) and an H-tube was the best crystallizing vehicle. Typical synthesis details can be seen in the



H-tube apparatus with $[\text{Fe}(\text{L})(\text{CN})_4]^{2-}$ on left

experimental section. Notably, when crystals begin to grow, they have to be kept in a sealed H-tube with some mother liquor present to prevent the crystals from drying out since single perfect crystals may contain solvent of crystallization in the lattice. Loss of this solvent from the crystals can result in the crystal lattice breaking down, and the crystals turning to powder.

Surprisingly, in the case of complex **3a** and **3b**, obtained from $[\text{Fe}^{\text{II}}(2,2'\text{-bipy})(\text{CN})_4]^{2-}$ and $[\text{Fe}^{\text{III}}(2,2'\text{-bipy})(\text{CN})_4]^-$, respectively, the crystal structures showed the same +2 charge on the iron centres. In keeping with the $\text{Fe}^{\text{III}} \rightarrow \text{Fe}^{\text{II}}$ reduction hypothesis similar reduction has been shown to occur in the heme-based NO carrier nitrophorin and in other Fe-protein systems (Ascenzi and Fasano, 2007). Hexacyanoferrate anion, particular ferricyanide ions are not extremely stable even in aqueous solution. Their oxidation/reduction processes from $\text{Fe}^{\text{II}} \rightarrow \text{Fe}^{\text{III}}$ and *vice versa* have also been studied in mixed cyano-bridged clusters (Parker *et al.*, 2002). Therefore, the reduction of the $\text{Fe}^{\text{III}} \rightarrow \text{Fe}^{\text{II}}$ in **3b** may be caused by the presence of cyanide which itself acting as the reducing agent in aqueous media. However, the four CN^- ligands of the Fe^{III} precursor are retained in the Fe^{II} product, **3b**, and thus free CN^- would have to be in the other 60% of product/solution not accounted for (see Experimental) Mn^{II} and methanol are the only other possible reductants in the reaction vessel. In future, it

would be instructive to use the precursor $[\text{Cr}^{\text{III}}(2,2'\text{-bipy})(\text{CN})_4]^-$.

The types of cyanide coordination are best monitored by infrared spectral studies. The assignments of the $\nu(\text{CN})$ bands of product compounds and of precursors in the present study are given in the Table 3.6. Typically, bridging cyanide ligands have higher $\nu(\text{CN})$ frequencies than the terminal cyanides (Nakamoto, 1963), since coordination usually weakens the ligand bond next to the coordination bonds, thus shifting the ligand stretching vibration to a lower frequency. As expected, the CN stretching band is shifted to higher wavenumbers by about 20 cm^{-1} compared to the tetracyanoferrate(II) building blocks when a CN group is bridged to a second metal ions. The IR bands due to coordinated chelate, $\nu(\text{NH})$ and $\nu(\text{OH})$ groups are given in the Experimental (synthesis) section.

Table 3.6 Vibrational frequencies of the cyanide ligand in the present study (cm^{-1}).

Sample	$\nu(\text{CN}), \text{cm}^{-1}$
$\text{K}_2[\text{Fe}^{\text{II}}(2,2'\text{-bipy})(\text{CN})_4]\cdot 3\text{H}_2\text{O}$	2037s
$\text{H}[\text{Fe}^{\text{III}}(2,2'\text{-bipy})(\text{CN})_4]\cdot 2\text{H}_2\text{O}$	2155s
$\text{K}_2[\text{Fe}^{\text{II}}(1,10\text{-phen})(\text{CN})_4]\cdot 4\text{H}_2\text{O}$	2030s
$\text{H}[\text{Fe}^{\text{III}}(1,10\text{-phen})(\text{CN})_4]\cdot 2\text{H}_2\text{O}$	2154s
$[\text{Fe}^{\text{II}}(2,2'\text{-bipy})(\text{CN})_4\text{Mn}^{\text{II}}]\cdot \text{MeOH}$ (3a)	2056s
$[\text{Fe}^{\text{II}}(2,2'\text{-bipy})(\text{CN})_4\text{Mn}^{\text{II}}(\text{H}_2\text{O})_2]$ (3b)	2051s
$[\text{Fe}^{\text{II}}(1,10\text{-phen})(\text{CN})_4\text{Cu}^{\text{II}}(\text{tn})(\text{H}_2\text{O})_2]\cdot 5\text{H}_2\text{O}$ (3c)	2056s
$[\text{Fe}^{\text{II}}(2,2'\text{-bipy})(\text{CN})_4\text{Cu}^{\text{II}}(\text{tn})]\cdot \text{H}_2\text{O}$ (3d)	2056s
$[\text{Fe}^{\text{II}}(2,2'\text{-bipy})(\text{CN})_4\text{Ni}^{\text{II}}(\text{en})_2]\cdot \text{solvent}$ (3e)	2051s

3.3.2 Structural Description of $[\text{Fe}^{\text{II}}(2,2'\text{-bipy})(\text{CN})_4\text{Mn}^{\text{II}}]\cdot\text{MeOH}$ (**3a**)

The X-ray single crystal structure analyses at 123(2) K reveals that compound **3a** crystallizes in the monoclinic system with space group $P2_1/c$ (No. 14). The asymmetric unit consists of two $[\text{Fe}^{\text{II}}(2,2'\text{-bipy})(\text{CN})_4]^{2+}$ anions, two Mn^{II} cations, and two methanol molecules of crystallization.

As shown in Figure 3.1, a crystallographically independent unit contains two types of iron (Fe1 and Fe2) and manganese (Mn1 and Mn2). Each Fe(II) atom is located in a distorted octahedral environment formed by two nitrogen atoms from a 2,2'-bipy ligand and four cyanide carbon atoms. The Fe–N_{2,2'-bipy} and Fe–C_{CN} bond lengths in **3a** range from 1.973(6) to 2.001(6) Å, and 1.868(7) to 1.920(7) Å, respectively. These values are in agreement with the Fe–N and Fe–C bond lengths as observed in the Fe(II) complexes such as $\text{K}_2[\text{Fe}(2,2'\text{-bipy})(\text{CN})_4]\cdot 2.5\text{H}_2\text{O}$ (Nieuwenhuyzen *et al.*, 1998) and $\text{K}_2[\text{Fe}(2,2'\text{-bipy})(\text{CN})_4]\cdot\text{H}_2\text{O}$ (Toma *et al.*, 2002). The three *trans* angles of [C–Fe–N] and [C–Fe–C] range from 171.7(3) to 175.7(3)°, which are somewhat bent from the ideal value of 180°. The Fe–C–N angles for bridging cyanide ligands range between 174.2(6) and 178.3(7)°.

The 2,2'-bipy ligand in **3a** exhibits usual acute N⋯N bite distances of 2.558(8) Å [N9⋯N10] and 2.578(8) Å [N11⋯N12]. The bite angles are 80.5(2) and 80.7(2)° for N9–Fe1–N10 and N11–Fe2–N12, respectively. These are one of the main factors accounting for the distortion from ideal octahedral geometry (90°) of Fe^{II}.

The 2,2'-bipy ligand, as a whole, is close to planar. The mean deviation (r. m. s. deviation of fitted atoms) from the best plane calculated using twelve atoms is 0.043 Å for the plane 1 (rings *A* and *B*) with the largest deviation is –0.149(8) Å at C18, whereas, r. m. s. deviation of fitted atoms is 0.074 Å with the largest deviation

of 0.171(8) Å at C27 for the plane 2 (rings *C* and *D*). The dihedral angle between the two planes is 3.9(1)°. The bond lengths and angles within the 2,2'-bipy groups are in agreement with that reported for the free 2,2'-bipy molecule (Merritt and Schroeder, 1956). The C1/C2/Fe1/N9/N10 and C5/C6/Fe2/N11/N12 sets of atoms define a five-membered chelate to Fe^{II}, and are close to being coplanar, with the largest deviation from their mean plane being 0.093(3) and -0.061(3) Å at N10 and N12, respectively.

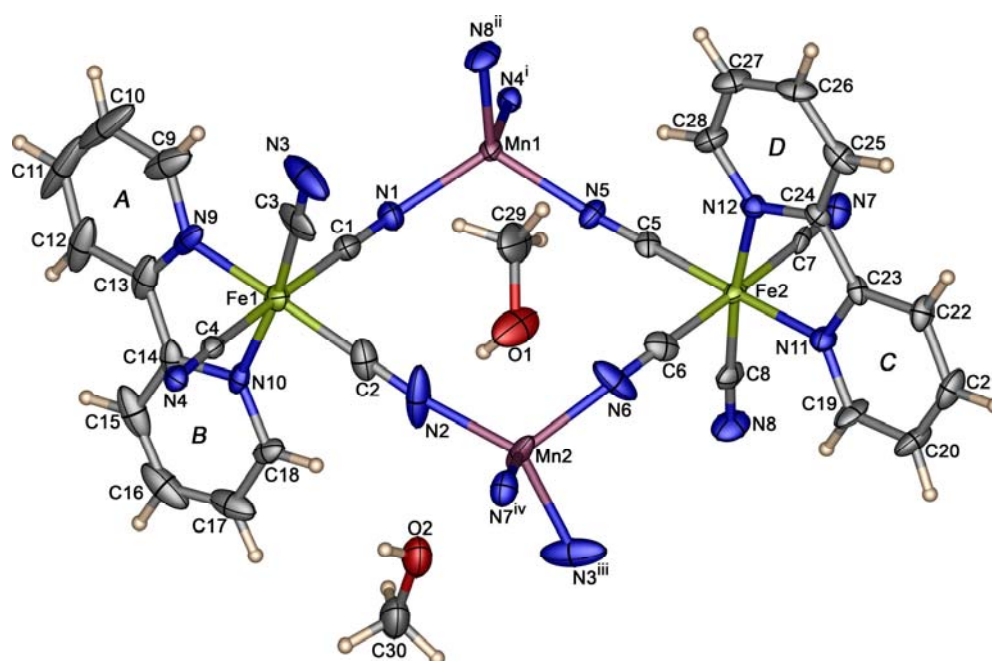


Figure 3.1 Thermal ellipsoid plot of a fragment at the 50% probability level containing the asymmetric unit with atom numbering and showing coordination environments of metals centre in **3a**. Hydrogen atoms are shown as small spheres of arbitrary radii. The labeling scheme, *A–D*, applied to the phenyl rings is used to identify the rings in subsequent discussion. Symmetry codes: (i) $-1+x, y, z$; (ii) $x, 0.5-y, -0.5+z$; (iii) $x, 0.5-y, 0.5+z$; (iv) $1+x, y, z$.

Interestingly, the Mn(II) centres adopt distorted tetrahedral geometry. Each Mn atom is coordinated by four nitrogen atoms from the cyanide-bridges of the $[\text{Fe}^{\text{II}}(2,2'\text{-bipy})(\text{CN})_4]^{2-}$ fragments. The Mn–N bond lengths in **3a** range from 2.057(6) to 2.114(6) Å, which compare well with those in other four-coordinated cyano-containing Mn(II) complexes such as 2.068(5) Å $[(4,4\text{-bipyH}_2)[\text{Mn}(\text{NCS})_4]$ (Chen *et al.*, 2000), and are comparable to the calculated average value (2.143 Å) for 31 tetrahedral Mn(II) complexes with a chromophore group MnN_4 as revealed by a CSD search from CONQUEST software version 5.26, update January 2008 (Allen, 2002). There are, however, slight differences in bond lengths and angles around the Mn(II) centre caused by the disordered methanol molecules of crystallization that are close to the Mn2 atoms. The relevant N–Mn–N bond angles vary between 92.7(3) and 128.2(4)°, and are therefore quite different to the ideal value of 109.5°, thus indicating the significant deviation from a regular tetrahedron. The Mn–N–C bond angles range from 156.2(6) to 176.8(10)°, which are somewhat more bent from linearity than are those of the Fe–N–C bond angles.

The bond lengths and angles within the cyanide ligand ranging from 1.151(10) to 1.171(11) Å are normal, and are comparable to the C–N bond distance in $\text{NaCN}\cdot 2\text{H}_2\text{O}$ (van Rij and Britton, 1978). From a bonding perspective, in the cyanide ions the carbon and nitrogen atoms act as π acceptor and σ donor, respectively. This Lewis acid–base character increases the π –bonding and σ –antibonding character of the Fe ion with the cyanide carbon and nitrogen atoms (Vahrenkamp *et al.*, 1997). Therefore, as expected, the $\text{Fe}^{\text{II}}\text{--C}_{\text{CN}}$ bond lengths in compound **3a** are shorter than the $\text{Mn}^{\text{II}}\text{--N}$ bond lengths.

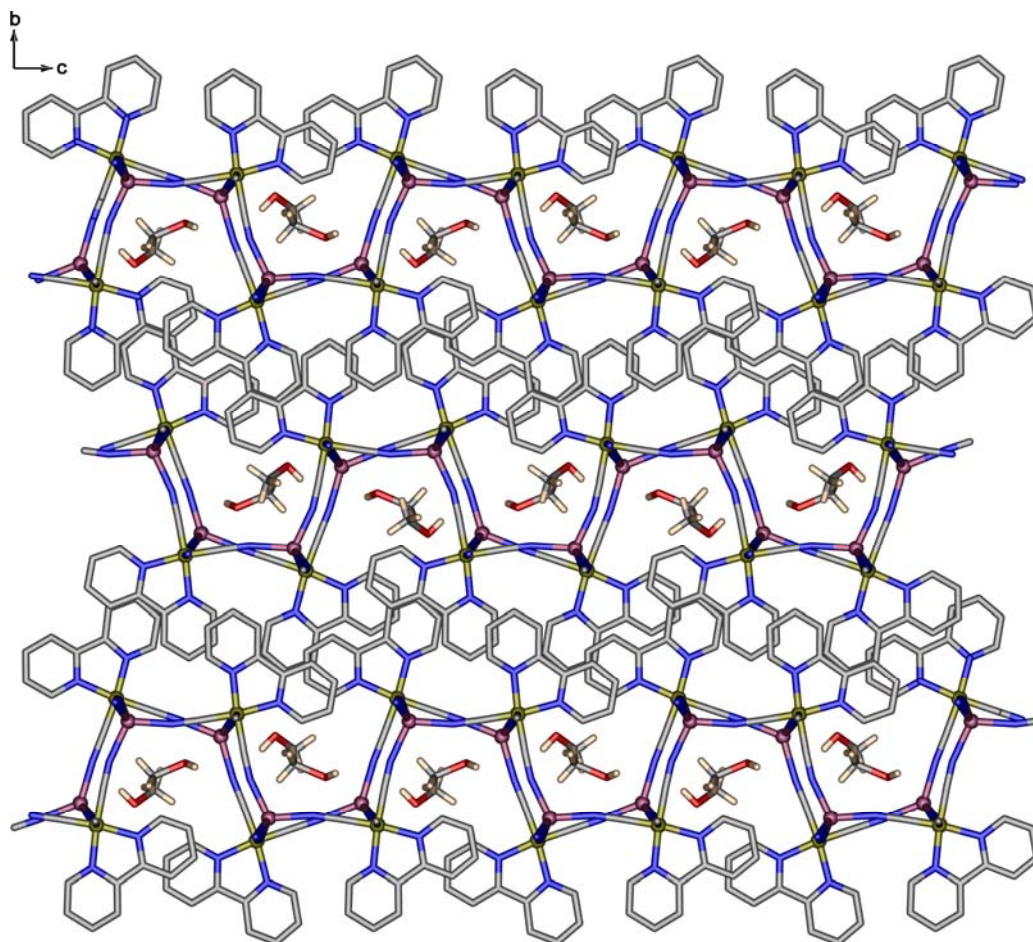


Figure 3.2 A projection along the a axis showing the 2-D corrugated sheets in **3a**.

Included methanol molecules occupy the corrugated sheets.

Each $[\text{Fe}^{\text{II}}(2,2'\text{-bipy})(\text{CN})_4]^{2-}$ unit uses four cyanide groups to bridge to four Mn^{II} cations. Simultaneously, each Mn^{II} atoms is linked to four $[\text{Fe}^{\text{II}}(2,2'\text{-bipy})(\text{CN})_4]^{2-}$ units to form neutral 2-D corrugated (4,4) sheets of $[\text{Fe}^{\text{II}}(2,2'\text{-bipy})(\text{CN})_4 \text{Mn}^{\text{II}}]$, and the methanol molecules of crystallization lie within the sheets as shown in Figure 3.2. Within the 2-D corrugated sheets, the $\text{M}\cdots\text{M}$ distances through the cyanide bridges and the $\text{M}\cdots\text{M}$ distances across the square windows vary from 4.997(1) to 5.163(1) and 6.250(1) to 7.813(1) Å, respectively, Figure 3.3.

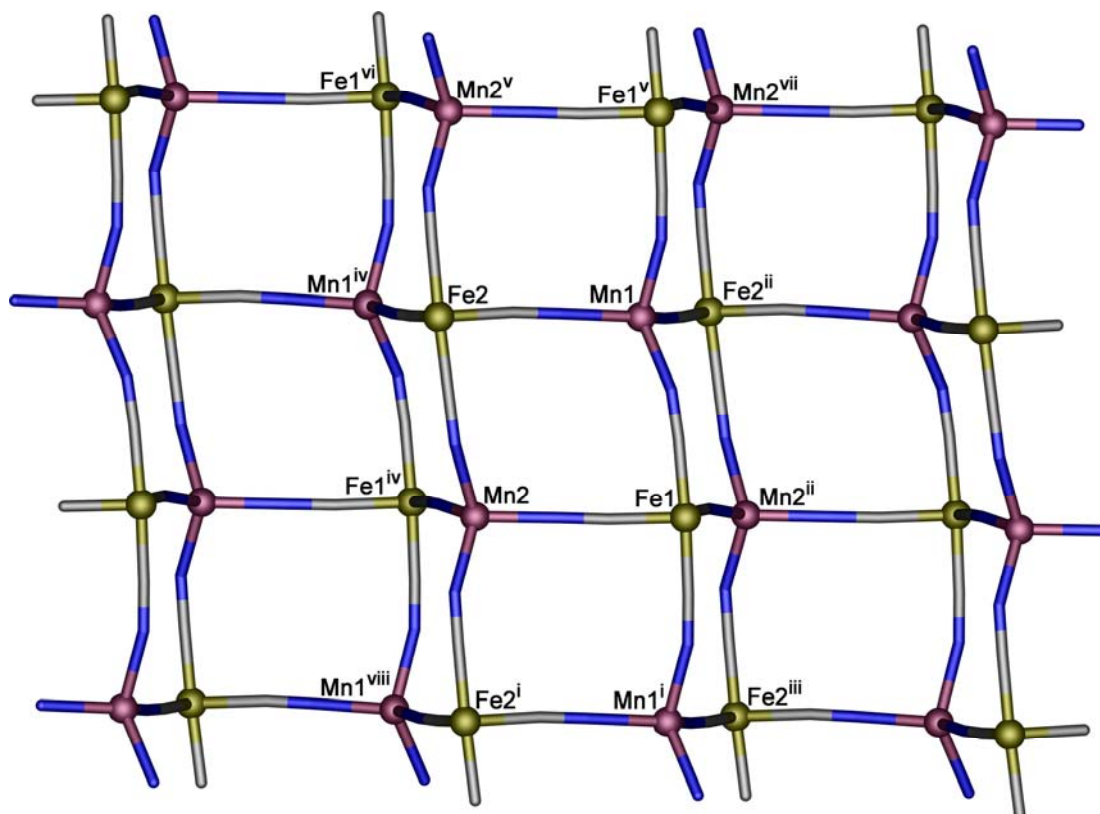


Figure 3.3 Schematic view of the 2-D corrugated sheets of the bimetallic skeleton formed by cyanide-bridged Fe(II) and Mn(II) atoms in **3a**. The M \cdots M separations are 4.997(1) [Fe1–Mn1], 5.096(1) [Fe1–Mn2], 5.036(1) [Fe1–Mn1ⁱ, Mn1–Fe1^v], 5.163(1) [Fe1–Mn2ⁱⁱ, Mn2–Fe1^{iv}], 5.027(1) [Fe2–Mn1], 5.072(1) [Fe2–Mn2], 5.050(1) [Fe2–Mn1^{iv}, Mn1–Fe2ⁱⁱ], and 5.003(1) Å [Fe2–Mn2^v, Mn2–Fe2ⁱ]. The M \cdots M distances across the squares are 7.813(1) [Fe1–Fe2], 7.219(1) [Fe1–Fe2ⁱⁱ, Fe2–Fe1^{iv}], 7.688(1) [Fe1–Fe2ⁱⁱⁱ, Fe2–Fe1^{vi}], 7.529(1) [Fe1–Fe2ⁱ] 6.392(1) [Mn1–Mn2], 6.808(1) [Mn1–Mn2ⁱⁱ], 6.701(1) [Mn1–Mn2^v], and 6.249(1) Å [Mn1–Mn2^{vii}]. Symmetry codes: (i) 1+x, y, z; (ii) x, 0.5–y, –0.5+z; (iii) 1–x, 0.5–y, –0.5+z; (iv) x, 0.5–y, 0.5+z; (v) –1+x, y, z; (vi) –1+x, 0.5–y, 0.5+z; (vii) –1+x, 0.5–y, –0.5+z; (viii) 1+x, 0.5–y, 0.5+z.

The packing of **3a** viewed down the crystallographic c axis is shown in Figure 3.4. The intercalated methanol molecules lie within the sheets. An extensive array of $C-H\cdots\pi$ and $\pi\cdots\pi$ type interactions between the sheets is also observed. For the $C-H\cdots\pi$ interactions, the carbon atoms of the 2,2'-bipy molecules act as hydrogen bond donors, and are oriented perpendicular to the mid-point of the $C\equiv N$ groups (hydrogen bond acceptors) of neighboring sheets. The $H\cdots\pi(C\equiv N)$ interatomic distances range from 2.578 to 2.875 Å, which are typical of literature values (Desiraju and Steiner, 1999). The 2,2'-bipy molecules are also themselves stacked, forming a slipped and strictly face-to-face $\pi\cdots\pi$ interaction. The value of the $C_g\cdots C_g$

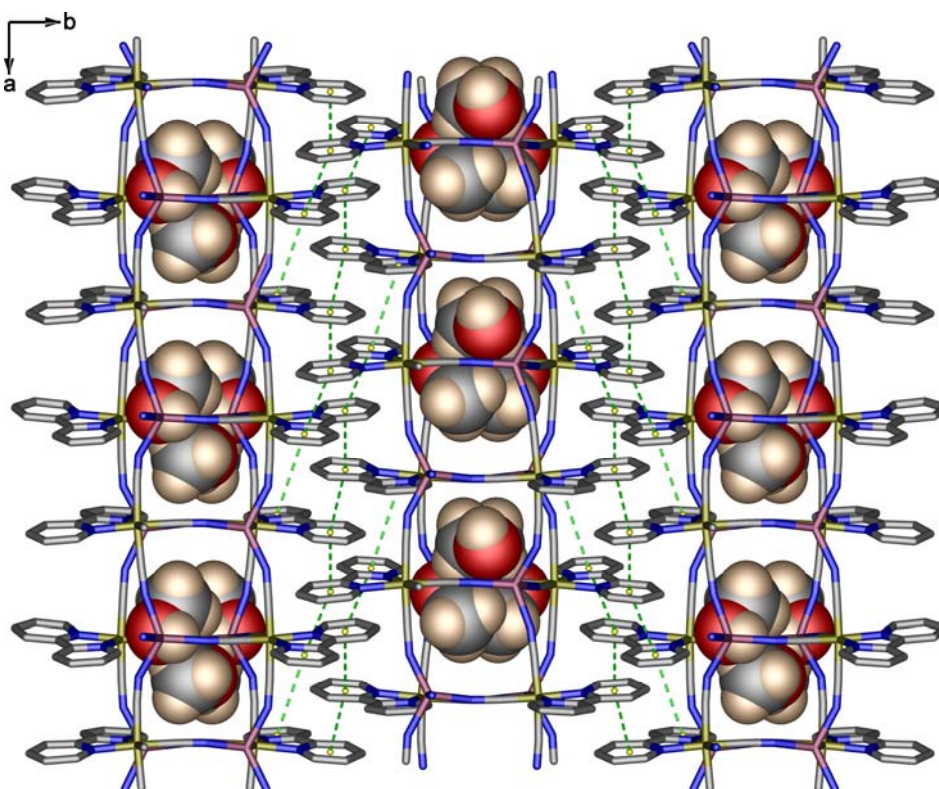


Figure 3.4 Packing diagram of **3a** viewed along the c axis showing $\pi\cdots\pi$ interactions between the 2-D corrugated sheets. Methanol molecules are represented as space-filling models.

distances range between 3.618 and 4.123 Å. These values may be indicative of weak $\pi\cdots\pi$ interactions (Janiak, 2000). The 2-D sheets in **3a** are thus cross-linked by a combination of C–H $\cdots\pi$ and weak $\pi\cdots\pi$ interactions into a 3-D supramolecular network. These interactions presumably contribute to the stabilization of the structure. Details of such supramolecular interactions in **3a** are given in Tables 3.7, and 3.8.

Table 3.7 Hydrogen bond geometries in **3a** (Å, °).

D–H \cdots A	d[D–H]	d[H \cdots A]	d[D \cdots A]	\angle [D–H–A]
C11–H11 \cdots A(C6 \equiv N6) ⁱⁱ	0.95	2.738	3.378	125.3
C15–H15 \cdots A(C1 \equiv N1) ⁱⁱⁱ	0.95	2.694	3.512	144.6
C17–H17 \cdots A(C7 \equiv N7) ^{iv}	0.95	2.875	3.806	167.1
C21–H21 \cdots A(C7 \equiv N7) ^v	0.95	2.737	3.406	128.1
C22–H22 \cdots A(C4 \equiv N4) ^{vi}	0.95	2.578	3.390	143.6
C26–H26 \cdots A(C4 \equiv N4) ^{vii}	0.95	2.765	3.432	129.9

A is the mid-point of the bridging cyano group of a neighboring chain. Symmetry codes: (i) x , $0.5-y$, $0.5+z$; (ii) $2-x$, $0.5+y$, $0.5-z$; (iii) $2-x$, $1-y$, $1-z$ (iv) $1+x$, $0.5-y$, $0.5+z$; (v) $1-x$, $-y$, $1-z$; (vi) $2-x$, $-0.5+y$, $0.5-z$; (vii) $-1+x$, $0.5-y$, $-0.5+z$.

Table 3.8 Geometrical parameters of π – π interactions in **3a** (Å, °).

π – π	Centre to centre distance (C _g \cdots C _g)	Closest distance of approach	Interplanar angle
ring <i>A</i> \cdots ring <i>B</i>	3.706	3.059(11)	2.1(1)
ring <i>A</i> \cdots ring <i>C</i>	3.926	3.193(11)	6.6(1)
ring <i>A</i> \cdots ring <i>D</i>	4.123	3.031(11)	0.0(2)
ring <i>B</i> \cdots ring <i>A</i>	3.706	3.169(11)	6.4(1)
ring <i>B</i> \cdots ring <i>D</i>	3.886	3.257(11)	9.9(1)
ring <i>C</i> \cdots ring <i>C</i>	3.618	3.291(8)	0.9(1)

What is notable in Figures 3.1 and 3.3 is that the desired CN-bridged square {Fe1/C1/N1/Mn1/N5/C5/Fe2/C6/N6/Mn2/N2/C2/Fe1} has been formed. However, it can not extend in to a square tube because of the two 2,2'-bipy ligands, and hence C4/N4 and C7/N7 extend outwards rather than at 90° to the square. The Mn(II) centres, of course, lack a blocking bidentate ligand.

3.3.3 Structural Description of [Fe^{II}(2,2'-bipy)(CN)₄Mn^{II}(H₂O)₂] (3b)

The single crystal X-ray structure analyses at 123(2) K reveals that compound **3b** is isostructural to [Ru^{II}(2,2'-bipy)(CN)₄Mn^{II}(H₂O)₂] (Xia *et al.*, 2007) a compound reported during this project. **3b** crystallizes in the high symmetry trigonal system with space group $R\bar{3}$ (No. 148). The asymmetric unit consists of one [Fe^{II}(2,2'-bipy)(CN)₄]²⁻ anion and one [Mn^{II}(H₂O)₂]²⁺ cation, as shown in Figure 3.5.

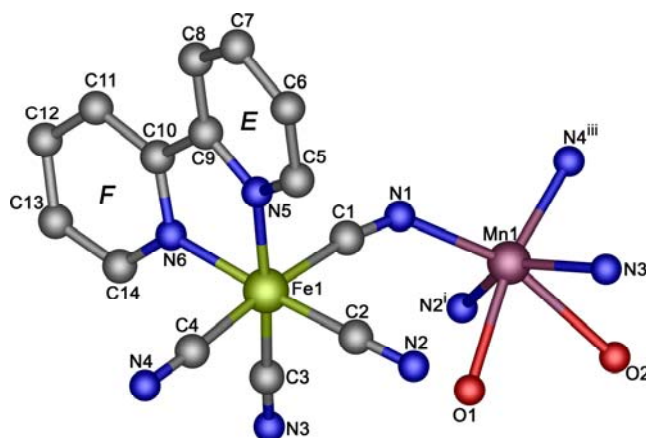


Figure 3.5 Ball and stick representation of the asymmetric unit with numbering scheme and showing the coordination environments of the metal centres in **3b**. Hydrogen atoms are omitted for clarity. The labeling scheme, *E-F*, applied to the phenyl rings is used to identify the rings in the subsequent discussion. Symmetry codes: (i) $x-y+1/3, x-1/3, -z+2/3$; (ii) $y+1/3, -x+y+2/3, -z+2/3$; (iii) $x, y, z-1$.

The Fe(II) centre is coordinated by two nitrogen atoms from one 2,2'-bipy and four cyanide carbon atoms, and has a distorted octahedral geometry. The Fe–C bond lengths range from 1.870(10) to 1.940(10) Å, whereas the Fe–N_{2,2'-bipy} bond lengths are 1.997(9) and 1.980(8) Å. The bond lengths and angles involving the 2,2'-bipy ligand are normal (Merritt and Schroeder, 1956). The whole 2,2'-bipy ligand is not planar with r. m. s. of 0.137 Å, and the largest deviation from the best plane being 0.179(9) at C6. The values of the bond lengths and angles within the [Fe^{II}(2,2'-bipy)(CN)₄]²⁻ unit are slightly different to those found in **3a**, *i.e.* the Fe–C–N angles range from 171.3(10) to 177.1(9)°, and are thus more bent from linearity.

The Mn(II) center is coordinated in a distorted octahedral geometry by four nitrogen atoms from four bridging cyanide groups and two oxygen atoms from water molecules. The Mn–N bond lengths range from 2.114(10) to 2.165(9) Å, whereas the Mn–O bond lengths are 2.340(9) and 2.480(20) Å. The Mn–N–C bond angles range from 140.6(9) and 175.4(9)°, and are much more significantly bent than the Fe–C–N bond angles above. The bond lengths and angles, however, for the [Mn^{II}(H₂O)₂]²⁺ moieties of **3b** are in accordance with those found in [Ru^{II}(2,2'-bipy)(CN)₄Mn^{II}(H₂O)₂] (Xia *et al.*, 2007).

As shown in Figures 3.6 and 3.7, the most significant structural feature of **3b** is the assembly of the two distinct types of building blocks, *i.e.* [Fe^{II}(2,2'-bipy)(CN)₄]²⁻ and [Mn^{II}(H₂O)₆]²⁺, to form remarkable neutral hydrophilic 1-D tubular coordination polymers, running along the crystallographic *a* axis. Each [Fe^{II}(2,2'-bipy)(CN)₄]²⁻ unit connects to four Mn(II) cations *via* cyanide groups. Simultaneously, each Mn(II) ions is linked to four Fe(II) ions. The tube can be described in terms of 18-membered {Fe₃Mn₃(CN)₆} rings (Figure 3.6c). Within this

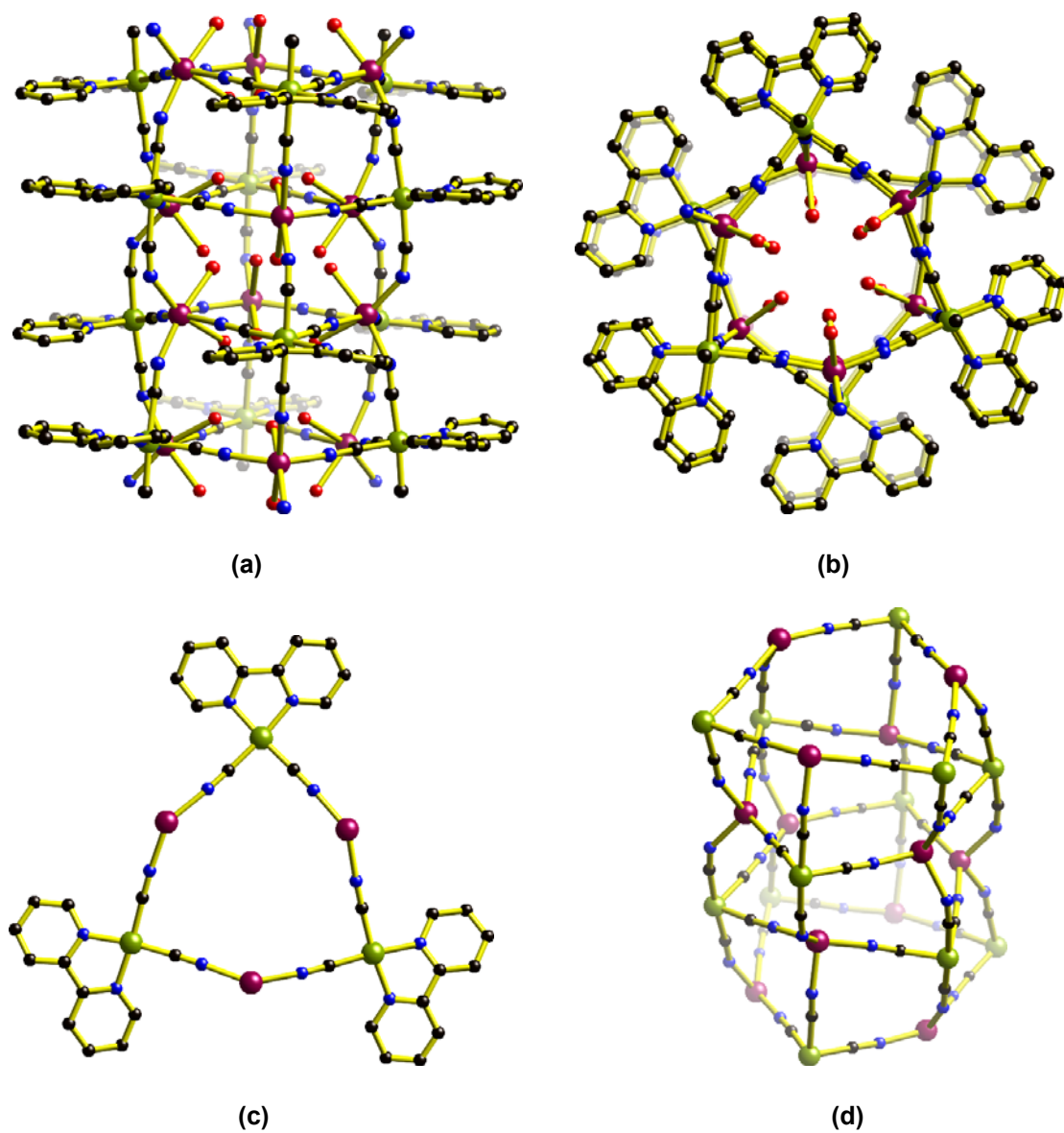


Figure 3.6 Views of (a) side, (b) top views of 1-D tubular structure, (c) Fe_3Mn_3 hexanuclear arrangement, and (d) schematic view of the tube topology (water and 2,2'-bipy molecules omitted for clarity) in **3b**.

open $\{\text{Fe}_3\text{Mn}_3\}$ hexanuclear arrangement, the angles of the three metal ions along the edges are $145.1(9)$ and $90.7(9)^\circ$ for $[\text{Mn}-\text{Fe}-\text{Mn}]$ and $[\text{Fe}-\text{Mn}-\text{Fe}]$, respectively. The r. m. s. deviation of fitted atoms from the best plane calculated using eighteen atoms in the ring is 0.196 \AA . These rings, which have a triangular shape, then stack so that each ring is staggered 60° to its neighbours. The stacked rings are then bridged by further cyanide ligands to generate the tube (Figure 3.6d).

The two side planes of the 1-D tube have a dihedral angle of $6.93(1)^\circ$. The cross dimension of the hexagon channel is *ca.* $9.925(2) \text{ \AA}$ (defined by the separation between Fe and Mn), which is slightly larger than that found for the Ru^{II} analog of 9.8 \AA (Xia *et al.*, 2007). The $\text{Fe}\cdots\text{Mn}$ separation across the cyanide bridges is $4.862(1) \text{ \AA}$.

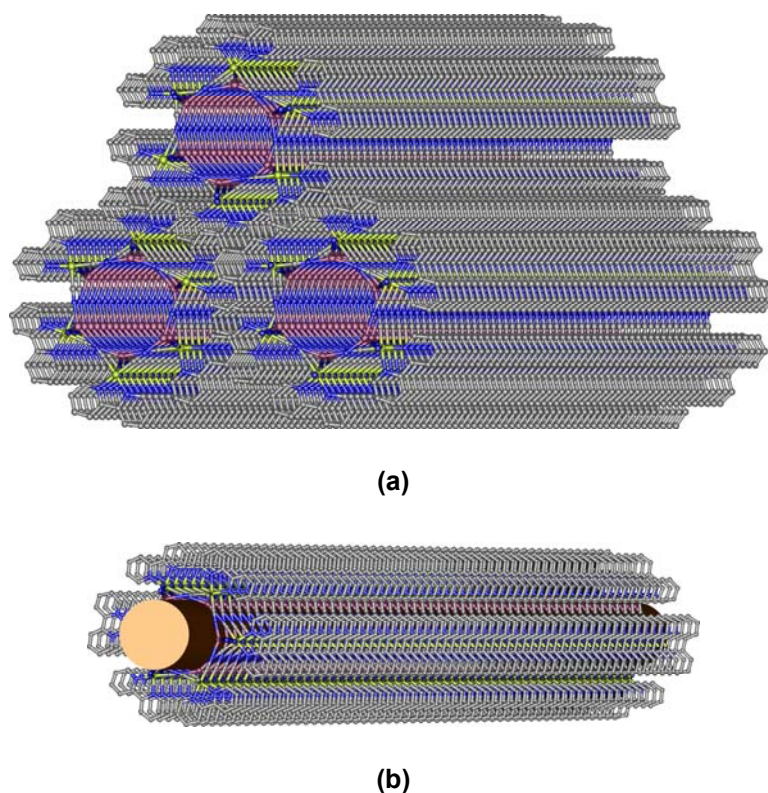


Figure 3.7 Views of (a) packing of the three and (b) single 1-D tubes in **3b**. The brown color defined the tube.

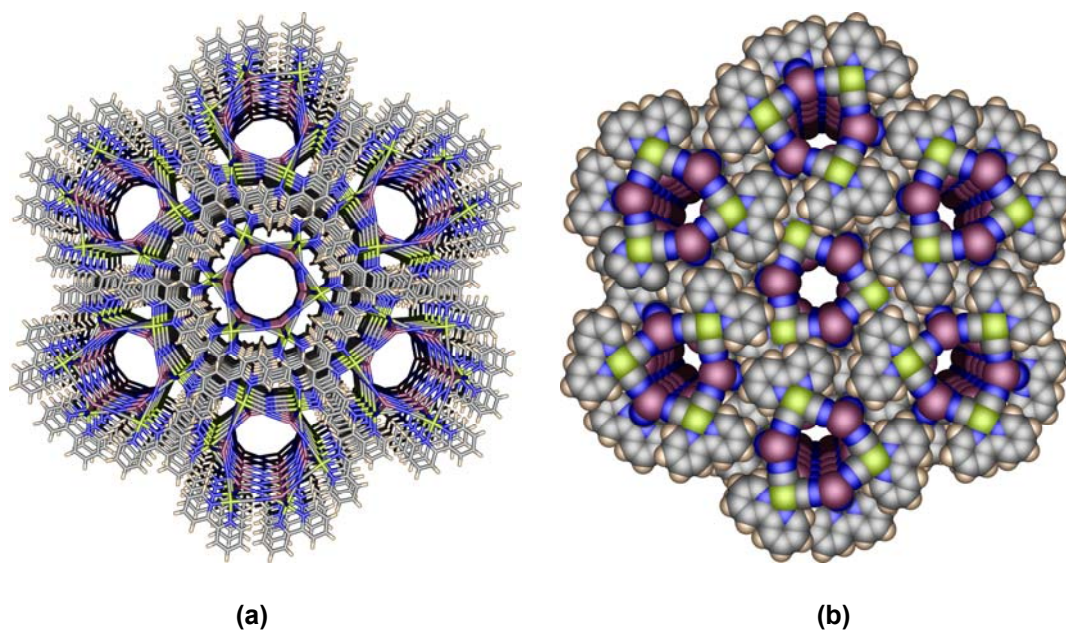


Figure 3.8 (a) Stick and (b) space filling representations of seven 1-D tubes in top view of **3b**. Water molecules are omitted.

As shown in Figure 3.8, one single nanotube is surrounded by six other nanotubes, and they extend in a parallel arrangement along the crystallographic c axis to form a 3-D supramolecular architecture *via* π - π interactions of overlapping phenyl rings, at interlayer distances of *ca.* 3.79 Å. These interactions help to increase the dimensionality into a 3-D supramolecular structure, and help to stabilize the crystal structure in **3b**.

In contrast to **3a**, there are no methanol molecules of crystallization observed in the structure of **3b**. This is perhaps surprising looking at the tubular channels. If only the arrangement of the Mn(II) centres and cyanide ligands are considered, then the geometrical characteristics of the Mn(II) ion in **3b** is very similar that of **3a**. Therefore the size of the clathrated solvents, *i.e.* water versus methanol is one factor

causing a significant difference between the structures of **3a** and **3b**. The topology observed in **3b** is very rare for cyanide-bridged bimetallic coordination polymers. A search from CSD (version 5.28, updates January 2008) and SciFinder (July 2008) yielded only one example, a Ru(II) analog (Xia *et al.*, 2007) of **3b**, reported so far. The initial aim of this work was to isolate square tubes, ideally of Fe^{III}/Mn^{II}, but it is gratifying to have made hexagonal tubes.

3.3.4 Structural Description of [Fe^{II}(1,10-phen)(CN)₄Cu^{II}(tn)(H₂O)₂] \cdot 5H₂O (**3c**)

The X-ray single crystal structure analyses at 123(3) K reveals that compound **3c** crystallizes in the triclinic system with space group $P\bar{1}$ (No. 2). **3c** contains a neutral cyanide-bridged Fe^{II}–Cu^{II} rectangular tetranuclear complex which resides on a centre of symmetry. The asymmetric unit consists of one [Fe^{II}(1,10-phen)(CN)₄]²⁻ anion, one [Cu^{II}(tn)(H₂O)₂]²⁺ cation, and five uncoordinated water molecules. A view of the core part of **3c**, with the atom-labeling scheme, is shown in Figure 3.9.

The Fe(II) centres are coordinated by two 1,10-phen nitrogen (Fe–N = 2.001(6) and 2.008(6) Å) and four cyanide carbon atoms (Fe–C = 1.874(6) to 1.929(7) Å), making a distorted octahedral geometry. The values of the bond lengths and angles involving the [Fe^{II}(1,10-phen)(CN)₄]²⁺ fragment are comparable to those observed in the following low-spin Fe(II) complexes: [Fe(1,10-phen)₂(CN)₂] \cdot 3H₂O (Zhuzhong *et al.*, 1996), K₂[Fe(2,2'-bipy)(CN)₄] \cdot 2.5H₂O (Nieuwenhuyzen *et al.*, 1998), and K₂[Fe(2,2'-bipy)(CN)₄] \cdot H₂O (Toma *et al.*, 2002). The Fe–C–N bond angle at the corners of the rectangle are 178.1(6) and 177.3(6)° for the [Fe1–C1–N1] and the [Fe1–C2–N2], respectively. The 1,10-phen ligand exhibits a typical acute N \cdots N bite distance of 2.615(7) Å (N5 \cdots N6) and bite angle of 81.4(2)° (N5–Fe1–N6). These are one of the main factors accounting for the distortion from ideal octahedral geometry

(90°). The 1,10-phen ligand as a whole is close to planar with maximum atomic deviation being 0.033(5) Å at the C15. The bond lengths and angles in the 1,10-phen ligands in **3c** agree well in the mean values of the free 1,10-phen ligand (Tian *et al.*, 1995), and in other 1,10-phen-containing Fe(II) complex of [FeCl₂(1,10-phen)₂] (Fu *et al.*, 2005).

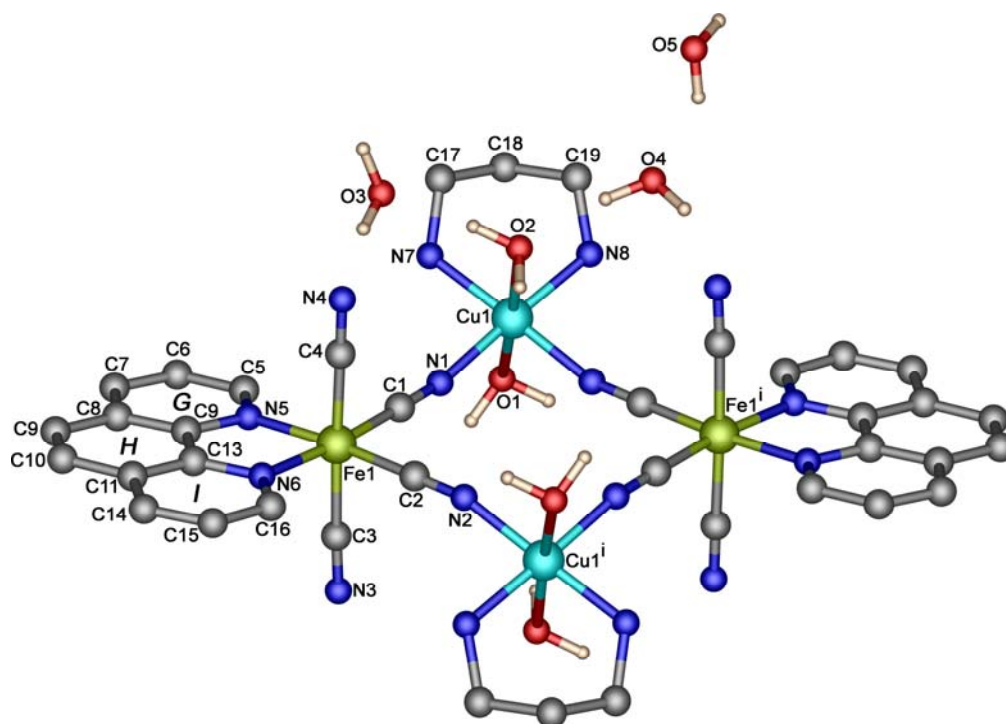


Figure 3.9 Ball and stick representation of the asymmetric unit in **3c** with numbering scheme and coordination environments of metals centre shown. The labeling scheme, *G–I*, applied to the phenyl rings are used to identify the rings in subsequent discussion. Symmetry code: (i) $-x, -y, -z$.

The Cu(II) centre has an elongated octahedral *trans* {CuN₄O₂} coordination geometry. The equatorial plane (N1, N2ⁱ, N7 and N8, symmetry code: (i) $-x, -y, -z$) is formed by two cyanide nitrogen atoms (Cu1–N1 = 1.982(5) Å and Cu1–N2ⁱ = 1.980(6) Å, symmetry codes: (i) $-x, -y, -z$) in *cis* positions and two nitrogen atoms of the chelated tn molecule in the *gauche* conformation (Cu1–N5 = 2.001(5) Å and Cu1–N6 = 2.008(5) Å). The Cu–N bond lengths in **3c** are comparable to the related complexes of [Fe^{II}(CN)₆{Cu^{II}(tn)}₂]·KCl·5H₂O (2.004–2.011 Å) and [{Cu^{II}(tn)}₂]·4H₂O (1.987–2.001 Å) (Triki *et al.*, 2006). The axial positions in the octahedron are occupied by two oxygen atoms of aqua ligands showing very long Cu–O distances of 2.630(5) and 2.470(5) Å for Cu1–O1 and Cu1–O2, respectively. These Cu–O values found in **3c** are in the range of semi-coordination (2.22–2.89 Å) for H₂O (Hathaway, 1973) caused by a Jahn-Teller effect. The {CuN₄O₂} geometric parameters of **3c** are comparable with the corresponding values in [Cu^{II}(tn)₂(H₂O)₂](S₂O₆), Cu–N = 2.021(2) and Cu–O = 2.572(2) Å (Kim *et al.*, 2003).

The acute angle subtended by the chelated tn ligand at the copper atom in **3c** is 95.0(2)°, comparable to the related bite angle of 94.1° in [{Cu^{II}(tn)}₂Fe^{II}(CN)₆]·KCl·5H₂O (Triki *et al.*, 2006), and slightly larger than that of 89.2° in [Fe^{II}(CN)₆Cu^{II}(tn)₂(H₂O)₂](F₂) (Emsley and Arif, 1988). The small bite angle causes the deviations from the ideal value of 90° *viz* 91.4(2), 87.4(2), 86.1(2), and 95.0(2)° for N1–Cu1–N2ⁱ, N1–Cu1–N7, N2ⁱ–Cu1–N8, and N7–Cu1–N8, respectively (symmetry code: (i) $-x, -y, -z$). The O1–Cu1–O2 bond angle is 173.4(2)°. The Cu–N–C_{CN} bond angles are significant bent at 160.6(5) and 160.2(5)° for Cu1–N1–C1 and Cu1–N2–C2, respectively. The Fe–C_{CN} bonds in compound **3c** are shorter than the

Cu–N_{CN} bonds, probably due to the stronger π -back donation from the Fe(II) ion to the cyanide groups.

The square cores are composed of alternate cyanide-bridged Fe(II) and Cu(II) ions. The four metal atoms occupy the corners and the four cyanide ligands act as edges. The values at the corners of the rectangle are close to right angles (C1–Fe1–C2 = 90.6(3)°, N1–Cu1–N2 = 91.4(2)°). The Fe \cdots Cu distances along the edges of the rectangles across bridging cyanides are 4.952(1) and 4.942(1) Å for Fe1 \cdots Cu1 and Fe1 \cdots Cu1ⁱ (symmetry code: (i) = $-x, -y, -z$), respectively. The values compare well with those observed in other cyanide-bridged Fe–Cu molecular squares complexes, such as 4.983(2) and 4.970(2) Å in [Fe^{II}₂Cu^{II}₂(μ -CN)₄(2,2'-bipy)₆](PF₆)₄·2H₂O·3CHCl₃ (Oshio *et al.*, 1999), 4.9747(7) and 4.9995(3) Å in [Fe^{II}₂Cu^{II}₂(μ -CN)₄(dmbpy)₄(impy)₂](ClO₄)₄·3CH₃OH·C₆H₆, where dmbpy = 4,4'-dimethyl-2,2'-bipyridine, impy = 2-(2-pyridyl)-4,4,5,5-tetramethyl-4,5-dihydro-1H-imidazolyl-1-oxy (Oshio *et al.*, 2002). These squares have more of the bidentate chelate (on Fe^{II}) and less CN[−] ligands than in **3c**.

An interesting structural feature of **3c** is that the *trans* coordinated water molecules on the Cu(II) centres hydrogen bond to neighboring square cores through O1 and O2 (2.832(7) Å) to give a 1-D tube-like structure along the crystallographic *c* axis, as shown in Figure 3.10. The closest metal \cdots metal distances between neighboring square cores is 6.699(1) Å.

Each coordinated water molecule is hydrogen bonded to three uncoordinated water molecules, with O \cdots O distances in the range of 2.779(7) to 2.865(13) Å. Two of these uncoordinated water molecules (O3 and O4) are also linked to the terminal cyanide nitrogens (N3 and N4) of a square core with O \cdots N distances between

2.873(7) and 2.958(7) Å. This is common in hydrated cyanometallates. The remaining uncoordinated water molecules (O5) are further linked to other uncoordinated water molecules (O4) with the O···O distances at 2.756(13) and 2.865(13) Å, forming a 1-D chain along the crystallographic *a* axis, as shown in Figure 3.11. Weak N–H···O and C–H···O hydrogen bonds (Desiraju and Steiner, 1999) are also observed in this compound. The values of the D···A distances are between 3.261(8) and 3.312(7), and 3.398(3) to 3.523(8) Å for N···O and C···O, respectively.

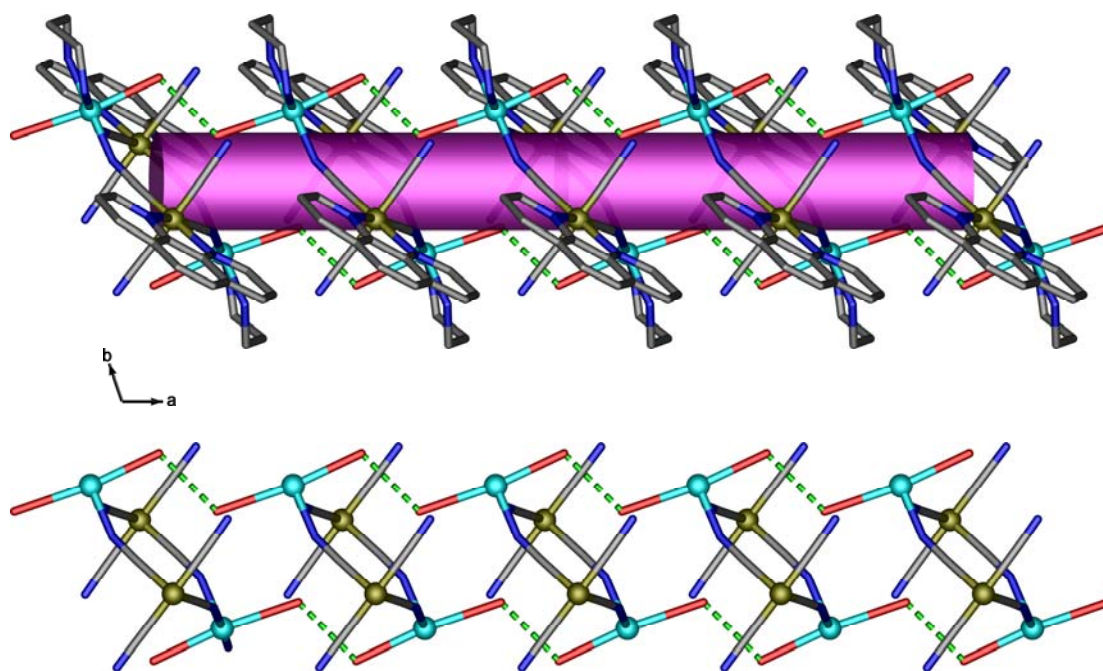


Figure 3.10 Views of 1-D tube like structure in **3c** propagated *via* hydrogen bonded parallel to the *a* axis. Hydrogen bonds are represented as dashed green lines.

Furthermore, the structure of compound **3c** showed the presence of C–H··· π and π ··· π bonding interactions which influence the crystal packing. These include C–H··· π , interactions involving the carbon atoms (C17 and C18) of the tn ligands and

π -cloud electrons on the 1,10-phen moieties (rings *E* and *F*). The values of the H \cdots centroid (C_g) distances and C–H \cdots C_g angles are 2.912(6) Å and 129°, and 2.693(7) Å and 148°, for C17–H17a \cdots $C_g(E)$ and C18–H18b \cdots $C_g(F)$, respectively.

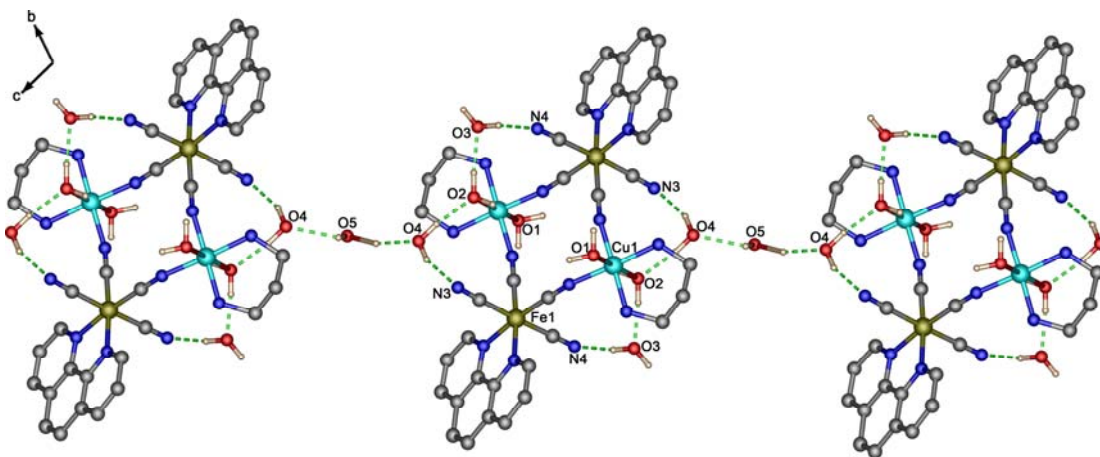


Figure 3.11 View of 1-D chain linked *via* O–H \cdots N and O–H \cdots O hydrogen bonds in **3c** along the *a* axis. C–H and N–H atoms on 1,10-phen and tn molecules have been omitted for clarity. Hydrogen bonds represented as dashed green lines.

The $\pi\cdots\pi$ type interactions between the 1,10-phen ligands also contribute to the stabilization the structure of **3c**. The 1,10-phen molecules are stacked to each other along the crystallographic *b* axis, thus leading to 2-D sheets as illustrated in Figure 3.12. The $C_g\cdots C_g$ distances between adjacent 1,10-phen moieties and the dihedral off-set angles are 3.734 Å and 3.1(4)°, and 3.643 Å and 0.0(4)° for $C_g(E)\cdots C_g(G^i)$, and $C_g(G)\cdots C_g(G^i)$, respectively (symmetry code: (i) 1+x, y, z). There are additional weak O/C–H $\cdots\pi$ type interactions between the uncoordinated waters or the 1,10-phen molecules and the mid-point of cyano groups. These interactions help

to enhance the dimensionality into a 3-D supramolecular structure. All relevant interactions in **3c** are listed in Tables 3.9 and 3.10.

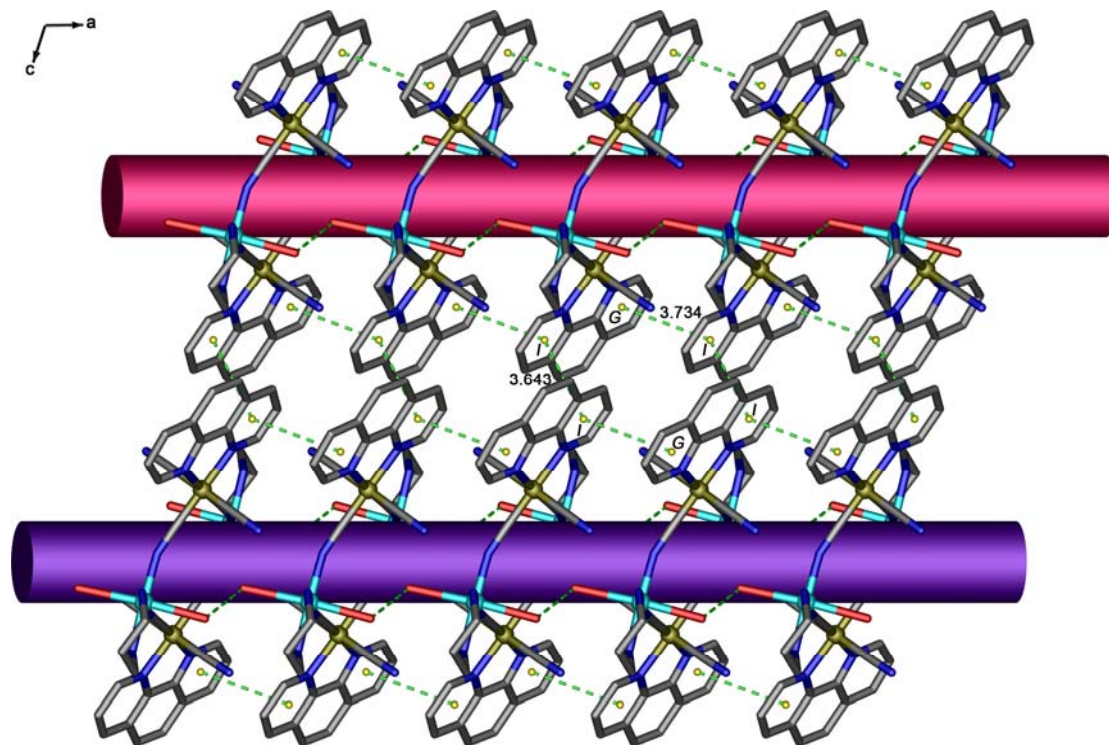


Figure 3.12 2-D sheet generated through a combination of self-complementary O–H···O hydrogen bonds and π – π interactions. The red and purple cylinders indicate the way to produce pseudo 1-D tubes.

It is interesting to contemplate why the desired square tubes did not form in **3c** since the four CN ligands around Fe(II) are in correct position as are the $\{\text{Fe}^{\text{II}}(1,10\text{-phen})\}$ and $\{\text{Cu}^{\text{II}}(\text{tn})\}$ ligands (Figure 3.9). Clearly, the Cu(II) centres “preferred” two *trans* H₂O molecules than the nitrogen atom from neighboring $[\text{Fe}^{\text{II}}(1,10\text{-phen})(\text{CN})_4]^{2-}$ groups. Perhaps dry organic solvents and organic soluble metal precursors are the way to go in the future.

Table 3.9 Hydrogen bond geometries in **3c** (Å, °).

D–H···A	d[D–H]	d[H···A]	d[D···A]	∠[D–H–A]
O1–H1w···N1 ⁱ	0.97(2)	2.54(5)	3.217(7)	127(5)
O1–H1w···A(C1≡N1) ^x	0.97	2.44	3.235	139
O1–H2w···N2 ⁱⁱ	0.97(2)	2.26(3)	3.202(7)	162(6)
O1–H2w···A(C2≡N2) ^x	0.97	2.44	3.235	139
O2–H4w···O1 ⁱⁱⁱ	0.97(2)	1.89(2)	2.832(7)	163(4)
O2–H3w···O3	0.96(2)	1.82(2)	2.779(7)	172(7)
O3–H6w···N4	0.97(2)	1.91(2)	2.873(7)	171(6)
O3–H5w···N4 ^{iv}	0.97(2)	2.00(3)	2.958(7)	167(5)
O4–H7w···O2	0.97(2)	1.86(3)	2.784(7)	160(7)
O4–H8w···N3 ^v	0.97(2)	1.95(3)	2.871(8)	159(5)
O5–H9w···O4	0.98(2)	1.88(8)	2.756(13)	148(12)
O5–H10w···O4 ^{vi}	0.98(2)	2.11(8)	2.865(13)	133(9)
N7–H7a···N4 ⁱⁱ	0.92	2.42	3.231(8)	148
N7–H7b···O3	0.92	2.61	3.312(7)	133
N8–H8b···N3 ⁱⁱⁱ	0.92	2.23	3.118(8)	161
N8–H8a···O4	0.92	2.56	3.261(8)	133
C5–H5···N4 ⁱⁱ	0.95	2.61	3.311(8)	131
C6–H6···N4 ⁱⁱ	0.95	2.86	3.422(9)	119
C10–H10···O5 ^{vii}	0.95	2.66	3.504(16)	148
C11–H11···O4 ^{viii}	0.95	2.47	3.398(8)	165
C11–H14···A(C3≡N3) ^{xii}	0.95	2.84	3.757	163
C17–H17a···C _g G ^{ix}	0.99	2.693(7)	3.602(7)	129
C17–H17b···A(C4≡N4) ^{xiii}	0.99	2.73	3.700	167
C18–H18a···O2 ⁱⁱ	0.99	2.53	3.523(8)	176
C18–H18b···C _g H ^{ix}	0.99	2.912(6)	3.605(7)	148
C19–H19a···O5 ⁱⁱ	0.99	2.58	3.474(14)	151

C_g is the centroids of ring. A is the mid-point of the bridging cyano group of a neighboring chain. Symmetry codes: (i) $-x+1, -y, -z$; (ii) $x+1, y, z$; (iii) $x-1, y, z$; (iv) $-x-1, -y-1, -z$; (v) $-x, -y, -z$; (vi) $-x-1, -y-1, -z-1$; (vii) $x+1, y, z+1$; (viii) $x, y, z+1$. (ix) $-x, -y-1, -z$; (x) $1-x, -y, -z$; (xi) $1+x, y, z$; (xii) $-x, -y, 1-z$; (xiii) $-x, -y-1, -z$.

Table 3.10 Geometrical parameters of π - π interactions in **3c** (Å, °).

π - π	Centre to centre distance (C _g ...C _g)	Closest distance of approach	Interplanar angle
ring <i>G</i> ...ring <i>I</i> ⁱ	3.734	3.204(9)	3.1(4)
ring <i>I</i> ...ring <i>I</i> ⁱ	3.643	3.436(15)	0.0(4)

Symmetry code: (i) 1+x, y, z.

3.3.5 Structural Description of [Fe^{II}(2,2'-bipy)(CN)₄Cu^{II}(tn)]·H₂O (**3d**)

A 1:1:1 molar ratio of [Fe^{II}(2,2'-bipy)(CN)₄], Cu(ClO₄)₂·6H₂O and tn was reacted to give brown-red needles of **3d**. The microanalysis of this crystalline product is consistent with the C, H and N values expected for the formula [Fe^{II}(2,2'-bipy)(CN)₄Cu^{II}(tn)]·H₂O. Despite the poor quality of the crystals, a data set was obtained that only to unambiguously establish the molecular square. Thus, only the molecular geometry or at least the bond connectivities are described. The bond lengths and angles as well as supramolecular interactions are not discussed here.

The unit cell parameters *a*, *b* and *c* are very similar, and the space group is identical to that in **3c**. The structure of **3d** is made up of neutral tetranuclear molecular rectangles of [Fe^{II}(2,2'-bipy)(CN)₄Cu^{II}(tn)]. The connectivity of the square core in **3d** is essentially the same to that of **3c**, which consists of cyanide-bridged Fe(II) and Cu(II) centrosymmetric rectangles, as shown in Figure 3.13. Again, each Fe(II) centre exhibits a distorted octahedral geometry with two pyridyl nitrogen atoms from a 2,2'-bipy ligand and four carbon atoms from the cyanide ligands.

Unlike in compound **3c**, the Cu(II) ions have a distorted square-planar geometry (pseudotetrahedral), and are coordinated by four nitrogen atoms: two from chelated tn N-donor ligands, and another two nitrogen atoms from two bridging

cyanide groups. Intriguingly and frustratingly, it is likely that this “out-of-plane” geometry around each Cu(II) prevents extension into square tube motifs, *via* N–C–Fe bridging to the next squares since bonded water is absent in **3d**.

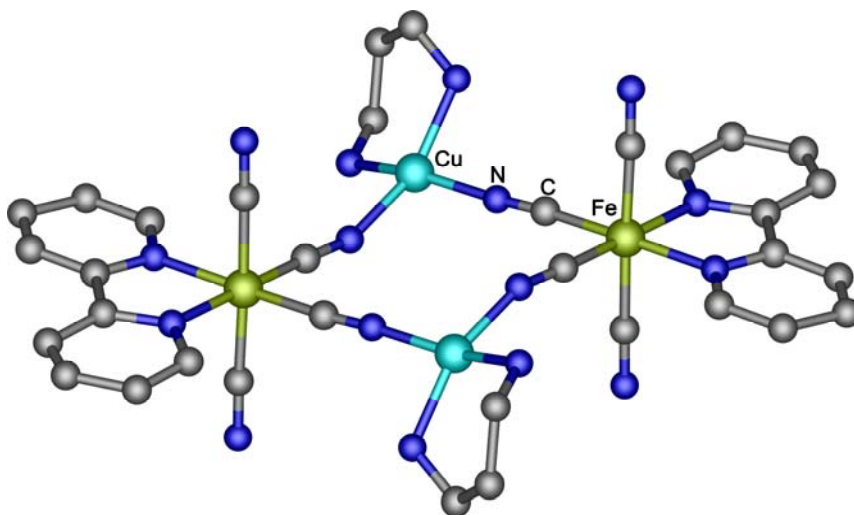


Figure 3.13 Ball and stick representation showing the atom connectivity and coordination environment in **3d**.

3.3.6 Structural Description of $[\text{Fe}^{\text{II}}(2,2'\text{-bipy})(\text{CN})_4]\text{Ni}^{\text{II}}(\text{en})_2 \cdot \text{Solvent}$ (**3e**)

Single crystal X-ray analysis at 123(2) K reveals that **3e** crystallizes in the monoclinic system with space group $P2_1/n$ (No. 14). The asymmetric unit consists of one $[\text{Fe}^{\text{II}}(2,2'\text{-bipy})(\text{CN})_4]^{2-}$ anion, one *cis*- $[\text{Ni}^{\text{II}}(\text{en})_2]^{2+}$ cation, and disordered clathrated solvent molecules as shown in Figure 3.14. Each of metal (II) centres lies on a general position. Since the mono-chelated precursor $[\text{Ni}(\text{en})(\text{H}_2\text{O})_4](\text{NO}_3)_2$ was used in synthesis, a rearrangement to the *bis* complex $[\text{Ni}(\text{en})_2(\text{H}_2\text{O})_2]^{2+}$ has occurred during reaction and crystallization, in low yield, of product **3e**.

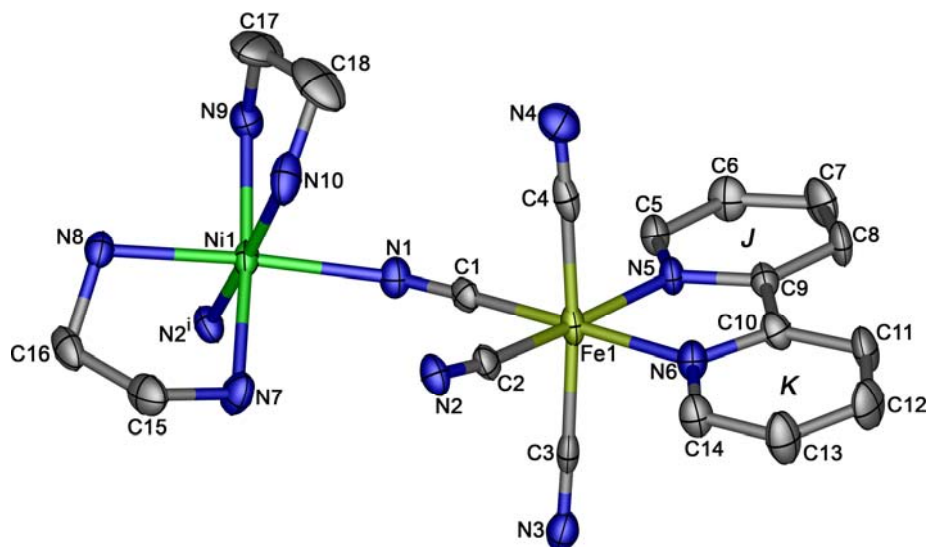


Figure 3.14 Thermal ellipsoid plot at the 50% probability level of **3e** containing coordination environments of metals centre shown. Disordered solvent molecules and hydrogen atoms are omitted. The labeling scheme, *J-K*, applied to the phenyl rings is used to identify the rings in subsequent discussion. Symmetry code: (i) $-1+x, y, z$.

The Fe(II) ions are coordinated by two 2,2'-bipy nitrogen atoms and four cyanide carbon atoms, taking a distorted octahedral geometry. The bond lengths and angles around the Fe(II) centres in **3e** are comparable to those found in **3a-3c**. The 2,2'-bipy ligand as a whole is close to planar. The mean deviation from the best plane calculated using all twelve atoms is 0.067 Å with the largest deviation being $-0.105(5)$ Å at C13. The bond lengths and angles within the 2,2'-bipy group compare well with those reported for the free 2,2'-bipy molecule (Merritt and Schroeder, 1956). The small bite angle of the bidentate 2,2'-bipy ligand is $80.4(1)^\circ$ for N5–Fe1–N6. This factor accounts for the distorted octahedral geometry of the Fe(II) centre from the ideal geometry (90°).

The Ni(II) centre exists in a distorted octahedral geometry defined by six nitrogen atoms. The equatorial positions are occupied by three nitrogen atoms of two en ligands (N7, N8, N9) and a cyano nitrogen atom (N1), whereas the nitrogen atom of one en ligand (N10) and a cyano nitrogen atom (N2ⁱ; (i) = -x, y-1/2, z-1/2) occupy the apical sites. The average Ni-N_{en} bond length is 2.113 Å, which agrees with those observed in the *bis*-{Ni^{II}(en)} complex such as [Ni(en)₂(py)₂](NO₃)₂ (Baldwin *et al.*, 1999). The average Ni-N_{CN} bond is 2.075 Å, which is slightly shorter than those of the Ni-N_{en} lengths. However, similar lengthening of the Ni-N_{en} bonds versus the Ni-N_{CN} bonds was observed in [$\{M^{III}(CN)_6\}_2\{Ni^{II}(en)_2\}_3$] $\cdot 2H_2O$, where M^{III} = Mn, Fe, Co, and Cr (Ohba *et al.*, 1997). The maximum deviation from the ideal octahedral geometry of the nickel centre is manifested in the angle variation from 90° to 84.8(2) and 95.2(2)° of the N1-Ni-N10 and N1-Ni-N2 angles, respectively, and the reduction from 180° for N1-Ni-N8 to 170.6(2)°.

The structure of **3e** consists of infinite 1-D zigzag bimetallic chains parallel to the *b* axis as shown in Figure 3.15. Within the chain, each [Fe^{II}(2,2'-bipy)(CN)₄]²⁻ unit connects to two *cis*-[Ni^{II}(en)₂]²⁺ moieties through two cyanide ions (C1N1 and C2N2) in the *cis* position, whereas the other two cyano groups (C3N3 and C4N4) remain terminal. The adjacent Fe \cdots Ni separations across the cyanide groups are 4.814(1) and 4.959(1) Å for Fe1 \cdots Ni1 and Fe1 \cdots Ni1ⁱ (symmetry code: i = -x, y+1/2, -z+1/2), respectively. The nearest interchain metal \cdots metal distances are 8.494(1) and 6.064(1) Å for the Fe1 \cdots Fe1ⁱ (symmetry code: i = -x, y-1/2, -z+1/2) and the Ni1 \cdots Ni1ⁱⁱ (symmetry code: ii = -x, y+1/2, -z+1/2), respectively. The linkage of cyanide-bridges in the *cis* position in a complex cation into zigzag chain as in **3e** was also observed in the structure of [$\{Fe^{III}(CN)_6\}_2\{Ni^{II}(en)_2\}_3$] $\cdot 2H_2O$ (Ohba *et al.*, 1994).

Intermolecular $\pi\cdots\pi$ interactions are a feature commonly observed in many compounds containing chelating aromatic planar molecules (Janiak, 2000). For **3e**, the shortest interplanar 2,2'-bipy \cdots 2,2'-bipy separation is 3.553(7) Å ($C_g(H)\cdots C_g(I)$ distances at 4.156 Å) with the dihedral angle between the planes being 0.0(2), indicating the existence of $\pi\cdots\pi$ interactions. N–H $\cdots\pi$ (ring *I*) interactions involving the *bis*-chelating en ligands and 2,2'-bipy moieties are also observed. The values of the H $\cdots\pi$ distances and N–H $\cdots\pi$ angles are 2.835(6) and 2.918(7) Å, and 111.3 and 113.8°, respectively. Relatively weak intermolecular C–H $\cdots\pi$ (C \equiv N) hydrogen bonding occurs between amine protons and π -acceptor sites on adjacent cyanide groups.

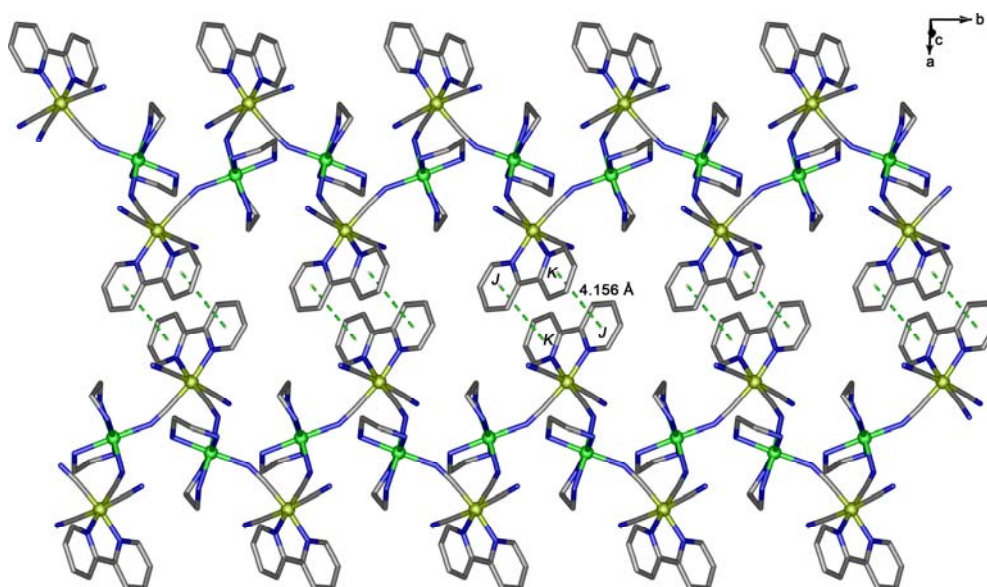


Figure 3.15 View of the 1-D zigzag chains in **3e** running parallel to the *b* axis.

Intermolecular π - π contacts represented by dotted green lines are observed between the 2,2'-bipy ligands of adjacent chains.

Furthermore, there is also extensive hydrogen bonds between the 1-D polymeric zigzag chains involving the clathrated solvent molecules and the terminal cyanide group of the $[\text{Fe}^{\text{II}}(2,2'\text{-bipy})(\text{CN})_4]^{2-}$ unit. Unfortunately, due to the high disorder in the intercalated solvent molecules, the positions of the atoms are very difficult to model. Therefore, the interactions are not discussed in detail. However, these interactions likely exist between the chains thus linking them into a novel 3-D supramolecular architecture as shown in Figure 3.16.

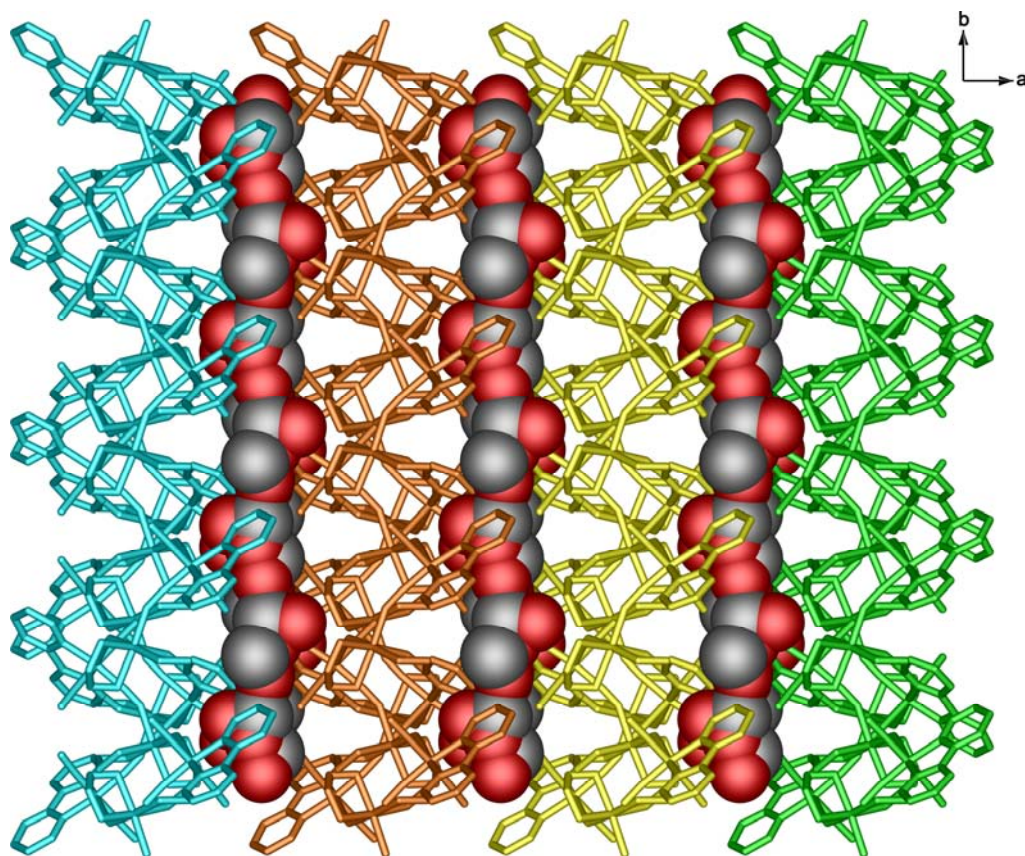


Figure 3.16 Stacking of four consecutive $\text{Fe}^{\text{II}}\text{-Ni}^{\text{II}}$ bimetallic chains of **3e** along the c axis. Included solvent is represented by the space filling models.

Magnetic measurements were made with the sample dispersed in Vaseline to eliminate field induced torquing of the crystallites (Kennedy and Murray, 1985). Typically, samples were ground with Vaseline, and a uniform mull was prepared. Measurements were made with both increasing and decreasing magnetic fields. The mass of the sample contained within the Vaseline mulls was determined by comparing the gram susceptibility of the neat crystalline with that of the mull, once corrections for the diamagnetic sample holder and Vaseline had been made, over a temperature range of not less than 30 K.

3.3.7 Magnetic Properties of $[\text{Fe}^{\text{II}}(2,2'\text{-bipy})(\text{CN})_4\text{Mn}^{\text{II}}]\cdot\text{MeOH}$ (**3a**)

The variable temperature magnetic susceptibility data of polycrystalline **3a** was measured in the 2–300 K temperature range under an applied field of 1 T. Plots of magnetic behaviours in **3a** are shown in Figure 3.17, in the form of effective magnetic moment (μ_{eff}) per 2Mn^{II} and 2Fe^{II} , versus the temperature. In accordance with the $1/\chi_{\text{M}}$ vs T plot, in the range 2–300 K, **3a** obey a Curie–Weiss $S = 5/2$ susceptibility behaviour with a positive Weiss constant of $\theta = 0.72$ K, indicating the presence of a ferromagnetic interaction, and $C = 7.93$ $\text{cm}^3 \text{mol}^{-1} \text{K}$. The room temperature μ_{eff} value of $8.01 \mu_{\text{B}}$ ($\chi_{\text{M}}T = 8.02$ $\text{cm}^3 \text{mol}^{-1} \text{K}$) for **3a** is slightly lower than the spin-only value of $8.37 \mu_{\text{B}}$ expected for a magnetically dilute spin system with two Fe^{II} ($S = 0$) and two Mn^{II} ions ($S = 5/2$), calculated for $g = 2.00$. As the temperature is decreased from 300 to *ca.* 50 K, the μ_{eff} values remain virtually constant then gradually increase, then abruptly to reach a maximum value of $9.53 \mu_{\text{B}}$ ($\chi_{\text{M}}T = 11.35$ $\text{cm}^3 \text{mol}^{-1} \text{K}$) at *ca.* 4 K, and finally decreases sharply to $8.47 \mu_{\text{B}}$ ($\chi_{\text{M}}T = 8.97$ $\text{cm}^3 \text{mol}^{-1} \text{K}$) at 2 K. This behavior is suggestive of either ferromagnetic coupling between the nearest neighbor high-spin Mn^{II} ($t_{2g}^3 e_g^2$) ions separated by *ca.* 6.5 Å

through the NC–Fe^{II}–CN pathways containing diamagnetic Fe^{II} ($t_{2g}^6 e_g^0$) centres, or *via* the non-covalent interactions (*i.e.* hydrogen bonding and π – π interactions), which is somewhat similar to that observed in the haptanuclear [$\{Mn^{II}(dmptacn)CN\}_6 Fe^{II}\}(ClO_4)_8 \cdot 5H_2O$, where $dmptacn = 1,4$ -bis(2-pyridylmethyl)-1,4,7-triazacyclononane (Parker *et al.*, 2002). There are no such weak interactions connecting the Mn(II) centres directly, so the bridging *via* $\{Fe^{II}(CN)_2\}$ is more likely.

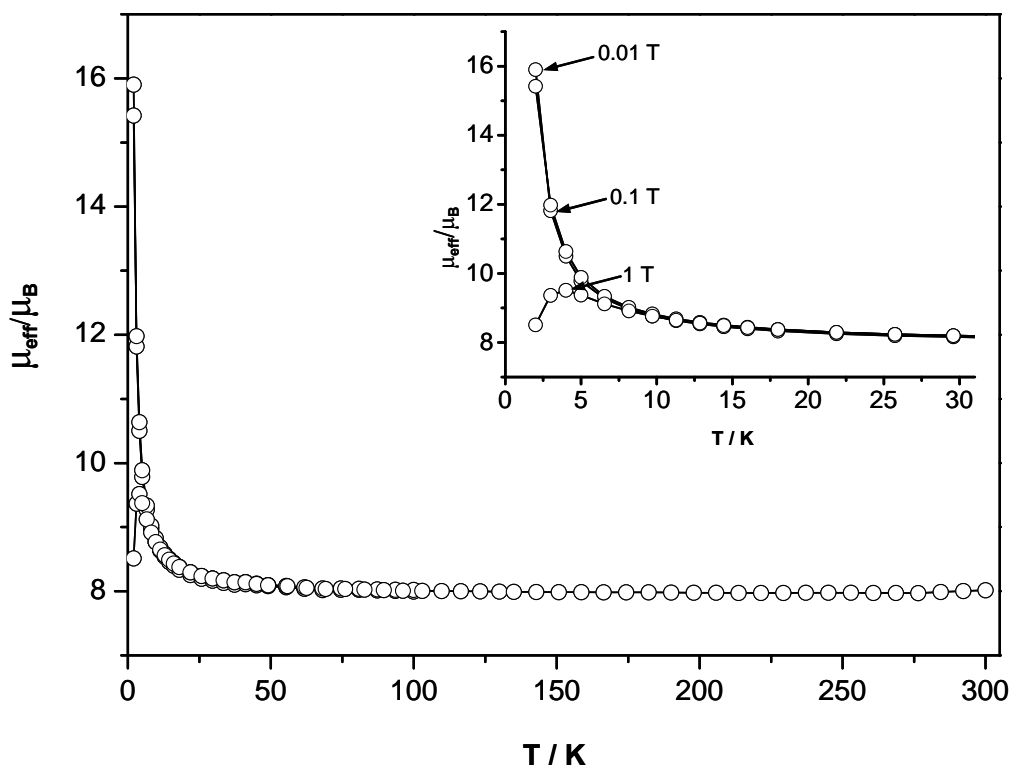


Figure 3.17 Plot of magnetic moment, per $2[Mn^{II}Fe^{II}]$, in fields of 0.01, 0.1 and 1 T for **3a**. The 2–30 K region is expanded in the insert. The solid lines are not calculated plots.

When small fields of 0.01 and 0.1 T are applied (insert of Figure), there is a rapid increase in the magnetic moment below 10 K, reaching a higher value at 2 K of

ca. $15.95 \mu_B$ ($\chi_M T = 31.80 \text{ cm}^3 \text{ mol}^{-1} \text{ K}$) and $15.58 \mu_B$ ($\chi_M T = 30.30 \text{ cm}^3 \text{ mol}^{-1} \text{ K}$) for 0.01 and 0.1 T fields, respectively. This field dependent behavior is suggesting of low lying Zeeman levels showing different thermal population as temperature varies, perhaps with saturation at higher field.

To further explore the origin of the ferromagnetic nature of the $\text{Mn}^{\text{II}} \cdots \text{Mn}^{\text{II}}$ interaction, and identify the coupled ground state, the magnetic field, H , dependence of DC magnetization (M) was investigated at various temperatures of 2, 3, 4, 5.5, 10 and 20 K, with magnetic fields up to 50000 Oe (0–5 T) using a SQUID magnetometer. The resulting magnetization isotherms for **3a** are shown in Figure 3.18, where the molar magnetization M is expressed in μ_B ($N\beta$) units, and M is expected to have the saturation value M_s , when H/kT becomes very large, according to the equation of $M_s = Ng\mu_B S$. In such a case the Mn^{II} single ion ground state is $S = 5/2$ and the magnetization (per 2Mn^{II} unit) should saturate to the value of $M = 10 \mu_B$ for two ferromagnetically coupled Mn^{II} ions, $S_{\text{TOTAL}} = 10/2$. Experimental data have shown that with the temperature at $T = 2.0 \text{ K}$, the magnetization adopts a value of $M = 10.0 N\mu_B$, which is very close to the theoretical value, and appears to be approaching saturation at the magnetic field $H = 50000 \text{ Oe}$. No long-range ordering or slow relaxation of the magnetization in **3a** was observed above 2 K evidenced by measurement of M in zero field (ZFCM) or in very small ($\sim 10 \text{ Oe}$) field cooling (FCM); the plots were identical (similar to Figure 3.21). Thus the repeat units Fe_2Mn_2 in Figure 3.1 show ferromagnetic coupling between Mn^{II} ions. The calculated magnetic moment value for a $S = 10/2$ level is $10.95 \mu_B$, this correspond to *ca.* $15.70 \mu_B$ observed in 0.01 and 0.1 T fields (Figure 3.17).

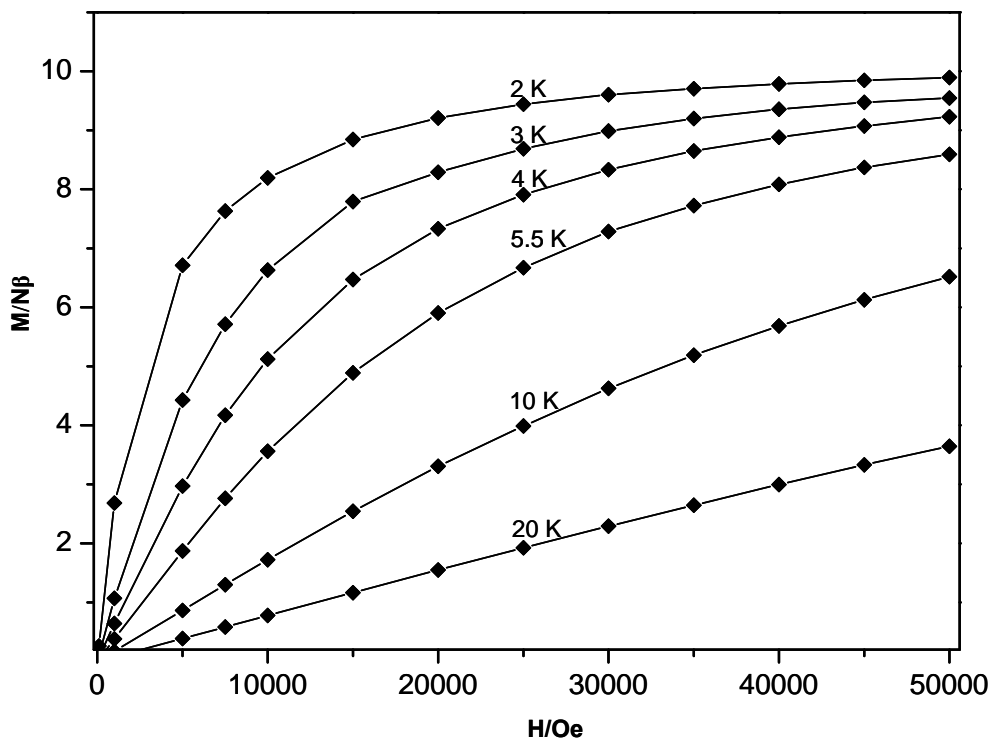


Figure 3.18 The DC magnetization isotherms (0–5 T) for **3a**, per $\text{Fe}^{\text{II}}\text{Mn}^{\text{II}}$.

3.3.8 Magnetic Properties of $[\text{Fe}^{\text{II}}(2,2'\text{-bipy})(\text{CN})_4\text{Mn}^{\text{II}}(\text{H}_2\text{O})_2]$ (**3b**)

The magnetic moments for **3b** were measured in the 2–300 K temperature range under an applied field of 1 T, and the plots of μ_{eff} vs T , per $\text{Fe}^{\text{II}}\text{Mn}^{\text{II}}$, are given in Figure 3.19. In accordance with ferromagnetism, the $1/\chi_{\text{M}}$ vs T plot, in the range 2–300 K, obeys the Curie-Weiss law with a positive Weiss constant of $\theta = 1.38$ K, and $C = 4.36 \text{ cm}^3 \text{ mol}^{-1} \text{ K}$. The μ_{eff} at room temperature, $5.93 \mu_{\text{B}}$ ($\chi_{\text{M}}T = 4.39 \text{ cm}^3 \text{ mol}^{-1} \text{ K}$), agrees with the spin-only value of $5.92 \mu_{\text{B}}$ expected for the magnetically dilute spin system with low-spin Fe^{II} ($S = 0$) and high-spin Mn^{II} ions ($S = 5/2$), assuming $g = 2.00$. Similar to the magnetic behavior observed in **3a**, on lowering the temperature, the μ_{eff} values remain constant between 300–50 K and gradually increase, then abruptly to reach a maximum value of $6.70 \mu_{\text{B}}$ ($\chi_{\text{M}}T = 5.61 \text{ cm}^3 \text{ mol}^{-1}$

K) at *ca.* 4 K, and finally decreases sharply to $6.00 \mu_B$ ($\chi_M T = 4.50 \text{ cm}^3 \text{ mol}^{-1} \text{ K}$) at 2 K. This behavior is similar to that observed in **3a**, suggesting a ferromagnetic coupling interaction between the nearest high-spin Mn^{II} ions through the low-spin Fe^{II} ions *via* bridging CN groups of the 1-D tube structure. This is more likely than *via* the non-covalent interactions (*i.e.* hydrogen bonding and π - π interactions) between the 1-D tubes.

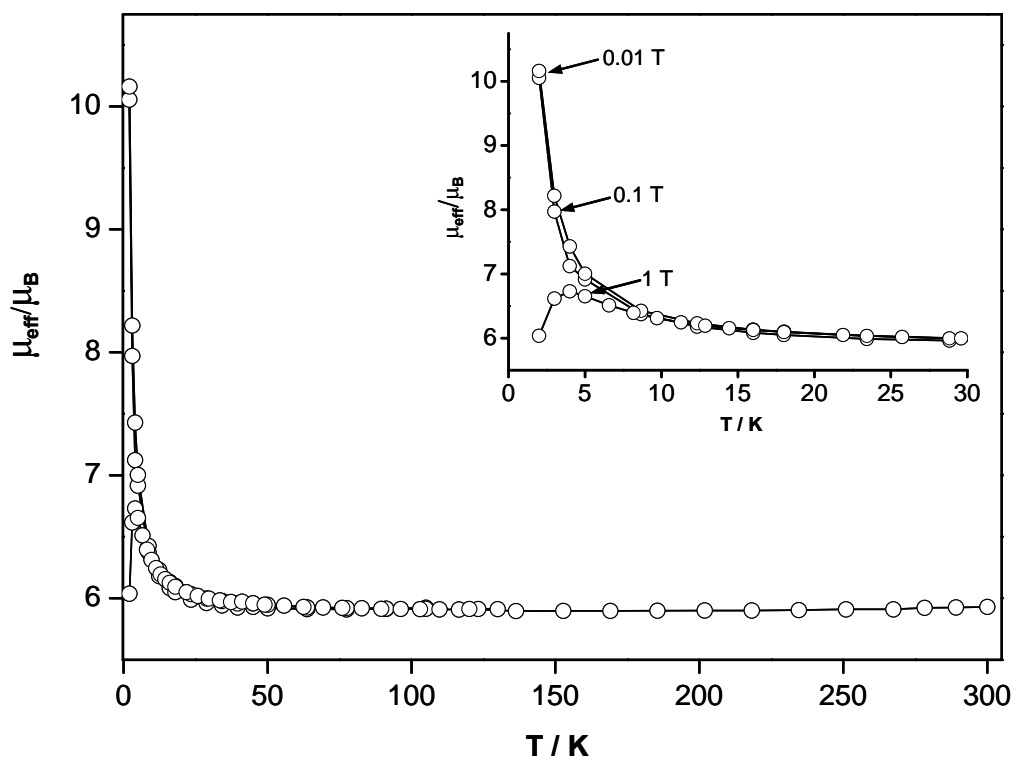


Figure 3.19 Plot of magnetic moment, per $[\text{Mn}^{\text{II}}\text{Fe}^{\text{II}}]$, in fields of 0.01, 0.1 and 1 T for **3b**. The 2–30 K region is expanded in the insert. The solid lines are not calculated plots.

As the applied field was decreased to values of 0.1 and 0.01 T, the μ_{eff} values increased rapidly below 10 K reaching a larger value of *ca.* $10.10 \mu_B$ ($\chi_M T = 12.75$

$\text{cm}^3 \text{mol}^{-1} \text{K}$) for both the 0.01 and 0.1 T fields at 2 K (insert of figure). For two ferromagnetically coupled $S = 5/2$ (Mn^{II}) ions, the $S = 10/2$ state should yield $\mu_{\text{eff}} \approx 10.90 \mu_{\text{B}}$ per $2\{\text{Fe}^{\text{II}}\text{Mn}^{\text{II}}\}$, *i.e.* $7.5 \mu_{\text{B}}$ per $\{\text{Fe}^{\text{II}}\text{Mn}^{\text{II}}\}$ lower than observed at the maximum for 1T and lower than the 2 K values in the smaller fields.

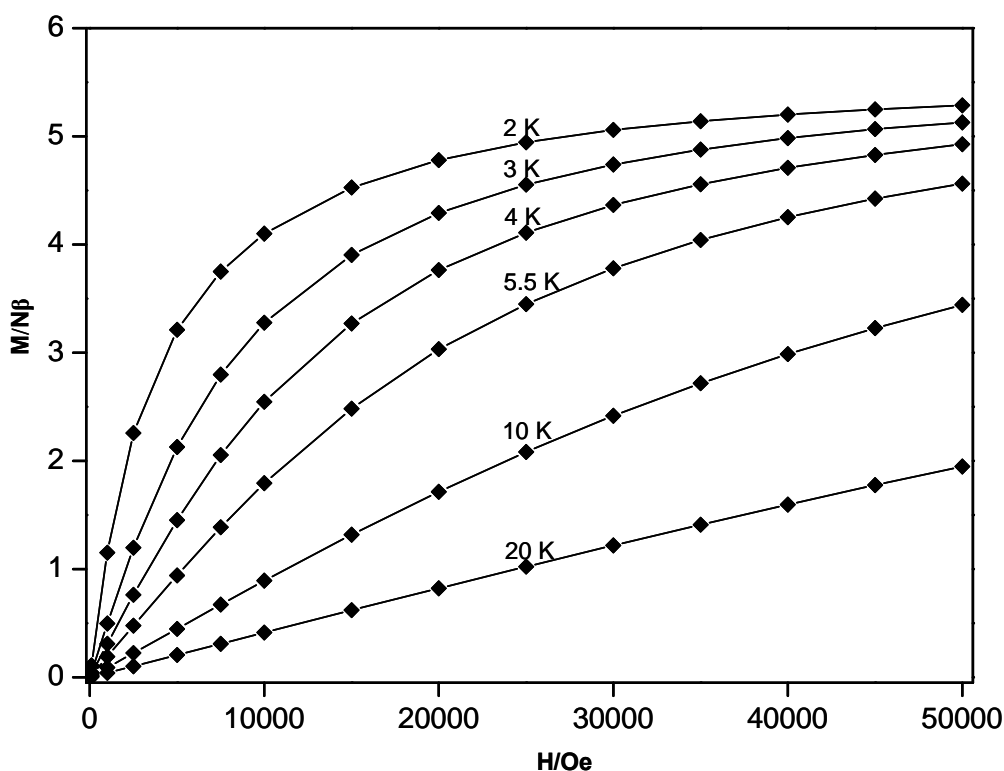


Figure 3.20 The DC magnetization isotherms (0–5 T) for **3b**, per $[\text{Mn}^{\text{II}}\text{Fe}^{\text{II}}]$.

Further, probing of the the low temperature region by measurements of magnetisation (M) isotherms (2–20 K) of **3b** yielded the plots shown in Figure 3.20. At 50000 Oe and 2 K, the magnetization, per $[\text{Mn}^{\text{II}}\text{Fe}^{\text{II}}]$, is nearly saturated with a value of $5.30 \mu_{\text{B}}$. The calculated saturation magnetization (M_s) for a spin-only system consisting of ferromagnetically coupled high-spin Mn^{II} ions ($S = 5/2$), assuming $g = 2.00$, is $10.0 \mu_{\text{B}}$ per Mn_2 , *i.e.* $5.0 \mu_{\text{B}}$ per Mn. Measurement of FCM and ZFCM show identical behaviour at temperatures 4–35 K as shown in Figure 3.21, indicating no

magnetic ordering occurs in the crystalline sample of **3b**. If ordering occurred the two curves would diverge at the T_C temperature. Thus, as in **3a**, ferromagnetic coupling occurs in **3b** between nearest Mn^{II} centers. There might be very weak tube–tube interactions.

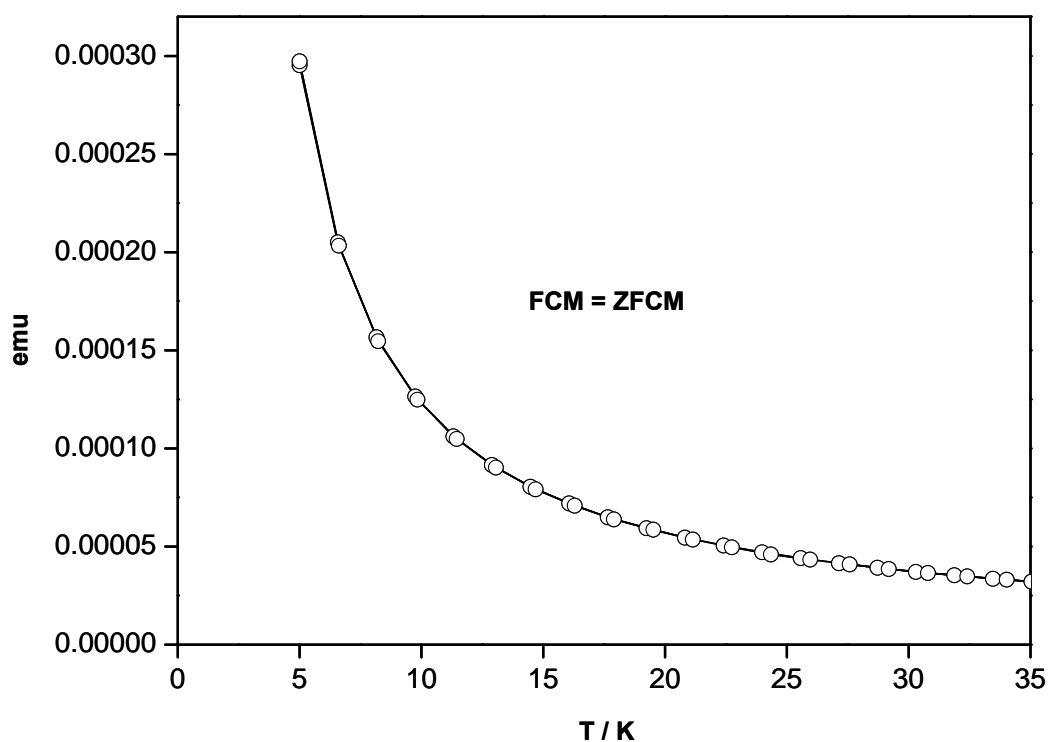


Figure 3.21 Temperature dependence (4–35 K) of FCM and ZFCM for **3b**, in emu units from the SQUID instrument.

3.3.9 Magnetic Properties of the Molecular Squares $[\text{Fe}^{\text{II}}(1,10\text{-phen})(\text{CN})_4$

$\text{Cu}^{\text{II}}(\text{tn})(\text{H}_2\text{O})_2 \cdot 5\text{H}_2\text{O}$ (**3c**) and $[\text{Fe}^{\text{II}}(2,2'\text{-bipy})(\text{CN})_4\text{Cu}^{\text{II}}(\text{tn})] \cdot \text{H}_2\text{O}$ (**3d**)

The magnetic susceptibilities of polycrystalline samples of **3c** and **3d** were measured as a function of temperature in the range of 2–300 K under an applied field of 1 T. The plots of the form of the effective magnetic moment (μ_{eff}) per $[\text{Cu}^{\text{II}}\text{Fe}^{\text{II}}]$

unit, versus the temperature for **3c** and **3d** are given in Figure 3.22. The magnetic properties of **3c** and **3d** are generally similar and behave essentially as two isolated paramagnetic Cu(II) centres with perhaps very weak antiferromagnetic coupling occurring between the d^9 Cu^{II} ($S = 1/2$) centers through the diamagnetic [Fe^{II}(2,2'-bipy)(CN)₄]²⁻, d^6 Fe^{II} ($S = 0$) centers. The values of μ_{eff} at 300 K are $2.02 \mu_{\text{B}}$ ($\chi_{\text{M}}T = 0.51 \text{ cm}^3 \text{ mol}^{-1} \text{ K}$) for **3c** and $1.78 \mu_{\text{B}}$ ($\chi_{\text{M}}T = 0.40 \text{ cm}^3 \text{ mol}^{-1} \text{ K}$) for **3d**. As the temperature decreases, the μ_{eff} values for the compounds remain almost constant until *ca.* 40 K, then decreases gradually in the 40–15 K range, and finally decreases sharply to reach *ca.* $1.05 \mu_{\text{B}}$ ($\chi_{\text{M}}T = 0.10 \text{ cm}^3 \text{ mol}^{-1} \text{ K}$) for **3c**, and $1.05 \mu_{\text{B}}$ ($\chi_{\text{M}}T = 0.14 \text{ cm}^3 \text{ mol}^{-1} \text{ K}$) for **3d** at 2 K. The $1/\chi_{\text{M}}$ versus T plots obey the Curie–Weiss law, $\chi_{\text{M}} = C/(T-\Theta)$, $C = 0.52$ and $0.35 \text{ cm}^3 \text{ mol}^{-1} \text{ K}$, with a negative Weiss constant (Θ) = -2.25 and -4.27 K for **3c** and **3d**, respectively. No differences between the magnetization (M) in zero-field cooling (ZFCM) and in field-cooling (FCM) samples are observed down to 2 K for both compounds, which indicates that no long-range magnetic ordering occurs, at least above 2 K.

The weak intra-square antiferromagnetic coupling is not surprising since the long Cu^{II}($S = 1/2$)–NC–Fe^{II}($S = 0$)–CN–Cu^{II}($S = 1/2$) pathway will lead to very weak coupling. The Cu^{II}($S = 1/2$)...Cu^{II}($S = 1/2$) distances, through the long diamagnetic NC–Fe^{II}–CN bridge (the empty d_{σ} orbital of the Fe^{II} ion), in both compounds are *ca.* 10 Å. The magnetic behaviour of **3c** and **3d** are also similar to those observed in the compounds $[\{\text{Cu}^{\text{II}}(\text{tn})\}_2\text{Fe}^{\text{II}}(\text{CN})_6] \cdot 4\text{H}_2\text{O}$ and $[\text{Cu}^{\text{II}}(\text{tnH})_2(\text{H}_2\text{O})_2\text{Fe}^{\text{II}}(\text{CN})_6] \cdot 2\text{H}_2\text{O}$ (Triki *et al.*, 2006).

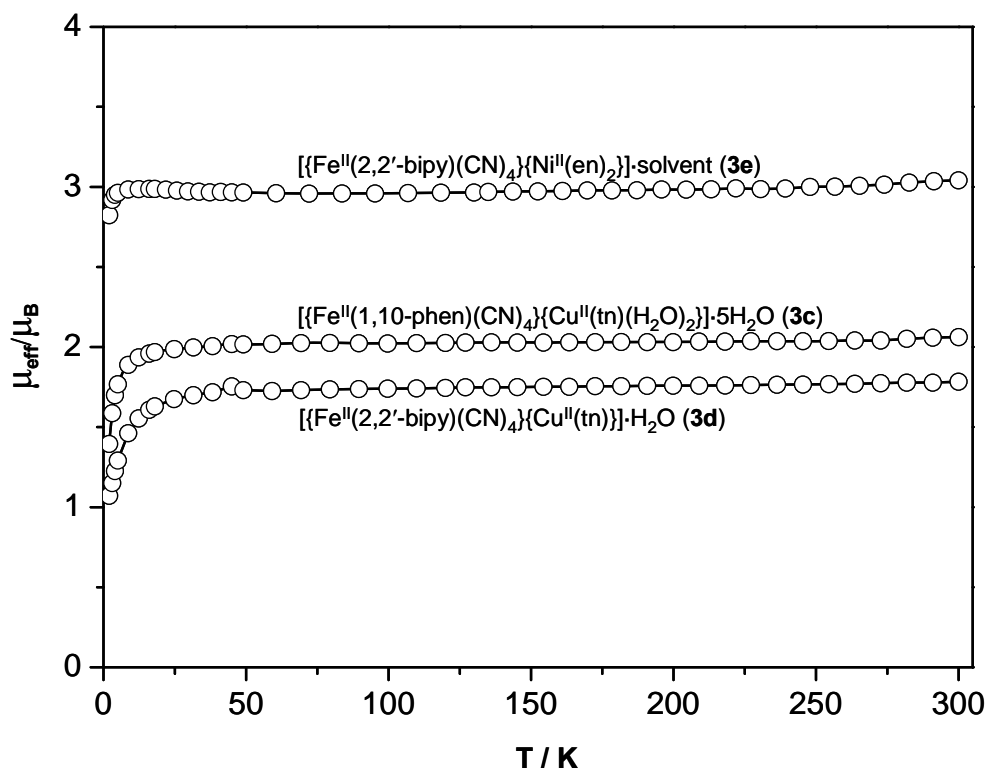


Figure 3.22 Plot of magnetic moment, per $[\text{Cu}^{\text{II}}\text{Fe}^{\text{II}}]$ for **3c-3d**, and per $[\text{Ni}^{\text{II}}\text{Fe}^{\text{II}}]$ for **3e**. The solid lines are not calculated plots.

3.3.10 Magnetic Properties of $[\text{Fe}^{\text{II}}(2,2'\text{-bipy})(\text{CN})_4\text{Ni}^{\text{II}}(\text{en})_2]\cdot\text{Solvent}$ (**3e**)

Variable temperature magnetic susceptibility data for a polycrystalline sample of **3e** were collected in the temperature range 2–300 K, in the form of μ_{eff} vs T , per $[\text{Fe}^{\text{II}}\text{Ni}^{\text{II}}]$ unit, (Figure 3.22). Again, due to the diamagnetic nature of the d^6 Fe^{II} ($S = 0$) centres, while Ni^{II} has a d^8 configuration ($S = 1$), the magnetic data in **3e** is therefore caused by the Ni^{II} ions. The μ_{eff} at room temperature of **3e** is $3.08 \mu_{\text{B}}$ ($\chi_{\text{M}}T = 1.10 \text{ cm}^3 \text{ mol}^{-1} \text{ K}$), which is typical of Ni^{II} ions. The μ_{eff} values for **3e** are practically independent of temperature in the range 300–50 K, then decreases gradually, and finally decreased sharply to reach $2.76 \mu_{\text{B}}$ ($\chi_{\text{M}}T = 0.95 \text{ cm}^3 \text{ mol}^{-1} \text{ K}$) for **3c** at 2 K. The $1/\chi_{\text{M}}$ versus T plots obeys the Curie–Weiss law, $\chi_{\text{M}} = C/(T-\Theta)$, $C = 1.13 \text{ cm}^3 \text{ mol}^{-1} \text{ K}$, with a negative Weiss constant (Θ) = -1.74 , respectively. The successive decrease of

χ_M and the negative Θ value suggest the operation of weak antiferromagnetic interaction between Ni^{II} ions through the diamagnetic $-\text{NC}-\text{Fe}^{\text{II}}-\text{CN}-$ bridges ($\text{Ni}^{\text{II}}\cdots\text{Ni}^{\text{II}} = ca. 10 \text{ \AA}$). In addition, the magnetic behaviour of **3e** is quite different behaviour to that found in $[\text{Fe}^{\text{II}}(\text{CN})_6\{\text{Ni}^{\text{II}}(\text{L})_2\}_3]\text{X}_2$, where L = 1,2-ethylenediamine, trimethylenediamine, X = PF_6^- , ClO_4^- (Fukita *et al.*, 1998) and $[\text{Ni}^{\text{II}}(\text{dmptacn})(\text{CN})_6\text{Fe}^{\text{II}}](\text{ClO}_4)_8 \cdot 7\text{H}_2\text{O}$, where dmptacn = 1,4-bis(2-pyridylmethyl)-1,4,7-triazacyclononane (Parker *et al.*, 2002), which all display weak ferromagnetic coupling *via* $\text{Ni}^{\text{II}}-\text{NC}-\text{Fe}^{\text{II}}-\text{CN}-\text{Ni}^{\text{II}}$ pathways.

3.4 Conclusions and Future Prospects

This study began with the rational design of making some new cyanide-bridged bimetallic materials having 1-D square tube motifs using a tetracyanoferrate of the formula $[\text{Fe}(\text{L})(\text{CN})_4]^{x-}$, where L = 1,10-phen, 2,2'-bipy, en, tn; $x = 1$ or 2, as building blocks. These ionic species were reacted with $[\text{M}(\text{L}')(\text{H}_2\text{O})_4]^{2+}$ where L' = en, tn, and while the desired square-tubes of the stoichiometry $[\text{Fe}(\text{L})(\text{CN})_4\text{M}(\text{L}')]$ have not been isolated, five new cyanide-bridged bimetallic compounds have been synthesized and characterized. Two of these are coordination polymers, one with a 2-D corrugated (4,4) sheets structure, of formula $[\text{Fe}^{\text{II}}(2,2'\text{-bipy})(\text{CN})_4\text{Mn}^{\text{II}}] \cdot \text{MeOH}$ (**3a**), the other with a 1-D hexagonal tube-like structure, of formula $[\text{Fe}^{\text{II}}(2,2'\text{-bipy})(\text{CN})_4\text{Mn}^{\text{II}}(\text{H}_2\text{O})_2]$ (**3b**). These materials were reproducibly synthesized *via* the self-assembly reactions of the $[\text{Fe}^{\text{II}}(2,2'\text{-bipy})(\text{CN})_4]^{2-}$ and $[\text{Fe}^{\text{III}}(2,2'\text{-bipy})(\text{CN})_4]^-$ building blocks respectively with $[\text{Mn}(\text{H}_2\text{O})_2]^{2+}$ in aqueous methanolic solution, respectively. Surprisingly, the synthetic process for **3b** involves the spontaneous reduction of the paramagnetic $[\text{Fe}^{\text{III}}(2,2'\text{-bipy})(\text{CN})_4]^-$ ion into the diamagnetic

$[\text{Fe}^{\text{II}}(2,2'\text{-bipy})(\text{CN})_4]^{2-}$ ion. Both compounds display similar ferromagnetic coupling between Mn^{II} ions. The ferromagnetic coupling probably arises because of the *ca.* 90° angle across the $\text{Mn}^{\text{II}}\text{-NC-Fe}^{\text{II}}\text{-CN-Mn}^{\text{II}}$ bridge at the corners of the squares. No long-range magnetic ordering occurs over the lattice down to 2 K owing to the diamagnetic nature of the $[\text{Fe}^{\text{II}}(2,2'\text{-bipy})(\text{CN})_4]^{2-}$ bridges combined with the weak intra-tube and tube-tube interactions in the case of **3b**.

Reactions of the $[\text{Fe}^{\text{II}}(1,10\text{-phen})(\text{CN})_4]^{2-}$ and $[\text{Fe}^{\text{II}}(2,2'\text{-bipy})(\text{CN})_4]^{2-}$ building blocks with the $[\text{Cu}^{\text{II}}(\text{tn})(\text{H}_2\text{O})_n]^{2+}$ cation in water reproducibly afforded single crystals of new examples of cyanide-bridged $\text{Fe}_2^{\text{II}}\text{-Cu}_2^{\text{II}}$ molecular squares, of formulae $[\text{Fe}^{\text{II}}(\text{CN})_4\text{Cu}^{\text{II}}(\text{tn})(\text{H}_2\text{O})_2]\cdot 5\text{H}_2\text{O}$ (**3c**) and $[\text{Fe}^{\text{II}}(\text{CN})_4\text{Cu}^{\text{II}}(\text{tn})]\cdot \text{H}_2\text{O}$ (**3d**). Even though each has the correct square geometry to form a square tube, they do not. An interesting structure of **3c** is that each square core is propagated by supramolecular $\text{O-H}\cdots\text{O}$ hydrogen bonds feature, into 1-D tube-like structure along the crystallographic *c* axis. Magnetic studies for **3c** and **3d** reveal a very weak antiferromagnetic exchange interaction (close to paramagnetism) between nearest Cu^{II} ions through the diamagnetic cyano- Fe^{II} ion, and again, no magnetic ordering occurs over the lattice down to 2 K.

In the last compound of formula $[\text{Fe}^{\text{II}}(2,2'\text{-bipy})(\text{CN})_4\text{Ni}^{\text{II}}(\text{en})_2]\cdot \text{solvent}$ (**3e**) was obtained from the slow diffusion reaction of $[\text{Fe}^{\text{II}}(2,2'\text{-bipy})(\text{CN})_4]^{2-}$ with $[\text{Ni}^{\text{II}}(\text{en})(\text{H}_2\text{O})_4]^{2+}$ in aqueous methanolic solution. The $[\text{Ni}^{\text{II}}(\text{en})(\text{H}_2\text{O})_4]^{2+}$ had rearranged to the $[\text{Ni}^{\text{II}}(\text{en})_2(\text{H}_2\text{O})_2]^{2+}$ form. **3e** shows a structure involving 1-D zigzag bimetallic chains that run parallel to the crystallographic *b* axis. This compound exhibits a weak antiferromagnetic intrachain interaction between the paramagnetic Ni(II) centers with no long-range magnetic ordering occurring. Thus, while the

desired square tubes have not been achieved, some beautiful CN-bridged bimetallic have been isolated, some with other tube motifs.

In future work, from the topological point of view, the Mn^{II} ions of the 1-D tube-like structure of $[\text{Fe}^{\text{II}}(2,2'\text{-bipy})(\text{CN})_4\text{Mn}^{\text{II}}(\text{H}_2\text{O})_2]$ (**3b**), could possibly be replaced by the other octahedral transition metal centres. In particular, the replacement of Mn^{II} by Fe^{II} ion, would offer an opportunity to achieve multifunctional materials involving spin-crossover (at the $\{\text{Fe}^{\text{II}}(\text{N})_4(\text{H}_2\text{O})_2\}$ centres) perhaps with porosity. To obtain the original target compounds $[\text{Fe}(\text{L})(\text{CN})_4\text{M}(\text{L}')]]$, the bonding of H_2O at $\text{M} = \text{Cu}^{\text{II}}$ (in **3c**) mean that dry solvent condition, and anhydrous precursor materials will need to be used. The projection of the tn ligand above the $\{\text{Cu}_2\text{Fe}_2\}$ square plane in **3d** mean that en ligand should be tried.

Due to the diamagnetic nature of the $[\text{Fe}^{\text{II}}(\text{bidentate})(\text{CN})_4]^{2-}$ building block, the substitution of the diamagnetic Fe^{II} ion ($S = 0$) for a paramagnetic M^{III} ion, such as Fe^{III} ($S = 1/2$), Cr^{III} ($S = 3/2$) or Ru^{III} ($S = 1/2$), is of great interest in achieving stronger exchange coupling and long-range magnetic ordering over the 3-D lattice. The $[\text{M}(\text{bidentate})(\text{CN})_4]$ building blocks have important implications also in developing future designs of novel cyanide-bridged supramolecular coordination compounds of the single-molecule magnet, SMMs (George *et al.*, 2000; Gatteschi and Sessoli, 2003; Beltran, and Long, 2005) or single-chain magnet, SCM (Lescouëzec *et al.*, 2005).

3.5 References

- Allen, F. H., Davies, J. E., Galloy, J. J., Johnson, O., Kennard, O., Macrae, C. F., Mitchell, E. M., Mitchell, G. F., Smith, J. M., and Watson, D. G. (1991). **J. Chem. Inf. Comput. Sci.** 31: 187-204.
- Ammala, P., Cashion, J. D., Kepert, C. M., Moubaraki, B., Murray, K. S., Spiccia, L., and West, B. O. (2000). **Angew. Chem., Int. Ed.** 112(9): 1754-1756.
- Ascenzi, P., and Fasano, M. (2007). **IUBMB Life** 59(11): 700-708.
- Arrio, M.-A., Sainctavit, Ph., Cartier dit Moulin, Ch., Brouder, Ch., de Groot, F. M. F., Mallah, T., and Verdaguer, M. (1996). **J. Phys. Chem.** 100(11): 4679-4684.
- Baldwin M. J., and Krause Bauerref, J. A. (1999). **Acta Crystallogr., Sect. C: Cryst. Struct. Commun.** 55: 1772-1773.
- Batten, S. R. (2001). **Curr. Opin. Solid State Mater. Sci.** 5(2-3): 107-114.
- Batten, S. R. (2004). **Encyclopedia of Supramolecular**; New York; Marcel Dekker, p. 1-13.
- Batten, S. R. (2005). **J. Solid State Chem.** 178(8): 2475-2479.
- Beltran, L. M. C., and Long, J. R. (2005). **Acc. Chem. Res.** 38(4): 325-334.
- Berlinguette, C. P., Vaughn, D., Cañada-Vilalta, C., Galán-Mascarós, J. R., and Dunbar, K. R. (2003). **Angew. Chem., Int. Ed.** 42(13): 1523-1526.
- Bernhardt, P. V., Bozoglian, F., Macpherson, B. P., and Martínez, M. (2005). **Coord. Chem. Rev.** 249(17-18): 1902-1916.
- Bradshaw, D., Claridge, J. B., Cussen, E. J., Prior, T. J., and Rosseinsky, M. J. (2005). **Acc. Chem. Res.** 38(4): 273-282.
- Buschmann, W. E., Paulson, S. C., Wynn, C. M., Girtu, M. A., Epstein, A. J., White,

- H. S., and Miller, J. S. (1998). **Chem. Mater.** 10(5): 1386-1395.
- Chapman, K. W., Chupas, P. J., and Kepert, C. J. (2005). **J. Am. Chem. Soc.** 127 (32): 11232-11233.
- Chapman, K. W., Southon, P. D., Weeks, C. L., and Kepert, C. J. (2005). **J. Chem. Soc., Chem. Commun.** (26): 3322-3324.
- Chen, H.-J., Zhang, L.-Z., Cai, Z.-G., Yang, G., and Chen, X.-M. (2000). **J. Chem. Soc., Dalton Trans.** (14): 2463-2466.
- Chippindale, A. M., Cheyne, S. M., and Hibble, S. J. (2005). **Angew. Chem., Int. Ed.** 44(48): 7942-7946.
- Chui, S. S.-Y., Lo, S. M.-F., Charmant, J. P. H., Orpen, A. G., and Williams, I. D. (1999). **Science** 283: 1148-1150.
- Crystal Maker. (2006). Crystal Maker Software, Yarnton, England.
- Culp, J. T., Park, J.-H., Frye, F., Huh, Y.-D., Meisel, M. W., and Talham, D. R. (2005). **Coord. Chem. Rev.** 249(23): 2642-2648.
- Desiraju, G. R., and Steiner, T. (1999). **The Weak Hydrogen Bond in Structural Chemistry and Biology.** Oxford University Press: Oxford.
- Dincá, M., Dailly, A., Liu, Y., Brown, C. M., Neumann, D. A., and Long, J. R. (2006). **J. Am. Chem. Soc.** 128(51): 16876-16883.
- Eddaoudi, M., Kim, J., Rosi, N., Vodak, D., Wachter, J., O'Keeffe, M., and Yaghi, O. M. (2002). **Science** 295(22): 469-472.
- Emsley, J., and Arif, M. (1988). **Inorg. Chim. Acta** 154(1): 17-20.
- Forster, P. M., and Cheetham, A. K. (2002). **Angew. Chem., Int. Ed.** 41(3): 457-459.
- Franz, P., Ambrus, P., Hauser, A., Chernyshov, D., Hostettler, M., Hauser, J., Keller, L., Krämer, K., Stoeckli-Evans, H., Pattison, P., Bürgi, H.-B., and Decurtins,

- S. (2004). **J. Am. Chem. Soc.** 126(50): 16472-16477.
- Fu, X.-C., Li, M.-T., and Wang, C.-G. (2005). **Acta Crystallogr. Sect. E: Struct. Rep. Online.** 61: m1221-m1222.
- Fukita, N., Ohba, M., Okawa, H., Matsuda, K., and Iwamura, H. (1998). **Inorg. Chem.** 37(5): 842-848.
- Gadet, V., Mallah, T., Castro, I., Verdaguer, M., and Veillet, P. (1992). **J. Am. Chem. Soc.** 114(23): 9213-9214.
- Gatteschi D., and Sessoli, R. (2003). **Angew. Chem., Int. Ed.** 42(3): 268-297.
- George, C., Dante, G., David, H. N., and Roberta, S. (2000). **MRS Bull.** 25(11): 66-71.
- Goto, M., Kogure, H. N., Ito, H., Tsubamoto, H., Nakabayashi, K., Kuroda, Y., and Sakai, T. (1986). **Inorg. Chem.** 25(10): 1684-1691.
- Guennic, L. B., Borshch, S., and Robert, V. (2007). **Inorg. Chem.** 46(26): 11106-11111.
- Henkel, G., and Krebs, B. (2004). **Chem. Rev.** 104(2): 801-824.
- Janiak, C. (2000). **J. Chem. Soc., Dalton Trans.** (21): 3885-3896.
- Janiak, C. (2003). **J. Chem. Soc., Dalton Trans.** (14): 2781-2804.
- Jensen, P., Batten, S. R., Fallon, G. D., Hockless, D. C. R., Moubaraki, B., Murray, K. S., and Robson, R. (1999). **J. Solid State Chem.** 145(2): 387-393.
- Kahn, O., and Martinez, C. J. (1998). **Science** 279: 44-48.
- Kennedy, B. J., and Murray, K. S. (1985). **Inorg. Chem.** 24(10): 1552-1557.
- Keper, C. J. (2006). **Chem. Commun.** (7): 695-700.
- Kitagawa, S., Kitaura, R., and Noro, S.-i. (2004). **Angew. Chem., Int. Ed.** 43(18): 2334-2375.

- Kesanli, B., Cui, Y., Smith, M. R., Bittner, E. W., Bockrath, B. C., and Lin, W. (2004). **Angew. Chem., Int. Ed.** 44(1): 72-75.
- Kaye, S. S., and Long, J. R. (2005). **J. Am. Chem. Soc.** 127(18): 6506-6507.
- Kaye, S. S., and Long, J. R. (2007). **Catal. Today** 120(3-4): 311-316.
- Kim, Y., Skelton, B. W., and White, A. H. (2003). **Acta Crystallogr., Sect. C: Cryst. Struct. Commun.** 59: m546-m548.
- Kosaka, W., Nomura, K., Hashimoto, K., and Ohkoshi, S.-I. (2005). **J. Am. Chem. Soc.** 127(24): 8590-8591.
- Leininger, S., Olenyuk, B., and Stang, P. J. (2000). **Chem. Rev.** 100(3): 853-908.
- Lescouëzec, R., Toma, L. M., Vaissermann, J., Verdaguer, M., Delgado, F. S., Ruiz-Pérez, C., Lloret, F., and Julve, M. (2005). **Coord. Chem. Rev.** 249(23): 2691-2729.
- Lescouëzec, R., Vaissermann, J., Ruiz-Pérez, C., Lloret, F., Carrasco, R., Julve, M., Verdaguer, M., Dromzee, Y., Gatteschi, D., and Wernsdorfer, W. (2003). **Angew. Chem., Int. Ed.** 42(13): 1483-1486.
- Maspoch, D., Ruiz-Molina, D., and Veciana, J. (2004). **J. Mater. Chem.** (18): 2713-2723.
- McDougall, G. J., and Hancock, R. D. (1980). **J. Chem. Soc., Dalton Trans.** (4): 654-658.
- Merritt, L. L., and Schroeder, E. (1956). **Acta Crystallogr., Sect. B: Struct. Sci.** 9: 801-804.
- Moliner, N., Muñoz, C., Létard, S., Solans, X., Menéndez, N., Goujon, A., Varret, F., and Real, J. A. (2000). **Inorg. Chem.** 39(23): 5390-5393.
- Moulton, B., and Zaworotko, M. J. (2002). **Curr. Opin. Solid State Mater. Sci.** 6:

117-123.

Munoz, M. C., Gaspar, A. B., Galet, A., and Real, J. A. (2007). **Inorg. Chem.** 46(20): 8182-8192.

Nakamoto, K. (1963). **Infrared Spectra of Inorganic and Coordination Compounds.** John Wiley & Sons, Inc., London.

Nihei, M., Ui, M., Yokota, M., Han, L., Maeda, A., Kishida, H., Okamoto, H., and Oshio, H. (2005). **Angew. Chem., Int. Ed.** 44(40): 6484-6487.

Niel, V., Martinez-Agudo, J. M., Muñoz, C., Gaspar, A. B., and Real, J. A. (2001). **Inorg. Chem.** 40(16): 3838-3839.

Nieuwenhuyzen, M., Bertram, B., Gallagher, J. F., and Vos, J. G. (1998). **Acta Crystallogr., Sect. C: Cryst. Struct. Commun.** 54: 603-606.

Ohba, M., Fukita, N., and Ōkawa, H. (1997). **J. Chem. Soc., Dalton Trans.** (10): 1733-1737.

Ohba, M., Maruono, N., Okawa, H., Enoki, T., and Latour, J. M. (1994). **J. Am. Chem. Soc.** 116(25): 11566-11567.

Ohba, M., and Ōkawa, H. (2000). **Coord. Chem. Rev.** 198(1): 313-328.

Ohkoshi, S., Ikeda, S., Hozumi, T., Kashiwagi, T., and Hashimoto, K. (2006). **J. Am. Chem. Soc.** 128(16): 5320-5321.

Oshio, H., Tamada, O., Onodera, H., Ito, T., Ikoma, T., and Tero-Kubota, S. (1999). **Inorg. Chem.** 38(25): 5686-5689.

Oshio, H., Yamamoto, M., and Ito, T. (2002). **Inorg. Chem.** 41(22): 5817-5820.

Parker, R. J., Spiccia, L., Moubaraki, B., Murray, K. S., Hockless, D. C. R., Rae, A. D., and Willis, A. C. (2002). **Inorg. Chem.** 41(9): 2489-2495.

Parker, R. J., Hockless, D. C. R., Moubaraki, B., Murray, K. S., and Spiccia, L.

- (1996). **Chem. Commun.** (24): 2789-2790.
- Robson, R., Abraham, B. F., Batten, S. R., Gable, R. W., Hoskins, B. F., and Liu, J. (1992). **In Supramolecular Architecture.** Bein, T., Ed.: American Chemical Society: Washington, DC: Chapter 19: pp 258-273.
- Salman, Z., Parolin, T. J., Chow, K. H., Keeler, T. A., Miller, R. I., Wang, D., Chakhalian, J., and MacFarlane, W. A. (2006). **Phys. Rev. B: Condens. Matter.** 374-375: 130-133.
- Sato, O. (2003). **Acc. Chem. Res.** 36(9): 692-700.
- Schilt, A. A. (1960). **J. Am. Chem. Soc.** 82(12): 3000-3005.
- Spiccia, L., Murray, K. S., and Young, J. F. (2004). **Inorg. Syn.** 34: 133-141.
- Szaciowski, K., Macyk, W., and Stochel, G. (2006). **J. Mater. Chem.** (47): 4603-4611.
- Tian, Y.-P., Duan, C.-Y., Xu, X.-X., and You, X.-Z. (1995). **Acta Crystallogr., Sect. C: Cryst. Struct. Commun.** 51: 2309-2312.
- Toma, L. M., Lescouëzec, R., Toma, L. D., Lloret, F., Julve, M., Vaissermann, J., and Andruh, M. (2002). **J. Chem. Soc., Dalton Trans.** (16): 3171-3176.
- Toma, L., Lescouëzec, R., Vaissermann, J., Herson, P., Marvaud, V., Lloret, F., and Julve, M. (2005). **New J. Chem.** 29(1): 210-219.
- Triki, S., Sala-Pala, J., Thétiot, F., Gómez-García, C. J., and Daran, J.-C. (2006). **Eur. J. Inorg. Chem.** 185-199.
- Wang, S., Zuo, J.-L., Zhou, H.-C., Choi, H. J., Ke, Y., Long, J. R., and You, X.-Z. (2006). **Angew. Chem., Int. Ed.** 43(44): 5940-5943.
- Ward, M. D. (2006). **Coord. Chem. Rev.** 250: 3128-3141.
- Verdaguer, M., Bleuzen, A., Marvaud, V., Vaissermann, J., Seuleiman, M., Desplanches,

- C., Sculler, A., Train, C., Garde, R., Gelly, G., Lomenech, C., Rosenman, I., Veillet, P., Cartier, C., Villain, F., and Verdaguer, M. (1999). **Coord. Chem. Rev.** 190-192: 1023-1047.
- Vahrenkamp, H., Gei, A., and Richardson, G. N. (1997). **J. Chem. Soc., Dalton Trans.** (20): 3643-3652.
- van Rij, C., and Britton, D. (1978). **Acta Crystallogr., Sect. B: Struct. Sci.** 34: 2080-2084.
- Xia, J., Shi, W., Chen, X.-Y., Wang, H.-S., Cheng, P., Liao, D.-Z., and Yan, S.-P. (2007). **J. Chem. Soc., Dalton Trans.** (23): 2373-2375.
- Yaghi, O. M., O'Keeffe, M., Ockwig, N. W., Chae, H. K., Eddaoudi, M., and Kim, J. (2003). **Nature** 423: 705-714.
- Zhang, Y.-Z., Gao, S., Wang, Z.-M., Su, G., Sun, H.-L., and Pan, F. (2005). **Inorg. Chem.** 44(13): 4534-4545.
- Zhuzhong, Z., Qinghin, M., Xiaozeng, Y., Guangwei, G., and Pei-Ju, Z. (1996). **Polyhedron** 15(15): 2655-2658.

CHAPTER IV

SUPRAMOLECULAR ARCHITECTURE

AND COORDINATION POLYMERS WITH $[\text{Ag}(\text{CN})_2]^-$

AS BUILDING BLOCK

4.1 Introduction

The crystal engineering of supramolecular architectures or metal organic coordination polymers has attracted great attention due to their potential use as functional solid materials (Robson *et al.*, 1992; Batten and Robson, 1998, Yaghi *et al.*, 2003). But, in many cases, it is quite difficult to control the desired solid state structures. Several factors such as (i) stereo electronic molecular information encoded in the ligands, (ii) size, charge and electronic structure, and (iii) external conditions, *eg.* solvent, counter ions, have a strong influence in the crystallization process on the formation of the solid state architectures. It is well known that noncovalent interactions (*eg.* hydrogen bonds, π - π and metallophilic interactions) have also presented a synthetic paradigm for the rational design and synthesis of functional materials in supramolecular chemistry (Desiraju, 2003).

The linear dicyanometallates of formula $[\text{M}^{\text{I}}(\text{CN})_2]^-$, where $\text{M}^{\text{I}} = \text{Ag}$ and Au , are of particular interest for use as bridging ligands for the construction of multidimensional cyanometalate coordination polymers exhibiting spin-crossover (SCO) phenomena (Niel *et al.*, 2002, Niel *et al.*, 2003; Niel *et al.*, 2005; Munoz *et al.*, 2007). These complex ligands have show versatile abilities to coordinate to metal ions

in different modes and numbers such as the (i) rod-shaped or a linear bridging motif (Dong *et al.*, 2003), (ii) a discrete anion playing the role of space filler (Omary *et al.*, 1996), and (iii) as a unidentate ligand blocking some coordination sites of a central atom (Soma and Iwamoto, 1998). Unlike other related two-connecting bridging ligands such as dicyanamide, $[\text{N}(\text{CN})_2]^-$, the $[\text{M}(\text{CN})_2]^-$ bridges can also possess the ability to further stabilize the polymeric structures through interactions between closed-shell $d^{10}\cdots d^{10}$ *argentophilic* ($\text{Ag}^I\cdots\text{Ag}^I$) or *aurophilic* ($\text{Au}^I\cdots\text{Au}^I$) interactions which effectively increase the dimensionality (Pyykko, 1997; Liu *et al.*, 2006). In addition, theoretical studies on dimeric models of linear two-coordinate complexes indicate that the strengths of such interactions are within the range of typical hydrogen bonds (Magnko *et al.*, 2002), the latter being perhaps the most widely applied tool for the increase of dimensionality and control of supramolecular architecture.

Recently, various coordination polymers have been discovered which employ the $[\text{Ag}(\text{CN})_2]^-$ ligand as a building block. For examples, 1-D chain $[\text{Cu}(4\text{-Mepy})_2\text{Ag}_2(\text{CN})_4]$ (Tričiková *et al.*, 2003), $[\text{Cu}(\text{en})_2][\text{Ag}_2(\text{CN})_3][\text{Ag}(\text{CN})_2]$, $[\text{Mn}(\text{NITpPy})_2][\text{Ag}(\text{CN})_2]_2$ (Dasna *et al.*, 2001), $[\text{Ni}(\text{tren})\text{Ag}(\text{CN})_2][\text{Ag}(\text{CN})_2]$ (Shorrocks *et al.*, 2002), $[\text{Cu}(\text{en})_2\text{Ag}_2(\text{CN})_4]$ (Černák *et al.*, 1998), $[\text{Ni}(\text{en})_2\text{Ag}(\text{CN})_2][\text{Ag}(\text{CN})_2]$ (Ren *et al.*, 2005), 2-D network $[\text{Ni}(\text{en})_2\text{Ag}_3(\text{CN})_5]$ (Zhang *et al.*, 1999), 2-D interpenetrating nets $[\text{Cu}(\text{en})\text{Cu}(\text{CN})_2\text{Ag}(\text{CN})_2]$ (Shorrocks *et al.*, 2002), $[\text{Ni}(\text{en})_2][\text{Ag}(\text{CN})_2]_2[\text{Ag}_2(\text{CN})_2]$ (Duriska *et al.*, 2006), 3-D networks $[\text{Ag}_4\text{Cd}_2(\text{tren})_2(\text{CN})_{6.5}][\text{Ag}(\text{CN})_{1.5}]$ (Zhang *et al.*, 2002), $[\text{Cu}(\text{dien})\text{Ag}(\text{CN})_2]_2[\text{Ag}_2(\text{CN})_3][\text{Ag}(\text{CN})_2]$ (Lescouëzec *et al.*, 2003), and 3-D doubly interpenetrating $[\text{Cd}(\text{pyz})\text{Ag}_2(\text{CN})_3\text{Ag}(\text{CN})_2]$ (Soma *et al.*, 1994).

The present work forms part of a research program on the chemistry of cyanide-bridged bimetallic coordination polymers with the primary aim of synthesizing 1-D tube-like motifs using $[M(\text{bidentate})(\text{CN})_4]^{2-}$ donors and $[M(\text{bidentate})(\text{solvent})_4]^{2+}$ acceptors as building blocks. A more general aim was to study the structural diversity and magnetic properties of cyanide-bridged and cyanometallate-bridged compounds. In this chapter, the initial aim was to use a linear dicyanoargentate $[\text{Ag}(\text{CN})_2]^-$ as bridging ligand to replace CN groups of the $[M(\text{bidentate})(\text{CN})_4]^{2-}$ building block (see Chapter III). The aromatic planar 2,2'-bipyridine (2,2'-bipy) bidentate ligand is used here to block two coordination sites in the acceptor group. This approach is expected to produce 1-D tube-like motifs of $[\text{Ag}(\text{CN})_2]$ bridged bimetallic coordination polymers. But other stoichiometries and topologies are possible even when $M^{\text{II}}:[\text{Ag}(\text{CN})_2]^-$ ratios of 1:1 are used. Thus, new supramolecular complexes can be formed that involve interactions such as argentophilic, hydrogen bonding, and $\pi \cdots \pi$ interactions. The synthesis and structures of four new mixed-metal compounds of $[\{\text{Ag}(\text{CN})_2\}_2\text{Mn}(2,2'\text{-bipy})_2] \cdot 2\text{H}_2\text{O}$ (**4a**), $[\text{Ag}(\text{CN})_2\text{Mn}(2,2'\text{-bipy})_2(\text{H}_2\text{O})]\text{Ag}(\text{CN})_2$ (**4b**) and two coordination polymers $[\text{Ag}_4(\text{CN})_7\{\text{Cd}(2,2'\text{-bipy})\}_2] \cdot [\text{ClO}_4]$ (**4c**) and $[\{\text{Ag}(\text{CN})_2\}_2\text{Cd}(2,2'\text{-bipy})]$ (**4d**) are described. **4a** and **4b** display supramolecular structures, while **4c** and **4d** are coordination polymers. Their structures contain $[\text{Ag}(\text{CN})_2]$ units which behave as building blocks as well as increasing the dimensionality and stabilizing the crystal structures through interactions of the argentophilic ($\text{Ag} \cdots \text{Ag}$), $\text{Ag} \cdots \text{N}$ and $\text{Ag} \cdots \pi$ types. The temperature dependent magnetic behavior of **4b** is also examined.

4.2 Experimental Section

4.2.1 Materials and Physical Measurements

KAg(CN)₂, Mn(ClO₄)₂·6H₂O, Mn(NO₃)₂·6H₂O, Cd(ClO₄)₂·6H₂O, and 2,2'-bipy were commercially available, and were used without further purification.

Caution!: Perchlorate salts of metal complexes with organic ligands are potentially explosive. Only small amounts of material should be prepared, and these should be handled with care. Cyanide is very poisonous. Great care should be taken that its salts do not come into contact with acid, which liberates highly toxic hydrogen cyanide gas. It should not be touched with the fingers; use a spatula or handle small pieces with pincers, and reactions were performed under a fume hood.

Microanalytical measurements (C, H, N) were performed by Campbell Microanalytical Laboratory, Chemistry Department, University of Otago, Dunedin, New Zealand. Infrared spectra of Nujol mulls were recorded using a diamond-ATR cell on a Bruker Opus/IR IFS 55 spectrometer in the range of 600–4000 cm⁻¹ (50 scans, resolution ±4 cm⁻¹). Variable-temperature magnetic susceptibility data were obtained by Dr. Boujemaa Moubaraki, Department of Chemistry, Monash University, using a Quantum Design MPMS 5 SQUID magnetometer for DC magnetization measurements.

4.2.2 Syntheses

Preparation of [{Ag(CN)₂}₂Mn(2,2'-bipy)₂]·H₂O (**4a**)

A crystalline sample of **4a** was obtained using the slow diffusion method in which an aqueous solution of 14 mL capacity was contained in an H-shaped tube and left in the dark. In a typical experiment, KAg(CN)₂ (40 mg, 0.2 mmol) was dissolved in 3 mL of distilled water to form a bright colorless solution, and this was pipetted

into one side of the H-tube. $\text{Mn}(\text{NO}_3)_2 \cdot 6\text{H}_2\text{O}$ (57 mg, 0.2 mmol) and 2,2'-bipy (31 mg, 0.2 mmol) were dissolved in 3 mL of distilled water to give a bright yellow aqueous solution, and this was pipetted into the other side arm of the H-tube. The H-tube was then carefully filled with distilled water. Upon slow diffusion for two weeks, pale-yellow shaped single crystals of **4a** were formed in the silver-containing side of the H-tube. Yield: 25 mg (63% based on $\text{KAg}(\text{CN})_2$). Anal. Found (calcd) for $\text{C}_{24}\text{H}_{20}\text{Ag}_2\text{MnN}_8\text{O}$ ($M_r = 705.14$ g/mol): C, 40.85(40.88); H, 2.80(2.79), N, 15.92(15.89). ATR-FTIR ($\nu_{\text{max}}/\text{cm}^{-1}$): 648m, 737s, 765s, 1013s, 1154m, 1312m, 1436s, 1471s, 1489s, 1575s, 1594m, 1630w, 2134s, 2155s, 3050w, 3089w, 3120w, 3468m, 3534br.

Preparation of $[\text{Ag}(\text{CN})_2\text{Mn}(2,2'\text{-bipy})_2(\text{H}_2\text{O})][\text{Ag}(\text{CN})_2]$ (4b**)**

The compound **4b** was prepared by a similar procedure to that described for **4a** above, in methanol/water (1:1, v/v) solution with $\text{Mn}(\text{ClO}_4)_2 \cdot 6\text{H}_2\text{O}$ being used instead of $\text{Mn}(\text{NO}_3)_2 \cdot 6\text{H}_2\text{O}$. X-ray quality pale-yellow block shaped single crystals of **4b** were formed in the silver-containing side after two weeks. Yield: 28 mg (70%). Anal. Found (calcd) for $\text{C}_{24}\text{H}_{18}\text{Ag}_2\text{MnN}_8\text{O}$ ($M_r = 705.14$ g/mol) C, 40.86(40.88); H, 2.57(2.79), N, 15.87(15.89). ATR-FTIR ($\nu_{\text{max}}/\text{cm}^{-1}$): 733s, 759s, 1013s, 1437s, 1472s, 1566m, 1575m, 1595s, 2142w, 2153s, 2611br, 2649br, 2664br, 2744br, 3097br, 3596br, 3619br, 3644br, 3679br, 3764br.

Preparation of $[\text{Ag}_4(\text{CN})_7\{\text{Cd}(2,2'\text{-bipy})_2\}]_2\text{ClO}_4$ (4c**)**

and $[\{\text{Ag}(\text{CN})_2\}_2\text{Cd}(2,2'\text{-bipy})]$ (4d**)**

The samples were prepared by a similar procedure to that described above for **4b**, in methanol/water (1:1, v/v) solution, and $\text{Cd}(\text{ClO}_4)_2 \cdot 6\text{H}_2\text{O}$ was used instead of

Mn(ClO₄)₂·6H₂O. X-ray quality colorless plate- (**4c**) and block- (**4d**) shaped single crystals were formed after two weeks.

Major phase **4c**: yield, 18.4 mg (46% based on KAg(CN)₂). Anal. Found (calcd) for C₃₇H₃₂Ag₄Cd₂ClN₁₅O₄ (*Mr* = 1562.63 g/mol): C, 37.01(36.13); H, 2.19 (2.06), N, 13.52(13.45). ATR-FTIR (ν_{max}/cm^{-1}): 736m, 762s, 1018m, 1154m, 1314m, 1438s, 1473s, 1489m, 1567m, 1577w, 1593w, 1601s, 2129w, 2139w, 2159s, 3053w, 3088w, 3112w, 3464w, 3535w.

Minor phase **4d**: yield, 2 mg (5% based on KAg(CN)₂). ATR-FTIR (ν_{max}/cm^{-1}): 737m, 767s, 1314m, 1439s, 1473s, 1576m, 1599s, 2130s, 2137m, 2155s, 2163m, 3051w, 3083w, 3109w, 3192w, 3471br, 3538br, 3847w.

4.2.3 X-Ray Crystallographic Study

Single crystals of **4a–4d** were mounted on a MiTeGen MicroMounts fiber in a small amount of oil and prior to measurements made by Dr. Suzanne M. Neville and Dr. Craig Forsyth, Monash University. Reflection intensities were collected on a Bruker X8 APEX CCD diffractometer (Mo K_{α} radiation, $\bar{\lambda} = 0.71073 \text{ \AA}$) and equipped with an Oxford Instruments nitrogen gas Cryostream. Empirical absorption corrections were applied to all data using SADABS (Blessing, 1995). The structures were solved using SHELXS-97 (Sheldrick, 1997) and refined on F^2 using SHELXL-97 (Sheldrick, 1997) with X-SEED (Barbour, 2001) as a graphics interface.

In the final cycles of refinement, all atoms except hydrogen atoms and disorder molecules were refined anisotropically. Hydrogen atoms attached to carbon atoms of 2,2'-bipy molecules were placed in idealized positions and constrained to ride on their parent atoms, with C–H distance at 0.95 Å, with $U_{\text{iso}}(\text{H}) = 1.2U_{\text{eq}}(\text{C})$.

For **4a** and **4b**, hydrogen atoms attached to oxygen atoms of the water molecules were located in a difference Fourier map and refined as riding in their as-found positions with a DFIX restraint of O–H distance at 0.90 Å, with $U_{\text{iso}}(\text{H}) = 1.2U_{\text{eq}}(\text{O})$.

For **4c**, the cyanide group, $\text{C}\equiv\text{N}$, was modeled as disordered over the symmetry site, with both atoms occupying the same site in the asymmetric unit and treated as a hybrid atom of 50% N and 50% C in the structure refinement. The ClO_4 anions were also disordered over inversion centers, and were refined with restrained Cl–O distances and the U_{iso} for the O atoms constrained to be the same.

Crystal data and details of the data collection, and structure refinement for **4a–4d** are summarized in Table 4.1. Selected interatomic bond lengths and angles for **4a–4d** are given in Tables 4.2–4.4. Intra- and intermolecular hydrogen bonds and geometrical parameters of π – π interactions for all compounds are provided in Tables 4.5 and 4.6, respectively. Other crystallographic data are given as supplementary material in a CIF in the attached CD-ROM.

Table 4.1 Summary of crystallographic data for the compounds **4a–4d**.

Identification code	4a	4b	4c	4d
Formula	C ₂₄ H ₂₀ Ag ₂ MnN ₈ O	C ₂₄ H ₁₈ Ag ₂ MnN ₈ O	C ₄₇ H ₃₂ Ag ₄ Cd ₂ ClN ₁₅ O ₄	C ₁₄ H ₈ Ag ₂ CdN ₆
<i>Mr</i>	705.14	705.14	1562.63	588.40
Crystal system	orthorhombic	monoclinic	monoclinic	monoclinic
Crystal color/habit	yellow/block	yellow/block	colorless/plate	colorless/block
Crystal size (mm)	0.22 × 0.14 × 0.10	0.25 × 0.25 × 0.13	0.25 × 0.25 × 0.10	0.25 × 0.13 × 0.13
Space group	<i>Pccn</i>	<i>P2₁/c</i>	<i>C2/c</i>	<i>P2₁/c</i>
<i>a</i> (Å)	21.6029(6)	15.0887(6)	27.4703(8)	11.1278(2)
<i>b</i> (Å)	14.4017(4)	14.3520(6)	14.3204(4)	21.7008(5)
<i>c</i> (Å)	16.6832(6)	12.8144(5)	16.1812(5)	15.5048(3)
α (°)	90	90	90	90
β (°)	90	112.241(2)	124.930(1)	107.630(1)
γ (°)	90	90	90	90
<i>V</i> (Å ³)	5190.5(3)	2568.5(1)	5218.7(3)	3568.2(1)
<i>Z</i> , <i>D</i> _{calc} (Mg m ⁻³)	8, 1.805	4, 1.823	4, 1.989	8, 2.191
Temperature (K)	123(2)	123(2)	123(2)	123(2)
μ (Mo <i>K</i> α) (mm ⁻¹), <i>F</i> (000)	2.01, 2760	2.03, 1380	2.38, 3008	3.36, 2208
θ range (°)	3.0 – 29.2°	3.0 – 29.2	2.6 – 27.5	1.7 – 27.5
Data completeness	0.997	1.000	0.997	0.997
Limiting indices <i>h</i>	–25 → 27	–17 → 17	–35 → 35	–19 → 19
<i>k</i>	–11 → 18	–17 → 12	–10 → 18	–18 → 12
<i>l</i>	–13 → 21	–15 → 15	–21 → 21	–16 → 16
<i>T</i> _{min} / <i>T</i> _{max}	0.721/0.818	0.631/0.779	0.588/0.797	0.487/0.669
Reflections collected/unique/ <i>R</i> _{int}	16095/4192/0.049	24156/4521/0.030	26563/5982/0.025	35928/8185/0.026
Data/restraints/parameters	4192/2/334	4521/0/333	5982/4/334	8185/0/415
<i>R</i> ₁ , <i>wR</i> ₂ [all data]	0.069, 0.091	0.027, 0.096	0.035, 0.115	0.024, 0.043
<i>R</i> ₁ , <i>wR</i> ₂ [<i>I</i> > 2 σ (<i>I</i>)]	0.043, 0.078	0.024, 0.088	0.029, 0.108	0.020, 0.041
Goodness of fit, <i>S</i>	1.06	0.80	0.93	1.10
$\Delta\rho$ _{min} , $\Delta\rho$ _{max} (e Å ⁻³)	0.68, –0.83	0.75, –0.56	1.87, –1.22	0.63, –0.63

Computer programs: Crystal Maker (2006), Diamond v. 3e (Brandenburg and Putz, 2006), SADABS (Blessing, 1995), SHELXL-97 (Sheldrick, 1997), SHELXS-97 (Sheldrick, 1997), and X-SEED (Barbour, 2001).

Table 4.2 Selected bond lengths and angles for **4a** and **4b** (Å, °). ^a

4a		4b	
Ag1–C1	2.068(5)	Ag1–C1	2.054(3)
Ag1–C2	2.060(5)	Ag1–C2	2.051(3)
Ag2–C3	2.059(5)	Ag2–C3	2.037(3)
Ag2–C4	2.048(5)	Ag2–C4	2.049(3)
Mn1–N1	2.177(4)	Mn1–O1	2.139(2)
Mn1–N3	2.186(4)	Mn1–N1	2.196(2)
Mn1–N5	2.267(3)	Mn1–N5	2.273(2)
Mn1–N6	2.279(3)	Mn1–N6	2.283(2)
Mn1–N7	2.240(3)	Mn1–N7	2.245(2)
Mn1–N8	2.277(3)	Mn1–N8	2.240(2)
C1–Ag1–C2	165.6(1)	C1–Ag1–C2	175.9(1)
C3–Ag2–C4	166.6(1)	C3–Ag2–C4	172.5(1)
Ag1–C1–N1	176.4(4)	Ag1–C1–N1	173.6(2)
Ag1–C2–N2	174.4(5)	Ag1–C2–N2	177.1(3)
Ag2–C3–N3	173.2(4)	Ag2–C3–N3	177.6(2)
Ag2–C4–N4	174.0(5)	Ag2–C4–N4	176.4(2)
Mn1–C1–N1	162.6(4)	Mn1–C1–N1	165.3(2)
Mn1–C3–N3	163.0(4)		

^a Estimated standard deviations of the least significant digits are given in parentheses.

Table 4.3 Selected bond lengths and angles for **4c** (Å, °). ^a

Ag1–C1	2.057(3)	Cd1–N3	2.265(3)
Ag1–C2	2.046(3)	Cd1–N5	2.372(2)
Ag2–C3	2.073(4)	Cd1–N6	2.360(3)
Ag2–C4/N4	2.110(3)	Cd1–N7	2.354(2)
Ag2–N2 ⁱ	2.525(3)	Cd1–N8	2.350(3)
Cd1–N1	2.295(3)		
C1–Ag1–C2	174.8(1)	N3–Cd1–N6	86.2(1)
C3–Ag2–C4	157.3(1)	N3–Cd1–N7	162.7(1)
C3–Ag2–N2 ⁱ	99.2(1)	N3–Cd1–N8	92.6(1)
N4–Ag2–N2 ⁱ	99.1(1)	N5–Cd1–N6	69.6(1)
N1–Cd1–N3	93.6(1)	N5–Cd1–N7	94.4(1)
N1–Cd1–N5	89.0(1)	N5–Cd1–N8	157.7(1)
N1–Cd1–N6	158.1(1)	N6–Cd1–N7	97.1(1)
N1–Cd1–N7	89.3(1)	N6–Cd1–N8	95.4(1)
N1–Cd1–N8	106.4(1)	N7–Cd1–N8	70.3(1)
N3–Cd1–N5	102.5(1)		

^a Estimated standard deviations of the least significant digits are given in parentheses.

Symmetry code: (i) $x-1/2, -y+1/2, z-1/2$.

Table 4.4 Selected bond lengths and angles for **4d** (Å, °). ^a

Ag1–C1	2.059(3)	Cd1–N7	2.334(2)
Ag1–C2	2.063(3)	Cd1–N9	2.407(2)
Ag2–C3	2.053(2)	Cd2–N2	2.277(2)
Ag2–C4	2.061(2)	Cd2–N4 ⁱⁱⁱ	2.387(2)
Ag3–C5	2.063(3)	Cd2–N6 ⁱ	2.290(2)
Ag3–C5	2.064(3)	Cd2–N8 ⁱⁱ	2.316(2)
Ag4–C6	2.054(3)	Cd2–N11	2.360(2)
Ag4–C7	2.050(3)	Cd2–N12	2.338(2)
Cd1–N1	2.269(2)	Ag1⋯Ag2 ^{iv}	3.3128(3)
Cd1–N3	2.348(2)	Ag2 ^v ⋯Ag3	3.2105(3)
Cd1–N5	2.257(2)		
C1–Ag1–C2	172.1(1)	N7–Cd1–N10	87.3(1)
C3–Ag2–C4	167.7(1)	N9–Cd1–N10	70.0(1)
C5–Ag3–C6	172.8(1)	N2–Cd2–N4 ⁱⁱⁱ	92.7(1)
C7–Ag4–C8	166.4(1)	N2–Cd2–N6 ⁱ	99.9(1)
N1–Cd1–N3	91.3(1)	N2–Cd2–N8 ⁱⁱ	95.0(1)
N1–Cd1–N5	102.6(1)	N2–Cd2–N11	92.9(1)
N1–Cd1–N7	91.9(1)	N2–Cd2–N12	159.7(1)
N1–Cd1–N9	163.0(1)	N4 ⁱⁱⁱ –Cd2–N6 ⁱ	89.8(1)
N1–Cd1–N10	93.3(1)	N4 ⁱⁱⁱ –Cd2–N8 ⁱⁱ	172.1(1)
N3–Cd1–N5	95.9(1)	N4 ⁱⁱⁱ –Cd2–N11	93.3(1)
N3–Cd1–N7	174.2(1)	N4 ⁱⁱⁱ –Cd2–N12	77.6(1)
N3–Cd1–N9	84.5(1)	N6 ⁱ –Cd2–N8 ⁱⁱ	87.7(1)
N3–Cd1–N10	87.7(1)	N6 ⁱ –Cd2–N11	166.5(1)
N5–Cd1–N7	87.9(1)	N6 ⁱ –Cd2–N12	97.8(1)
N5–Cd1–N9	94.1(1)	N8 ⁱⁱ –Cd2–N11	87.3(1)
N5–Cd1–N10	163.4(1)	N8 ⁱⁱ –Cd2–N12	95.3(1)
N7–Cd1–N9	90.9(1)	N11–Cd2–N12	70.1(1)

^a Estimated standard deviations of the least significant digits are given in parentheses. Symmetry codes: (i) $x+1, -y-1/2, z+1/2$; (ii) $-x+1, y-1/2, -z+1/2$; (iii) $-x+2, y-1/2, -z-1/2$; (iv) $-x+2, -y, -z$; (v) $x-1, y, z$.

Table 4.5 Hydrogen bond geometries for **4a** and **4b** (Å, °). ^a

D–H⋯A	d[D–H]	d[H⋯A]	d[D⋯A]	∠[D–H–A]
4a				
O1–H1 _w ⋯N2	0.88(1)	2.12(2)	2.982(5)	167(7)
O2–H2 _w ⋯N4	0.89(1)	2.15(2)	3.031(6)	167(6)
C7–H7⋯O1 ⁱ	0.95	2.48	3.383(7)	158.8
C22–H22⋯O2 ⁱⁱ	0.95	2.50	3.451(7)	175.4
C12–H12⋯π (C)	0.95	2.508(7)	3.430(8)	142.4
4b				
O1–H1 _w ⋯N4 ⁱⁱⁱ	0.72(3)	2.04(4)	2.747(4)	167(3)
O1–H2 _w ⋯N2 ^{iv}	0.74(5)	2.00(5)	2.745(4)	179(5)
C23 ^v –H23 ^v ⋯π (F)	0.95	2.924(3)	3.747(3)	130.7
C24 ^v –H24 ^v ⋯π (F)	0.95	2.951(3)	3.771(3)	126.8
4c				
C6–H6⋯O3	0.95	2.78	3.297(10)	115.0
C12–H12⋯O3 ^{vi}	0.95	2.56	3.290(10)	133.6
C15–H15⋯O2	0.95	2.54	3.179(14)	124.5
C17 ^{vii} –H17 ^{vii} ⋯π (I)	0.95	2.592(3)	3.540(3)	166.0
4d				
C26 ^{viii} –H26 ^{viii} ⋯π (M)	0.95	2.977(4)	3.539(4)	132.5
C27 ^{viii} –H27 ^{viii} ⋯π (M)	0.95	2.544(4)	3.539(4)	127.6

^a Estimated standard deviations of the least significant digits are given in parentheses. Symmetry codes: (i) 1/2+x, 2–y, 1/2–z; (ii) 1/2–x, 2–y, –z–1; (iii) 1–x, 1–y, –z; (iv) x, 1.5–y, 0.5–z. (v) –x, 1–y, 2–z; (vi) x, 1/2–y, z–1/2; (v) x, 1/2–y, z–1/2; (vi) x–1/2, 3/2–y, z–1/2; (vii) x, 1–y, z–1/2; (viii) x, 1+y, z.

Table 4.6 Geometrical parameters of π - π interactions in **4a–4d** (\AA , $^\circ$). ^a

π - π	Centre to centre distance ($C_g \cdots C_g$)	Closest distance of approach	Interplanar angle
4a			
ring <i>A</i> ··ring <i>C</i>	3.839	3.402(7), C16	4.2(3)
ring <i>B</i> ··ring <i>D</i>	4.148	3.571(6), C21	5.3(3)
4b			
ring <i>E</i> ··ring <i>F</i>	4.208	3.231(4), C12	19.2(1)
ring <i>G</i> ··ring <i>H</i>	3.830	3.402(4), N8	2.7(1)
4c			
ring <i>I</i> ··ring <i>J</i>	3.781	3.368(3), C12	6.6(1)
ring <i>K</i> ··ring <i>L</i>	3.746	3.361(4), C22	2.9(1)
4d			
ring <i>M</i> ··ring <i>O</i>	4.531	2.695(6), C19	15.6(1)
ring <i>O</i> ··ring <i>P</i>	3.772	3.220(3), C27	2.6(1)

^a Estimated standard deviations of the least significant digits are given in parentheses.

4.3 Results and Discussion

4.3.1 Synthesis and ATR-IR Spectra

Reaction of $\text{Mn}(\text{NO}_3)_2 \cdot 6\text{H}_2\text{O}$ or $\text{Mn}(\text{ClO}_4)_2 \cdot 6\text{H}_2\text{O}$, $\text{K}[\text{Ag}(\text{CN})_2]$, and 2,2'-bipy in a 1:1:1 molar ratio in an aqueous or methanol/water solutions afforded pale-yellow block-shaped single crystals of the new complexes $[\{\text{Ag}(\text{CN})_2\}_2\text{Mn}(2,2'\text{-bipy})_2] \cdot \text{H}_2\text{O}$ (**4a**) and $[\text{Ag}(\text{CN})_2\text{Mn}(2,2'\text{-bipy})_2(\text{H}_2\text{O})]\text{Ag}(\text{CN})_2$ (**4b**) in good yields. The crystallizing solvent and the counter anions have profound effects on the structures of the products. Both compound have $\text{Ag}(\text{CN})_2:\text{Mn}:2,2'\text{-bipy}$ ratios of 2:1:2, thus a mole equivalent of Mn(II) remains in solution. A methanol/water solution of $\text{Cd}(\text{ClO}_4)_2 \cdot 6\text{H}_2\text{O}$ containing one equivalent of 2,2'-bipy with a methanol/water solution of one equivalent of $\text{K}[\text{Ag}(\text{CN})_2]$ afforded a major product of colorless plate shaped crystals of $[\text{Ag}_4(\text{CN})_7\{\text{Cd}(2,2'\text{-bipy})\}_2]\text{ClO}_4$ (**4c**) and traces of block-shaped crystals of $[\{\text{Ag}(\text{CN})_2\}_2\text{Cd}(2,2'\text{-bipy})]$ (**4d**). Interestingly, compound **4c** has $\text{Ag}(\text{CN})_2:\text{Cd}:2,2'\text{-bipy}$ ratios of 2:1:2, while **4d** has 2:1:1. Attempts to grow crystals using $\text{Fe}(\text{ClO}_4)_2 \cdot x\text{H}_2\text{O}$, $\text{Co}(\text{ClO}_4)_2 \cdot 6\text{H}_2\text{O}$, $\text{Ni}(\text{ClO}_4)_2 \cdot 6\text{H}_2\text{O}$, and $\text{Zn}(\text{ClO}_4)_2 \cdot 6\text{H}_2\text{O}$ instead of $\text{Mn}(\text{ClO}_4)_2 \cdot 6\text{H}_2\text{O}$ or $\text{Cd}(\text{ClO}_4)_2 \cdot 6\text{H}_2\text{O}$ using the same procedure as in **4b** were unsuccessful. Despite many attempts, the crystals obtained were always very small, often twinned and of poor quality.

Bridging or terminal cyano groups can usually be differentiated by the positions of the corresponding infrared $\nu(\text{CN})$ stretching absorption bands. Typically, bridging CN ligands have higher stretching frequencies than the terminal CN ligand (Nakamoto, 1963). The solid state IR spectrum of $\text{K}[\text{Ag}(\text{CN})_2]$ had $\nu(\text{CN})$ band at 2134 cm^{-1} . The CN stretching region of the solid state IR spectrum of **4a** and **4b** is consistent with the presence of bridging cyano groups with $\nu(\text{CN})$ at 2155s and 2153s

cm^{-1} , and terminal cyano groups at 2134s and 2142w cm^{-1} , respectively. The infrared spectrum of **4c** had a $\nu(\text{CN})$ band at 2159s cm^{-1} . **4d** has $\nu(\text{CN})$ bands at 2154s and 2163s cm^{-1} , at higher wavenumbers than that of free $\text{K}[\text{Ag}(\text{CN})_2]$, indicating all the cyano groups are bridging. These results are consistent with the single crystal X-ray studies.

4.3.2 Structural Description of $[\{\text{Ag}(\text{CN})_2\}_2\text{Mn}(2,2'\text{-bipy})_2]\cdot\text{H}_2\text{O}$ (**4a**)

4a crystallizes in a monoclinic system with the space group $P2_1/n$ (No. 14). The asymmetric unit consists of one $[\text{Mn}(2,2'\text{-bipy})_2]^{2+}$ fragment and two distinct $[\text{Ag}(\text{CN})_2]^-$ units in general positions, and half of two water molecules of crystallization on a special positions, in Figure 4.1. The structure consists of discrete metal complexes and intercalated water molecules.

The Mn(II) center is *cis* six-coordinated by four 2,2'-bipy nitrogen and two cyanide nitrogen atoms to form a distorted octahedral geometry. The Mn–N_{2,2'-bipy} bond lengths range from 2.240(3) to 2.279(3) Å, and are comparable to those observed in other 2,2'-bipy containing manganese(II) complexes; *cis*- $[\text{Mn}(2,2'\text{-bipy})_2(\text{NCS})_2]$ (Veidis *et al.*, 1981) and *cis*- $[\text{Mn}(2,2'\text{-bipy})_2(\text{Cl})_2]$ (Lumme and Lindell, 1988). The Mn–N_{CN} bond lengths at 2.177(4) and 2.186(4) Å are slightly shorter than the Mn–N_{2,2'-bipy} bond lengths. Similar shorter bonds for Mn–N_{CN} versus Mn–N_{2,2'-bipy} in **4a** are observed in *cis*- $[\text{Mn}(2,2'\text{-bipy})_2(\text{NCS})_2]$ (Veidis *et al.*, 1981), *cis*- $[\text{Mn}(1,10\text{-phen})_2(\text{NCS})_2]$ (Hollenman *et al.*, 1994), and *cis*- $[\text{Mn}(1,10\text{-phen})_2(\text{dca})_2]$ (Wang *et al.*, 2000). The Mn–N–C bond angles are 162.6(4) and 163.0(4)°.

The two $[\text{Ag}(\text{CN})_2]^-$ units in **4a** is somewhat bent. The C–Ag–C bond angles range from 165.6(1) to 166.6(1)°, and the Ag–C–N bond angles are in the 173.2(4) and 176.4(4)° range. The Ag–C bond lengths range from 2.048(5) to 2.068(5) Å.

These values are slightly different to that reported for the free $\text{Ag}(\text{CN})_2$ molecules (Victoria *et al.*, 2005) caused by the cyanide group from $\text{Ag}(\text{CN})_2$ bridging to the manganese (II) centre.

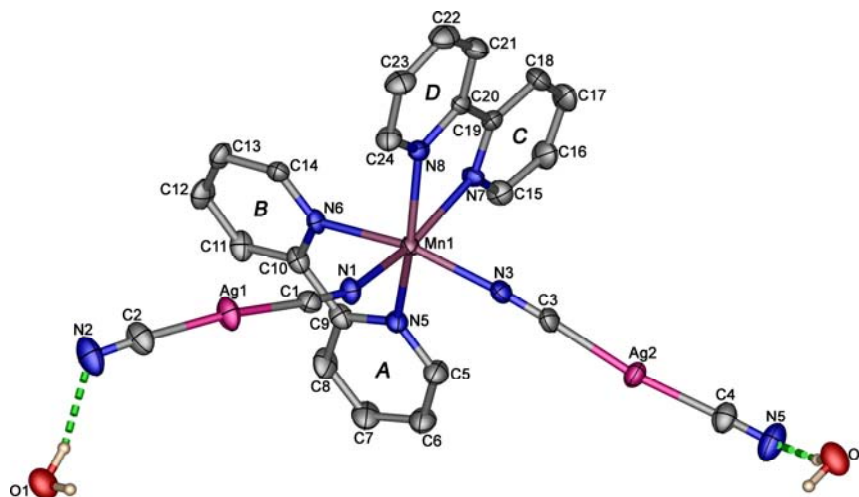


Figure 4.1 Perspective view of **4a** with the atom-numbering scheme. Displacement ellipsoids are drawn at the 50% probability level. Hydrogen atoms are shown as small spheres of arbitrary radii. The labeling scheme, *A–D*, applied to the phenyl rings are used to identify the rings in subsequent discussion.

The 2,2'-bipy ligands in **4a** are essentially planar. A maximum deviation of $-0.082(3)$ Å is observed at atom N8 from the least-squares plane of ring *D*. The bond lengths and angles within the 2,2'-bipy ring (1.333(5) to 1.482(6) Å and 115.4(4) to 124.0(5)°) are all normal and compare well with those observed for the free 2,2'-bipy molecules (Merritt and Schroeder, 1956). The dihedral angle between the least-squares planes through the two 2,2'-bipy ligands containing rings *A/B* and rings *C/D* is 78.7(1)°. The bite angle of 2,2'-bipy is 72.2(1) and 72.8(1)° for N5–Mn1–N6 and

N7–Mn1–N8, respectively. This is one of the main factors accounting for this distortion from ideal octahedral geometry (angle of 90°) of the Mn(II) centre.

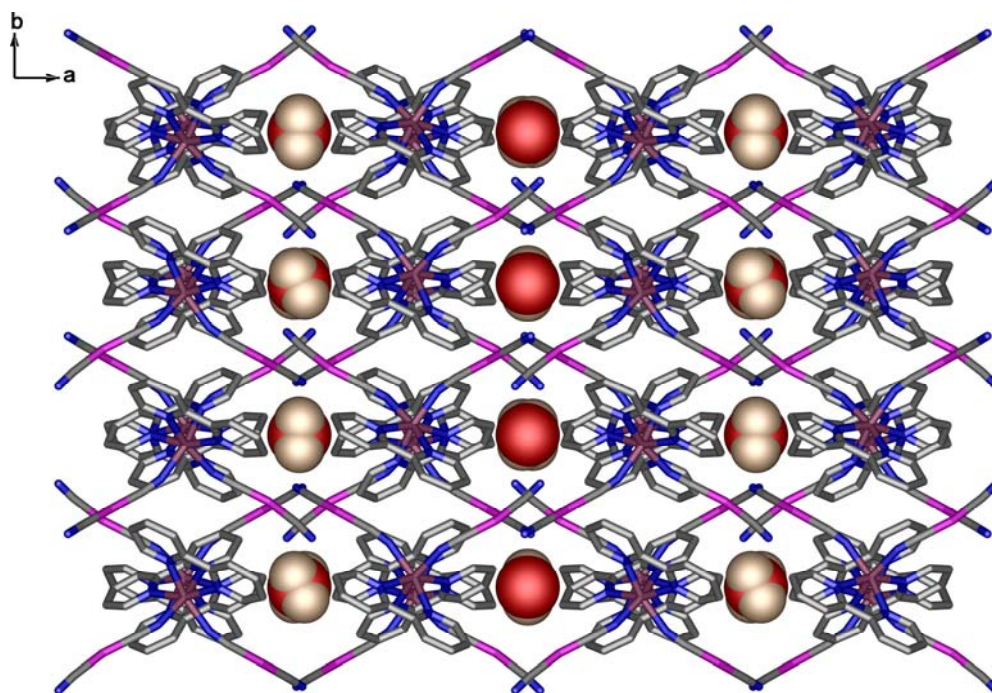


Figure 4.2 Packing diagram of **4a** view along the c axis. Included water molecules are represented as space-filling model.

The crystal packing view along the crystallographic c axis in **4a** is shown in Figure 4.2. A number of supramolecular interactions are observed within the solid state packing. The unligated N-end (nitrile) of the monodentate $[\text{Ag}(\text{CN})_2]$ anions, N4, is bonded at $2.753(4)$ Å to the Ag1 atoms of adjacent component into chains running parallel to the a direction, Figure 4.3a. The value of this $\text{Ag}\cdots\text{N}$ contact in **4a** is well below the sum of the van der Waals radii [1.72 (Ag) + 1.54 (N) = 3.26 Å] (Bondi, 1964) and within the range of other $\text{Ag}\cdots\text{N}$ interactions (2.7 – 3.1 Å) reported in the literature (Withersby *et al.*, 1997; Batten *et al.*, 1998; Janiak *et al.*, 1999). The

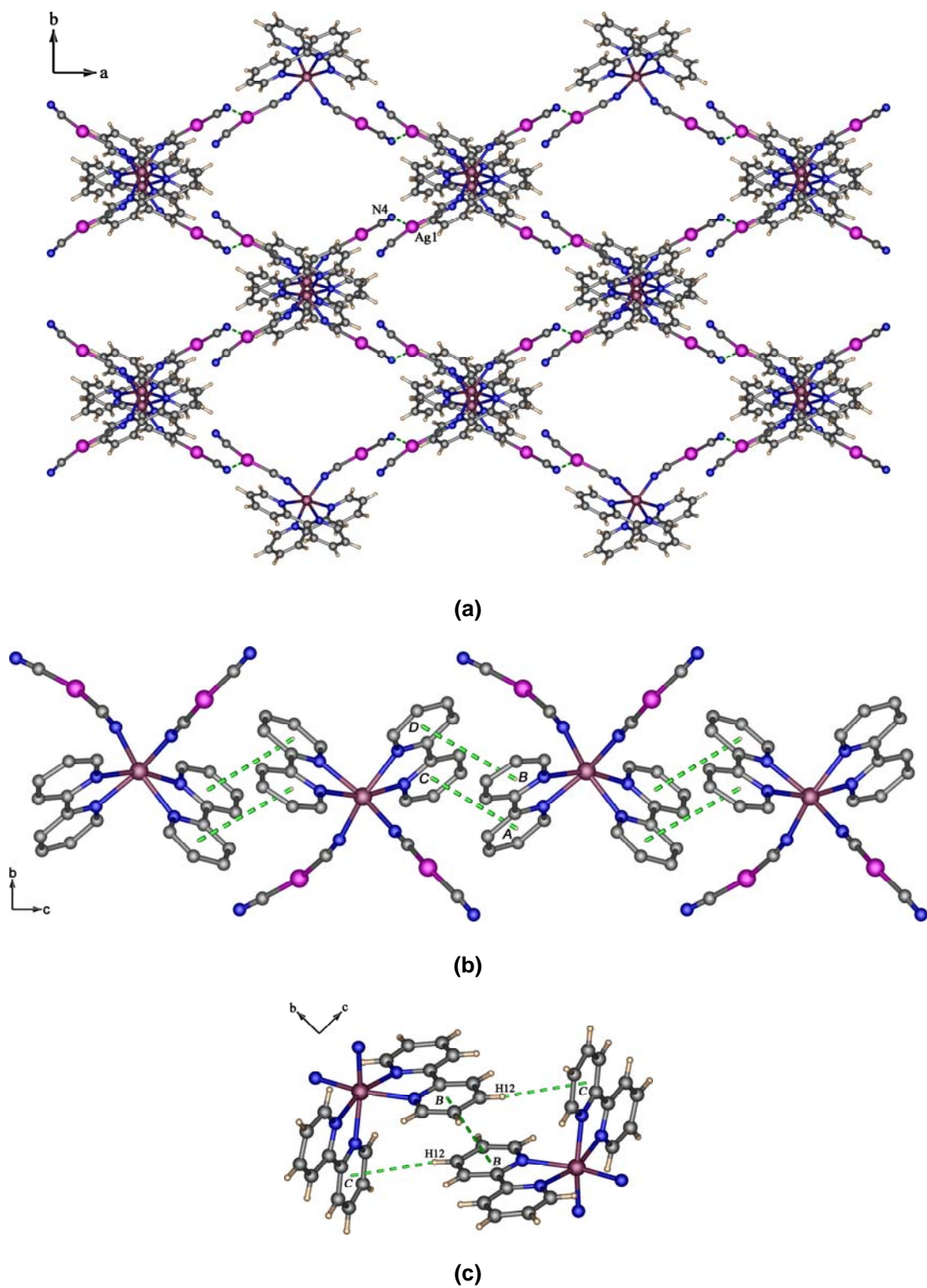


Figure 4.3 Views of supramolecular interactions in **4a** (a) $\text{Ag}\cdots\text{N}$, (b) $\pi\cdots\pi$ and (c) P4AE $\text{C}-\text{H}\cdots\pi$ interactions.

chains are then interconnected through offset head-to-head π - π interactions (*off*) between the pyridyl groups of the 2,2'-bipy ligands as shown in Figure 4.3b. The closest distances of approach between the pyridyl rings are 3.402(7) and 3.571(6) Å for ring *A*··ring *C* and ring *B*··ring *D*, respectively. Ring *C* reinforces the supramolecular structure of **4a** by additional C-H·· π edge-to-face type interactions from hydrogen atoms, H12, of the stacked aryl rings, pointing towards the faces of aryl rings *C* at a distance of 2.508(7) Å. This result in centrosymmetric, achiral, parallel fourfold aryl embraces (P4AE), containing one *off* interaction, and two *ef* interactions (Dance and Scudder, 1996) as illustrated Figure 4.3c. These interactions are associated to give the resulting 2-D square grid, and are further linked together between grids to form 3-D supramolecular architectures along the crystallographic *c* axis as shown in Figure 4.4.

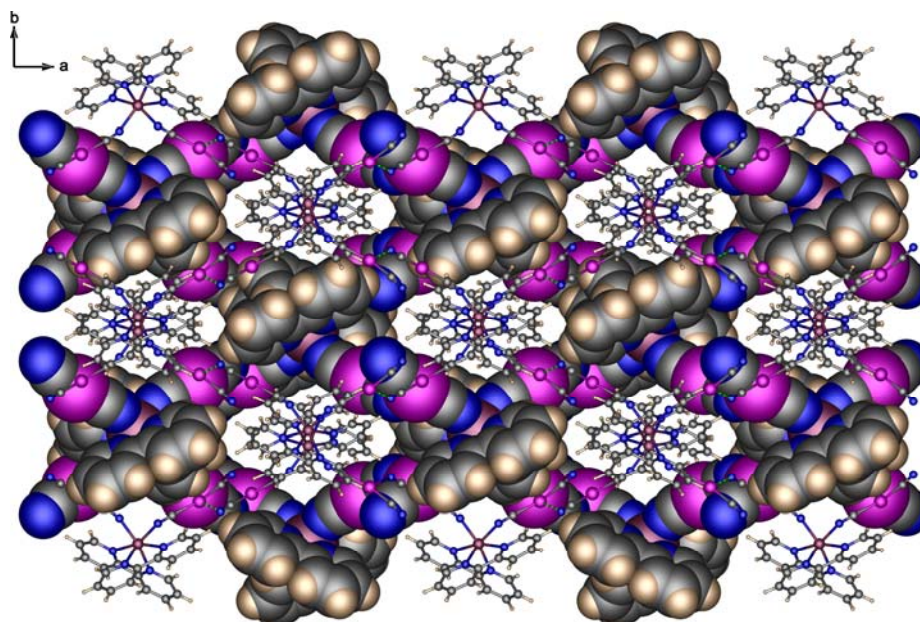


Figure 4.4 Crystal packing in **4a** along the *c* axis showing a single (space-filling) and second (ball and stick) square grids formed *via* Ag··N, C-H·· π and π ·· π interactions.

In order to investigate the argentophilic ($\text{Ag}\cdots\text{Ag}$) interactions, a CSD (version 5.29 updates January 2008) search was carried out with the help of the ConQuest (version 1.10) program (Allen *et al.*, 1991). The result for a search on complexes having $\text{Ag}\cdots\text{Ag}$ interactions between two $[\text{Ag}(\text{CN})_2]$ fragments with the $\text{Ag}\cdots\text{Ag}$ contact constrained to be less than the sum of van der Waals radii of two Ag atoms, 3.44 Å (Bondi, 1964), is illustrated in Figure 4.5. A typical range for these $\text{Ag}\cdots\text{Ag}$ contacts is *ca.* 2.95 to 3.30 Å. The interchain $\text{Ag}\cdots\text{Ag}$ separation in **4a** is 3.847(1) Å, which is greatly longer than the sum of its van der Waals radii. Thus, this value is considered to be a very weak van der Waals contact.

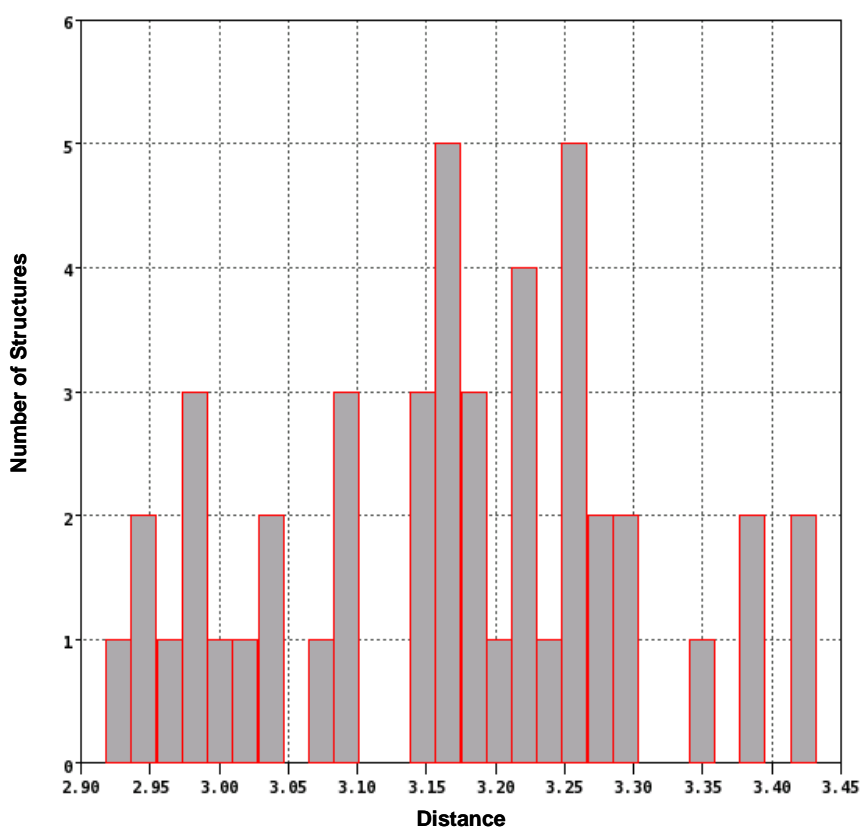


Figure 4.5 Histogram plot of distribution of $\text{Ag}\cdots\text{Ag}$ contacts between two $[\text{Ag}(\text{CN})_2]$ fragments obtained from the CSD (version 5.29 updates January 2008).

Furthermore, the uncoordinated water molecules of O1 and O2 act as both hydrogen bond donors and acceptors participating in two strong ($\text{O-H}\cdots\text{N} = 2.982(5)$ and $3.031(6)$ Å) and two weak ($\text{C-H}\cdots\text{O} = 3.383(7)$ and $3.451(7)$ Å) hydrogen bonds, thereby producing an infinite chain running parallel to the c direction, as shown in Figure 4.6.

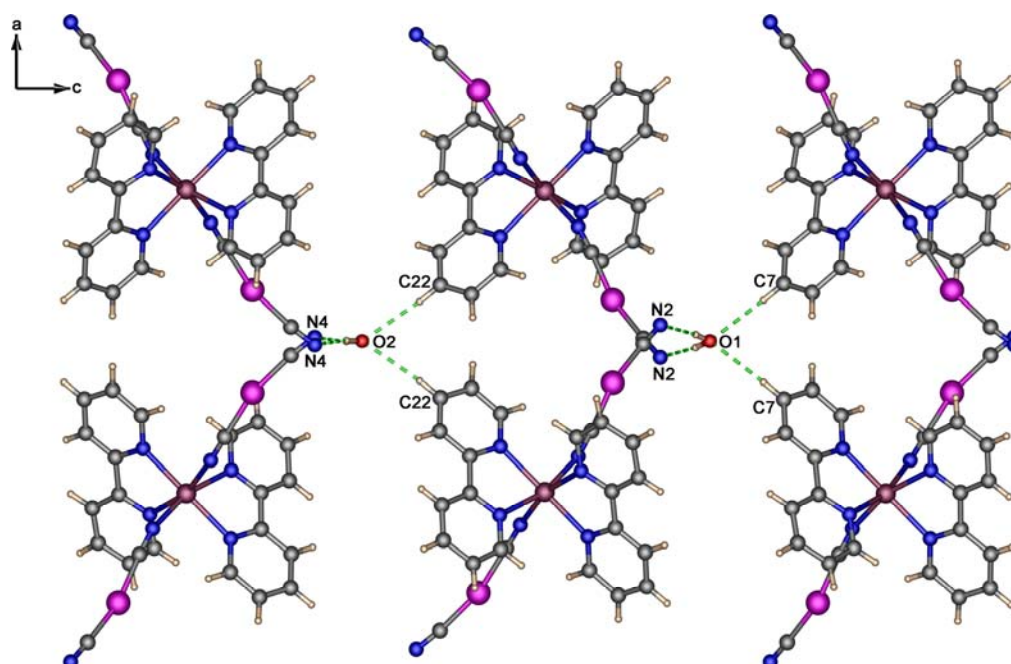


Figure 4.6 Part of the crystal structure of **4a**, showing the formation of an infinite $\text{O-H}\cdots\text{N}$ and $\text{C-H}\cdots\text{O}$ chain running parallel to the c direction.

4.3.3 Structural Description of $[\text{Ag}(\text{CN})_2\text{Mn}(2,2'\text{-bipy})_2(\text{H}_2\text{O})]\cdot\text{Ag}(\text{CN})_2$ (**4b**)

Unlike compound **4a**, the single crystal X-ray diffraction analyses of **4b** revealed that a water molecule is coordinated to the Mn(II) centre, and there is also one isolated $[\text{Ag}(\text{CN})_2]$ anion. **4a** crystallizes in the monoclinic space group $P2_1/c$ (No. 14). The asymmetric unit contains one $[\text{Ag}(\text{CN})_2\text{Mn}(2,2'\text{-bipy})_2(\text{H}_2\text{O})]^+$ cation and one uncoordinated $[\text{Ag}(\text{CN})_2]^-$ anions in general positions, Figure 4.7.

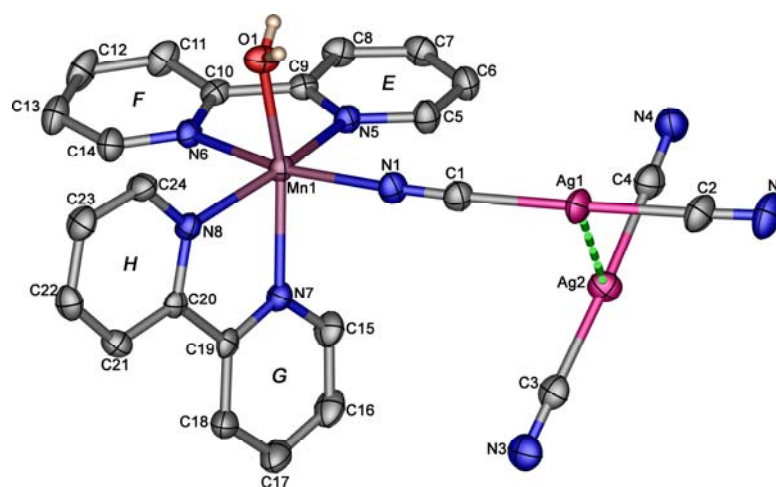


Figure 4.7 Perspective view of **4b** with the atom-numbering scheme. Displacement ellipsoids are drawn at the 50% probability level. Hydrogen atoms are omitted for clarity. The labeling scheme, *E–G*, applied to the phenyl rings are used to identify the rings in subsequent discussion.

Again, the Mn(II) centre is *cis* six-coordinated by four 2,2'-bipy nitrogen, one cyanide nitrogen, and one water oxygen atoms, taking a distorted octahedral geometry. The dihedral angle of the 2,2'-bipy planes of $78.3(1)^\circ$ in **4b** is essentially the same as that found in **4a**. The Mn–N_{CN} (2.196(2) Å) and the Mn–N_{2,2'-bipy} bond lengths (2.240(3) to 2.273(3) Å) are comparable to that found in **4a**.

The two [Ag(CN)₂][−] groups in **4b** are almost linear with the C–Ag–C bond angles ranging from $172.5(1)$ to $175.9(1)^\circ$ and the Ag–C–N bond angles in the $171.9(2)$ to $176.7(3)^\circ$ range. The bond lengths and angles involving the 2,2'-bipy molecules are comparable to those of **4a**. The bite angles of 2,2'-bipy molecules are respectively at $71.8(1)$ and $72.9(1)^\circ$ for N5–Mn1–N6 and for N7–Mn1–N8, which is one of the main factors accounting for the distortion of manganese(II) centre.

A significant difference between the structures of **4a** and **4b** is the presence of the *argentophilic* (Ag \cdots Ag) interactions and the absence of Ag \cdots N interactions and weak C–H \cdots O hydrogen bonds in **4b**. As shown in Figure 4.8a, the [Mn(2,2'-bipy)₂(H₂O)Ag(CN)₂]⁺ cation and [Ag(CN)₂][−] anion portions make contact to each other *via* argentophilic interactions and generate a 1-D zigzag chain parallel to the crystallographic *c* axis. The Ag \cdots Ag contacts are 3.188(1) and 3.775(1) Å for Ag1–Ag2 and Ag1^{*i*}–Ag2 (symmetry code: (*i*) = *x*, 1.5–*y*, *z*–0.5), respectively. The dihedral angles between two [Ag(CN)₂][−] fragments are 84.0(1)° [N1–C1–Ag1–C2–N2 and N3–C3–Ag2–C4–N4] and 83.5(1)° [N1^{*i*}–C1^{*i*}–Ag1^{*i*}–C2^{*i*}–N2^{*i*} and N3–C3–Ag2–C4–N4, symmetry code: (*i*) = *x*, 1.5–*y*, *z*–0.5]. For these Ag \cdots Ag contacts, one is significantly shorter and one longer than the sum of the van der Waals radii of two Ag(I) centers, 3.44 Å (Bondi, 1964). Therefore, the former and latter interactions indicate the presence of strong argentophilic and weak van der Waals interactions, respectively. There is an additional hydrogen bonding interaction between O1 and N2 at 2.745(4) Å which helps to stabilize the chain. Each chain in **4b** is linked through weak $\pi\cdots\pi$ stacking interactions with the shortest C \cdots C distance between the pyridine rings of adjacent chains being 3.231(4) Å, thus creating a 2-D array parallel to the crystallographic *c* axis as shown in Figure 4.8b.

There are additional O \cdots N hydrogen bonding (O1 \cdots N4 = 2.745(4) Å) and π – π stacking interactions of the pyridine rings between the 2-D arrays which hold the components together into a 3-D supramolecular structure as well as make the crystal structure more stable (Tables 4.5 and 4.6).

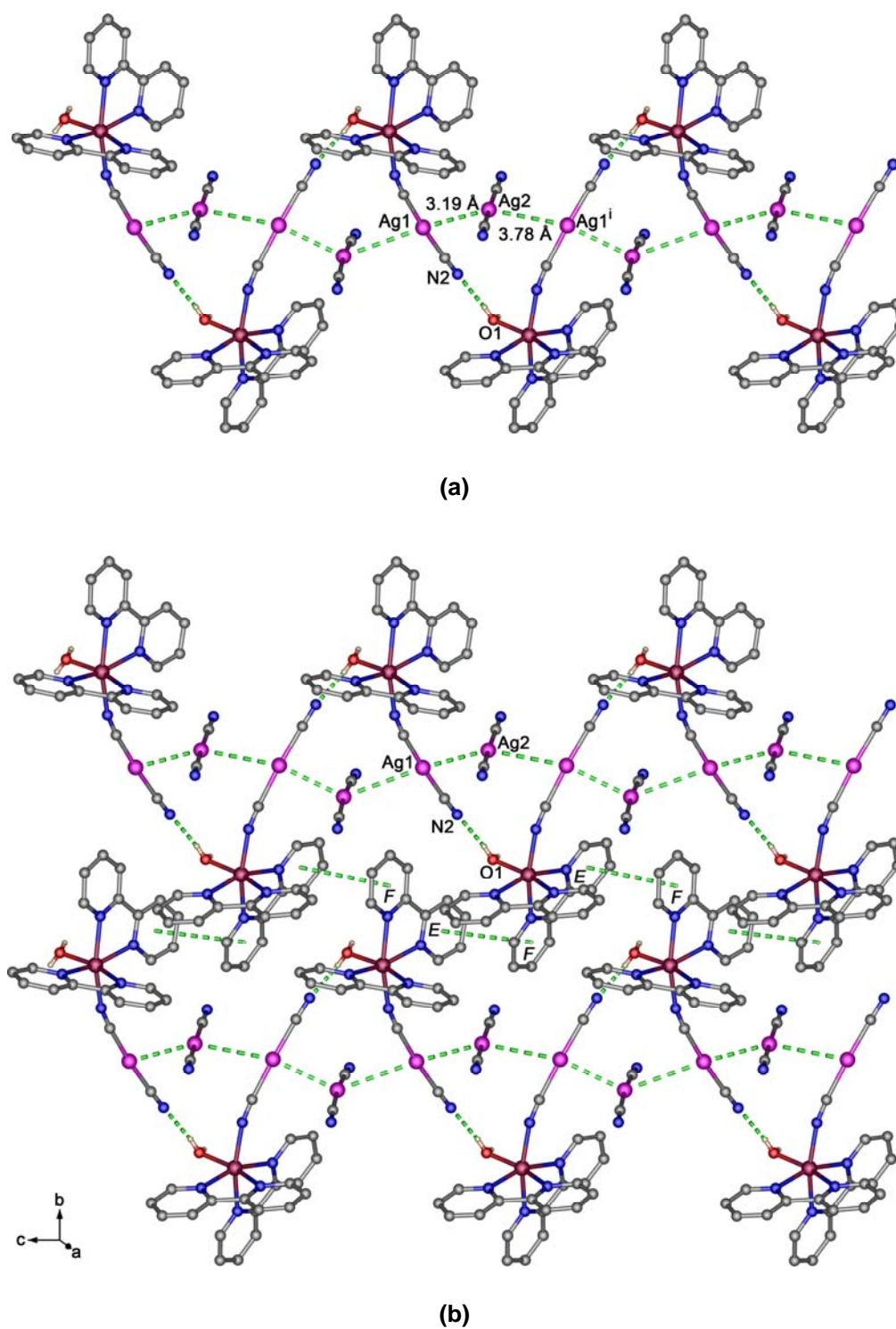


Figure 4.8 The 2-D sheet in **4b** *via* intermolecular O–H···N hydrogen bonds, Ag···Ag, and π ··· π interactions.

4.3.4 Structural Description of $[\text{Ag}_4(\text{CN})_7\{\text{Cd}(2,2'\text{-bipy})\}_2]\text{ClO}_4$ (**4c**)

4c crystallizes in the monoclinic space group $C2/c$ (No. 15). The structure consists of 1-D polymer ladders of $[\text{Ag}_4(\text{CN})_7\{\text{Cd}(2,2'\text{-bipy})\}_2]$ cations, charge balanced by disordered $[\text{ClO}_4]$ counter anions, Figure 4.9. Similar to the coordination environment of the Mn(II) ion in **4a**, the Cd(II) centre in **4c** is *cis* six-coordinated by four 2,2'-bipy nitrogen and two cyanide nitrogen atoms, and adopts a distorted octahedral coordination geometry. The Cd–N_{2,2'-bipy} bond lengths (2.240(3) and 2.279(3) Å) are somewhat shorter than the Cd–N_{CN} bonds lengths (2.265(3) and 2.295(3) Å). The dihedral angle between the least-squares planes through the two 2,2'-bipy ligands containing rings *I/J* and *K/L* is 72.5(1)°.

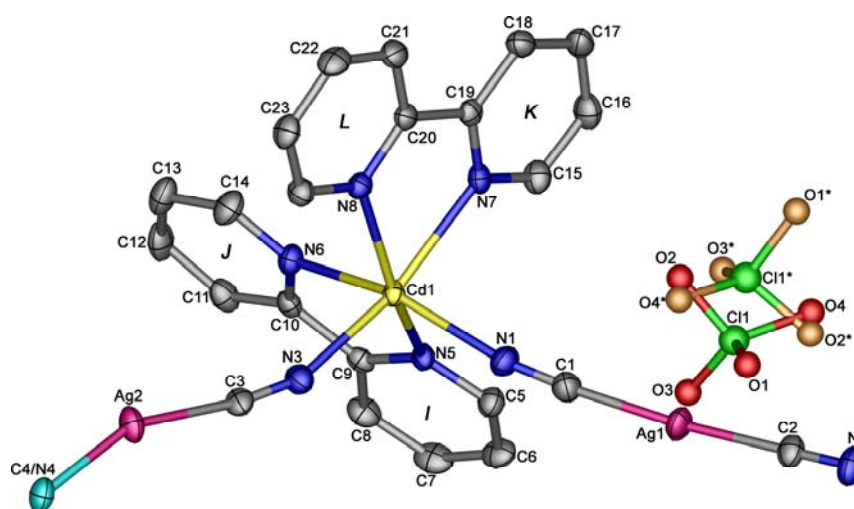


Figure 4.9 Perspective view of **4c** with the atom-numbering scheme. Displacement ellipsoids are drawn at the 50% probability level. Hydrogen atoms are omitted for clarity. The labeling scheme, *I–L*, applied to the phenyl rings are used to identify the rings in the subsequent discussion.

Two different environments can be distinguished for the Ag(I) atoms. Ag1 is coordinated to the Cd(II) centre through the N1 cyanide, and to Ag2 *via* the N2 cyanide, while Ag2 is similarly bonded to the Cd(II) centre through the N3 atom and to another Ag2 *via* the C4/N4 atom in which crystallographic occupancy of C/N atoms in cyanide was 0.5 for each. The $[\text{Ag1}(\text{CN})_2]^-$ and $[\text{Ag2}(\text{CN})_2]^-$ groups in **4c** do not have similar geometrical characteristics. Site Ag1 is almost linear, while the Ag2 site is more bent. The C–Ag–C bond angles are $174.8(1)$ and $157.3(1)^\circ$ for C1–Ag1–C2 and C3–Ag2–C4/N4, respectively. The Ag–C–N bond angles are in the range $170.0(3)$ to $176.6(3)^\circ$. The Ag–C bond lengths range from $2.046(3)$ to $2.073(3)$ Å which is similar to those found in **4a** and **4b**.

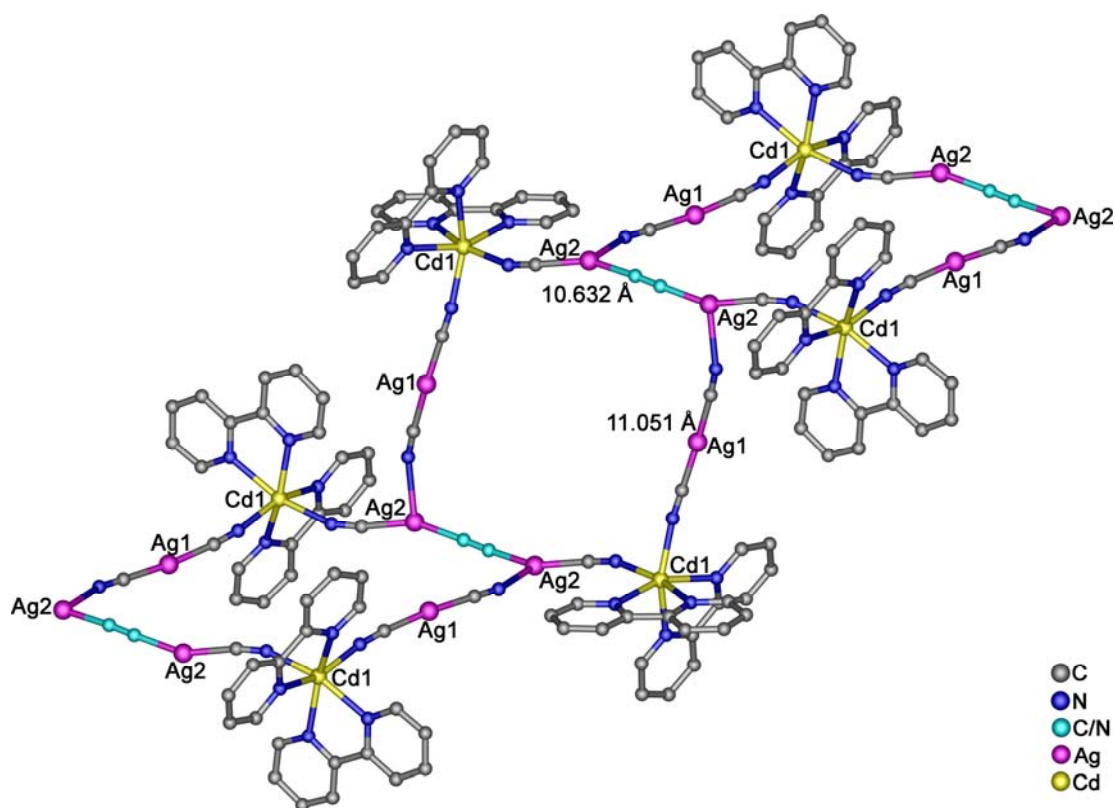


Figure 4.10 View of 1-D ladder like chain in **4c**.

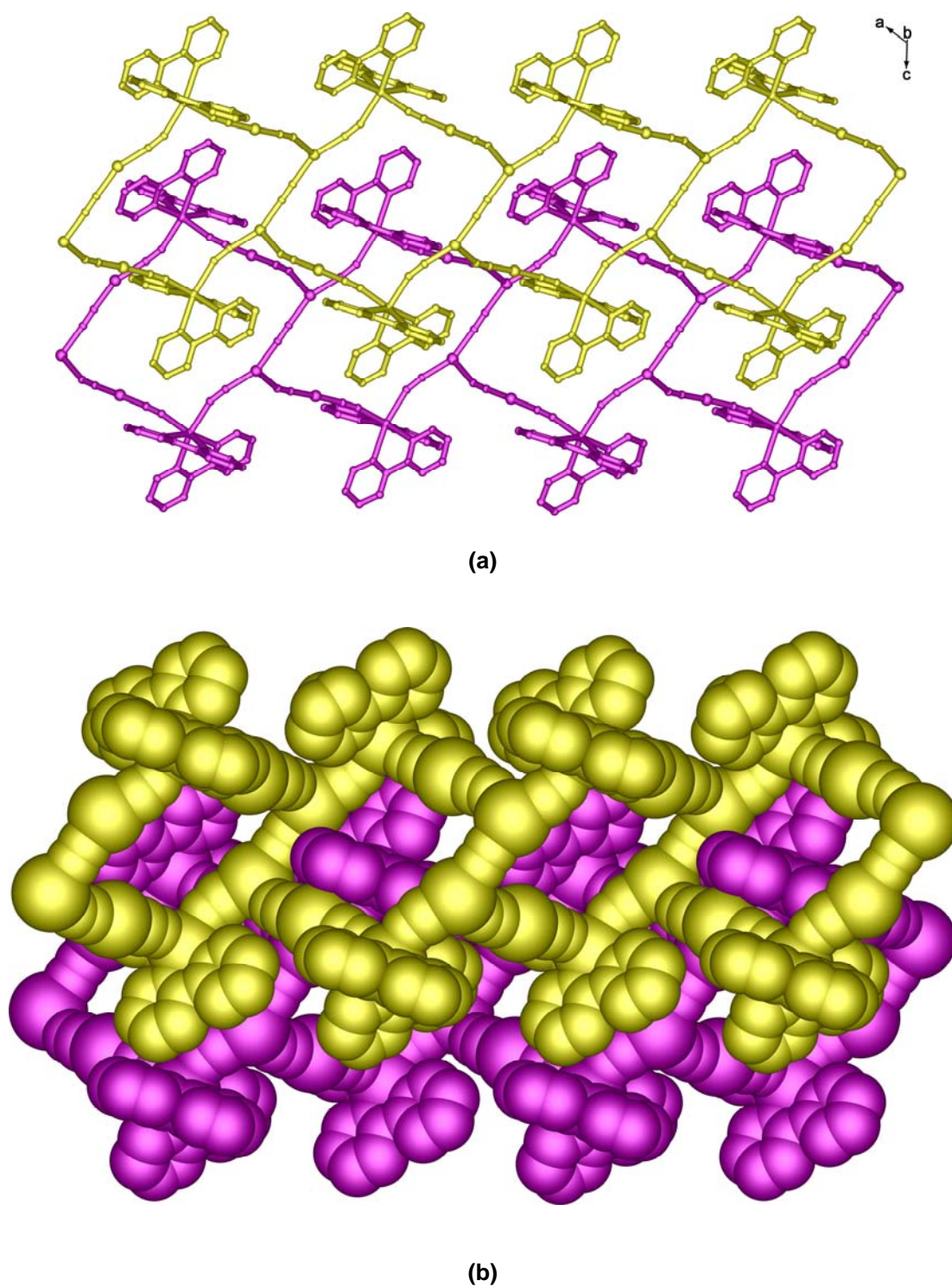


Figure 4.11 (a) Ball and stick and (b) space-filling representation showing two ladder chains in **4c** viewed along the *b* axis.

As shown in Figures 4.10 and 4.11, cationic ladders are generated. The sides of the ladders are built by $[\text{Cd}(2,2'\text{-bipy})]^{2+}$ moieties being bridged by $[\text{Ag}_2(\text{CN})_3]^-$ groups. The rungs are created by the disordered C4/N4 cyanide bridging between Ag2 atoms. The dimension of the 24-membered square cavities is $10.632(3) \times 11.051(3)$ Å. Each square is occupied by a $[\text{Cd}(2,2'\text{-bipy})_2]^{2+}$ fragment from a neighboring ladder chain and a $[\text{ClO}_4]^-$ counter anion. There is no intermolecular $\text{Ag}\cdots\text{Ag}$ contact less than 3.44 Å (Bondi, 1964). The shortest intermolecular $\text{Ag}\cdots\text{Ag}$ distance of 4.043(1) Å is too long to be regarded as a significant argentophilic interaction. There are, however, weak interactions of $\text{Ag}1\cdots\pi$ (ring *J*) at 3.374(1) Å between the ladders.

The adjacent ladder chains are further aggregated into 2-D sheets through the offset head-to-head π - π interactions with the closest distance of approach between the pyridyl rings of 2,2'-bipy molecules of adjacent chains being 3.361(4) Å, as shown in Figure 4.12.

It is also worthwhile to note that the 2-D sheets form a 3-D supramolecular structure *via* an intermolecular edge-to-face $\text{C-H}\cdots\pi$ interaction. The H13 atoms point toward the faces of aryl rings *I* at a distance of 2.608(3) Å. A view of the crystal packing along the *b* axis is presented in Figure 4.13. The included $[\text{ClO}_4]^-$ counter anions are located between the cationic chains, and interact with the 2,2'-bipy of the cationic chains, forming $\text{C}\cdots\text{O}$ hydrogen bonds with the distances ranging from 3.179(14) to 3.297(10) Å (Table 4.5). These weak hydrogen bonds no doubt help to stabilize the supramolecular 3-D framework of **4c**.

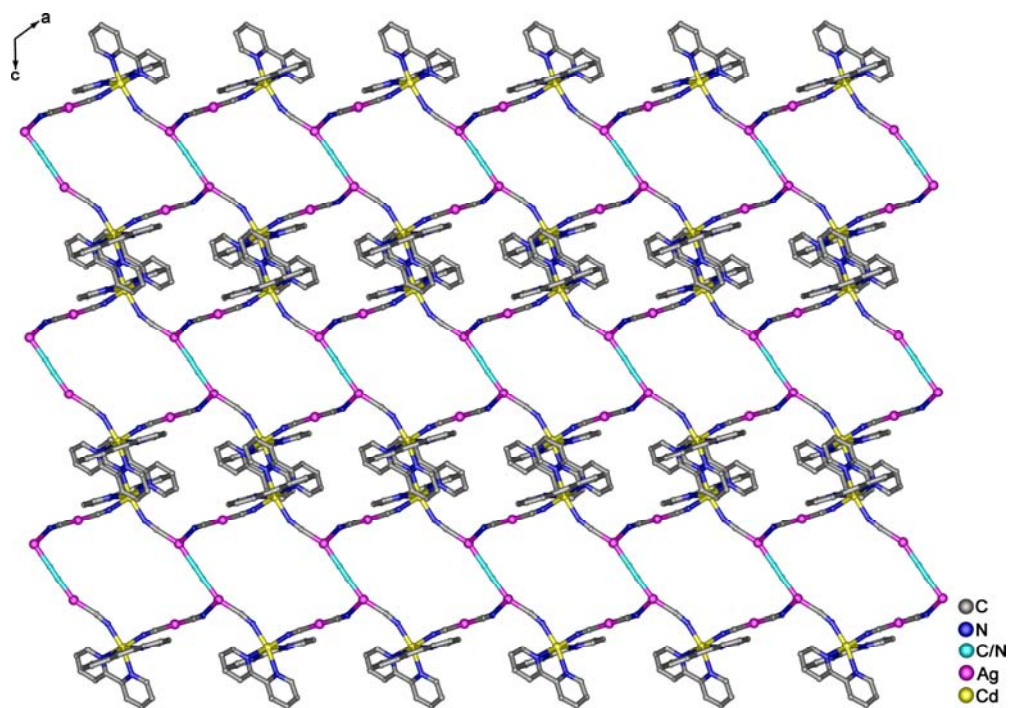


Figure 4.12 The 2-D sheet in **4c** *via* intermolecular $\pi \cdots \pi$ interactions.

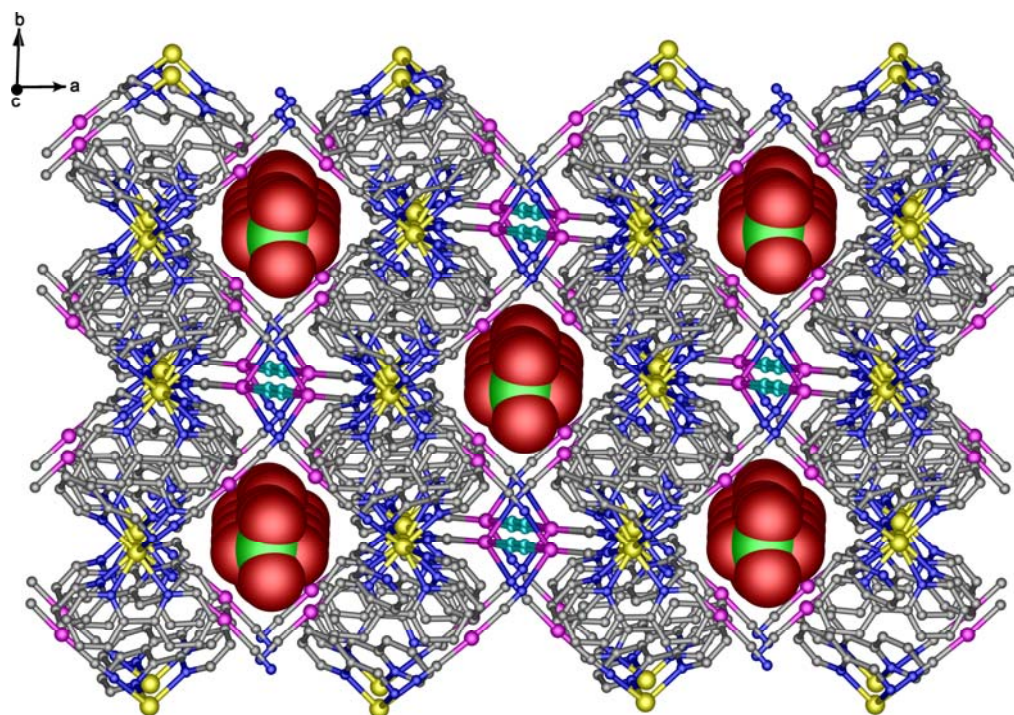


Figure 4.13 Crystal packing in **4c** along the *a* axis. Included perchlorate counter anions represented as space-filling model.

4.3.5 Structural Description of $[\{\text{Ag}(\text{CN})_2\}_2\text{Cd}(2,2'\text{-bipy})]$ (**4d**)

4d was separated from the same reaction as **4c**. Single crystal X-ray analysis reveals that **4d** is composed of an interpenetrated polymeric structure without the present of any solvent molecules. **4d** crystallizes in the monoclinic space group $P2_1/c$ (No. 14). The asymmetric unit contains two independent Cd(II) and four distinct Ag(I) centers, all of which each lie on general positions, Figure 4.14.

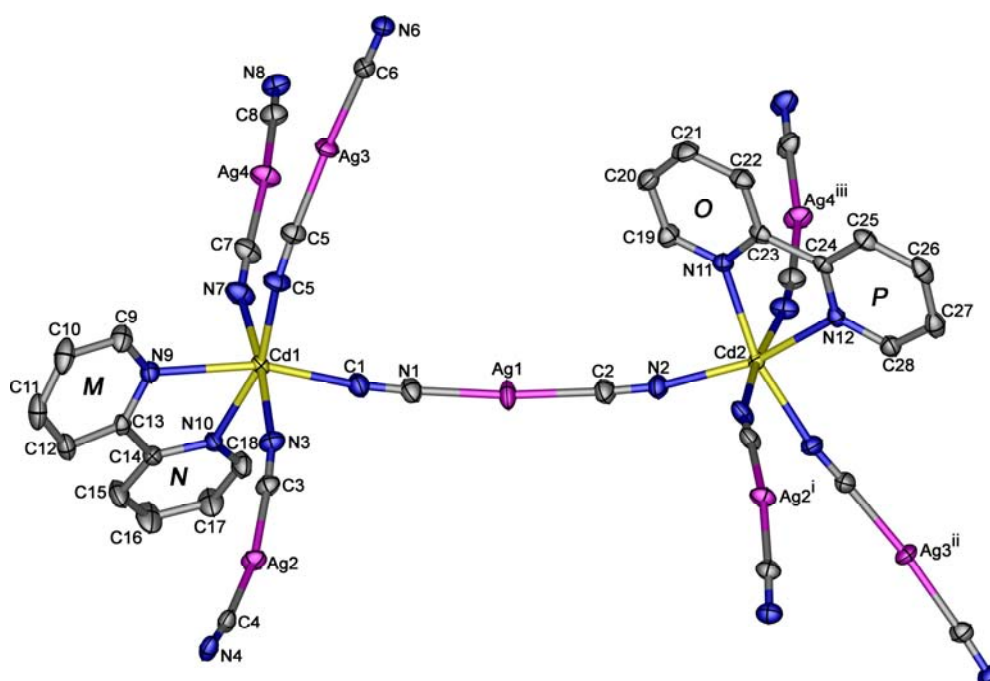


Figure 4.14 Perspective view of **4d** with the atom-numbering scheme. Displacement ellipsoids are drawn at the 50% probability level. Hydrogen atoms are omitted for clarity. The labeling scheme, M – P , applied to the phenyl rings are used to identify the rings in subsequent discussion. Symmetry codes: (i) $2-x, -1/2-y, -1/2-z$; (ii) $1+x, -1/2-y, 1/2+z$; (iii) $1-x, -1/2+y, 1/2-z$.

The Cd(II) center has a slightly distorted $\{CdN_6\}$ octahedral coordination sphere with two 2,2'-bipy nitrogen and four cyanide nitrogen atoms. The Cd–N_{2,2'-bipy} bond lengths in **4d** range from 2.350(3) to 2.372(2) Å, and are slightly longer than the Cd–N_{CN} bond lengths, 2.257(2) and 2.387(2) Å. The four [Ag(CN)₂] groups in **4d** are very similar, and are somewhat bent. The C–Ag–C bond angles are in the 166.4(1) to 172.8(1)° range, while the Ag–C–N bond angle range from 171.9(2) to 176.7(3)°. The Ag–C bond lengths vary in the range 2.050(3) to 2.064(3) Å, and are essentially the same as those found in **4c**. It should be noted that the 2,2'-bipy ligand coordinated to Mn²⁺ centre is not planar. R. m. s. deviation of fitted atoms from the best plane calculated using twelve atoms (rings *M/N*) is 0.20 Å with the largest deviation being 0.297(2) Å at C12. The dihedral angle between the two planes is 23.6(1)°.

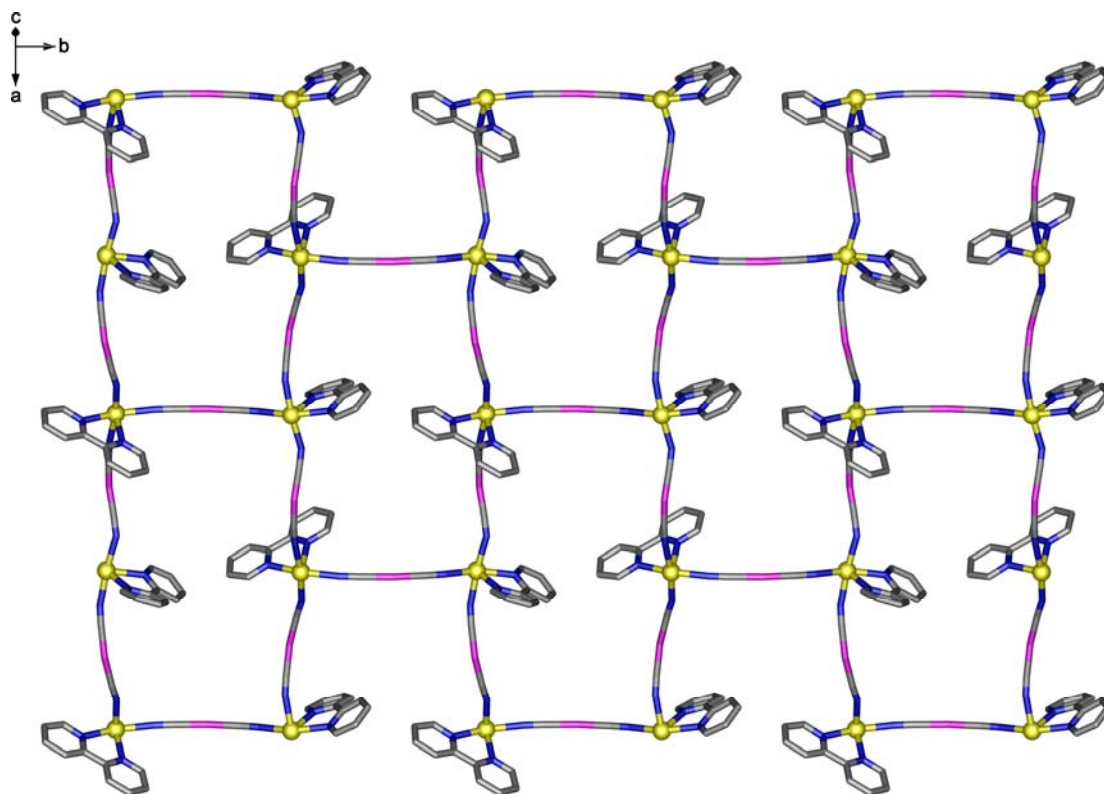


Figure 4.15 The 2-D sheet with the (6,3) topology in **4c**.

The Cd(II) ions are linked by the four different types of $[\text{Ag}(\text{CN})_2]^-$ ligands into a 3-D network. The net may be described in terms of 2-D sheets in which the $[\text{Cd}(2,2'\text{-bipy})]^{2+}$ moieties are bridged by the Ag1, Ag2 and Ag4 containing anions. These sheets have a brickwork like (6,3) topology, Figure 4.15, with the rectangular windows having the dimensions $10.526(2) \times 21.650(2) \text{ \AA}$. Each sheet is then bridged by the Ag3 anions to both the sheet above and the sheet below, to give an overall 3-D net, Figure 4.16. The Ag3 anions bridge the two types of $[\text{Cd}(2,2'\text{-bipy})]^{2+}$ groups, and create square windows. An overall 4-connected net is created, with both types of Cd(II) atoms acting as 4-connecting nodes. Both nodes are topologically equivalent, and thus the net has the Schläfli symbol $4^2.6^3.8$ (Batten and Robson, 1998).

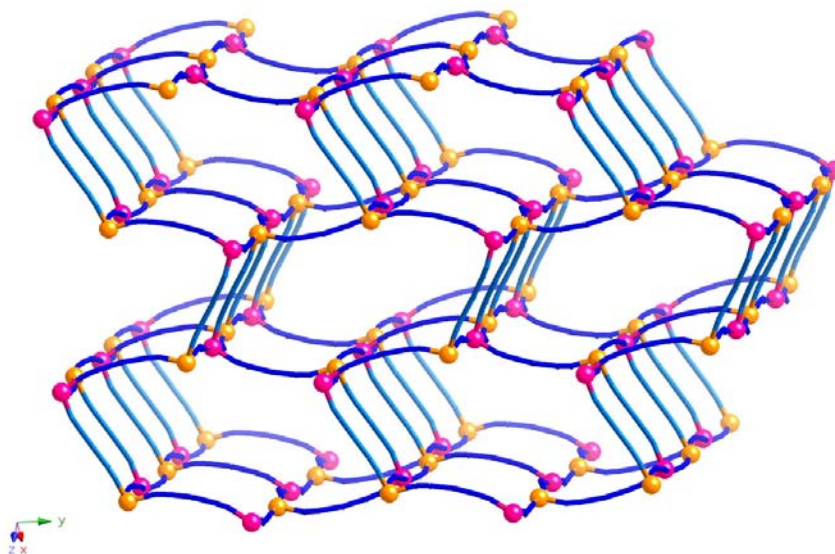


Figure 4.16 Schematic view of the 3-D 4-connected network with $4^2.6^3.8$ topology for **4d**.

The 3-D net resulting the construction of two types of 1-D open channels along the crystallographic b axis, as shown in Figures 4.16 and 4.17. The edge length of the 1-D channel is *ca.* 10.8 Å but no guest molecules are encapsulated in the channels. Instead, the channels of a single 3-D net provide enough space for two other identical nets to interpenetrate, yielding three interpenetrating 3-D nets (4-connected), as shown in Figure 4.18.

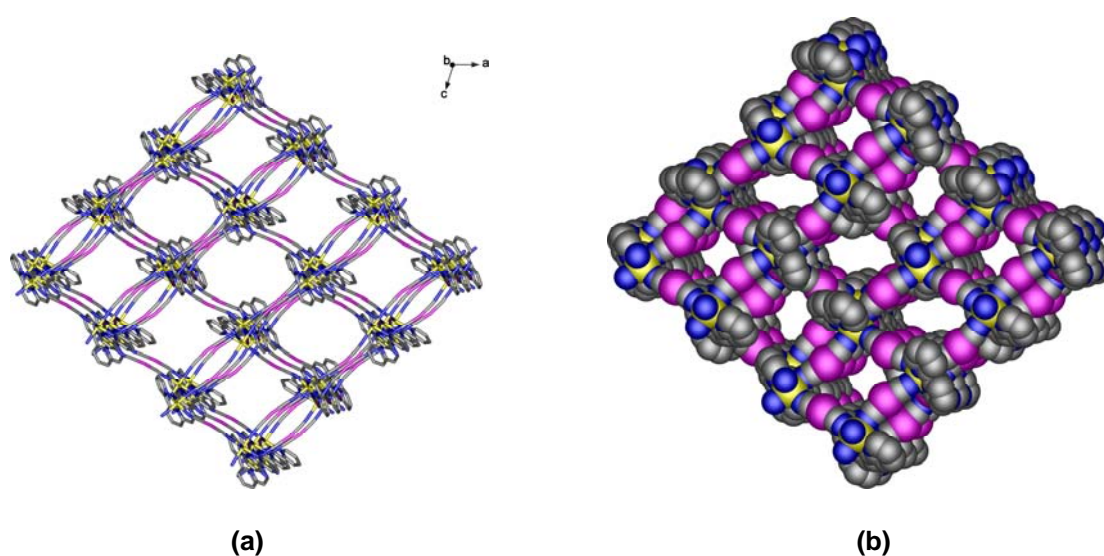


Figure 4.17 (a) Wires/sticks and (b) space filling representations of single 3-D framework with 1-D channels in **4d** viewed along the b axis.

An additional factor that also appears to influence the packing of the structure is weak C–H \cdots π hydrogen bonding between the 2,2'-bipy ligands of the adjacent nets. H \cdots π (ring M) separations are 2.544(4) and 2.977(4) Å. As mentioned above, this interaction causes the pyridyl rings (M and N) of the 2,2'-bipy ligands to not be coplanar but be twisted by 23.6(1)°. The interactions observed in **4d** presumably assist the formation interpenetrated nets, similar to the triple interpenetrated 3-D SCO polymers of [Fe(pmd)(H₂O){M(CN)₂}₂] \cdot H₂O, where pmd = pyrimidine, M = Ag or

Au (Neil *et al.*, 2003). Indeed, it is possible that the Fe(II) analogues of **4d** would show SCO features.

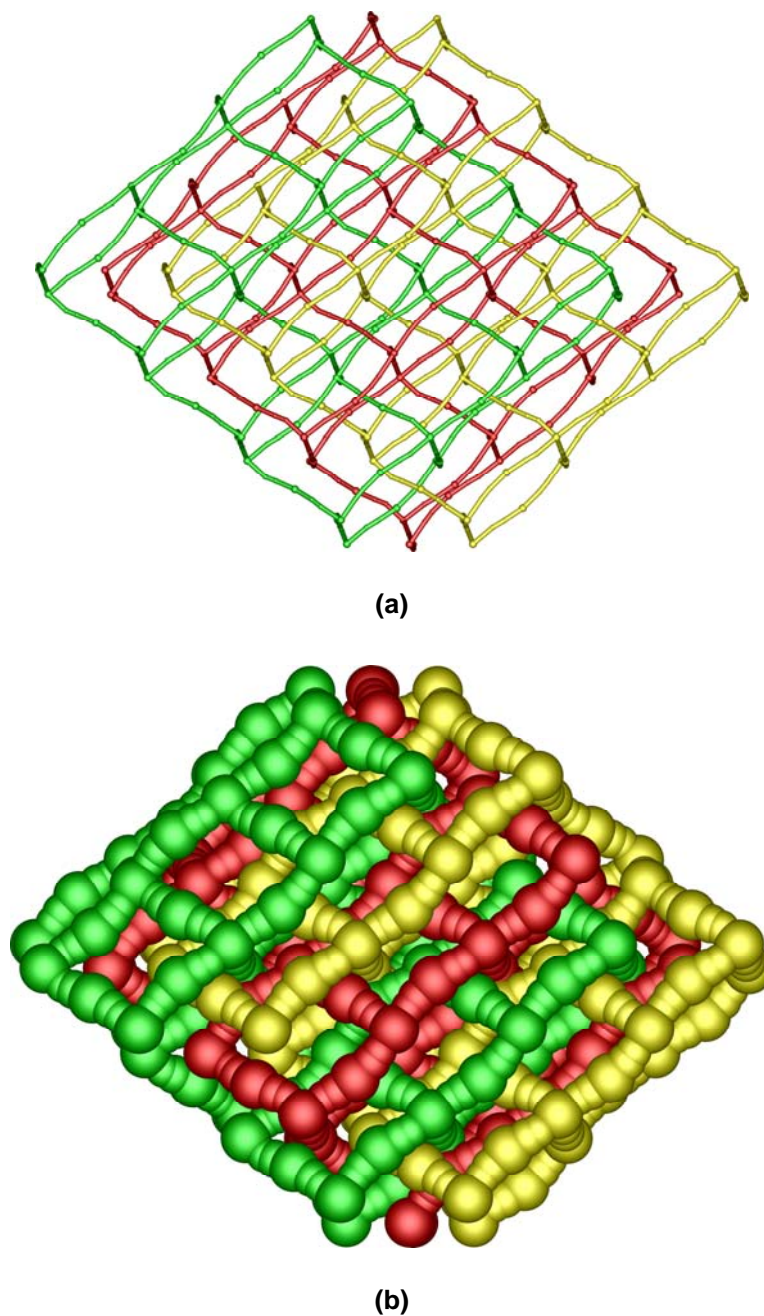


Figure 4.18 (a) Ball and stick and (b) space-filling representations of the interpenetrating nets along the *b* axis of **4d**, the alternating frameworks are shown in yellow, red and green. The 2,2'-bipy molecules are omitted for clarity.

In addition, although these 1-D channels of single 3-D nets have significant size, despite the occurrence of interpenetration of second and third 3-D nets which reduces the void volume, there is no significant void space as calculated by PLATON (Spek, 1995).

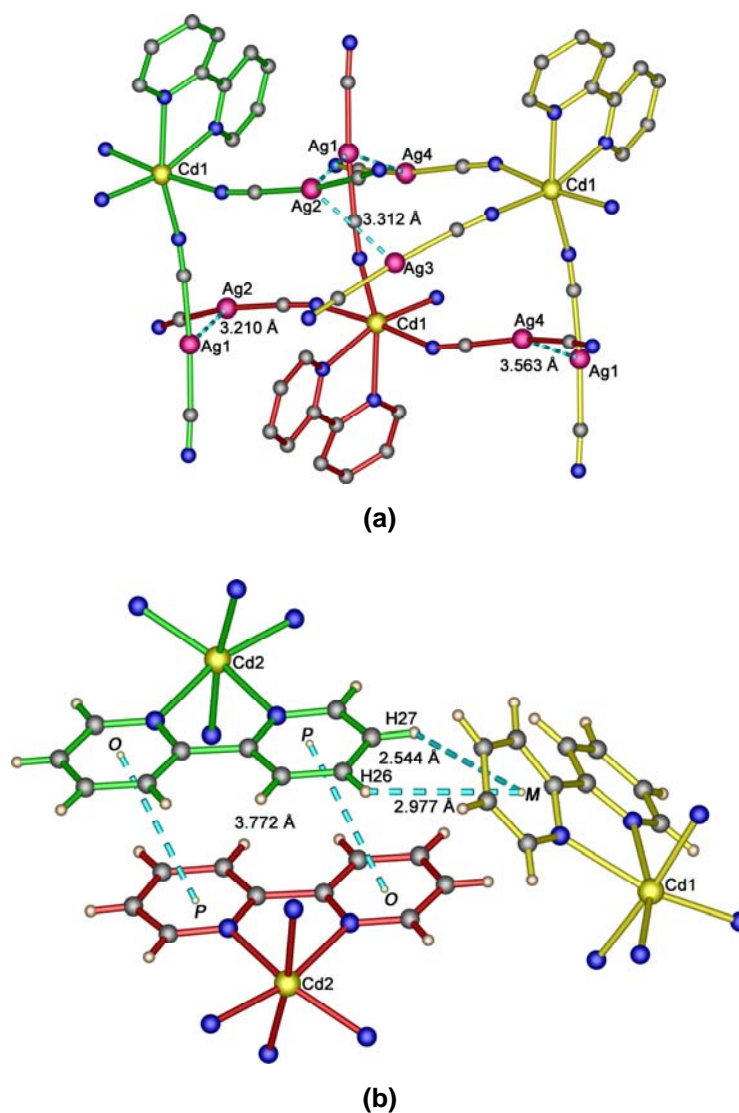


Figure 4.19 Views of a fragment of the alternating nets in **4d** showing (a) the Ag...Ag argentophilic and (b) C-H... π and π ... π interactions (dotted lines).

4.3.6 Magnetic Properties of $[\text{Ag}(\text{CN})_2\text{Mn}(2,2'\text{-bipy})_2(\text{H}_2\text{O})]\cdot\text{Ag}(\text{CN})_2$ (**4b**)

Complex **4b** shows a Curie-Weiss dependence of χ_{Mn} versus temperature as shown in Figure 4.20, with the corresponding μ_{eff} values being independent of temperature, $5.8 \mu_{\text{B}}$, indicating no spin-spin coupling is occurring in agreement with the crystal structure.

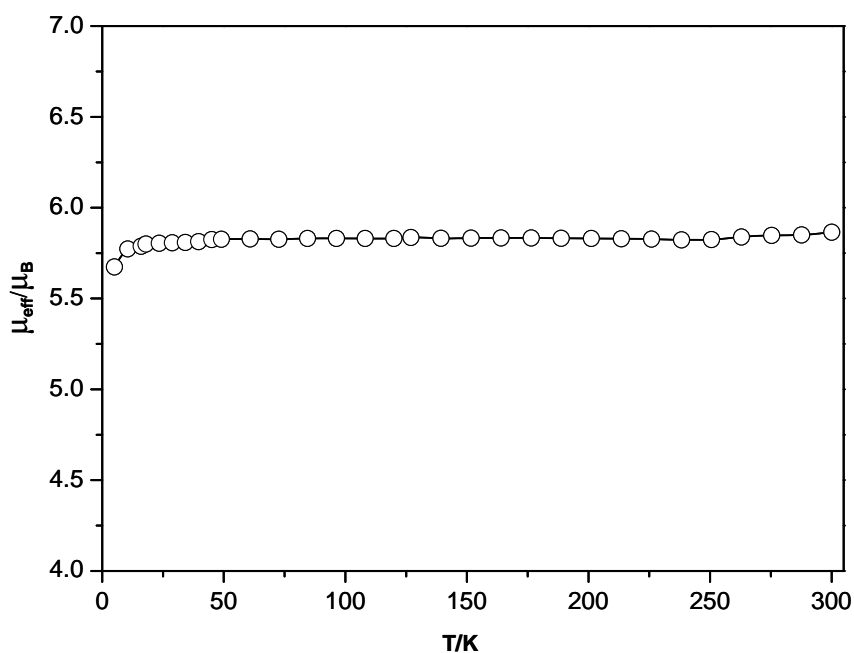


Figure 4.20 Plot of magnetic moment in field of 1 T for **4b**. The solid lines are not calculated plots.

4.4 Conclusions

At a synthetic level, the used of a $[\text{Ag}(\text{CN})_2]^-:\text{M}^{\text{II}}:2,2'\text{-bipy}$ mole ratio of 1:1:1 led in only one case, **4d**, to the stoichiometry $\text{M}^{\text{II}}:2,2'\text{-bipy}$ of 1:1, desired in the aim of making square tube topologies. The other compounds, **4a–4c**, all crystallized with the *cis*-(2,2'-bipy)₂M fragments in mononuclear or polynuclear compounds, showing that this is a stable moiety. Perusal of Figure 4.15 show that, in **4d** the square “rings” have the four *cis*-oriented $[\text{Ag}(\text{CN})_2]^-$ group required to construct

tubes. However, because the 2,2'-bipy chelates are not all on the “outer” blocking position of each square, this allows bridging to continue to join the squares, “side ways”, into extended grids. In the *cis*-(2,2'-bipy)₂M-containing species **4a–4c**, the tubes can not, of course, form.

Despite this, the [Ag(CN)₂][−] is a useful building block for the construction of various supramolecular coordination polymers. Among the four complexes, argentophilic (Ag⋯Ag) and other noncovalent interactions of Ag⋯N, Ag⋯π, strong (O–H⋯N) or weak (C–H⋯O, C–H⋯π) hydrogen bonds and π⋯π interactions have an impact on the overall structures as well as playing important roles in increasing supramolecular structural dimensionality.

The influence of Ag⋯N and Ag⋯Ag interactions is apparent on the structures of **4a** and **4b**, respectively, which increase in dimensionality from 0- to 1-D chains. In both complexes, dimensionality is then increased from 1-D chain to 3-D supramolecular network *via* hydrogen bonds and π⋯π interactions. **4c** and **4d** are novel heterobimetallic Cd(II)–Ag(I) cyano bridged coordination polymers. The former forms a 1-D ladder like structure and the latter consists of triply interpenetrating square-grid nets. Although **4c** displays no Ag⋯Ag interactions, there are Ag⋯π, C–H⋯O and π⋯π interactions cross-linked between the 1-D thus yielding a 3-D supramolecular structure. Triply interpenetrated 3-D nets of **4d** are stabilized by a number of Ag⋯Ag contacts as well as weak C–H⋯π and π⋯π interactions. Paramagnetic behaviour with zero antiferromagnetic coupling has been observed in **4b**, in accord with the long Mn^{II}–NC–Ag^I–CN–Mn^{II} covalent bridging. The Mn^{II}–NC–Ag^I–CN–(H₂O)–Mn^{II} bridges in **4b**, were not conducive to spin-spin coupling.

4.5 References

- Allen, F. H., Davies, J. E., Galloy, J. J., Johnson, O., Kennard, O., Macrae, C. F., Mitchell, E. M., Mitchell, G. F., Smith, J. M., and Watson, D. G. (1991). **J. Chem. Inf. Comput. Sci.** 31: 187-204.
- Assefa, Z., Shankle, G., Patterson, H. H., and Reynolds, R. (1994). **Inorg. Chem.** 33(10): 2187-2195.
- Batten, S. R., and Robson, R. (1998). **Angew. Chem. Int. Ed.** 37(11): 1460-1494.
- Batten, S. R., Hoskins, B. F., and Robson, R. (1998). **New J. Chem.** 22(2): 173-175.
- Blessing, R. H. (1995). **Acta Crystallogr., Sect. A: Found. Crystallogr.** 51: 33-38.
- Barbour, L. J. (2001). **J. Supra. Chem.** 1(4-6): 189-191.
- Brandenburg, K., and Putz, H. (2006). **DIAMOND**. Version 3.1e. Crystal Impact GbR, Bonn, Germany.
- Černák, J., Chomič, J., Gravereau, P., Orendáčová, A., Orendáč, M., Kováč, J. Feher, A., and Kappenstein, C. (1998). **Inorg. Chim. Acta** 281: 134-140.
- Colacio, E., Lloret, F., Kivekals, R., Suárez-Varela, J., Sunberg, M. R., and Uggla, R. (2003). **Inorg. Chem.** 42(2): 560-565.
- Crystal Maker. (2006). Crystal Maker Software, Yarnton, England.
- Dance, I., and Scudder, M. (1996). **Chem. Eur. J.** 2(5): 481-486.
- Dasna, I., Golhen, S., Ouahab, L., Daro, N., and Sutter, J.-P. (2001). **Polyhedron** 20 (11-14): 1371-1374.
- Desiraju, G. R. (2003). **Crystal Design: Structure and Function**. 1st ed. Publisher: Chichester: John Wiley Sons Ltd.
- Desiraju, G. R., and Steiner, T. (1999). **The Weak Hydrogen Bond in Structural Chemistry and Biology**. Oxford University Press.

- Dong, W., Wang, Q.-L., Si, S.-F., Liao, D.-Z., Jiang, Z.-H., Yan, S.-P., and Cheng, P. (2003). **Inorg. Chem. Commun.** 6: 873-876.
- Duriska, M. B., Batten, S. R., and Price, D. J. (2006). **Aus. J. Chem.** 59(1): 26-29.
- Emsley, J. (1998). **The Elements**. 3rd ed., Oxford University Press, New York.
- Fernandez, E. J., Lopez-de-Luzuriaga, J. M., Monge, M., Rodriguez, M. A., Crespo, O., Gimeno, M. C., Laguna, A., and Jones, P. G. (1998). **Inorg. Chem.** 37(23): 6002-6006.
- Hermann, H. L., Boche, G., and Schwerdtfeger, P. (2001). **Chem. Eur. J.** 7(24): 5333-5342.
- Hollenman, S. R., Parker, O. J., and Breneman, G. L. (1994). **Acta Crystallogr., Sect. C: Cryst. Struct. Commun.** 50: 867-869.
- Janiak, C. (2000). **J. Chem. Soc., Dalton Trans.** (21): 3885-3896.
- Janiak, C., Uehlin, L., Wu, H.-P., Klüfers, P., Piotrowski, H., and Scharmann, T. G. (1999). **J. Chem. Soc., Dalton Trans.** (17): 3121-3131.
- Lescouëzec, R., Vaissermann, J., Ruiz-Pérez, C., Lloret, F., Carrasco, R., Julve, M., Verdaguer, M., Dromzee, Y., Gatteschi, D., and Wernsdorfer, W. (2003). **Angew. Chem. Int. Ed.** 42(13): 1483-1486.
- Leznoff, D. B., Xue, B.-Y., Batchelor, R. J., Einstein, F. W. B., and Patrick, B. O. (2001). **Inorg. Chem.** 40(23): 6026-6034.
- Liu, X., Guo, G.-C., Fu, M.-L., Liu, X.-H., Wang, M.-S., and Huang, J.-S. (2006). **Inorg. Chem.** 45(9): 3679-3685.
- Magnko, L., Schweizer, M., Rauhut, G., Schütz, M., Stoll, H., and Werner, H.-S. (2002). **Phy. Chem. Chem. Phys.** 4: 1006-1013.
- Merritt, L. L., and Schroeder, E. (1956). **Acta Crystallogr.** 9: 801-804.

- Munoz, M. C., Gaspar, A. B., Galet, A., and Real, J. A. (2007). **Inorg. Chem.** 46 (20): 8182-8192.
- Niel, V., Munoz, M. C., Gaspar, A. B., Galet, A., Levchenko, G., and Real, J. A. (2002). **Chem. Eur. J.** 8(11): 2446-2453.
- Niel, V., Thompson, A. L., Goeta, A. E., Enachescu, C., Hauser, A., Galet, A., Munoz, M. C., and Real, J. A. (2005). **Chem. Eur. J.** 11(7): 2047-2060.
- Niel, V., Thompson, A. L., Muñoz, M. C., Galet, A., Goeta, A. E., and Real, J. A. (2003). **Angew. Chem. Int. Ed.** 42(32): 3760-3763.
- Omary, M. A., Webb, T. R., Assefa, Z., Shankle, G. E., and Patterson, H. H. (1998). **Inorg. Chem.** 37(6): 1380-1386.
- Pyykko, P. (1997). **Chem. Rev.** 97(3): 597-636.
- Ren, Y.-P., Long, L.-S., Huang, R.-B., and Zheng, L.-S. (2005). **Appl. Organomet. Chem.** 19: 1070-1071.
- Robson, R., Abraham, B. F., Batten, S. R., Gable, R. W., Hoskins, B. F., and Liu, J. **In Supramolecular Architecture.** Bein, T., Ed.: American Chemical Society: Washington, DC, 1992: Chapter 19: pp. 258-273.
- Sheldrick, G. M. (1997). **SHELXL-97**: A program for crystal structure refinement. University of Geottinger: Germany.
- Sheldrick, G. M. (1997). **SHELXS-97**: A program for automatic solution of crystal structure. University of Geottinger: Germany.
- Shorrock, C. J., Xue, B.-Y., Kim, P. B., Batchelor, R. J., Patrick, B. O., and Leznoff, D. B. (2002). **Inorg. Chem.** 41(25): 6743-6753.
- Soma, T., and Iwamoto, T. (1996). **Inorg. Chem.** 35(7): 1849-1856.

- Soma, T., Yuge, H., and Iwamoto, T. (1994). **Angew. Chem. Int. Ed.** 33(15-16): 1665-1666.
- Spek, A. L. (1995). **PLATON**. Molecular Geometry Program. University of Utrecht, The Netherlands.
- Tričiková, L., Potočňák, I., and Chomič, J. (2003). **Transition Met. Chem.** 28(7): 808-815.
- Victoria, U., Thorsten, P., and Hans, H. (2005). **Angew. Chem. Int. Ed.** 44(18): 2794-2797.
- Withersby, M. A., Blake, A. J., Champness, N. R., Hubberstey, P., Li, W. S., and Schroder, M. (1997). **Angew. Chem. Int. Ed.** 36(21): 2327-2329.
- Zhang, H., Cai, J., Feng, X.-L., Li, T., Li, X.-Y., and Ji, L.-N. (2002). **Inorg. Chem. Commun.** 5(9): 637-641.
- Zhang, H.-X., Chen, Z.-N., Su, C.-Y., Ren, C., and Kang, B.-S. (1999). **J. Chem. Crystallogr.** 29(12): 1239-1243.

CHAPTER V

SYNTHESIS, STRUCTURE, AND

MAGNETIC PROPERTIES OF 3-D CYANIDE-BRIDGED

HOMOMETALLIC COORDINATION POLYMERS

5.1 Introduction

The design and synthesis of polymeric cyano bridged metal complexes has received much attention over the past three decades due to their interest in the fields of magnetic (Verdaguer *et al.*, 1999; Ohba and Ōkawa, 2000, Černák *et al.*, 2002), electrochemical (Karyakin, 2001), and microporous features (Hoskins and Robson, 1990; Zheng *et al.*, 2005; Kepert, 2006; Chapman and Chupas, 2007). The diamagnetic, square-planar anions $[\text{M}(\text{CN})_4]^{2-}$, where M = Ni, Pt, and Pd, are ideal building blocks for constructing of coordination polymers, due to the ability of the four cyanide groups to connect to other metal atoms, and thus build up molecular assemblies either heterometallic or homometallic with various degrees of dimensionality (Muga *et al.*, 2004). Among such materials were the first 2-D Hofmann-like structures of formula $[\text{Fe}(\text{py})_2\text{Ni}(\text{CN})_4]$, where py = pyridine, exhibiting spin-crossover (SCO) properties (Kitazawa *et al.*, 1996). In this system, the $[\text{Ni}(\text{CN})_4]^{2-}$ moiety acts as an anionic “ligand” in the related fashion to the anionic ligand NCS^- observed, for example, in 3-D structure of iron(II) SCO compounds of $[\text{Fe}_2(\text{azpy})_4(\text{NCS})_4] \cdot (\text{guest})$, azpy = *trans*-4,4'-azopyridine (Halder *et al.*, 2002).

Following this early work by Kitazawa *et al* and Real *et al* reported the use of 2-connecting pyridine ligands such as pyrazine to increase the dimensionality of coordination polymers, resulting in 3-D Hofmann structures of the type $[\text{Fe}(\text{pyz})\text{M}^{\text{II}}(\text{CN})_4]$, where pyz = pyrazine, M^{II} = Ni, Pd, Pt (Niel *et al.*, 2001; Bonhommeau *et al.*, 2005). Similar structural motifs were obtained when aliphatic bidentate amines were used in the $\text{Cd}-[\text{Ni}(\text{CN})_4]^{2-}$ system (Kitazawa *et al.*, 1991). These pyrazine-bridged compounds have similar cooperative SCO properties and characteristic change of color upon spin change, and to the pyridine 2-D species. From a reactivity point of view, Iwamoto and co-workers showed that the rigidity of the Hofmann type clathrate frameworks allows for shape and size selective inclusion of organic solvents or water molecules to fill up the void space stabilizing the crystal structure. The absorption and/or desorption of guest molecules may reveal potential applications in the areas of separation and catalysis (Nishikiori and Iwamoto, 1986; Park and Iwamoto, 1992; Yuge and Iwamoto, 1993; 1994; Yuge *et al.*, 1995; Yuge, Noda and Iwamoto, 1996).

The tetracyanometallate moieties (generally formed by d^8 metal ions) are low-spin and diamagnetic, and thus cannot exhibit intrinsic spin and magnetic properties as do the $S = 1/2$ entities such as d^5 (low-spin) $[\text{Fe}^{\text{III}}(\text{CN})_6]^{3-}$. Therefore, from a magnetic point of view, the use of $[\text{M}^{\text{II}}(\text{CN})_4]^{2-}$ building blocks has received little attention for designing magnetically ordered coordination polymers, but they can provide second neighbor magnetic interactions across the five atom NC–Ni–CN bridge. Importantly, the cyanide ligand can also participate in noncovalent interactions such as hydrogen bonding and weaker electrostatic contacts. It has been suggested that hydrogen bonds and π – π interactions between neighbouring aromatic

rings may serve as weak exchange pathways between paramagnetic centers (Goodson *et al.*, 1994; Van Langenberg *et al.*, 1997). Such a situation was observed in the complex $[\text{Ni}(\text{CN})_4\text{Cu}(\text{en})_2]$, where en = 1,2-diaminoethane (Oredáč *et al.*, 1995). This compound has structure consisting of 1-D 2,2-*TT* chains of composition $[-\text{Cu}(\text{en})_2-\text{N}\equiv\text{C}-\text{Ni}(\text{CN})_2-\text{C}\equiv\text{N}-]_n$, ($T = \textit{trans}$), formed by $[\text{Ni}(\text{CN})_4]^{2-}$ anions linked *via* two cyano groups in the *trans* position to $[\text{Cu}(\text{en})_2]^{2+}$ cations. Low-temperature magnetic and thermodynamic studies indicated that this compound behaved as a 2-D magnet in which hydrogen bonds mediate the exchange coupling. Following this example, a series of 1-D cyanide-bridged bimetallic coordination polymers constructed from $[\text{M}(\text{CN})_4]^{2-}$ acting as the bridge between four-coordinate *bis*(diamine) metal(II) complex, have been structurally and magnetically studied. The most representative examples of these types of complexes were discovered by Černák and co-workers (Černák *et al.*, 2002).

As mentioned in Chapter I (section 1.6) the present work forms part of a research program on the chemistry of cyanide-bridged bimetallic coordination polymers with a primary aim being the synthesis of 1-D tube-like motifs using $[\text{M}(\text{bidentate})(\text{CN})_4]^{2-}$ and $[\text{M}(\text{bidentate})(\text{solvent})_4]^{2+}$ building blocks, where bidentate blocks the 2- and 3-D directions. A more general aim of the project was to study the structural diversity and magnetic properties of cyanide-bridged compounds. In this chapter some novel cyanide-bridged compounds of the types $[\text{Ni}(\text{CN})_4\text{Ni}(\text{en})]\cdot 2\text{H}_2\text{O}$ (**5a**) and $[\text{Ni}(\text{CN})_4\text{Ni}(\text{tn})]\cdot \text{H}_2\text{O}\cdot \text{MeOH}$ (**5b**), having 3-D homometallic frameworks are described, in which the complex anions $[\text{Ni}(\text{CN})_4]^{2-}$ was employed as building block. These compounds are formed reproducibly in high yield (>80%) by a slow diffusion method at room temperature. The $[\text{Ni}(\text{CN})_4]^{2-}$ compound did not, of

course, contain a bidentate chelate and thus the method could not yield tube-like product. The preparation of these compounds and their magnetostructural investigation are presented here.

5.2 Experimental Section

5.2.1 Materials and Physical Measurements

$\text{Ni}(\text{NO}_3)_2 \cdot 6\text{H}_2\text{O}$, $\text{Ni}(\text{ClO}_4)_2 \cdot 6\text{H}_2\text{O}$, $\text{K}[\text{Ni}(\text{CN})_4] \cdot \text{H}_2\text{O}$, en, and tn were commercially available, and were used without further purification. Precursor complex $[\text{Ni}(\text{en})(\text{H}_2\text{O})_4](\text{NO}_3)_2$ was prepared according to the method reported in Chapter III.

Caution!: Cyanide containing compounds are very poisonous. Great care was taken so that its salts did not come into contact with acid, which would liberate highly toxic hydrogen cyanide gas. Cyanide salts should not be touched with the fingers, a spatula was used or small pieces with pincers were handled, and reactions were performed under a fume hood.

Microanalytical measurements (C, H, N) were performed by Campbell Microanalytical Laboratory, Chemistry Department, University of Otago, Dunedin, New Zealand. Infrared spectra of Nujol mulls were recorded using a diamond-ATR cell on a Bruker Opus/IR IFS 55 spectrometer in the range of $600\text{--}4000\text{ cm}^{-1}$ (50 scans, resolution $\pm 4\text{ cm}^{-1}$). Thermogravimetric analysis (TGA) was performed on a Perkin-Elmer TGA 7 thermogravimetric analyzer in the air with a heating rate of $10\text{ }^\circ\text{C}/\text{min}$. Variable-temperature magnetic susceptibility data were obtained by Dr. Boujemaa Moubaraki, Monash University using a Quantum Design MPMS 5 SQUID magnetometer for DC magnetization measurements.

5.2.2 Syntheses

Preparation of $[\text{Ni}(\text{CN})_4\text{Ni}(\text{en})]\cdot 2\text{H}_2\text{O}$ (**5a**)

A crystalline sample of **5a** was obtained using a slow diffusion method in which an aqueous solution of 14 mL capacity was contained in an H-shaped tube, and left in the dark. In a typical experiment procedure, $[\text{Ni}(\text{en})(\text{H}_2\text{O})_4](\text{NO}_3)_2$ (158 mg, 0.5 mmol) was dissolved in 3 mL of distilled water to form a bright blue solution and this was pipetted into one side of the H-tube. $\text{K}_2[\text{Ni}(\text{CN})_4]\cdot\text{H}_2\text{O}$ (120 mg, 0.5 mmol) was dissolved in 3 mL of distilled water to give a bright yellow solution, and this was pipetted into the other side arm of the H-tube. The H-tube was then carefully filled with distilled water. Upon slow diffusion over a period of two weeks, pink block-shaped single crystals of **5a** were formed in the $[\text{Ni}(\text{en})(\text{H}_2\text{O})_4](\text{NO}_3)_2$ containing side of the H-tube. Yield: 96 mg, 80% based on $\text{K}_2[\text{Ni}(\text{CN})_4]\cdot\text{H}_2\text{O}$. Anal. Found (calcd) for $\text{C}_6\text{H}_{12}\text{N}_6\text{Ni}_2\text{O}_2$ ($M_r = 317.59$ g/mol): C, 22.89(22.70); H, 3.75(3.81), N, 26.33 (26.46). ATR-FTIR ($\nu_{\text{max}}/\text{cm}^{-1}$): 669w, 959w, 1019m, 1070w, 1095w, 1317w, 1395w, 1452w, 1597s, 1982w, 2163s, 2324w, 2867w, 2908w, 2960w, 3189w, 3285m, 3340m, 3580m, 3857s. μ_{eff} (300 K) = 3.03 μ_{B} .

Preparation of $[\text{Ni}(\text{CN})_4\text{Ni}(\text{tn})]\cdot\text{H}_2\text{O}\cdot\text{MeOH}$ (**5b**)

A sample of **5b** was prepared following the procedure described above for **5a** using aqueous methanolic (1:1, v/v) solutions. Typically, $\text{Ni}(\text{NO}_3)_2\cdot 6\text{H}_2\text{O}$ (150 mg, 0.5 mmol) and tn (40 mg, 0.5 mmol) were dissolved in 3 mL of MeOH/H₂O to form a blue solution of $[\text{Ni}(\text{tn})(\text{H}_2\text{O})_n]^{2+}$ (in situ), and this was pipetted into one side of a H-tube. $\text{K}_2[\text{Ni}(\text{CN})_4]\cdot\text{H}_2\text{O}$ (120 mg, 0.5 mmol) was dissolved in 3 mL of MeOH/H₂O to give a bright yellow solution, and this was pipetted into the other arm. The H-tube was then carefully filled with MeOH/H₂O solution. Slow diffusion for two weeks

yielded pink-blue block-shaped crystals of **5b** in the $[\text{Ni}(\text{tn})(\text{H}_2\text{O})_n]^{2+}$ containing side. Yield: 120 mg, 85% based on $\text{K}_2[\text{Ni}(\text{CN})_4]\cdot\text{H}_2\text{O}$. Anal. Found (calcd) for $\text{C}_8\text{H}_{16}\text{N}_6\text{Ni}_2\text{O}_2$ ($M_r = 345.64$ g/mol): C, 27.68(27.80); H, 4.53(4.67), N, 24.29 (24.31). ATR-FTIR ($\nu_{\text{max}}/\text{cm}^{-1}$): 640w, 910m, 1016m, 1073w, 1140w, 1279w, 1399w, 1430w, 1457m, 1599m, 2158s, 2830w, 2871w, 2932w, 2972w, 3272m, 3342m, 3455w, 3549w, 3616w. $\mu_{\text{eff}}(300\text{ K}) = 2.99 \mu_{\text{B}}$.

5.2.3 X-Ray Crystallographic Study

Single crystals with dimensions $0.12 \times 0.14 \times 0.20$ mm (**5a**) and $0.08 \times 0.14 \times 0.26$ mm (**5b**) were mounted on a MiTeGen MicroMounts fiber in a small amount of oil and quench cooled to 123(2) K prior to measurements made by Dr. Suzanne M. Neville, Monash University. Reflection intensities were collected on a Bruker X8 APEX CCD diffractometer (Mo K_α radiation, $\bar{\lambda} = 0.71073$ Å) and equipped with an Oxford Instruments nitrogen gas Cryostream. Empirical absorption corrections were applied to all data using SADABS (Blessing, 1995). The structures were solved using SHELXS-97 (Sheldrick, 1997) and refined on F^2 using SHELXL-97 (Sheldrick, 1997) with X-SEED (Barbour, 2001) as a graphics interface.

In the final model all non-hydrogen atoms were given anisotropic atomic displacement parameters. For **5a**, hydrogen atoms attached to oxygen atoms of the water molecules were located in a difference Fourier map and were isotropically. Hydrogen atoms bound to carbon or nitrogen atoms of en molecule were positioned geometrically and refined as riding atoms with C–H and N–H distances of 0.97 and 0.86 Å, respectively, and $U_{\text{iso}}(\text{H})$ values of $1.2U_{\text{eq}}(\text{C},\text{N})$. In compound **5b**, the tn molecule exhibits disorder across the pseudo mirror plane with refined occupancies of approximately 1:1. Standard DFIX and SIMU restraints were used for the dimensions

of the disordered molecule. The disorder in hydrogen occupancy on this molecule was refined using two hydrogen atom sites and the correct geometry was induced using DFIX and DANG restraints (Shelxl-97). A DFIX restraint was also used to refine the hydrogen atoms of water and methanol molecules. Crystal data and details of the data collection, and structure refinement are summarized in Table 5.1. Selected interatomic bond lengths and angles for compounds **5a** and **5b** are given in Table 5.2. Intra- and intermolecular hydrogen bonds in compounds are provided in Table 5.3.

Table 5.1 Summary of crystallographic data for the compounds **5a** and **5b**.

Identification code	5a	5b
Formula	C ₆ H ₁₂ N ₆ Ni ₂ O ₂	C ₈ H ₁₆ N ₆ Ni ₂ O ₂
<i>Mr</i>	317.59	345.64
Crystal system	monoclinic	tetragonal
Crystal color/habit	pink/block	blue/block
Crystal size (mm)	0.12 × 0.14 × 0.20	0.26 × 0.14 × 0.08
Space group	<i>C2/c</i>	<i>P4mbm</i>
<i>a</i> (Å)	11.5925(7)	13.8269(4)
<i>b</i> (Å)	8.9108(5)	13.8269(4)
<i>c</i> (Å)	12.4542(7)	7.0038(4)
β (°)	113.475(2)	90
<i>V</i> (Å ³)	1180.02(12)	1339.01(9)
<i>Z</i>	8	4
<i>D</i> _{calc} (Mg m ⁻³)	1.788	1.715
Temperature (K)	123(2)	123(2)
μ (Mo <i>K</i> α) (mm ⁻¹)	3.19	2.82
<i>F</i> (000)	648	712
θ range (°)	3.0 – 27.5	2.9 – 30.0
Data completeness	0.95	1.00
Limiting indices <i>h</i>	–13 → 15	–17 → 16
<i>k</i>	–11 → 11	–17 → 17
<i>l</i>	–15 → 15	–9 → 7
<i>T</i> _{min} / <i>T</i> _{max}	0.591/0.682	0.528/0.806
Reflections collected/unique	5508/1289	4754/879
<i>R</i> _{int}	0.024	0.030
Data/restraints/parameters	1204/0/91	842/4/78
<i>R</i> ₁ , <i>wR</i> ₂ [all data]	0.022, 0.050	0.027, 0.062
<i>R</i> ₁ , <i>wR</i> ₂ [<i>I</i> > 2 σ (<i>I</i>)]	0.019, 0.049	0.025, 0.061
Goodness of fit, <i>S</i>	1.10	1.17
$\Delta\rho$ _{min} , $\Delta\rho$ _{max} (e Å ⁻³)	0.44, –0.47	0.52, –0.54

Computer programs: Crystal Maker (2006), Diamond v. 3.1e (Brandenburg and Putz, 2006), SADABS (Blessing, 1995), SHELXL-97 (Sheldrick, 1997), SHELXS-97 (Sheldrick, 1997), and X-SEED (Barbour, 2001).

Table 5.2 Selected bond lengths and angles for **5a** and **5b** (Å, °). ^a

[Ni(CN)₄Ni(en)]·2H₂O (5a)			
Ni1–N1	2.060(1)	Ni2–C2	1.860(1)
Ni1–N2	2.094(1)	C1–N1	1.145(2)
Ni1–N3 ⁱ	2.090(1)	C2–N3	1.152(2)
Ni2–C1	1.865(1)	Ni1…Ni1 ⁱⁱ	15.5247(7)
Ni1…Ni2	5.0613(3)	Ni2…Ni2 ⁱⁱⁱ	16.3115(7)
N1–Ni1–N2	93.4(1)	Ni1–C3–N2	106.5(1)
C1–Ni2–C2	91.7(1)	Ni2–C1–N1	176.9(1)
Ni1–C1–N1	174.1(1)	Ni2–C2–N3	177.9(1)
[Ni(CN)₄Ni(tn)]·H₂O·MeOH (5b)			
Ni1–N1	2.100(2)	Ni3–C2	1.865(3)
Ni1–N2	2.077(2)	C1–N2	1.151(4)
Ni1–N3	2.079(2)	C2–N3	1.144(4)
Ni2–C1	1.865(3)	Ni1…Ni1 ^{iv}	7.3909(10)
Ni1…Ni2	5.0911(4)	Ni1…Ni3 ^{iv}	9.8784(5)
Ni1…Ni3	5.0320(2)	Ni2…Ni2 ^v	7.0038(4)
N1–Ni1–N2	88.4(1)	Ni1–N2–C1	176.3(2)
N1–Ni1–N3	87.6(1)	Ni1–N3–C2	163.5(2)
N2–Ni1–N3	92.5(1)	Ni2–C1–N2	176.8(2)
Ni1–N1–C3	121.6(2)	Ni3–C2–N3	178.8(2)

^a Estimated standard deviations of the least significant digits are given in parentheses. Symmetry codes: (i) $-x+1/2, y+1/2, -z+1/2$; (ii) $1-x, 1-y, -z$; (iii) $0.5+x, 0.5+y, -1+z$; (iv) $-x, 1-y, z$; (v) $x, y, -1+z$.

Table 5.3 Hydrogen bond geometries for **5a** and **5b** (Å, °). ^a

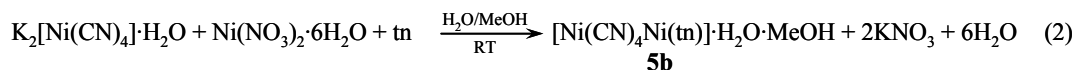
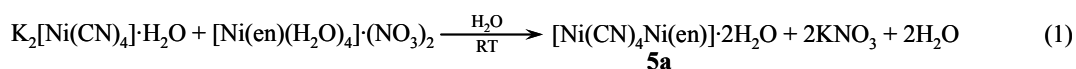
D–H⋯A	d[D–H]	d[H⋯A]	d[D⋯A]	∠[D–H–A]
5a				
N2–H2a⋯O1	0.82(2)	2.30(2)	3.078(3)	160(2)
N2–H2b⋯O1i	0.89(3)	2.43(3)	3.272(3)	159(2)
O1–H1a⋯A(C1≡N1) ⁱⁱ	0.94(6)	2.82	3.640	146
O1–H1b⋯A(C2≡N3) ⁱⁱⁱ	1.09(8)	2.04	3.000	147
5b				
N1–H1b⋯O1	0.92	2.22	3.060(5)	152
O1–H1⋯O2 ^{iv}	0.90(2)	1.96(2)	2.847(9)	171(5)
C3–H3b⋯O1 ^v	0.99	2.85	3.315(6)	109
O2–H2⋯A(C1≡N1)	0.91(7)	2.50	3.283	145
O2–H2⋯A(C2≡N3) ^{vi}	0.91(7)	3.06	3.566	117

^a Estimated standard deviations of the least significant digits are given in parentheses. *A* is the mid-point of the bridging cyano group of a neighboring chain. Symmetry codes: (i) 0.5–*x*, 0.5+*y*, 0.5–*z*; (ii) 0.5+*x*, 0.5+*y*, *z*; (iii) 0.5–*x*, 1.5–*y*, 1–*z*. (iv) –*x*, *y*, *z*; (v) 0.5–*x*, 0.5–*y*, 1–*z*; (vi) *x*, *y*, –*z*.

5.3 Results and Discussion

5.3.1 Syntheses

The compounds [Ni(CN)₄Ni(en)]·2H₂O (**5a**) and [Ni(CN)₄Ni(tn)]·H₂O·MeOH (**5b**) were synthesized (close to quantitatively) by slow evaporation of aqueous solution for **5a**, and an aqueous/methanolic (1:1, v,v) solution for **5b**. H-shaped tubes were employed, and left in the dark at room temperature. The syntheses involved equations 1 and 2, respectively.



Attempts to grow single crystals of $[\text{Ni}(\text{CN})_4\text{Ni}(\text{tn})]\cdot 2\text{H}_2\text{O}$ in aqueous solution using the same procedure as in **5a** were unsuccessful. So the mixed solvent was used. Change of counter ions from $\text{Ni}(\text{NO}_3)_2\cdot 6\text{H}_2\text{O}$ to $\text{Ni}(\text{ClO}_4)_2\cdot 6\text{H}_2\text{O}$ does not have any significant effect on the nature of the products, provided the reactant ratios of 1:1 remain the same. This is perhaps not surprising since anions are not in the product. More significantly, the dimensionality of cyanide-bridged homometallic coordination polymers in the $\text{Ni}(\text{CN})_4\text{-Ni-L}$ system (where $\text{L} = \text{en}$ or tn) is increased by controlling the stoichiometry of Ni:L . In the present system, the reaction of $\text{L:Ni:Ni}(\text{CN})_4$ in the molar ratio of 1:1:1 yielded 3-D network structures in **5a** and **5b** (below). In contrast, Černák and co-workers used 2 mole equivalents of en per Ni , $[\text{Ni}(\text{en})_2(\text{H}_2\text{O})_2]^{2+}$, and obtained coordination polymers containing 1-D chains of $[\text{Ni}(\text{CN})_4\text{Ni}(\text{en})_2\}$. At higher en:Ni ratios (1:3), $[\text{Ni}(\text{CN})_4\text{Ni}(\text{en})_3\}$ was produced (Černák *et al.*, 2002).

5.3.2 Structural Description of $[\text{Ni}(\text{CN})_4\text{Ni}(\text{en})]\cdot 2\text{H}_2\text{O}$ (**5a**)

Compound **5a** crystallizes in the monoclinic system with space group $C2/c$ (No. 15). The structure is a neutral 3-D nickel cyanide framework. The detailed coordination environments for both kinds of metal ions in the lattice are shown in Figure 5.1. The asymmetric unit contains nine non-hydrogen atoms with two crystallographically distinct Ni atoms. Atoms Ni1 and Ni2 lie on 2-fold rotation axes

and inversion centers, respectively. The uncoordinated lattice water molecule lies on a general position.

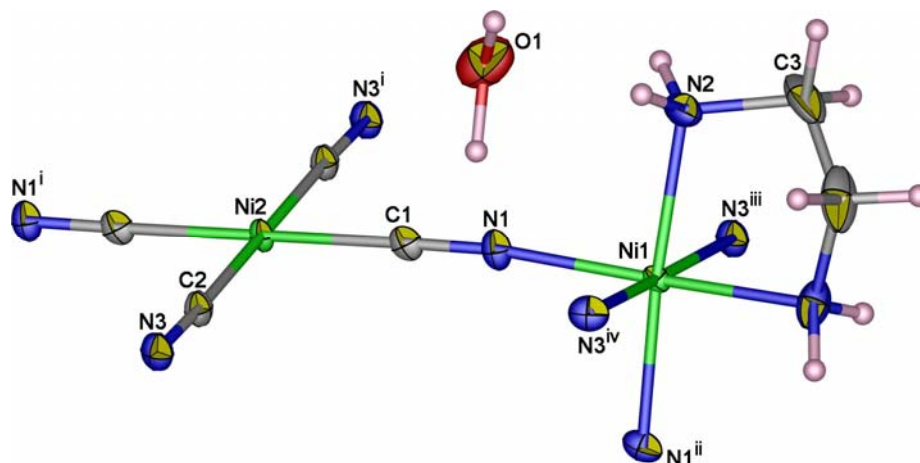


Figure 5.1 View of **5a** with the atom-numbering scheme. Displacement ellipsoids are drawn at the 50% probability level. Hydrogen atoms are shown as small spheres of arbitrary radii. Symmetry codes: (i) $0.5-x, 0.5-y, 1-z$; (ii) $-x, y, 0.5-z$; (iii) $0.5+x, 0.5+y, z$; (iv) $0.5-x, 0.5+y, 0.5-z$; (v) $-x, y, 0.5-z$.

The central Ni1 atom exhibits octahedral geometry. Of the six nitrogen atoms, four positions are occupied in the equatorial plane by two bridging cyano groups and a chelating en molecule. The remaining two nitrogen atoms belong to two N-bonded bridging cyano groups situated in the axial sites. The chelating en molecule has the *gauche* conformation. The angle between the planes N2–Ni1–N2ⁱ and C3–Ni1–C3ⁱ (symmetry operation: (i) $-x, y, 0.5-z$) is $28.3(1)^\circ$. This value is comparable with the value of $24.1(8)^\circ$ and $25.6(7)^\circ$ observed in $[\text{Ni}(\text{CN})_4\text{Ni}(\text{en})_2] \cdot 2.16\text{H}_2\text{O}$ (Černák *et al.*, 1990), and $29.6(3)^\circ$ found for the anhydrous complex $[\text{Ni}(\text{CN})_4\text{Ni}(\text{en})_2]$ (Černák *et al.*, 1988). The largest deviation from the least squares plane for Ni1 through

$N1/N1^i/N2/N2^i$ is $-0.081(1)$ Å at $N2^i$ (symmetry operation: (i) $-x, y, 0.5-z$). The Ni1 center is exactly located in the plane. The Ni– N_{en} distance of $2.094(1)$ Å is comparable with those observed in the analogues en complexes $[Ni(en)(H_2O)_4](NO_3)$ (McDougall and Hancock, 1980) and $[Ni(en)(H_2O)_4]\cdot SO_4\cdot 2H_2O$ (Healy *et al.*, 1984). Moreover, the distances Ni– N_{en} are a little shorter than the bond distances of the same type in some *bis*(en), $[Ni(en)_2(H_2O)_2][ClO_4]_2$ (Minacheva *et al.*, 1974), or *tris*(en), $[Ni(en)_3][NO_3]_2$ (Korp *et al.*, 1980) complexes. This means that the en ligand in compound **5a** is bonded more strongly than in *bis*(en) or *tris*(en) complexes. The Ni– N_{CN} distances exhibit different values. Namely, the Ni–N1 bonds ($2.064(1)$ Å) in the *cis* position with respect to the bridging cyano groups are somewhat shorter compared to that in the *trans* position of Ni–N3 ($2.092(1)$ Å). A similar elongation of the *trans*-positioned bonds versus *cis*-positioned bonds was observed the $[Ni(CN)_4Ni(en)_2]$, (Černák *et al.*, 1988) and $[Ni(CN)_4M(en)_2]_2(PhNH_2)$, where $M^{II} = Cd, Zn, Cu$ and Ni (Yuge and Iwamoto, 1994).

The overall mean $C\equiv N$ bond length of $1.149(2)$ Å is also in accordance with the sum of the triple bond radii of C and N atoms (0.603 and 0.55 Å, respectively) found in the work of Pauling (1960). Looking at the Ni– $N\equiv C$ angle, Ni1–N1 \equiv C1 at $174.1(1)^\circ$ is less bent than Ni1–N3 \equiv C2, $167.1(1)^\circ$.

The Ni2 atom has a NiC_4 chromophore, and exhibits a slightly deformed square planar geometry. The maximum deviation of the C atoms from the least-squares plane through the $[Ni(CN)_4]^{2-}$ ion (defined by C1/N1/C2/N3/Ni2/C1ⁱ/N1ⁱ/C2ⁱ/N3ⁱ (symmetry operation: (i) $0.5-x, 0.5-y, 1-z$) is $0.489(2)$ Å for C1ⁱ. This means that the $[Ni(CN)_4]^{2-}$ anion is not quite as planar as in the compound $Na_2[Ni(CN)_4]\cdot 3H_2O$, the largest deviation in that plane being 0.027 Å at 295 K and

0.022 Å at 30 K (Ptasiewicz-Bak *et al.*, 1998). Comparison of the structural parameters of the $[\text{Ni}(\text{CN})_4]^{2-}$ anion with other tetracyanonickelates(II) complexes shows that the bond lengths and angles have typical values, and are similar to those found in $[\text{Ni}(\text{CN})_4\text{Ni}(\text{en})_2]$ and $[\text{Ni}(\text{CN})_4\text{Ni}(\text{en})_2]\cdot 2.16\text{H}_2\text{O}$ complexes, reported by Černák and co-workers (1988; 1990).

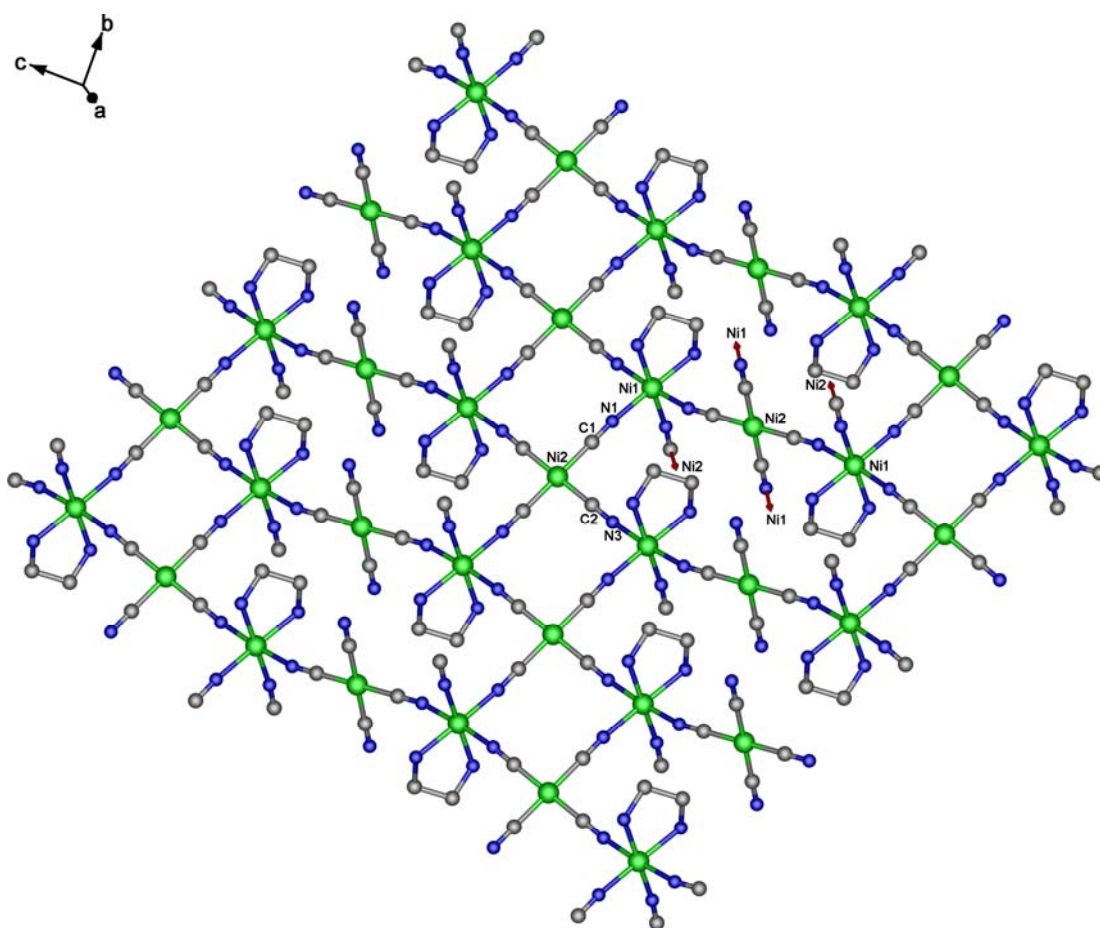


Figure 5.2 The 2-D sheet motif in **5a**. Hydrogen atoms and water molecules are omitted for clarity.

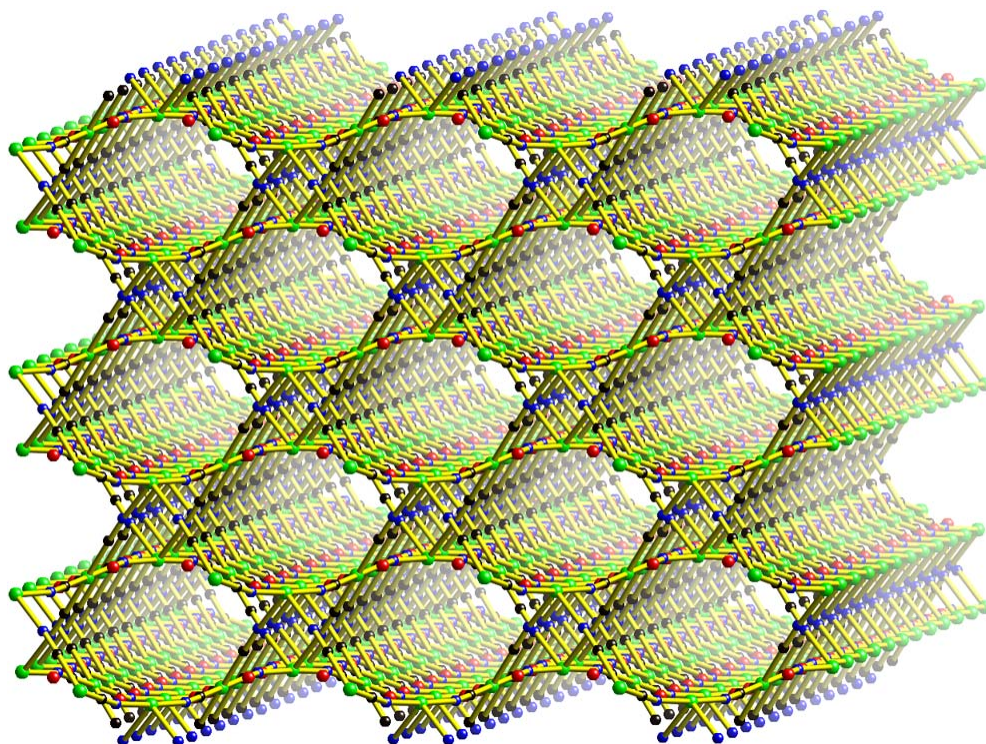


Figure 5.3 Projection of the 3-D network structure of **5a** viewed slightly offset from the *c* axis, en molecules are omitted.

Each $[\text{Ni}(\text{CN})_4]^{2-}$ is coordinated to four $[\text{Ni}(\text{en})]^{2+}$ cations through four cyano nitrogen atoms to form a 2-D sheet motif with alternating fused rows of twenty four-member $\text{Ni}_8(\text{CN})_8$ rings and square shaped $\text{Ni}_4(\text{CN})_4$ rings, as shown in Figure 5.2. This topology is similar to that found in $[\text{NdM}(\text{bpym})(\text{H}_2\text{O})_4(\text{CN})_6]\cdot 3\text{H}_2\text{O}$, where $\text{bpym} = 2,2'$ -bipyrimidine, $\text{M} = \text{Fe}$ and Co (Ma *et al.*, 2001). Within this arrangement, the $\text{Ni}\cdots\text{Ni}$ distance across the cyanide ligands is $5.0613(3)$ Å. The shortest $\text{Ni}\cdots\text{Ni}$ distances across the square rings of the sheets are $15.5247(7)$ and $16.3115(7)$ Å for $\text{Ni1}\cdots\text{Ni1}^{\text{i}}$ and $\text{Ni2}\cdots\text{Ni2}^{\text{ii}}$ (symmetry codes: (i) $1-x, 1-y, -z$; (ii) $0.5+x, 0.5+y, -1+z$), respectively. As shown in Figure 5.3, the overall 3-D network is generated by these 2-D sheets being mutually connected to neighbouring sheets through $\text{Ni2}-\text{C1}\equiv\text{N1}$

–Ni1 linkages. Water molecules are located in the lattice, and the cavities are filled by the coordinated en ligands (not shown in Figure). In addition, each nickel center acts as four-connected node and gives a binodal network with the Schläfli symbol $(4^2.8^4)(4^2.8^4)$ (Batten and Robson, 1998).

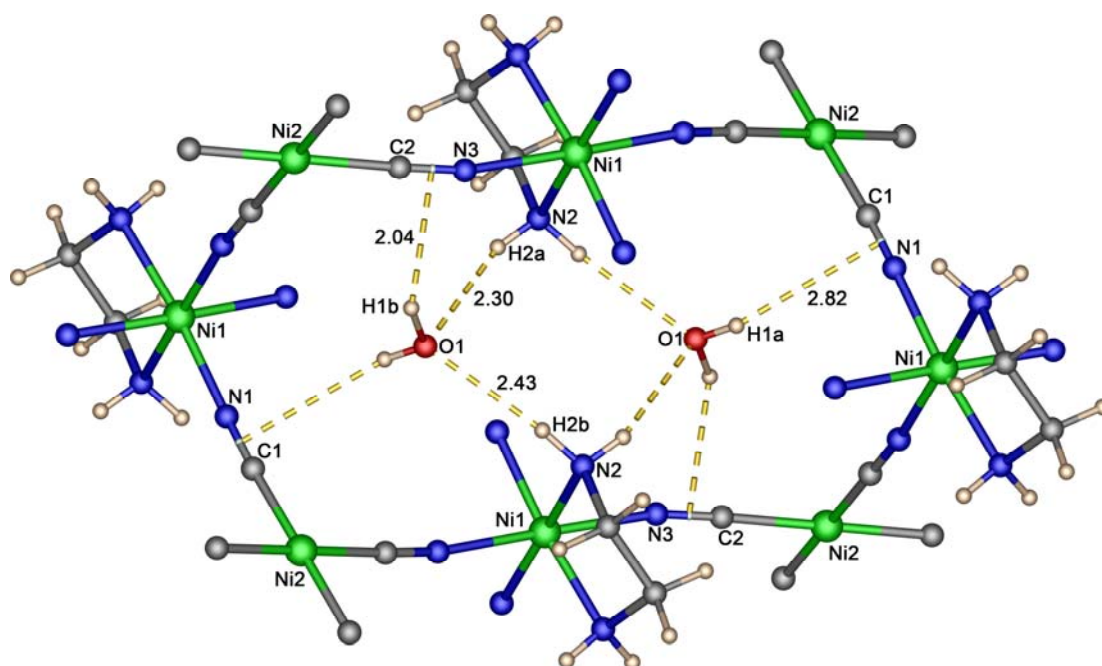


Figure 5.4 The detailed view of the hydrogen bonds in the **5a**. Hydrogen bonds are represented by dotted lines.

As stated previously, hydrogen bonds may serve as an exchange pathway between paramagnetic centers. The observed intra- and intermolecular hydrogen bonds are given in Table 5.3. As shown in Figure 5.4, atom N2 in the coordinated en ligand forms hydrogen bonds to atom O1 of the solvent water molecule with distances of 3.078(3) and 3.272(3) Å. The N2–N–O1 angle is *ca.* 160°. In turn, atoms H1a and H1b of the water molecule (O1) are oriented perpendicular to the mid-point (*A*) of the C1≡N1 (0.5+*x*, 0.5+*y*, *z*) and C2≡N3 (0.5–*x*, 1.5–*y*, 1–*z*) at 2.82 and 2.04 Å

for $H1a \cdots A(C1 \equiv N1)$ and $H1b \cdots A(C2 \equiv N3)$, respectively. The $O1-H-A$ angle is in between 146 and 147° . These observed distances and angles are suggesting weak interactions with the π molecular orbital of the cyano groups at the limited of such interactions (Saenger and Jeffrey, 1991), with the $C2 \equiv N3$ interaction being considering stronger.

5.3.3 Structural Description of $[Ni(CN)_4Ni(tn)] \cdot H_2O \cdot MeOH$ (**5b**)

Compound **5b** crystallizes in the tetragonal system with space group $P4mbm$ (No. 127). The asymmetric unit with the atom-numbering scheme is shown in Figure 5.5, and consists of a half $[Ni(tn)]^{2+}$ cation, half a $[Ni(CN)_4]^{2-}$ anion (0.25 Ni2, 0.25 Ni3), and isolated disordered water and methanol molecules.

Ni1 exhibits a distorted NiN_6 octahedral geometry, coordinating to two nitrogen atoms from the chelating tn ligand ($Ni-N_{tn} = 2.100(3)$ Å), and four cyano groups atoms ($Ni-N_{tn} = 2.075(3)$ and $2.078(3)$ Å). The chelating tn molecule is disordered about a crystallographic mirror plane with equal site occupation factors. The $Ni-N \equiv C$ bond angles fall into two groups. $Ni1-N2 \equiv C1$ is nearly linear ($176.7(2)^\circ$), whereas $Ni1-N3 \equiv C2$ deviates significantly from linearity ($163.4(3)^\circ$). Ni2 and Ni3 are located on special positions $(0, 1/2, 1/2)$ and $(0, 0, 0)$, respectively. Each Ni2 ion is coordinated by four cyanide ligands in a square planar arrangement. All four of the cyanide groups then bridge to the Ni1 atoms. The $Ni2-C$ bond distance is $1.864(3)$ Å. This value is normal and comparable to that observed in **5a**, and those reported for other the bimetallic complexes of $[Ni(CN)_4]^{2-}$ building blocks, such as $[Ni(CN)_4Ni(en)_2]$ and $[Ni(CN)_4Ni(en)_2] \cdot 2.16H_2O$ (Černák *et al.*, 1988; 1990). The $Ni-C \equiv N$ bond angles are almost linear and range from $177.3(3)$ to $179.0(3)^\circ$,

indicative of strong directional bonding as the π orbitals of the cyano ligands interact with the d orbitals of the metal center. The average $\text{C}\equiv\text{N}$ bond length of $1.150(3)$ Å is found to be similar to that in **5a**.

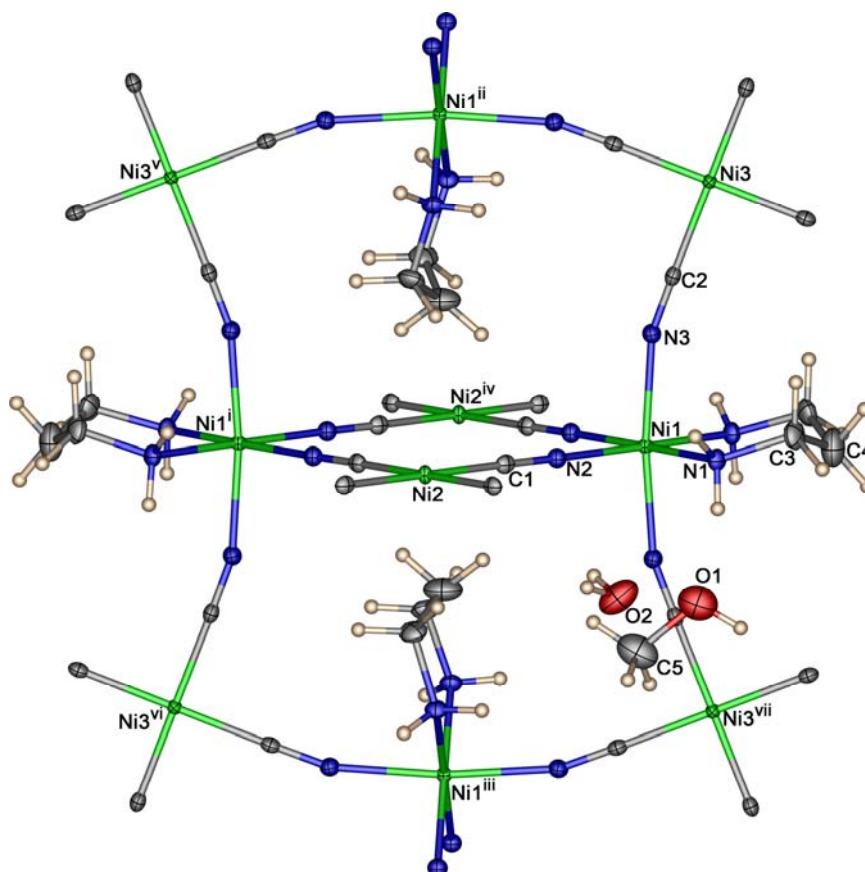


Figure 5.5 Perspective view of part of the structure in **5b** showing coordination environments around the Ni metals. Displacement ellipsoids are drawn at the 50% probability level. Hydrogen atoms are shown as small spheres of arbitrary radii. Symmetry codes: (i) $-x, 1-y, -z$; (ii) $1-x, y, z$; (iii) $x, -y, 1$; (iv) $x, y, -1+z$; (v) $x, 1+y, z$; (vi) $-1/2+x, 1/2-y, -z$; (vii) $1/2+x, 1/2-y, -z$.

As depicted in Figure 5.6, the structure of compound **5b** contains pairs of $[\text{Ni}(\text{tn})]^{2+}$ cationic groups bridged by $[\text{Ni}(\text{CN})_4]^{2-}$ anions in a *cis* fashion, generating $[\text{Ni}_2\text{-Ni}_2]$ squares with the $\text{Ni1}\cdots\text{Ni2}$ distance across the cyanide ligands being 5.0914(4) Å. Each square is linked to another two others through shared Ni2 atoms, creating a 1-D chain parallel to the crystallographic *c* axis. These 1-D chains are further connected by $\text{Ni1-C}\equiv\text{N-Ni3}$ linkages along the crystallographic *a* axis with a $\text{Ni1}\cdots\text{Ni3}$ distance of 5.0320(2) Å, to create a column network as shown in Figure 5.7. Within the column, the shortest intermolecular $\text{Ni}\cdots\text{Ni}$ distances are 7.3909(10), 9.8784(5), and 7.0038(4) Å for $\text{Ni1}\cdots\text{Ni1}^{\text{i}}$, $\text{Ni1}\cdots\text{Ni3}^{\text{i}}$, and $\text{Ni2}\cdots\text{Ni2}^{\text{ii}}$ (symmetry codes: (i) $-x, 1-y, z$; (ii) $x, y, -1+z$), respectively. The underlying net is a trinodal 4-connected net with the Schläfli symbol $(4^2.8^4)(4.6^5)_2(6^4.8^2)$, where the symbols represent the nodes in the order Ni2, Ni1, and Ni3. The 3-D network structure in **5b** viewed from an angle slightly displaced from the crystallographic *c* axis is depicted in Figure 5.8.

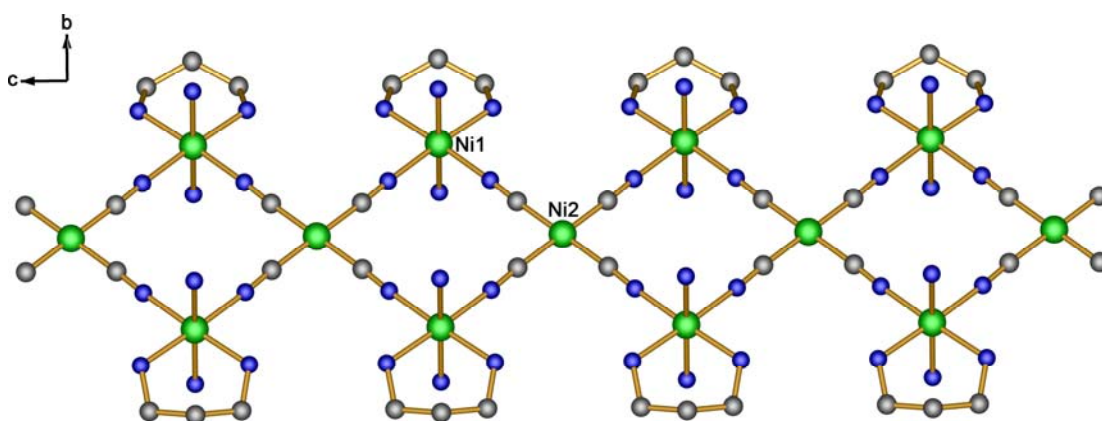


Figure 5.6 View of 1-D of a square shaped $[\text{Ni-Ni}]$ core in **5b** parallel to the *c* axis.

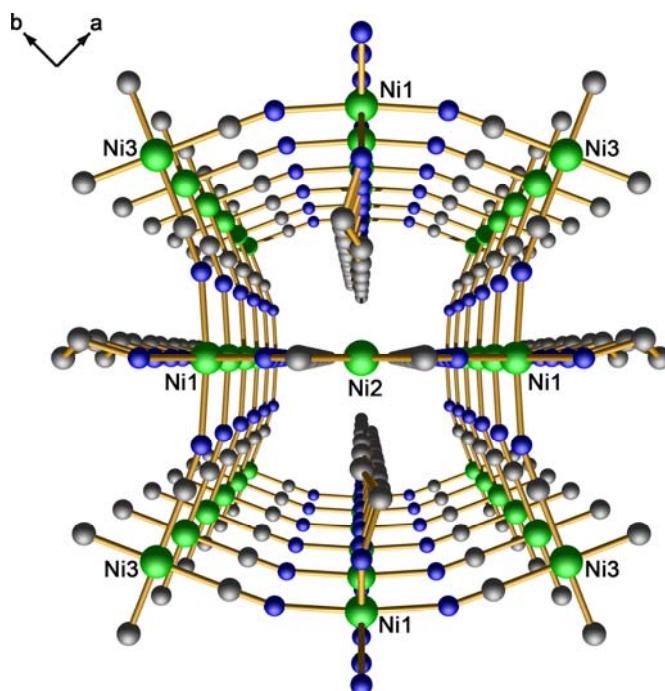


Figure 5.7 Perspective view of column structure in **5b** along the *c* axis.

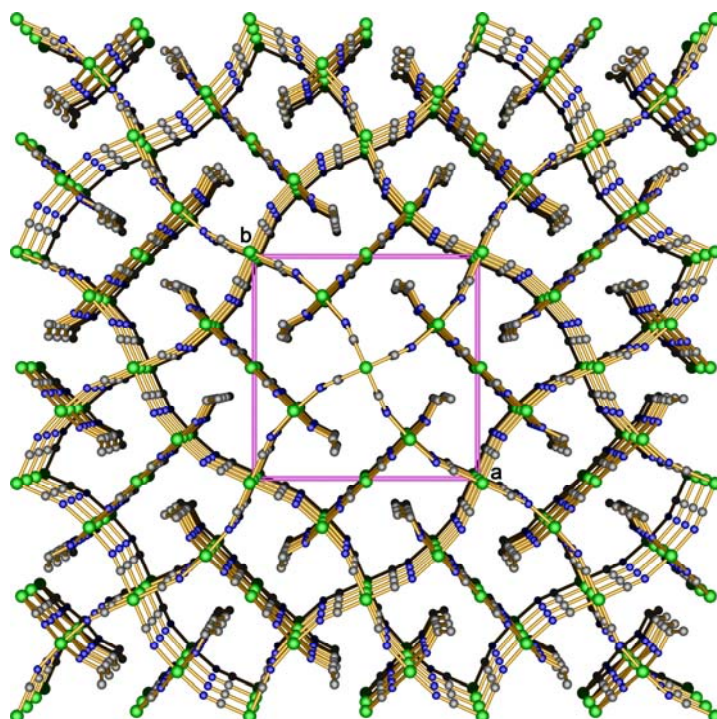


Figure 5.8 Perspective view of the cell packing in **5b** along the *c* axis. Hydrogen atoms and methanol molecules are omitted for clarity.

The crystal structure of **5b** is stabilized by N/O/C–H···O hydrogen bonds and O–H··· π interactions, Table 5.3. As can be seen in Figure 5.9, the hydroxyl groups of the methanol (O1) act as hydrogen bond donor to the oxygen atom of lattice water (O2) molecules ($\text{O1–H1a}\cdots\text{O2}^i = 2.847(9)$ Å, symmetry code: (i) $-x, y, z$), and also act as a hydrogen bond acceptors toward nitrogen (N1) and carbon atoms (C3) of the tn ligands ($\text{N1–H1a}\cdots\text{O1} = 3.060(5)$ Å, $\text{C3–H3b}\cdots\text{O1}^i = 3.315(6)$ Å, symmetry code: (i) $0.5-x, 0.5-y, 1-z$). Atom H2 of the water molecule (O2) is oriented perpendicular to the mid-point (*A*) of the $\text{C1}\equiv\text{N1}$ (x, y, z) and $\text{C2}\equiv\text{N3}$ ($x, y, -z$) cyanide groups. The $\text{H2}\cdots A$ bond lengths and the $\text{O2–H2–}A$ angles are $2.50(8)$ Å, $145(7)^\circ$ and $3.06(8)$ Å, $117(8)^\circ$ for $\text{O2–H2}\cdots A(\text{C1}\equiv\text{N1})$ and $\text{O2–H2}\cdots A(\text{C2}\equiv\text{N3})$, respectively. These values may be considered as weak O–H··· π interactions (Saenger and Jeffrey, 1991).

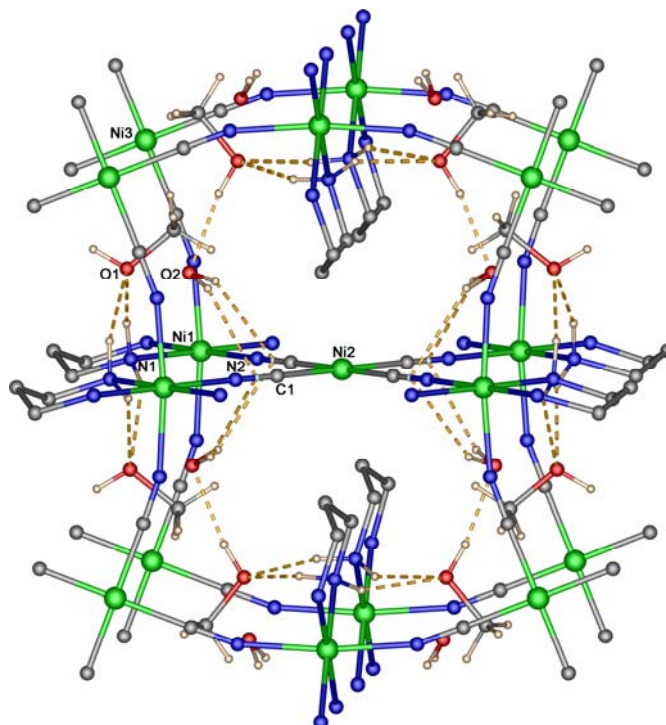


Figure 5.9 The detailed view of the hydrogen bonds in **5b**. Hydrogen bonds are represented by dotted lines.

The network structures of these two compounds are completely different as schematic depicted shown in Figure 5.10. Despite the similar formulae, the size of the aliphatic diamine ligand and the solvated molecules influences the orientations of the linkages, generating different networks for these two compounds.

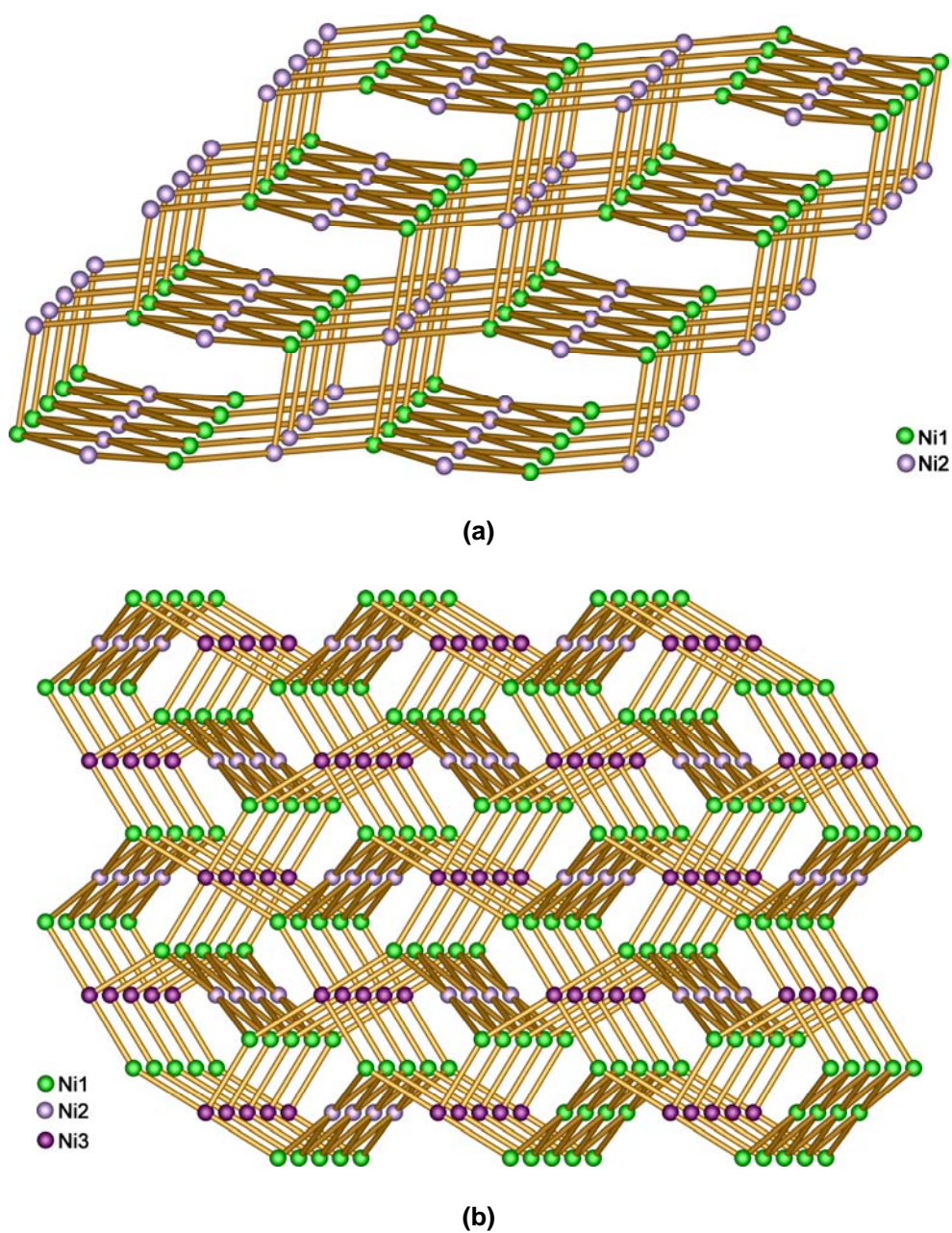


Figure 5.10 Schematic views of the 3-D 4-connected network for (a) **5a** and (b) **5b**.

5.3.4 Magnetic Properties

Variable temperature magnetic susceptibility data for polycrystalline samples of **5a** and **5b** were collected in the temperature range 4–300 K. The magnetic behaviours of **5a** and **5b** are very similar. Plots of magnetic behaviours in **5a** and **5b** are shown in Figure 5.11, in the form of the molar magnetic susceptibility (χ_M^{-1}) or effective magnetic moment (μ_{eff}) per 2Ni^{II} , versus the temperature.

DC magnetic susceptibilities were measured in a field of 1 T. The observed value of μ_{eff} per $\{2\text{Ni}^{\text{II}}\}$ unit at 300 K is $3.03 \mu_B$, where μ_B = the Bohr magneton ($\chi_M T = 1.15 \text{ cm}^3 \text{ mol}^{-1} \text{ K}$) for **5a** and $2.99 \mu_B$ ($\chi_M T = 1.12 \text{ cm}^3 \text{ mol}^{-1} \text{ K}$) for **5b**, which is expected for the magnetically dilute system consisting of square planar Ni^{II} ($S = 0$) and octahedral Ni^{II} ($S = 1$). These μ_{eff} values for **5a** and **5b** are slightly higher than those observed for the 1-D compounds: $[\text{Ni}(\text{CN})_4\text{Ni}(\text{pn})_2]\cdot\text{H}_2\text{O}$ ($2.75 \mu_B$), $[\text{Ni}(\text{CN})_4\text{Ni}(\text{tn})_2]\cdot\text{H}_2\text{O}$ ($2.75 \mu_B$), $[\text{Ni}(\text{CN})_4\text{Ni}(\text{dien})]\cdot 2\text{H}_2\text{O}$ ($2.78 \mu_B$), and $[\text{Ni}(\text{CN})_4\text{Ni}(\text{trien})]\cdot\text{H}_2\text{O}$ ($2.80 \mu_B$) at room temperature, where pn = 1,2-diaminopropane, tn = 1,3-diaminopropane, dien = diethylenetriamine, and trien = triethylenetetraamine (Zhan *et al.*, 2000). On lowering the temperature, the μ_{eff} values for the compounds remain almost constant until 50 K, then decreases gradually in the 50–15 K range, and finally decreases sharply to reach 2.77 and $2.57 \mu_B$ at 4 K for **5a** and **5b**, respectively, the sharp decrease being due to zero-field split of $S = 1$ states. The $1/\chi_M$ versus T plot obeys the Curie–Weiss law, $\chi_M = C/(T-\Theta)$, $C = 0.56$ and $0.41 \text{ cm}^3 \text{ mol}^{-1} \text{ K}$, with a negative Weiss constant (Θ) = -0.48 and -0.37 K for **5a** and **5b**, respectively. These results might indicate the existence of a weak antiferromagnetic interaction. No differences between the magnetization (M) in zero-field cooling (ZFCM) and in field-cooling (FCM) samples are observed down to 4 K for both compounds, which

indicates that no long-range magnetic ordering occurs, at least above 4 K. This is not surprising considering the long $\text{Ni}^{\text{II}}(S = 1)\text{-NC-Ni}^{\text{II}}(S = 0)\text{-CN-Ni}^{\text{II}}(S = 1)$ pathway which will lead to very weak coupling. The $\text{Ni}^{\text{II}}(S = 1)\cdots\text{Ni}^{\text{II}}(S = 1)$ distances in both compounds are approximately 10.1 Å.

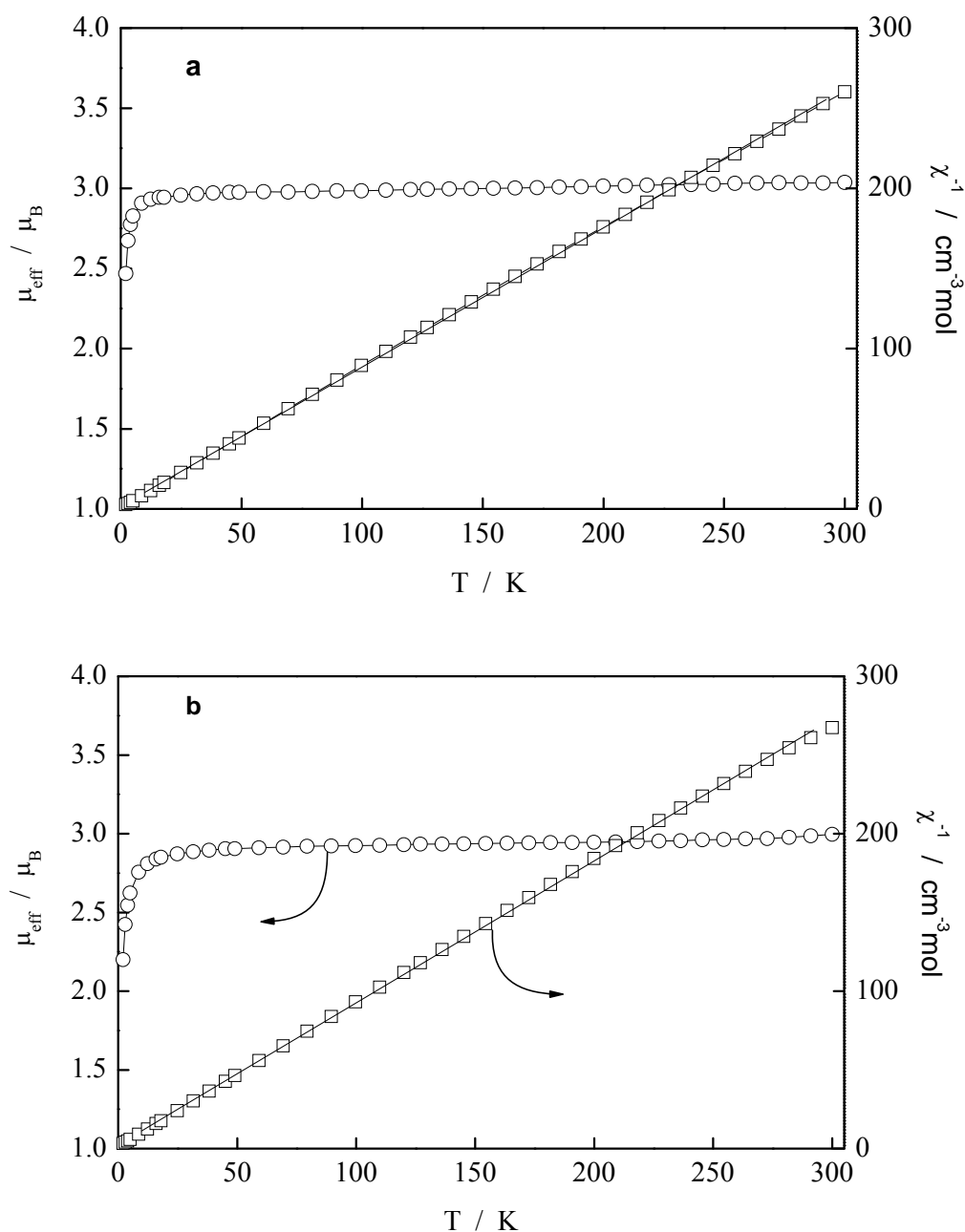


Figure 5.11 Temperature dependent magnetic behaviours of (a) 5a and (b) 5b.

5.3.5 ATR-FTIR Spectra

Comparison of the infrared spectral patterns for compounds **5a**, **5b**, and the precursor $K_2[Ni(CN)_4] \cdot H_2O$ are shown in Figure 5.12. The assignments of the vibrational bands of these compounds are given in the Table 5.4. The IR spectra of the $Ni(CN)_4$ group in the clathrate, $[Ni(CN)_4Ni(dabn)] \cdot 1.5benzene$ (Kasap and Özcelik, 1997), and $[Ni(CN)_4Ni(dapn)] \cdot Toluene$ (Kasap *et al.*, 1998) are also listed in Table 5.4 for comparison.

In the solid state spectra, the infrared spectral features of the compounds **5a** and **5b** in the range 3000 to 600 cm^{-1} are similar to each other. Strong absorption band at 2162 and 2154 cm^{-1} observed in the IR spectrum are assigned to the bridging cyano groups for **5a** and **5b**, respectively. Typically, bridging CN ligands have higher stretching frequencies than the terminal CN ligand (Nakamoto, 1963). As expected, the CN stretching band is shifted to higher wavenumbers than those for the free $[Ni(CN)_4]^{2-}$ when a CN group is bridged to a second metal. Such frequency shifts were also observed for other compounds which all of the CN group of square planar $[Ni(CN)_4]^{2-}$ moiety were coordinated with a second metal (Kasap *et al.*, 1997; Demirci, and Kantarci, 1998). Broad absorption bands at 3460–3185 cm^{-1} for **5a** are assigned to $\nu(NH)$ frequencies from NH_2 groups involved in hydrogen bonds (Nakamoto, 1963), for **5a**, and a sharp absorption band around 3658–3550 cm^{-1} is attributed to $\nu(OH)$ of hydrated water (Sorrell, 1988). The bands appears between 3616 to 3272 cm^{-1} for **5b** are due to $\nu(OH)$ from water and methanol molecules. This is consistent with the presence of solvated of water and methanol molecules observed in the single crystal X-ray studies. Broad absorption band at 3480–3160 cm^{-1} for **5b** are assigned to $\nu(NH)$ frequencies.

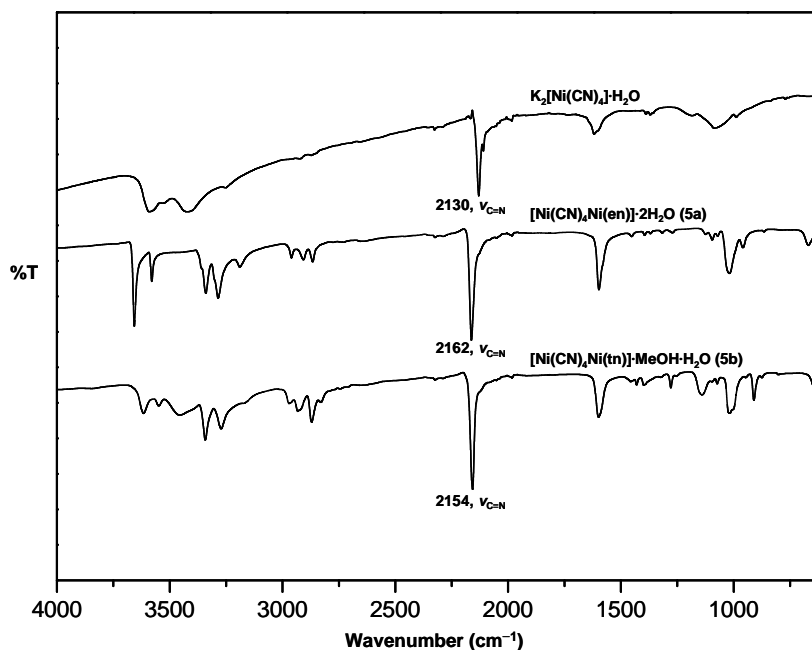


Figure 5.12 ATR-FTIR spectra of $K_2[Ni(CN)_4] \cdot H_2O$, **5a** and **5b**.

5.3.6 Differential Thermal Analysis and Thermal Gravimetric Analysis

Single crystal X-ray structure analysis of compounds **5a** and **5b**, reveals that crystallize solvent molecules exist in the lattice (Figures 5.4 and 5.10). From the topological point of view, these solvate molecules have the ability to leave the host lattice. The investigation of inclusion of guest solvent molecules and the thermal stability of the framework in compounds **5a** and **5b**, has therefore been monitored by DTA/TGA analysis on polycrystalline sample. The profile consists of two distinguished stages corresponding to the initial release of solvent molecules, and then the organic molecules and cyano groups decomposing. The framework structures of both compounds were found to be stable in the solid state up to *ca.* 320 °C. The thermal decomposition curve for **5a** and **5b** plotted as a function of temperature versus percent weight loses are shown in Figures 5.13 and 5.14, respectively.

Table 5. 4 Vibrational frequencies for compounds **5a** and **5b** (cm⁻¹).

Assignment	K ₂ [Ni(CN) ₄]·H ₂ O	5a	5b	[Ni(CN) ₄ Ni(dabn)] ^a	[Ni(CN) ₄ Ni(dapn)] ^b
$\nu(\text{OH})$	3591brsh, 3425brsh	3658vs, 3580ssh	3615br, 3549br	–	–
$\nu(\text{NH})$	–	3340s, 3285s, 3189m	3458sbr, 3342s, 3272m	3356s, 3294s	3363s, 3298m
$\nu(\text{CH})$	–	2960w, 2911w, 2867w	2972wsh, 2931wsh, 2870m	2950s, 2912m, 2879m	2954s, 2927m, 2877m, 2858m
$\nu(\text{C}\equiv\text{N})$	2130vs	2162vs	2154vs	2169vs	2170vs
$\delta(\text{NH}_2)$	–	1598s	1598s	1587w	1581vs
$\delta(\text{CH}_2)$	–	1452w	1430w	1460m	1475m
$\nu(\text{CN})$	–	1096w, 1082msh	1096w, 1082msh	1068vw, 1057m	1059w, 1020w

The symbols ν and δ to valence and in-plane vibrations, respectively.

ν = very, s = strong, m = medium, w = weak, br = broad, sh = shoulder

^a [Ni(CN)₄Ni(dabn)]·1.5benzene, dabn = 1,4-diaminobutane (Kasap *et al.*, 1998)

^b [Ni(CN)₄Ni(dapn)]·Toluene, dapn = 1,5-diaminopentane (Kasap *et al.*, 1998)

The dehydration process of **5a** is a single step in the range from room temperature to 110 °C. The weight loss is 10.0% which smaller than the theoretical value of 11.3%, corresponding to the loss of two water molecules. It leads to broad endothermic peaks. The second step has a sharp mass loss and broad endothermic in the 320–417 °C temperature range. Two for these broader losses occur below 590 °C the observed total weight loss of 51.9% in the range 320–590 °C, corresponding to the decomposition of en molecule and cyanides (calculated 51.7%), and to the collapse of the framework. The final thermal decomposition product is presumably a mixture of NiO. The total observed weight loss (61.9%) is in agreement with the calculated (63.4%).

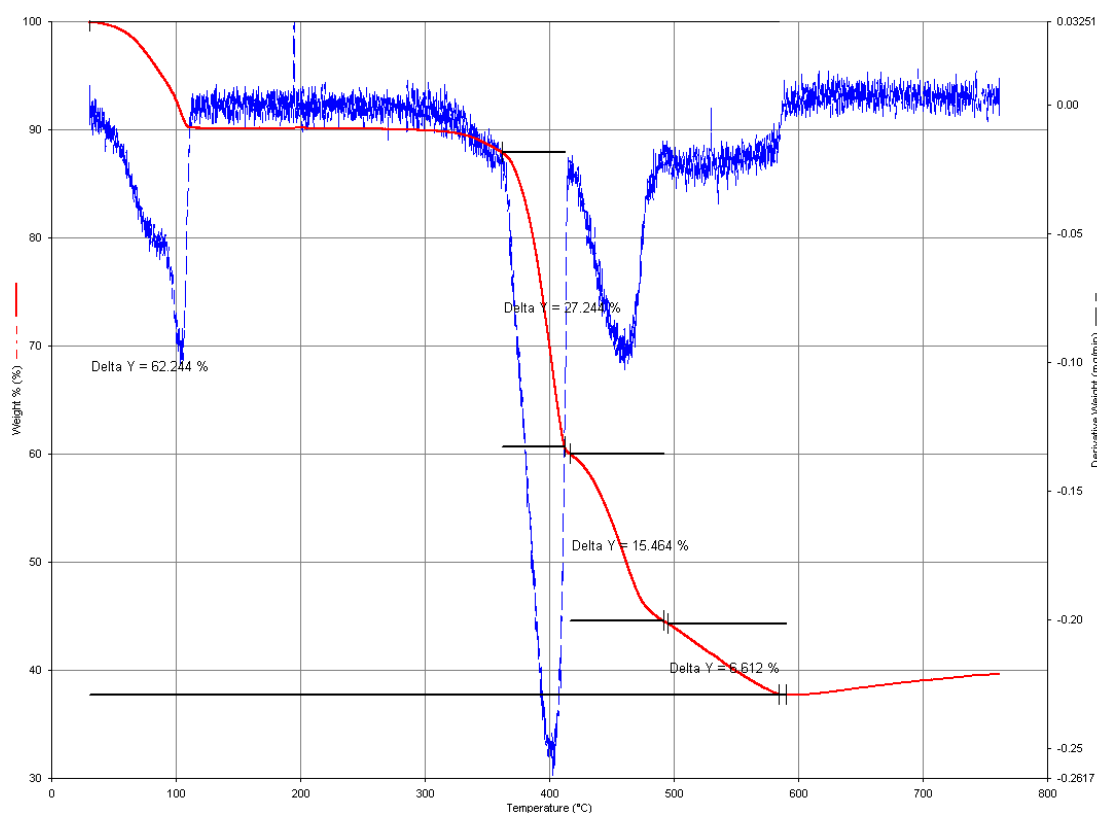


Figure 5.13 TGA (red) and DTA (blue) profiles for **5a**.

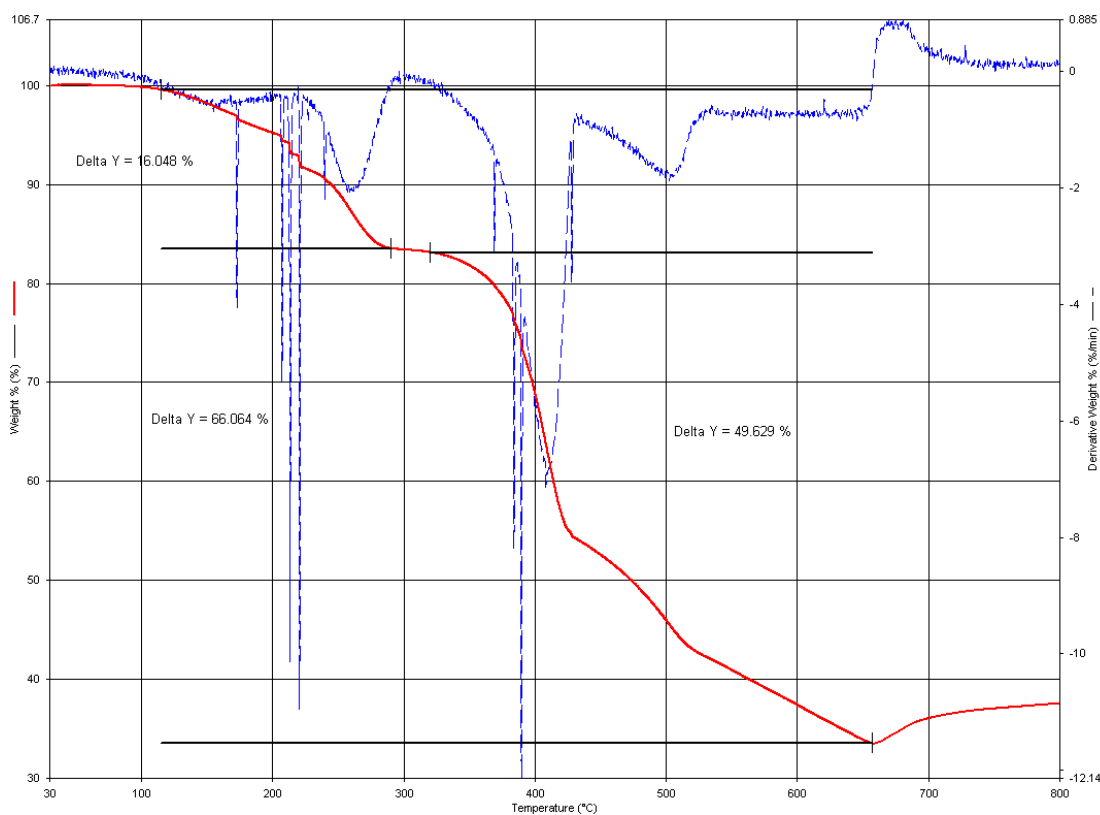


Figure 5.14 TGA (red) and DTA (blue) profiles for **5b**. The very sharp blue lines of derivative DTA due to the possible moving of sample during heating and should be ignored.

The thermal decomposition of **5b** is similar to the thermal decomposition of **5a** and can be described in the same way. In the first endothermic two-stages, broad step observed in the temperature rang 105–280 °C has a weight loss of 16.1% due to the loss of solvent water and methanol molecules (calculated 16.0%). The framework structure of **5b** was found stable in the solid state up to *ca.* 320 °C which similar to that found in **5a**. The decomposition then proceeds continuously into the second endothermic and sharp step finished at 660 °C. The corresponding observed weight loss of 49.6% which corresponds to the decomposition of *tn* molecules and cyanides

(calculated 51.5%). The final thermal decomposition product is a mixture of NiO. The total observed weight loss (66.1%) is in agreement with the calculated one (66.0%).

5.4. Conclusions

Reaction of diamagnetic square-planar complex of tetracyanonickelate(II), $[\text{Ni}(\text{CN})_4]^{2-}$, with $[\text{Ni}(\text{L})(\text{H}_2\text{O})_n]^{2+}$, where L = en (**5a**) and tn (**5b**), provided 3-D cyanide-bridged homometallic coordination polymers of $[\text{Ni}(\text{CN})_4\text{Ni}(\text{en})]\cdot 2\text{H}_2\text{O}$ (**5a**) and $[\text{Ni}(\text{CN})_4\text{Ni}(\text{tn})]\cdot \text{H}_2\text{O}\cdot \text{MeOH}$ (**5b**). The framework structures of these 3-D species show similar but not identical networks, with some beautiful structural details and hydrogen bonding interactions for solvate molecules. Thermogravimetric studies show that the solvate molecules are removed prior to complex decomposition. These exhibit paramagnetic behavior at the octahedral Ni(II) centers with little or no spin coupling occurring across either $\text{Ni}(\text{CN})_4$ or hydrogen bonding pathways. Further work on such novel framework systems could involve exploration of their porosity and to see if Ni center replaced by Fe(II) to probably yield 3-D SCO $\{\text{FeN}_6\}$ species somewhat related to Hofmann phases (see also Chapter VI).

5.5 References

- Barbour, L. J. (2001). **J. Supra. Chem.** 1(4-6): 189-191.
- Batten, S. R., and Robson, R. (1998). **Angew. Chem., Int. Ed.** 37: 1461-1494.
- Blessing, R. H. (1995). **Acta Crystallogr., Sect. A: Found. Crystallogr.** 51: 33-38.
- Bonhommeau, S., Molnár, G., Galet, A., Zwick, A., Real, J.-A., McGarvey, J. J., and Bousseksou, A. (2005). **Angew. Chem., Int. Ed.** 44(26): 4069-4073.
- Brandenburg, K., and Putz, H. (2006). **DIAMOND**. Version 3.1e. Crystal Impact GbR, Bonn, Germany.
- Chapman, K. W., and Chupas, P. J. (2007). **J. Am. Chem. Soc.** 129(33): 10090-10091.
- Černák, J., Orendáč, M., Potočňák, I., Chomič, J., Orendáčová, A., Skoršepa, J., and Feher, A. (2002). **Coord. Chem. Rev.** 224(1-2): 51-66.
- Černák, J., Chomič, J., Baloghová, D., and Dunaj-Jurco, M. (1988). **Acta Crystallogr., Sect. C: Cryst. Struct. Commun.** 44: 1902-1905.
- Černák, J., Chomič, J., Domiano, P., Ori, O., and Andreetti, G. D. (1990). **Acta Crystallogr., Sect. C: Cryst. Struct. Commun.** 46(11): 2103-2107.
- Černák, J., Lipkowski, J., Čižmár, E., Orendáčová, A., Orendáč, M., Feher, A., and Meisel, M. W. (2003). **Solid State Sci.** 5: 579-585.
- Crystal Maker. (2006). Crystal Maker Software, Yarnton, England.
- Francesconi, L. C., Corbin, D. R., Clauss, A. W., Hendrickson, D. N., and Stucky, G. D. (1981). **Inorg. Chem.** 20(7): 2078-2083.
- Goodson, P. A., Glerup, J., Hodgson, D. J., Michelsen, K., and Rychlewska, U. (1994). **Inorg. Chem.** 33(2): 359-366.
- Halder, G. J., Kepert, C. J., Moubaraki, B., Murray, K. S., and Cashion, J. D. (2002).

Science 298: 1762-1765.

Healy, P. C., Patrick, J. M., and White, A. H. (1984). **Aus. J. Chem.** 37(5): 921-928.

Hoskins, B. F., and Robson, R. (1990). **J. Am. Chem. Soc.** 112(4): 1546-1554.

Karyakin, A. (2001). **Electroanalysis** 13(10): 813-819.

Kasap, E., Saglam, S., and Kantarci, Z. (1998). **ARI** 50(4): 217-219.

Kasap, E., Saglam, S., and Kantarci, Z. (1998). **ARI** 50(4): 220-222.

Keper C. J. (2006). **Chem. Commun.** 695.

Kitazawa, T., Gomi, Y., Takahashi, M., Takeda, M., Enomoto, M., Miyazaki, A., and Enoki, T. (1996). **J. Mater. Chem.** 6(1): 119-121.

Kitazawa, T., Mizushima, Y., Shiraha, J., Ryoko, T., Katoh, A., Hasegawa, T., Nishikiori, S. L., and Iwamoto, T. (1991). **Inclusion Phenom. Mol. Recognit. Chem.** 10(1): 29-37.

Korp, J. D., Bernal, I., Palmer, R. A., and Robinson, J. C. (1980). **Acta Crystallogr., Sect. B: Struct. Sci.** 36: 560-564.

Ma, B.-Q., Gao, S., Su, G., and Xu, G.-X. (2001). **Angew. Chem., Int. Ed.** 40(2): 434-437.

McDougall, G. J., and Hancock, R. D. (1980). **J. Chem. Soc., Dalton Trans.** (4): 654-658.

Minacheva, L. Kh., Antsyshkina, A. S., and Porai-Koshits, M. A. (1974). **J. Struct. Chem.** 3: 408-414.

Muga, I., Gutiérrez-Zorrilla, J. M., Vitoria, P., Román, P., Lezama, L., and Beitia, J. I. (2004). **Eur. J. Inorg. Chem.** (9): 1886-1893.

Nakamoto, K. (1963). **Infrared Spectra of Inorganic and Coordination Compounds.** John Wiley & Sons, Inc., London.

- Nishikiori, S., and Iwamoto, T. (1986). **Inorg. Chem.** 25(6): 788-794.
- Niel, V., Martinez-Agudo, J. M., Munoz, M. C., Gaspar, A. B., and Real, J. A. (2001). **Inorg. Chem.** 40(16): 3838-3839.
- Ohba, M., and Ōkawa, H. (2000). **Coord. Chem. Rev.** 198(1): 313-328.
- Park, K. M., and Iwamoto, T. (1992). **Chem. Commun.** (1): 72-74,
- Pauling, L. (1960). **The Nature of the Chemical Bond**. 3rd ed. Ithaca, New York: Cornell University Press.
- Ptasiewicz-Bak, H., Olovsson I., and McIntyre, G. J. (1998). **Acta Crystallogr., Sect. B: Struct. Sci.** 54: 600-612.
- Saenger, W., and Jeffrey, G. A. (1991). **Hydrogen Bonding in Biological Structures**. Berlin/Heidelberg: Springer-Verlag.
- Scorrell, T. N. (1988). **Interpreting Spectra of Organic Molecules**. University Science Books: Mill Valley, CA.
- Sheldrick, G. M. (1997). **SHELXL-97**: A program for crystal structure refinement. University of Geottinger; Germany.
- Sheldrick, G. M. (1997). **SHELXS-97**: A program for automatic solution of crystal structure. University of Geottinger: Germany
- Van Langenberg, K., Batten, S. R., Berry, K. J., Hockless, D. C. R., Moubaraki, B., and Murray, K. S. (1997). **Inorg. Chem.** 36(22): 5006-5015.
- Verdaguer, M., Bleuzen, A., Marvaud, V., Vaissermann, J., Seuleiman, M., Desplanches, C. Sculler, A., Train, C., Garde, R., Gelly, G., Lomenech, C., Rosenman, I., Veillet, P., Cartier, C., and Villain, F. (1999). **Coord. Chem. Rev.** 190-192: 1023-1047.
- Yuge, H., and Iwamoto, T. (1993). **J. Chem. Soc., Dalton Trans.** (18): 2841-2847.

Yuge, H., and Iwamoto, T. (1994). **J. Chem. Soc., Dalton Trans.** (8): 1237-1242.

Yuge, M., Mamada, A., Asai, M., Nishikiori, S.-i., and Iwamoto, T. (1995). **J. Chem. Soc., Dalton Trans.** (19): 3195-3205.

Yuge, H., Noda, Y., and Iwamoto, T. (1996). **Inorg. Chem.** 35(7): 1842-1848.

Zhan, S.-z., Guo, D., Zhang, X.-y., Du, C.-x., Zhu Y., and Yang, R.-n. (2000). **Inorg. Chim. Acta** 298(1): 57-62.

Zheng, J.-M., Batten, S. R., and Du, M. (2005). **Inorg. Chem.** 44(10): 3371-3373.

CHAPTER VI

SYNTHESIS, STRUCTURES, AND SPIN-CROSSOVER PROPERTIES OF INFINITE 3-D FRAMEWORK IRON(II) CONTAINING ORGANODINITRILE BRIDGING LIGANDS

6.1 Introduction

Prussian blue analogues (PBs) and closely related polymeric metal cyanides have a remarkable history in coordination chemistry and have aroused intensive interest due to their magnetostructural feature and potential application in many fields (Itaya *et al.*, 1986; Ohba and Ōkawa, 2000; Gütllich *et al.*, 2001; Culp *et al.*, 2005; Roy *et al.*, 2008). The archetypical PB, $[\text{Fe}_4\{\text{Fe}(\text{CN})_6\}_3] \cdot x\text{H}_2\text{O}$, has a cubic network structure in which the Fe atoms lie at the lattice points and the cyanide groups are bridging (Buser *et al.*, 1977). It orders ferromagnetically below $T_C = 5.6$ K (Herren *et al.*, 1980). Many methods have been developed over the last 50 years for the synthesis of PB and PBs. In 1960, Pauling and Pauling reported the first “*Super-PB*” of trisilver cobalt(III) hexacyanide, $\text{Ag}_3[\text{Co}(\text{CN})_6]$, from powder X-ray data. The structure contains NC–Ag–CN bridges between two cobalt metal ions to form three interpenetrating frameworks, with the edge of the unit cube having a value of *ca.* 10.2 Å (Pauling and Pauling, 1960). Much later, Robson and co-workers reported a single crystal structure of the related compound $\text{Rb}[\text{Cd}\{\text{Ag}(\text{CN})_2\}_3]$. The structure contains

three identical, independent and interpenetrating of α -Po-related 3-D nets, with an approximately linear NC–Ag–CN connector in place of the CN of the parent of PB. The Cd \cdots Cd distance of cuboid edge connectors is 24.5 Å, whereas, the other three solid diagonals of the cuboid are contracted with the Cd \cdots Cd distance of 16.5 Å and remain equivalent to each other (Hoskins *et al.*, 1994). In order to address the challenge and obtain 3-D super PBs, Fischer and co-workers used a planar Me₃Sn⁺ fragment as spacer to replace each Ag(I) ion of super PB. The resulting 3-D framework organotin(IV) polymer [(Me₃Sn)₃Co(CN)₆] has a Co \cdots Co separation across the N–Sn–N spacer of *ca.* 9.5 Å (Behrens *et al.*, 1992). Following these studies, several more 3-D super PB complexes, *eg.* [(Me₂Sn)₃{Co(CN)₆}₂] \cdot 6H₂O (Siebel *et al.*, 2000), [(Me₃Sn)₃M(CN)₆], where M = Co and Ir (Poll *et al.*, 2001) were also prepared having different M \cdots M separations across the spacers.

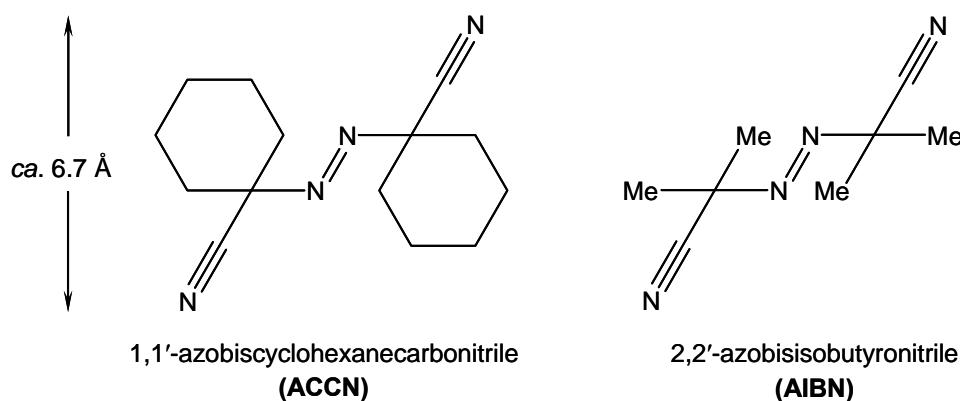
Many polymeric structures have been reported of “molecular” CN[−] type structures and clusters containing chelating co-ligands such as [{Ni^{II}(bpm)₂}₃{Fe^{III}(CN)₆}₂] \cdot 7H₂O, bpm = bis(1-pyrazolyl)methane (Van Langenberg *et al.*, 1997) and [Ni^{II}(tn)₂]₃[Fe^{III}(CN)₆]₂ \cdot X, tn = diaminopropane, X = ClO₄, BF₄, PF₆ (Ohba *et al.*, 1997). Charged dinitrile of the dca type, N(CN)₂[−], have been used in studies of [M{N(CN)₂}₂] compounds that form 3-D networks and display long-range magnetic order in most case, where M = Cr, Mn, Fe, Co, Ni and Cu (Batten and Murray, 2003).

The polymeric approach has also been used for the construction of Fe(II) SCO compounds (Real *et al.*, 1995; Kahn and Martinez, 1998). This strategy consists of linking together the SCO sites by covalent bridges into extended polymeric structures. In 1999, the first example of a 3-D polymeric complex, [Fe(btr)₃](ClO₄)₂, btr = tris(4,4'-bis-1,2,4-triazole), exhibiting a cooperative SCO has been reported by Kahn

and co-workers (Garcia *et al.*, 1999). Subsequently, Real *et al* reported 3-D SCO Hofmann-like networks $[\text{Fe}^{\text{II}}(\text{pz})\text{M}^{\text{II}}(\text{CN})_4] \cdot n\text{H}_2\text{O}$, where $\text{pyz} = \text{pyrazine}$, $\text{M} = \text{Ni}$, $n = 2$; Pd , $n = 2.5$, and Pt , $n = 2.5$, and found that their magnetic and chromatic properties changed abruptly and they displayed thermal- and pressure-induced hysteresis at temperatures close to room temperature (Niel *et al.*, 2001). The assembly of $[\text{M}^{\text{I}}(\text{CN})_2]^-$ groups, $\text{Fe}(\text{II})$, and pyrimidine afforded triply interpenetrated, porous 3-D SCO polymers of formula $[\text{Fe}(\text{pmd})(\text{H}_2\text{O})\{\text{M}^{\text{I}}(\text{CN})_2\}_2] \cdot \text{H}_2\text{O}$, where $\text{M}^{\text{I}} = \text{Ag}$ and Au , $\text{pmd} = \text{pyrimidine}$ (Niel *et al.*, 2003). Murray and Kepert (2004) described 3-D SCO materials incorporating 2-connecting di-pyridyls and these showed very interactive guest dependent effects. Most of the more open framework $\text{Fe}(\text{II})$ SCO coordination polymers incorporate N-donating heterocyclic type ligands of the linked di-triazole or di-tetrazole (Grunert *et al.*, 2004; Absmeier *et al.*, 2006). Neutral organonitrile bridged spacer using $\text{NC}-\text{R}-\text{CN}$ ligands are much less well known. One example with $\text{R} = (\text{CH}_2)_4$ has been used in dinuclear $\text{Fe}(\text{II})$ SCO compounds (Batten *et al.*, 2004). The anionic dinitrile, $\text{N}(\text{CN})_2^-$ (dca), has also been used as a bridge in dinuclear SCO compounds (Ortega-Villar *et al.*, 2005; Murray, 2008).

An early report by Zuur and co-workers deal with neutral dinitrile ligands and the influence of linking azo groups on complex formation (Zuur *et al.*, 1984). This group synthesized a number of compounds of the type $[\text{M}(\text{AIBN})_3][\text{InCl}_4]_2$ where M is Fe , Co , Ni , and Zn , AIBN is a potential bridging, 2-connecting dinitrile, 2,2'-azobisisobutyronitrile. They studied their spectral and magnetic properties and concluded that three ligand molecules are used for complete octahedral coordination as evidenced by the optical ($d-d$) and IR spectra. Interestingly, the iron(II)-complex was reported to exhibit a high spin-low SCO transition with the magnetic moment

dropping from $5.9 \mu_B$ at room temperature to $4.6 \mu_B$ at 70 K. However, there was no crystal structure explored. Therefore, it prompted us in the present work to confirm and elucidate the structure and magnetism using the same AIBN ligand, and a related one, Scheme 1. In this chapter is reported the synthesis, single crystal structural and magnetic and Mössbauer spectral investigation of complexes of formula $[\text{Fe}^{\text{II}}(\text{L})_3][\text{M}^{\text{III}}\text{Cl}_4]_2$, where L is either 1,1'-azobiscyclopentanecarbonitrile (ACCN) or 2,2'-azobisisobutyronitrile (AIBN), $\text{M}^{\text{III}} = \text{Fe}$ or In . It will be shown that, they have 3-D α -Po type framework structures. The compounds synthesized were $[\text{Fe}^{\text{II}}(\text{AIBN})_3][\text{In}^{\text{III}}\text{Cl}_4]_2$ (**6a**), $[\text{Fe}^{\text{II}}(\text{AIBN})_3][\text{Fe}^{\text{III}}\text{Cl}_4]_2$ (**6b**), $[\text{Fe}^{\text{II}}(\text{ACCN})_3][\text{In}^{\text{III}}\text{Cl}_4]_2$ (**6d**), and $[\text{Fe}^{\text{II}}(\text{ACCN})_3][\text{Fe}^{\text{III}}\text{Cl}_4]_2$ (**6e**). The crystal structure of $[\text{Fe}^{\text{II}}(\text{AIBN})\text{H}_2\text{O}][\text{Fe}^{\text{III}}\text{Cl}_4]_2$ (**6c**), which was a minor phase separated from the reaction producing **6b**, is also briefly described.



Scheme 1 The ligands (left) ACCN and (right) AIBN used for this study. They are capable of binding to two metal ions *via* the $\text{C}\equiv\text{N}$ nitrogen donors but not *via* the azo group.

As indicated above, there are a number of polynuclear Fe(II) SCO network structures known using 2-connecting di-triazoles and di-tetrazoles but none are known using dinitriles. Compounds **6a** and **6b** are thus the first example of 3-D Fe(II) SCO containing dinitrile ligands.

6.2 Experimental Section

6.2.1 Materials and Physical Measurements

FeCl₂, FeCl₃, InCl₃, ACCN, and AIBN were purchased from commercial sources and used without further purification.

Microanalytical measurements (C, H, N) were performed by Campbell Microanalytical Laboratory, Chemistry Department, University of Otago, Dunedin, New Zealand. Infrared spectra of Nujol mulls were recorded using a diamond-ATR cell on a Bruker Opus/IR IFS 55 spectrometer in the range of 600–4000 cm⁻¹ (50 scans, resolution ±4 cm⁻¹). Thermogravimetric analysis (TGA) was performed on a Perkin-Elmer TGA 7 thermogravimetric analyzer in the air with a heating rate of 10 °C/min. Variable-temperature magnetic susceptibility data were obtained by Dr. Boujemaa Moubaraki, School of Chemistry, Monash University, using a Quantum Design MPMS 5 SQUID magnetometer for DC magnetization measurements. Mössbauer measurements were obtained by Assoc. Prof. Dr. John D. Cashion, School of Physics, Monash University. The spectra were measured using a conventional constant acceleration drive with a symmetrical saw-tooth waveform. The source of ⁵⁷Co in rhodium was maintained at room temperature. Fresh crystalline samples were loaded into a piston type Perspex holder. The holder was placed in a cold-finger type cryostat in good thermal contact with a reservoir containing liquid nitrogen. The

spectra were fitted to Lorentzian lines, with the matching lines of a doublet constrained to have the same intensity and line width. Isomer shifts were calibrated against the spectrum of α -iron.

6.2.2 Syntheses

Preparation of $[\text{Fe}^{\text{II}}(\text{AIBN})_3][\text{In}^{\text{III}}\text{Cl}_4]_2$ (**6a**)

Method #1: A single crystal of **6a** suitable for X-ray crystallographic analysis was obtained by slow diffusion in which MeNO_2 solutions of 14 mL capacity were contained in an H-shaped tube and allowed left in the dark. In a typical experiment, FeCl_2 (62 mg, 0.5 mmol) and InCl_3 (220 mg, 1 mmol) were dissolved in 3 mL of MeNO_2 to form a bright yellow-brown solution and this was pipetted into one side of the H-tube. AIBN (250 mg, 1.5 mmol) was dissolved in 3 mL of MeNO_2 to give a colorless solution and this was pipetted into the other side arm of the H-tube. The H-tube was then carefully filled with MeNO_2 . Upon slow diffusion for three weeks, yellow block-shaped single crystals of **6a** were formed in the iron-indium-containing side of the H-tube. Yield: 20 mg, 32% based on FeCl_2 .

Method #2: The route of Zuur *et al.*, (1984) was followed. FeCl_2 (62 mg, 0.5 mmol), InCl_3 (220 mg, 1 mmol) and AIBN (250 mg, 1.5 mmol) were dissolved in 15 mL of MeNO_2 with vigorous stirring. After 24 hrs of stirring under N_2 , a white precipitate of **6a** was filtered off and washed with small amount of MeNO_2 and diethyl ether subsequently and dried in vacuum over P_2O_5 . Yield: 50 mg, 82% based on FeCl_2 . The IR spectrum of this sample is similar to that of the sample obtained by the slow diffusion method above. Found (calcd) for $\text{C}_{24}\text{H}_{36}\text{Cl}_8\text{FeIn}_2\text{N}_{12}$ ($M_r = 1061.73$ g/mol): C, 27.11(27.15); H, 3.40(3.42), N, 15.78(15.83). ATR-FTIR ($\nu_{\text{max}}/\text{cm}^{-1}$): 717w, 856w, 958w, 1178s, 1217s, 1369m, 1388m, 1438w, 1461w, 1599m,

1982w, 2051w, 2166w, 2286m, 2314w, 2944w, 2996m, 3404w. TGA (under air ambient, rate 10 °C min⁻¹) $-\Delta w$ (122–130 °C) = 45.8%, corresponding to loss of AIBN molecules (46.4% theory). μ_{eff} (300 K) = 5.28 μ_{B} .

Preparation of [Fe^{II}(AIBN)₃][Fe^{III}Cl₄]₂ (6b) and [Fe^{II}(AIBN)(H₂O)][Fe^{III}Cl₄]₂ (6c)

Single crystals of **6b** and **6c** were synthesized from the same reaction and were prepared following the procedure described above for **6a**, except that FeCl₃ was used instead of FeCl₂ and without InCl₃. Typically, FeCl₃ (81 mg, 0.5 mmol) was dissolved in 3 mL of MeNO₂ to form a yellow-brown solution and this was pipetted into one side of the H-tube. AIBN (250 mg, 1.5 mmol) was dissolved in 3 mL of MeNO₂ to give a colorless solution and this was pipetted into the other side arm of the H-tube. The H-tube was then carefully filled with MeNO₂. Upon slow diffusion for two weeks, yellow block-shaped (**6b**) and pale yellow plate (**6c**) single crystals were formed in the iron-containing side of the H-tube. Yield: 21 mg, 27% (**6b**) and 4 mg 5% (**6c**) based on FeCl₃. Anal. Found (calcd) for **6b**, C₂₄H₃₆Cl₈Fe₃N₁₂ (*Mr* = 943.79 g/mol): C, 30.52(30.54); H, 3.82(3.85), N, 17.78(17.81). ATR-FTIR (ν_{max} /cm⁻¹): 713m, 853w, 951w, 1176s, 1216s, 1367m, 1385m, 1440m, 1464m, 1609m, 1642w, 1982w, 2051w, 2165w, 2242w, 2282s, 2945w, 2998m, 3458br. μ_{eff} (250 K) = 9.90 μ_{B} .

Preparation of [Fe^{II}(ACCN)₃][In^{III}Cl₄]₂ (6d)

Method #1: Single crystals of **6c** were prepared following the procedure described above for **6a**, except that ACCN was used instead of AIBN. In a typical experiment procedure, FeCl₂ (62 mg, 0.5 mmol) and InCl₃ (220 mg, 1 mmol) were dissolved in 3 mL of MeNO₂ to form a bright yellow-brown solution and this was

pipetted into one side of the H-tube. ACCN (360 mg, 1.5 mmol) was dissolved in 3 mL of MeNO₂ to give a colorless solution and this was pipetted into the other side arm of the H-tube. The H-tube was then carefully filled with MeNO₂. Upon slow diffusion for three weeks, yellow block shaped single crystals of **6c** were formed in the iron-indium-containing side of the H-tube. Yield: 33 mg, 54% based on FeCl₂.

Method #2: The route of Zuur *et al.*, (1984) was followed. FeCl₂ (62 mg, 0.5 mmol), InCl₃ (220 mg, 1 mmol) and ACCN (360 mg, 1.5 mmol) were dissolved in 15 mL of MeNO₂ and vigorous stirring for 24 hrs. The resulting white precipitate was filtered off and washed with small amount of MeNO₂ and diethyl ether subsequently and dried in vacuum over P₂O₅. Yield: 55 mg, 90% based on FeCl₂. The IR spectrum of this sample is similar to that of the sample obtained by the slow diffusion method, above. Anal. Found (calcd) for C₄₂H₆₀Cl₈FeIn₂N₁₂ (*Mr* = 1184.17 g/mol): C, 27.14 (27.15); H, 3.40(3.42), N, 15.82(15.83). ATR-IR (ν_{max}/cm^{-1}): 851w, 906m, 943m, 1071w, 1163w, 1256w, 1285w, 1442s, 1556w, 2116w, 2276w, 2862m, 2936w, 2949s, 3466w. μ_{eff} (300 K) = 5.26 μ_{B} .

Preparation of [Fe^{II}(ACCN)₃][Fe^{III}Cl₄]₂ (**6e**)

Single crystals of **6d** were prepared following the procedure described above for **6b**, except that ACCN was used. Pale yellow block-shaped single crystals of **6d** were formed in the iron-containing side of the H-tube. Yield: 35 mg, 43% based on FeCl₃. Anal. Found (calcd) for C₄₂H₆₀Cl₈Fe₃N₁₂ (*Mr* = 1184.17 g/mol): C, 42.54 (42.60); H, 5.09(5.11), N, 14.15(14.19). ATR-FTIR (ν_{max}/cm^{-1}): 854w, 957w, 1173s, 1223s, 1369m, 1388m, 1438w, 1461w, 1602m, 1991w, 2063w, 2177w, 2239m, 2301w, 2941w, 3002m, 3414w. μ_{eff} (300 K) = 9.59 μ_{B} .

6.2.3 X-Ray Crystallographic Study

Single crystals of **6a–6e** were mounted on MiTeGen MicroMounts fibers in a small amount of oil prior to measurements made by Dr. Suzanne M. Neville and Dr. Craig Forsyth, Monash University. Reflection intensities were collected on a Bruker X8 APEX CCD diffractometer using Mo $K\alpha$ ($\lambda = 0.71073$ Å) radiation and equipped with an Oxford Instruments nitrogen gas Cryostream. Empirical absorption corrections were applied to all data using SADABS (Blessing, 1995). The structures were solved using SHELXS and refined on F^2 using SHELXL-97 (Sheldrick, 1997) with X-SEED (Barbour, 2001) as a graphics interface.

In the final cycles of refinement, all atoms except hydrogen atoms were refined anisotropically. Hydrogen atoms were placed in geometrically idealized positions and constrained to ride on their parent atoms, with C–H = 0.99 Å and $U_{\text{iso}}(\text{H}) = 1.2U_{\text{eq}}(\text{C})$ for CH groups, and with C–H = 0.97 Å and $U_{\text{iso}}(\text{H}) = 1.5U_{\text{eq}}(\text{C})$ for methyl groups.

For **6c**, hydrogen atoms attached to oxygen atoms of the water molecules were located in a difference Fourier map and refined as riding in their as-found positions with a DFIX restraint of O–H distance at 0.90 Å, with $U_{\text{iso}}(\text{H}) = 1.2U_{\text{eq}}(\text{O})$. For **6a** was refined as a racemic twin using the TWIN and BASF commands in SHELXL-97 (Sheldrick, 1997). The twin law was (0 1 0 / 1 0 0 / 0 0 -1) and the final value of the BASF parameter was 0.471(17) for 103 K and 0.029(2) for 233 K.

Crystal data and details of the data collection and structure refinement for compounds **6a–6c** and **6c–6d** are summarized in Tables 6.1 and 6.2, respectively. Selected interatomic bond lengths and angles for compounds **6a–6b**, **6c**, and **6d–6e** are given in Tables 6.3, 6.4, and 6.6, respectively. The hydrogen bonds geometries for

6c are given in Table 6.5. The bond lengths and angles and other crystallographic data are given as supplementary material in the CIF which can be found on the attached CD-ROM.

Table 6.1 Summary of crystallographic data for the compounds **6a–6b**.

Identification code	6a		6b	
Temperature (K)	103	233	103	233
Formula	C ₂₄ H ₃₆ Cl ₈ FeIn ₂ N ₁₂	C ₂₄ H ₃₆ Cl ₈ FeIn ₂ N ₁₂	C ₂₄ H ₃₆ Cl ₈ Fe ₃ N ₁₂	C ₂₄ H ₃₆ Cl ₈ Fe ₃ N ₁₂
<i>Mr</i>	1061.73	1061.73	943.80	943.80
Crystal system	trigonal	trigonal	trigonal	trigonal
Crystal color/habit	red/block	yellow/block	red/block	yellow/block
Crystal size (mm)	0.10 × 0.10 × 0.10	0.10 × 0.10 × 0.10	0.13 × 0.13 × 0.13	0.13 × 0.13 × 0.13
Space group	<i>R</i> -3 (No. 148)	<i>R</i> -3 (No. 148)	<i>R</i> -3 (No. 148)	<i>R</i> -3 (No. 148)
<i>a</i> (Å)	14.6031(3)	14.7130(10)	14.4521(2)	14.5996(3)
<i>b</i> (Å)	14.6031(3)	14.7130(10)	14.4521(2)	14.5996(3)
<i>c</i> (Å)	36.917(2)	37.436(5)	36.345(1)	36.966(1)
α (°)	90	90	90	90
β (°)	90	90	90	90
γ (°)	120	120	120	120
<i>V</i> (Å ³)	6817.9(5)	7018.1(12)	6574.3(2)	6823.8(4)
<i>Z</i>	6	6	6	6
<i>D</i> _{calc} (Mg m ⁻³)	1.552	1.507	1.430	1.378
μ (Mo <i>K</i> α) (mm ⁻¹)	1.82	1.77	1.50	1.44
<i>F</i> (000)	3144	3144	2868	2868
θ range (°)	1.7 – 25.0	3.2 – 25.0	1.7 – 27.5	2.5 – 27.5
Data completeness	0.978	0.998	1.000	0.998
Limiting indices <i>h</i>	-14 → 17	-17 → 13	-18 → 11	-12 → 11
<i>k</i>	-17 → 10	-10 → 17	-10 → 18	-16 → 13
<i>l</i>	-38 → 41	-44 → 36	-47 → 45	-11 → 18
<i>T</i> _{min} / <i>T</i> _{max}	0.839/0.839	0.843/0.843	0.829/0.829	0.835/0.835
Reflections collected/unique	10095/2617	9731/2754	14219/3369	14333/3485
<i>R</i> _{int}	0.030	0.035	0.032	0.042
Data/restraints/parameters	2293/0/144	2269/0/146	2878/0/143	2338/0/143
<i>R</i> ₁ , <i>wR</i> ₂ [all data]	0.085, 0.170	0.090, 0.173	0.050, 0.090	0.084, 0.139
<i>R</i> ₁ , <i>wR</i> ₂ [<i>I</i> > 2 σ (<i>I</i>)]	0.077, 0.161	0.075, 0.158	0.042, 0.085	0.056, 0.123
Goodness of fit, <i>S</i>	1.07	1.10	1.04	1.07
$\Delta\rho_{\min}$, $\Delta\rho_{\max}$ (e Å ⁻³)	1.85, -1.51	0.73, -0.87	1.35 -1.24	0.77 -0.86

Computer programs: Crystal Maker (2006), Diamond v. 3e (Brandenburg and Putz, 2006), SADABS (Blessing, 1995), SHELXL-97 (Sheldrick, 1997), SHELXS-97 (Sheldrick, 1997), and X-SEED (Barbour, 2001).

Table 6.2 Summary of crystallographic data for the compounds **6c–6e**.

Identification code	6c	6d	6e
Temperature (K)	123	123	123
Formula	C ₁₆ H ₂₈ Cl ₈ Fe ₃ N ₈ O ₂	C ₄₂ H ₆₀ Cl ₈ FeIn ₂ N ₁₂	C ₄₂ H ₆₀ Cl ₈ Fe ₃ N ₁₂
<i>Mr</i>	815.61	1302.12	1184.17
Crystal system	monoclinic	triclinic	triclinic
Crystal color/habit	yellow/plate	yellow/block	yellow/block
Crystal size (mm)	0.25 × 0.20 × 0.05	0.03 × 0.03 × 0.03	0.14 × 0.14 × 0.14
Space group	<i>P</i> 2 ₁ / <i>n</i> (No. 14)	<i>P</i> -1 (No. 2)	<i>P</i> -1 (No. 2)
<i>a</i> (Å)	9.3413(2)	10.9464(5)	10.9068(9)
<i>b</i> (Å)	12.9995(3)	15.9076(7)	15.8580(11)
<i>c</i> (Å)	14.4027(4)	16.1604(7)	16.1047(12)
α (°)	90	89.592(2)	89.575(3)
β (°)	97.4790(10)	89.682(2)	89.485(2)
γ (°)	90	86.288(2)	85.889(2)
<i>V</i> (Å ³)	1734.07(7)	2808.0(2)	2778.1(4)
<i>Z</i>	2	2	2
<i>D</i> _{calc} (Mg m ⁻³)	1.562	1.540	1.416
μ (Mo K α) (mm ⁻¹)	1.88	1.49	1.20
<i>F</i> (000)	820	1312	1220
θ range (°)	1.8 – 25.0	1.8 – 25.0	1.3 – 25.0
Data completeness	0.967	0.994	0.926
Limiting indices <i>h</i>	-13 → 12	-13 → 12	-11 → 12
<i>k</i>	-18 → 18	-18 → 18	-18 → 14
<i>l</i>	-19 → 17	-19 → 17	-19 → 15
<i>T</i> _{min} / <i>T</i> _{max}	0.650/0.912	0.956/0.956	0.845/0.887
Reflections collected/unique	12762/3843	41135/9828	13125/9045
<i>R</i> _{int}	0.019	0.036	0.116
Data/restraints/parameters	3610/2/175	8105/0/586	6822/0/586
<i>R</i> ₁ , <i>wR</i> ₂ [all data]	0.027, 0.054	0.044, 0.073	0.108, 0.210
<i>R</i> ₁ , <i>wR</i> ₂ [<i>I</i> > 2 σ (<i>I</i>)]	0.025, 0.052	0.033, 0.069	0.078, 0.176
Goodness of fit, <i>S</i>	1.06	1.07	1.05
$\Delta\rho_{\min}$, $\Delta\rho_{\max}$ (e Å ⁻³)	0.45, -0.35	0.81, -0.81	0.80, -0.87

Computer programs: Crystal Maker (2006), Diamond v. 3e (Brandenburg and Putz, 2006), SADABS (Blessing, 1995), SHELXL-97 (Sheldrick, 1997), SHELXS-97 (Sheldrick, 1997), and X-SEED (Barbour, 2001).

Table 6.3 Selected bond lengths and angles for $[\text{Fe}^{\text{II}}(\text{AIBN})_3]^{2+}$ cations in **6a** and **6b** at selected temperatures (\AA , $^\circ$).^a

	$[\text{Fe}^{\text{II}}(\text{AIBN})_3][\text{In}^{\text{III}}\text{Cl}_4]_2$ (6a)		$[\text{Fe}^{\text{II}}(\text{AIBN})_3][\text{Fe}^{\text{III}}\text{Cl}_4]_2$ (6b)	
	103 K	233 K	103 K	233 K
Fe1–N1	2.000(6)	2.139(6)	1.945(2)	2.133(3)
Fe2–N4	2.177(6)	2.175(6)	2.176(2)	2.171(3)
Fe1 \cdots Fe2	10.4375(3)	10.5398(7)	10.3110(1)	10.4408(2)
Fe1 \cdots Fe1 ⁱ	14.6031(3)	14.7130(10)	14.4521(2)	14.5996(3)
Fe2 \cdots Fe2 ⁱⁱ	14.9169(6)	15.0955(14)	14.7106(3)	14.9295(5)
C1–N1	1.131(9)	1.120(9)	1.133(3)	1.118(4)
C4–N4	1.144(8)	1.124(8)	1.139(3)	1.135(4)
N2–N3	1.221(8)	1.215(8)	1.231(3)	1.222(4)
C1–C2	1.486(11)	1.479(10)	1.481(3)	1.478(5)
C3–C4	1.481(9)	1.495(9)	1.486(3)	1.492(4)
C2–N2	1.465(10)	1.473(10)	1.482(3)	1.480(4)
C3–N3	1.514(9)	1.490(9)	1.491(3)	1.486(4)
N1–Fe1–N1 ⁱⁱⁱ	89.2(2)	89.6(2)	89.1(1)	89.2(1)
N1–Fe1–N1 ^{iv}	90.8(2)	90.4(2)	90.9(1)	90.7(1)
N1–Fe1–N1 ^v	180	180	180	180
N4–Fe2–N4 ^{vi}	87.3(2)	87.5(2)	87.1(1)	87.1(1)
N4–Fe2–N4 ^{vii}	92.7(2)	92.5(2)	92.9(1)	92.8(1)
N4–Fe2–N4 ^{viii}	180	180	180	180

^a Estimated standard deviations of the least significant digits are given in parentheses. Symmetry codes: (i) $x, 1+y, z$; (ii) $x-2/3, y-1/3, z-1/3$; (iii) $y+2/3, -x+y+1/3, -z+4/3$; (iv) $-y, x-y-1, z$; (v) $-x+2/3, -y-2/3, -z+4/3$; (vi) $y+1/3, -x+y+2/3, -z+5/3$; (vii) $-y+1, x-y, z$; (viii) $-x+4/3, -y+2/3, -z+5/3$.

Table 6.4 Selected bond lengths and angles for $[\text{Fe}^{\text{II}}(\text{AIBN})(\text{H}_2\text{O})]^{2+}$ cations in $[\text{Fe}^{\text{II}}(\text{AIBN})(\text{H}_2\text{O})][\text{Fe}^{\text{III}}\text{Cl}_4]_2$, **6c** at 123 K (Å, °). ^a

Fe1–N1	2.144(1)	N2–N3	1.228(2)
Fe1–N4 ⁱ	2.171(1)	C1–C2	1.487(2)
Fe1–O1	2.083(1)	C3–C4	1.488(2)
C1–N1	1.135(2)	C2–N2	1.494(2)
C4–N4	1.135(2)	C3–N3	1.489(2)
Fe1⋯Fe1 ⁱ	10.3521(2)	Fe1⋯Fe1 ⁱⁱ	12.9995(3)
Fe1⋯Fe1 ⁱⁱⁱ	16.1444(4)		
N1–Fe1–N1 ^{iv}	180	N4 ^{iv} –Fe1–N4 ^v	180
N1–Fe1–N4 ^v	85.5(1)	N4 ^{iv} –Fe1–O1	91.1(1)
N1–Fe1–N4 ^{vi}	94.4(1)	N4 ^v –Fe1–O1	88.8(1)
N1–Fe1–O1	90.5(1)	O1–Fe1–O1 ^{iv}	180
N1–Fe1–O1 ^{iv}	89.4(1)		

^a Estimated standard deviations of the least significant digits are given in parentheses. Symmetry codes: (i) $1/2-x, 1/2+y, 1/2-z$; (ii) $x, 1+y, z$; (iii) $x-1/2, 1/2-y, 1/2-z$; (iv) $-x, -y, -z+1$; (v) $x-1/2, -y+1/2, z-1/2$; (vi) $-x+1/2, y-1/2, -z+3/2$; (vii) $-x+1/2, y+1/2, -z+3/2$.

Table 6.5 Hydrogen bond geometries for $[\text{Fe}^{\text{II}}(\text{AIBN})(\text{H}_2\text{O})][\text{Fe}^{\text{III}}\text{Cl}_4]_2$, **6c** (Å, °). ^a

D–H⋯A	[D–H]	[H⋯A]	[D⋯A]	[D–H–A]
O1–H1⋯Cl4 ⁱ	0.80(1)	2.54(1)	3.266(1)	150(1)
O1–H2⋯Cl1	0.81(1)	2.37(1)	3.168(1)	163(2)

^a Estimated standard deviations of the least significant digits are given in parentheses. Symmetry code: (i) $1/2-x, 1/2+y, 1/2-z$.

Table 6.6 Selected bond lengths and angles for $[\text{Fe}^{\text{II}}(\text{ACCN})_3]^{2+}$ cations in **6d** and **6e** at 123 K (\AA , $^\circ$). ^a

	$[\text{Fe}^{\text{II}}(\text{ACCN})_3][\text{In}^{\text{III}}\text{Cl}_4]_2$ (6d)	$[\text{Fe}^{\text{II}}(\text{ACCN})_3][\text{Fe}^{\text{III}}\text{Cl}_4]_2$ (6e)
Fe1–N11	2.164(3)	2.159(5)
Fe1–N21	2.150(3)	2.160(5)
Fe1–N31	2.140(3)	2.142(5)
Fe1–N41	2.123(3)	2.125(5)
Fe1–N51	2.172(3)	2.179(5)
Fe1–N61	2.164(3)	2.159(5)
Fe1 \cdots Fe1 ⁱ	10.6461(9)	10.6032(17)
Fe1 \cdots Fe1 ⁱⁱ	10.8428(9)	10.8290(17)
Fe1 \cdots Fe1 ⁱⁱⁱ	10.9464(5)	10.9068(9)
Fe1 \cdots Fe1 ^{iv}	10.9464(5)	10.9068(9)
Fe1 \cdots Fe1 ^v	11.9861(9)	11.9265(18)
Fe1 \cdots Fe1 ^{vi}	12.0096(9)	11.9705(17)
C11–N11	1.147(4)	1.131(8)
C21–N21	1.143(4)	1.131(8)
C31–N31	1.138(4)	1.143(8)
C41–N41	1.142(4)	1.130(8)
C51–N51	1.142(4)	1.145(8)
C61–N61	1.143(4)	1.160(8)
C12–N12	1.499(4)	1.506(8)
C22–N22	1.489(4)	1.479(8)
C32–N32	1.502(4)	1.501(8)
C42–N42	1.483(4)	1.471(8)
C52–N52	1.484(4)	1.489(7)
C62–N62	1.486(4)	1.484(8)
N11–Fe1–N21	179.1(1)	179.2(1)
N11–Fe1–N31	90.3(1)	89.8(2)
N11–Fe1–N41	89.6(1)	89.6(2)
N11–Fe1–N51	90.2(1)	90.4(1)
N11–Fe1–N61	89.6(1)	89.2(1)

Table 6.6 (Continued).

	$[\text{Fe}^{\text{II}}(\text{ACCN})_3][\text{In}^{\text{III}}\text{Cl}_4]_2$ (6d)	$[\text{Fe}^{\text{II}}(\text{ACCN})_3][\text{Fe}^{\text{III}}\text{Cl}_4]_2$ (6e)
N21–Fe1–N31	89.7(1)	90.3(2)
N21–Fe1–N41	90.3(1)	90.2(2)
N21–Fe1–N51	88.9(1)	88.8(1)
N21–Fe1–N61	91.1(1)	91.4(1)
N31–Fe1–N41	178.1(1)	178.3(2)
N31–Fe1–N51	88.8(1)	88.9(1)
N31–Fe1–N61	88.8(1)	88.5(2)
N41–Fe1–N51	89.3(1)	89.5(2)
N41–Fe1–N61	93.0(1)	93.0(2)
N51–Fe1–N61	177.6(1)	177.4(1)

^a Estimated standard deviations of the least significant digits are given in parentheses. Symmetry codes: (i) $2-x, 1-y, -z$; (ii) $2-x, 1-y, 1-z$; (iii) $1+x, y, z$; (iv) $x-1, y, z$; (v) $2-x, -y, -z$; (vi) $2-x, -y, 1-z$.

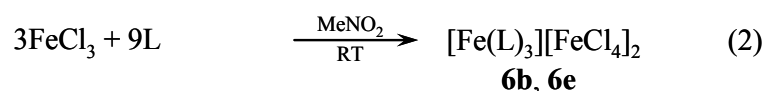
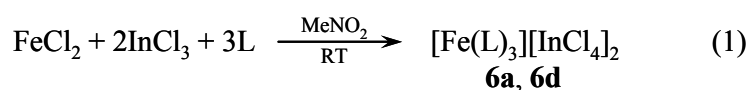
6.3 Results and Discussion

6.3.1 Syntheses and Characterizations

The iron(II) compounds are air- and moisture-sensitive solids. To isolate compounds **6a**, **6b**, **6d** and **6e** reproducibly, from MeNO₂ solutions, it is necessary to remove all traces of air and moisture. The experiments were therefore performed under N₂. During the synthesis of **6b**, if traces of air moisture are present, the minor product of the aqua complex of **6c** is obtained in *ca.* 5% yields.

$[\text{Fe}^{\text{II}}(\text{L})_3][\text{In}^{\text{III}}\text{Cl}_4]_2$, where L is AIBN (**6a**) and ACCN (**6d**), were obtained as pale-yellow block shaped crystals by the reactions of anhydrous FeCl₂, InCl₃, and L mixed in MeNO₂, in a 1:2:3 molar ratio. An H-shaped tube was employed and the solution left in the dark at room temperature. When 3 equivalents of L were slowly diffused into 1 equivalent of anhydrous FeCl₃ in MeNO₂, yellow block-shaped

crystals of **6b** (L is AIBN) and **6e** (L is ACCN) were also isolated. Curiously, the balanced chemical equations representing the syntheses of the crystalline products **6b** and **6e** do not correspond to the actual stoichiometric ratio of reactants used, when $3\text{FeCl}_3 + 9\text{L}$ is considered since Fe(III) is reduced, in part, to Fe(II). The dinitrile groups on the ligands may function as reducing agents. The syntheses involved equations 1 and 2, respectively.



Single crystals of all compounds are unstable and sensitive to oxidation or hydrolysis, when they are taken from the mother liquor and exposed to moist air. Yellowish powder compounds are thus formed. A white powder sample of **6a** was prepared according to the literature (Zuur *et al.*, 1981), and was phase pure as judged by microscopic visual examination and microelemental analysis. The IR spectra of the compounds provide spectral evidence for the occurrence of bridging organonitrile ligands. The CN stretching band is shifted to higher wave numbers compare to those for the free AIBN (2243m cm^{-1}) or ACCN (2237m cm^{-1}) ligands. The bridging coordinated organonitrile group frequency is now higher when a cyanide group is bridged to a second metal: 2286m (**6a**), 2274m (**6b**), 2241m (**6d**), and 2239m cm^{-1} (**6e**). TGA showed that 3-D nets of compound **6a** are thermally stable up to *ca.* 120°C after lose the AIBN ligands.

6.3.2 Structural Description of $[\text{Fe}^{\text{II}}(\text{AIBN})_3][\text{M}^{\text{III}}\text{Cl}_4]_2$, $\text{M}^{\text{III}} = \text{In}$ (**6a**), Fe (**6b**)

The X-ray single crystal structure analysis was performed at 103 and 223(2) K using the same crystal. At both temperatures the compounds have isomorphous structures of formula $[\text{Fe}^{\text{II}}(\text{AIBN})_3][\text{M}^{\text{III}}\text{Cl}_4]_2$, where $\text{M}^{\text{III}} = \text{In}$ (**6a**) and Fe (**6b**), and crystallize in the trigonal space group $R\bar{3}$ (No. 148). There is no crystallographic phase transition as the temperature is lowered. The asymmetric unit with atomic numbering is shown in Figure 6.1 (**6a** uses the same numbering as in **6b**). It contains two crystallographically independent Fe atoms, half of two $[\text{MCl}_4]$ anions, and one AIBN molecule. All metal ions lie on special position of the three fold inversion axis and have an inversion center. The midpoint of the AIBN ligands coincides with an inversion center. At 233 K, all the Fe(II) ions are in the HS state. At 103 K, however, the Fe1 site is now characteristic of the Fe(II) ion in the LS state, while the Fe2 site remains characteristic of Fe(II) ion in the HS state.

HS–HS complex structure ($T = 233$ K). Each Fe atom is coordinated by six nitrogen atoms from each of six AIBN ligands. At 233 K, the Fe–N bond lengths in the FeN_6 coordination core of **6a** (2.139(6) Å for Fe1 and 2.175(6) Å for Fe2) correspond to the values found for **6b** (2.133(3) Å for Fe1 and 2.171(3) Å for Fe2). These values are typical of a HS Fe(II) complex with six similar N-donor atoms as observed for the 3-D polymeric SCO of $[\text{Fe}(\text{btr})_3][\text{ClO}_4]_2$, where btr = tris(4,4'-bis-1,2,4-triazole) (Garcia *et al.*, 1999) and $[\text{Fe}(\text{pbtz})_3][\text{ClO}_4]_2$, where pbtz = 1,3-di(tetrazol-2-yl)propane (Bronisz, 2007).

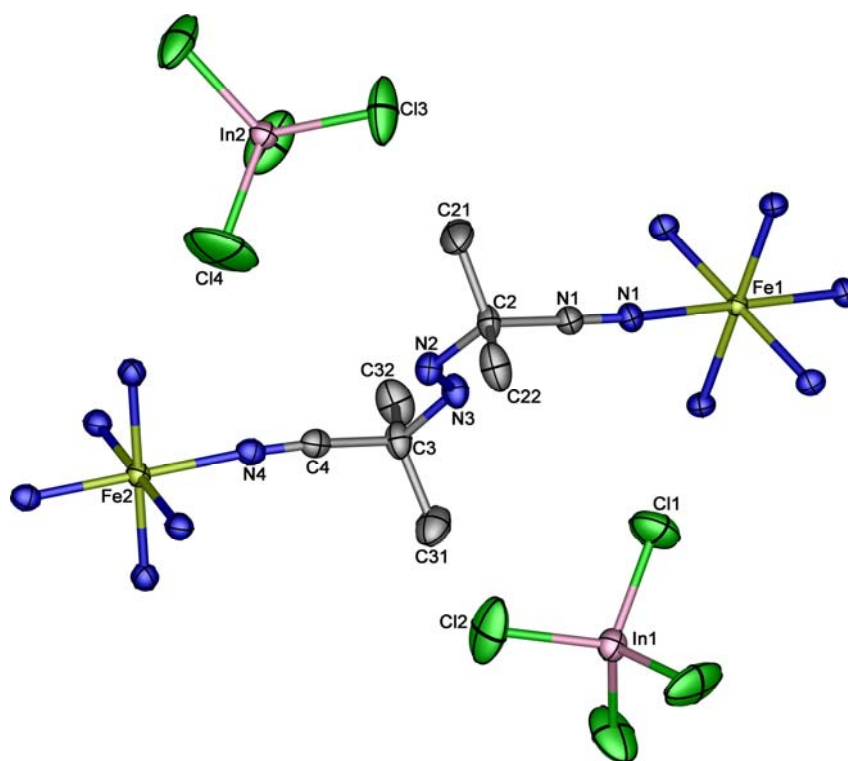


Figure 6.1 View showing asymmetric unit with the atom numbering in **6a**. Thermal ellipsoids are drawn at the 50% probability level at 103 K. The hydrogen atoms are omitted for clarity. Compound **6b** is isostructural.

The Fe2 octahedron ($\text{N4-Fe2-N4}' = 87.5(2)\text{--}92.5(2)^\circ$ for **6a** and $87.1(1)\text{--}92.8(1)^\circ$ for **6b**) is slightly more distorted from the ideal geometry (90°) than that found in the Fe1 octahedron ($\text{N1-Fe1-N1}' = 89.6(2)\text{--}90.4(2)^\circ$ for **6a**, and $89.2(1)\text{--}90.7(1)^\circ$ for **6b**). However, this distortion remains limited, as shown by the values (close to 180 or 90°) of the N–Fe–N angles (Table 6.3). The octahedral angular distortion around the Fe2 centre in **6a** and **6b**, defined as Σ , the sum of the deviations from 90° (the trigonal distortion angle = 0 for a perfect octahedron) of the twelve [N–Fe–N] angles ($\Sigma = 30.0^\circ$ for **6a**, and 33.8° for **6b**), is large compared with the Fe1 centres ($\Sigma = 4.8^\circ$ for **6a**, and 8.4° for **6b**). The Fe–N–C bond angles range

respectively from 170.7(6)–174.4(5)° and 170.5(2)–172.6(2)° for **6a** and **6b** and are somewhat bent from strict linearity. This is one factor accounting for the distortion from ideal octahedral geometry of the Fe(II) centre in the present compounds.

The bridging AIBN ligands for both compounds have an *S*-shaped conformation. All atoms except those of the methyl groups are nearly planar. For the plane consists of the best plane of eight atoms (N1, C1, C2, N2, N3, C3, C4, N4) referred to the orthogonalized axial system, the r. m. s. deviation of fitted atoms is 0.019 and 0.020 Å with the largest deviation being 0.044(6) and 0.0043(3) at N2 (which is in the double bond) for **6a** and **6b**, respectively. The atoms of the two methyl groups are not of course in the plane. The conformation of the AIBN ligand can also be described by the torsion angles: N1–C1–C2–N2 = 169.2(1)° for **6a** and 166.3(3)° for **6b**, N4–C4–C3–N3 = –142.1(2)° for **6a** and –130.01(1)° for **6b**. The N1⋯N4 separations are 6.609(7) and 6.601(3) Å for **6a** and **6b**, respectively. These values are slightly shorter than those of 6.67 Å for the free AIBN ligands (Argay and Sasvári, 1971). The Fe1⋯Fe2 separations across the AIBN ligands are 10.5398(7) and 10.4408(2) Å for **6a** and **6b**, respectively.

HS–LS complex structure (*T* = 103 K). On cooling to 103 K, the Fe–N bond lengths are markedly temperature dependent as depicted in Figure 6.2 and listed in Table 6.3. The Fe1–N1 bond lengths (**6a** = 2.000(6) Å, **6b** = 1.945(2) Å) are shorter than those for the Fe2–N4 bonds (**6a** = 2.177(6) Å, **6b** = 2.176(2) Å). The Fe–N bond lengths exhibit significantly different values within experimental error (3σ) as large as *ca.* 0.1–0.2 Å ($\Delta d[\text{Fe–N}] = 0.1$ for **6a** and 0.2 Å for **6b**). HS

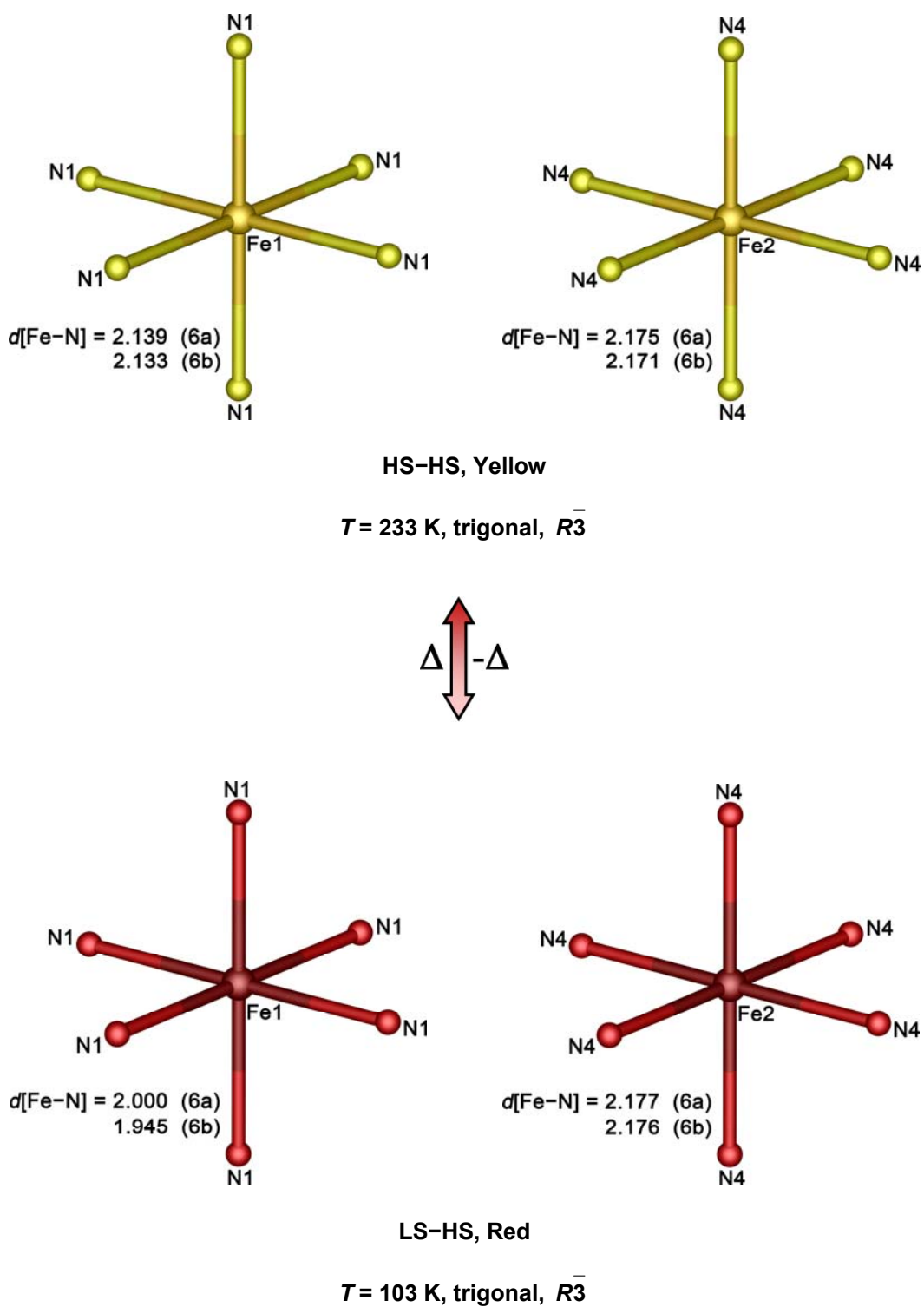


Figure 6.2 Comparison of Fe–N bond lengths in **6a** and **6b** at 103 and 233 K.

octahedral complexes of transition metal ions, *i.e.* d^6 Fe(II), are expected to display larger radii, and hence longer metal-ligand bonds than their LS counterparts upon moving from HS, $S = 2$ to LS, $S = 0$ (Gütlich *et al.*, 1994). Therefore, the long Fe–N bonds in **6a** and **6b** indicate the presence of a HS iron(II) ion, whereas, the short Fe–N bonds point to a LS configuration of the iron(II) ion. This shortening of the Fe–N bond lengths after lowering temperatures is a characteristic feature of the HS \rightarrow LS transition which was similar to that observed in other Fe(II) SCO complexes: $[\text{Fe}(\text{btzb})_3][\text{PF}_6]_2$, where $\text{btzb} = 1,4\text{-bis}(\text{tetrazol-1-yl})\text{butane-N}_4,\text{N}_4'$ (Grunert *et al.*, 2004), $[\text{Fe}(n\text{ditz})_3][\text{ClO}_4]_2$, where $n = 4\text{-}9$, $\text{ditz} = \text{bis}(\text{tetrazol-1-yl})\text{alkane-N}_4,\text{N}_4'$ (Absmeier *et al.*, 2006), $[\text{Fe}(\text{NCS})_2(\text{bpbd})_2] \cdot \{\text{acetone}\}$, $\text{bpbd} = 2,3\text{-bis}(4'\text{-pyridyl})\text{-}2,3\text{-butanediol}$ (Neville *et al.*, 2007), and $[\text{Fe}(\text{NCSe})_2(\text{cddt})] \cdot 2(\text{MeOH})$ and $[\text{Fe}(\text{NCS})_2(\text{cddt})] \cdot 2(\text{MeOH})$, where $\text{cddt} = 2\text{-chloro-}4,6\text{-bis}(\text{di-pyrid-2-ylamino})\text{-}1,3,5\text{-triazine}$ (Neville *et al.*, 2007). The Fe1–N1 distances are decreased by 6.8 and 9.8% on going from the HS (233 K) to the LS (103 K) state for **6a** and **6b**, respectively.

In the 103 K structure, the N1–Fe1–N1' bond angles for the LS form vary from $89.2(2)\text{-}90.8(2)^\circ$ and $89.1(1)\text{-}90.9(1)^\circ$, and are slightly different for the N4–Fe2–N4' angles in the HS species that adopt values of $87.3(2)\text{-}92.7(2)^\circ$ and $87.1(1)\text{-}92.9(1)^\circ$ for **6a** and **6b**, respectively. Indeed, the decreasing of temperature shows a significant increasing of deformation of the octahedral geometry about the Fe centre as defined by Σ , the sum of the deviations from 90° from twelve [N–Fe–N] angles. As depicted in Figure 6.3, the Fe1N₆ chromophore in the LS state shows a significantly greater distortion of the coordination octahedron and is more

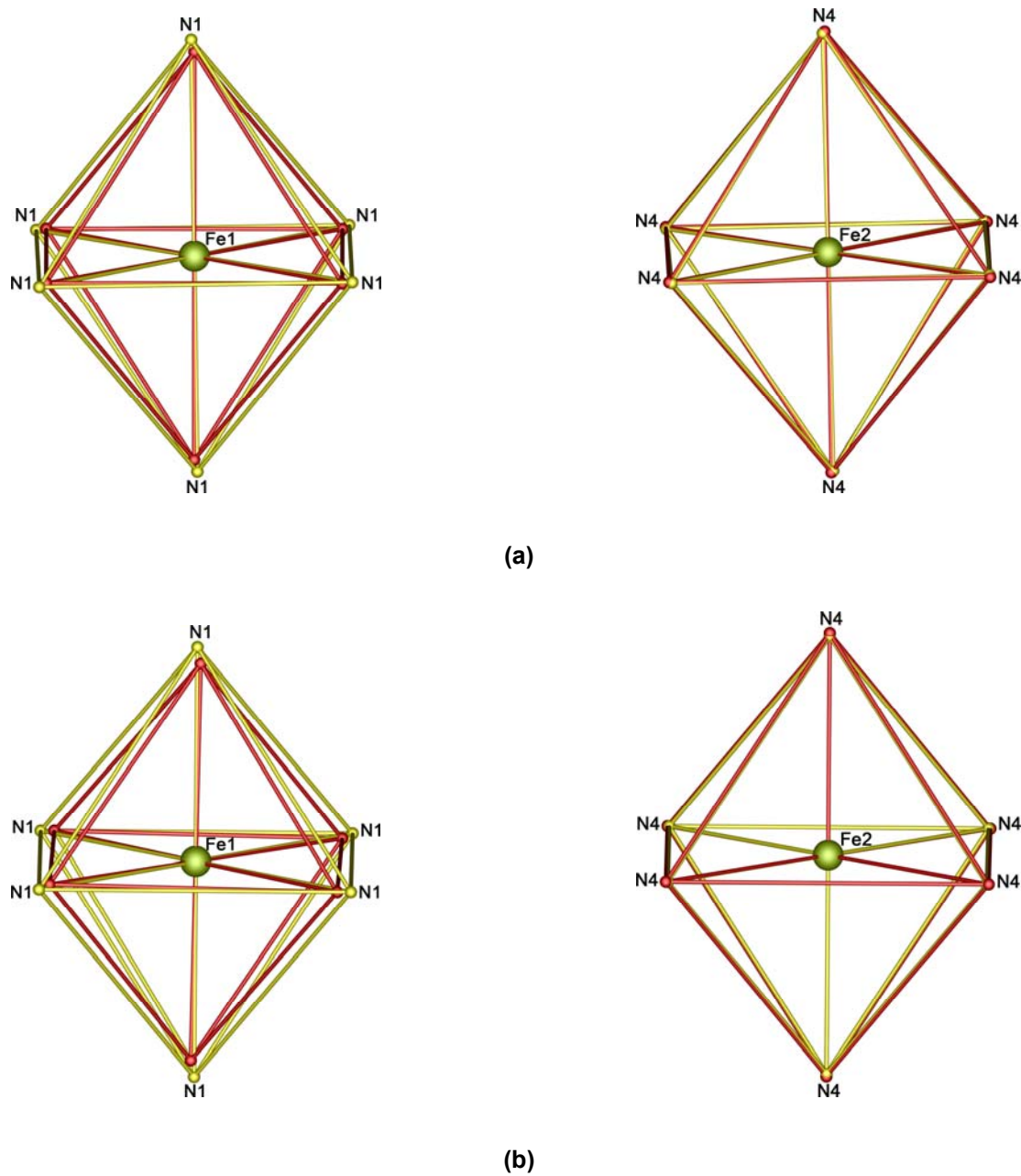


Figure 6.3 Schematic representation for comparison of distorted octahedral geometry around Fe(II) centres in (a) **6a** and (b) **6b** at 103 (red) and 233 K (yellow).

compressed in comparison to the Fe_2N_6 core in the HS species following the HS \rightarrow LS transition: Fe1: $\Sigma = 4.8^\circ$ at 233 K $\rightarrow 9.6^\circ$ at 103 K for **6a**; $\Sigma = 8.4^\circ$ at 233 K $\rightarrow 10.8^\circ$ at 103 K for **6b**; Fe2: $\Sigma = 30.0^\circ$ at 233 K $\rightarrow 32.4^\circ$ at 103 K for **6a**, 33.8° at 233 K $\rightarrow 34.8^\circ$ at 103 K for **6b**. The slight distortion observed in the present compounds is not unusual for Fe(II) SCO complexes, with similar behaviour observed for other 3-D polymeric compounds (Garcia *et al.*, 1999; Bronisz, 2007).

The AIBN bridging ligands show small changes in bond lengths with temperature as shown in Figure 6.4. The main structural modification of the AIBN molecule between 233 and 103 K concerns the coordination sphere of the Fe1 site and torsion angle changes in AIBN. The N1–C1–C2–N2 torsion angle is reduced from $169.2(1)^\circ$ at 233 K to $151.7(5)^\circ$ at 103 K for **6a**, but is increased from $166.3(3)^\circ$ at 233 K to $171.5(1)^\circ$ at 103 K for **6b**. Furthermore, the torsion of N4–C4–C3–N3 is reduced from $-142.2(1)^\circ$ at 233 K to $-117.1(2)^\circ$ at 103 K for **6a**, and is weakly reduced from $-130.1(1)^\circ$ at 233 K to $-128.4(2)^\circ$ at 103 K for **6b**. R. m. s. deviation of fitted atoms is 0.023 and 0.024 Å with the largest deviation being $-0.036(5)$ and $-0.043(1)$ Å at C2 for **6a** and **6b**, respectively. The largest deviation of atoms at 103 K is now C2 (at N2, at 233 K). These values indicate that the AIBN molecule reorientates when cooling temperature. The temperature dependence can also be demonstrated by the intramolecular N1 \cdots N4 separation, which increases by 0.8% from 6.609(7) and 6.601(3) Å at 233 K to 6.666(8) and 6.658(2) Å at 103 K for **6a** and **6b**, respectively. The Fe1 \cdots Fe2 separations across the AIBN ligands in **6a** decreases by 1% from 10.5398(7) Å at 233 K to 10.4375(3) Å at 103 K, whereas in **6b**, it decreases by 1.2% from 10.4408(2) Å at 233 K to 10.3110(1) Å at 103 K.

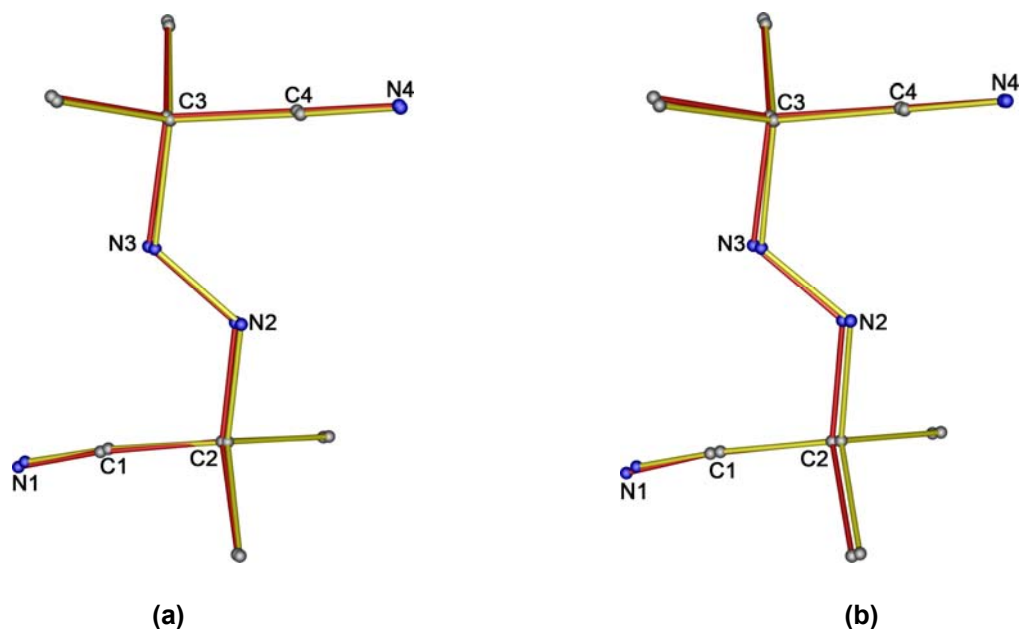


Figure 6.4 Views of AIBN ligands in (a) **6a** and (b) **6b** at 103 (red) and 233 K (yellow).

Of greater significance is the comparison between the unit cell parameters at the two collection temperatures. The cell volume of the unit cell decreases from 7018.1(12) and 6823.8(4) Å³ at 233 K to 6817.9(5) and 6574.3(2) Å³ at 103 K for **6a** ($\Delta V = 3\%$) and **6b** ($\Delta V = 3.8\%$), respectively. The largest change in cell dimensions was for the *c* axis ($\Delta c = 1.4\%$ for **6a**, 1.7% for **6b**). The changes in the *a* and *b* axes are considerably smaller ($\Delta a/b = 0.7\%$ for **6a**, 0.9% for **6b**). The characteristic feature of **6a** and **6b** is the thermochromic effect observed in which the HS \rightarrow LS transition is accompanied by a concomitant change from yellow (233 K) to red (103 K). In summary, between the FeN₆ chromophores in compounds **6a** and **6b** show that, the Fe₂ core at 103 K does not reveal any significant differences to that at 233 K, whereas

the Fe1 core undergoes the thermally induced SCO transition between the two temperatures. We see later in the magnetism description this transition occurs between 100 and 150 K for **6a** and 100–200 K for **6b**.

In addition, the geometry of the $[\text{M}^{\text{III}}\text{Cl}_4]$ counter anion in all compounds is distorted tetrahedral. The basic trends in the M–Cl bond lengths in **6a** and **6b** at selected temperatures are consistent with the trend in the ionic radii between Fe and In in which the M–Cl bond lengths decrease with decrease in the ionic radii of the central metal ions. As expected, the bond lengths of $\text{Fe}^{\text{III}}\text{–Cl}$ [2.170(7)–2.184(8) Å at 103 K and 2.142(3)–2.170(2) Å at 233 K] are shorter than those of the $\text{In}^{\text{III}}\text{–Cl}$ bonds [2.298(3)–2.317(4) Å at 103 K and 2.294(3)–2.308(5) Å at 233 K]. The bond lengths and angles around the anions metal centre at the collected temperatures are typical and comparable to those observed in other four-coordinated Fe(III) or In(III) complexes: 2.15–2.31 Å for $(\text{SbzSbz})_2[\text{FeCl}_4]\text{Cl}$, where $\text{SbzSbz} = 3,5\text{-diphenyl-1,2-dithiolium}$ (Mason, *et al.*, 1974), and 2.30–2.36 Å for $(\text{Et}_4\text{N})[\text{InCl}_4]$ (Trotter, *et al.*, 1969).

The extended structure consists of a 3-D cationic host framework of $[\text{Fe}(\text{AIBN})_3]^{2+}$ which is charged balance by two “guest” $[\text{MCl}_4]^-$ anions. The Fe(II) centres are six-connected and each Fe(II) atom connects to six other Fe(II) atoms through the nitrile nitrogens of the AIBN ligands to give a 3-D α -Po like network (Batten and Robson, 1998), as shown in Figure 6.5. This topology is identical to those found in other 3-D α -Po-related nets, *eg.* three interpenetrating framework structures in the “*Super-Prussian-Blue*” of $[\text{Ag}_3\text{Co}(\text{CN})_6]$ (Pauling and Pauling, 1968),

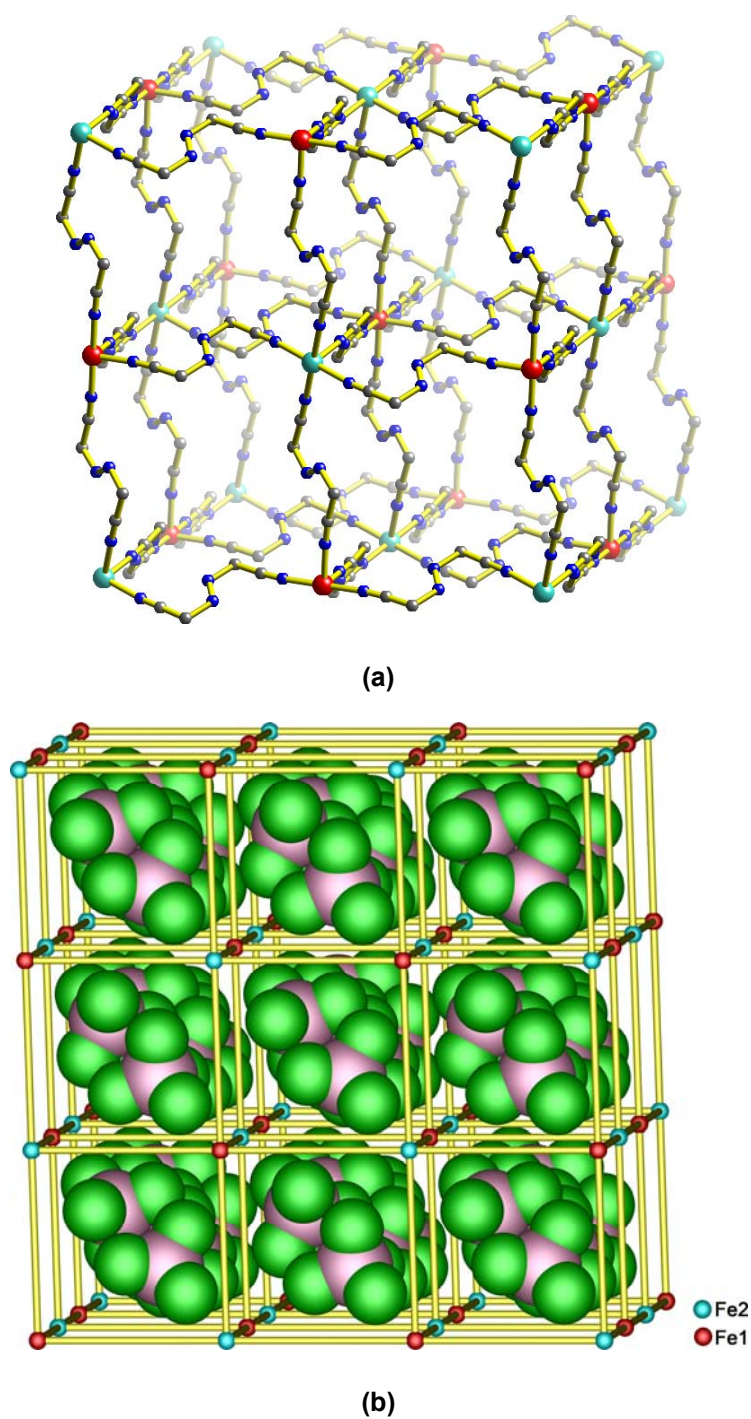


Figure 6.5 (a) Views of the 3-D net in the structure of **6a** at 103 K. Methyl groups and counter anions are omitted for clarity. (b) Schematic presentation of the α -Po related net in **6a**. Counter anions and AIBN molecules are represented as space-filling model and yellow solid lines, respectively. Compound **6b** is isostructural.

Rb[Cd{Ag(CN)₂}₃] (Hoskins *et al.*, 1994), [(Me₃Sn)₃Rh(SCN)₆] (Siebel and Fischer, 1997), and two interpenetrating nets of [M(dca)₂(4,4'-bipy)], where M = Fe, Co, and Ni (Jensen *et al.*, 2002). Within each of the rhombohedral channels are two independent [MCl₄] counter anions. These ions sterically prevent interpenetration of the coordination networks in a similar way to that of [CoCp₂]⁺ guest cations ions in a 3-D non-interpenetrating open-framework of (CoCp₂)[Fe(μ -CNSnMe₃NC)₃] (Schwarz *et al.*, 1995).

A surprising aspect of the structures in **6a** and **6b** is the absence of significant intermolecular hydrogen bonds. There are no intermolecular C \cdots Cl contacts of less than 3.45 Å in lengths (Bondi, 1964). The shortest intermolecular C \cdots Cl contact has H \cdots Cl and C \cdots Cl distances of 2.90 and 3.463(12) Å, respectively, both too long to be regarded as a significant C–H \cdots Cl hydrogen bond. The decreasing of the temperature does not involve any differences in the structures of the polymeric network. Therefore, only electrostatic forces and van der Waals interactions appear to contribute to the stabilization of the structures in **6a** and **6b**.

6.3.3 Structural Description of [Fe^{II}(AIBN)H₂O][Fe^{III}Cl₄]₂ (**6c**)

A few yellow plate crystals of **6c** were obtained as a minor product, and were separated by eye from **6b**. The X-ray single crystal structure analysis was only determined at 123 K. The compound crystallizes in the monoclinic space group $P2_1/n$ (No. 14). The asymmetric unit comprises one Fe atom on a special position and one AIBN ligand, one coordinated water, and one FeCl₄ counter anions in general position, Figure 6.6. The crystal structure of **6c** is made up of the packing of 2-D (4,4) topology polymeric [Fe^{II}(AIBN)H₂O]²⁺ cations and [Fe^{III}Cl₄][−] anions perpendicular to the crystallographic *b* axis.

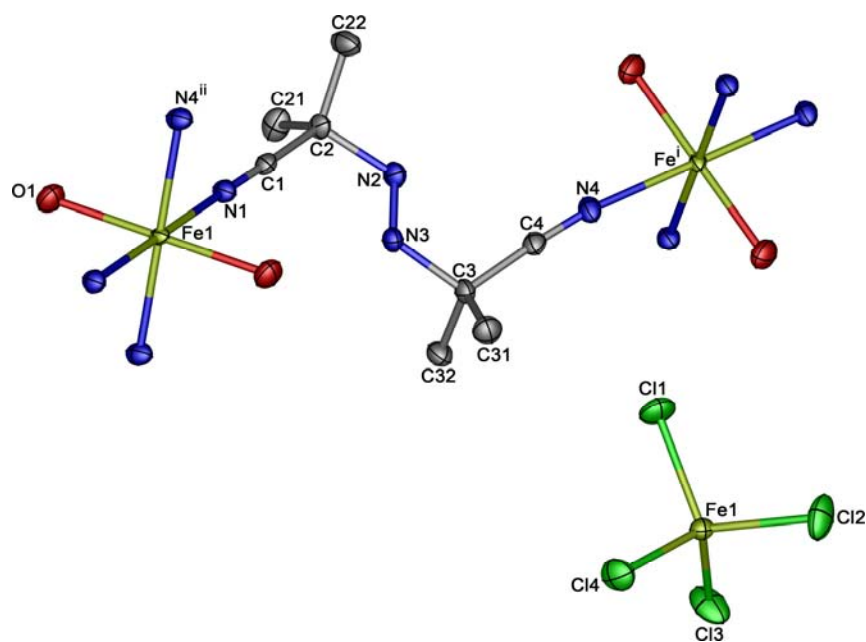


Figure 6.6 View showing the asymmetric unit with the atom numbering in **6c**.

Thermal ellipsoids are drawn at the 50% probability level at 123 K. The hydrogen atoms are omitted for clarity. Symmetry codes:

The Fe(II) ion is coordinated by four AIBN nitrogen ligands in the equatorial plane while two water molecules occupy the axial positions, forming a somewhat distorted FeN_4O_2 octahedral geometry. The Fe–N bond lengths of 2.144(1) [Fe1–N1] and 2.171(1) Å [Fe1–N4ⁱ; (i) = $x-1/2, 1/2-y, z-1/2$] are not significantly different within experimental error (3σ) and are comparable to those Fe–N bond lengths for the HS species in **6a** and **6b**. The Fe1–O1 bond length of 2.083(1) Å is well within the sum of the Fe/O van der Waals radii of 3.59 Å (Bondi, 1964). The values of the N–Fe1–N and N–Fe1–O angles between adjacent atoms are in the range 85.5(1)–94.4(1)°. This shows a strong deviation from the ideal octahedral geometry caused by the coordination of four AIBN ligands and two coordinated water

molecules. The deformation of the octahedral geometry as defined by Σ , the sum of the deviations from 90° from four $[\text{N}-\text{Fe}-\text{N}]$ angles and eight $[\text{N}-\text{Fe}-\text{O}]$ is 23.7° .

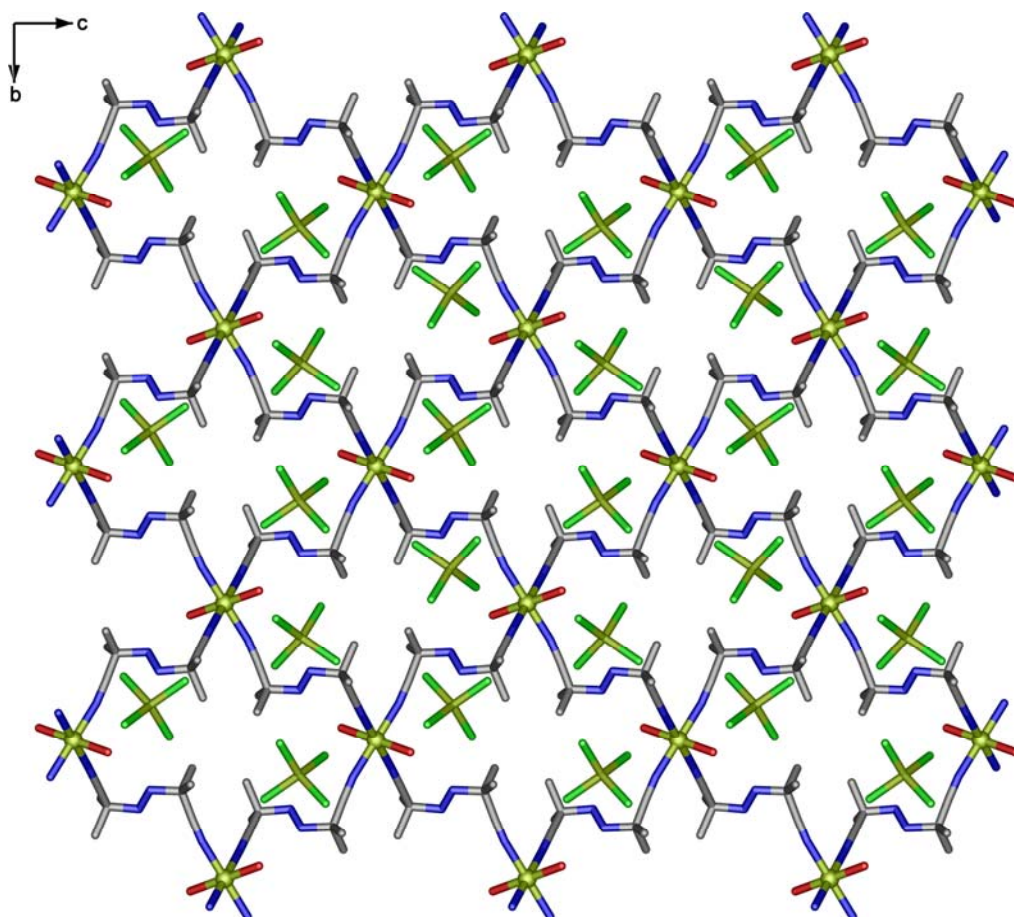


Figure 6.7 View of 2-D (4,4) sheets in **6c** along the *b* axis.

As shown in Figure 6.7, viewed perpendicular to the crystallographic *b* axis, the bridging AIBN ligands in **6c** have again an *S* shaped conformation, with a $\text{N1}\cdots\text{N4}$ separation of $6.544(1)$ Å, and then link the Fe(II) ions into a 2-D sheet topology. The cavities in the sheet exhibit rhombohedral grids with a Fe to Fe dimension of $10.3521(2) \times 10.3521(2)$ Å (the Fe \cdots Fe separation across the AIBN ligand) which is somewhat shorter than those of **6a** and **6b**. The Fe \cdots Fe distances across the windows

are 12.9995(3) and 16.1444(4) Å. The sheets pack on each other with an interlayer separation of 11.1659(2) Å (Fe \cdots Fe).

The coordination geometry around the Fe(III) centre of the Fe^{III}Cl₄ counter anions is a distorted tetrahedron. The bond lengths and angles around the Fe(III) ions are typical and comparable to those observed in **6b**. These counter anions are located between the sheets as shown in Figure 6.8. The 2-D sheet associates into a 3-D structure *via* O \cdots Cl bonds formed between the apical coordination water molecules and Cl atoms of the counter anions (Table 6.5), aligned along the crystallographic *b* axis.

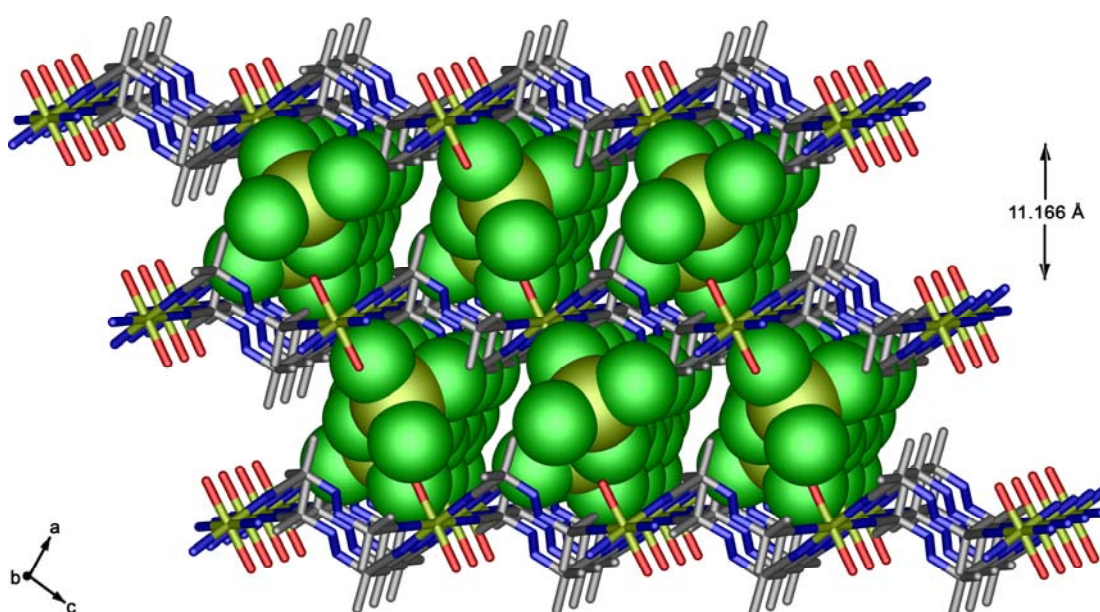


Figure 6.8 View slightly offset from the *b* axis showing the 2-D layered structure in **6c**. Inclusion of Fe^{III}Cl₄ is represented by the space filling models. Hydrogen atoms are omitted for clarity.

6.3.4 Structural Description of $[\text{Fe}^{\text{II}}(\text{ACCN})_3][\text{M}^{\text{III}}\text{Cl}_4]_2$, $\text{M}^{\text{III}} = \text{In}$ (**6c**), **Fe** (**6d**)

A CSD search, with the help of the ConQuest program (version 1.10) in the January 2008 release of the CSD version 5.29 (Allen, 1991), showed that there have been no reports on the crystal structure of compounds involving the ACCN ligand. X-ray single crystal structure analysis at 123 K reveals that compounds **6d** and **6e** are isomorphous and crystallize in a triclinic system with the space group $P\bar{1}$ (No. 2). The asymmetric unit contains one Fe atom, half of two crystallographically independent $[\text{M}^{\text{III}}\text{Cl}_4]$ ions, and half of six ACCN molecules as shown in Figure 6.9. The complex molecule is located on a general position, thus losing the crystallographic three fold symmetry in the solid state as they exist in compounds **6a** and **6b** (*vide infra*).

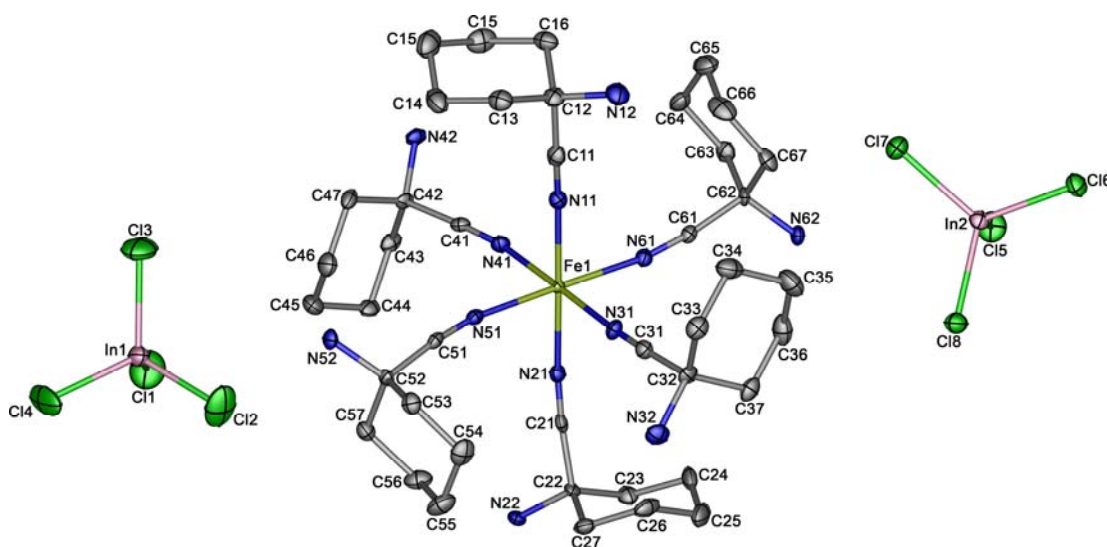


Figure 6.9 A view showing asymmetric unit with the atom numbering in **6c**. Thermal ellipsoids are drawn at the 50% probability level at 123 K. The hydrogen atoms are omitted by simplicity. **6d** is isostructural.

The Fe–N bond lengths in **6d** range from 2.123(3) to 2.172(3) Å, and correspond closely to those in **6e**, which range from 2.125(3) to 2.2.179(3) Å. These values are characteristic of the HS form of Fe(II) ions, and are comparable to those observed for the HS species in **6a** and **6b**. The Fe–N–C bond angles range from 166.9(2) to 176.0(2)° and 168.4(5) to 177.6(5)° for **6d** and **6e**, respectively, and are somewhat different from those in **6a–6c**. This change probably results from the steric effect of the R group in the ACCN ligand, which may compress all the Fe–N–C bond angles, resulting in a marked expansion and simplification of the lattice.

The bond distances and angles within the tetrahedral [M^{III}Cl₄] counter anions in **6d** and **6e** agree with those in the **6a** and **6b** analogues. The bond lengths and angles involving the ACCN dinitrile ligands are comparable to those for the AIBN ligands in **6a–6c**.

Compounds **6d** and **6e** show an extended framework similar to those of **6a** and **6b**, but more distorted, being made up of a 3-D polymeric cationic network of [Fe(ACCN)₃]²⁺ and uncoordinated [M^{III}Cl₄] anions where M = Fe (**6c**). In (**6d**), as shown in Figure 6.10. Within the network each ACCN molecule bridges two Fe(II) ions and six ACCN molecules are coordinated to each iron(II) ion in an *S* shaped conformation. Such a bridging fashion of the neighboring Fe(II) ions is propagated in three directions, leading to the formation of a 3-D network. Comparing the structures of **6a–6b** with **6d–6e**, the replacement of the two methyl groups by a cyclopentane group has little effect on the overall topology. However, the Fe···Fe separations across the ACCN ligands range from 10.6461(9) to 12.0096(9) and 10.6032(17) to 11.9705(17) Å for **6d** and **6e**, respectively, and are significantly different to those observed in **6a** and **6b** (Tables 6.3 and 6.6).

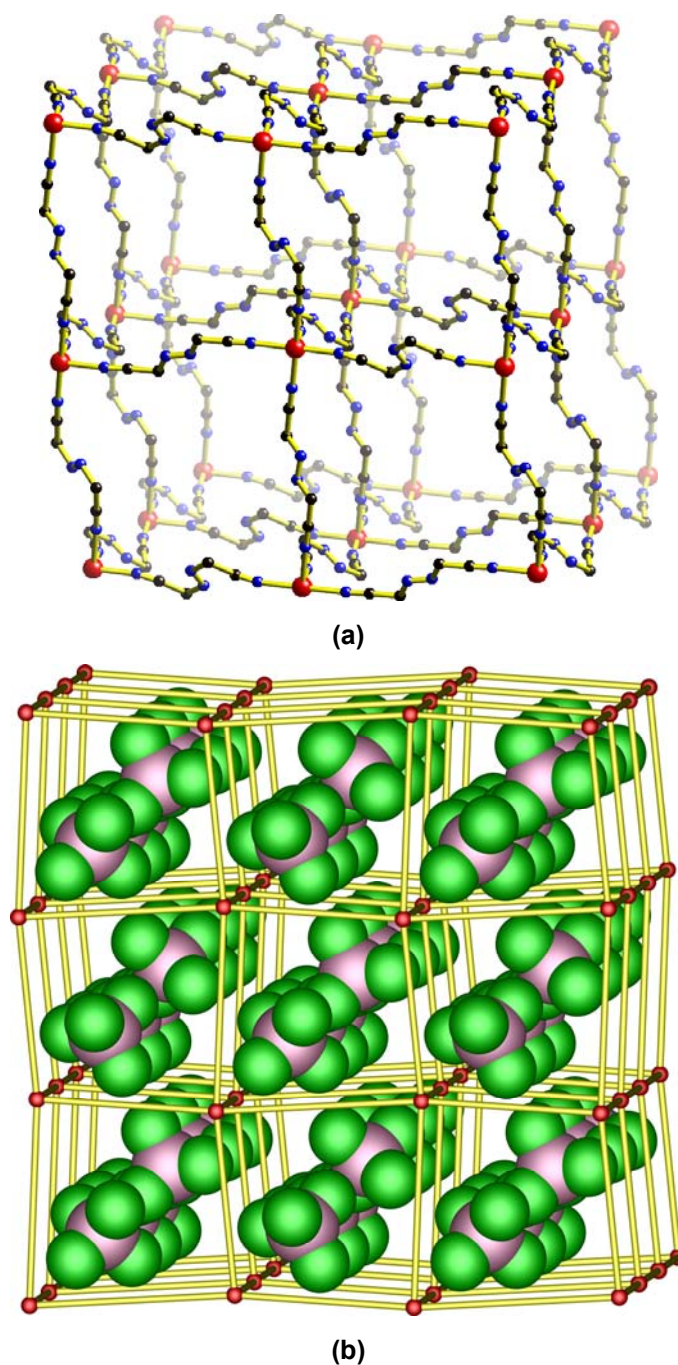


Figure 6.10 (a) A view of the 3-D net in the structure of **6d** at 123 K. Cyclopentane groups and $[\text{In}^{\text{III}}\text{Cl}_4]^-$ counter anions are omitted for clarity. (b) Schematic presentation of the α -Po-related net in **6d**. Inclusion of counter anions and ACCN molecules represented as space-filling model and yellow solid lines, respectively. Compound **6e** is isostructural.

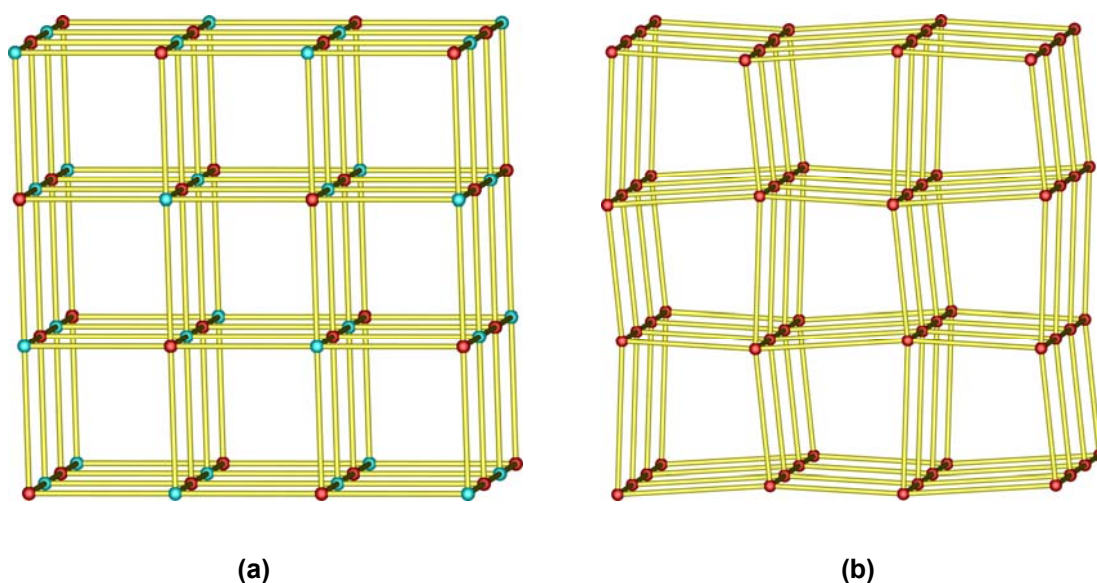


Figure 6.11 Schematic presentation in comparison of the α -Po related net for (a) **6a–6b** and (b) **6d–6e**. The red spheres correspond to Fe1, sky-blue spheres to Fe2. The ACCN or AIBN molecules are represented as yellow solid lines. Included counter anions are omitted.

In addition, similarly to that observed in compounds **6a** and **6b**, there are no conventional hydrogen bonds observed in **6d** and **6e**. There are, however, electrostatic forces and van der Waals interactions which help to stabilize the overall structures.

6.3.5 Magnetism

In order to characterize the spin state (HS vs LS) and any crossover spin transitions, the temperature dependent magnetic susceptibility measurements were performed over a 2–300 K range on freshly prepared samples. Once crystallized the sample has to be kept under a nitrogen atmosphere and put into the SQUID instrument as quickly as possible. The magnetic properties of compounds **6a–6b** and

6c–6d are represented in Figure 6.12 in the form of a $\chi_M T$ versus T plot, where χ_M is the molar magnetic susceptibility per Fe (**6a**, **6b**) and per 3Fe (**6d**, **6e**) and T is the temperature (the plots in the forms of the effective magnetic moment, μ_{eff} , versus T of compounds **6a–6b** and **6c–6d** are also provided in Figure 6.13). The magnetic behaviors of compounds **6a** and **6b** show that they undergo an incomplete spin transition, whereas no SCO occurs in **6c** and **6d** and they remain HS at all temperatures.

For **6a**, $\chi_M T$ (per Fe^{II} ion) is equal to $3.48 \text{ cm}^3 \text{ K mol}^{-1}$ ($\mu_{\text{eff}} = 5.28 \mu_B$) at 300 K, which is the expected value for the Fe(II) ions in the HS octahedral state. Upon lowering the temperature, $\chi_M T$ remains almost constant until 150 K, below this temperature, the $\chi_M T$ changes sharply to attain a value of $2.15 \text{ cm}^3 \text{ K mol}^{-1}$ ($\mu_{\text{eff}} = 4.15 \mu_B$) at 100 K. It then remains practically constant down to 50 K with this $\chi_M T$ value. In the plateau region, the compound is a mixture of HS ($S = 2$) and LS ($S = 0$) states in approximately 60% HS and 40% LS. The presence of the HS state of the paramagnetic fraction is in agreement with the results of the X-ray diffraction studies. Upon further lowering of the temperature below 40 K, $\chi_M T$ decreases again, reaching a value of $1.05 \text{ cm}^3 \text{ K mol}^{-1}$ ($\mu_{\text{eff}} = 2.90 \mu_B$) at 2 K. This decrease may be attributed to the zero-field splitting (ZFS) of the residual HS sites of the Fe(II) $^5A_{2g}$ states. In the warming mode, the $\chi_M T$ versus T is the same as observed in the cooling mode, which indicates the absence of any thermal hysteresis or thermal trapping. The T_C ($= T_{1/2}$) value of the spin transition at Fe1 sites is 118 K.

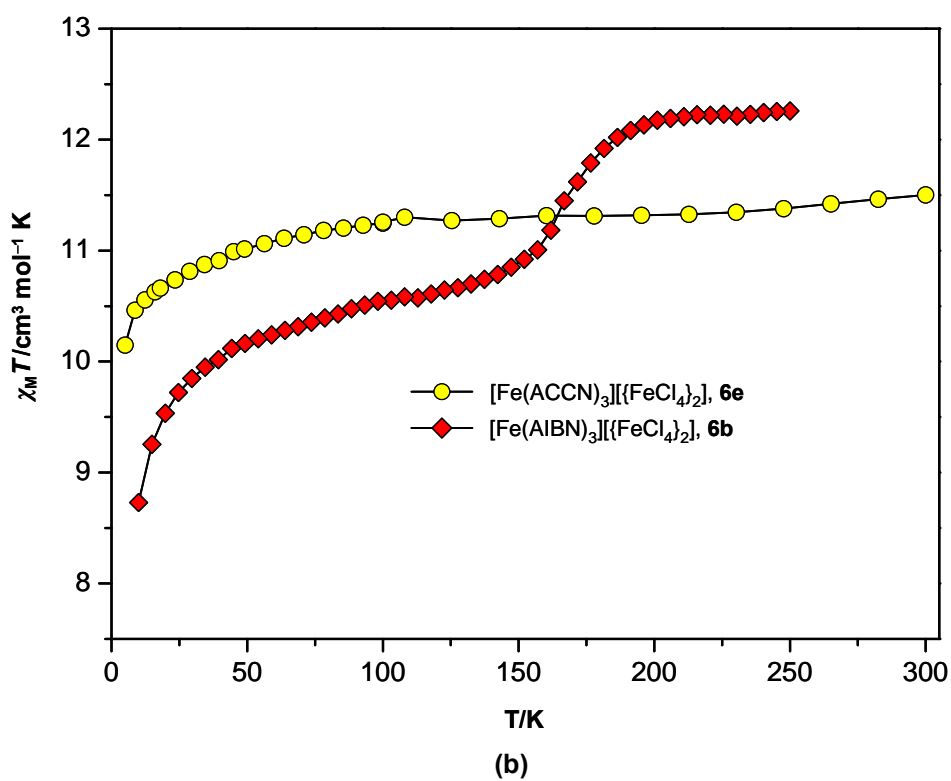
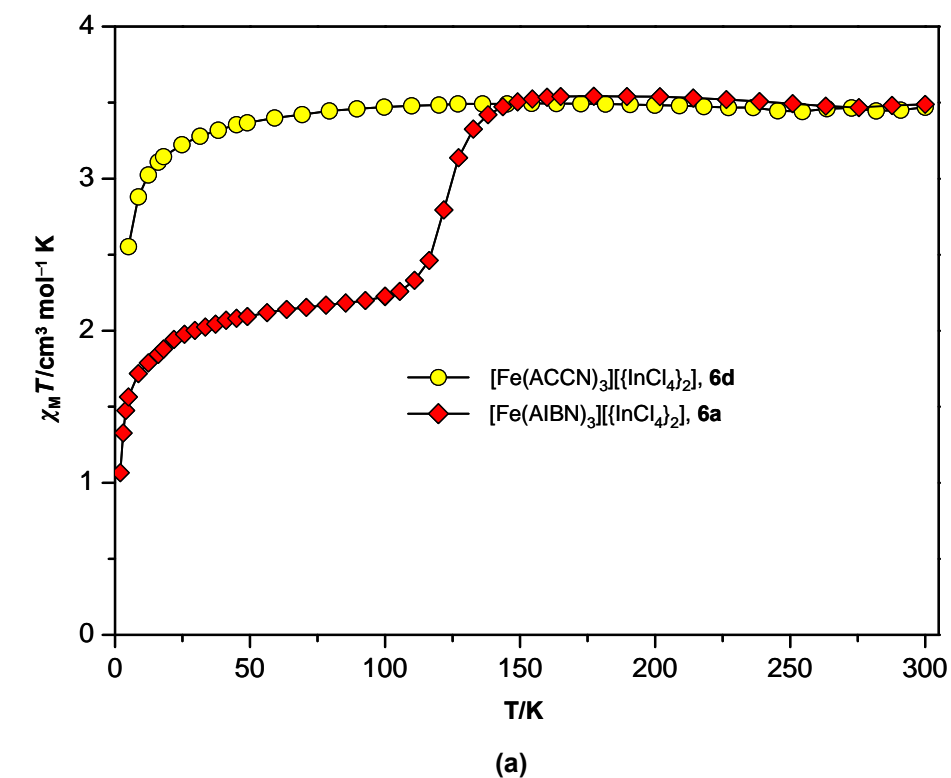


Figure 6.12 Magnetic behavior for compounds (a) **6a–6d** and (b) **6b–6e** in the form of $\chi_M T$ vs T plots.

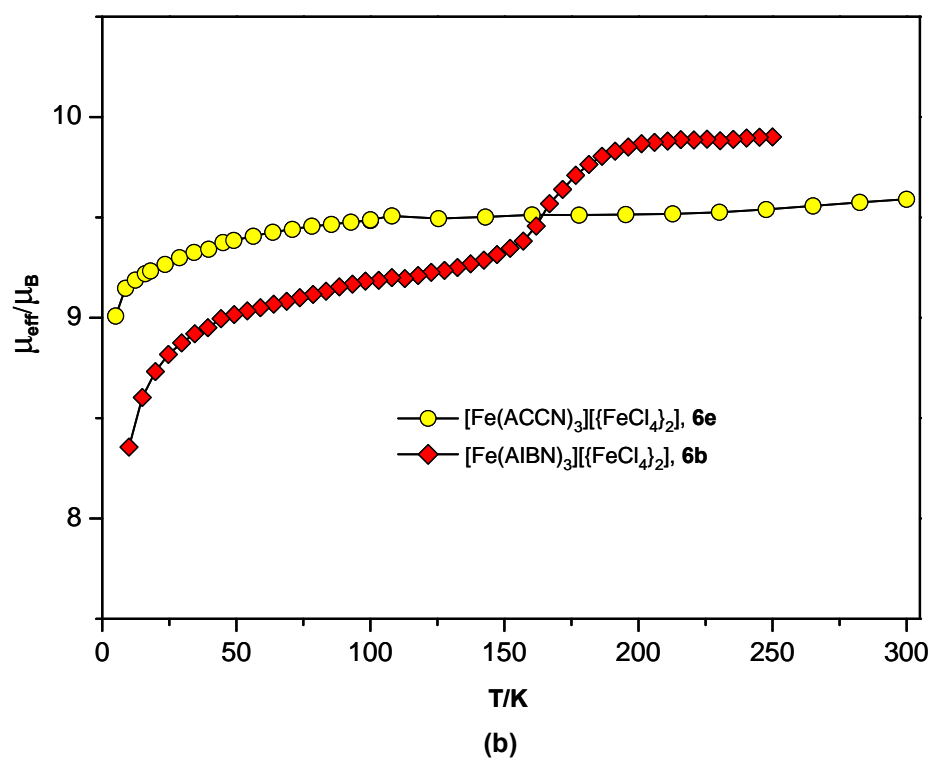
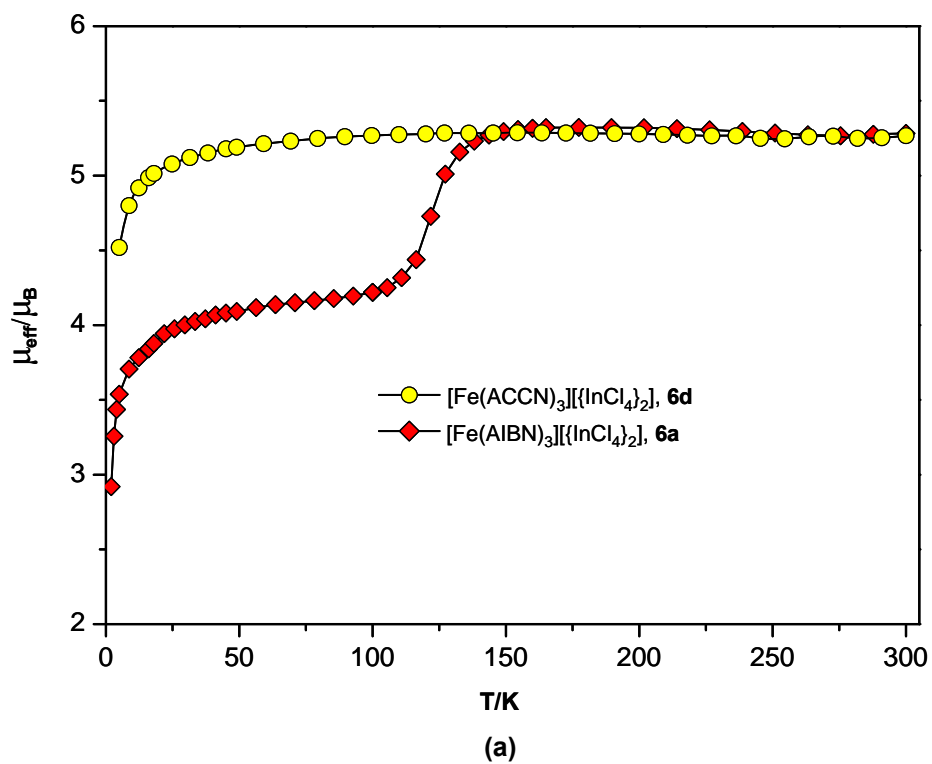


Figure 6.13 Magnetic behavior for compounds **6a–6d** and **6b–6e** in the form of μ_{eff} vs T plots.

For **6b**, $\chi_M T$ per mol is equal to $12.3 \text{ cm}^3 \text{ K mol}^{-1}$ ($\mu_{\text{eff}} = 9.92 \mu_B$) at 250 K. This $\chi_M T$ value in the HS form, calculated per 3Fe ions ($\text{Fe}^{\text{II}}, S = 2; 2\text{Fe}^{\text{III}}, S = 5/2$) is significantly larger than that of **6a** ($\text{Fe}^{\text{II}}, S = 2; 2\text{In}^{\text{III}}, S = 0$) due to the HS d^5 $[\text{Fe}^{\text{III}}\text{Cl}_4]^-$ counter anions. Upon cooling, the $\chi_M T$ values remain almost constant until *ca* 200 K. Below this temperature, the $\chi_M T$ values undergo a gradual decrease at the spin transition to reach a plateau value of *ca.* $10.5 \text{ cm}^3 \text{ K mol}^{-1}$ ($\mu_{\text{eff}} = 9.17 \mu_B$), with a small gradual decrease between 100–50 K, then more rapidly due to ZFS of $[\text{Fe}^{\text{II}}(\text{AIBN})_3]^{2+}$ and $[\text{Fe}^{\text{III}}\text{Cl}_4]^-$ HS centres to reach $8.8 \text{ cm}^3 \text{ K mol}^{-1}$ at 10 K. No thermal hysteresis was observed in this compound. The $T_{1/2}$ value is *ca.* 170 K, higher than in **6a**. After correcting χ_M for two HS Fe(III) ions ($2 \times 0.0145 \text{ cm}^3 \text{ mol}^{-1}$), the proportion of HS Fe(II) undergo SCO is *ca.* 50%.

The magnetic behaviors of **6d** and **6e** are characteristic of Fe(II) compounds in the HS state in agreement with the crystal structure data. The $\chi_M T$ value at 300 K are $3.45 \text{ cm}^3 \text{ K mol}^{-1}$ ($\mu_{\text{eff}} = 5.26 \mu_B$) and $11.50 \text{ cm}^3 \text{ K mol}^{-1}$ ($\mu_{\text{eff}} = 9.59 \mu_B$) for **6d** and **6e**, respectively. These $\chi_M T$ values are almost constant in the range 50–300 K and display Curie-Weiss behaviors; **6d**: $C = 3.12 \text{ cm}^3 \text{ K mol}^{-1}$, $\Theta = -0.87 \text{ K}$; **6e**: $C = 6.28 \text{ cm}^3 \text{ K mol}^{-1}$, $\Theta = -0.50 \text{ K}$. At the temperatures lower than 50 K, $\chi_M T$ decreases due to the occurrence of ZFS of the $S = 2$ state of the HS species.

6.3.6 Mössbauer Spectroscopy

These spectra were measured on samples **6a** and **6b** by Associate Professor John D. Cashion, School of Physics, Monash University, and were used to complement the magnetic susceptibility data and shed light on the spin states and spin transitions. Spectra are shown in Figures 6.14 and 6.15, and the values of the isomer shift, δ (IS), and quadrupole splitting, ΔE_Q (QS), half-width at half-height, Γ , and area

%, are given in Table 6.7. Many fitting attempts were made (eg. five different fits for **6a** at 295 K) and Table 6.7 contains the fit judged to be the most compatible with the structural and magnetic data as well as a low fitting value of χ^2 .

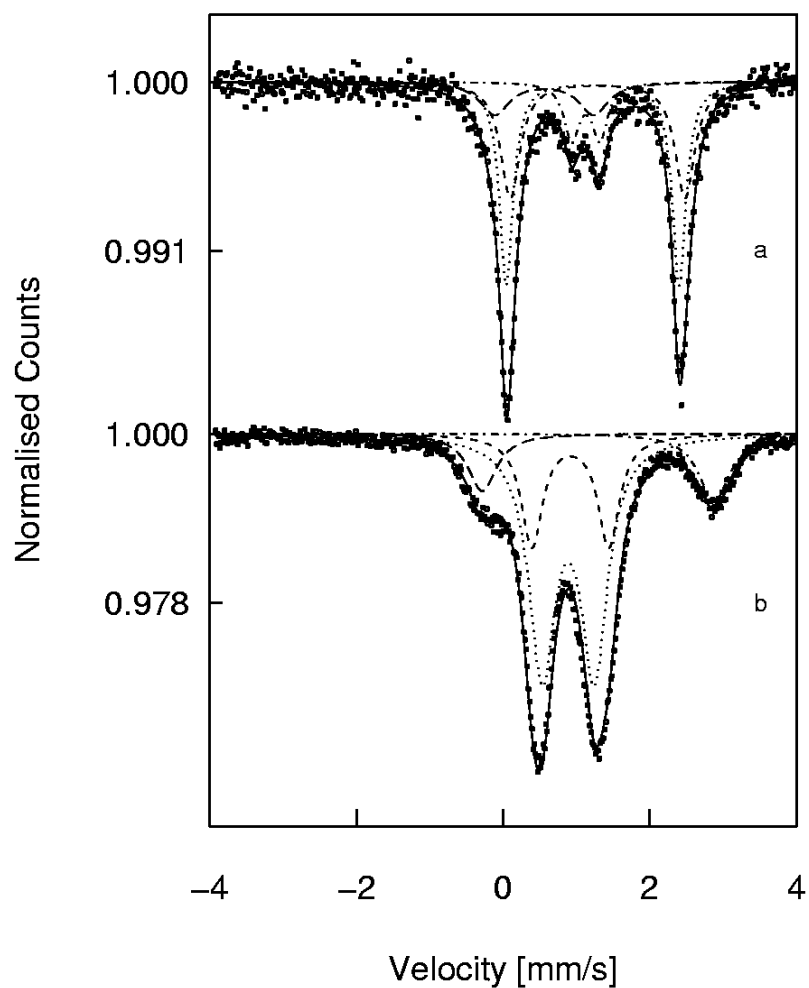


Figure 6.14 ^{57}Fe Mössbauer spectra of $[\text{Fe}^{\text{II}}(\text{AIBN})_3][\text{In}^{\text{III}}\text{Cl}_4]_2$ (**6a**) recorded at (a) 77 and (b) 295 K.

The room temperature spectrum of **6a** was fitted to four quadrupole doublets. Two doublets are assigned to similar HS sites and make up 73% of the area, in agreement with the crystal structure. They have typical HS isomer shifts and quadrupole splitting values, *viz* $\delta = 1.29 \text{ mm s}^{-1}$, $\Delta E_Q = 2.38 \text{ mm s}^{-1}$ (site 1) and $\delta = 1.22 \text{ mm s}^{-1}$, $\Delta E_Q = 2.36 \text{ mm s}^{-1}$ (site 2). Surprisingly, a 14% area doublet due to LS Fe(II) was observed, in view of the magnetism, but this sometime occurs. It showed $\delta = 0.56 \text{ mm s}^{-1}$, $\Delta E_Q = 1.35 \text{ mm s}^{-1}$. A fourth doublet with $\delta = 1.13 \text{ mm s}^{-1}$, $\Delta E_Q = 0.38 \text{ mm s}^{-1}$ helps with the fitting but can not be assigned. At 77 K, only one HS doublet, of area 18% was resolved ($\delta = 1.30 \text{ mm s}^{-1}$, $\Delta E_Q = 3.16 \text{ mm s}^{-1}$), the high value of ΔE_Q compared to the 295 K value being quite common for HS Fe(II). This agrees with the occurrence of one HS site in the structure. Interestingly, two LS doublets were resolved with a total area of 82%. This does not agree with the structure or magnetism, the latter showing 40% of LS Fe(II) and 60% of HS. Factors such as the Lamb effect can make Mössbauer areas different to known spin state concentrations, but the differences here are rather large.

Complex **6b** contains HS tetrahedral anions, $[\text{Fe}^{\text{III}}\text{Cl}_4]^-$, with $\delta \approx 0.2\text{--}0.3 \text{ mm s}^{-1}$, $\Delta E_Q \approx 0.27\text{--}0.4 \text{ mm s}^{-1}$ (Table 6.7). The room temperature spectrum has two other quadrupole doublets, a HS with $\delta = 1.16 \text{ mm s}^{-1}$, $\Delta E_Q = 2.94 \text{ mm s}^{-1}$, as the structure would suggest, and a LS with $\delta = 0.57 \text{ mm s}^{-1}$, $\Delta E_Q = 0.70 \text{ mm s}^{-1}$, the latter in tiny % area as expected. This LS line increases in intensity (13%) at 77 K, and to 24% at 4.2 K, although the latter is masked by the $[\text{Fe}^{\text{III}}\text{Cl}_4]^-$ doublet and thus has a lower δ than expected. The HS line at 4.2 has similar δ and ΔE_Q values to those at 77 K (Table 6.7) and to those of **6a**. It has area ratio of 1.5:1 (HS:LS) compared to *ca.* 1:1 from the magnetism and crystal data.

In summary, the Mössbauer data are generally in agreement with the magnetic and crystal structure but there are some differences, as described above.

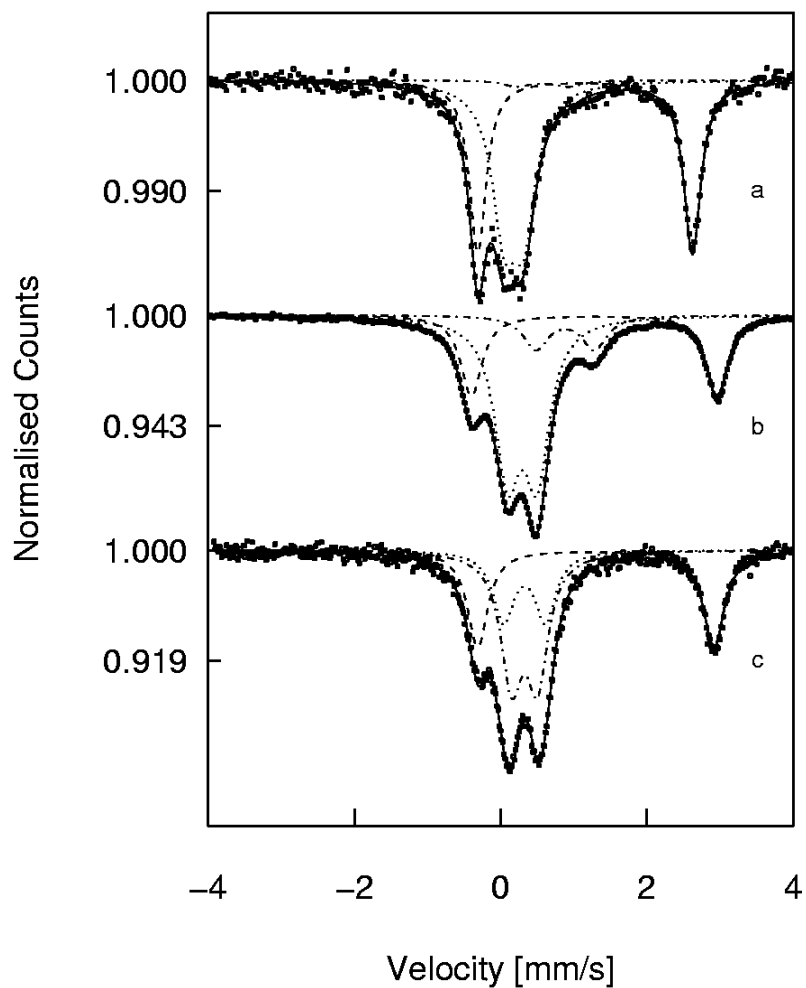


Figure 6.15 ^{57}Fe Mössbauer spectra of $[\text{Fe}^{\text{II}}(\text{AIBN})_3][\text{Fe}^{\text{III}}\text{Cl}_4]_2$ (**6b**) recorded at (a) 4.2, (b) 77, and (c) 295 K.

Table 6.7 Mössbauer data for $[\text{Fe}^{\text{II}}(\text{AIBN})_3][\text{M}^{\text{III}}\text{Cl}_4]_2$, $\text{M}^{\text{III}} = \text{In}$ (**6a**), Fe (**6b**).

Sample	T [K]	$\delta^{[\text{a}]}$ [mm s^{-1}]	ΔE_Q [mm s^{-1}]	$\Gamma^{[\text{b}]}$ [mm s^{-1}]	Area Ratio [%]	Assignment
6a	295	1.29(1)	2.38(1)	0.32	33(20)	HS(1)
		1.22(1)	2.36(1)	0.22	40(20)	HS(1)
		1.13(1)	0.38(2)	0.24	12(1)	?
		0.56(3)	1.35(6)	0.48	14(2)	LS
	77	1.30(1)	3.16(1)	0.48	18(1)	HS(1)
		0.92(1)	1.05(3)	0.35	23(7)	LS(1)
		0.89(1)	0.71(2)	0.44	59(7)	LS(2)
6b	295	1.16(1)	2.94(1)	0.28	46(1)	HS
		0.57(9)	0.70(2)	0.44	3(2)	LS
		0.18(1)	0.27(1)	0.40	51(2)	$[\text{Fe}^{\text{III}}\text{Cl}_4]^-$
	77	1.28(1)	3.36(1)	0.35	27(1)	HS
		0.88(2)	0.80(2)	0.41	13(1)	LS
		0.20(1)	0.40(1)	0.41	60(1)	$[\text{Fe}^{\text{III}}\text{Cl}_4]^-$
	4.2	1.30(1)	3.23(1)	0.34	33(1)	HS
		0.33(1)	0.57(10)	0.34	24(35)	LS
		0.33(1)	0.35(10)	0.36	44(35)	$[\text{Fe}^{\text{III}}\text{Cl}_4]^-$

^[a] Isomer shift data are reported with respect to iron foil.

^[b] Full line width at half-height.

6.4 Conclusions

Using the polymeric approach (Kahn *et al.*, 1998), five new Fe(II) coordination polymers containing the dinitrile bridging ligands AIBN and ACCN have been synthesized using one-pot assembly reaction, and have been structurally characterized. Four of the compound of type $[\text{Fe}^{\text{II}}\text{L}_3][\text{Fe}^{\text{III}}\text{Cl}_4]_2$ are an exceedingly moisture-sensitive solids, thus all syntheses were carried out under a nitrogen atmosphere in order to avoid oxidation/hydrolysis. The general crystal structures consist of a 3-D α -Po like net, except for the minor phase of a diaqua derivative **6c** that were separated from crystals of **6b**, and it has a 2-D sheet-like structure. Of these, **6a** and **6b** crystallize in a highly symmetrical $R\bar{3}$ phase. There are two crystallographically independent Fe(II) octahedrally distorted sites covalently linked *via* the nitrile nitrogen atom of AIBN bridges molecule with the Fe \cdots Fe separation *ca.* 10.5 Å. The metal atoms lie on special positions of the threefold axis as well as on inversion center. The AIBN compounds **6a** and **6b** are particular noteworthy in displaying an interesting SCO transition. This confirms the early prediction by Zuur and co-workers (1984). The SCO transitions were characterized by use of temperature dependent magnetic susceptibility (2–300 K) and Mössbauer effect spectral measurements (4.2, 77 and 295 K) together with single crystal X-ray crystallography (103 and 233 K). The data revealed that both compounds **6a** and **6b** exhibit incomplete “half” SCO phenomena at $T_{1/2} = 118$ and 170 K, respectively, with no thermal hysteresis. Only half of the Fe(II) sites (Fe1) undergo the HS \rightarrow LS transition. The reason for this is not clear except to note that one Fe site (Fe1) is different, even in the all HS form, to the offer Fe site (Fe2) and might be disposed to undergo SCO. There is no accompanying crystallographic phase change; the $R\bar{3}$

phase is retained both at 103 and 233 K. A difference between **6a** and **6b** is of course, the anion ($[\text{InCl}_4]^-$ and $[\text{FeCl}_4]^-$), but there are no anion...cation interactions. There are also subtle changes in the conformation and torsion angles of the AIBN bridging ligand across the spin transition temperatures.

For **6d** and **6e**, there is only one crystallographically unique Fe(II) center, when the ACCN ligand was used instead of the AIBN ligand. Thus the symmetry of the lattice is lowered from trigonal to triclinic with a change in the space group from $R\bar{3}$ to $P\bar{1}$ phase as AIBN is replaced ACCN (*vide infra*). On the basis of the topological perspective, **6d** and **6e** have essentially the same as those found in **6a** and **6c** but more distorted. This might be caused by the size of *R* groups on the organodinitrile ligands, *i.e.* dimethyl in AIBN and cyclopentane in ACCN. No SCO transition was observed in compounds **6d** and **6e** as evidenced by of temperature dependent magnetic susceptibility and single crystal X-ray crystallographic analysis at 123 K. The HS state of Fe(II) ion persists between 50–300 K. At lower temperatures, the magnetism displays a typical decrease in $\chi_M T$ due to the occurrence of zero-field splitting (ZFS) of the high spin $S = 2$ states. This lack of SCO in **6d** and **6e** presumably relates to the six ACCN ligands providing a weaker octahedral ligand field at Fe(II) than do the six AIBN nitrile N-donors.

Temperature induced phase transitions are of great importance in solid state chemistry, including SCO materials, and investigation of the temperature dependence of a structure can reveal much about how structure variation affects physical properties (Herbstein, 2006). However, no compounds in the present study show temperature dependent on solid-state arrangements.

Up to now, only a few 3-D open network of Fe(II) SCO compounds have been reported. Most examples in this field are coordination polymer species based on N-donating heterocyclic groups linked as a spacer (Garcia *et al.*, 1999; Absmeier *et al.*, 2006; 2007; Bronisz, 2007). The presented result shows that use groups of organodinitrile ligands provides a new class and significantly expands known examples of the Fe(II) SCO compounds with high dimensionality of polymeric structure. Construction of such materials creates the conditions for further investigation of the influence of the ligands, *eg.* linker group between $-C\equiv N$, as well as the guest counter anion molecules on the coordination polymers architecture, and also on the chemical and physical properties (magnetic, photomagnetic) of such compounds.

6.4 References

- Absmeier, A., Bartel, M., Carbonera, C., Jameson, G. N. L., Weinberger, P., Caneschi, A., Mereiter, K., Létard, J.-F., and Linert, W. (2006). **Chem. Eur. J.** 12(8): 2235-2243.
- Absmeier, A., Bartel, M., Carbonera, C., Jameson, G. N. L., Werner, F., Reissner, M., Caneschi, A., Létard, J.-F., and Linert, W. (2007). **Eur. J. Inorg. Chem.** (19): 3047-3054.
- Allen, F. H., Davies, J. E., Galloy, J. J., Johnson, O., Kennard, O., Macrae, C. F., Mitchell, E. M., Mitchell, G. F., Smith, J. M., and Watson, D. G. (1991). **J. Chem. Inf. Comput. Sci.** 31: 187-204.
- Argay G., and Sasvári, K. (1971). **Acta Crystallogr., Sect. B: Struct. Sci.** 27: 1851-1858.
- Barbour, L. J. (2001). **J. Supramol. Chem.** 1(4-6): 189-191.
- Batten, S. R., Bjernemose, J., Jensen, P., Leita, B. A., Murray, K. S., Moubaraki, B., Smith, J. P., and Toftlund, H. (2004). **J. Chem. Soc., Dalton Trans.** (20): 3370-3375.
- Batten, S. R., and Murray, K. S. (2003). **Coord. Chem. Rev.** 246(1-2): 103-130.
- Batten, S. R., and Robson, R. (1998). **Angew. Chem. Int. Ed.** 110(11): 1558-1595.
- Blessing, R. H. (1995). **Acta Crystallogr., Sect. A: Found. Crystallogr.** 51: 33-38.
- Bondi, A. (1964). **J. Phys. Chem.** 68(3): 441-451.
- Brandenburg, K., and Putz, H. (2006). **DIAMOND**. Version 3.1e. Crystal Impact GbR, Bonn, Germany.
- Bronisz, R. (2007). **Inorg. Chem.** 46(16): 6733-6739.

- Buser, H. J., Schwarzenbach, D., Petter, W., and Ludi, A. (1977). **Inorg. Chem.** 16(11): 2704-2710.
- Carlucci, L., Ciani, G., Proserpio, D. M., and Rizzato, S. (2002). **CrystEngCommun.** (22): 121-129.
- Crystal Maker (2006). Crystal Maker Software, Yarnton, England.
- Culp, J. T., Park, J.-H., Frye, F., Huh, Y.-D., Meisel, M. W., and Talham, D. R. (2005). **Coord. Chem. Rev.** 249(23): 2642-2648.
- Garcia, Y., Kahn, O., Rabardel, L., Chansou, B., Salmon, L., and Tuchagues, J. P. (1999). **Inorg. Chem.** 38(21): 4663-4670.
- Grunert, C. M., Schweifer, J., Weinberger, P., Linert, W., Mereiter, K., Hilscher, G., Muller, M., Wiesinger, G., and van Koningsbruggen, P. J. (2004). **Inorg. Chem.** 43(1): 155-165.
- Gütlich, P., Garcia, Y., and Woike, T. (2001). **Coord. Chem. Rev.** 219-221: 839-879.
- Gütlich, P., Hauser, A., and Spiering, H. (1994). **Angew. Chem. Int. Ed.** 33(20): 2024-2054.
- Halder, G. J., Kepert, C. J., Moubaraki, B., Murray, K. S., and Cashin, J. D. (2002). **Science** 298: 1762-1765.
- Herbstein, F. H. (2006). **Acta Crystallogr., Sect. B: Struct. Sci.** 62: 341-383.
- Herren, F., Fischer, P., Ludi, A., and Haelg, W. (1980). **Inorg. Chem.** 19(4): 956-959.
- Hoskins, B. F., Robson, R., and Scarlett, N. V. Y. (1994). **J. Chem. Soc., Chem. Commun.** (18): 2025-2026.
- Itaya, K., Uchida, I., and Neff, V. D. (1986). **Acc. Chem. Res.** 19(6): 162-168.

- Jensen, P., Batten, S. R., Moubaraki, B., and Murray, K. S. (2002). **J. Chem. Soc., Dalton Trans.** (19): 3712-3722.
- Kahn, O., and Martinez, C. J. (1998). **Science** 279: 44-48.
- Mason, R., Robertson, G. B., and Rusholme, G. A. (1974). **Acta Crystallogr., Sect. B: Struct. Sci.** 30: 906-910.
- Murray, K. S. (2008). **Eur. J. Inorg. Chem.** (20): 3101-3121.
- Murray, K. S., and Kepert, C. J. (2004). **Top. Curr. Chem.** 233: 195-228.
- Neville, S. M., Leita, B. A., Offermann, D. A., Duriska, M. B., Moubaraki, B., Chapman, K. W., Halder, G. J., and Murray, K. S. (2007). **Eur. J. Inorg. Chem.** (8): 1073-1085.
- Neville, S. M., Moubaraki, B., Murray, K. S., and Kepert, C. J. (2007). **Angew. Chem. Int. Ed.** 119(12): 2105-2108.
- Niel, V., Martinez-Agudo, J. M., Munoz, M. C., Gaspar, A. B., and Real, J. A. (2001). **Inorg. Chem.** 40(16): 3838-3839.
- Niel, V., Thompson, A. L., Muñoz, M. C., Galet, A., Goeta, A. E., and Real, J. A. (2003). **Angew. Chem. Int. Ed.** 42(32): 3760-3763.
- Ohba, M., and Ōkawa, H. (2000). **Coord. Chem. Rev.** 198(1): 313-328.
- Ohba, M., Ōkawa, H., Fukita, N., and Hashimoto, Y. (1997). **J. Am. Chem. Soc.** 119 (5): 1011-1019.
- Ortega-Villar, N., Thompson, A. L., Muñoz, M. C., Ugalde-Saldívar, V. M., Goeta, A. E., Moreno-Esparza, R., and Real, J. A. (2005). **Chem. Eur. J.** 11(19): 5721-5734.
- Pauling, L., and Pauling, P. (1968). **Proc. Nat. Acad. Sci. U.S.A.** 60: 362-367.

- Poll, E.-M., Olbrich F., Samba, S., Fischer, R. D., Avalle, Paolo, Apperley, D. C., and Harris, R. K. (2001). **J. Solid State Chem.** 157(2): 324-338.
- Real, J. A., Andrés, E., Muñoz, M. C., Julve, M., Granier, T., Bousseksou, A., and Varret, F. (1995). **Science** 268: 265-267.
- Roy, X., Thompson, L. K., Coombs, N., and MacLachlanref, M. J. (2008). **Angew. Chem. Int. Ed.** 47(3): 511-514.
- Schwarz, P., Siebel, E., Fischer, R. D., Apperley, D. C., Davies, N. A., and Harris, R. K. (1995). **Angew. Chem. Int. Ed.** 34(11): 1197-1199.
- Sheldrick, G. M. (1997). **SHELXL-97**: A program for crystal structure refinement. University of Geottinger: Germany.
- Sheldrick, G. M. (1997). **SHELXS-97**: A program for automatic solution of crystal structure. University of Geottinger: Germany.
- Siebel, E., and Fischer, R. D. (1997). **Chem. Eur. J.** 3(12): 1987-1991.
- Siebel, E., Fischer, R. D., Davies, N. A., Apperley, D. C., and Harris, R. K. (2000). **J. Organomet. Chem.** 604: 34-42.
- Trotter, J., Einstein, F. W. B., and Tuck, D. G. (1969). **Acta Crystallogr., Sect. B: Struct. Sci.** 25: 603-604.
- van der Sluis, P., and Spek, A. L. (1990). **Acta Crystallogr., Sect. A: Found. Crystallogr.** 46: 194-201.
- Van Langenberg, K., Batten, S. R., Berry, K. J., Hockless, D. C. R., Moubaraki, B., and Murray, K. S. (1997). **Inorg. Chem.** 36(22): 5006-5015.
- Zuur, A. P., Driessen, W. L., and Everstijn, P. L. A. (1981). **Inorg. Nucl. Chem. Lett.** 17: 15-18.

CHAPTER VII

HYDRO/SOLVOTHERMAL

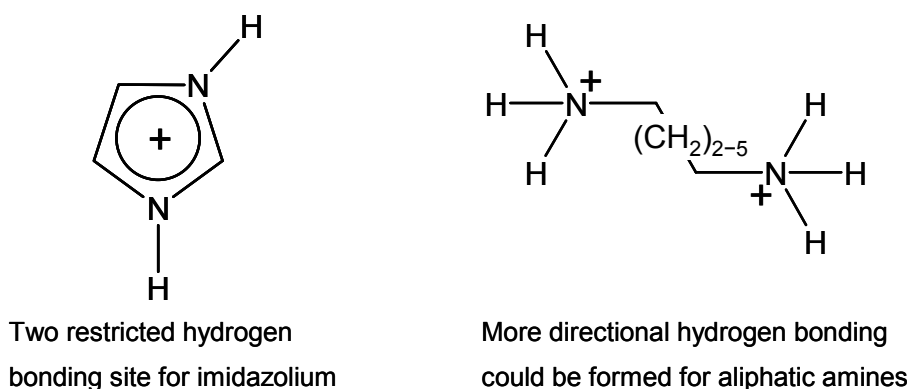
SYNTHESIS OF NEW HYBRID ORGANIC–INORGANIC

VANADIUM OXIDES COMPOUNDS

7.1 Introduction

Framework materials based on organic-inorganic hybrids involving metal oxides and organic templates are of great contemporary interest in the fields of material science and chemical research. They have a topological diversity with a rich variety of structure types and bonding geometries (Smith, 1988; Cheetham *et al.*, 1999; Lee *et al.*, 2003) that allows potential applications in the fields of catalysis, magnetism, photochemistry, and sorption (Williams *et al.*, 2000; Clearfield and Wang, 2002; MasPOCH *et al.*, 2007). In the last few years, polymers of such hybrids, particularly those involving vanadium oxide and a secondary transition metal have been made using a hydrothermal approach with an aliphatic amine as a template that provides space-filling or charge-compensation and thus acts as a structure directing agent (Chirayil *et al.*, 1998; Chesnut *et al.*, 1999; Hagrman *et al.*, 2001). Many of these compounds are frameworks built from edge- and corner-sharing of VO₄ tetrahedra, square VO₅ pyramids, or VO₆ octahedra (Zavalij and Whittingham, 1999). They have been investigated for application as secondary cathode materials (Höwing *et al.*, 2003; Whittingham, 2004), and as oxidative catalysts (Sadakane *et al.*, 2007).

The present work forms part of exploration of hitherto unreported organic-inorganic hybrids involving vanadium oxide. One focus of this research is to use the aromatic diamine planar geometry of imidazole and hydrothermal syntheses to introduce secondary inorganic metal sites. This molecule is different from the aliphatic diamines previously used (Law *et al.*, 2000; Law and Williams, 2000; Williams *et al.*, 2000) in terms of basicity, size, shape, ligation ability, hydrogen bond capacity and charge and this could allow different and more diverse framework structures, Scheme 1.



In the syntheses the inorganic-organic hybrid solids, two major types interactions are usually affecting the geometries of the structure: (i) coordination and covalent bonds connecting the metal center and appropriate ligand types, and (ii) hydrogen bonds between organic solid and the metal oxide framework. Upon protonation, the imidazolium gives a conjugate acid with $pK_a = 6.5$. It is less base compare to ordinary aliphatic organic amines, which the pK_a usually 9–11. More imidazole has to be added in order to increase the pH of the reaction mixture, and this might also affect the stoichiometric ratio of the organic moiety:metal and creates thus the structure diversity. Moreover, the imidazolium does not possesses terminal NH_3R^+ ammonium ions and it offer limited hydrogen bonds forming capability due to it rigid structure in compare with normal aliphatic organoammonium, thus the structural directing effect of it is believed to behaves quite different from the ordinary straight chain aliphatic diamines.

Scheme 1

Many hybrid organic-inorganic vanadium oxide structures have been determined by single crystal X-ray diffraction. A search of the Cambridge Structure Database (Allen *et al.*, 1995) shows that despite many of these materials displaying disorder that effects the resulting physical properties, the structures have usually only been evaluated at room temperature. Temperature induced phase transitions are of great importance in solid state chemistry (Herbstein, 2006) and investigation of the temperature dependence of a structure can reveal much about how structure variation affects physical properties.

In this chapter report the hydro/solvothermal synthesis and characterization of five new single crystal structures of hybrids organic-inorganic vanadium oxide compounds in which parts of the inorganic frameworks are constructed by $\{VO_4\}$ tetrahedra. The compounds were $[Mn_3(OH)_2(V_4O_{13})][ImH]$ (**7a**), $[Mn(Im)_4V_2O_6]$ (**7b**), $[Co(Im)_4V_2O_6]$ (**7c**), $[Ni(Im)_4V_2O_6]$ (**7d**), and $[Mn(Im)_3(DMSO)V_2O_6]$ (**7e**). The crystal structures and temperature dependence of three isomorphous of **7b-7d** are also investigated.

7.2 Experimental Section

7.2.1 Materials and Physical Measurements

$Mn(CH_3COO)_2 \cdot 4H_2O$, $Co(CH_3COO)_2 \cdot 4H_2O$, $Ni(CH_3COO)_2 \cdot 4H_2O$, V_2O_5 , and imidazole (Im) were purchased from commercial sources and used without further purification. The synthesis was carried out in a 23 ml Teflon-lined stainless autoclave under autogenous pressure with a filling capacity of about 25% (safety information for hydrothermal bomb techniques, Chainok, 2004).

The morphology of the crystalline products and heavy element ($> \text{Na}$) compositions were observed by a scanning electron microscope (Jeol model JSM-6400 SEM) equipped with an energy dispersive X-ray fluorescence microanalyzer (WDX-100 EDX attachment). Elemental analysis was performed by Medac Ltd., UK. FTIR spectra were recorded in the range $370\text{--}4000\text{ cm}^{-1}$ on a Perkin-Elmer model Spectrum GX FTIR spectrometer using KBr pellets. The phase purity of materials was established using a PW1830 Powder X-ray diffractometer with a graphite monochromator using a 1.5418 \AA Cu $K\alpha$ X-radiation source at room temperature (scanning rate: $0.025\text{ }^\circ/\text{s}$; scan range: $2\text{--}55^\circ$). Thermogravimetric analysis (TGA) was performed on a Perkin-Elmer TGA 7 thermogravimetric analyzer in the air with a heating rate of $10\text{ }^\circ\text{C}/\text{min}^{-1}$.

7.2.2 Syntheses

Preparation of $[\text{Mn}_3(\text{OH})_2(\text{V}_4\text{O}_{13})][\text{ImH}]$ (**7a**)

A single crystal of **7a** suitable for X-ray crystallographic analysis was obtained by hydrothermal synthesis. A typical procedure was to mix V_2O_5 (0.18 g, 1.0 mmol), $\text{Mn}(\text{CH}_3\text{COO})_2\cdot 4\text{H}_2\text{O}$ (0.25 g, 1.0 mmol) in the presence of Im (0.40 g, 5.88 mmol), and then dissolve the mixture with distilled water (5 mL, 444 mmol). The solution was then stirred for two hours in air to form an orange yellow mixture. The final reaction mixture was then placed in a Teflon container, sealed in a 23 mL bomb, placed in an oven, heated from room temperature to $120\text{ }^\circ\text{C}$, and maintained at $120\text{ }^\circ\text{C}$ under autogenous pressure for 5 days. After cooling, the product was filtered off from the bright yellow mother liquor, washed with distilled water, and dried overnight at room temperature. Orange plate like crystals of **7a** was easily separated from a yellow-brown powder by hand under an optical microscope. The yield was 20% (0.04

g) based on V_2O_5 . Anal. Found (Calcd) for $C_3H_6N_2O_{15}Mn_3V_4$ ($Mr = 679.69$ g/mol): C, 5.22(5.31)%, H, 0.75(0.89)%, N, 3.96(4.13)%. FTIR (ν_{max}/cm^{-1}): 3126w, 3018w, 2840w, 1516m, 1480w, 1431m, 1327m, 1262w, 1004m, 1042s, 901s, 752s, 625s, 564m.

Preparation of $[Mn(Im)_4V_2O_6]$ (**7b**)

Single crystals of **7b** were prepared following the procedure described above for **7a** above. A mixture of V_2O_5 (0.18 g, 1.0 mmol), $Mn(CH_3COO)_2 \cdot 4H_2O$ (0.25 g, 1.0 mmol), Im (0.80 g, 11.75 mmol), and distilled H_2O (5 mL, 444 mmol) was sealed in a 23 ml Teflon-lined stainless-steel autoclave. The brown-orange solution was heated to 120 °C and held at 120 °C for 5 days. After cooling, the product was filtered off, washed with distilled water, and dried overnight at room temperature. Orange-yellow block shaped crystals were easy to separate from a yellow-brown powder by hand under an optical microscope. The yield was 90% (0.14 g) based on V_2O_5 . Anal. Found (Calcd) for $C_{12}H_{16}MnN_8O_6V_2$ ($Mr = 679.69$ g/mol): C, 27.43 (27.45)%, H, 2.98(3.07)%, N, 21.37(21.34)%. EDX; V:Mn = 2:1. FTIR (ν_{max}/cm^{-1}): 3430w, 3126w, 3048w, 2942w, 2840w, 1536m, 1492w, 1480w, 1431m, 1327m, 1262w, 1094m, 1065s, 927s, 790s, 655s, 614m, 547m. TGA (under air, rate 5 °C min^{-1}) $-\Delta w$ (150–650 °C) = 52.1%, corresponding to loss of imidazole molecules (51.9% theory).

Preparation of $[Co(Im)_4V_2O_6]$ (**7c**)

Single crystals of **7c** was prepared analogously to **7b** in which $Co(CH_3COO)_2 \cdot 4H_2O$ was used instead of $Mn(CH_3COO)_2 \cdot 4H_2O$. Orange-red block shaped crystals were easy to separate from a purple powder. The yield was 95% (0.15 g) based on

V₂O₅. Anal. Found (Calcd) for C₁₂H₁₆CoN₈O₆V₂ (*Mr* = 529.13 g/mol): C, 27.41 (27.19)%, H, 2.92(3.04)%, N, 21.16(21.14)%. EDX; V:Co = 2:1. FTIR (ν_{max}/cm^{-1}): 3401w, 3122w, 3042w, 2935w, 2836w, 1534m, 1490w, 1479w, 1427m, 1326m, 1262w, 1091m, 1065s, 925s, 788s, 654s, 612m, 546m. TGA (under air, rate 5 °C min⁻¹) $-\Delta w$ (175–630 °C) = 52.0%, corresponding to loss of imidazole molecules (51.5% theory).

Preparation of [Ni(Im)₄V₂O₆] (7d)

Single crystals of **7d** was prepared analogously to **7b** in which Ni(CH₃COO)₂·4H₂O was used instead of Mn(CH₃COO)₂·4H₂O. Blue block shaped crystals were easy to separate from a brown blue powder. The yield was 90% (0.14 g) based on V₂O₅. Anal. Found (Calcd) for C₁₂H₁₆NiN₈O₆V₂ (*Mr* = 528.90 g/mol): C, 26.97 (27.25)%, H, 2.97(3.05)%, N, 21.07(21.19)%. EDX; V:Ni = 2:1. FTIR (ν_{max}/cm^{-1}): 3991w, 3118w, 3039w, 2931w, 2834w, 1533m, 1488w, 1473w, 1425m, 1324m, 1262w, 1089m, 1065s, 924s, 787s, 654s, 611m, 541m. TGA (under air, rate 5 °C min⁻¹) $-\Delta w$ (180–625 °C) = 51.9%, corresponding to loss of imidazole molecules (51.5% theory).

Preparation of [Mn(DMSO)(Im)₃V₂O₆] (7e)

Using the same stoichiometric ratio of the V₂O₅, Mn(CH₃COO)₂·4H₂O, and Im and reaction condition as in **7b**, but with the solvent changed from distilled H₂O to DMSO (2 mL, 20.2 mmol), yellow-brown plate like crystals were obtained and separated from a brown powder. The yield was 90% (0.17 g) based on V₂O₅. Anal. Found (Calcd) for C₁₁H₁₈MnN₆O₇S₁V₂ (*Mr* = 535.20 g/mol): C, 24.41(24.69)%, H, 2.92(3.39)%, N, 15.64(15.70)%. EDX; V:Mn = 2:1. FTIR (ν_{max}/cm^{-1}): 3430w, 3126w,

3048w, 2942w, 2840w, 1536m, 1492w, 1480w, 1431m, 1327m, 1262w, 1094m, 1065s, 927s, 787s, 655s, 614m, 547m. TGA (under N₂, rate 5 °C min⁻¹) $-\Delta w$ (195-670 °C) = 50.3%, corresponding to loss of organic molecules (49.8% theory).

7.2.3 X-Ray Crystallographic Study

Single crystal X-ray data were collected either on a Bruker SMART APEX 1000 CCD diffractometer (HKUST) or on an Enraf-Nonius KappaCCD diffractometer (SUT and ANU). Reflection intensities were collected using graphite monochromated Mo $K\alpha$ radiation ($\lambda = 0.71073$ Å). Structures were solved by direct methods and expanded using Fourier techniques. The structures were refined by full matrix on F^2 by SHELXTL (Sheldrick, 1997) for **7a** and **7e** or on F with use of RAELS06 (Rae, 2006) for **7b-7d**. In the final cycles of refinement, all atoms except hydrogen atoms and disordered molecules were refined anisotropically. However, special crystal structure refinement details for each compound are described below.

7a: The imidazolium molecules were found to be disordered, and were modeled in two different orientations. The total occupancy of both orientations was fixed to one. Restraints were applied to the displacement parameters of this disordered molecule.

7b-7d: Refinement of the low temperature $I4_1/a$ phase used origin choice 2 of the *International Tables for X-ray Crystallography*, Vol. A (Hahn, 1995), and 317 variables to describe 64 non hydrogen atom positions and 36 hydrogen atom positions. A separate scale constant for reflections with l odd was added for the Co structure. The second of eight imidazoles in the asymmetric unit was found to be disordered. All hydrogen atoms were reinserted in geometrically sensible positions after each refinement cycle and given atom displacement parameters defined by the

12 variable *TL* rigid body model (Rae, 1975) that described the anisotropic atom displacement parameters of the corresponding imidazole (or disordered imidazole). The centres of action for the librations were located on the associated *M* atom. A common set of refinable local orthonormal coordinates were used to impose equal planar geometry on every imidazole, their origins and orientations being independently determined. The 2-fold rotation related components of the disordered imidazole were constrained to be coplanar with the coordinating nitrogens coincident. The metal atoms and oxygen atoms were refined as isolated anisotropic atoms. Atoms *M2* and *M3* lie on 2-fold axes.

Refinement of the high temperature $P4_2/n$ phases used origin choice 2 (Hahn, 1995), and 174 variables to describe 40 non hydrogen atom positions and 24 hydrogen atom positions. The first and second of the four imidazoles in the asymmetric unit were described as 1:1 disordered and given labels 1a and 1b, and 2a and 2b. All other atoms were modelled as being ordered. All hydrogen atoms were reinserted in geometrically sensible positions after each refinement cycle and given atom displacement parameters defined by the rigid body models for the atoms to which they were attached. The two disordered imidazoles are attached to the *M1* atom and their atoms were modelled to have a common *T* rigid model parametrisation plus individual librations about the relevant *M1*–N bonds. The other two imidazoles were attached to *M2* and were also modelled to have a common *T* rigid model parametrisation plus individual librations about the relevant *M2*–N bonds. A common set of refinable local orthonormal coordinates were used to impose equal planar geometry on every imidazole, their origins and orientations being independently determined. Restraints were used to match the *M1*–N bond distances of each

component of a disordered imidazole. Restraints were also used to initially restrain second nearest neighbour $M1-C$ distances but these restraints were reduced to minimal importance in the final refinement cycle. The metal atoms and oxygen atoms were refined as isolated anisotropic atoms. Atoms $M1$ and $M2$ lie on 2-fold axes.

For $M = Ni$, the low temperature $P2/n$ phase was described using 287 variables to describe 60 non-hydrogen atoms and 32 hydrogen atom positions in the asymmetric unit. Only the sixth of eight imidazoles is not hydrogen bonded and a mixed scattering factor description was used to justify the atom labeling. A model for C62 as $(1-\delta_1)f_C + \delta_1f_N$ and N62 as $(1-\delta_2)f_C + \delta_2f_N$, where $\delta_1 + \delta_2 = 1$ gave $\delta_1 = 0.035$ (25). All hydrogen atoms were reinserted in geometrically sensible positions after each refinement cycle and give atom displacement parameters defined by the rigid body models applying to the atoms to which they were attached. In the asymmetric unit, pairs of imidazoles are attached to non equivalent Ni atoms on 2-fold axes and were given rigid body T model parameters constrained by this symmetry (Rae, 1975). Additional L model parameters (6 per imidazole) centered on the relevant Ni were also included to describe the imidazole atom displacement parameters by $4 \times (4 + 2 \times 6) = 64$ variables. A common set of refinable local orthonormal coordinates were used to impose equal planar geometry on the imidazoles, their origins and orientations being independently refined. No restraints were used. The metal and oxygen atoms were refined as independent anisotropic atoms. The crystals were found to be 0.746 (3):0.254 twinned assuming a 90° rotation about \mathbf{b} as the twinning operation and allowing for the overlap of adjacent reflections modeling the observed intensity using the function $Y = 0.746 (3) |F_1|^2 + 0.254 P |F_2|^2$ where $P = 0.5 - 0.5 \sin(\pi(d - d_0)/2d_0)$

if $d < 2d_0$, 0 otherwise. d is the separation in reciprocal space of overlapping twin component reflections and d_0 was refined to be $0.1397(5) a^*$.

The data collection and structure refinement details for **7a–7e** at selected temperatures are listed in Tables 7.1–7.4. Detailed refinement statistics for **7b–7d** are given in Table 7.5. Other crystallographic data of compounds **7a–7e** are given as supplementary material in the CIF which can be found on the attached CD-ROM.

Table 7.1 Summary of crystallographic data for the compounds **7a** and **7e**.

Identification code	7a	7e
Formula	C ₃ H ₇ Mn ₃ N ₂ O ₁₅ V ₄	C ₁₁ H ₁₈ MnN ₆ O ₇ SV ₂
<i>Mr</i>	679.69	535.20
Crystal system	triclinic	monoclinic
Crystal color/habit	orange/plate	yellow-brown/plate
Crystal size (mm)	0.15 × 0.15 × 0.10	0.33 × 0.23 × 0.13
Space group	<i>P</i> -1 (No. 2)	<i>P</i> 2 ₁ / <i>n</i> (No. 14)
<i>a</i> (Å)	5.005(1)	10.125(2)
<i>b</i> (Å)	8.107(1)	14.784(3)
<i>c</i> (Å)	10.170(2)	13.668(3)
<i>α</i> (°)	84.87(3)	90
<i>β</i> (°)	87.52(3)	92.51(3)
<i>γ</i> (°)	80.84(3)	90
<i>V</i> (Å ³)	405.61(1)	2044.1(7)
<i>Z</i>	1	4
<i>D</i> _{calc} (Mg m ⁻³)	2.783	1.739
Temperature (K)	100(2)	298(2)
<i>μ</i> (Mo <i>Kα</i>) (mm ⁻¹)	4.54	1.651
<i>F</i> (000)	648	1076.0
<i>θ</i> range (°)	3.4 – 28.0	2.03 – 25.0
Data completeness	0.95	0.99
Limiting indices <i>h</i>	-6 → 6	-12 → 11
<i>k</i>	-10 → 10	-10 → 17
<i>l</i>	-13 → 13	-15 → 16
<i>T</i> _{min} / <i>T</i> _{max}	0.511/0.635	0.528/0.806
Reflections collected/unique	3890/1096	10238/2580
<i>R</i> _{int}	0.075	0.055
Data/restraints/parameters	1589/10/124	3591/0/253
<i>R</i> ₁ , <i>wR</i> ₂ [all data]	0.046, 0.070	0.069, 0.163
<i>R</i> ₁ , <i>wR</i> ₂ [<i>I</i> > 2σ(<i>I</i>)]	0.077, 0.077	0.099, 0.151
Goodness of fit, <i>S</i>	1.03	0.98
Δρ _{min} , Δρ _{max} (e Å ⁻³)	0.68, -0.97	0.98, -0.64

Computer programs: Diamond v. 3e (Brandenburg and Putz, 2006), SADABS (Blessing, 1995), SHELXL-97 (Sheldrick, 1997), SHELXS-97 (Sheldrick, 1997).

Table 7.2 Summary of crystallographic data for the compound **7b** at selected temperatures.

Identification code	7b				
Temperature (K)	100(2)	200(2)	279(2)	283(2)	295(2)
Formula	C ₁₂ H ₁₆ MnN ₈ O ₆ V ₂	C ₁₂ H ₁₆ MnN ₈ O ₆ V ₂	C ₁₂ H ₁₆ MnN ₈ O ₆ V ₂	C ₁₂ H ₁₆ MnN ₈ O ₆ V ₂	C ₁₂ H ₁₆ MnN ₈ O ₆ V ₂
<i>Mr</i>	525.13	525.13	525.13	525.13	525.13
Crystal system	tetragonal	tetragonal	tetragonal	tetragonal	tetragonal
Crystal color/habit	orange-yellow/block	orange-yellow/block	orange-yellow/block	orange-yellow/block	orange-yellow/block
Crystal size (mm)	0.16 × 0.14 × 0.09	0.16 × 0.14 × 0.09	0.16 × 0.14 × 0.09	0.16 × 0.14 × 0.09	0.16 × 0.14 × 0.09
Space group	<i>I</i> 4 ₁ / <i>a</i> (No. 88)	<i>I</i> 4 ₁ / <i>a</i> (No. 88)	<i>I</i> 4 ₁ / <i>a</i> (No. 88)	<i>P</i> 4 ₂ / <i>n</i> (No. 86)	<i>P</i> 4 ₂ / <i>n</i> (No. 86)
<i>a</i> (Å)	23.0354(3)	23.0473(3)	23.0645(3)	16.3271(2)	16.3615(2)
<i>b</i> (Å)	23.0354(3)	23.0473(3)	23.0645(3)	16.3271(2)	16.3615(2)
<i>c</i> (Å)	29.6005(3)	29.6521(3)	29.6897(3)	14.8304 (2)	14.8030(2)
<i>α</i> (°)	90	90	90	90	90
<i>β</i> (°)	90	90	90	90	90
<i>γ</i> (°)	90	90	90	90	90
<i>V</i> (Å ³)	15706.9(3)	15750.5(3)	15794.1(3)	3953.40(9)	3962.74(9)
<i>Z</i>	32	32	32	8	8
<i>D</i> _{calc} (Mg m ⁻³)	1.777	1.772	1.767	1.765	1.760
<i>μ</i> (Mo <i>Kα</i>) (mm ⁻¹)	1.61	1.61	1.61	1.61	1.61
<i>F</i> (000)	8416.0	8416.0	8416.0	2004.0	2004.0
<i>θ</i> range (°)	2.6 – 30.0	2.6 – 30.0	2.6 – 30.0	2.6 – 30.0	2.6 – 30.0
Data completeness	0.99	1.00	1.00	0.99	0.99
Limiting indices <i>h</i>	–31 → 32	–32 → 25	–32 → 30	–22 → 21	–23 → 16
<i>k</i>	–32 → 32	–32 → 27	–32 → 32	–22 → 22	–23 → 16
<i>l</i>	–30 → 41	–41 → 41	–41 → 41	–19 → 20	–20 → 19
<i>T</i> _{min} / <i>T</i> _{max}	0.684/0.767	0.708/0.768	0.707/0.765	0.678/0.765	0.672/0.765
Reflections collected/unique	106159/11464	96520/11499	109552/11539	55800/5769	54609/5784
<i>R</i> _{int}	0.058	0.061	0.059	0.055	0.059
Data/parameters	8019/317	7205/317	6608/317	4293/174	4271/174
<i>R</i> ₁ , <i>wR</i> ₂ [<i>I</i> > 3σ(<i>I</i>)]	0.032, 0.046	0.033, 0.046	0.035, 0.050	0.048, 0.075	0.040, 0.060
Goodness of fit, <i>S</i>	1.47	1.45	1.56	2.59	2.06
Δ <i>ρ</i> _{min} , Δ <i>ρ</i> _{max} (e Å ⁻³)	1.22, –0.98	0.76, –0.70	1.08, –0.70	2.14, –1.24	1.11, –0.80

Computer programs: COLLECT (Nonius BV, 1997–2000), HKL SCALEPACK (Otwinowski and Minor, 1997), DENZO and SCALEPAK (Otwinowski and Minor, 1997), SIR97 (Altomare *et al.*, 1999), RAELS06 (Rae, 2006), ORTEP (Burnett and Johnson, 1996), and Diamond V.3e (Brandenburg and Putz, 2006).

Table 7.3 Summary of crystallographic data for the compound **7c** at selected temperatures.

Identification code	7c			
Temperature (K)	100(2)	170(2)	180(2)	295(2)
Formula	C ₁₂ H ₁₆ CoN ₈ O ₆ V ₂	C ₁₂ H ₁₆ CoN ₈ O ₆ V ₂	C ₁₂ H ₁₆ CoN ₈ O ₆ V ₂	C ₁₂ H ₁₆ CoN ₈ O ₆ V ₂
<i>Mr</i>	529.13	529.13	529.13	529.13
Crystal system	tetragonal	tetragonal	tetragonal	tetragonal
Crystal color/habit	orange-red/block	orange-red/block	orange-red/block	orange-red/block
Crystal size (mm)	0.25 × 0.19 × 0.18	0.25 × 0.19 × 0.18	0.25 × 0.19 × 0.18	0.25 × 0.19 × 0.18
Space group	<i>I</i> 4 ₁ / <i>a</i> (No. 88)	<i>I</i> 4 ₁ / <i>a</i> (No. 88)	<i>P</i> 4 ₂ / <i>n</i> (No. 86)	<i>P</i> 4 ₂ / <i>n</i> (No. 86)
<i>a</i> (Å)	22.8606(3)	22.8863(3)	16.2544(2)	16.2666(3)
<i>b</i> (Å)	22.8606(3)	22.8863(3)	16.2544(2)	16.2666(3)
<i>c</i> (Å)	29.2658(3)	29.2700(3)	14.5532(2)	14.6057(2)
<i>α</i> (°)	90	90	90	90
<i>β</i> (°)	90	90	90	90
<i>γ</i> (°)	90	90	90	90
<i>V</i> (Å ³)	15294.5(3)	15331.1(3)	3845.1(1)	3864.7(1)
<i>Z</i>	32	32	8	8
<i>D</i> _{calc} (Mg m ⁻³)	1.839	1.835	1.829	1.819
<i>μ</i> (Mo <i>Kα</i>) (mm ⁻¹)	1.86	1.86	1.86	1.86
<i>F</i> (000)	8480.0	8480.0	2012.0	2012.0
<i>θ</i> range (°)	2.6 – 30.0	2.6 – 30.0	2.6 – 30.0	2.6 – 30.0
Data completeness	1.00	0.99	0.99	1.000
Limiting indices <i>h</i>	–32 → 32	–32 → 32	–22 → 22	–22 → 22
<i>k</i>	–32 → 30	–32 → 30	–22 → 22	–22 → 22
<i>l</i>	–41 → 41	–41 → 41	–20 → 20	–20 → 20
<i>T</i> _{min} / <i>T</i> _{max}	0.636/0.720	0.639/0.719	0.658/0.721	0.662/0.720
Reflections collected/unique	127079/11163	107994/11199	59858/5608	57596/5657
<i>R</i> _{int}	0.059	0.057	0.046	0.059
Data/parameters	7414/318	6461/318	4475/174	3905/174
<i>R</i> ₁ , <i>wR</i> ₂ [<i>I</i> > 3σ(<i>I</i>)]	0.035, 0.056	0.040, 0.065	0.032/0.050	0.033/0.047
Goodness of fit, <i>S</i>	1.85	2.10	1.80	1.56
Δ <i>ρ</i> _{min} , Δ <i>ρ</i> _{max} (e Å ⁻³)	1.20, –1.13	2.40, –1.40	1.07, –0.53	0.72, –0.55

Computer programs: COLLECT (Nonius BV, 1997–2000), HKL SCALEPACK (Otwinowski and Minor, 1997), DENZO and SCALEPAK (Otwinowski and Minor, 1997), SIR97 (Altomare *et al.*, 1999), RAELS06 (Rae, 2006), ORTEP (Burnett and Johnson, 1996), and Diamond V.3e (Brandenburg and Putz, 2006).

Table 7.4 Summary of crystallographic data for the compound **7d** at 100(2) and 295(2) K.

Identification code	7d	
	100(2)	295(2)
Temperature (K)	100(2)	295(2)
Formula	C ₁₂ H ₁₆ NiN ₈ O ₆ V ₂	C ₁₂ H ₁₆ NiN ₈ O ₆ V ₂
<i>Mr</i>	528.90	528.90
Crystal system	monoclinic	tetragonal
Crystal color/habit	blue/block	blue/block
Crystal size (mm)	0.40 × 0.21 × 0.18	0.40 × 0.21 × 0.18
Space group	<i>P</i> 2/ <i>n</i> (No. 2)	<i>P</i> 4 ₂ / <i>n</i> (No. 86)
<i>a</i> (Å)	16.1379(3)	16.1988(2)
<i>b</i> (Å)	14.3657(2)	16.1988(2)
<i>c</i> (Å)	16.3422(4)	14.5589(2)
<i>α</i> (°)	90	90
<i>β</i> (°)	90.1205(9)	90
<i>γ</i> (°)	90	90
<i>V</i> (Å ³)	3788.64(13)	3820.27(8)
<i>Z</i>	8	8
<i>D</i> _{calc} (Mg m ⁻³)	1.855	1.839
<i>μ</i> (Mo <i>Kα</i>) (mm ⁻¹)	2.0	2.0
<i>F</i> (000)	2128.0	2
<i>θ</i> range (°)	2.6 – 30.0	2.6 – 30.0
Data completeness	0.99	1.00
Limiting indices <i>h</i>	–22 → 22	–22 → 22
<i>K</i>	–20 → 19	–22 → 22
<i>L</i>	–23 → 23	–20 → 19
<i>T</i> _{min} / <i>T</i> _{max}	0.619/0.712	0.630/0.703
Reflections collected/unique	53813/11073	48877/5581
<i>R</i> _{int}	0.055	0.047
Data/parameters	9089	4334
<i>R</i> ₁ , <i>wR</i> ₂ [<i>I</i> > 3σ(<i>I</i>)]	0.039, 0.053	0.031, 0.048
Goodness of fit, <i>S</i>	1.67	1.70
Δ <i>ρ</i> _{min} , Δ <i>ρ</i> _{max} (e Å ⁻³)	2.30, –2.32	0.81, –0.65

Computer programs: COLLECT (Nonius BV, 1997-2000), HKL SCALEPACK (Otwinowski and Minor, 1997), DENZO and SCALEPAK (Otwinowski and Minor, 1997), SIR97 (Altomare *et al.*, 1999); RAELS06 (Rae, 2006), ORTEP (Burnett and Johnson, 1996), and Diamond V.3e (Brandenburg and Putz, 2006).

Table 7.5 Refinement statistics for the compounds **7b–7d** at selected temperatures.

Temperature (K)	Class	Number of reflections	$R(F)$	$R(F^2)$	$wR(F)$	GoF
7b at 100(2)	1	4749	0.027	0.039	0.044	1.56
	2	3540	0.054	0.080	0.063	1.61
	1 + 2	8289	0.033	0.042	0.050	1.58
	1 + 2 + 3	11464	0.055	0.046	0.057	1.53
7b at 200(2)	1	4515	0.028	0.041	0.043	1.49
	2	2914	0.059	0.089	0.063	1.54
	1 + 2	7429	0.034	0.044	0.049	1.51
	1 + 2 + 3	11499	0.065	0.050	0.058	1.44
7b at 279(2)	1	4432	0.030	0.043	0.045	1.55
	2	2436	0.071	0.108	0.076	1.72
	1 + 2	6868	0.037	0.046	0.053	1.64
	1 + 2 + 3	11539	0.080	0.053	0.065	1.56
7b at 283(2)	1	4397	0.049	0.064	0.076	2.61
	1 + 3	5769	0.065	0.067	0.079	2.38
7b at 295(2)	1	4352	0.041	0.068	0.060	2.06
	1 + 3	5784	0.058	0.071	0.065	1.92
7c at 100(2)	1	4687	0.028	0.040	0.047	1.77
	2	3186	0.092	0.125	0.109	2.46
	1 + 2	7873	0.040	0.044	0.065	2.08
	1 + 2 + 3	11163	0.066	0.048	0.073	1.96
7c at 170(2)	1	4592	0.033	0.047	0.054	1.98
	2	2411	0.146	0.210	0.161	2.94
	1 + 2	7003	0.047	0.051	0.075	2.36
	1 + 2 + 3	11199	0.085	0.057	0.086	2.13
7c at 180(2)	1	4450	0.032	0.044	0.051	1.84
	1 + 3	5608	0.043	0.046	0.054	1.77
7c at 295(2)	1	3990	0.034	0.045	0.048	1.60
	1 + 3	5657	0.059	0.050	0.056	1.55
7d at 100(2)	1	9244	0.040	0.059	0.054	1.70
	1 + 3	11073	0.049	0.061	0.056	1.62
7d at 295(2)	1	4420	0.032	0.044	0.049	1.73
	1 + 3	5581	0.044	0.046	0.053	1.66

Class 1: Reflection with $I > 3\sigma(I)$ and $h + k + l$ even. *Class 2:* Reflection with $I > 3\sigma(I)$ and $h + k + l$ odd. *Class 3:* Reflection all with $I < 3\sigma(I)$ and not included in the refinement. Average of F^2 for Class 2 relative to Class 1 is 0.111 (100(2) K), 0.098 (200(2) K), and 0.082 (279(2) K) for **7b**, 0.066 (100(2) K), and 0.044 (170(2) K) for **7c**.

7.3 Results and Discussion

7.3.1 Syntheses and Characterization

The temperature of the reaction is of crucial importance for the crystallization of M/V/O/imidazole products. Experiments conducted at temperatures between 160 and 200°C gave black brown powders that do not contain imidazole, as verified by IR studies. These materials were not characterized further. However, maintaining the temperature of the crystallization reaction between 110 and 120 °C generally gave two product components (a crystalline material and powder). Therefore, in this study temperature of reactions of vanadium oxide with a secondary metal in the presence of imidazole was generally controlled near 120 °C to produce nice crystalline products. Time also played an important role affecting the morphology and particle size of crystallized products. To grow single crystals with dimensions 0.2–0.4 mm, suitable for X-ray crystallography, it is necessary to increase the reaction time, typically to 4–5 days.

In order to assignment of single crystal for analyzed with a laboratory X-ray crystallography, SEM is also one of powerful method to provided a good indication of single crystal character. SEM pictures of compounds **7a–7e** are shown in Figure 7.1. The morphology of a single crystals of **7a** are often intergrown plate like crystal with size of *ca.* 1.0–2.0 mm. Beside, **7b–7d** are observed to be similar that in hexagonal-shaped single crystals with particle diameter of *ca.* 1.0–2.0 mm, whilst that of **7e** are stacked in a random fashion *ca.* 0.5–1.0 mm in size. It is evidence that these particles are particularly clear and large enough to be determining with a single crystal X-ray diffractometer. In addition, for all compounds the EDX analysis confirmed the presence of M and V in *ca.* 1:2 ratio in crystalline materials.

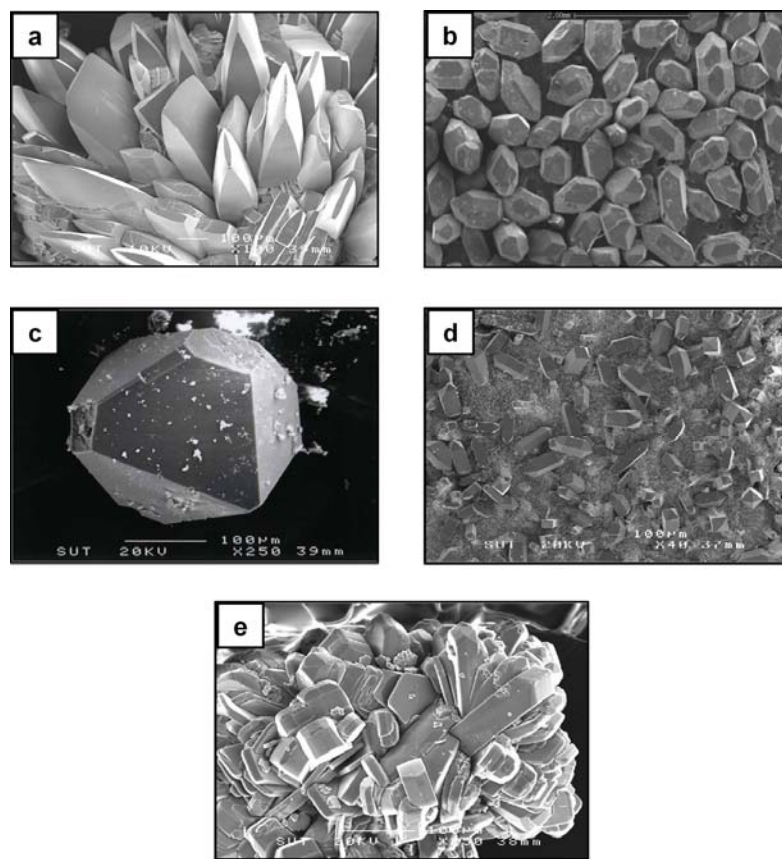


Figure 7.1 SEM pictures of (a) **7a**, (b) **7b**, (c) **7c**, (d) **7d**, and (e) **7e**.

The balanced chemical equations representing the syntheses of the products do not always correspond to the actual stoichiometric ratio of the reactants that are required to maximize the product yields. This is not surprising as other products are also formed. There are at least five factors which influence the composition and structure of the reaction products: stoichiometry, temperature, reaction times, concentration, and pH. Although we were not able to clarify fully the effect of each of these factors, some distinct tendencies were observed from the many synthetic trials. The conditions reported in the sample preparation section are optimum for preparing the compounds in highly crystalline form. The compounds are phase pure by microscopic examination, microelemental analysis, and powder X-ray diffraction. As

shown in Figure 7.2, the room temperature PXRD patterns of bulk materials of compounds correspond well in position with the simulated one on the basis of the single crystal data, indicating the phase purity of the synthesized sample.

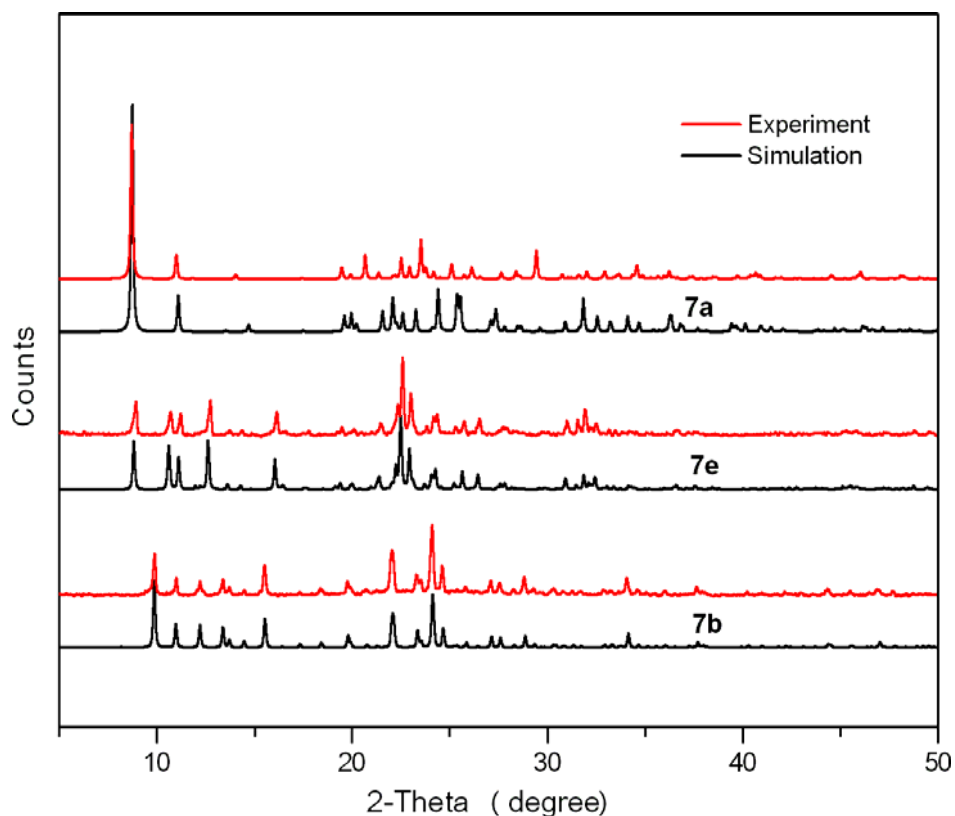


Figure 7.2 Simulation and experiment PXRD patterns of **7a**, **7b**, and **7e**. **7c** and **7d** are isostructure to **7b**.

7.3.2 Structural Description of $[\text{Mn}_3(\text{OH})_2(\text{V}_4\text{O}_{13})][\text{ImH}]$ (**7a**)

Compound **7a** crystallizes in the centrosymmetric triclinic space group $P\bar{1}$ with $Z = 1$. The structure consists of an open 3-D anionic framework which is charged balance by imidazolium cations. The asymmetric unit contains sixteen non-hydrogen atoms, out of which twelve belong to the inorganic framework and five to the protonated aromatic amine ligand, Figure 7.3. There are two crystallographically

independent vanadium atoms and two distinct manganese atoms. The oxidation states of the metals are determined by bond valence sum (Brown and Altermatt, 1985; Brese and O'Keeffe, 1991) to be Mn^{II} , Mn^{III} , and V^{V} . Therefore, **7a** is a mixed-valence manganese metal. The Mn–O bond distances vary from 1.895(4) to 2.225(4) Å (mean 2.087 Å) and the V–O distances in the range 1.639(4)–1.799(4) Å (mean 1.716 Å). Selected interatomic bond lengths for compound **7a** are given in Table 7.6.

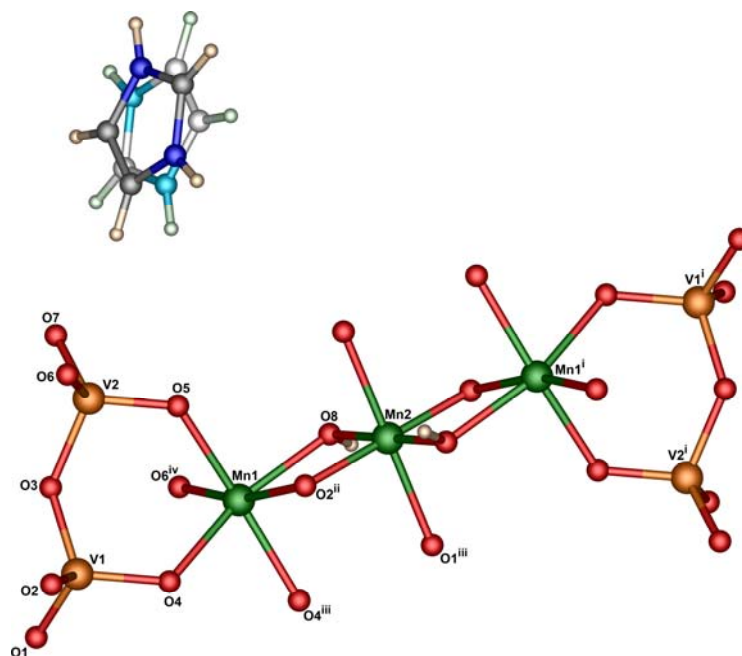


Figure 7.3 Ball and stick representation of the asymmetric unit with numbering scheme and showing the coordination environments of the metal centres in **7a**. The two orientations of the disordered imidazolium are shown in different colors. Symmetry codes: (i) $-x, 1-y, -1-z$; (ii) $1-x, -y, -1-z$; (iii) $-x, -y, -1-z$; (iv) $-1+x, y, z$.

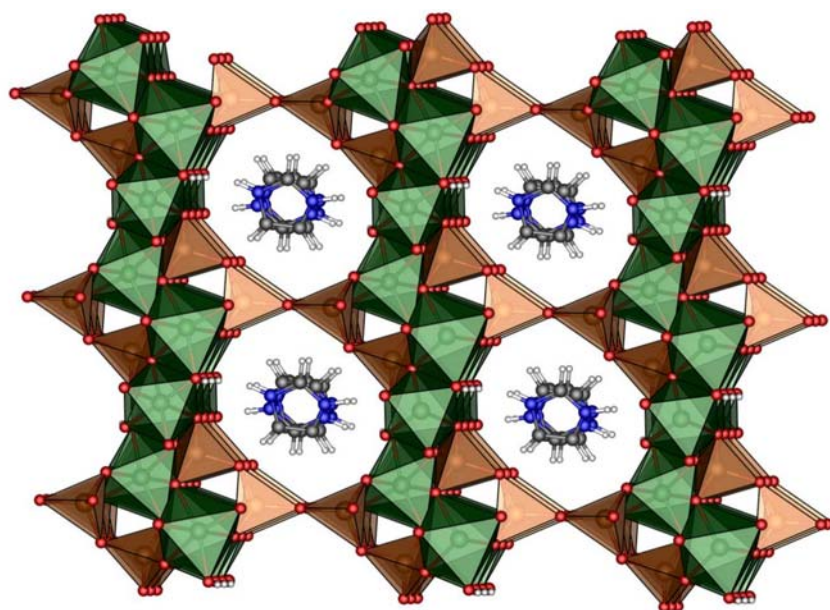
Table 7.6 Selected bond lengths (Å) for **7a**.^a

Mn1–O2 ⁱ	2.187(4)	V1–O1	1.666(3)
Mn1–O4	2.157(3)	V1–O2	1.748(3)
Mn1–O4 ⁱⁱ	2.204(3)	V1–O3	1.777(3)
Mn1–O5	2.159(4)	V1–O4	1.698(3)
Mn1–O6 ⁱⁱⁱ	2.119(4)	V2–O3	1.799(3)
Mn1–O8	2.119(4)	V2–O5	1.636(4)
Mn2–O1 ⁱⁱ	2.187(4)	V2–O6	1.649(4)
Mn2–O2 ⁱ	2.157(3)	V2–O7	1.780(1)
Mn2–O8	1.895(3)		

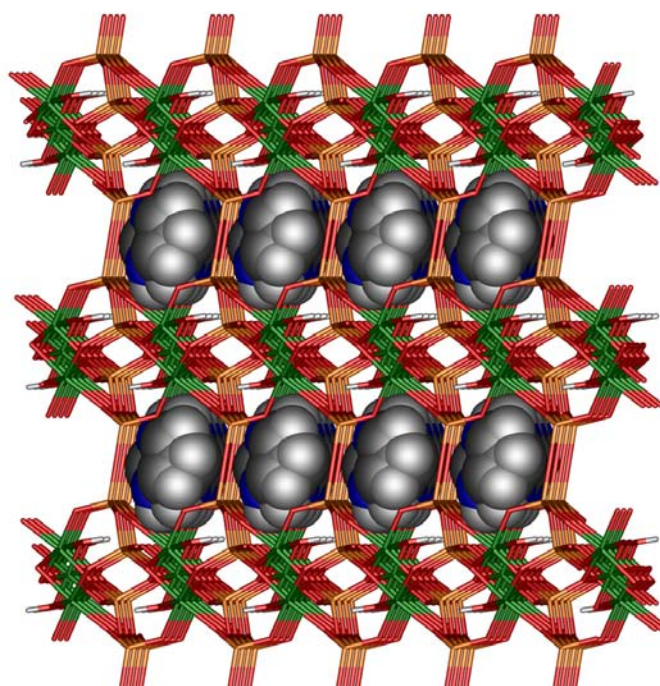
^a Estimated standard deviations are given in parentheses.

Symmetry codes: (i) $1-x, -y, -1-z$; (ii) $-x, -y, -1-z$; (iii) $x, y, z-1$.

The anionic framework of **7a** comprises of 1-D ladder chains of [Mn₃] trimer blocks. The Mn ladders are then linked together into a 3-D structure by tetravanadate [V₄O₁₃] units along the crystallographic *a* axis, as shown in Figure 7.4a. The formation of an open 3-D framework can alternatively be described as constructed by the secondary building unit (SBU) of Mn₃V₄O₂₄ clusters in which this cluster is built by VO₄ tetrahedra and MnO₆ octahedra linked through their edges and corners. The cluster of the SBU is capped together in the *b* axis to form the 2-D layer and further connected by V–O–V linkages forming the 3-D structure, which possesses 1-D channels, as depicted in Figure 7.4b. These hydrophilic channels are ten-membered rings and occupied by disordered imidazolium cations. As shown in Figure 7.5, the channel dimensions are approximately 7.9×10.2 Å. This channel is somewhat longer when comparing to the most common zeolites such as mordenite (5.3×8.4 Å) and stilbite (5.3×8.3 Å), and those of AIPO families such as AIPO-C (5.6×8.4 Å) and AIPO-D (4.8×9.0 Å). The imidazolium molecules are in close proximity and form



(a)



(b)

Figure 7.4 (a) Polyhedral and ball-and-stick representation of **7a** viewed approximately along the a axis, and (b) wires/stick and space-filling representation viewed along the b axis of **7a**. The disordered imidazolium molecules are located in the middle of the channels.

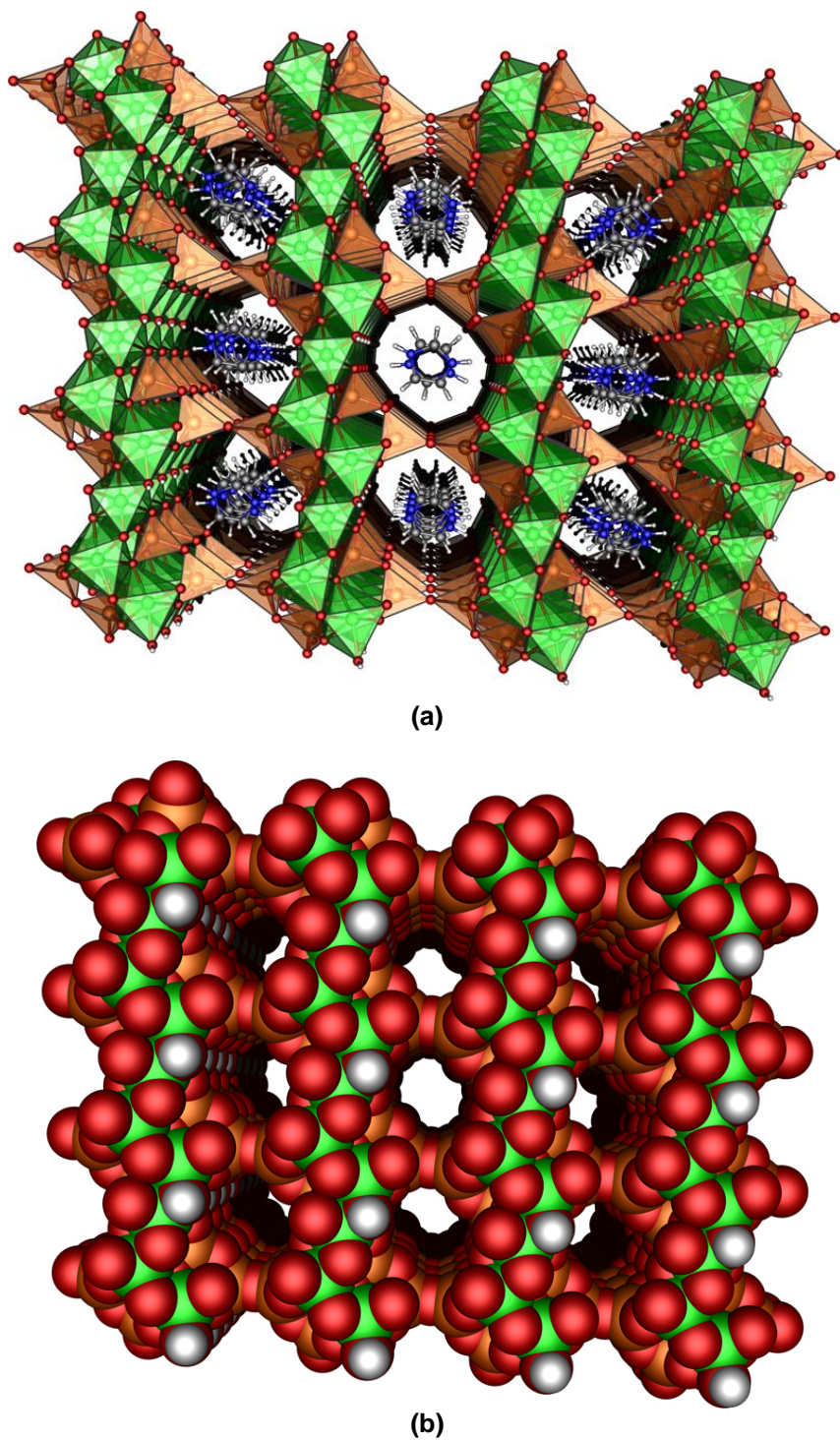


Figure 7.5 Perspective views of (a) polyhedral and (b) space-filling representations of anionic framework in **7a** along the crystallographic *a* axis.

C–H···O and N–H···O hydrogen bond interactions to the inorganic framework, thus, playing a crucial role in the stability of the open framework structure in **7a**. The (D···A) distances are in the range 2.777(3)–3.125(3) Å and D–H···A angles > 140°.

7.3.3 Investigation of the Structure and Phase Transitions of $[M(\text{Im})_4\text{V}_2\text{O}_6]_\infty$, $M = \text{Mn}$ (**7b**), Co (**7c**), Ni (**7d**)

Largest principal libration tensor for the imidazoles of the low and high temperature phases are summarized in Tables 7.7 and 7.8. Angle between normals to planes of pseudo symmetry related imidazoles for the low and high temperature phases of the compounds **7b–7c** are given in Tables 7.9 and 7.10. Selected bond lengths at 100(2) K for the compounds **7b** and **7c** are listed in Tables 7.11 and 7.12. The hydrogen bonding at 100(2) and 295(2) K is described in Tables 11 and 12. The bond lengths and angles, hydrogen bonds geometry, and other crystallographic data at all experiment temperatures are given as supplementary material in the CIF which can be found on the attached CD-ROM.

Structural Description of the $I4_1/a$ Phase

Compounds $\text{C}_{12}\text{H}_{16}\text{MN}_8\text{O}_6\text{V}_2$, $M = \text{Mn}$ (**7b**), Co (**7c**), Ni (**7d**), have isomorphous structures. The room temperature structure ($Z = 8$) in space group $P4_2/n$ (No. 86) is reversibly transformed to a body centred structure ($Z = 32$) in space group $I4_1/a$ (No. 88) at 281(2) K for **7b** and 175(2) K for **7c**. The asymmetric unit along with the atomic numbering for the $I4_1/a$ structures are shown in Figure 7.6a. This Figure is drawn for **7b** down a direction 10° away from $\mathbf{a} + \mathbf{b}$ with \mathbf{c} vertical. In the $P4_2/n$ phase the two halves of the asymmetric unit become related by a 2-fold rotation axis parallel to \mathbf{c} and passing through $M1$. Four crystallographically independent VO_4 tetrahedra

are in general positions. Atoms *M2* and *M3* lie on 2-fold rotation axes that contain -4 sites. Atom *M1* lies approximately on a 4_1 screw axis that corresponds to a 4_2 axis in the $P4_2/n$ structure. There are eight imidazole groups, seven of which are involved in hydrogen bonding. The imidazol labeled with a 2 is not hydrogen bonded, and is disordered with occupancy ratios that refined to **7b**: 0.776(11):0.224 at 100(2) K, 0.698(12):0.302 at 200(2) K, 0.618(13):0.382 at 279(2) K, and **7c**: 0.425(15):0.575 at 100(2) K, 0.389(18):0.611 at 170(2) K.

The coordination polyhedra observed for the four vanadium atoms exhibit distorted $[\text{VO}_4]$ tetrahedral coordination geometry with three μ_2 -O atoms and a terminal oxygen atom. The bond valence sums (Brown and Altermatt, 1985; Brese and O'Keeffe, 1991) indicate that all the vanadium is pentavalent. Each vanadium tetrahedron is connected *via* μ_2 -O atoms. The pair (V1 and V2), likewise (V3 and V4), are mutually linked together through corner sharing of μ_2 -O atoms (O2 and O5), likewise (O8 and O11) to form $[\text{V}_4\text{O}_{12}]^{4-}$ tetranuclear rings about a centre of inversion. This anionic cluster of $[\text{V}_4\text{O}_{12}]^{4-}$ resembles the prototypical structure observed in $(\text{Bu}_4\text{N})_3\text{HV}_4\text{O}_{12}$ (Fuchs *et al.*, 1976), and $(\text{PPh}_4)_2\text{V}_4\text{O}_{11}$ (Sharma *et al.*, 2002). The O3, O6, O9, and O12 atoms are terminal. The remaining oxygens of O1, O4, O7, and O10 connect the relevant VO_4 tetrahedron to a *M* atom that displays a distorted octahedral geometry coordinated through a nitrogen donor to four imidazole groups atoms in an equatorial plane and two oxygen atoms from the anionic $[\text{V}_4\text{O}_{12}]$ clusters in axial positions. The metal atoms are not coplanar with respect to the imidazoles and this presumably is to satisfy packing and hydrogen bonding demands.

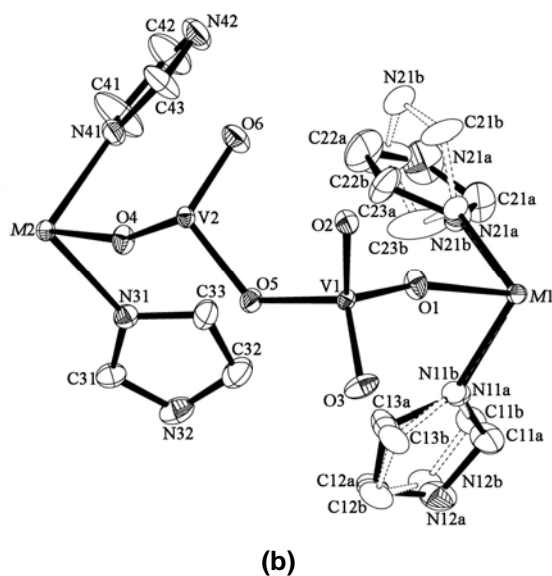
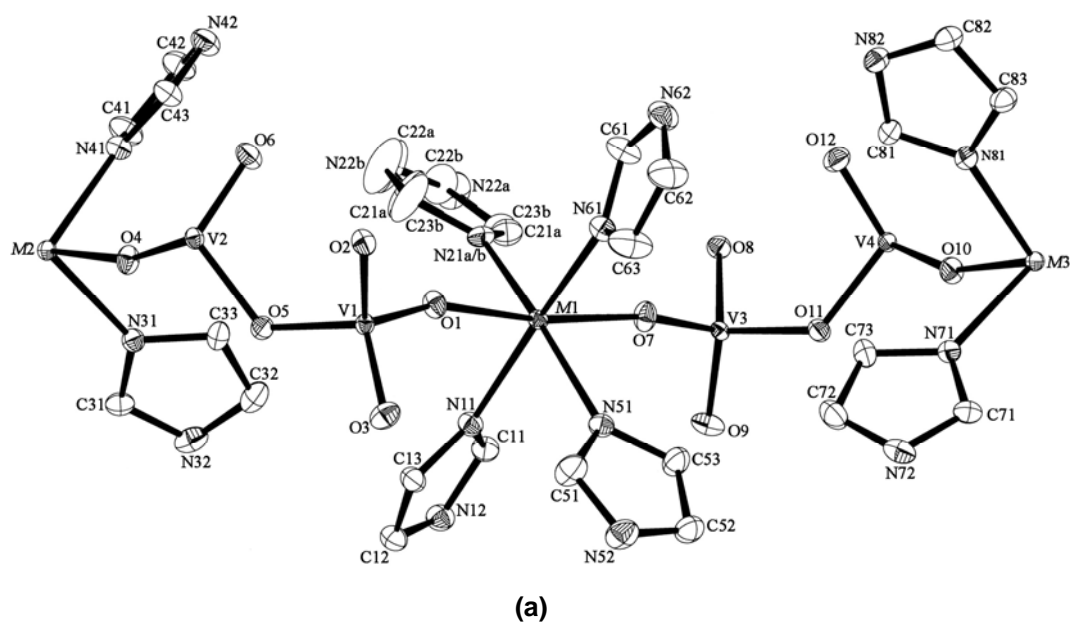


Figure 7.6 Shows the asymmetric unit of (a) the $I4_1/a$ at 100(2) K, and (b) the $P4_2/n$ at 295(2) K structures of **7a** down equivalent directions with 50 and 25% displacement ellipsoids, respectively. Environment on the right of the 2-fold axis in Figure 7.6a transforms to the environment as depicted the left of the axis. Hydrogen atoms are omitted for clarity.

Figure 7.7a shows a single layer of the $I4_1/a$ structure at $z = 1/2$ projected down the c axis. The framework consists of cyclic $[V_4O_{12}]$ tetramers interconnected by MN_4O_2 octahedra. The topology of framework is defined by two cyclic sub-motifs, namely, four VO_4 tetrahedra corner connected to form a eight membered $\{V_4O_4\}$ small rings, and the four MN_4O_2 octahedra and eight VO_4 tetrahedra further connected to form a twenty four membered $\{M_4V_8O_{12}\}$ large rings. The 4_1 screw axis causes the centres of the small and large rings to alternate along the c direction with $1/4c$ spacing (*ca.* 7.4 Å). Eight imidazoles connected to four different M atoms fill cavities centred on pseudo inversion centres. Views of a polyhedral representation, showing 2-D layer of $I4_1/a$, $P4_2/n$, and $P2/n$ structures are illustrated in Figure 7.8 in which coordinated imidazole ligand project outside the bimetallic oxide layers are omitted.

Figures 7.9a and 7.9b show the environment about such a site $3/4$, $1/4$, $1/2$. The pseudo inversion relates imidazoles equivalent to those labeled 1, 2, 3, and 4 to those labeled 5, 6, 7, and 8, respectively. The available hydrogen attached to the non metal-coordinated nitrogen of the imidazole is involved in hydrogen bonding to an oxygen atom for all imidazoles except that labeled 2. The bond connectivity is centrosymmetric for all the imidazoles except those labeled 2 and 6. The hydrogen bonds are of similar length (*ca.* 2.8 Å) and connect equivalents of N12, N32, N42, N52, N62, N72, and N82 to equivalents of O12, O11, O3, O6, O9, O5, and O9, respectively. However only the orientations of the imidazoles labeled 3 and 7 maintained a reasonably exact inversion relationship.

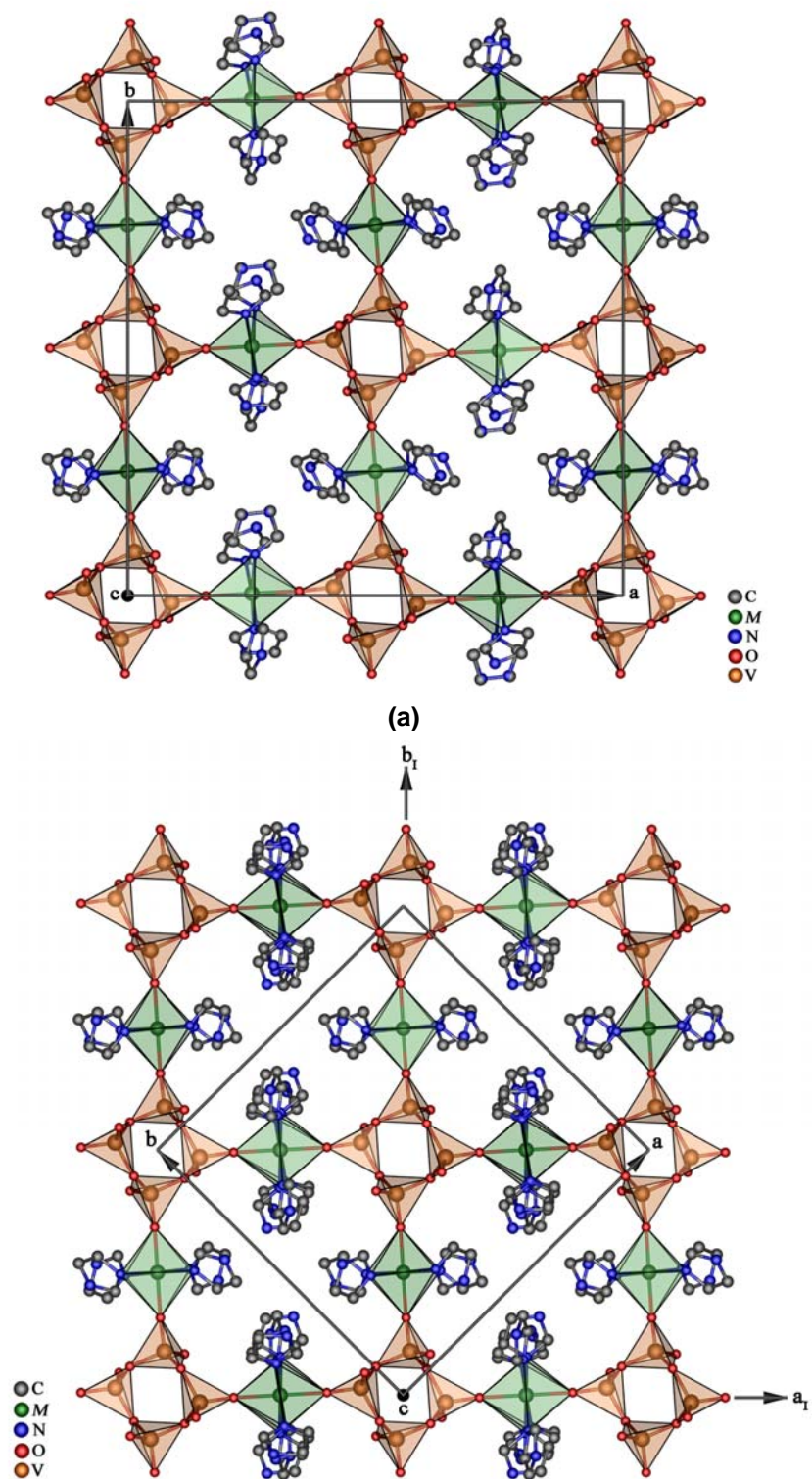


Figure 7.7 Polyhedral representations of single layer of compounds at (a) $I4_1/a$ and (b) $P4_2/n$, viewed along the crystallographic c axis. The layers are at $z = 1/2$ for $I4_1/a$, and $z = 1$ for $P4_2/n$.

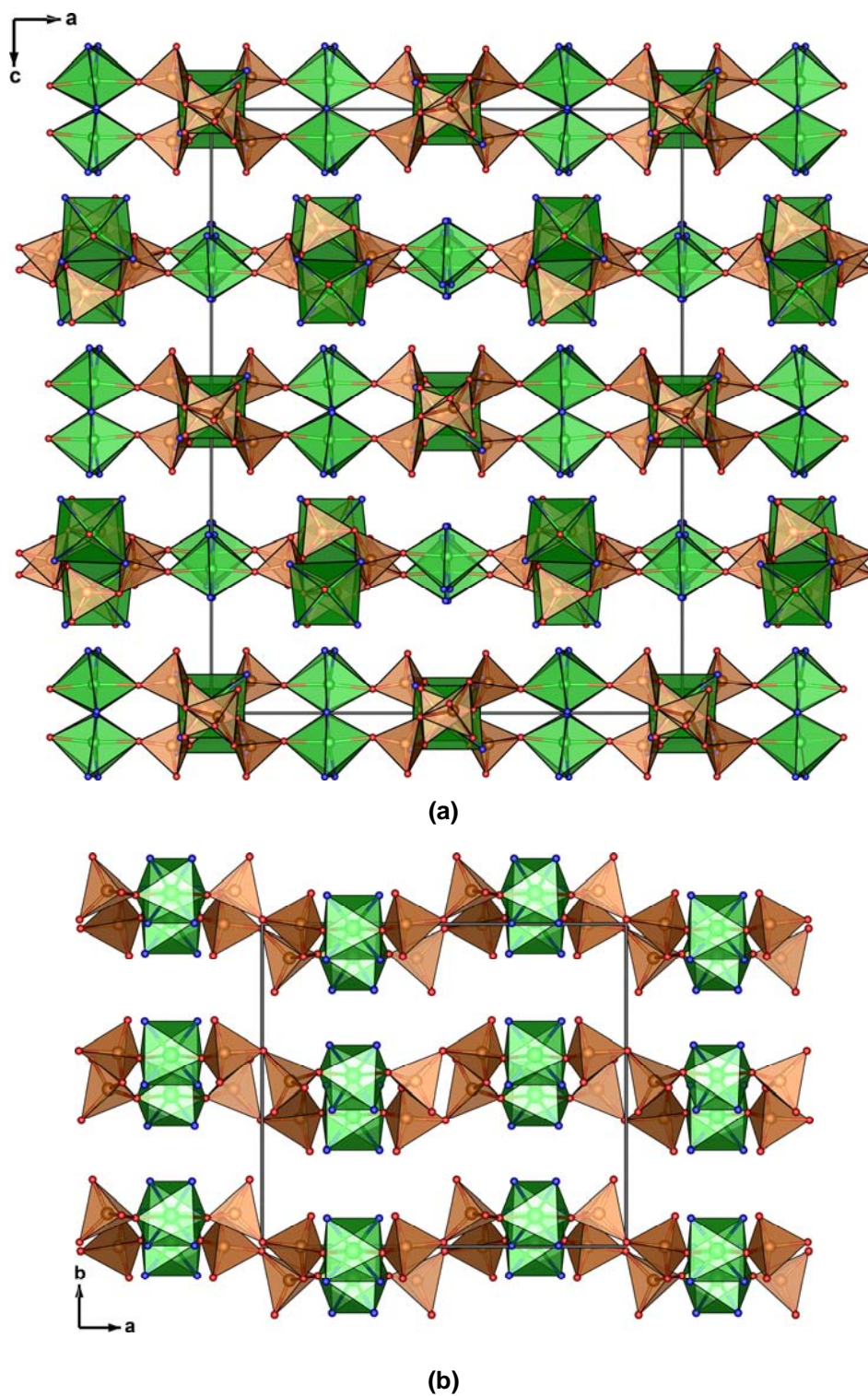


Figure 7.8 Polyhedral representations of inorganic layers of compounds at (a) $I4_1/a$ for **7b** and **7c**, (b) $P2/n$ for **7d**, and (c) $P4_2/n$ for **7b–7c**.

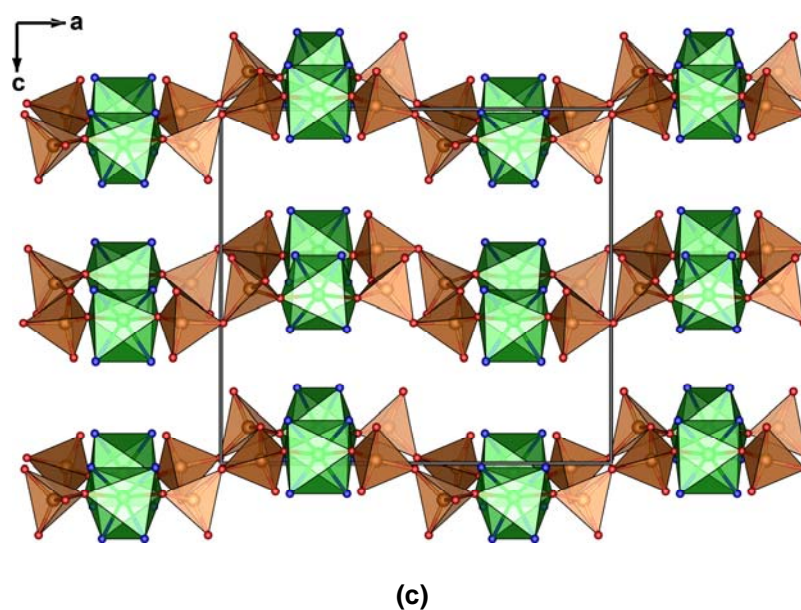


Figure 7.8 (Continued)

Description of the $P4_2/n$ phase

The high temperature phase crystallizes in space group $P4_2/n$ (no. 86), with eight formula units per unit cell. The asymmetric unit is illustrated in Figure 7.6b for **7b**, and is related to the asymmetric unit of the $I4_1/a$ phase by the transformation $x_p = x_1 + y_1 - 1$, $y_p = -x_1 + y_1 + 1$, $z_p = 2z_1$ and occupies half the volume. This corresponds to relating two axial systems with a common origin so that $\mathbf{a}_p = 1/2(\mathbf{a}_1 + \mathbf{b}_1)$, $\mathbf{b}_p = 1/2(-\mathbf{a}_1 + \mathbf{b}_1)$, $\mathbf{c}_p = 1/2\mathbf{c}_1$. Figures 7.6a and 7.6b are drawn down the same direction. What was a 4_1 screw axis passing approximately through $M1$ is now a 4_2 screw axis containing a 2-fold rotation that relates two asymmetric units. Atoms $M1$ and $M2$ both lie on 2-fold axes. $M2$ is on an axis containing -4 sites. The coordination geometry around the metal centres is identical to the low temperature $I4_1/a$ phase.

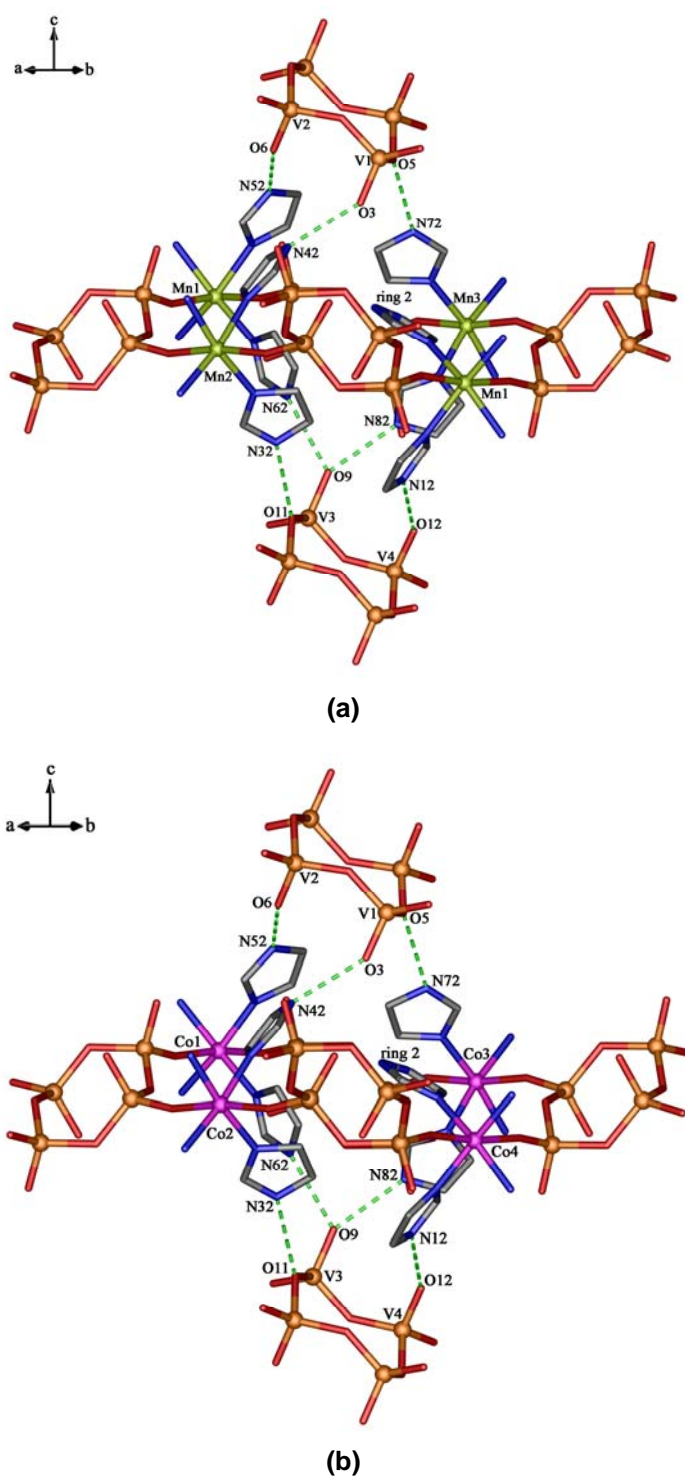
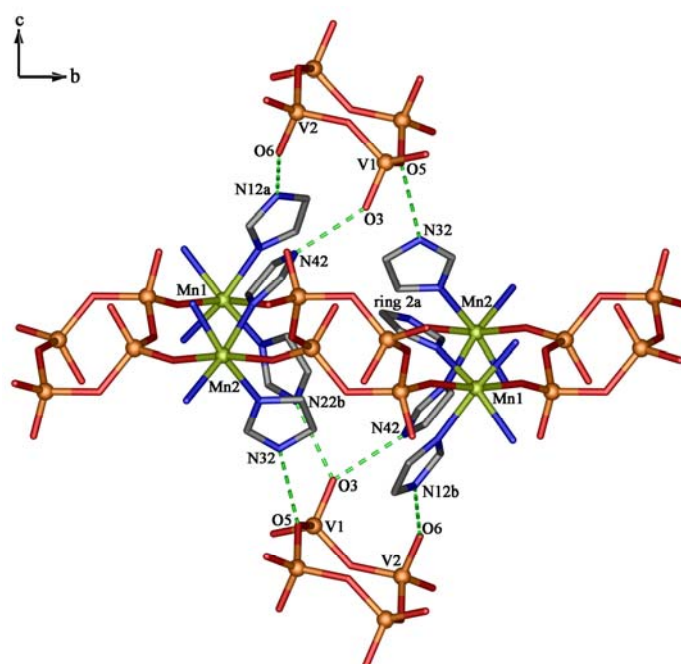
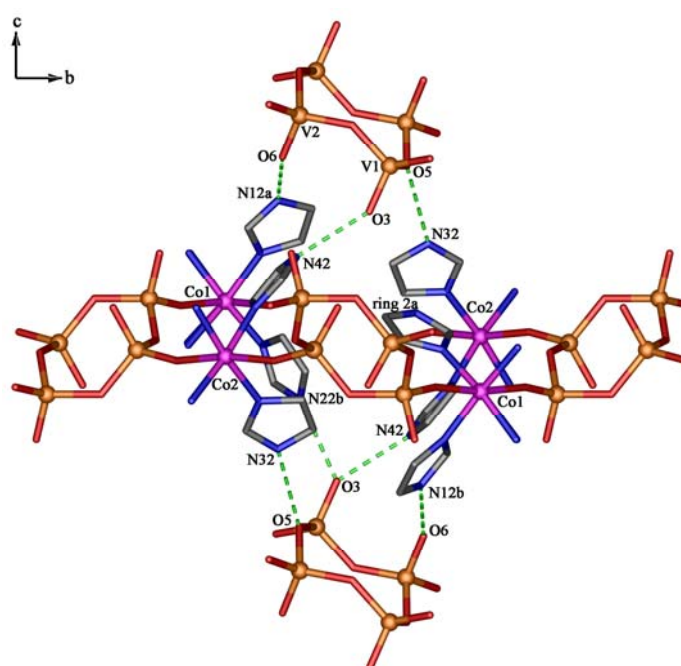


Figure 7.9 Hydrogen bonds about the pseudo inversion centers $3/4$, $1/4$, $1/2$ for the $I4_1/a$ structure at 100(2) K of (a) **7b**, (b) **7c**, and 0 , $1/2$, 1 for the $P4_2/n$ structure at 295(2) K of (c) **7b**, (d) **7c**. The 1:1 disorder of the $P4_2/n$ structure is not shown.



(c)



(d)

Figure 7.9 (Continued).

The imidazoles 1 and 2 attached to *M1* were each disordered over two positions whereas this was found to be unnecessary for imidazoles 3 and 4 attached to *M2*. Again the metal atoms were not constrained to lie in the plane of the attached imidazoles. The occupancy refinement suggested ratios of 1:1 which were subsequently fixed.

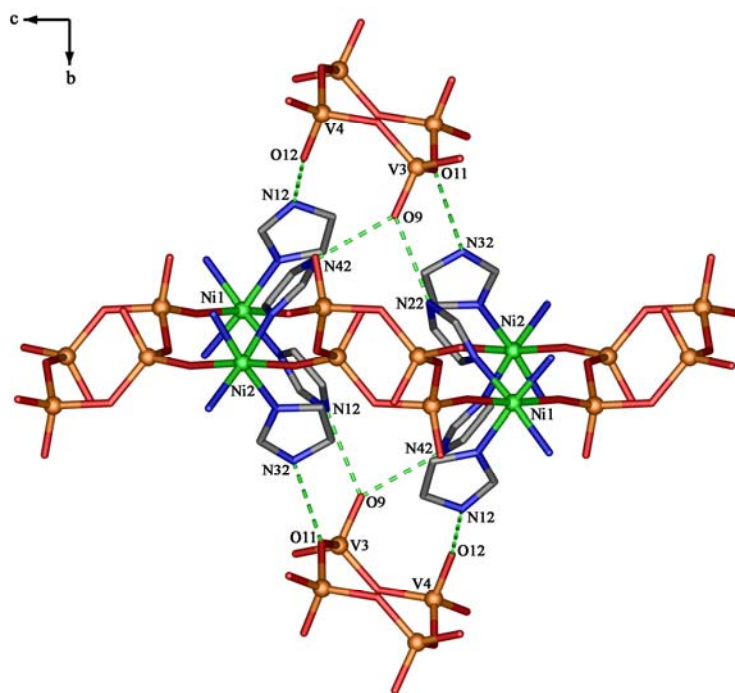
The hydrogen bond connectivity is equivalent to the *I4₁/a* phase if one simply imposes exact inversions in the centre of the cavities containing eight imidazoles as required by the space group *P4₂/n*. Figures 7.9c and 7.9d shows the environment of the cavity at 0, 1/2, 1, after ordering across the inversion centre to best approximate the *I4₁/a* phase, imidazoles 1 to 8 of *I4₁/a* phase corresponding to imidazoles 1b, 2a, 3, 4, 1a, 2b, 3, 4 of *P4₂/n* phase. It is seen that the major difference between the two phases is that imidazoles 4 and 8 that were not inversion equivalent in the *I4₁/a* phase have joined imidazoles 3 and 7 in becoming inversion related in the *P4₂/n* phase. To switch between inversion related descriptions of the cavity only requires a change in the hydrogen bond connectivity for imidazoles 2 and 6, 2 becoming hydrogen bonded and 6 losing its hydrogen bond. The other changes simply involve reorienting the imidazoles without a change of hydrogen bond connectivity.

The description of the *P4₂/n* phase has departed from the model implied by disordering the *I4₁/a* structure so as to simplify the refinements allowing each of the refinements above the transition temperature to have a well behaved refinement. We have ignored the inherent coplanar disorder of imidazole 2 in the *I4₁/a* structure. Likewise imidazoles 3 and 4 of the *P4₂/n* structure should in principle be replaced by pairs of half occupancy imidazoles. Instead we rely on rigid body atom displacement parameters to indicate what is going on.

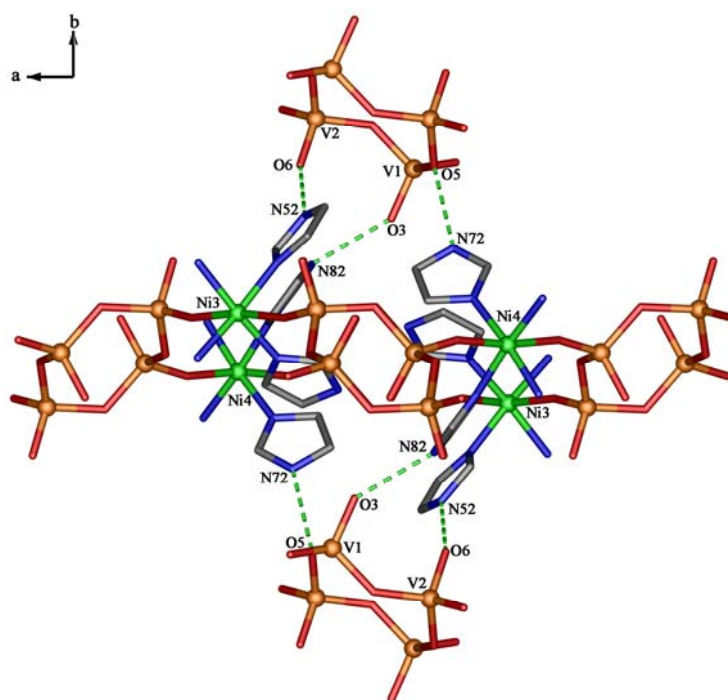
Columns parallel to *c* direction of imidazoles attached to *M1* are propagated by 4_1 and 4_3 screw axes. The inversion centres within the cavities containing eight imidazoles obviously applies almost exactly in the ordered cavity model for imidazoles 3 and 4, blocking communication between columns parallel to *c* direction of imidazoles attached to *M1* in the $P4_2/n$ structure. The ability to switch between the inversion related environments of a cavity only exists above the transition temperature and the requirements to become ordered in space group $I4_1/a$ is revealed by studying the $P4_2/n$ structure just above the transition point.

Structural Description of the $P2/n$ Phase

The ordering of the disordered $P4_2/n$ structure to create a $P2/n$ structure allows the lost 4_2 symmetry operation to create twinned components related by a 90° rotation about the monoclinic axis. Imidazoles 1 to 8 of the $P2/n$ asymmetric unit correspond to imidazoles 1a, 2b, 3, 4, 1b, 2a, 3, 4 of the $P4_2/n$ asymmetric unit. Rings 1 to 4 are obtained by the transformation $x = x_p, y = z_p, z = y_p$ and imidazoles 5 to 8 are obtained by a further transformation $x' = -z+1, y' = y-1/2, z' = x+1/2$. Imidazoles 1 to 4 and their inversion equivalents create a centrosymmetric cavity in which all eight imidazoles are involved in hydrogen bonding whereas imidazoles 5 to 8 and their inversion equivalents create a centrosymmetric cavity in which only six imidazoles are involved in hydrogen bonding. Imidazole 6 is not used for hydrogen bonding. Figures 7.10a and 7.10b show the hydrogen bonds about the inversion centers at 0, 1, $1/2$ and $1/2, 1/2, 1/2$, respectively. The angles between the normals to the imidazole planes for rings 5 to 8 and rings 1 to 4 transformed by the pseudo symmetry operation $-z+1, y-1/2, x+1/2$ are 48.0° (1, 5), 71.3° (2, 6), 1.4° (3, 7), and 13.6° (4, 8) at 100(2) K respectively.



(a)



(b)

Figure 7.10 Hydrogen bonds about the inversion centres (a) 0, 1, 1/2, and (b) 1/2, 1/2, 1/2 for the ordered $P2/n$ structure of **7d** at 100(2) K.

Change of Structure with Temperature

The cell dimensions for each temperature are given in Tables 7.2-7.4. Although the unit cell volume decreases with decrease in temperature, (**7b**, $V = 3962.7(1) \text{ \AA}^3$ at 295(2)K, $3953.4(1) \text{ \AA}^3$ at 283(2) K, $V/4 = 3948.5(1) \text{ \AA}^3$ at 279(2) K, $3937.6(1) \text{ \AA}^3$ at 200(2) K, $3926.7(1) \text{ \AA}^3$ at 100(2) K; **7c**, $V = 3864.7(1) \text{ \AA}^3$ at 295(2) K, $3845.04(9) \text{ \AA}^3$ at 180(2) K, $V/4 = 3832.8(1) \text{ \AA}^3$ at 170(2) K, $3823.6(1) \text{ \AA}^3$ at 100(2) K; **7d**, $V = 3820.27(1) \text{ \AA}^3$ at 295(2) K, and $3788.63(1) \text{ \AA}^3$ at 100(2) K), the **c** axis actually increases sharply near the $P4_2/n$ to $I4_1/a$ transition temperature when approached from above (**7b**, $c = 14.8030(2) \text{ \AA}$ at 295(2) K, $14.8304(2) \text{ \AA}$ at 283(2) K, $c/2 = 14.8448(2) \text{ \AA}$ at 279(2) K, $14.8261(2) \text{ \AA}$ at 200(2) K, $14.8002(2) \text{ \AA}$; **7c**, $14.6057(2) \text{ \AA}$ at 295(2) K, $14.5532(2) \text{ \AA}$ at 180(2) K, $c/2 = 14.6350(2) \text{ \AA}$ at 170(2) K, $14.6329(2) \text{ \AA}$ at 100(2) K; **7d**, $14.5589(2) \text{ \AA}$ at 295(2) K, $14.3657(2) \text{ \AA}$ at 100(2) K). It should be pointed out that the transition temperature for the Co structure was not as well defined as for the Mn structure, presumably because the smaller unit cell for the Co structures causes what may be described as a “*sticking gate effect*”. The low temperature Co structure persists above the transition temperature if the unit cell is determined within ten minutes and the high temperature structure has similar persistence below the transition temperature.

Indeed the low temperature Co structure was shown to have stacking faults requiring the use of two scale constants, K_1 for l even and K_2 for l odd, where $K_2/K_1 = 0.819(4)$ at 100(2) K and $0.653(5)$ at 170(2) K. No such adjustments to the low temperature Mn structure (**7b**) was necessary. The 170(2) K structure of Co (**7c**) is not as good as the other refinements and one suspect that K_2 may have been varying with time during data collection. Residual peaks on the heavy atoms, most noticeable when

a single scale is used, persist to a lesser extent for the 170(2) K structure but not the 100(2) K structure.

The largest principal values of the libration tensor in radians² for each imidazole ring are given in Tables 7.7 and 7.8, using the labelling of the $I4_1/a$ structure. Tables 7.9 and 7.10 give the departure from equivalence of the imidazole rings using the difference in degrees between the directions of the normals to the planes of the imidazoles after one of each pair of rings has been transformed by a pseudo 2-fold rotation axis parallel to c so as to create pseudo superposition. The structures obtained above the transition temperature have rings (3, 7) and rings (4, 8) exactly equivalent but with a substantial libration about the relevant $M-N$ bond. The entry in Table 7.10 marked (*) are obtained by evaluating $2\sqrt{L_{ii}}$, where L_{ii} is the largest principal value of the libration tensor in radians² and then converting to degrees. By comparing libration parameters above and below the transition temperatures it is reasonable to assume the libration for imidazoles (3, 7) does not come from a disorder.

It is to be noted that the imadazole rings have effectively no change in their pseudo equivalence except for rings 4 and 8 where the increase in libration with lowering temperature above the transition for the Mn structure (**7b**) is worthy of note. The amount rings have to move to invert the environment of a pseudo inversion centre is given by the values in Tables 7.7 and 7.8 implying a big change for rings 2 and 6. As can be see in Figure 7.6a, a rotation of ring 6 by about 130° to take up the alternative position must involve rotating ring 8 out of the way while this ring maintains its hydrogen bond connection. Looking at **7b** at 283(2) K (Table 7.8) the major libration parameter for rings (4, 8) is very similar to the value expected for a

1:1 disorder of the 279(2) K structure (Table 7.7). The smaller libration parameter at 295(2) K could suggest that the distribution of rings 4 and 8 is less bimodal and more gaussian, reducing the mean square displacement. This suggests that at 283(2) K reasonably sized domains are already ordered in space group $I4_1/a$. The increase in the **c** axis as the temperature is lowered above the transition temperature facilitates the transition from disorder to order. It is to be noted that in **7c**, the libration of ring 8 in the 295(2) K and 180(2) K structures is much smaller suggesting this gate is usually stuck in a near closed position. Things are only a bit better at 170(2) K, the libration increasing with the increase in the interlayer repeat. This suggests the transition temperature for **7c** is nearer 170(2) than 180(2) K.

Table 7.7 Largest principal libration values (radians²) for the imidazoles of the low temperature phase ($I4_1/a$ for **7b**, **7c**, and $P2/n$ for **7d**). ^a

Imidazole ring	Libration Tensor (radians ²)					
	7b at 100 K	7b at 200 K	7b at 279 K	7c at 100 K	7c at 170 K	7d at 100 K
1	0.0009(3)	0.004(1)	0.0105(3)	0.0046(9)	0.007(1)	0.009(1)
2	0.025(1)	0.030(1)	0.0437(4)	0.034(1)	0.039(2)	0.034(1)
3	0.0016(1)	0.0026(1)	0.0050(1)	0.0026(5)	0.0044(6)	0.0009(1)
4	0.0092(8)	0.017(1)	0.0254(4)	0.0060(7)	0.0033(4)	0.0046(7)
5	0.018(1)	0.026(1)	0.0354(6)	0.024(1)	0.029(2)	0.0055(9)
6	0.023(1)	0.044(4)	0.0700(1)	0.034(1)	0.053(3)	0.012(1)
7	0.0044(6)	0.006(1)	0.0110(2)	0.0040(6)	0.008(1)	0.0002(5)
8	0.0053(7)	0.010(1)	0.0263(5)	0.0127(1)	0.051(3)	0.0007(1)

^a Estimated standard deviations are given in parentheses.

Table 7.8 Largest principal libration values (radians²) for the imidazoles of the high temperature phase.^a

Imidazole ring	Libration Tensor (radians ²)				
	7b at 283 K	7b at 295 K	7c at 180 K	7c at 295 K	7d at 295 K
1b	0.025(3)	0.018(3)	0.015(2)	0.013(2)	0.012(2)
2a	0.016(3)	0.031(4)	0.0621(3)	0.071(4)	0.101(4)
3	0.014(2)	0.015(2)	0.009(1)	0.015(1)	0.013(1)
4	0.286(7)	0.102(3)	0.0330(1)	0.035(2)	0.030(1)
1a	0.050(5)	0.050(4)	0.041(2)	0.024(2)	0.027(1)
2b	0.122(7)	0.147(6)	0.206(6)	0.291(9)	0.254(8)
3	0.014(2)	0.015(2)	0.009(1)	0.015(1)	0.013(1)
4	0.286(7)	0.102(3)	0.0330(1)	0.035(2)	0.030(1)

^a Estimated standard deviations are given in parentheses.

Table 7.9 Departure from equivalence of pseudo symmetry related imidazoles for the low temperature phase (*I4₁/a* for **7b**, **7c**, and *P2/n* for **7d**).

Imidazole ring		Angle between normals to planes (°)					
		7b at 100 K	7b at 200 K	7b at 279 K	7c at 100 K	7c at 170 K	7d at 100 K
1	5	25.0	24.2	22.9	25.6	25.3	48.0
2	6	127.6	129.0	130.1	124.5	124.2	71.3
3	7	3.1	3.1	2.7	2.4	2.2	1.4
4	8	52.8	53.4	52.4	55.5	55.1	13.6

Table 7.10 Departure from equivalence of pseudo symmetry related imidazoles for the high temperature phase.

Imidazole ring		Angle between normals to planes (°)				
		7b at 283 K	7b at 295 K	7c at 180 K	7c at 295 K	7d at 295 K
1a	1b	23.6	23.0	29.8	23.1	34.9
2a	2b	122.6	114.1	108.0	109.5	109.8
3	3	14.0*	14.0*	11.0*	14.0*	13.1*
4	4	59.2*	36.7*	20.8*	21.4*	19.7*

*Evaluated as $2\sqrt{L_{ii}}$, see text.

When the same approach is applied to **7d**, there is clear evidence that (see Tables 7.7 to 7.10) imidazoles 1 and 5 and not imidazoles 4 and 8 are associated with the phase transition that changes the hydrogen bonding of imidazoles 2 and 6. It is reasonable to surmise that the mechanism for ordering that pushes imidazoles 4 and 8 out of the way to allow imidazoles 2 and 6 to switch hydrogen bonding arrangements has been closed down because of the smaller Ni atom, and been replaced by an alternative mechanism that involves a monoclinic distortion of the unit cell and the creation of alternate layers of different hydrogen bonding. As seen from Figure 7.10, the extra hydrogen bonds in Figure 7.10a compared to Figure 7.10b makes the *c* axis of 16.3422(2) Å longer than the *a* axis of 16.1379(2) Å. The distortion is not present in the high temperature form of **7d** and suggests that all cavities contain seven hydrogen bonded imidazoles for the $P4_2/n$ structures.

Bond lengths and angles

Bond lengths are in remarkably good agreement over the whole temperature range and are most reliable for the 100(2) K structures in space group $I4_1/a$. The Mn–N distances range from 2.216(1) to 2.264(1) Å, mean 2.253(1) Å, and the Mn–O distances range from 2.126(1) to 2.202(1) Å, mean 2.154 Å. If the Mn1–N21 bond is omitted since this imidazole is disordered, then the Mn–N range is 2.216(1) to 2.264(1) Å, mean 2.251 Å. These are slightly longer than the bond lengths for Co and Ni, namely, Co–N distances range from 2.109(1) to 2.156(1) Å, mean 2.137 Å, and the Co–O distances range from 2.074(2) to 2.140(2) Å, mean 2.100 Å. If the Co1–N21 bond is omitted, then the Co–N range is 2.057(1) to 2.100(1) Å, mean 2.076 Å. The Ni–N distances range from 2.109(1) to 2.156(1) Å, mean 2.137 Å, and the Ni–O distances range from 2.074(2) to 2.140(2) Å, mean 2.100 Å. However, it

should be noted that the imidazole not involved a hydrogen bonding always had the shortest $M-N$ bond in all refinements.

The bond lengths around V fall into three groups, (i) those involving oxygens bridging (μ_2-O) vanadium atoms, (ii) those involving oxygens bringing (μ_2-O) a vanadium and an M atom, and (iii) those involving terminal oxygens. For the Mn structure, V–O distances (i) vary from 1.796(1) to 1.820(1) Å, mean 1.807 Å, V–O distances (ii) vary from 1.640(1) to 1.651(1) Å, mean 1.644 Å, and V–O distances (iii) vary from 1.633(1) to 1.650(1) Å, mean 1.640 Å. For the Co structure, V–O distances (i) vary from 1.798(1) to 1.827(1) Å, mean 1.811 Å, V–O distances (ii) vary from 1.635(2) to 1.650(2) Å, mean 1.643 Å, and V–O distances (iii) vary from 1.637(1) to 1.653(1) Å, mean 1.643 Å. For the Ni structure, V–O distances (i) vary from 1.798(2) to 1.831(2) Å, mean 1.816 Å, V–O distances (ii) vary from 1.640(2) to 1.651(2) Å, mean 1.649 Å, and V–O distances (iii) vary from 1.630(1) to 1.649(1) Å, mean 1.641 Å. The O–V–O bond angles range from 107.3(1) to 112.9(1)°, mean value 109.5° for Mn, from 107.3(1) to 113.0(1)°, mean value 109.5° for Co, and from 107.4(1) to 111.5(1)°, mean value 109.5° for Ni. It is seen that the tetrahedral angles around V are corresponding to the ideal value of 109.5°.

Table 7.11 Selected bond lengths of **7b** and **7c** at 100(2) K (Å).^a

	7b , Mn	7c , Co
M1–N11	2.262(1)	2.143(1)
M1–N21a	2.260(1)	2.138(2)
M1–N21b	2.260(1)	2.138(2)
M1–N51	2.262(1)	2.139(1)
M1–N61	2.216(1)	2.109(1)
M2–N31	2.264(1)	2.156(1)
M2–N41	2.252(1)	2.130(1)
M3–N71	2.257(1)	2.147(1)
M3–N81	2.246(1)	2.131(1)
M1–O1	2.157(1)	2.112(2)
M1–O7	2.202(1)	2.140(2)
M2–O4	2.132(1)	2.075(2)
M3–O10	2.126(1)	2.074(2)
V1–O1	1.651(1)	1.650(2)
V1–O2	1.796(1)	1.798(2)
V1–O3	1.637(1)	1.641(2)
V1–O5	1.820(1)	1.827(2)
V2–O2 ⁱ	1.804(1)	1.811(2)
V2–O4	1.644(1)	1.643(2)
V2–O5	1.812(1)	1.809(2)
V2–O6	1.638(1)	1.642(2)
V3–O7	1.640(1)	1.635(2)
V3–O8	1.796(1)	1.798(2)
V3–O9	1.650(1)	1.653(2)
V3–O11	1.810(1)	1.817(2)
V4–O8 ⁱⁱ	1.806(1)	1.810(2)
V4–O10	1.641(1)	1.642(2)
V4–O11	1.814(1)	1.814(2)
V4–O12	1.633(1)	1.637(2)

^a Estimated standard deviations are given in parentheses.

Symmetry codes: (i) $-x+2, -y+1, -z+1$; (ii) $-x+1, -y+1, -z+1$.

Table 7.12 Selected bond lengths of **7d** at 100(2) K (Å). ^a

Ni1–N11	2.062(1)	V1–O3	1.643(2)
Ni1–N21	2.057(1)	V1–O5	1.831(2)
Ni2–N31	2.100(1)	V2–O2 ⁱ	1.810(2)
Ni2–N41	2.068(1)	V2–O4	1.649(2)
Ni3–N51	2.085(1)	V2–O5	1.820(2)
Ni3–N61	2.055(2)	V2–O6	1.641(2)
Ni4–N71	2.102(1)	V3–O7	1.646(2)
Ni4–N81	2.080(1)	V3–O8	1.798(2)
Ni1–O1	2.111(2)	V3–O9	1.649(2)
Ni2–O4	2.057(2)	V3–O11	1.823(2)
Ni3–O7	2.121(2)	V4–O8 ⁱⁱ	1.818(2)
Ni4–O10	2.077(2)	V4–O10	1.650(2)
V1–O1	1.651(2)	V4–O11	1.821(2)
V1–O2	1.809(2)	V4–O12	1.630(2)

^a Estimated standard deviations are given in parentheses.

Symmetry codes: (i) $-x+1, -y+2, -z+1$; (ii) $-x+1, -y+1, -z+2$.

Table 7.13 Hydrogen bond geometries for **7b** and **7c** at 100(2) and 295(2) K (Å, °). ^{a§}

<i>T</i> (K)	D–H⋯A	d[D–H]	d[H⋯A]		d[D⋯A]		∠[D–H⋯A]	
			7b	7c	7b	7c	7b	7c
100(2)	N12–H1N12⋯O12 ⁱ	0.86	1.97	1.96	2.774(2)	2.754(2)	163	154
100(2)	N32–H1N32⋯O11 ⁱⁱ	0.86	2.07	2.12	2.890(2)	2.912(2)	159	154
100(2)	N42–H1N42⋯O3 ⁱⁱⁱ	0.86	2.00	2.00	2.791(2)	2.775(2)	153	149
100(2)	N52–H1N52⋯O6 ⁱ	0.86	1.96	1.93	2.782(2)	2.757(2)	161	162
100(2)	N62–H1N62⋯O9 ⁱⁱⁱ	0.86	2.02	2.04	2.851(2)	2.853(2)	161	157
100(2)	N72–H1N72⋯O5 ^{iv}	0.86	1.99	2.05	2.764(2)	2.796(2)	149	145
100(2)	N82–H1N82⋯O9 ⁱⁱⁱ	0.86	1.92	1.91	2.762(2)	2.758(2)	166	167
295(2)	N12b–H1N12b⋯O6 ^v	0.86	1.96	1.99	2.797(4)	2.808(5)	165	160
295(2)	N22b–H1N22b⋯O3 ^{vi}	0.86	2.03	2.02	2.875(3)	2.860(4)	167	166
295(2)	N32–H1N32⋯O5 ^{vii}	0.86	2.07	2.07	2.871(2)	2.865(3)	154	154
295(2)	N42–H1N42⋯O3 ^{vi}	0.86	1.97	1.93	2.773(3)	2.763(3)	155	162

^a Estimated standard deviations are given in parentheses.

Symmetry codes: (i) $-y+5/4, x-1/4, z-1/4$; (ii) $y+1/4, -x+3/4, -z+3/4$; (iii) $y+1/4, -x+5/4, z+1/4$; (iv) $y+1/4, -x+7/4, -z+3/4$; (v) $y-1/2, -x+1, z-1/2$; (vi) $y-1/2, -x+1, z+1/2$; (vii) $-y+1/2, x, -z+3/2$.

[§]Hydrogen bond geometry at other temperatures (200(2), 279(2), 283(2) K for **7b** and 170(2), 180(2) K for **7c** is given in the CIF which can be found on the attached CD-ROM.

Table 7.14 Hydrogen bond geometries for **7d** at 100(2) and 295(2) K (Å, °). ^a

<i>T</i> (K)	D–H⋯A	d[D–H]	d[H⋯A]	d[D⋯A]	∠[D–H⋯A]
100(2)	N12–H1N12⋯O12 ⁱ	0.86	1.98	2.732(2)	145.7
100(2)	N22–H1N22⋯O9 ⁱⁱ	0.86	2.10	2.893(2)	152.9
100(2)	N32–H1N32⋯O11 ⁱⁱⁱ	0.86	2.21	2.950(2)	144.0
100(2)	N42–H1N42⋯O9 ⁱⁱⁱ	0.86	1.94	2.743(2)	154.5
100(2)	N52–H1N52⋯O6 ^{iv}	0.86	1.90	2.716(2)	159.0
100(2)	N72–H1N72⋯O5 ^v	0.86	2.03	2.815(2)	151.1
100(2)	N82–H1N82⋯O3	0.86	2.13	2.829(2)	137.9
295(2)	N12a–H1N12a⋯O6 ^{vi}	0.86	1.92	2.722(3)	154.0
295(2)	N12b–H1N22b⋯O6 ^{vi}	0.86	1.92	2.757(3)	163.8
295(2)	N22b–H1N22b⋯O3 ^{vii}	0.86	2.10	2.924(2)	159.7
295(2)	N32–H1N32⋯O5 ^{viii}	0.86	2.15	2.913(2)	147.7
295(2)	N42–H1N42⋯O3 ^{vii}	0.86	2.00	2.771(2)	148.7

^a Estimated standard deviations are given in parentheses.

Symmetry codes: (i) $-x+1/2, y, -z+3/2$; (ii) $-x+1/2, y+1, -z+3/2$; (iii) $x-1/2, -y+1, z-1/2$; (iv) $x, y-1, z$; (v) $-x+1, -y+1, -z+1$; (vi) $y-1/2, -x+1, z-1/2$; (vii) $y-1/2, -x+1, z+1/2$; (viii) $-y+1/2, x, -z+3/2$.

7.3.2 Structural Description of [Mn(DMSO)(Im)₃V₂O₆] (7e)

Compound **7d** crystallizes in a monoclinic system, space group $P2_1/n$ ($Z = 4$). There are two crystallographically independent V atoms and a Mn atom in the asymmetric unit, Figure 7.11. The V sites exhibit distorted tetrahedral coordination geometry with a terminal O atom (mean V=O = 1.631 Å) and three μ_2 -O atoms (mean V–O = 1.789(1) Å). The V⁵⁺ oxidation state for two unique vanadium cations is supported by valence sum calculation (Brown and Altermatt, 1985; Brese and O'Keeffe, 1991). The Mn atom is octahedrally coordinated by three N atoms from imidazole ligands (mean Mn–N = 2.229 Å), one O atom from DMSO solvate (Mn–O

= 2.304(1) Å), and two μ_2 -O atoms from each distorted $\{\text{VO}_4\}$ tetrahedra (mean Mn–O = 2.217 Å). Selected interatomic bond lengths for compound **7d** are given in Table 7.15.

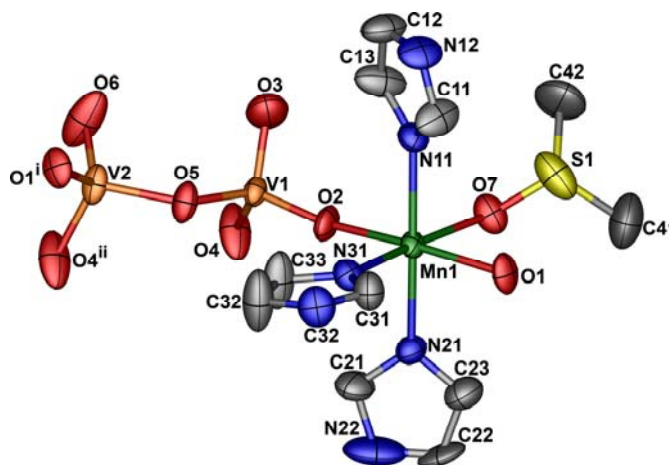


Figure 7.11 Thermal ellipsoid plot of a fragment of **7e** at the 30% probability level containing its asymmetric unit with atom numbering and showing coordination environments of metals centre. Hydrogen atoms are omitted for clarity. Selected bond lengths (Å) for **7e**: Mn1–N11 = 2.212(5), Mn1–N21 = 2.213(5), Mn1–N31 = 2.258(5), Mn1–O1 = 2.134(4), Mn1–O2 = 2.118(4), Mn1–O7 = 2.304(4), V1–O2 = 1.641(4), V1–O3 = 1.614(5), V1–O4 = 1.777(4), V1–O5 = 1.792(4), V2–O1ⁱ = 1.645(4), V2–O4ⁱⁱ = 1.795(5), V1–O5 = 1.780(4), V1–O6 = 1.608(5). Symmetry codes: (i) $-1/2+x, 1/2-y, 1/2+z$; (ii) $-x, -y, 2-z$.

The framework structure of **7e** is constructed by $[\text{V}_4\text{O}_{12}]^{4-}$ building units covalently linked to $\text{Mn}(\text{Im})_3(\text{DMSO})$ moieties through the bridging oxo groups along the crystallographic a axis, Figure 7.10. The imidazole ligands and DMSO solvate decorate the layer on the periphery. The framework connectivity in **7e** is similar to that of **7b–7d**. However, the major difference is the replacement of one equatorial imidazole on $\text{Mn}(\text{II})$ with a coordinated DMSO solvent molecule resulting in the loss of 4_2 symmetry lowering the symmetry to 2_1 . The $\{\text{V}_4\text{O}_{12}\}$ cluster of **7e** exhibits approximate C_{2v} symmetry, while that in $P4_2/n$ phase of **7b–7d** is about C_{2h} symmetry.

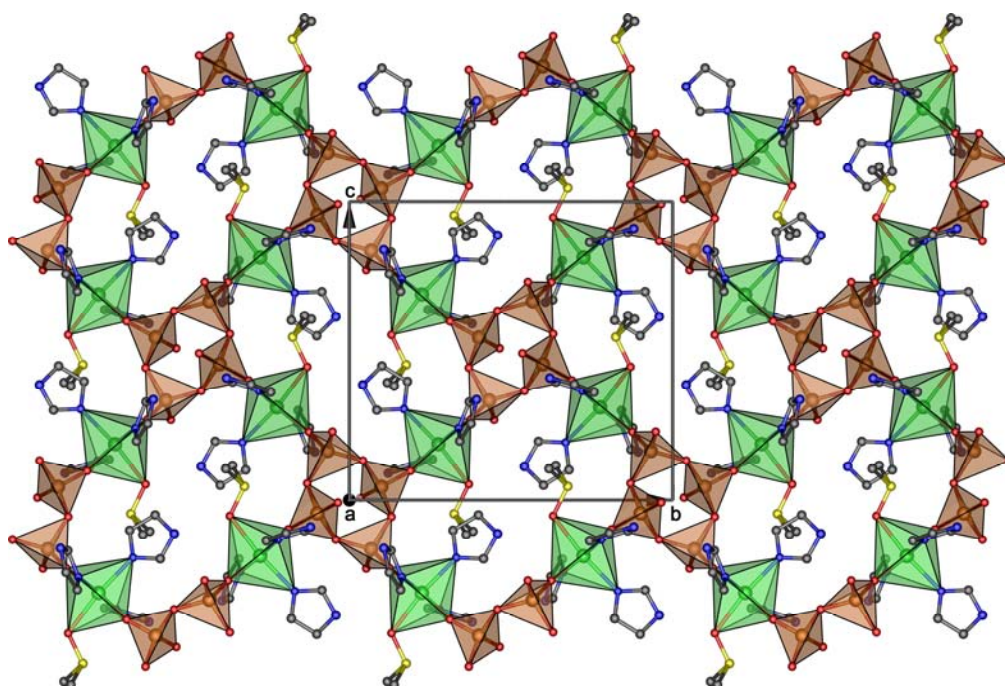


Figure 7.12 Polyhedral representations of single layer of compound **7e**, viewed along the crystallographic a axis. The layer is at $z = 1/2$.

As shown in Figure 7.13, **7e** has a 2-D polymeric layer structure viewed along the crystallographic *b* axis. The supramolecular network is formed through N–H···O hydrogen bond interactions, Table 7.15, between coordinated imidazole ligands on manganese centers and bridging oxo groups or terminal vanadyl sites above and below from adjacent layers. These interactions help to stabilize the assembly as well as increase the dimensionality of the structure.

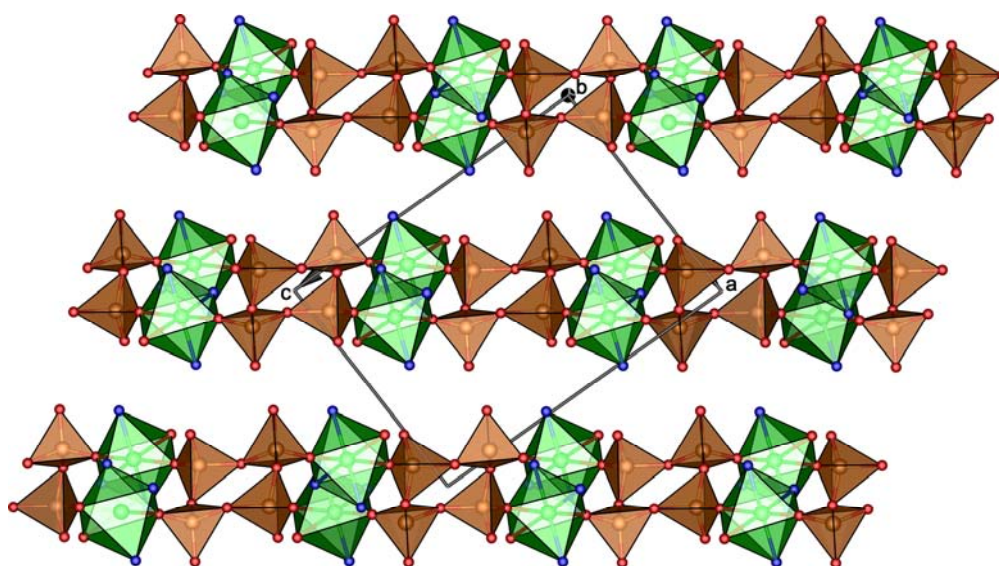


Figure 7.13 Polyhedral representations of a portion of bimetallic inorganic layers of compound **7e**, viewed along the crystallographic *b* axis.

Table 7.15 Hydrogen bond geometries for **7e** (Å, °).^a

D–H···A	d[D–H]	d[H···A]	d[D···A]	∠[D–H···A]
N12–H12b···O6 ⁱ	0.86	1.92	2.739(8)	157.8
N22–H22b···O6 ⁱⁱ	0.86	2.40	3.231(11)	163.9
N32–H32b···O7 ⁱⁱⁱ	0.86	2.02	2.861(7)	166.2

^a Estimated standard deviations are given in parentheses.

Symmetry codes: (i) $-x-1/2, 1/2+y, 3/2-z$; (ii) $1+x, y, z$; (iii) $1/2-x, 1/2+y, 3/2-z$.

7.4 Conclusions

In this study, five new hybrid organic-inorganic vanadium oxide complexes with interesting structural motifs have been synthesized through the reactions of various stoichiometry of V_2O_5 , M^{II} ($M = Mn, Co, Ni$), and the aromatic planar molecule of Im ligand under mild hydro/solvothermal conditions. The successful isolation of this species not only provides an intriguing example of hybrid organic-inorganic framework materials, but also may open up possibilities for the design of new polyoxometallates (POM)-based materials and inorganic oxide microstructure as well as zeolites analog.

Compounds **7b–7e** has 2-D layer structure that constructed from the basic building units of VO_4 tetrahedra and MN_4O_2 octahedra, and the Im ligand acts as a structure directing agent. An isomorphous structures of formulae $[M(Im)_4V_2O_6]$, where $M = Mn$ (**7b**), **Co** (**7c**), **Ni** (**7d**), are particular noteworthy in displaying an interesting order-disorder crystallographic phase transition between the $P4_2/n$ at 295(2) K and $I4_1/a$ (**7b** and **7c**) or $P2/n$ (**7d**) at 100(2) K. For the DMSO solvothermal synthesis of **7e**, the replacement of one equatorial imidazole on Mn(II) with a covalently coordinated DMSO results in a loss of symmetry lowering the space group to $P2_1/n$ at 295(2) K, but the topologically is similar to those observed in **7b–7d**.

Remarkably, the new 3-D mixed-valence manganese metal zeolite analog **7a** can be obtained from similar the building units of VO_4 tetrahedra as found in those **7b–7e**. Compound **7a** has an anionic open 3-D inorganic framework in which the organic counterions of $[ImH]^+$ are located in 1-D tunnels generated from ten-membered rings $[Mn_4V_6]$ rings, and play role as a template that provides space-filling or charge-compensation. This compound could be significant in terms of the potential

applications in acid catalysis and magnetic materials. The successful preparation of compound **7a** further confirms the power of the hydrothermal reactions for isolation new metal oxide hybrids as well as the microporous solid of inorganic oxide which such solid materials may be support in the development of nanoscience and nanotechnology in the future.

7.5 References

- Allen, F. H., Davies, J. E., Galloy, J. J., Johnson, O., Kennard, O., Macrae, C. F., Mitchell, E. M., Mitchell, G. F., Smith, J. M., and Watson, D. G. (1991). **J. Chem. Inf. Comput. Sci.** 31: 187-204.
- Altomare, A., Burla, M. C., Camalli, M., Cascarano, G. L., Giacovazzo, C., Guagliardi, A., Moliterni, A. G. G., Polidori, G., and Spagna, R. (1999). **J. Appl. Crystallogr.** 32: 115-119.
- Blessing, R. H. (1995). **Acta Crystallogr., Sect. A: Found. Crystallogr.** 51: 33-38.
- Brandenburg, K., and Putz, H. (2006). **DIAMOND**. Version 3.1e. Crystal Impact GbR, Bonn, Germany.
- Brese, N. E., and O'Keeffe, M. (1991). **Acta Crystallogr., Sect. B: Struct. Sci.** 47: 192-197.
- Brown, I. D., and Altermatt, D. (1985). **Acta Crystallogr., Sect. B: Struct. Sci.** 41: 244-247.
- Burnett, M. N., and Johnson, C. K. (1996). **ORTEP-III**. Report ORNL-6895. Oak Ridge National Laboratory, Tennessee, USA.
- Cheetham, A. K., Férey, G., and Loiseau, T. (1999). **Angew. Chem. Int. Ed.** 38: 3268-3292.

- Clearfield, A., and Wang, Z. (2002). **J. Chem. Soc., Dalton Trans.** (15): 2937-2947.
- Chainok, K. (2004). **M. Sc. Thesis.** Suranaree University of Technology.
- Chesnut, D. J., Hagrman, D., Zapf, P. J., Hammond, R. P., LaDuca, R., Haushalter R. C., and Zubieta J. (1999). **Coord. Chem. Rev.** 190-192: 737-769.
- Chirayil, T., Zavalij, P. Y., and Whittingham, M. S. (1998). **Chem. Mater.** 10(10): 2629-2640.
- Creagh, D. C., and McAuley, W. J. (1995). **International Tables for X-ray Crystallography.** Vol. C, Table 4.2.6.8, Dordrecht: Kluwer Academic Publishers. pp 219-222.
- Fuchs, J., Mahjour, S., and Pickardt, J. (1976). **Angew. Chem. Int. Ed.** 15(6): 374-375.
- Hahn, Th. (1995). **International Tables for X-ray Crystallography.** Vol. A. Dordrecht: Kluwer Academic Publishers. pp 344-345 and 350-351.
- Hagrman, P. J., Finn, R. C., and Zubieta, J. (2001). **Solid State Sci.** 3(7): 745-774.
- Herbstein, F. H. (2006). **Acta Crystallogr., Sect. B: Struct. Sci.** 62: 341-383.
- Höwing, J. Gustafsson, T., and Thomas, J. O. (2003). **Acta Crystallogr., Sect. B: Struct. Sci.** 59: 747-752.
- Law, T. S.-C., Sung, H. H.-Y., and Williams, I. D. (2000). **Inorg. Chem. Commun.** 3(8): 420-423.
- Law, T. S.-C., and Williams, I. D. (2000). **Chem. Mater.** 12(8): 2070-2072.
- Lee, J. S., Lee, Y.-J., Tae, E. L., Park, Y. S., and Yoon, K. B. (2003). **Science** 301: 818-821.
- Maspoch, D., Ruiz-Molina, D., and Veciana J. (2007). **Chem. Soc. Rev.** (5): 770-818.

- Nonius. (1998). **COLLECT**. Nonius BV, Delft, The Netherlands.
- Otwinowski, Z., and Minor, W. (1997). **Methods in Enzymology**. Vol. 276, Macromolecular Crystallography, Part A, edited by Carter Jr, C. W. and Sweet, R. M., New York: Academic Press. pp 307-326.
- Oxford Cryosystems. (1997). 600 Series Cryostream Cooler Operation and Instruction Guide, Oxford Cryosystems, Oxford, UK.
- Rae, A. D. (1975). **Acta Crystallogr., Sect. A: Found. Crystallogr.** 31: 560-570.
- Rae, A. D. (2006). **RAELS06**: A Comprehensive Constrained Least Squares Refinement Program. Australian National University, Canberra, Australia.
- Sadakane, M., Watanabe, N., Katou, T., Nodasaka, Y., and Ueda, W. (2007). **Angew. Chem. Int. Ed.** 46(9): 1493-1496.
- Sharma, S., Ramanan, A., Zavalij, P. Y., and Whittingham, M. S. (2002). **CrystEng Commun.** 40(100): 601-604.
- Smith, J. V. (1988). **Chem. Rev.** 88(1): 149-182.
- Whittingham, M. S. (2004). **Chem. Rev.** 104(10): 4271-4302.
- Williams, I. D., Law, T. S-C., Sung, H. H-Y., Wen, G-H., and Zhang, X-X. (2000). **Solid State Sci.** 2(1): 47-55.
- Zavalij, P. Y., and Whittingham, M. S. (1999). **Acta Crystallogr., Sect. B: Struct. Sci.** 55: 627-663.

CHAPTER VIII

CONCLUDING REMARKS

The underlying direction of the work leading to this thesis is along the lines of structure function relationships of hybrid organic-inorganic materials wherein the inorganic portion forms metal-connected networks that contain the organic moieties as templates, inclusions, or decorations. At the same time work reported herein demonstrates some common laboratory techniques and practices for single crystal growth and prediction of the arrangement of molecules or ions as they assemble in the solid metallosupramolecular structure which is a network incorporating both inorganic and organic components.

Initial synthesis of a new compound often gives an impure sample, as evidenced by color or morphology. The challenge of producing pure products of the hybrid compounds reported herein, by either bench top or hydrothermal methods, was met. Even so the precipitate sample from any one reaction mixture may still appear inhomogeneous due to mixtures of single crystals, polycrystalline powder, or amorphous material. Such mixtures may even appear to be different colors. This apparent inhomogeneity of a product can be discounted by comparing the powder X-ray diffractogram from the bulk sample with the pattern calculated from the single crystal analysis. Other techniques such as elemental analyses, electron probe, thermal analysis, and spectroscopy may also be used to support the structure analysis to reinforce the veracity of the correlation between structures and properties.

The first portion of this thesis provides a review on X-ray crystal structures of hybrid organic-inorganic materials that have formed in attempts to bridge different aspects of solid state supramolecular chemistry and molecular crystal engineering, and also to understand their structures-properties correlations.

Solid state phase transitions is an important subject that has been widely explored in organic crystals, and is of considerable commercial interest, particularly in the pharmaceutical industry where different polymorphic forms of drugs may have different bioavailability, and require different processing and formulation. It is also found that compounds with polymorphic forms exhibit various types of structural phase transition on external perturbations such as temperature, pressure, and/or light, which may affect the resulting physical properties. The utilization of routine analytical and spectroscopic laboratory tools for investigation of solid-state transformation is sometimes restricted. Therefore, in order to ascertain the possibility of phase transition, variable temperature X-ray diffraction, magnetic susceptibility, Mössbauer, FTIR, and thermal analysis measurements are demonstrated to be useful methods.

Specific examples of phase transition studies in this thesis are described in Chapters VI and VII. The order-disorder structural phase transition was observed in the polymeric isomorphous compounds of formula $[M(\text{Im})_4\text{V}_2\text{O}_6]_\infty$, where M = Mn, Co, Ni, Im = imidazole. The phase transition was studied by single crystal X-ray diffraction between 100 and 295 K. It was observed that the room temperature $P4_2/n$ disordered phase is reversibly transformed to the $I4_1/a$ ordered phase below 281 K for Mn and 175 K for Co. The ordered phase of Ni was found to have space group $P2/n$ at

100 K. The phase transition mechanisms of these compounds were affected by a change of the hydrogen bond connectivity.

Another particularly interesting phase change is the magnetic spin-crossover (SCO) behavior found in the 3-D framework of formula $[\text{Fe}(\text{AIBN})_3][\text{MCl}_4]_2$ where $\text{M} = \text{Fe}^{\text{III}}$ and In^{III} . The SCO transitions were characterized by use of temperature dependent magnetic susceptibility (2–300 K) and Mössbauer effect spectral measurements (4.2, 77 and 295 K) together with single crystal X-ray crystallography (103 and 233 K). The data revealed that the AIBN compounds exhibit incomplete “half” SCO phenomena with no accompanying crystallographic phase change.

Taking into account for the solid state phase transition, in the cases of formal $[\text{M}(\text{Im})_4\text{V}_2\text{O}_6]$ and the later $[\text{Fe}(\text{AIBN})_3](\text{MCl}_4)_2$ compounds are considered to be crystallographic first order phase transition and magnetic spin transition between two electronic states (high spin \rightarrow low spin) in molecular chemistry, respectively, as evidence through careful investigation on such methods mentioned above. It is noteworthy that the phase transition should also be confirmed by differential scanning calorimetric (DSC) measurements. This will help to obtain the information required.

A number of coordination polymers and supramolecular compounds with diversified architectures and other interesting features of supramolecular interactions such as hydrogen bonds and π - π stacking, network interpenetration, and molecular topology are observed in this thesis. An impressive example from the present study is the formation of the remarkable neutral hydrophilic 1-D tubular structure of the cyanide-bridged bimetallic coordination compound $[\text{Fe}(2,2'\text{-bipy})(\text{CN})_4\text{Mn}(\text{H}_2\text{O})_2]$. This compound displays ferromagnetic behavior without any magnetic ordering in the temperature range explored (2–300 K). From the topological point of view, the Mn^{II}

ions of the 1-D tube-like structure of $[\text{Fe}(2,2'\text{-bipy})(\text{CN})_4\text{Mn}(\text{H}_2\text{O})_2]$ could possibly be replaced by other octahedral transition metal centers which would offer an opportunity to achieve multifunctional materials involving spin-crossover ($\{\text{Fe}^{\text{II}}(\text{N})_4(\text{H}_2\text{O})_2\}$ centers) perhaps with porosity.

Another a beautiful example is the formation of new 3-D open-framework manganese vanadates of $[\text{ImH}][\text{Mn}_3(\text{OH})_2(\text{V}_4\text{O}_{13})]$, in which anionic oxide frameworks with ten-membered ring channels have assembled around the cationic organic guests. This compound is very interesting due to the mixed-valence $[\text{Mn}^{\text{II}}\text{--Mn}^{\text{III}}\text{--Mn}^{\text{II}}]$ trimer blocks, herein observed for the first time in a manganese vanadate solid framework. These could be remarkable redox catalyst as well as promising candidates for other applications like adsorptive and ion-exchange behavior.

Since the properties of any material are largely due to its structure, control over the structure allows manipulating these properties. This thesis has demonstrated how small changes in structure (from synthetic strategy or from physical stimuli such as temperature change) lead to changes in specific target properties (*i.e.* magnetism or other phase). Presently, many important applications of materials chemistry can be found in the electronics, energy, medical, and processing industries. Therefore, new materials designed by chemists will certainly continue to have our impact on our economy and the world.

APPENDICES

APPENDIX A

CRYSTALLOGRAPHIC INFORMATION FILES

(CD-ROM)

Directory of Crystallographic Information Files

ID Code	Compound	Temperature (K)
2a	[Ag ₂ (bmtz)(ClO ₄)]ClO ₄	123(2)
2b	[Ag(bmtz)]ClO ₄ ·MeCN	123(2)
2c	[{Ag(tcm)} ₂ (H ₂ bmtz)(MeCN)]	123(2)
2d	[{Ag(tcm)} ₂ bmtz]	123(2)
2e	[Ag(bptz)(NO ₃)]	123(2)
2f	[H ₂ bptz](NO ₃) ₂	123(2)
3a	[Fe(2,2'-bipy)(CN) ₄ Mn]·MeOH	123(2)
3b	[Fe(2,2'-bipy)(CN) ₄ Mn(H ₂ O) ₂]	123(2)
3c	[Fe(1,10-phen)(CN) ₄ Cu(tn)(H ₂ O) ₂]·5H ₂ O	123(2)
3e	[Fe(2,2'-bipy)(CN) ₄ Ni(en) ₂]·Solvent	123(2)
4a	[{Ag(CN) ₂ } ₂ Mn(2,2'-bipy) ₂]·H ₂ O	123(2)
4b	[Ag(CN) ₂ Mn(2,2'-bipy) ₂ (H ₂ O)][Ag(CN) ₂]	123(2)
4c	[Ag ₄ (CN) ₇ {Cd(2,2'-bipy)} ₂]ClO ₄	123(2)
4d	[{Ag(CN) ₂ } ₂ Cd(2,2'-bipy)]	123(2)
5a	[Ni(CN) ₄ Ni(en)]·2H ₂ O	123(2)
5b	[Ni(CN) ₄ Ni(tn)]·H ₂ O·MeOH	123(2)
6a_100	[Fe(AIBN) ₃][InCl ₄] ₂	103(2)
6a_233	[Fe(AIBN) ₃][InCl ₄] ₂	233(2)
6b_100	[Fe(AIBN) ₃][FeCl ₄] ₂	103(2)
6b_233	[Fe(AIBN) ₃][FeCl ₄] ₂	233(2)

ID Code	Compound	Temperature (K)
6c	[Fe(AIBN)H ₂ O][FeCl ₄] ₂	123(2)
6d	[Fe(ACCN) ₃][InCl ₄] ₂	123(2)
6e	[Fe(ACCN) ₃][FeCl ₄] ₂	123(2)
7a	[Mn ₃ (OH) ₂ (V ₄ O ₁₃)][ImH]	100(2)
7b_100	[Mn(Im) ₄ V ₂ O ₆]	100(2)
7b_200	[Mn(Im) ₄ V ₂ O ₆]	200(2)
7b_279	[Mn(Im) ₄ V ₂ O ₆]	279(2)
7b_283	[Mn(Im) ₄ V ₂ O ₆]	283(2)
7b_295	[Mn(Im) ₄ V ₂ O ₆]	295(2)
7c_100	[Co(Im) ₄ V ₂ O ₆]	100(2)
7c_200	[Co(Im) ₄ V ₂ O ₆]	170(2)
7c_279	[Co(Im) ₄ V ₂ O ₆]	180(2)
7c_283	[Co(Im) ₄ V ₂ O ₆]	295(2)
7c_295	[Co(Im) ₄ V ₂ O ₆]	295(2)
7d_100	[Ni(Im) ₄ V ₂ O ₆]	100(2)
7d_295	[Ni(Im) ₄ V ₂ O ₆]	295(2)
7e	[Mn(DMSO)(Im) ₃ V ₂ O ₆]	295(2)

APPENDIX B

SUPPLEMENTARY MATERIAL

Chapter II

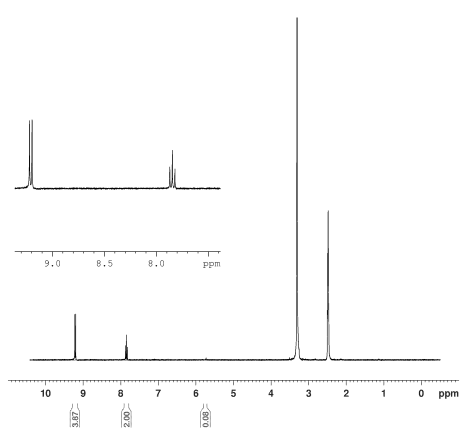


Figure B2.1 ^1H NMR for the bmtz ligand.

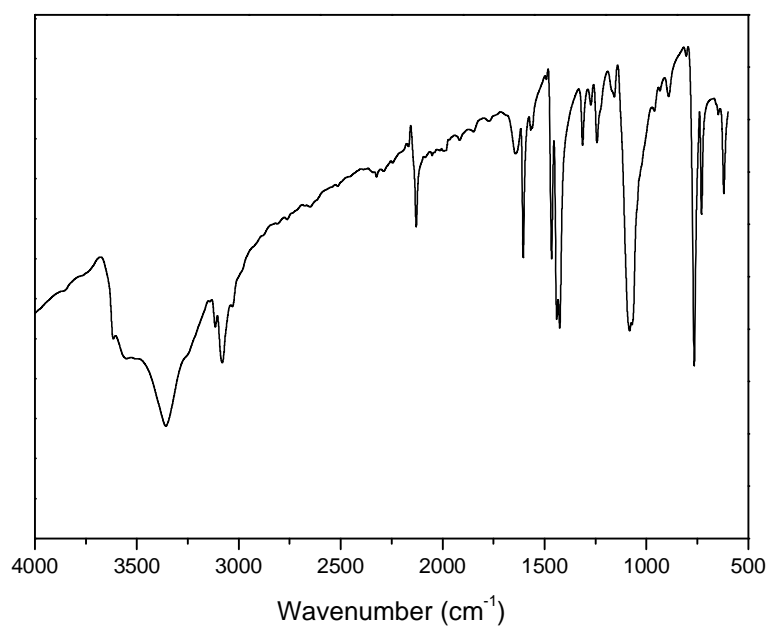


Figure B2.2 The IR spectrum for **2a**.

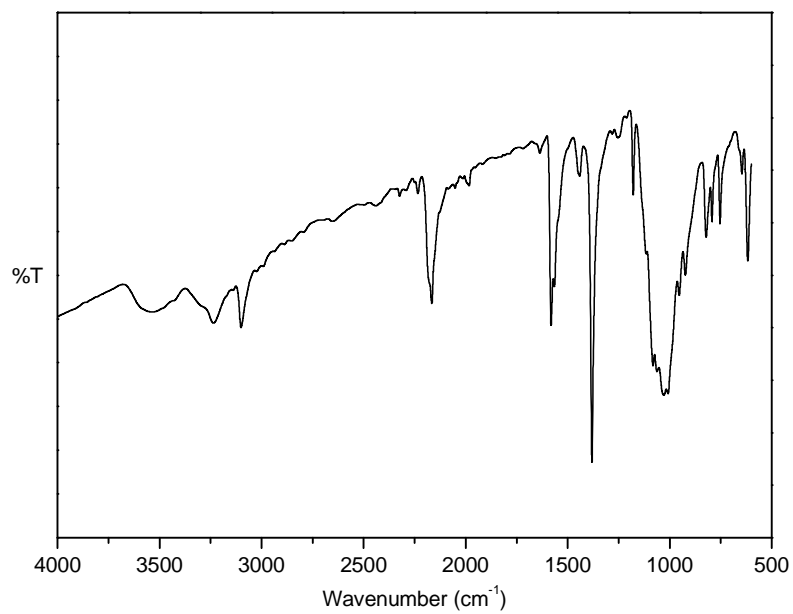


Figure B2.3 The IR spectrum for **2b**.

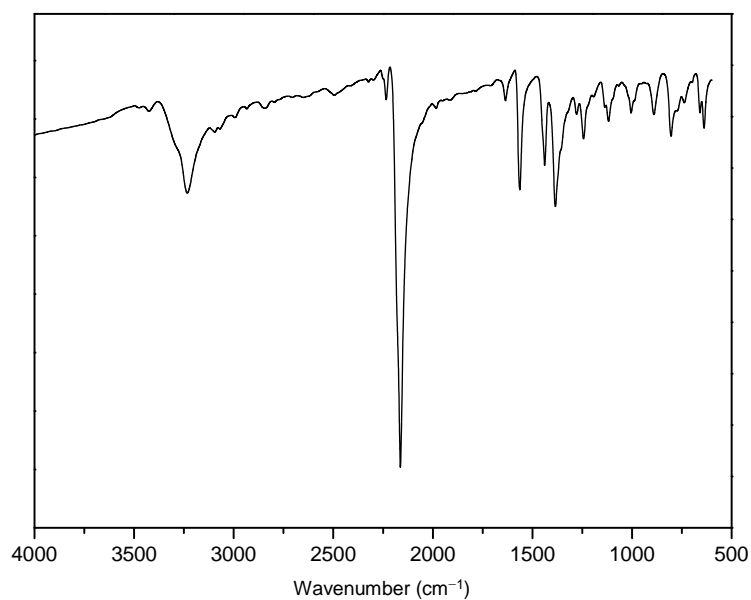


Figure B2.4 The IR spectrum for **2c**.

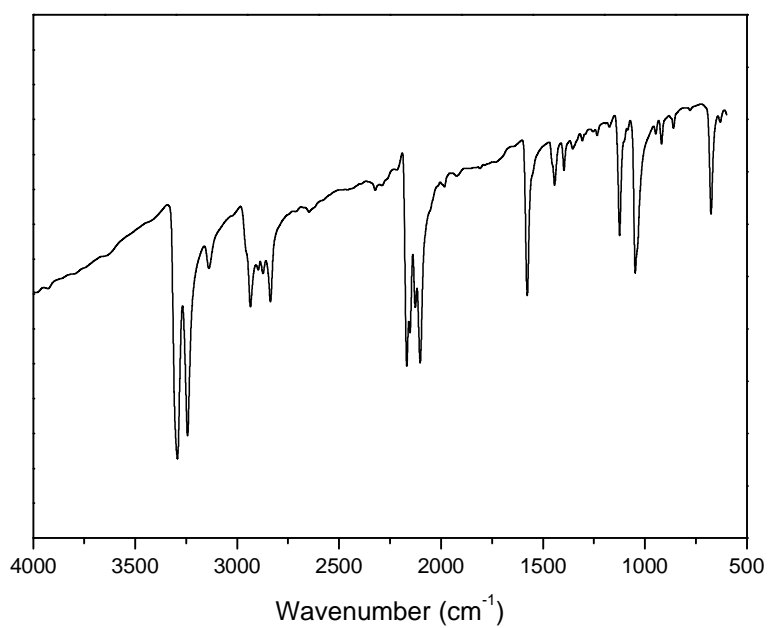


Figure B2.5 The IR spectrum for **2d**.

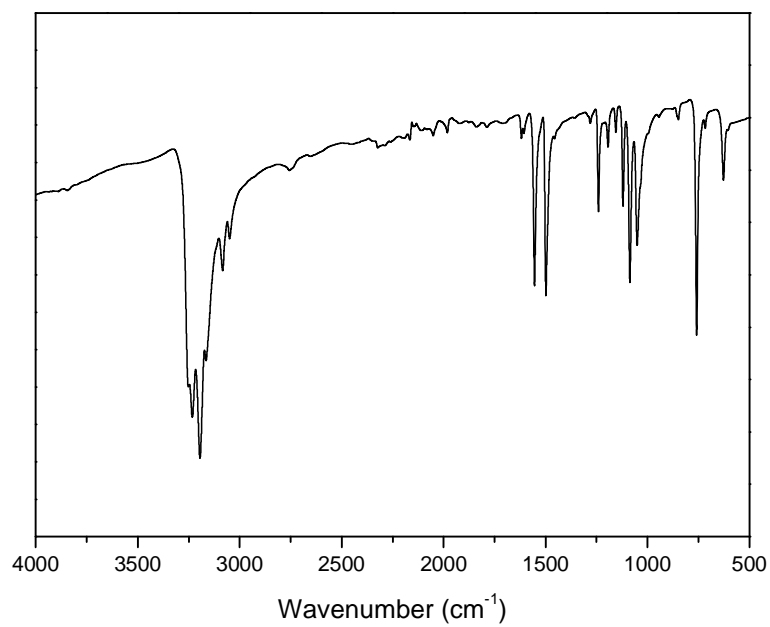


Figure B2.6 The IR spectrum for **2e**.

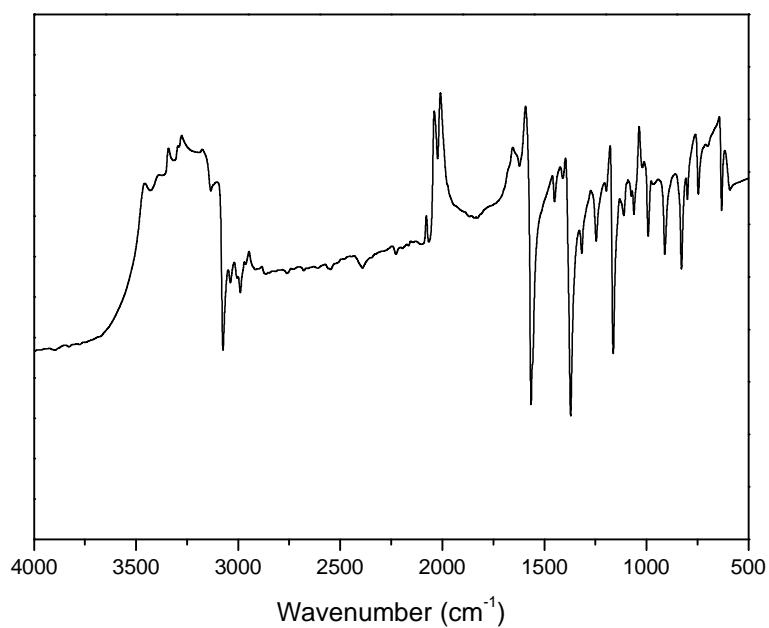


Figure B3.1 The IR spectrum for **2f**.

Chapter III

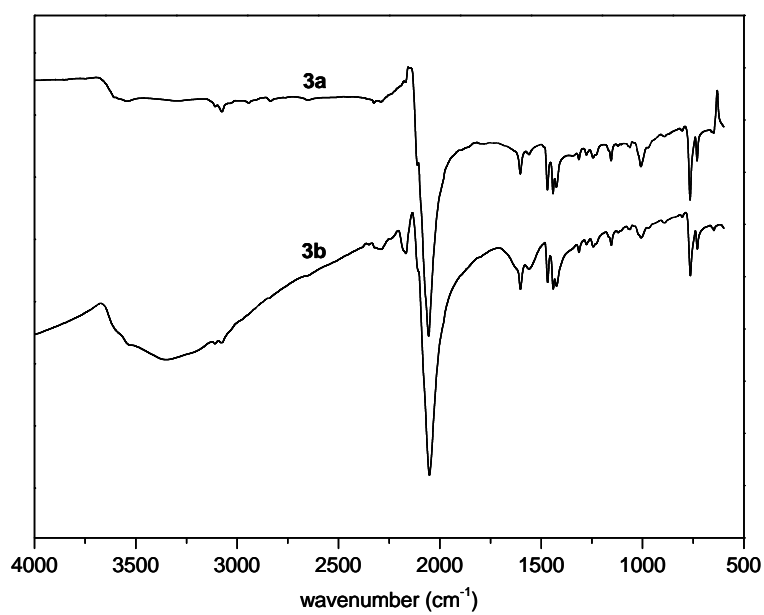


Figure B3.1 The IR spectrum for **3a-3b**.

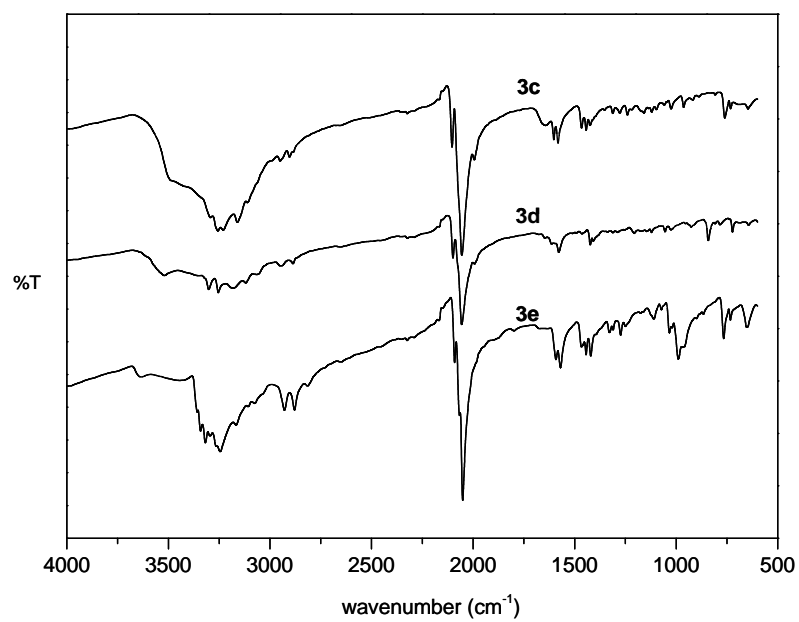


Figure B3.2 The IR spectrum for **3c-3e**.

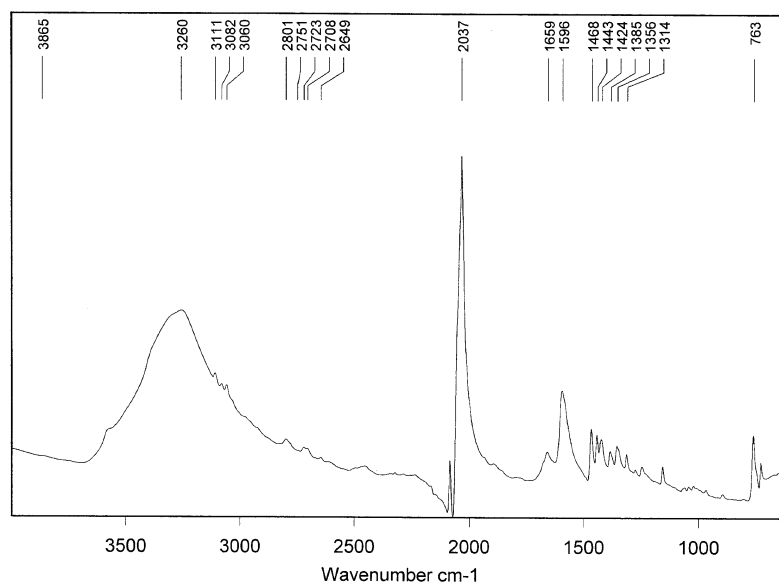


Figure B3.3 The IR spectrum for K₂[Fe^{II}(2,2'-bipy)(CN)₄]·3H₂O.

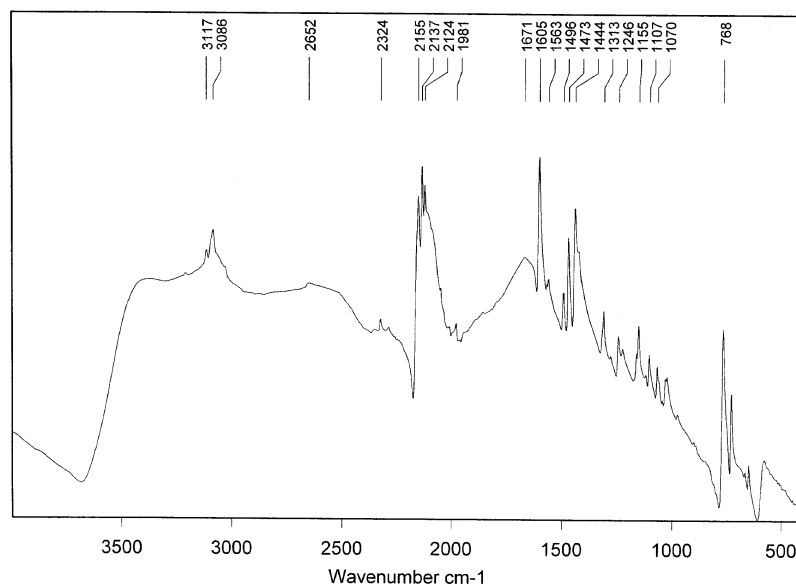


Figure B3.4 The IR spectrum for $\text{H}[\text{Fe}^{\text{III}}(2,2'\text{-bipy})(\text{CN})_4]\cdot 2\text{H}_2\text{O}$.

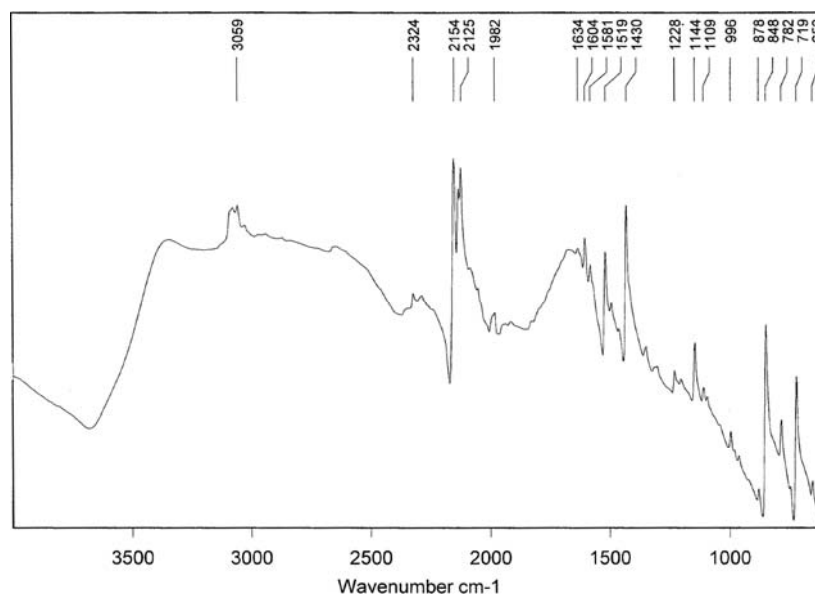


Figure B3.5 The IR spectrum for $\text{H}[\text{Fe}^{\text{III}}(1,10\text{-phen})(\text{CN})_4]\cdot 2\text{H}_2\text{O}$.

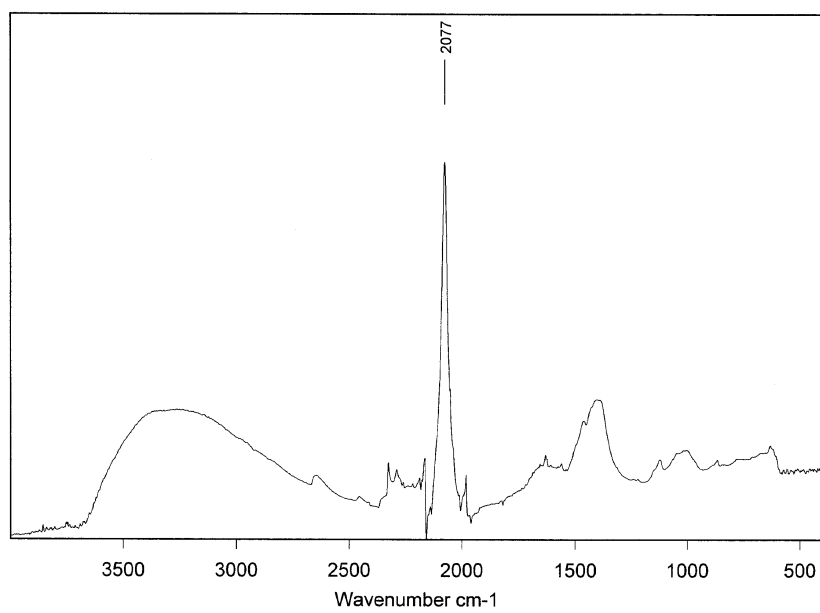


Figure B3.6 The IR spectrum for KCN.

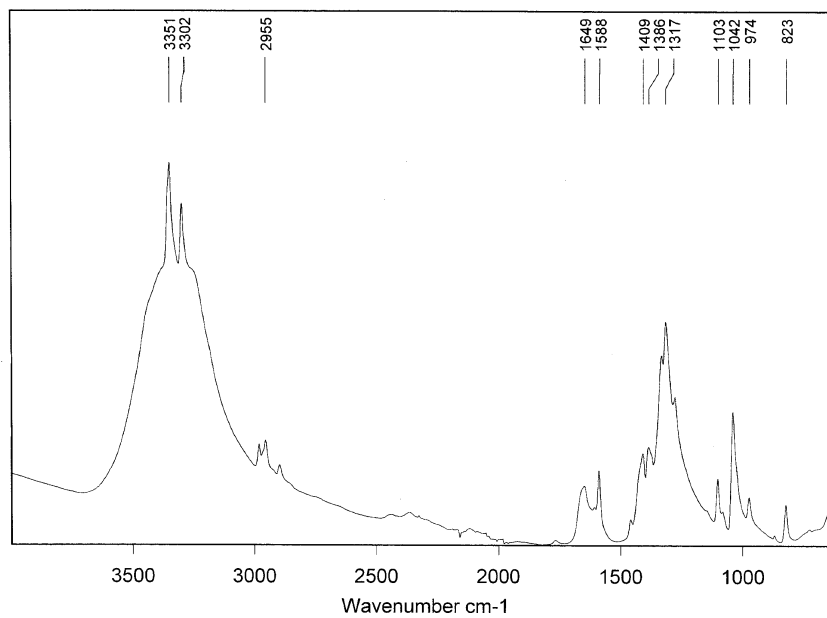


Figure B3.7 The IR spectrum for [Ni(en)(H₂O)₄](NO₃)₂.

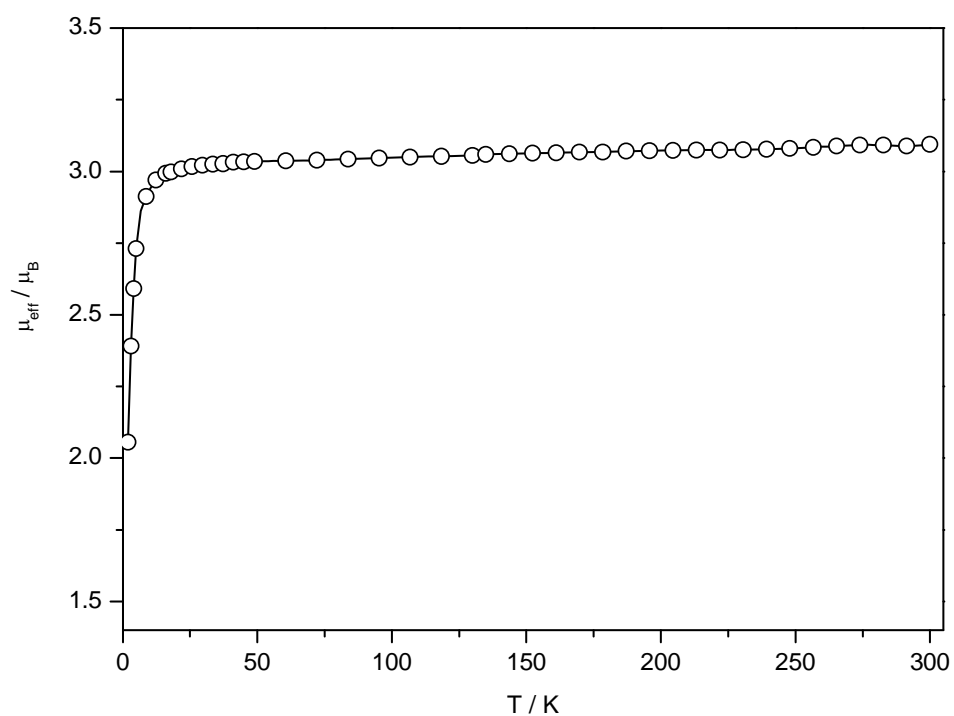


Figure B3.8 Plot of magnetic moment, per $[\text{Ni}^{\text{II}}]$, for $[\text{Ni}(\text{en})(\text{H}_2\text{O})_4](\text{NO}_3)_2$.

Chapter IV

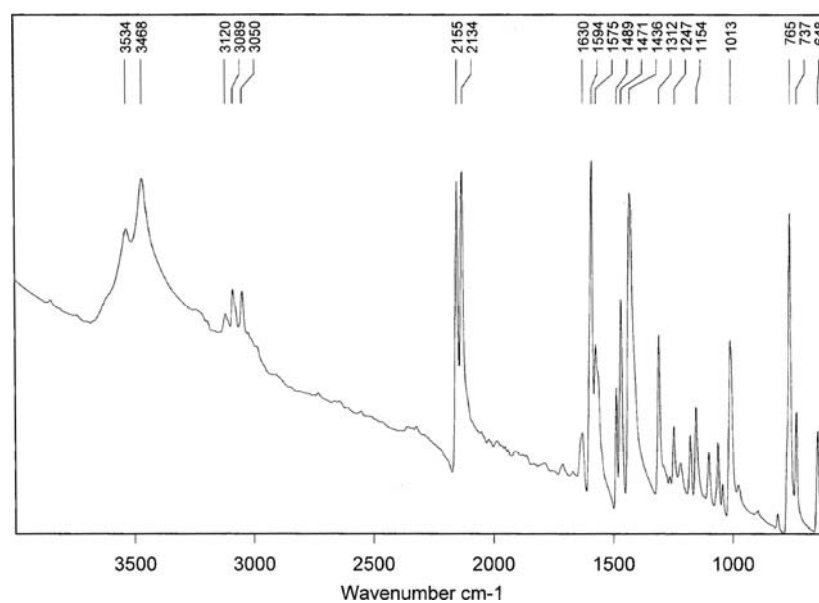


Figure B4.1 The IR spectrum for **4a**.

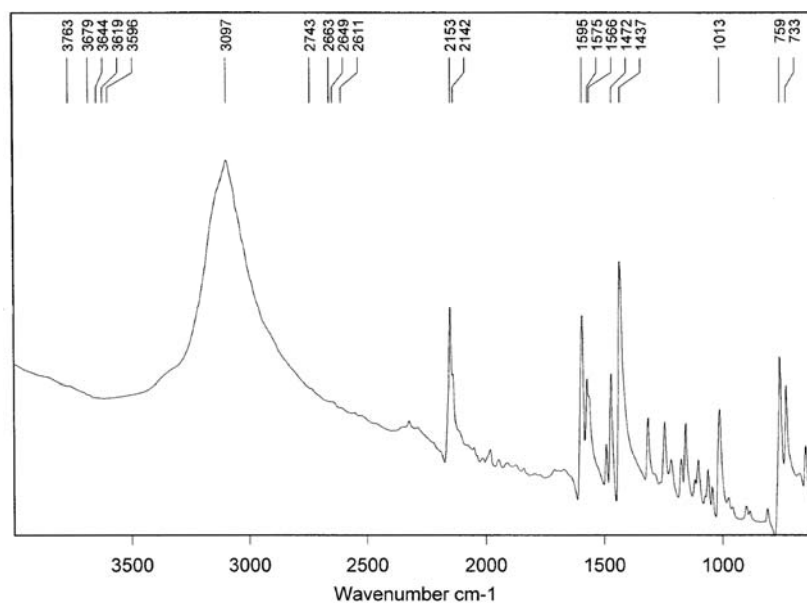


Figure B4.2 The IR spectrum for **4b**.

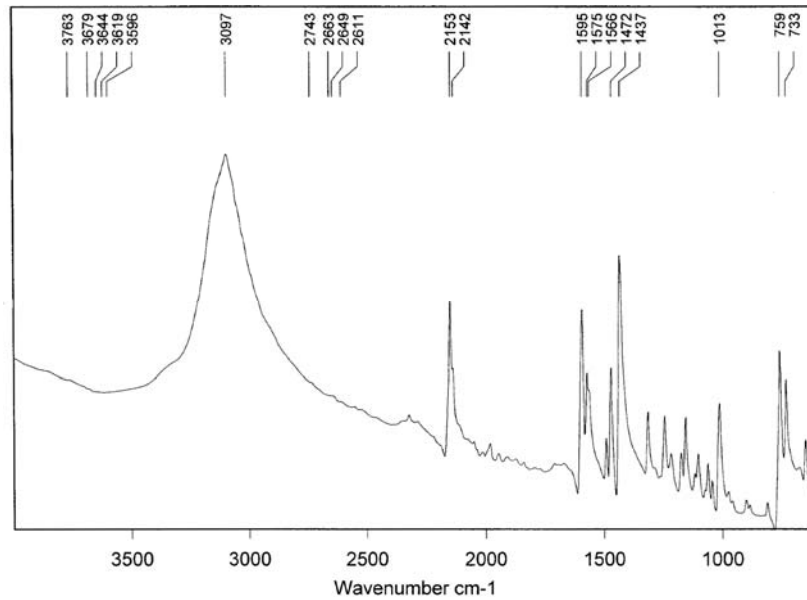


Figure B4.3 The IR spectrum for **4c**.

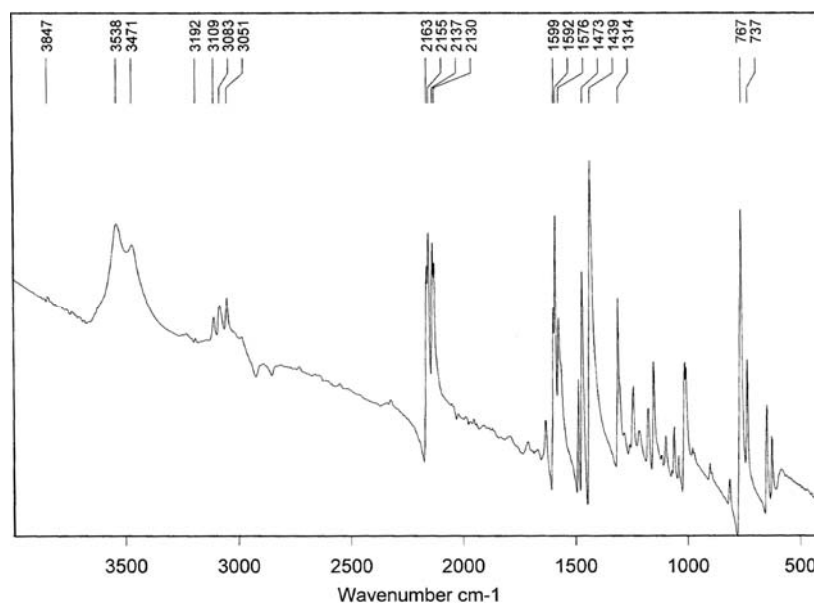


Figure B4.4 The IR spectrum for **4d**.

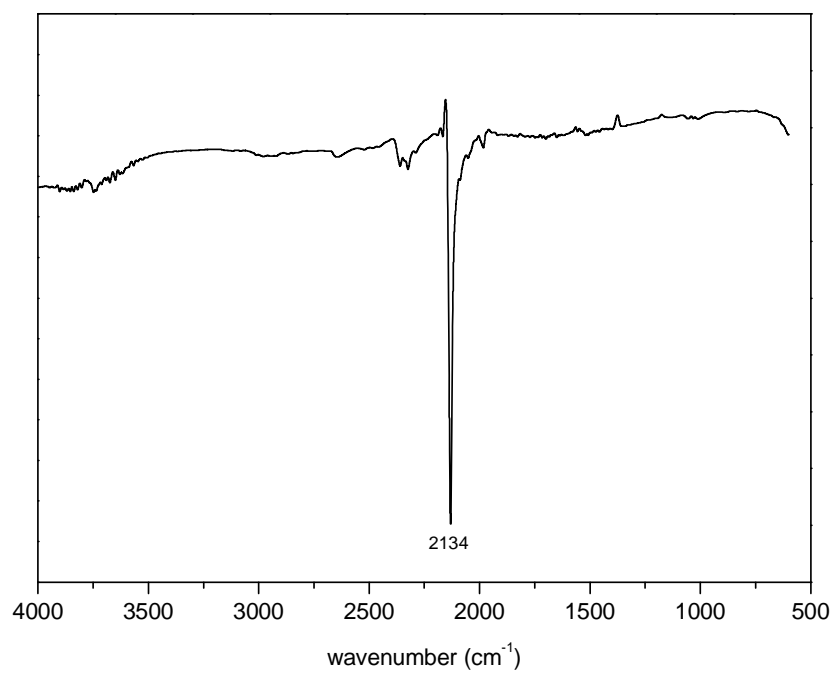


Figure B4.5 The IR spectrum for K[Ag(CN)₂].

Chapter VI

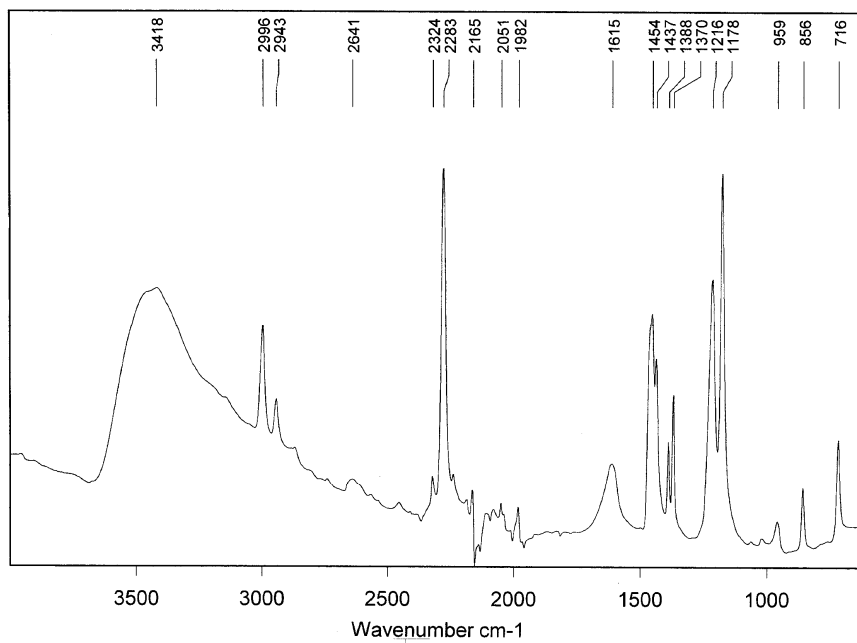


Figure B6.1 The IR spectrum for 6a.

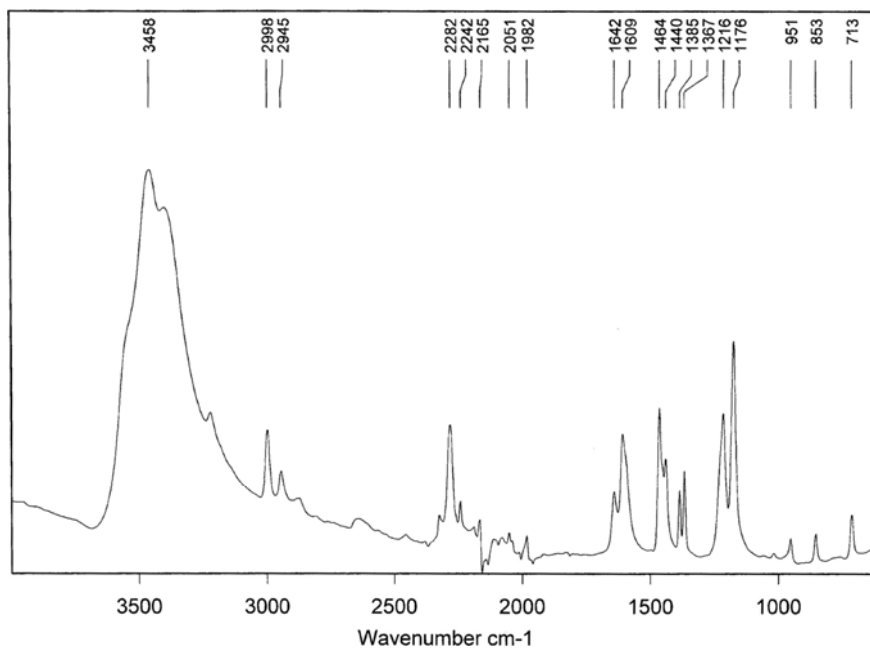


Figure B6.2 The IR spectrum for 6b.

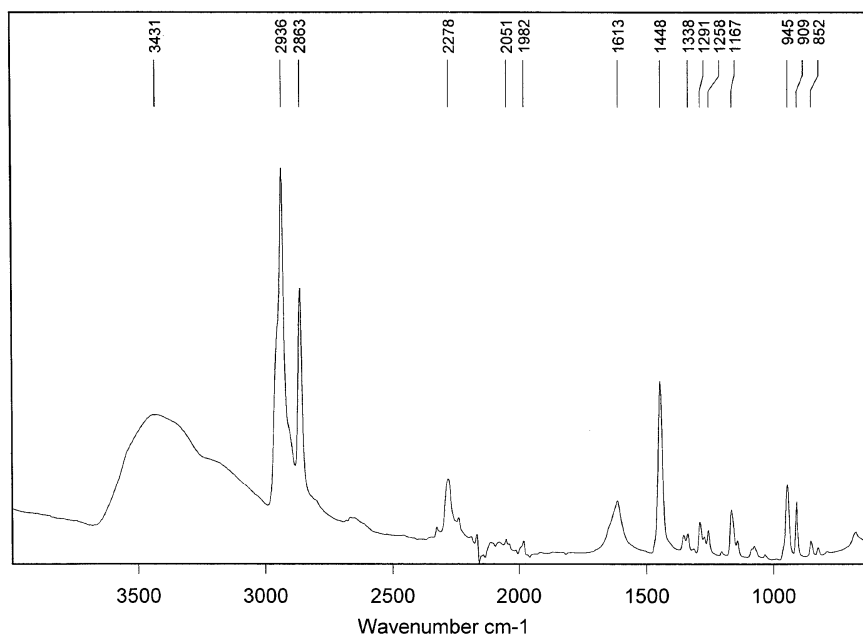


Figure B6.3 The IR spectrum for **6d**.

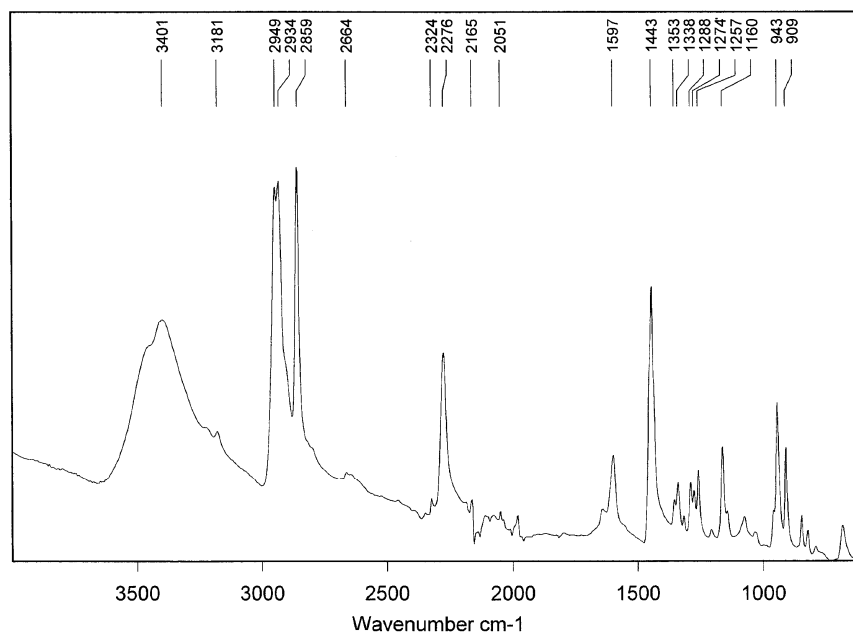


Figure B6.4 The IR spectrum for **6e**.

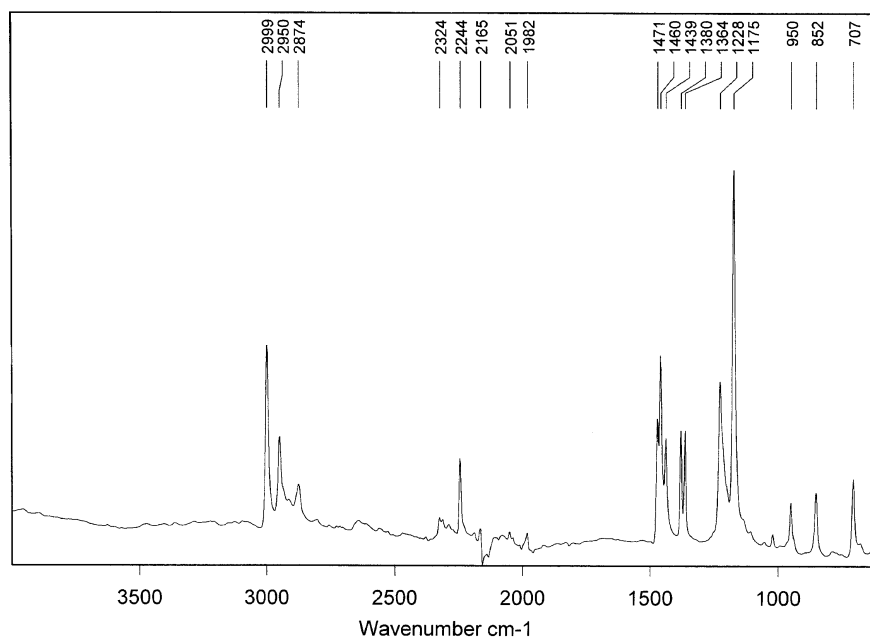


Figure B6.5 The IR spectrum for the AIBN ligand.

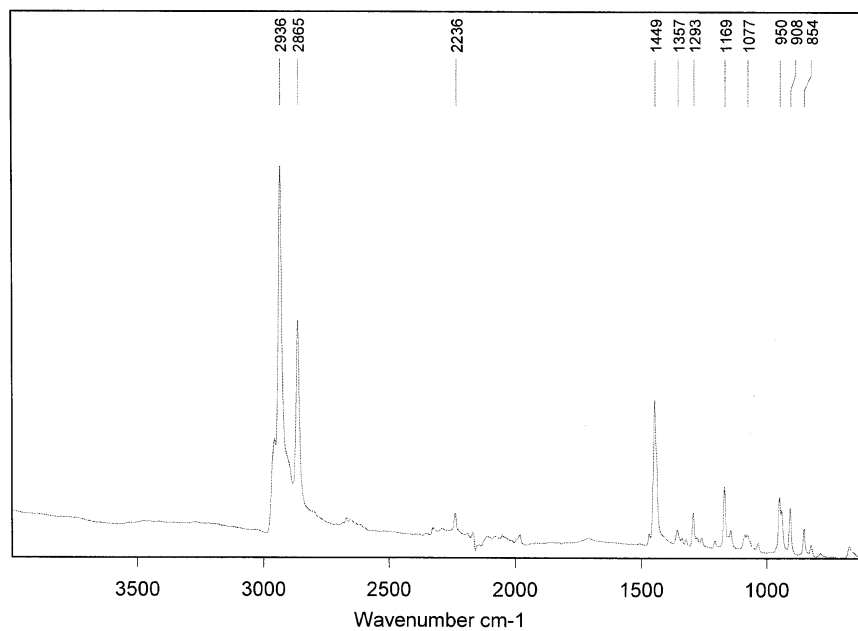


Figure B6.6 The IR spectrum for the ACCN ligand.

Chapter VII

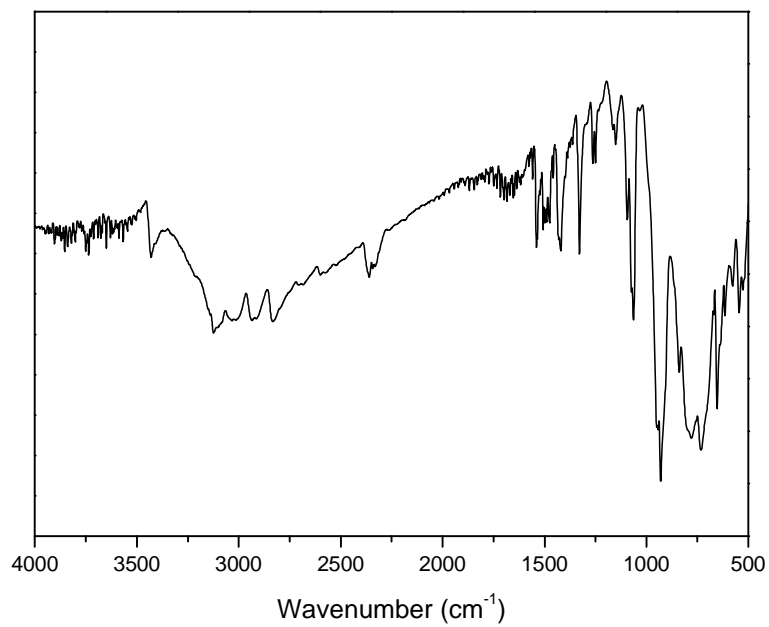


Figure B7.1 The IR spectrum for **7a**.

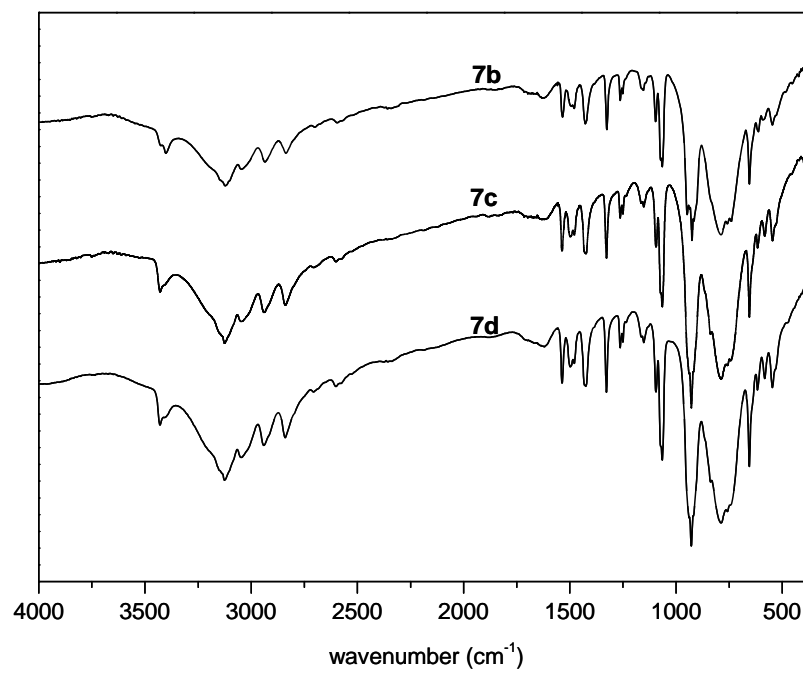


Figure B7.2 The IR spectrum for **7b-7d**.

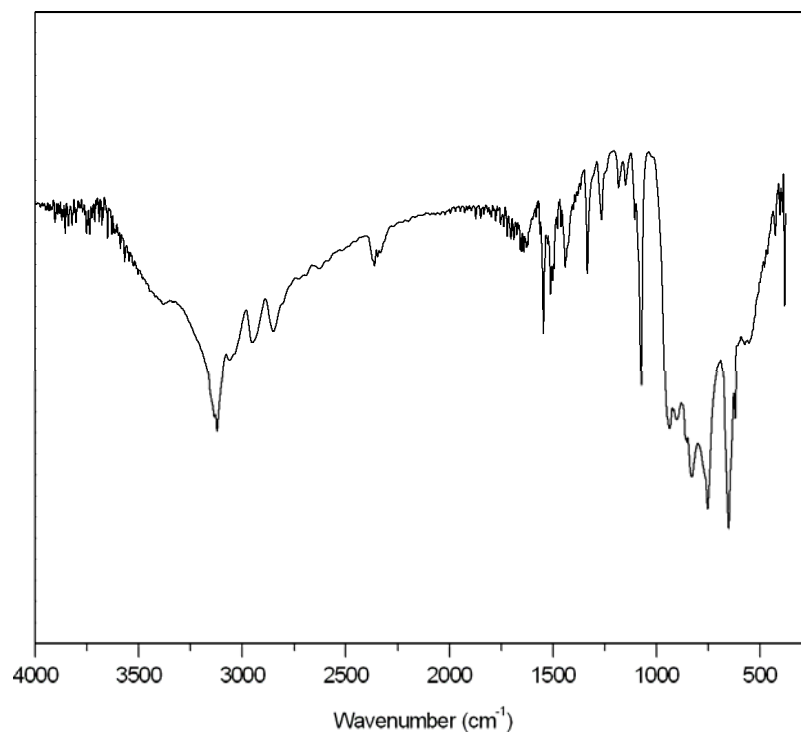


Figure B7.3 The IR spectrum for **7e**.

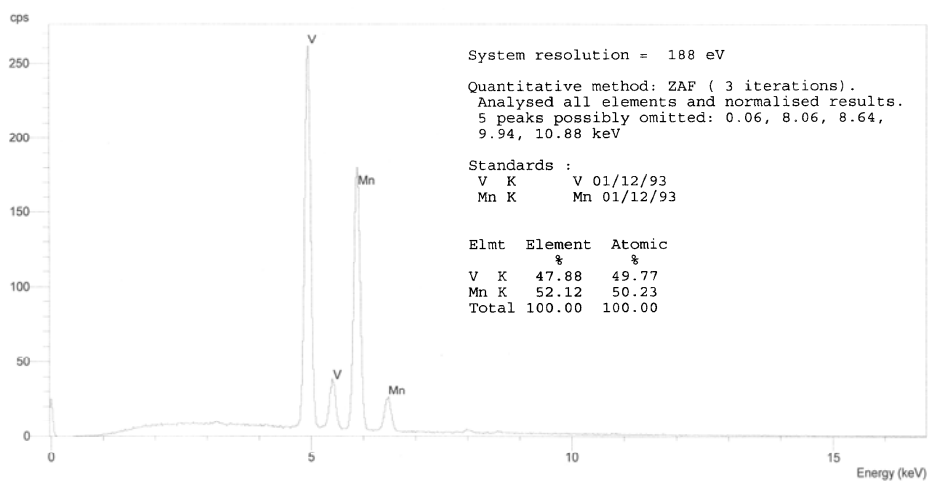


Figure B7.4 The EDX spectrum for **7b**.

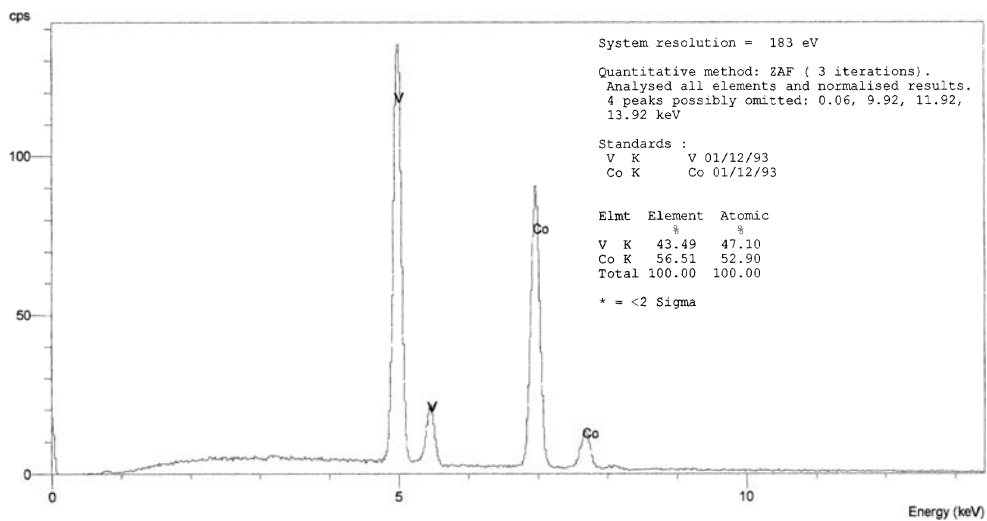


Figure B7.5 The EDX spectrum for 7c.

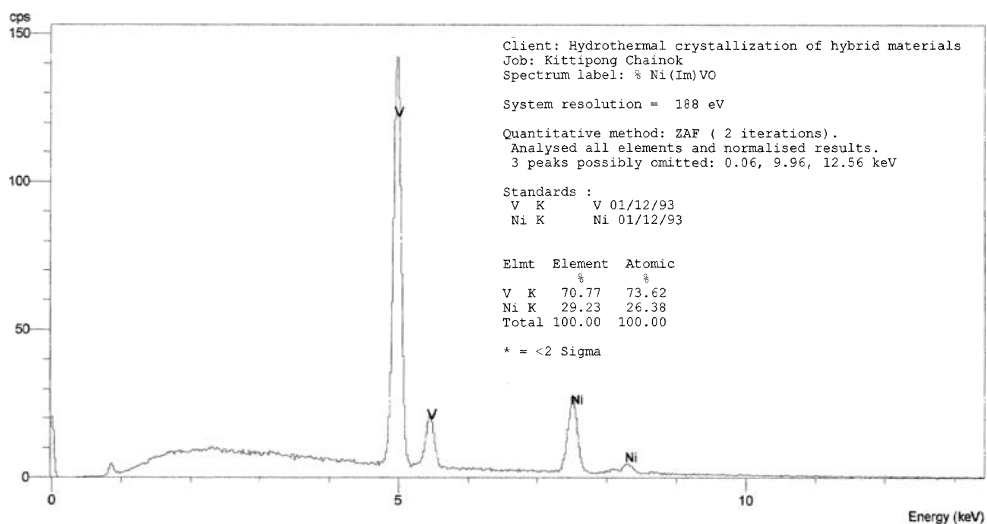


Figure B7.6 The EDX spectrum for 7d.

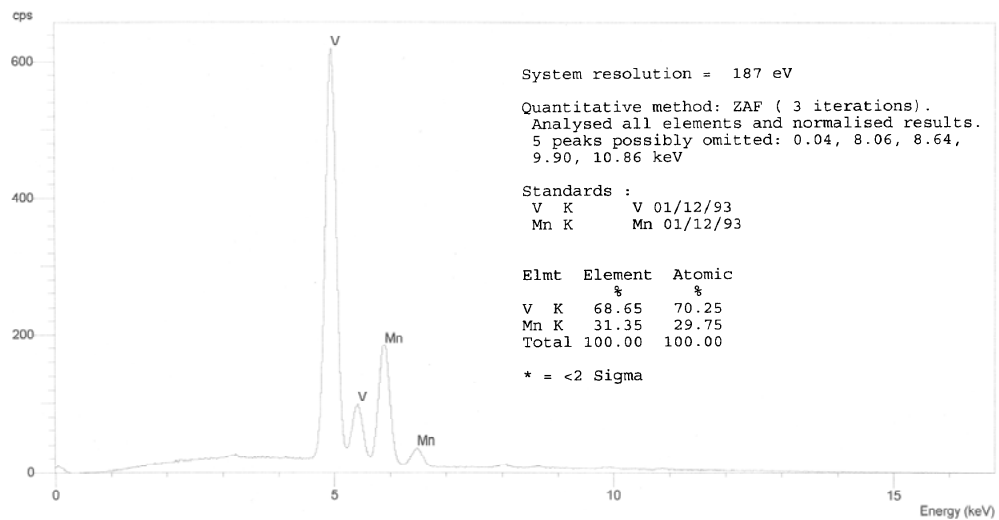


Figure B7.7 The EDX spectrum for **7e**.

APPENDIX C

SUBMITTED ABSTRACTS AND PRESENTATIONS

2009

1. Haller, K. J., **Chainok, K.**, Rae, A. D., Willis, A. C., Williams, I. D. Structure and Phase Transitions of the Polymeric Organic-Inorganic Hybrids: $M(\text{imidazole})_4\text{V}_2\text{O}_6$, $M = \text{Mn, Co, Ni}$. The 2009 Annual American Crystallographic Association Meeting. 25-30 July 2009, Sheraton City Centre Hotel, Toronto, Ontario, Canada.
2. **Chainok, K.**, Haller, K. J., Batten, S. R., Murray, K. S. Ferromagnetic Coupling in $\text{Fe}^{\text{II}}-\text{Mn}^{\text{II}}$ Cyanide-Bridged Bimetallic Coordination Polymer with 1-D Nanotube-like and 2-D Corrugated Sheet Structures. *Pure and Applied Chemistry International Conference (PACCON 2009)*. 14-16 January 2009, Naresuan University, Phitsanulok, Thailand.

2008

3. **Chainok, K.**, Batten, S. R., Murray, K. S., Haller, K. J. Spin-Crossover Studies on 3-D Framework Fe(II) Organonitrile Compounds. *The 34th Congress on Science and Technology of Thailand*. 31 October - 2 November 2008, Queen Sirikit National Convention Center, Bangkok, Thailand.
4. **Chainok, K.**, Rae, A. D., Willis, A. C., Williams, I. D., Haller, K. J. Investigation of Phase Transition of Hybrid Inorganic-Organic Metal Vanadate. *XXI Congress of the International Union of Crystallography*. 23-31 August 2008, Osaka, Japan.

5. **Chainok, K.**, Neville, S. M., Moubaraki, B., Batten, S. R., Murray, K. S., Haller, K. J. Synthesis, Structures, and Magnetic Properties of 3-D Network Cyanide-Bridged Homometallic Ni^{II}–Ni^{II} Coordination Polymers. *SmartMat08 & IWOFM-2*. 22-25 April 2008, Chiang Mai, Thailand.

2007

6. **Chainok, K.**, Neville, S. M., Moubaraki, B., Batten, S. R., Murray, K. S., Haller, K. J. Antiferromagnetic Properties of Cyanide-Bridged Homometallic Coordination Polymers. *2007 Inorganic Symposium*. 14 December 2007, Monash University, Melbourne, Australia.
7. **Chainok, K.**, Haller, K. J., Williams, I. D., Rae, A. D. Structural Studies of Hybrid Inorganic–Organic Vanadate Frameworks. *The 6th National Symposium on Graduate Research*. 7-8 September 2007, Mahidol University, Salaya Campus, Thailand.
8. **Chainok, K.** Hybrid Inorganic–Organic Composites: Synthesis, Crystal Structures, and Properties. *Invited Seminar in Chemistry*. 26 September 2007. Ramkhamhaeng University, Bangkok, Thailand.
9. **Chainok, K.**, Haller, K. J., Neville, S. M., Moubaraki, B., Batten, S. R., Cashion, J. D., Murray, K. S. Crystal Structure and Magnetic Properties of Cyanide-Bridged Bimetallic Coordination Polymers. *SCANZ 2007 Conference - Crystal XXV*. 10-13 April 2007. Hunter Valley, New South Wales, Australia.

2006

10. **Chainok, K.**, Neville, S. M., Moubaraki, B., Batten, S. R., Murray, K. S., Haller, K. J. Ferromagnetic Coupling in a Fe^{II}–Mn^{II} Cyanide Sheet Structure. *2006 Inorganic Symposium*. 8 December 2006, RMIT University, Melbourne, Australia

11. **Chainok, K.**, Haller, K. J., Williams, I. D. Hydrothermal Synthesis and Structural Studies of Organically Modified Metal Vanadate Framework. *2006 Inorganic Symposium*. 8 December 2006, RMIT University, Melbourne, Australia.
12. Krachodnok, S., **Chainok, K.**, Haller, K. J., Sung, H. H-Y., Shek, F. L-Y., Williams, I. D. Synthesis and Structures of Organically Modified Zinc Vanadates. *Joint Conference of the Asian Crystallographic Association and the Crystallographic Society of Japan, AsCA06/CrSJ, Meeting*. 20-23 November 2006, EPOCHAL conference venue, Tsukuba, Japan.
13. Pimdee, W., **Chainok, K.**, Haller, K. J. Hydro/Solvothermal Synthesis and Structural Characterization of Two New 2D Layered Manganese Vanadates. *The 32nd Congress on Science and Technology of Thailand*. 10-12 October 2006, Queen Sirikit National Convention Center, Bangkok, Thailand.
14. **Chainok, K.**, Haller, K. J., Sung, H. H-Y., Williams, I. D. Organically Modified Manganese Vanadates Solid Frameworks. *2006 ICMR Summer School on Porous Materials*. 30 July - 12 August 2006, University of California, Santa Barbara, USA.
15. **Chainok, K.**, Haller, K. J., Sung, H. H-Y., Williams, I. D. Synthesis and Characterization of Novel 2D Organic-Inorganic Hybrid Cobalt and Nickel Vanadates. *The 2006 Annual American Crystallographic Association*. 22-27 July 2006, Honolulu, Hawaii, USA.

2005

16. **Chainok, K.**, Haller, K. J. Organic-Inorganic Hybrid Supramolecular Materials: Synthesis and Characterization of Layer Structure Metal Vanadate Compounds. *The 31st Congress on Science and Technology of Thailand*. 19-21 October 2005,

Suranaree University of Technology, Nakhon Ratchasima, Thailand.

17. Srisopba, S., **Chainok, K.**, Haller, K. J. Hydrothermal Synthesis and Structural Characterization of An Organic-Inorganic Hybrid Vanadium Oxide Materials. *The 31th Congress on Science and Technology of Thailand*. 19-21 October 2005, Suranaree University of Technology, Nakhon Ratchasima, Thailand.
18. **Chainok, K.**, Haller, K. J., Sung, H. H-Y., Williams, I. D. Noncovalent Interactions in a Three Component Supramolecular Structure. *XX Congress of the International Union of Crystallography*. 23-31 August 2005, Florence, Italy.
19. **Chainok, K.**, Haller, K. J. Synthesis and Characterization of Organic-Inorganic Hybrid Cobalt Vanadates: $[\text{Co}_2(\text{Im})_8\text{V}_4\text{O}_{12}]$, Im = imidazole. *Seminar on Nano Material Fabrication Technologies*. 28-29 July 2005, Lotus Pang Suan Keaw, Chaing Mai, Thailand.

2004

20. **Chainok, K.**, Haller, K. J. Sung, H. H-Y., Williams, I. D. Supramolecular Structure of $[(\text{ImH})^+]^2[\text{Co}(\text{H}_2\text{O})_6]^{2+}[\text{Co}(\text{TMA})_2(\text{H}_2\text{O})_4]^{4-}$. *The 30th Congress on Science and Technology of Thailand*. 19-21 October 2004, Impact Exhibition and Convention Center, Muang Thong Thani, Bangkok, Thailand.
21. **Chainok, K.**, Haller, K. J. Supramolecular Interactions in $[\text{Co}(\text{picoline})_3]\cdot\text{H}_2\text{O}$. *The 4th National Symposium on Graduate Research*. 10-11 August 2004, Lotus Pang Suan Keaw, Chaing Mai, Thailand.
22. **Chainok, K.**, Haller, K. J. Hydrothermal Synthesis, Characterization, and Supramolecular Structure of $[\text{Co}(\text{C}_6\text{H}_4\text{O}_2\text{N})_3]\cdot\text{H}_2\text{O}$. *The 6th Conference of the Asian Crystallographic Association, AsCA'04*. 27-30 June 2004, Hong Kong University of Science and Technology, Hong Kong.

2003

23. **Chainok, K.**, Krachodnok, S., Haller, K. J. Hydrothermal Synthesis and Characterization of $(\text{NH}_3\text{CH}_2\text{CH}_2\text{CH}_2\text{NH}_3)^{2+}[(\text{VO})_2(\text{VO}_4)_2]^{2-}$. *The 29th Congress on Science and Technology of Thailand*. 20-22 October 2003, Golden Jubilee Convention Hall, Khon Kean University, Thailand.
24. **Chainok, K.**, Haller, K. J. Hydrothermal Synthesis and Characterization of a Micro porous Cobalt Vanadium Oxide Framework Compound. *The 10th Tri-University International Joint Seminar & Symposium*. 18-21 October 2003, Mie University, Japan.

2002

25. **Chainok, K.**, Haller, K. J., Williams, I. D. Structure of the Missing $[\text{Cu}_2(\text{terephthalate})_4]$ "Paddle-Wheel" Coordination Polymer. *The 28th Congress on Science and Technology of Thailand*. 24-26 October 2002, Queen Sirikit National Convention Center, Bangkok, Thailand.
26. **Chainok, K.**, Haller, K. J. Molecular Structure of 2-Hydroxy-N-(2-Aminosallylidene)Aniline. *The 3rd National Symposium on Graduate Research*. 18-19 August 2002, Suranaree University of Technology, Nakhon Ratchasima, Thailand.

2001

27. Kunapongkitti, S., **Chainok, K.**, Haller, K. J. Synthesis and Characterization of Four-Coordinate Nickel Nitrosyl Bis-Triphenyl Phosphine Halide Complexes. *The 27th Congress on Science and Technology of Thailand*. 16-18 October 2001, Hadyai, Songkla, Thailand.

CURRICULUM VITAE

KITTIPONG CHAINOK

BORN: May 26, 1977, Nakhon Ratchasima, Thailand

EDUCATION

Sep 2004 – Dec 2008 Ph.D. in Chemistry, Suranaree University of Technology
Jul 2001 – Aug 2004 M.Sc. in Chemistry, Suranaree University of Technology
Jul 1996 – Sep 2000 B.Sc. in Chemistry, Ramkhamhaeng University

PROFESSIONAL EXPERIENCE

Oct 2007 – Jul 2008 Visiting Scholar, Monash University
Apr 2007 – Aug 2008 Visiting Scholar, ANU
Sep 2006 – Mar 2007 Visiting Scholar, Monash University
Jul – Aug 2006 Summer School on Porous Materials, UCSB
May – Jun 2006 Visiting Research, HKUST

SCHOLARSHIPS, HONORS, AND AWARDS

2009 PACCON Outstanding Oral Presentation Award; 2008, 2005, 2004 IUCr Young Scientist Travel Grant; 2007 Endeavour Research Fellowship; 2006 ICMR Summer School Grant; 2006 Endeavour Asia Award; 2006 SUT Outstanding Research Award; 2004 IUCr Outstanding Presentation Award; 2003 SUT & Mie Univ. Travel Grant; 2002 SUT Research Grant for Master Degree Study

PROFESSIONAL AFFILIATIONS AND ACTIVITIES

Member of the Chemistry Society of Thailand, Member of the American Crystallographic Association (ACA), Member of the Society of Crystallographers in Australia and New Zealand (SCANZ), Captain of SUT Football Team (2003-2004)